Transactions of the ASME®

FLUIDS ENGINEERING DIVISION
Technical Editor
DEMETRI P. TELIONIS (1999)
Assistant to the Editor
J. E. POWELL
Executive Secretary
PAT WHITE (1999)
Calendar Editor
M. F. ACKERSON

Associate Technical Editors
R. E. A. ARNDT (1995)
P. R. BANDYOPADHYAY (1997)
M. GHARIB (1995)
A. F. GHONIEM (1995)
F. GIRALT (1997)
H. HASHIMOTO (1996)
J. A. C. HUMPHREY (1997)
O. C. JONES (1995)
G. E. KARNIADAKIS (1995)
J. H. KIM (1996)
R. W. METCALFE (1995)
L. NELIK (1995)
W.-F. NG (1995)
M. W. REEKS (1996)
W. S. SARIC (1995)
M. M. SINDIR (1997)
D. E. STOCK (1996)
S. P. VANKA (1996)

BOARD ON COMMUNICATIONS
Chairman and Vice-President
R. MATES

Members-at-Large
T. BARLOW, N. H. CHAO, A. ERDMAN, G. JOHNSON, L. KEER, E. M. PATTON, S. PATULSKI, S. ROHDE, R. SHAH, F. WHITE, J. WHITEHEAD, K. T. YANG

OFFICERS OF THE ASME
President, **D. T. KOENIG**
Exec. Director
D. L. BELDEN
Treasurer
R. A. BENNETT

PUBLISHING STAFF
Managing Director, Engineering
CHARLES W. BEARDSLEY
Director, Technical Publishing
JANET M. WEINRIB
Managing Editor, Technical Publishing
CYNTHIA B. CLARK
Managing Editor, Transactions
CORNELIA MONAHAN
Production Assistant
MARISOL ANDINO

Transactions of the ASME, Journal of Fluids Engineering (ISSN 0098-2202) is published quarterly (Mar., June, Sept., Dec.) for $175.00 per year by The American Society of Mechanical Engineers, 345 East 47th Street, New York, NY 10017. Second class postage paid at New York, NY and additional mailing offices. POSTMASTER: Send address changes to Transactions of the ASME, Journal of Fluids Engineering, c/o THE AMERICAN SOCIETY OF MECHANICAL ENGINEERS, 22 Law Drive, Box 2300, Fairfield, NJ 07007-2300.
CHANGES OF ADDRESS must be received at Society headquarters seven weeks before they are to be effective. Please send old label and new address.
PRICES: To members, $40.00, annually: to nonmembers, $175.00. Add $30.00 for postage to countries outside the United States and Canada.
STATEMENT from By-Laws. The Society shall not be responsible for statements or opinions advanced in papers or . . . printed in its publications (B7.1, Par. 3).

INDEXED by Applied Mechanics Reviews and Engineering Information, Inc. Canadian Goods & Services Tax Registration #126148048.

Journal of Fluids Engineering

Published Quarterly by The American Society of Mechanical Engineers

VOLUME 117 • NUMBER 3 • SEPTEMBER 1995

(Contents continued on p. 330)

(Contents continued)

Technical Briefs

Announcements and Special Notices

Journal of Fluids Engineering

Editorial

Electronic publishing is here. It is here, at ASME and the *Journal of Fluids Engineering*. This Journal has made available to its readers the JFE Data Bank as early as December 1992 and last year expanded modestly its electronic services (see editorial of September 1994). We now use the electronic medium to make available color frames or video as well as text or appendices that do not fit in the printed space. Soon, the ASME Transactions will be available on CD-ROM. ASME has also launched a broader electronic information network through its ASMENET. Information on this service is available through Sara Stephens (stephens@asme.org).

What does all this mean for our readership? A new level of convenience will definitely be available. One will be able to recall earlier journal issues more easily, without bringing down and leafing through heavy volumes. More importantly, the published material will constitute a data base. A user will be able to carry out a search with key words, with authors' names, etc. But the mode of our operation may also change. The professional publishers behind this move correctly foresee some of the changes that will inevitably ensue. For example, they argue that the established pattern of "publish and distribute" will be reversed. Our papers will be first distributed electronically and then published. Yet in a way, this has been the practice already, at least in scientific publications. Most of us distribute early versions of our work to selected colleagues in the form of engineering reports or dissertations or conference papers. Our contributions are available in some form or another, years before they appear in archival journals. But the electronic medium will bring about changes that may eventually upset our established patterns of operation entirely, the ultimate and most frightening to our generation being the total elimination of paper, i.e., the traditional printing and binding.

Skeptics may wonder whether such ideas are premature and somewhat farfetched. But I believe that the availability of the electronic medium will lead naturally and effortlessly to significant changes in our mode of operation within no more than a year or two. This is essentially due to the fact that suddenly, we will have practically no limitation in space. The availability of electronic space could not come at a more appropriate time. In recent years, most scientific publications and the JFE in particular, have been under great pressure to limit their expansion in pages, while the number of submitted papers and the backlog of accepted papers was growing monotonically. We are already allowing the material of some papers to spill over to the electronic medium. The reader should not think that we intend to publish more papers and inevitably reduce the quality of contributions to JFE. The aim is to provide more space to high-quality contributions.

In its recent meeting at the Summer FED Conference, the JFE Editorial Board decided to formalize this process. The number of pages allotted to each article will be controlled more carefully. Authors may be asked to reduce the size of their papers as much as possible, aiming at six or even less pages for the printed version. However, a longer version will also be accepted to appear only electronically. The editors are willing to review the longer version, making suggestions on how an article can be reduced to its shorter printed form. There will be some limitation on the text of the longer version of the paper as well, but the number of figures and the volume of digital data will be virtually unlimited. Lengthy derivations or computer program listings could also appear in the form of appendices.

At first sight, this mode of operation may appear contributing to the proliferation of published material but actually, the opposite will be true. The availability of the electronic version of contributions will allow the editors to insist that the short version of a paper, namely the printed version be more concise and focused. In fact, the unique opportunity is now available to insist that space be devoted to define clearly the specific contributions of each article to the permanent literature but also its usefulness and its possible applications to fluids engineering. Some may fear that this procedure will require extra work on the part of authors and editors since each contribution will require two papers. But a ten- or twelve-page paper will be easily shortened to six, if entire nonessential sections, like the description of experimental facilities, the derivation of equations, details of numerical schemes, or discussion of experimental uncertainty or numerical accuracy are replaced by a five-line description. We should not forget that all this information will only be a few keyboard strokes away.

Let us expand upon the more exciting possibilities, and more drastic changes, some of which may happen naturally while others could require bold action on the part of authors and editors. Here for example is another established process which may be reversed. We can go from "review and publish" to "publish and review." This could work as follows: Papers are automatically published electronically, as soon as they are submitted. This could be a special section of the electronic medium which will be reserved for articles under consideration. These articles are immediately open for electronic peer review by anyone who wants to offer criticism. Simultaneously, an editor invites specific reviewers to provide criticism and these reviews can be either added to the open bulletin-board type of publication or can be communicated directly to the editor. In response to all comments; and following the advice of the editor, authors revise their paper. The editor then, if satisfied, places the paper at another level or another category in the electronic file and the process is repeated until a paper receives the endorsement of the editorial board and is placed in the final electronic journal and in its shorter form is printed on paper. One of the innovations that this process entails is that it will avail to the readership comments and criticism, on a paper under consideration. We can see both advantages and disadvantages for such an approach and these deserve more thought and debate.

There is another established pattern of operation which most of us never question. Once a paper appears in an archival journal, it cannot be changed simply because it is impossible to change something that already appeared in print. Many would argue that this is the way it should be. Contributions should be

cast in concrete for posterity. They probably feel that this is a basic element of the archiving process. Well, now we may actually question this mode of operation as well. What is really wrong with an alive paper? A paper that authors can continue expanding and improving as long as they like, while all its editions are dated and are electronically available. Today, many of us find ourselves fragmenting the publication of our work into many short papers because we want to show progress to our sponsors, and some of us would need to beef up résumés. It would make much more sense if all new data and all new ideas can be incorporated on the same paper where they belong. I believe that this mode of operation should improve the quality of publications and reduce drastically the actual number of papers. Editors should be able to recognize for example, that new submitted material is a corollary or an addendum to a recent publication and instruct the authors to improve their earlier paper by adding this new material to it. The repetition of a lengthy introduction, derivations and so much material that is necessary to make a paper stand alone will thus be eliminated. We can then naturally go back to the normal mode of publishing one paper for a three- to four-year project instead of spreading the material to five or six papers in different journals. Promotion and tenure committees may have to reconsider their criteria but this will be their problem. There are minor nuisances we may have to eliminate. For example, we wouldn't be able to refer to an article by the year, volume, and month but, today, I am sure that this could be worked out very easily.

There may be many more ideas, and the JFE Editorial board would like to have the input of the readership. You could do this electronically of course, simply by offering a comment to this editorial. For directions, please refer to the box "Access to the Electronic JFE" at the end of any issue. In this issue, it appears on page 544.

The Editor

Measuring Unsteady Velocity Profiles and Integral Parameters Using Digital Image Processing of Hydrogen Bubble Timelines

S. D. Bruneau[1]
Research Assistant.

W. R. Pauley
Assistant Professor.
Mem. ASME

Department of Aerospace Engineering,
The Pennsylvania State University,
University Park, PA 16802

To aid in the investigation of artificially generated turbulent spots a technique was developed to make instantaneous measurements of full velocity profiles in an unsteady water boundary layer. These profiles were used to document the unsteady behavior of scalar descriptors such as the displacement thickness. The classical hydrogen bubble flow visualization technique was augmented to yield quantitative information by incorporating digital image processing of videotaped boundary layer flow. Digital images were converted into velocity fields using a corrected time-of-flight technique. The capability and limitations of this method in both steady and unsteady flows have been verified using an analytical uncertainty analysis and through comparison with laser-Doppler anemometry measurements. Recommendations are made for effective use of this technique.

1 Introduction

There are several techniques suitable for making instantaneous single-point velocity measurements in a boundary layer. The most common are hot wire anemometry and laser Doppler anemometry. To obtain descriptions of unsteady velocity profiles with these traditional techniques the measurement system must be translated to each location in the velocity profile. Multiple realizations of an unsteady event can be measured and an ensemble-averaged or phase-averaged description of the unsteady boundary-layer event can be recorded. Alternatively, instantaneous full velocity profiles can be obtained using a "rake" comprised of multiple hot wires. Unfortunately, rakes or groups of hot wires can cause significant flow disturbances and are complex to calibrate due to the requirement that each probe have its own electrical bridge and calibration coefficients.

To overcome the limitations imposed by single point measurement techniques several full-field measurement schemes which use particle imaging or flow marking have been developed. Many of these techniques are capable of delivering instantaneous fields of scalar and vector quantities. Adrian (1991) presented a detailed review of many of these techniques which include tomographic interferometry, planar laser-induced fluorescence, nuclear-magnetic-resonance imaging, laser-speckle velocimetry, particle-tracking velocimetry, and particle imaging velocimetry. The possibilities they offer are extensive. The main drawback with most of them for use in investigating unsteady flow fields is the need for highly-resolved images obtained at a rapid rate. Thus far this has required the use of photographic film, although highly resolved video array detectors are now being investigated that promise to remove this limitation.

The objective of the present research was to obtain unsteady boundary layer profiles using automated processing of hydrogen bubble timelines produced by the electrolysis of water at a wire placed normal to a test surface. Records of the hydrogen bubble lines yield the instantaneous description of the unsteady profile, $u(y, t)$. The emphasis was on accurately and rapidly obtaining unsteady integral desriptors of the boundary layer such as the unsteady displacement and momentum thicknesses. These boundary layer descriptors can be tied to the acoustic excitation due to the unsteady velocity field of the boundary layer undergoing transition to turbulence (Krane and Pauley, 1995). The large quantity of information and unsteady nature of the flow made the use of traditional photographic techniques impractical. Although observation of hydrogen bubble timelines has been used extensively in the past along with traditional photography, the focus of this effort was to develop automated digital image processing to convert the video pictures to useful velocity information. To confirm their validity the measurements were compared with measurements made using a laser Doppler anemometer.

2 Test Flow: An Artificially Generated Turbulent Spot

The driving motivation for developing the present velocity measurement technique was the need to characterize the far-field effects of the unsteady development of turbulent spots. In the past, researchers have used fast response probes to study artificially initiated turbulent spots, among them Schubauer and Klebanoff (1955) and Wygnanski et al. (1982) who have documented the general shape and characteristics of turbulent spots. Much is known about turbulent spots. For example, features such as the spread angle and the propagation velocity have been determined (Fig. 1). Immediately following the spot is a "calmed region" characterized by a "full" velocity profile which is more stable than the surrounding laminar flow or Blasius profile. The mean velocity profiles in the interior of the spot are similar to a turbulent boundary layer. Scalar descriptors such as the displacement thickness and momentum thickness change rapidly within the spot. The maximum height of the spot is approximately equal to the thickness of a hypothetical turbulent boundary layer which originates at the streamwise location where the spot is triggered, and the height of the leading interface's overhang corresponds roughly to the thickness of the laminar boundary layer (Riley and Gad-el-Hak, 1985).

There is evidence, mainly from flow visualization, that there exist several structures, possibly hairpinlike vortices, within a single spot. It has been observed that the number of structures increases as the spot convects downstream (Sankaran et al.,

[1] Presently Research Engineer, Marotta Scientific Controls, Montville, NJ 07045.

Contributed by the Fluids Engineering Division for publication in the JOURNAL OF FLUIDS ENGINEERING. Manuscript received by the Fluids Engineering Division June 17, 1993; revised manuscript received April 25, 1995. Associate Technical Editor: W. S. Saric.

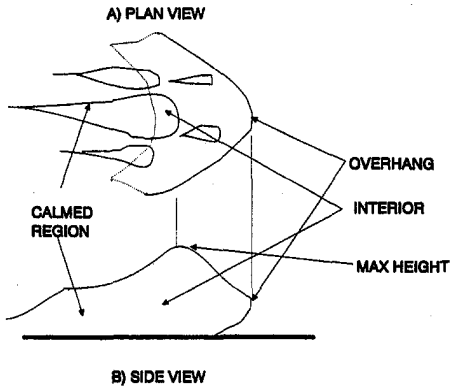

Fig. 1 The turbulent spot characteristics: (*a*) in plan view and (*b*) in side view

1991a, b). When the averaging is conditioned on either the trailing or leading edges of the spot, details associated with the internal structures are smeared. Ensemble averaging smears out all but the largest scales. Ensemble-averaged data lends itself well to obtaining the scalar descriptors of turbulent spots such as the arrival time, convection velocity, and unsteady displacement thickness. The goal of this investigation was to develop and verify the accuracy of the hydrogen bubble wire technique, augmented by digital image processing, as an efficient tool for measuring the large-scale characteristics of turbulent spots for use in predicting their far-field effects. Previous studies (i.e., Lauchle, 1991) have shown that the largest scales are dominant in determining the noise production.

3 Background of Hydrogen Bubble Technique

E. W. Geller (1954) is recognized as the originator of hydrogen bubble flow visualization. He observed the evolution of gases as he tried to improve upon Wortmann's technique in his masters thesis. At the Douglas Aircraft Company D. W. Clutter and A. M. O. Smith (1961) developed the technique which uses the bubbles produced by electrolysis at a wire as a flow marker. A fine wire mounted perpendicular to the flow serves as the cathode, or negative electrode, in a DC circuit, and another element of a material such as brass or graphite serves as the anode. The production of hydrogen occurs on the wire when it is excited by an electric pulse. If the polarity is reversed and the fine wire is excited as the anode, oxygen bubbles are produced. Exciting the wire as a cathode is preferable because hydrogen bubbles are approximately half as large as oxygen bubbles and serve as better flow tracers due to their smaller buoyancy force. By electrically pulsing the wire, hydrogen bubble "clouds" are formed which are swept from the wire by the flow. Milazzo (1963) showed that the passage of current occurs immediately after the voltage is applied. The resulting thin lines of bubbles deform to the shape of the local velocity profile $u(y, t)$. By pulsing the wire at a constant frequency, these bubble lines mark the flow at constant time intervals known as timelines.

Quantitative analysis of hydrogen bubble timelines was introduced by Schraub et al. (1965). They used the technique to measure time-dependent velocity fields in low-speed water flows. Since Schraub et al. several others have utilized the technique to make quantitative measurements. Davis and Fox (1967) used hydrogen bubble wires in clear tubes and Kim et al. (1971) applied them in turbulent boundary layers. Lu and Smith (1985) reviewed the previous work done using manual processing of the images and extended the technique to employ automated digital image processing in obtaining turbulence statistics. Lu and Smith (1991) further employed their technique to investigate near-wall bursting characteristics. To derive velocity information from the timelines, video frames were analyzed. The local velocity was established using time-of-flight techniques. The local bubble-line velocity at each y location was approximated as

$$u_b(y, t) = \frac{\Delta x}{\Delta t}$$

where Δx is the horizontal displacement between any two bubble timelines and Δt is the period of time between wire pulses. Applying this method to bubble trajectories at several heights, instantaneous velocity profiles were obtained.

Schraub et al. (1965) outlined several possible contributors to uncertainty in the measurements. The present study encountered many of the same sources and some additional ones due to the incorporation of automated digital image processing. The terms which yield a large uncertainty interval, and hence are the dominant contributors to the total uncertainty in the velocity, were singled out. To obtain the overall error in an instantaneous measurement, the error associated with both Δx and Δt must be identified and taken into account. The errors associated with Δt and the scaling factors associated with Δx are negligible compared with the errors in Δx itself. Schraub et al. found that the potential error in the displacement scaling factor and framing speed contributed less than one fifth of the total uncertainty in the Δx term. The total uncertainty in Δx is comprised of the following factors:

1 Measuring Δx on film.
2 Averaging effects in changing velocity field.
3 Possible displacement of the bubble due to secondary velocities (v and w).
4 Response of the bubbles to fluctuations.
5 Resolution problems due to finite bubble size and due to finite averaging intervals.
6 Bubble rise due to buoyancy.
7 Velocity defect behind the bubble generating wire.

Schraub et al. used manual techniques for measuring Δx. They noted that errors exist as a result of human error, friction in their film reader, optical distortions, and film-image resolution. An Eulerian velocity field at a point in time and space, u_b

Nomenclature

a = radius of a bubble
C = constant in wake correction (1.7)
d = diameter of hydrogen bubble wire
g = acceleration of gravity
H = boundary layer shape factor, δ^*/Θ
t = time
u, v, w = components of mean velocity
U = freestream velocity
u_b = velocity of a bubble
V_b = volume of a bubble
x, y, z = Cartesian coordinate system
Δx = spacing between bubble lines
Δt = time between bubble lines
δ^* = boundary layer displacement thickness, $\int_0^\infty [1 - (u/U)]dy$
δ_{99} = location where $u = 0.99U$ (boundary layer thickness)
ν_f = kinematic viscosity of water
ρ_f = density of water
ρ_g = density of bubble
Θ = boundary layer momentum thickness, $\int_0^\infty (u/U)[1 - (u/U)]dy$

$= u_b(x, y, t)$, is calculated using the Lagrangian time-averaged velocity of marker bubbles over a small time interval. Averaging uncertainties arise from the use of a marker method where the Eulerian velocity in the flow field at a point in space and time $u(x, y, z, t)$ is predicted by calculating the Lagrangian time-averaged velocity of marker bubbles over a small spatial interval. Lu and Smith (1985) assumed that the Eulerian velocity was equal to the Lagrangian timeline velocity because of the limited transit distance between bubble timelines and the relatively short averaging time. Their results substantiated this assumption.

Bubble displacement due to secondary velocities (v and w) is dependent upon the flow characteristics. Large bubble displacements may introduce errors into the estimates of Δx and thus u. The hydrogen bubble method assumes that the observed streamwise distance between bubble lines results from the true x-direction component of velocity. Lu and Smith (1991) used the hydrogen bubble wire technique to study the near-wall bursting in a turbulent boundary layer. It might be argued that the bursting process is related to (or at least similar in many ways to) the formation of turbulent spots and therefore would be expected to generate similar levels of three-dimensionality. Lu and Smith (1985) have shown that for small differential distances between bubble lines, the much smaller magnitudes of the v and w velocity components relative to u have a small influence on bubble line deformation. Through comparison with accepted boundary layer statistics they showed that the hydrogen bubble wire technique produces similar results to single hot wires at a given measurement location in a turbulent boundary layer. Compared to the LDA, both single hot wires and the hydrogen bubble technique exhibit some error due to secondary velocities. The present data are, therefore, comparable to that which can be obtained with a rake of many closely-spaced single hot wires.

Uncertainties in Δx arise because the bubbles do not respond instantaneously to changes in the fluid velocity surrounding it. According to Davis and Fox (1967) a bubble leaving the wire takes 0.1 ms to attain a velocity of 98 percent of the fluid velocity. It is a good approximation, therefore, to neglect this error source. To correct for the wake effects of the wire, Lu and Smith (1985) utilized an equation for wake defect given by Abernathy et al. (1977),

$$\frac{(u - u_b)}{u} = C\left(\frac{x}{d}\right)^{-1/2}$$

where u is the true fluid velocity, u_b is the measured bubble velocity, x is the distance of the bubble from the generating wire, d is the wire diameter, and C is a coefficient which depends on both the local Reynolds number and the wire drag coefficient. Lu and Smith (1991) found $C = 1.7$ to yield a reasonable fit of the data from their water channel facility for a wire diameter Reynolds number of 3.6. Our Reynolds number, which ranged from 6.7 to 9.9, is of similar magnitude so we adopted their value for this coefficient. They note that this corrected velocity is not a true instantaneous velocity due to use of the Taylor hypothesis which assumes that the corrected Lagrangian timeline velocity reflects the local Eulerian velocity. They further state, however, that the limited transit distance and short averaging time results in close agreement with accepted hot-wire probe data for turbulence statistics, evidence which supports the validity of using this hypothesis.

The choice of electrode size, material, and location contributes to the success of the hydrogen bubble technique. Matsui et al. (1977) studied the effects of electrode material and electrode size to determine the effects on the production of hydrogen. They experimented with two wires, a 30 μm diameter platinum and a 10 μm tungsten wire. On the 30 μm wire, extremely small, densely spaced bubbles were generated at the surface. Neighboring bubbles combined into larger ones, and in the course of time the number of bubbles decreased. Their sizes were not uniform, being 0.5 to 1.5 times the diameter of the wire. The 10 μm wire was quite different; bubbles generated near the wire were evenly distributed and did not coalesce. They noted that the bubble size remained fairly uniform and concluded that in a low speed flow a sufficiently thin generating wire is superior for generating the smallest bubbles. In addition, these bubbles are least affected by buoyancy. Matsui et al. (1977) obtained the best results using tungsten wire. Lu and Smith (1991) obtained good results using a 20 μm diameter platinum wire.

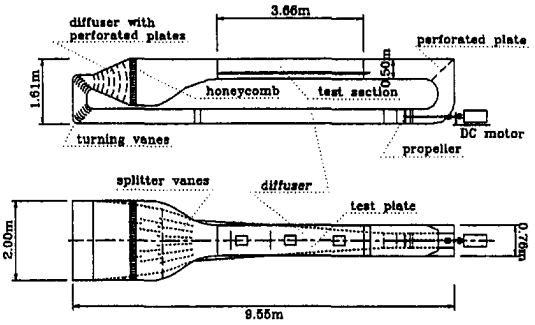

Fig. 2 Aerospace engineering laminar flow water channel

Schraub et al. (1965) noted that the material used to make bubble generation wires is not critical except with respect to corrosion and fragility. Stainless steel wires are usually strongest and easiest to handle. Platinum is usually preferred because it does not corrode, and it appears to accumulate dirt less rapidly. Due to experimental considerations, the material chosen for the present experiments was stainless steel wire because of its strength. Two wire sizes were tested to optimize performance, 50 μm and 25 μm. The 25 μm stainless-steel wire was not strong enough to handle the force of the oncoming flow and yielded regardless of tension. The 50 μm wire held its perpendicular position and produced bubbles which were sufficient to produce a sharp image in the video.

4 Facility: Open Surface Laminar Flow Water Channel

The tests were conducted in a closed-circuit, open surface laminar flow water channel. Details of the flow loop are shown in Fig. 2. Further details can be found in Krane and Pauley (1995). Turbulent spots were generated by an impulsive jet ejected from a small hole in the test plate. A 0.5 mm hole located 53 cm from the leading edge was fed by a peristaltic pump driven by a stepper motor under computer control. The pulse strength for the jet was determined using flow visualization with a fluorescene dye sheet on the test surface. The smallest jet capable of consistently triggering the spots was chosen.

LDA surveys revealed the quality of the baseline flow in the test section. Figure 3(a) shows good agreement between the centerline laminar boundary layer profile and the Blasius solution. The minimum physical spacing from the wall for the closest data point was 0.032 cm for this profile and for all LDA results reported in this paper. An upper bound on the turbulence intensity of the freestream flow was found to be 0.3 percent (the noise threshold of our LDA system). In addition, there were regions of wall contamination which spread at approximately 10° from the wall, limiting the area over which a laminar boundary layer existed on the test surface. The sidewall contamination limits the measurement of turbulent spots to the upstream 2 meters of the test plate. However, the freestream velocity was found to have very good streamwise and spanwise uniformity in this region. The ensemble averaged profiles reported

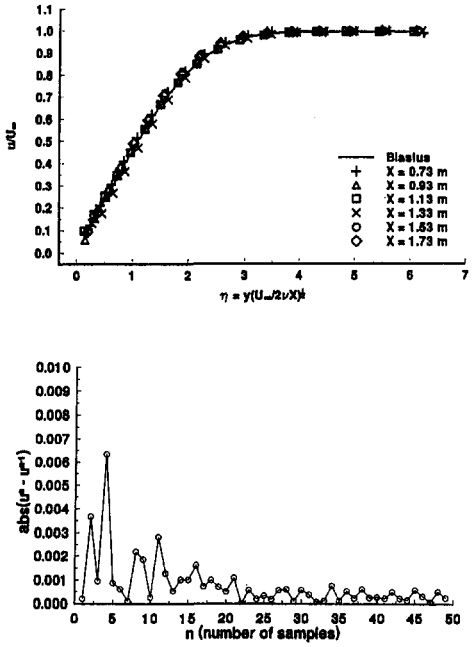

Fig. 3 (*a*) and (*b*) Qualification of the flow facility using LDA measurements: (*a*) velocity profiles cast in similarity coordinates at several *x*-locations compared to the Blasius solution and (*b*) convergence of the ensemble averaged velocity

in this paper were obtained using 30 realizations of the turbulent spots. Figure 3(*b*) shows the convergence of an ensemble averaged velocity in the flow for an increasing number of realizations. In this figure, the ordinate is the time average of the absolute value of the difference between the average of n samples and the average of $n - 1$ samples. Acceptable convergence is achieved after 30 realizations.

The hydrogen bubble wire is held normal to the test surface using a removable port plug mounted in the test plate which contains an electrically-insulated attachment. The wire is sealed at the test plate. The wire is held above the test section by a mount which provides the important capability to set and continually maintain a constant wire tension. The maintenance of constant tension is critically important since the wires quickly decay and stretch during use. In these experiments no sodium-based electrolytes were added to the water to enhance bubble production, a common practice, due to concerns about corrosion of the aluminum test fixtures which was a severe problem.

Lighting was provided from the side of the test section opposite the camera. Many orientations of the light source were tried. It was found that positioning the light at approximately 45 degrees off-axis in a forward scatter orientation, pointing downstream, provided the best lighting for the procedure. A 150-watt arc lamp was focused into a circular beam and a convex lens was used to concentrate the light on a small region of interest in the boundary layer. In addition, a second 150 watt floodlamp was oriented 45 deg off-axis pointing upstream, to fully illuminate the wall region. The lighting scheme that was used is shown in Fig. 4(*a*).

The technique employed to obtain hydrogen bubble lines was similar to that of Schraub et al. (1965) and Lu and Smith (1985, 1991). However, their electronics were replaced at the logic level by a computer-resident interface card and associated software. One important constraint that was placed on the system was to limit the voltage applied to the electrical circuit to 100 volts for safety reasons. It was generally observed that higher voltages are always better and therefore the voltage is limited by other considerations such as the maximum current that can be passed through a small wire without it burning up and by safety. For our chosen maximum voltage, the duration of the wire pulse signal was chosen to obtain the sharpest line of bubbles possible while generating a sufficient bubble density to produce an image which registered on the video camera. The ideal pulse duration fell in a range from 1 to 9 ms depending on flow velocity.

The video taping and bubble production must be in synchronous operation. A schematic of the system used is shown in Fig. 4(*b*). At each new video frame the bubble line must be at the same "growth" stage. In order to achieve this coordination the camera must trigger the bubble production (i.e., the video camera records an event which it triggers). The video camera, a SONY video 8 Handycam/pro, delivers an National Television Standards Committee (NTSC) composite video signal. The video signal from the camera is filtered by a bandpass filter to produce a trigger signal for use in initiating the wire pulse. The video signal from the camera triggers a MetraByte DAS-16 multifunction high speed analog/digital, input/output, expansion board installed in an IBM PC AT personal computer. The DAS-16 generates a 5-volt pulse which excites a solid state DC relay. The solid state relay energizes a 95-volt DC source to pulse the bubble wire. Finally, the bubbles due to the pulse are recorded by the video camera which had originally triggered the event and the "cycle" begins again. This cycle takes place at the camera's framing rate of 30 Hz. The shutter speed of the camera is $\frac{1}{1000}$ of a second which freezes the image.

5 Digital Image Processing Hardware

An image processing system made by Data Translation Inc. was used to convert videotape of hydrogen bubble images into digital arrays. The processing hardware included a DT2871 Color Frame Grabber, a DT2869 Video Decoder/Encoder, and a DT2858 Auxiliary Frame Processor board. All were operated by a Dell Corp. 386-based personal computer. The DT2871 Color Frame Grabber captures and displays images in real time. On this board an image is stored in three separate 512 × 512 × 8 bit buffers, one for hue, one for intensity, and one for saturation. The DT2869 then converts the NTSC composite

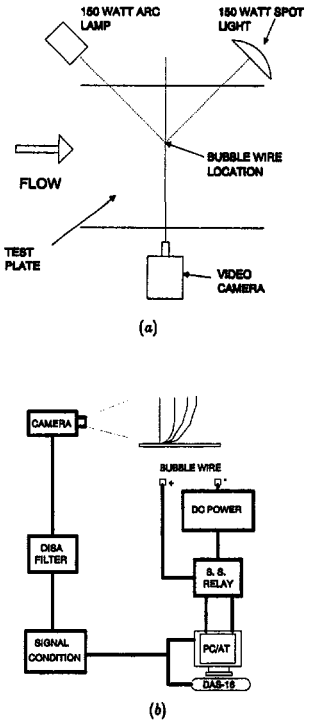

Fig. 4 (*a*) and (*b*) Configurations for hydrogen bubble wire technique (*a*) lighting scheme and (*b*) system definition

color video signal into an RS-170 RGB format. The DT2858 Auxiliary Frame Processor works in conjunction with the DT2871 to perform mathematically-intensive operations on individual frame buffers at high speeds, greatly accelerating execution time. Each image requires 1 Mbyte of memory.

For the hydrogen bubble technique to work, each frame must be analyzed individually. The Sony camera has a freeze frame and frame advance capability. Unfortunately, when such cameras freeze an image the synchronization information needed to convert the NTSC composite video into the RS-170 format is lost. The vertical and horizontal synchronization information contained in video signals is critical in forming a high quality image. When the sync pulses are missing, the image can exhibit problems such as skewness and jitter. To provided the expected signal format from the camera to the frame grabber an IDEN IVT-7 Time Base Corrector (TBC) was used. The TBC strips the incoming sync information from the video signal and replaces it with an RS-170 RGB sync signal in order to match the DT2871 requirements. The TBC also has a frame/field freeze feature to enhance the image by removing jitter and/or skewness and a quality image is captured and prepared for manipulation to obtain the desired flow description.

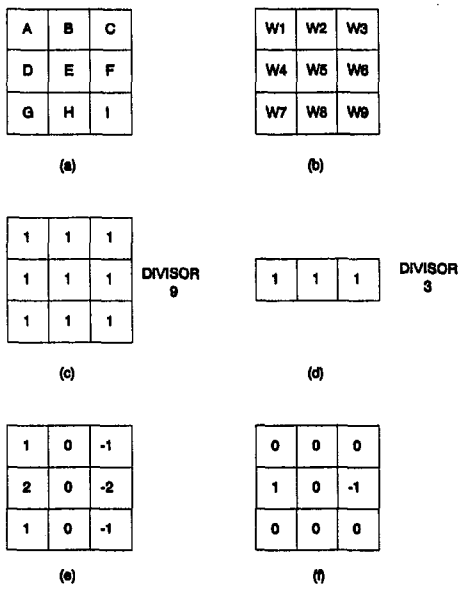

Fig. 5 (*a–f*) Coefficient masks for image processing

6 Image Processing Procedure

To obtain velocity profiles the locations of the edges of each timeline must be established and the corresponding distance between the timelines must be calculated. There are several techniques which may be used to detect the edges in an image. Vertical line enhancement is a technique often used to highlight lines that are one pixel wide. This technique is not effective for hydrogen bubble lines, however, because the bubble timelines are generally several pixels wide. Optimal thresholding is a technique which statistically analyzes a histogram of the intensity values in a region of interest. The problem with this technique is that non-uniformity in lighting the boundary layer region extending from the wall to the freestream leads to situations where noise in the freestream has a higher intensity than the timelines in the wall region; if a threshold is set for the wall region, the software responds to noise in the freestream, generating substantial error. The best results are obtained using a gradient/Laplacian method which utilizes the intensity distribution across a row of pixels at a single height above the wall. This process locates the edge of a bubble line by computing the maximum negative intensity gradient. This maximum occurs at the leading edge of the bright timeline on the dark background.

Coefficient or "convolution" masks (digital filters) were used to obtain weighted quantities and gradients. Each element in the pixel neighborhood, $A - I$ (Fig. 5(a)), was multiplied by its respective weighting coefficient, $W1 - W9$ (Fig. 5(b)). The result of this multiplication replaces the value at the center of the mask, $I_{i,j}$, i.e.:

$$I_{i,j} = W_1A + W_2B + W_3C + W_4D + W_5E + W_6F + W_7G + W_8H + W_9I$$

For example, a low pass filter mask operates simply by multiplying each neighbor by 1, adding them, and dividing by the number of neighbors (neighborhood averaging). Gradient masks of the Sobel operator type were used. The first derivative was obtained using the 3×3 Sobel operator shown in Fig. 5(e). It smooths noise and provides the gradient in the x direction. The Sobel operator is essentially a central difference method. The weighting of the Sobel operator increases the smoothing of the neighboring pixels making the derivative less sensitive to noise. Weighting the pixels closest to the center yields additional smoothing (Gonzalez and Wintz, 1987). The second derivative mask (Fig. 5(f)) is a simplified Sobel operator which is also a central difference scheme. Lowpass filters, or averages, were chosen over median filters because they smooth the intensity distribution while leaving the overall shape of the distribution unchanged. Median filters present the possibility of altering the overall shape of the distribution especially at the edge locations.

The intensity distribution across a row of pixels in an image has a sinusoidal shape (Fig. 6(a)). The high intensity represents a bright bubble-line and the low intensity represents a dark background. Each row of the intensity buffer was lowpass filtered using the mask in Fig. 5(d). The gradient across a row was taken using the mask in Fig. 5(e). Taking the derivative of the gradient, or the second derivative of intensity, yields the position where the maximum of the first derivative is located. This position is the leading edge of a timeline. Since noise components also yield gradients, the software might recognize these noise components as timeline edges. This problem is resolved by recognizing that the gradient at a timeline edge is much larger than the gradient of a noise component. The mean magnitude of the gradient across a row was calculated and each pixel tested against it. If the value was above the mean, it remained unchanged. If the value was below the mean, it was set to zero (Fig. 6(b)). This is known as threshold filtering. Manual inspection of several cases confirmed that the gradients due to noise fell beneath the mean value threshold. With this "cleaned" gradient distribution, another derivative was taken to yield the maximum values using the mask in Fig. 5(f).

In order to calculate the velocity profile, the first three bubble lines are considered. The most upstream bubble line in every frame is a cloud of bubbles still attached to the wire. The second is free of the wire but has not yet moved through a complete interval at the time of the exposure. The time interval between the bubble line still attached to the wire and the first bubble line downstream is unknown due to the complexity of the bubble formation and shedding process. The interval between the second and third timelines is a complete $\frac{1}{30}$ s, the framing rate of the camera, therefore, these lines are used to determine thevelocity. An additional incentive for using the second and third lines rather than trying to utilize the first line is that the error due to the wake of the wire is most pronounced just after the wire. The second and third lines are beyond the region strongly affected by the wire.

Images were sent individually to the frame grabber using the camera frame advance capability. Once the edge points were found by the software the edge pixels were assigned a value corresponding to black or white. Since there are discontinuities in this trace of the edges due to lighting irregularities, another

lowpass filtering was performed using the mask in Fig. 5(*c*), leaving a continuous profile. Measuring the distance between the second and third lines was achieved by counting the pixels between the two and applying the correct pixel scaling to obtain the true distance.

Velocity was measured using a time of bubble flight technique. The measured bubble velocity, u_b, was corrected for wire wake effects using the correction scheme described previously. This procedure yielded the instantaneous streamwise velocity, $u(y, t)$. In the region very close to the wall (0–4 mm) lighting nonuniformity was a problem and the processing software had difficulty interpreting the bubble timelines. Also in this region bubble buoyancy was a problem. Schraub et al. (1965) showed that bubble buoyancy effects are important when the ratio of the bubble rise velocity to the local flow velocity is below $\frac{1}{50}$. It was found that the $\frac{1}{50}$th velocity criteria is reached at approximately the height above the wall below which the lighting becomes too faint for the software to detect the timelines. The lighting and buoyancy problems were both eliminated by replacing the measured profile between the wall and the $\frac{1}{50}$th criteria point with a least-squares third-order polynomial fit (see further discussion below).

7 Results and Discussion

Falkner Skan Velocity Profile Test. To obtain an estimate of the accuracy possible using the image processing procedure with "perfect" bubble lines a known profile was plotted on paper, videotaped, and then processed using our procedure. This scheme isolated the uncertainty due to the digital image processing procedure from that due to irregularity in bubble generation or due to wire interference. This established the best possible performance using our camera and the magnitude of the error due to limitations in the resolution resulting from finite pixel spacing. A Falkner Skan similarity solution was used as a test case. The flow chosen was that for a flow against a wedge of half angle $\pi/2$. The comparison between the known solution and that predicted by the reduction scheme was quite good with an average error of 1.5 percent (Fig. 7). At distances from the wall greater than 0.1 cm, the error was less than ±1 percent. Below 0.1 cm the technique loses accuracy because several time lines mesh together, causing difficulty in distinguishing individual lines.

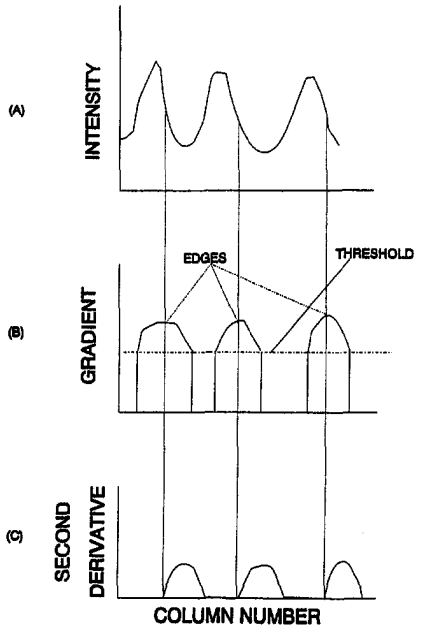

Fig. 6 (*a–c*) Edge detection scheme

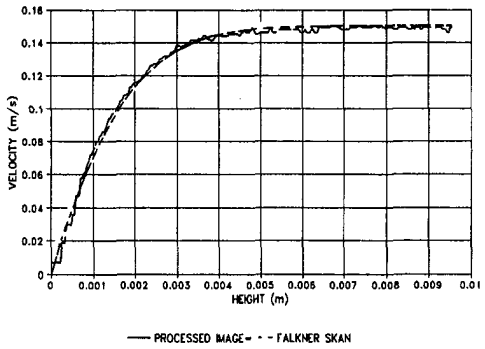

Fig. 7 Falkner skan actual and processed velocity profiles

The distance between two bubble lines in this test profile ranged from 110 pixels at the outer edge of the boundary layer down to zero pixels near the wall. Therefore, the penalty for not resolving the true edge of any timeline to a precision greater than one pixel is much larger when the region of interest is near the wall. In the actual experiments the camera field of view was dictated by the expected size of the unsteady turbulent spot. It was required that the camera field of view extend to approximately 4 cm above the plate to ensure that an entire turbulent spot could be captured in one picture. This requirement limited the option of magnifying the image to obtain a greater number of pixels between timelines. The magnification chosen yielded a y-scale of 0.012 cm/pixel and an x-scale of 0.016 cm/pixel. Pixel resolution between timelines in the actual images ranged from 32 pixels at 15 cm/s to 48 pixels at 22 cm/s in the freestream. This resolution leaves an error band of approximately 2–3 percent. If the scope of this study were only laminar profiles, the region of interest would have been about 2 cm high, and a near doubling of the resolution described above would be possible.

Analytical Uncertainty Analysis. In addition to the uncertainty in measuring Δx due to the limited number of pixels available, which was detailed in the previous section, an estimate was made of the potential uncertainty in tracking bubbles. Lu and Smith (1985) showed that the Eulerian field velocity equals the Lagrangian time-averaged velocity due to the short distance and averaging time. In addition, uncertainty due to limitations in the response of bubbles to fluctuations was shown by Davis and Fox (1967) to be negligible. The response of the bubbles to buoyancy, however, cannot be neglected. Schraub et al. (1965) suggested the use of a correction when the vertical rise velocity divided by the local mean velocity was above $\frac{1}{50}$. They also determined that the bubble diameter ranged from $\frac{1}{2}$ to 1 wire diameters. Based on one wire diameter of 50 μm, the terminal rise velocity for the present experiments was calculated at 0.0014 m/s. Therefore, when the mean velocity, $u(y, t)$, fell below 6.8 cm/s, a third order polynomial least-squares fit was employed to fit the profile down to the wall.

The choice of the third-order polynomial fit was based on the work of Lu and Smith (1991). They showed that the simplest minimum function which fits the time-dependent velocity behavior in the wall sublayer is a third-order polynomial. This function provides for a linear profile near the wall and instantaneous fluctuations in both the streamwise pressure gradient and its gradient normal to the wall. They determined that this fit gave good agreement with published data for the law-of-the-wall region in a low-Reynolds-number turbulent boundary layer. The three constants were determined using a best-fit curve through twelve points. The first point was located at the wall ($y = 0$). The second point was located where the bubble rise velocity was $\frac{1}{50}$th of the local flow velocity. The remaining ten points corresponded to the next 10 pixels above the $\frac{1}{50}$th criteria point. Using points stretching up into the profile provided for

a curve fit that matched the slope of the profile near the $\frac{1}{50}$th criteria point. Results for the laminar profiles show that the curve fit adequately corrected for the buoyancy effect near the wall.

To quantify the error associated with the trajectory of the bubbles due to buoyancy, averaging effects, and the response of bubbles to the flow dynamics, an analytical study was performed. The study involved tracking a line of bubbles in a known flowfield. It was assumed that the bubbles do not modify the flowfield. Twenty bubbles were tracked for a time interval of $\frac{1}{15}$ seconds. This produced a data set similar to that obtained from digitizing a photograph in an actual experiment. The time interval used to compute the velocity was $\frac{1}{30}$ seconds. From the analytical bubble field the indicated velocity was found using the horizontal distance between the two bubble lines. The resulting velocity profile was compared to the analytical velocity profile used to calculate the flowfield through which the bubbles had been propagating.

The analytical model of a bubble in an unsteady flow follows from the studies of Maxey and Riley (1983) and Hoffman (1988). The vector equation for the trajectory of a rigid, spherical bubble in an unsteady flow is as follows:

$$\rho_b V_b \frac{du_b}{dt} = V_b(\rho_b - \rho_f)g + \rho_f V_b \frac{Du}{Dt} + 6\pi\rho_f \nu_f a(u - u_b) + \frac{1}{2}\rho_f V_b\left(\frac{Du}{Dt} - \frac{du_b}{dt}\right)$$

(1) (2) (3) (4) (5)

where V_b is the bubble volume, u_b is the bubble velocity, ρ_b and ρ_f are the bubble and fluid density respectively, ν_f is the fluid viscosity, a is the bubble radius, and u is the given flowfield. The rate of change in the position of the bubble is used to predict the velocity of the bubble using the expression $u_b = dx_b/dt$. The significance of each term in the equation above is:

1 Mass of the particle times its acceleration.
2 Buoyancy term.
3 Force due to the pressure gradient in the fluid surrounding the bubble, caused by the acceleration of the fluid.
4 Viscous resistance of the spherical bubble.
5 Force required to accelerate the "added mass."

The assumptions are that the bubble is rigid and retains its shape. The bubble is also assumed to be a solid sphere which allows the use of the Stokes drag term. Since this part of the analysis is an estimate only, the above method is suitable to establish a best-case accuracy estimate for the velocity calculation.

The expression above was used to track bubble trajectories using an iterative scheme. Bubble paths were calculated through a $\frac{1}{15}$ second travel time employing sixty time steps. Twenty bubbles were given initial positions from zero for the first bubble near the wall to 7.6 cm away from the wall, each spaced 2 mm apart. A contrived flowfield was devised to simulate an unsteady velocity profile passing the wire. The perturbation is sinusoidal and is roughly similar to that which would result from the passage of a convecting spanwise vortex. The streamwise velocity component was altered with a vertical component with a magnitude 17 percent as large. The function describing this velocity field is

$$\mathbf{V} = C_1 y^n x^{1/2} \frac{U_\infty}{D^m}(1 + C_2 \cos(\omega t))\hat{e}_x - \frac{C_1}{6} y^{n+1} x^{-1/2} \frac{U_\infty}{D^m}(1 + C_2 \cos(\omega t))\hat{e}_y$$

The constants were chosen to roughly match the upstream portion of a passing turbulent spot. The constant C_1 was set to match the experiment freestream velocity at the outer edge of the profile. The constant C_2 matches the magnitude of the time-dependence, D is the vortex diameter, and the frequency, $\omega = \pi/4$ 1/s, matches the period of the time dependence. The constants n and m determine the shape of the profile and its spatial development by controlling the dependence on x and y.

Four test cases were run for representative perturbation magnitudes at a freestream velocity of $U = 0.19$ m/s. The results obtained by processing the bubble locations were compared with the known analytical profile. Complete details of this study can be found in Bruneau and Pauley (1992). In summary, Case 1 spanned the time interval from 0 to $\frac{1}{15}$ seconds and resulted in an error that ranged from 0.4 percent in the freestream to 0.5 percent near the wall. The error in δ^* was 0.37 percent. Case 2 spanned a time interval from 29/30 to 31/30 seconds, chosen to cause the cosine term to change sign at mid time interval. The velocity error ranged from 1.3 percent in the freestream to 0.3 percent near the wall. Case 3 spanned the same time interval with stronger time dependence. The error in the resulting velocity varied from 0.9 percent in the freestream to 0.02 percent near the wall and the error in the displacement thickness was 0.36 percent. To provide a stringent test of the method, Case 4, which spanned the interval from 0 to $\frac{1}{15}$ seconds, was run to simulate a strongly adverse streamwise pressure gradient approaching boundary layer separation. The resulting error varied from 3.5 percent in the freestream to 1.7 percent near the wall. The error in δ^* remained quite low, however, at 0.12 percent. It was observed that even with instantaneous local velocity errors of 3–5 percent, the error in the integral quantity, δ^*, was much less. The ability of integration to offset some of the error which results from the use of differencing and the ability to obtain instantaneous integral parameters is a significant benefit provided by this hydrogen bubble wire technique.

Hydrogen Bubble Technique Versus LDA in a Laminar Boundary Layer. The technique was tested in the laminar flow facility through a range of velocities. It is constrained by limits in operational parameters, namely wire voltage, current, and pulse duration, which dictate the velocity interval where accurate bubble response to the fluid is obtained. At low flow velocity, bubble buoyancy limits the potential accuracy. At high flow velocity, bubble clouds exhibit excessive spreading. As bubbles of varying size are created and swept off of the wire at high speeds, the various sized bubbles are affected in different ways, causing spreading. This spreading contributes to uncertainty in interpreting the edges of the bubble lines. It was found that spreading and buoyancy were the two major limitations in addition to the pixel resolution of the image processing system.

It was desired to establish a lower limit on the allowable freestream velocity. When the ratio of the bubble rise velocity to mean local fluid velocity near the wall approaches $\frac{1}{50}$ there is unacceptable distortion in the profile. From this height down to the wall a curve fit was needed. With a freestream velocity of 15 cm/s, the point at which curve fitting began was approximately 4.5 mm (approximately 12 percent of the boundary layer). Lowering the velocity further entails curve fitting a larger portion of the profile which would introduce considerable potential error in the integral quantities of interest. An additional problem arising from very low freestream velocities was a tendency toward significant coalescence of the bubbles originating at the base of the wire. This coalescence of bubbles resulted in the timelines grouping together and "climbing." This mass of bubbles is generated in the low velocity portion of the boundary layer where the bubble vertical rise rate is predominant. The software indicates zero velocity when the lines merge due to the fact that it is looking for the separation of the timelines.

The upper end of the allowable velocity range is dictated by the velocity at which the spreading of the bubble lines hinders resolution of the edge. Varying the pulse duration between 1

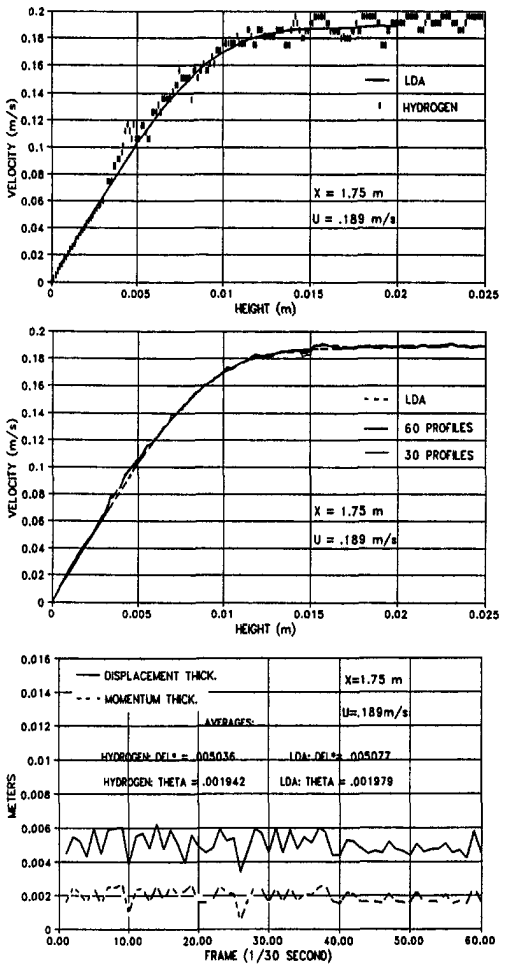

Fig. 8 (*a–c*) Evaluation of hydrogen bubble results for 19 cm/s case ($\Delta t = \frac{1}{30}$ s). (*a*) Instantaneous hydrogen bubble versus LDA, (*b*) time-averaged hydrogen bubble versus LDA, (*c*) hydrogen bubble integral parameters versus time.

and 10 ms revealed that there was not a linear relationship between the pulse duration and the width of the bubble cloud. The bubble line width changes slightly while the density of the bubble cloud changes dramatically. Best results are obtained when the pulse duration is increased with velocity in order to make the bubble clouds more dense and less sensitive to spreading. Above 22 cm/s, however, the combination of voltage and current available to produce hydrogen gas at the wire was essentially exhausted as the spreading could not be overcome by increasing the pulse duration. The spreading of the bubbles in the freestream lead to severe lighting non-uniformity as bubbles of varying size were exposed to varying buoyancy forces. To overcome this limitation the next step would be to increase the voltage. With the 100 volt limit the technique is effectively limited to a range of freestream velocities between 15 and 22 cm/s.

Instantaneous and time-averaged hydrogen bubble velocity profiles were compared to time-averaged LDA surveys for a laminar boundary layer. The LDA surveys used for this comparison were comprised of data taken at 30 heights above the wall and were averaged over 30 seconds. A typical instantaneous hydrogen bubble profiles for 19 cm/s is shown in Fig. 8(a). The results indicate freestream velocity errors of approximately ±5 percent and substantially larger errors (approximately 10 percent) near the wall (but above the region of the third-order polynomial fit). Lu and Smith (1985) observe similar uncertainties and report ±5 percent at $y^+ = 165$ and ±20 percent very near the wall. Time averaging of the results decreased the error for all test velocities. The time average for the 19 cm/s case is shown in Fig. 8(b). For the time-averaged profiles the agreement between the hydrogen bubble wire results and the measurements made with the LDA are better than ±2 percent. The instantaneous integral parameters were also investigated. Figure 8(c) shows the comparison of integral parameters between the instantaneous and time-averaged hydrogen bubble technique and the time-averaged LDA measurements at 19 cm/s. In a laminar flow the integral parameters should remain constant. However, fluctuations were observed due to non-uniform bubble production and due to the curve fit near the wall. The RMS of these fluctuations is typically 5 to 10 percent.

Hydrogen Bubble Technique Versus LDA for Measuring Turbulent Spot. Laminar profile tests established the accuracy of the method and its velocity range. The next step was measuring the flow field during the passage of a turbulent spot, a transient event. The velocity profiles vary from laminar to nominally turbulent and then back to laminar. During this turbulent spot passage the hydrogen bubbles which track the flow encounter complex velocity profiles. Because of the strong velocity gradients, this test case is a challenging application of the hydrogen bubble technique.

It was found that the technique needed to be modified somewhat for highly unsteady flows. The criteria for fitting the portion of the velocity profile with velocity magnitude below $\frac{1}{30}$th of the freestream velocity was modified. The original adaptive technique proved to be unsatisfactory because deformed profiles met the $\frac{1}{30}$th criteria at various y locations within the region of interest, often far from the wall, while other profiles did not meet the criteria until very close to the wall where the lighting intensity was too weak for good resolution. To overcome these limitations the region fit by the profile was fixed at a set height corresponding to the location where the $\frac{1}{30}$th criteria was met by the undisturbed laminar profile. This was also close to the height where the lighting became too dim for the image processing software to recognize timelines (about 2.5 mm from the wall). Since the region of interest stretched to 3.65 cm, the curve-fit area made up only 6.8 percent of the entire profile.

The goal in using the hydrogen bubble technique to investigate turbulent spots was to obtain instantaneous measurements of the displacement thickness, δ^*, versus time for individual spot realizations using the measured profiles. Of the three speeds tested with laminar profiles, the freestream velocity of 19 cm/s yielded the least error in the δ^* calculation. For this reason it was chosen as the speed for investigation of the turbulent spot. The centerline port at $x = 1.75$ m from the leading edge was chosen as the location to position the wire. To keep the post-processing time to a minimum, it was desirable to delay the data processing until the disturbance had propagated from the turbulent spot generator to near the measurement location. The experimental control was set to begin pulsing the hydrogen bubble wire six seconds after the turbulent spot was generated and to end approximately 8.5 seconds later. This time interval covered the most dynamic portion of the spot passage. The duration of the entire spot passage was about 25 seconds from laminar profile back to laminar profile. The total processing effort included 250 frames per spot (each $\frac{1}{30}$th of a second apart) for a total of 7500 frames.

LDA data was obtained for use in validating the results obtained using the hydrogen bubble technique. Forty turbulent spot realizations were generated and measured at each of 22 y locations. Ensemble averaging was performed based on the actuation of the spot generator. From the ensemble-averaged velocity $u(y, t)$ the displacement thickness $\delta^*(t)$ was calculated. A similar ensemble averaging procedure was performed using 30 hydrogen bubble realizations. The results of this comparison shown in Fig. 9 demonstrate good agreement between the two techniques. The results at two times during the develop-

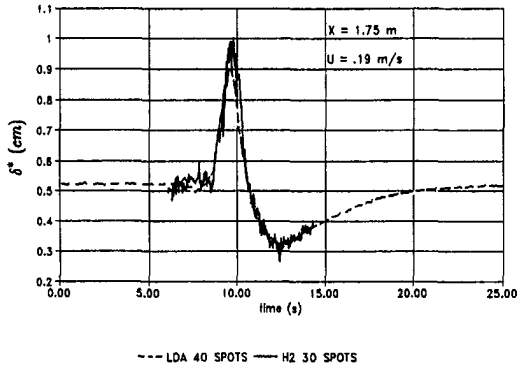

Fig. 9 Ensemble-averaged δ^* versus time for hydrogen bubble and LDA

ment were chosen for detailed further investigation, $t = 7.6$ and 9.75 seconds. At $t = 7.6$ seconds the hydrogen bubble technique indicates an upward trend in the displacement thickness while the LDA shows a downward trend. At $t = 9.75$ seconds the hydrogen bubble method yielded a higher value of maximum δ^*. Inspection of the ensemble-averaged velocity profiles from the two methods at these times helps in understanding the discrepancy (Figs. 10(a) and (b)). From the comparison of the two velocity profiles in each figure, it is evident that the hydrogen bubble method is susceptible to the severe gradients within the spots.

Figures 11(a–f) illustrate the deformation of the timelines around $t = 9.75$ seconds. Figure 11(a) shows laminar flow timelines for comparison with the remaining video images. The next four images (Figs. 11(b–e)) are sequential video images from one realization (spot #1). The last image (Fig. 11(f)) is the processed video image corresponding to Fig. 11(e). In each case, there is variation in the distance between the timelines, from the freestream to the wall. This variation in Δx with height results in the distorted velocity profiles. The quality of the timelines remains good—The timelines retain their bubble

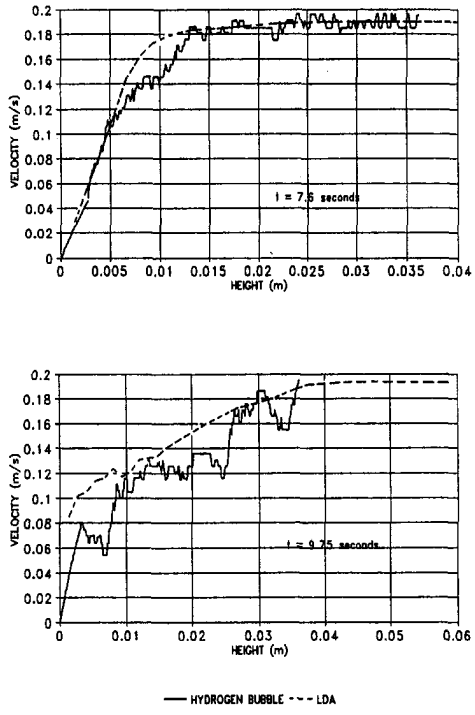

Fig. 10 (a) and (b) Hydrogen bubble and LDA ensemble-averaged velocity profiles at $t = 7.6$ and 9.75 seconds

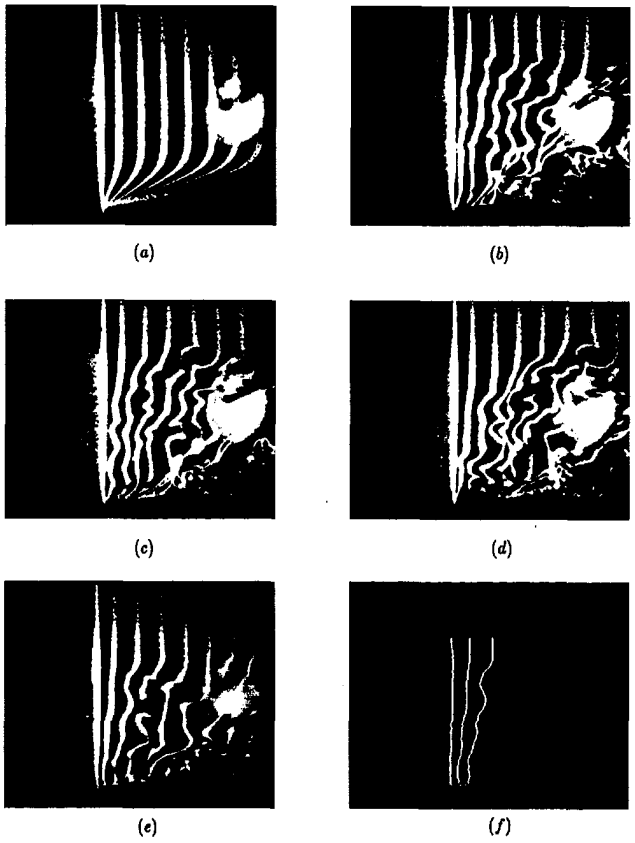

Fig. 11 (a–f) Actual sequential video frames near 9.75 sec. for turbulent spot passage: (a) laminar flow timelines (for comparison); timelines at (b) 9.73, (c) 9.77, (d) 9.80, and (e) 9.83 s (f) processed video image at 9.83 s

density and do not experience significant bubble spreading. The likely difficulty at these two locations arrises from not measuring instantaneous Lagrangian velocity of the bubbles but instead using averaged values over the interval. Ensemble-averaging captures the large-scale fluctuations in the flowfield but fails to yield information about the substructures within. In order to obtain a definitive analysis of the difference in results, a second technique to measure instantaneous velocities would need to be developed for comparison with the hydrogen bubble method.

Investigation of the instantaneous traces of δ^* from the hydrogen bubble method versus the LDA ensemble average result shows that each spot not only follows the overall scales described by the averaged results but also the individuality of each spot (Figs. 12(a) and (b)). It is evident that there is a histogram of peaks, arrival times, periods, and sharpness. The data in these plots is raw data and has not been filtered in any way. Each spot has substantial fluctuation throughout the realization; it was found that for the 19 cm/s laminar case, the rms about the mean δ^* value was approximately eight percent. For the turbulent spots the rms in the instantaneous traces is considerably greater than twelve percent.

It is unclear whether the fluctuations in the hydrogen bubble results are due primarily to uneven bubble formation or if the fluctuations represent the substructures within the spot. The fluctuations in the displacement thickness observed in the laminar boundary layer suggest that the method itself is a substantial contributor to the rms in the signal. Clearly these results suggest that the practice of ensemble averaging has a significant potential for missing high-frequency, small-scale fluctuations that could significantly modify the instantaneous local displacement thickness. Fortunately for the study of boundary layer transition noise, these are known to be inefficient producers of noise. This

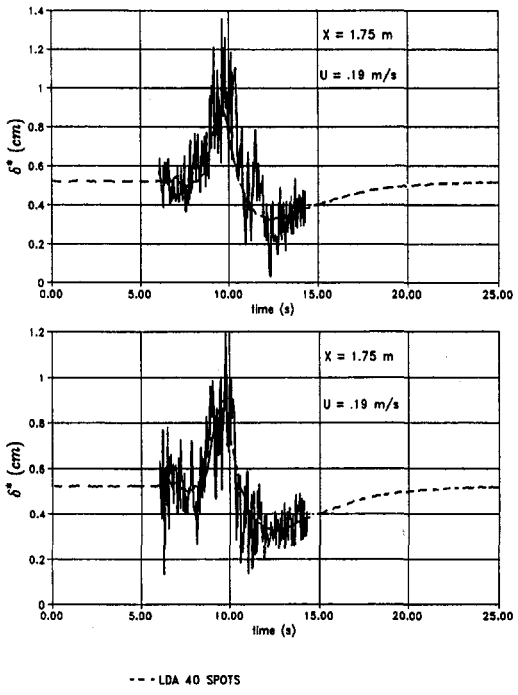

Fig. 12 (*a*) and (*b*) Instantaneous δ^* versus time for selected turbulent spots using hydrogen bubble technique. Spots (*a*) # 10 and (*b*) 20 of the 30 spot data set.

high-frequency unsteadiness must be considered whenever this technique is to be utilized.

8 Conclusions and Recommendations

The results obtained in this study both analytically and experimentally show that the hydrogen bubble method is a valid technique for flow measurements. The analytical error estimates compared reasonably well with the experimental results suggesting that the dominant sources of error have been accounted for. The hydrogen bubble wire method is very sensitive to the pixel resolution between timelines. It is also sensitive to severe gradients within the turbulent spots. The allowable operating velocity is constrained by bubble buoyancy effects for the low velocities and by spreading of the bubble timelines at high velocities. These limitations could potentially be expanded either way by adjusting the electrical conditions of the apparatus itself, particularly by allowing the use of higher voltages.

An analytical study using a laminar boundary layer profile substantiated the claim that the Eulerian field velocity can be represented by the Lagrangian time-averaged velocity of the bubbles. The instantaneous velocity results calculated at all velocities and time intervals yielded a maximum error of 5 percent in the freestream to 10 percent near the wall. The integral parameters showed fairly good consistency but exhibited sensitivity to either bubble generation non-uniformity or the curve-fitting procedure down by the wall, as the rms about the means was about 5–10 percent for a laminar boundary layer. The δ^* values in the turbulent spot passings yielded localized inconsistencies with the ensemble-averaged LDA results. The hydrogen bubble method deviated from the LDA results during periods of very large gradients in the boundary layer profile as might be expected.

It is not clear whether the LDA ensemble averaging scheme smears out the overall magnitude of the peaks in δ^* or whether the hydrogen bubble method accentuates the peaks due to its error band. A second instantaneous velocity profile measurement scheme is not presently available. It can be concluded that the errors due to buoyant motion of the bubbles deep in the boundary layer were successfully removed by implementing a third-order least-squares curve fit near the wall. One enhancement which might significantly improve the response to unsteady flow fields would be speeding up the pulse frequency, as long as the timelines fully detach from the generating wire. However, if any of the parameters are changed, many other parameters such as voltage, current, or pulse duration must also change. As an example, closer spacing of the timelines would further exacerbate the limitations in accuracy due to the available pixel spacing. This in turn would make a higher resolution camera necessary.

Acknowledgments

The authors wish to acknowledge the support of the Office of Naval Research code 1125 OA.

References

Abernathy, F. H., Bertschy, J. R., and Chin, R. W., 1977, "Turbulence Spectra Using Laser Doppler Anemometry and Selective Seeding," *Proceedings of 5th Symposium on Turbulence,* Paterson, G. K., Zakin, J. L. eds., University Missouri-Rolla, pp. 133–142.

Adrian, R. J., 1991, "Particle-Imaging Techniques for Experimental Fluid Mechanics," *Annual Review of Fluid Mechanics,* Vol. 23, pp. 261–304.

Bruneau, S. D., and Pauley, W. R., 1992, "Digital Image Processing of Hydrogen Bubble Lines for Instantaneous Velocity Profiles," Technical Report No. TR 92-10, Applied Research Laboratory, Pennsylvania State University.

Clutter, D. W., and Smith, A. M. O., 1961, "Flow Visualization by Electrolysis of Water," *Aerospace Engineering,* Vol. 18, pp. 24–76.

Davis, W., and Fox, R. W., 1967, "An Evaluation of the Hydrogen Bubble Technique for the Quantitative Determination of Fluid Velocities Within Clear Tubes," ASME *Journal of Basic Engineering,* Dec., pp. 771–776.

Geller, E. W., 1954, An Electrochemical Method of Visualizing the Boundary Layer, Master's thesis, Dept. of Aeronautical Engineering, Mississippi State College.

Gonzalez, R. C., and Wintz, P., 1987, *Digital Image Processing,* 2nd Ed., Addison Wesley, Reading, MA.

Hoffman, G. H., 1988, "The Trajectory of a Gas Bubble in an Axisymmetric Turbulent Boundary Layer," Department of the Navy, Space and Naval Warfare Systems Command Technical Memorandum, File no. 88-136.

Kim, H. T., Kline, S. J., and Reynolds, W. C., 1971, "The Production of Turbulence Near a Smooth Wall in a Turbulent Boundary Layer," *Journal of Fluid Mechanics,* Vol. 50, pp. 133–60.

Krane, M. H., and Pauley, W. R., 1995, "Estimation of the Direct Acoustic Radiation From a Transitional Boundary Layer Using Velocity Measurements," *Journal of Sound and Vibration,* Vol. 181, No. 5, pp. 737–763.

Lauchle, G. C., 1991, "Hydroacoustics of Transitional Boundary Layer Flow," *Applied Mechanics Review,* Vol. 44, No. 12, pp. 517–531.

Lu, L. J., and Smith, C. R., 1985, "Image Processing of Hydrogen Bubble Flow Visualization for Determination of Turbulence Statistics and Bursting Characteristics," *Experiments in Fluids,* Vol. 3, pp. 349–356.

Lu, L. J., and Smith, C. R., 1991, "Use of Flow Visualization Data to Examine Spatial-Temporal Velocity and Burst-Type Characteristics in a Turbulent Boundary Layer," *Journal of Fluid Mechanics,* Vol. 232, pp. 303–340.

Matsui, T., Nagata, H., and Yasuda, H., 1977, "Some Remarks on Hydrogen Bubble Technique for Low Speed Water Flows," *Flow Visualization,* A. Asanuma, ed.

Maxey, M. R., and Riley, J. J., 1983, "Equations of Motion for a Small Rigid Sphere in a Non-Uniform Flow," *Physics of Fluids,* Vol. 26, pp. 883–889.

Milazzo, G., 1963, *Electrochemistry, Theoretical Principles and Practical Applications,* Elsevier, Amsterdam.

Riley, J. J., and Gad-el-Hak, M., 1985, "The Dynamics of Turbulent Spots," *Frontiers in Fluid Mechanics,* Davis, S. H., and Lumley, J. L., eds., Springer, New York, pp. 123–155.

Sankaran, R., Antonia, R. A., Bisset, D. K., and Sokolov, M., 1991a, "Flow Patterns and Organization Within Turbulent Spots," *Physics of Fluids A,* pp. 1560.

Sankaran, R., Sokolov, M., and Antonia, R. A., 1991b, "Substructures in a Turbulent Spot," *Journal of Fluid Mechanics,* Vol. 197, pp. 389–414.

Schraub, F. A., Kline, S. J., Henry, J., Runstadler, P. W., and Littell, A., 1965, "Use of Hydrogen Bubbles for Quantitative Determination of Time Dependent Velocity Fields in Low Speed Water Flows," ASME *Journal of Basic Engineering,* June, pp. 429–444.

Schubauer, G. B., and Klebanoff, P. S., 1955, "Contributions to the Mechanics of Boundary Layer Transition," NACA TN 3489.

Wygnanski, I., Zilberman, M., and Haritonidis, J. H., 1982, "On the Spreading of a Turbulent Spot in the Absence of a Pressure Gradient," *Journal of Fluid Mechanics,* Vol. 123, pp. 69–90.

M. Priven
CAMERI-Coastal and Marine Engineering Research Institute, Technion City, Haifa 32000, Israel

J. F. Atkinson
Department of Civil Engineering, State University of New York at Buffalo, Buffalo, NY 14260

G. A. Bemporad
ISMES Spa, V.le G. Cesare 29, 24100 Bergamo, Italy

H. Rubin
Department of Civil Engineering, State University of New York at Buffalo, Buffalo, NY 14260

Theoretical Study of a Laminar Jet in a Double-Diffusion Environment*

The flow field development associated with the injection of negatively, neutrally, and positively buoyant fluid layers into a stratified environment was analyzed in this study. The analysis considered two-dimensional (horizontal slot) fluid injection under laminar conditions in either temperature-stratified, salinity-stratified or double-diffusive stratified environments. The major features characterizing the buoyant layer development were identified. A numerical model, which integrates in a local reference frame the equations governing mass, momentum, heat and salinity fluxes, was developed. The model was used to examine the characteristic flow patterns for the two-dimensional buoyant discharges of interest in this study. It was also possible to show that double-diffusion effects may significantly influence the development of initially neutral fluid layers and cause a certain vertical deviation.

1 Introduction

The injection of buoyant fluid layers into a stratified environment is a common feature in environmental and industrial problems. The natural water bodies receiving the liquid waste are usually subject to nonuniform temperature and salinity profiles and the fluid is normally injected under turbulent conditions. The environmental impact of the discharged pollutants depends on the efficiency of the mixing processes. These processes are characterized by the size and stratification of the receiving water body and by the buoyancy and momentum of the injected flow (e.g., Jirka and Akar, 1991).

There have been many studies of turbulent jet properties. In contrast, relatively little work has been done to examine the characteristics of a laminar jet injected into a stratified environment. Laminar or transition to turbulent flow conditions may appear for turbulent jet injection in a stratified environment after a point of "*jet collapse*" (e.g., Roberts and Matthews, 1987). These fluids are also of interest for some industrial applications. For example, Kaghazchi (1988) investigated the possibility of using laminar jets as a suitable means by which liquid-liquid reactions could be effectively investigated. A specific application of laminar jets is with solar ponds, where heat collection and storage may be generated by a water body having salinity increasing with depth. Moreover, an increase in solar pond performance may be obtained by applying advanced methodologies which involve the establishment of a stratified flowing layer in the bottom part of the pond gradient zone (Keren et al., 1991, 1993). This layer is created and maintained by injecting and withdrawing laminar jets of different temperature and salinity.

In this study we examine the behavior of a laminar jet injected into a stratified environment. The jet may be positively, negatively or neutrally buoyant and the stratification may be by temperature, salinity or both (i.e., possibly double-diffusive). The problem definition sketch is shown in Fig. 1. In general, gradients are assumed to be constant and negative, namely temperature and salinity increase with depth. However, for temperature stratification the temperature gradient is positive.

2 Hydrodynamics of the Fluid Injection and Withdrawal

Theoretical and experimental investigations of laminar flows in a stratified environment were initially concerned with the movement of obstacles in stratified fluid. Pao (1968) investigated the laminar flow generated by the movement of a finite thin flat plate, and determined the velocity profile of the shear layer above the plate. In this study it was found that the flow was governed by the ratio between the Reynolds number Re and the Richardson number Ri, defined as

$$\mathrm{Re} = \frac{UL}{\nu} \quad \mathrm{Ri} = \frac{g}{\varrho_0}\frac{d\varrho}{dz}\frac{L^2}{U^2} \qquad (1a\text{–}b)$$

U is the flat plate velocity, L is the flat plate length, ϱ and ϱ_0 are the density and the reference density, respectively, ν is the kinematic viscosity and g is the gravitational acceleration. Experimental data showed that for higher values of the Re/Ri ratio, namely dominant inertia forces, velocity oscillations spread out vertically with slight attenuation. Instead, for lower values of Re/Ri, namely the stratification was dominant, velocity oscillations rapidly decreased with height. Pao (1968) and Browand and Winant (1971) presented analytical solutions for the velocity in the laminar shear layer. The two-dimensional flow was assumed incompressible, viscous and subject to the Boussinesq approximation; the ambient fluid was stably stratified. However, as the same authors cautioned, the predicted streamline pattern could be hardly realized in practice, because of a streamline overturning which could produce a statically unstable density distribution.

Browand and Winant (1972) performed experiments where an horizontally moving cylinder in a stratified fluid pushed ahead of it a long tongue or slug of almost stagnant fluid moving at the speed of the cylinder. Qualitative pictures of the upstream flow were obtained by first placing dye in a large region in front of the cylinder, and then pulling the cylinder through the dye. The experimental measurements showed large unstable regions above and below the centerplane. Browand and Winant (1972) assumed as a measure of the upstream wake thickness the distance between the points above and below the centerplane where the slug density became equal to the ambient density.

* Parts of this study were presented at the 3rd International Conference on Progress in Solar Ponds, El Paso, Texas, May 1993 and at the 2nd International Conference on Water Pollution, Milan, Italy, June 1993.

Contributed by the Fluids Engineering Division for publication in the Journal of Fluids Engineering. Manuscript received by the Fluids Engineering Division October 2, 1993; revised manuscript received August 31, 1994. Associate Technical Editor: M. Gharib.

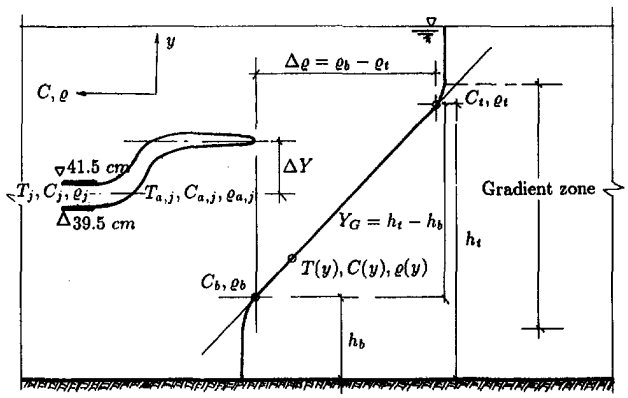

Fig. 1 Problem definition sketch

In a parallel theoretical and experimental study, Maxworthy (1972) found a similarity between the flow generated by the cylinder movement and a slug intrusion into a stratified environment. The fluid was injected into a salinity stratified environment through a two-dimensional slot; the fluid density was equal to the ambient density at the injection level. The slug length, l, and the thickness near the source were found to increase proportionally to $t^{5/6}$ and $t^{1/6}$, respectively, where t is time from the beginning of the experiment. No evaluation was performed on the buoyant jet vertical deviation from its initial level. Maxworthy (1972) mentioned that the accuracy of his experimental data was not sufficient to check the vertical spreading intensity. These experiments on fluid injection were characterized by Reynolds number Re = 5.9 − 245. The Reynolds number Re was defined as in eq. (1*a*), where the flat plate length L was replaced by the jet thickness d.

Manins (1976) described the intrusion of a homogeneous fluid into a salinity stratified environment. His data showed that $l \propto t$ for practically all the runs. There was no evidence of a $t^{5/6}$ dependence as found by Maxworthy (1972) in experiments with low Reynolds numbers (Re < 100). Instead, a $t^{5/6}$ dependence of the intrusion length could be confirmed only at higher Reynolds numbers (but still laminar). Density profiles measured before and after the fluid intrusion showed an asymmetry about the intrusion level. This phenomenon was explained by Manins (1976) as caused by the different boundary conditions at the top and bottom of the gradient zone: fluid below the intrusion level was relatively quiescent, while fluid above that level was rising as fluid was added in the flume. The density gradient was not changed significantly, although a certain shift could be observed above and below the fluid intrusion. This fact suggested that density transport due to fluid recirculation was not present. In both studies by Maxworthy (1972) and Manins (1976), the outflow from the test flume was not taken into consideration, whereas this factor should play an important role during the flow establishment and in steady-state conditions. No experiment was performed on the injection of buoyant fluid layers.

Fluid withdrawal from a stratified environment induces a flow pattern which is basically asymmetrical and unsteady (e.g., Imberger, 1980). During selective withdrawal, the sink removes fluid from the withdrawal layer, and steepens the density gradient within that region. This fluid is replaced by water from above the sink level, while the liquid below the sink is subject to circulation.

The injection of a very viscous fluid, as the Reynolds number of the flow tends to zero, satisfies the Stokes equations for creeping flow and the resulting fluid injection may be termed as creeping jet. A description and analytical solution for such flows are given by Schlichting (1933). The velocity distribution of the creeping plane jet was calculated by Tatsumi and Kakutani (1958). For larger values of the longitudinal coordinate x the flow becomes nearly uniform. As Re increases, the jet becomes more concentrated and less stable, finally breaking up and becoming turbulent.

The stability of the two-dimensional laminar jet was analyzed by Tatsumi and Kakutani (1958) and subsequently by Kaplan (1964). These authors analysed the stabilizing influence of viscosity for Re < 100. Kaplan (1964) computed the complete neutral line and mapped the region of instability by integrating the complete Orr-Sommerfield equations. A qualitative estimate of the critical Reynolds number for a jet in a neutral environment was found to be $\mathrm{Re}_c = 4$ at $K = 0.2$, where K is the dimensionless wave number.

Linear stability analysis, performed in conditions of neutral stratification, shows that the fluid layer injection develops a velocity profile which is unstable. However, if the receiving ambient is stably stratified, a sufficient condition for stability is Ri > $\frac{1}{4}$ everywhere in the fluid (e.g., Miles, 1961). The breaking-up of the creeping jet may therefore be controlled by the stable stratification, with no damaging effects caused on the fluid stratification by the fluid injection.

Based on the above review, the following conclusions may be reached:

(*a*) very few studies have been performed on low Reynolds number fluid injection into a singly stratified environment;

Nomenclature

B = buoyancy flux, $[L^4T^{-3}]$
C = salinity concentration [%]
C_D = drag coefficient [dimensionless]
C_p = specific heat, $[L^2T^{-2}{}^\circ\mathrm{C}^{-1}]$
d = layer width, $[L]$
g = gravitational acceleration, $[LT^{-2}]$
Fr = densimetric Froude number, [dimensionless]
l = slug length, $[L]$
L = flat plate length, $[L]$
l_M, l_N, l_Q = characteristic length scales, $[L]$
N = buoyancy frequency, $[T^{-1}]$
q_e = entrainment discharge, $[L^2T^{-1}]$
Ra = thermal Rayleigh number, [dimensionless]
Re = Reynolds number, [dimensionless]
Rs = solute Rayleigh number, [dimensionless]
R_ϱ = stability ratio, [dimensionless]
$R_{\varrho,j}$ = jet stability ratio, [dimensionless]
t = time, $[T]$
$\mathbf{v}$ = velocity vector, $[LT^{-1}]$
x = longitudinal coordinate, $[L]$
y = vertical coordinate, $[L]$
α = entrainment coefficient, [dimensionless]
β_T = thermal expansion coefficient $[^\circ\mathrm{C}^{-1}]$
β_C = solutal expansion coefficient $[\%^{-1}]$
ΔY = vertical deviation, $[L]$
κ_C = solute diffusivity, $[L^2T^{-1}]$
κ_T = thermal diffusivity, $[L^2T^{-1}]$
ν = kinematic viscosity, $[L^2T^{-1}]$
ϱ = density, $[ML^{-3}]$
η = jet referenced coordinate, $[L]$
ζ = jet referenced coordinate, $[L]$

Subscripts and Superscripts

a = ambient characteristics
b = bottom of stratified zone
j = jet initial values
t = top of stratified zone

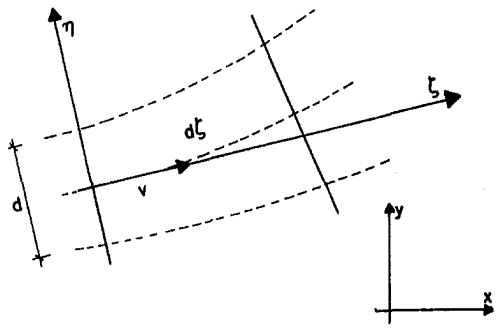

Fig. 2 Two-dimensional flow geometry

(*b*) no studies have been performed on laminar fluid injection into a double-diffusion environment;

(*c*) the importance of double-diffusion effects on the stability of the stratified water body subject to buoyant layer injection is an issue still to be investigated;

(*d*) previous experiments did not consider any outflow mechanism from the test tank, leading to unsteady flow conditions in the experimental flume.

3 Numerical Model Development

A mathematical model was developed to analyze the general behaviour of a low Re buoyant jet in a stratified water body. The model essentially routes the injected fluid layer through the domain of interest by solving, in a local reference frame, the equations of conservation of mass flux, momentum flux, heat and salinity flux. The present mathematical model assumes pressure deviations from hydrostatic to be negligible; entrainment, diffusion and dissipation terms are included.

For the control volume sketched in Fig. 2, the equations expressing conservation of mass flux, momentum flux, heat and salinity flux are:

$$\frac{d}{d\zeta}\left[\int_A \varrho|\mathbf{v}|(\zeta,\eta)dA\right] = \varrho_a q_e \tag{2}$$

$$\frac{d}{d\zeta}\left[\int_A \varrho|\mathbf{v}|^2(\zeta,\eta)e_x dA\right] = -2\varrho C_D|\mathbf{v}|^2 e_x$$

$$\frac{d}{d\zeta}\left[\int_A \varrho|\mathbf{v}|^2(\zeta,\eta)e_y dA\right] = -2\varrho C_D|\mathbf{v}|^2 e_y + \varrho g\int_A \frac{\varrho_a-\varrho(\zeta,\eta)}{\varrho_a}dA \tag{3a–b}$$

$$\frac{d}{d\zeta}\left[\int_A \varrho C_p|\mathbf{v}|(\zeta,\eta)T(\zeta,\eta)dA\right] = \varrho_a C_p q_e T_a - 2\varrho_a\kappa_T\frac{(T-T_a)}{d}$$

$$\frac{d}{d\zeta}\left[\int_A \varrho|\mathbf{v}|(\zeta,\eta)C(\zeta,\eta)dA\right] = \varrho_a q_e C_a - 2\varrho_a\kappa_C\frac{(C-C_a)}{d} \tag{4a–b}$$

Here $\chi = (\zeta, \eta)$ is the orthogonal reference system oriented according to the velocity vector $\mathbf{v} = (v_x, v_y) = (v_\zeta, v_\eta)$ and $\mathbf{e} = (e_x, e_y) = (v_x, v_y)/|\mathbf{v}| = (e_\zeta, e_\eta)$ is a unit vector oriented according to the jet velocity vector; q_e is the entrainment discharge; ϱ is the jet density; d is the injected layer width; C_D is the drag coefficient; T is the temperature; C is the solute concentration; C_p is the specific heat; κ_T and κ_C are the thermal and solute diffusivities, respectively. The subscript a refers to ambient characteristics. In Eq. (4) the temperature and solute gradients at the jet surface are approximated as $(T - T_a)/d$ and $(C - C_a)/d$, respectively. The entrainment discharge is assumed to be proportional to the velocity vector as follows

$$q_e = 2\alpha|\mathbf{v}| \tag{5}$$

where α is an empirical coefficient. The set of Eqs. (2)–(4) is completed by the following equation of state:

$$\varrho(T, C) = \varrho_0[1. - \beta_T(T - T_0) + \beta_C(C - C_0)] \tag{6}$$

where β_T and β_C are the thermal and solutal expansion coefficients, respectively, and subscript 0 refers to a reference state.

We assume the different variables to be constant across the layer width (top hat method), namely a function only of the axis of the local reference system oriented according to the velocity vector. Under this assumption, introducing Eq. (5) into the integral governing equations, Eqs. (2)–(4), we obtain the following equations of:

Mass continuity

$$\frac{d}{d\zeta}(\varrho d|\mathbf{v}|) = 2\alpha\varrho_a|\mathbf{v}| \tag{7}$$

Momentum

$$\frac{d}{d\zeta}[\varrho d|\mathbf{v}|v_x] = -2\varrho C_D|\mathbf{v}|^2\frac{v_x}{|\mathbf{v}|}$$

$$\frac{d}{d\zeta}[\varrho^d|\mathbf{v}|v_y] = -2\varrho C_D|\mathbf{v}|^2\frac{v_y}{|\mathbf{v}|} + \varrho dg\frac{\varrho_a-\varrho}{\varrho_a} \tag{8a–b}$$

Heat and solute transport

$$\frac{d}{d\zeta}(\varrho d|\mathbf{v}|T) = 2\alpha\varrho_a|\mathbf{v}|T_a - 2\varrho_a\frac{\kappa_T}{C_p}\frac{(T-T_a)}{d}$$

$$\frac{d}{d\zeta}(\varrho d|\mathbf{v}|C) = 2\alpha\varrho_a|\mathbf{v}|C_a - 2\varrho_a\kappa_C\frac{(C-C_a)}{d} \tag{9a–b}$$

Equations (7)–(9), together with Eq. (6), represent a nonlinear system of six equations in the six unknowns ϱ, v_x, v_y, d, T and C. The fluid layer is discharged at vertical position Y_j, with jet width d_j, initial velocity $\mathbf{v}_j$, temperature T_j and solute concentration C_j (see Fig. 1). The fluid is injected into an ambient environment with linear temperature and solute concentration gradients G_T and G_C, respectively. The gradients are $G_T = (T_b - T_t)/Y_G$ and $G_C = (C_b - C_t)/Y_G$, where subscript b refers to a bottom value and subscript t refers to a value at the top of the stratified region, and Y_G is the depth of this region.

4 Characteristic Length Scales of the Jet Injection

The significant length scales defined for the analysis of jet injection into a stratified fluid are (e.g., Roberts and Matthews, 1987; Jirka and Akar, 1991)

$$l_Q = \frac{Q}{M^{1/2}} \quad l_M = \frac{M^{3/4}}{B^{1/2}} \quad l_N = \frac{M^{1/4}}{N^{1/2}} \tag{10a–c}$$

where

$$N = \left(-\frac{g}{\varrho_{a,j}}\frac{d\varrho_a}{dy}\right)^{1/2}$$

is the buoyancy frequency, ν is the kinematic viscosity, Q and M are the kinematic fluxes of volume and momentum, respectively, B is the buoyancy, and $\varrho_{a,j}$ is the ambient density at the injection level. l_Q characterizes the distance from the origin over which the source volume flux exerts a dynamic influence on the flow field, (this length scale is essentially the nozzle diame-

ter); l_M characterizes the distance from the origin over which the momentum flux is important relative to the buoyancy flux; and l_N is a length scale which characterizes the strength of the source momentum flux relative to stratification. Following previous studies (e.g., Roberts and Matthews, 1987) the jet vertical deviation can be expressed as:

$$\frac{\Delta Y}{l_N} = f\left(\frac{l_Q}{l_N}, \frac{l_M}{l_N}, \frac{M^{1/2}}{\nu}\right) \tag{11}$$

l_N is chosen as the normalizing length scale as this will always be important for the present problem, while l_Q and l_M may or may not be important, depending on the conditions. The third ratio in Eq. (11) is not relevant for the present analysis on fluid injection at low Reynolds numbers. This vertical deviation may be also characterized by an exit jet Froude number defined as (Johnstone and Zangrando, 1988):

$$Fr = |\mathbf{v}_j|\left(d_j g \frac{(\varrho_j - \varrho_{a,j})}{\varrho_{a,j}}\right)^{-1/2} \tag{12}$$

where ϱ_j is the initial jet density and d_j is the initial jet width.

Experiments of Roberts and Matthews (1987) with turbulent jets showed that because of stable stratification the jet turbulence would collapse at a certain distance from the injection slot. For jets of small volume flux, generated by a point source, they showed that the collapse distance could be expressed as $\zeta_m = C_1 l_N$, where C_1 for nonbuoyant jets ranged from 2.1 to 3.6. After collapse, the flow intrudes horizontally as a layer of constant thickness, i.e., the entrainment is significantly reduced.

Jirka and Akar (1991) considered the development of a horizontal jet in a stratified environment. In this study, the characteristic length was defined as $l'_N = M^{1/3}/N^{1/2}$. This definition is the two-dimensional equivalent of the definition given in eq. (10c), which was for three-dimensional flow. According to Jirka and Akar (1991), when $\zeta/l'_N \ll O(1)$, where ζ is the velocity oriented coordinate, the effect of density stratification is negligible, while $\zeta/l'_N \gg O(1)$ implies that the initial jet momentum is no longer important and a density current will then form at the terminal level.

These results were incorporated into the numerical model proposed in the previous section. The experiments on laminar jet injection into stratified environment reported by Priven et al. (1995) showed that in most cases a turbulent cloud could appear in the region close to the injection slot. For this reason, the concept of "collapse distance" was introduced into the mathematical model. It was assumed that the jet collapse would occur conventionally at a distance $\zeta \simeq \gamma \cdot l'_N$, where $1 < \gamma < 10$. For $\zeta \leq \gamma \cdot l'_N$ salt and temperature diffusion were assumed to be of turbulent type, and therefore κ_T and κ_C were increased by two orders of magnitude with respect to the molecular values. Moreover, for $\zeta \geq \gamma \cdot l'_N$, entrainment was assumed negligible. By using $\gamma = 5$ we obtained good agreement between numerical and experimental data (see Priven et al., 1995).

5 Initial Behavior of the Injected Fluid

In order to characterize the initial behaviour of the injected buoyant fluid, as well as the capability of the fluid layer to maintain a horizontal direction along the flume after the initial stages, it is helpful to define a jet stability number $R_{\varrho,j}$ as

$$R_{\varrho,j} = \frac{\beta_C \Delta C_j}{\beta_T \Delta T_j} \tag{13}$$

where

$$\Delta C_j = C_j - C_{a,j}$$

$$\Delta T_j = T_j - T_{a,j}$$

T_j, C_j and ϱ_j are the temperature, salinity concentration and density of the injected fluid; $T_{a,j}$, $C_{a,j}$ and $\varrho_{a,j}$ are the ambient fluid temperature, salinity concentration and density at the level of injection, respectively. The magnitude of $R_{\varrho,j}$ can help to determine the initial behaviour of the buoyant fluid layer. This jet stability number is equivalent to the ratio of thermal and solute Rayleigh numbers, $R_\varrho = \mathrm{Rs}/\mathrm{Ra} = \beta_C \Delta C/\beta_T \Delta T$, generally used to characterize the stability of double-diffusion systems (e.g., Sherman and Imberger, 1991). Here ΔC and ΔT are the temperature and salinity differences between the top and the bottom of the double-diffusion system.

Table 1 Initial behavior of the injected fluid layer

Case (I)	T_j	C_j	$R_{\varrho,j}$	Behavior
1	$T_j = T_{a,j}$	$C_j = C_{a,j}$	—	neutral
2	$T_j > T_{a,j}$	$C_j = C_{a,j}$	$R_{\varrho,j} = 0$	rise
3	$T_j < T_{a,j}$	$C_j = C_{a,j}$	$R_{\varrho,j} = 0$	drop
4	$T_j = T_{a,j}$	$C_j > C_{a,j}$	—	drop
5a	$T_j > T_{a,j}$	$C_j > C_{a,j}$	$R_{\varrho,j} > 1$	drop
5b	$T_j > T_{a,j}$	$C_j > C_{a,j}$	$R_{\varrho,j} = 1$	neutral
5c	$T_j > T_{a,j}$	$C_j > C_{a,j}$	$R_{\varrho,j} < 1$	rise
6	$T_j < T_{a,j}$	$C_j > C_{a,j}$	$R_{\varrho,j} < 0$	drop
7	$T_j = T_{a,j}$	$C_j < C_{a,j}$	—	rise
8	$T_j > T_{a,j}$	$C_j < C_{a,j}$	$R_{\varrho,j} < 0$	rise
9a	$T_j < T_{a,j}$	$C_j < C_{a,j}$	$R_{\varrho,j} > 1$	rise
9b	$T_j < T_{a,j}$	$C_j < C_{a,j}$	$R_{\varrho,j} = 1$	neutral
9c	$T_j < T_{a,j}$	$C_j < C_{a,j}$	$R_{\varrho,j} < 1$	drop

Table 1 represents 13 possible cases related to variations in T_j and C_j with respect to $T_{a,j}$ and $C_{a,j}$. The density difference between the injected and the ambient fluid, which drives the initial behavior of the jet, becomes:

$$\frac{\varrho_j - \varrho_{a,j}}{\varrho_0} = -\beta_T \Delta T_j + \beta_C \Delta C_j = (R_{\varrho,j} - 1)\beta_T \Delta T_j \tag{14}$$

The condition $R_{\varrho,j} = 1$ therefore characterizes an initially neutrally buoyant jet. The value of $R_{\varrho,j}$ is not defined for $\Delta T_j = 0$.

As shown in Table 1, there are only three cases ($I = 1$, 5b and 9b) which represent neutral fluid injection. In Case 1 $R_{\varrho,j}$ cannot be defined, and only for this Case 1 the fluid is able to keep an horizontal direction at some distance after injection. In cases 5b and 9b, instead, the fluid will undergo vertical motion because of the different rates of heat and salinity diffusion. In Case 5b, for example, the injected fluid is initially neutral. Then, since temperature diffuses faster than salt, the temperature of the injected fluid rapidly matches the ambient one. At this point, the injected fluid becomes heavier and starts to drop. A similar situation occurs in Case 9b, where the faster heat diffusion makes the layer positively buoyant soon after injection.

In Case 2 the fluid is injected with a temperature higher than the ambient, so that the injected fluid initially rises. Case 3 is analogous to Case 2; here the fluid layer initially drops because of the lower injection temperature. In Case 4 the fluid layer initially drops due to the higher salinity in the injected fluid. In Case 5a the fluid layer initially drops because the density difference caused by salinity is higher than the density difference caused by temperature. The ratio $R_{\varrho,j} > 1$ identifies such conditions. The opposite conditions occurs in case 5c, where the fluid layer initially rises; here $R_{\varrho,j} < 1$. In Case 6 both temperature and salinity differences cause the fluid layer to drop. Analogously, in Case 8 both temperature and salinity differences cause the fluid layer to rise. In both cases $R_{\varrho,j} < 0$. In Case 7 the lower salinity causes the injected fluid to rise. Finally, in cases 9a and 9b both the temperature and salinity of the injected fluid are lower than the temperature and salinity of the ambient fluid. In these two last cases, the jet initially drops or rises according to the value of $R_{\varrho,j}$, as shown in Table 1.

This preliminary analysis can only determine the initial behavior of the jet. The numerical experiments described in the

Table 2 Summary of numerical experiments

Run	T_b	T_t	C_b	C_t	T_ϱ	G_T	G_C
1	66.0	34.0	12.0	8.0	1.795	80.0	10.0
2	66.0	34.0	14.0	6.0	3.59	80.0	20.0
3	66.0	34.0	16.0	4.0	5.385	80.0	30.0

following section will enable a better understanding of the long-term behavior of a buoyant jet in a double-diffusive system.

6 Numerical Simulations

The set of Eqs. (7)–(9) was integrated numerically; these equations could be written in the following symbolic form:

$$\frac{d\mathbf{w}}{d\zeta} = \mathcal{F}(\mathbf{w}); \quad \mathbf{w} = \varrho d|\mathbf{v}|\{1, v_x, v_y, T, C\}^T \quad (15)$$

where $\varrho = \varrho(T, C)$, Eq. (6). An explicit numerical integration of Eq. (15) determines the values of the variables in $\mathbf{w}$ at location $\zeta_{(i+1)}$ given the values of the variables in $\mathbf{w}$ at location $\zeta_{(i)}$. Initial conditions for the numerical scheme are the jet width d_j, the jet velocity $\mathbf{v}_j$, the jet temperature T_j and the jet solute concentration C_j. The explicit scheme adopts an iterative procedure over n, which determines the solution at $(i + 1)$ as follows:

$$\mathbf{w}_{(i+1)}^{(n+1)} = \mathbf{w}_{(i)} + \mathcal{F}\left(\frac{\mathbf{w}_{(i)} + \mathbf{w}_{(i+1)}^{(n)}}{2}\right)\Delta\zeta \quad (16)$$

The above iterations are performed until the difference between successive solutions is below a given threshold ϵ.

The following values were used in the numerical simulations: $g = 9.8$ m/s^2, $\kappa_T/C_p = 1.4 \cdot 10^{-7}$ m^2 s^{-1}, $\kappa_C = 1.5 \cdot 10^{-9}$ m^2 s^{-1}, $\varrho_0 = 1000$, kg m^{-3}, $\beta_T = 4.7 \cdot 10^{-4}$°C^{-1}, $\beta_C = 6.8 \cdot 10^{-3}$‰$^{-1}$, $T_0 = 4$°C and $C_0 = 0$ (e.g. Zangrando and Fernando, 1991). To determine the value of the drag coefficient C_D, we can consider that according to Maxworthy (1972) there is a similarity between the laminar jet flow and the slug propagation in front of a moving cylinder in a stratified environment. The drag coefficient for rounded bodies is influenced by the value of Re. In this study the values of the drag coefficient C_D for a sphere moving through a fluid were obtained from Shames (1962). For instance, for moderate Reynolds numbers typical to our simulations, namely Re $\simeq$ 100, Shames (1962) reports $C_D \simeq 2$. The value of $\alpha = 0.1$, valid for the zone before the point of jet collapse, was determined through calibration of the model with experimental results (Priven et al., 1995).

The numerical experiments were performed assuming a stratified zone of depth equal to 40.0 cm; the jet was injected at a level of 20.0 cm from a plane slot 2.0 cm wide. The simulations considered the stratification conditions shown in Table 2. All jets were discharged with an initial velocity of 0.5 cm s^{-1}.

All three numerical simulations shown in Table 2 considered initially neutral jets, i.e., the density difference between the jet and ambient fluid at the injection level was set equal to zero (see Eq. (14)). Since the fluid was initially neutrally buoyant $R_{\varrho,j} = 1$. Figure 3 shows the computed jet deviations from the horizontal direction for different stratifications as a function of the temperature difference between the jet and the ambient fluid, ΔT_j. The jet was routed throughout the ambient fluid up to a distance of 100 m. These results show that the injection of an initially neutral fluid, with $\Delta T_j \neq 0$ and $\Delta C_j \neq 0$, does not guarantee an horizontal trajectory.

In fact, the faster heat dissipation rapidly makes the initially neutral jet either heavier or lighter than the ambient fluid. Consequently, the jet rises or drops due to buoyancy force. Only fluid injection characterized by $\Delta T_j = 0$ and $\Delta C_j = 0$ is able to guarantee an horizontal trajectory. Figure 3 also shows that smaller jet deviations are obtained for higher ambient fluid stratification, and viceversa. Moreover, the jet vertical deviation is symmetrical about the injection slot level for positively and negatively buoyant jets.

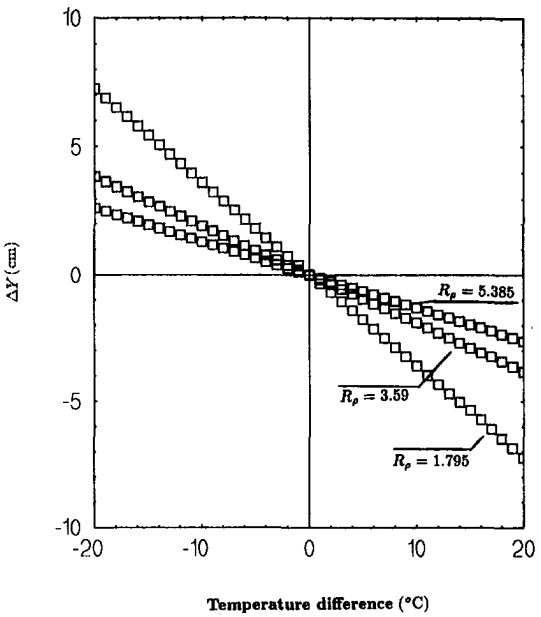

Fig. 3 Buoyant layer deviation from the horizontal versus the temperature difference ΔT_j for various double-diffusion environments [x = 100 m]

Figure 4 shows the development of an initially neutral fluid layer after its injection; the ambient characteristics are given in Table 2, run 3. The jet stability ratio in this simulation is $R_{\varrho,j} = 1$. However, since the injected fluid is characterized by temperature and salinity concentration lower than the ambient fluid, a certain vertical deviation is expected. The jet initially maintains its horizontal trajectory, given the high entrainment rate which characterizes the zone before the jet collapse, namely ζ

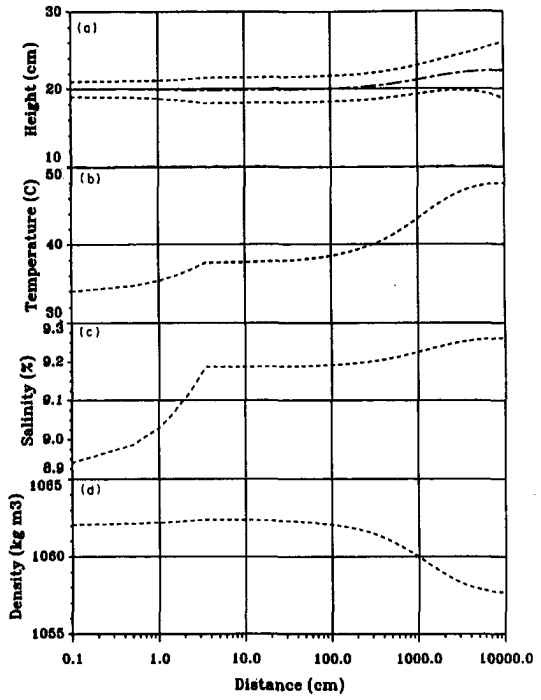

Fig. 4 Development of the characteristics of an initially neutral fluid in a doubly stratified ambient fluid

$< \zeta_m$. In this initial zone, temperature and salinity concentration rapidly tend to the ambient values. After the point of jet collapse the entrainment of the ambient fluid is significantly reduced and molecular heat and salt diffusivity characterize the heat and salt transfer. Note that the kink in Fig. 4 corresponds to $\zeta < \zeta_m$. Given the difference between the heat and salt diffusivities, as well as the difference between the thermal and the solutal expansion rate, the jet experiences a positive buoyancy over a length of 100 m. An analogous behaviour could be seen for an initially neutral jet, whose temperature and salinity concentrations were higher then the ambient fluid at the level of injection.

7 Concluding Comments

The present theoretical analysis on the development of a buoyant fluid layer under laminar flow conditions concerns jet behaviour in a stratified environment, particularly its stability and vertical motion due to buoyancy. The behavior of buoyant and nonbuoyant fluid layers injected into a double-diffusion environment was investigated by integrating numerically the equations of transport in a local reference frame. Results from previous dimensional analysis identified the length scales associated with fluid injection into a stratified stagnant flow under laminar flow conditions. A stability parameter $R_{\varrho,j}$, for fluid injection into a double-diffusion environment, was defined to characterize the initial vertical displacement of the buoyant or neutral jet. An initially neutral buoyant jet may be obtained by injecting fluid having the same temperature and salinity as the ambient fluid, case 1 of Table 1; under these conditions, the jet maintains its horizontal direction. An initially neutral jet may also be obtained by injecting a fluid having different temperature and salinity from the ambient fluid, case 5b and 9b of Table 1. However, in this case, the jet may eventually undergo vertical deviation. Thus, the injection of an initially neutral fluid layer was not sufficient to prevent vertical deviation of the jet itself.

Theoretical and experimental results relevant to turbulent jets were applied in the present numerical model. The "collapse distance" concept was used to calculate the jet fluid properties immediately after injection and at the point when any turbulence generated by buoyancy or convection in the region close to the injection slot is damped by the stable stratification. Experimental evidence of the theoretical results presented in this paper is the subject of additional studies by the same authors (Priven et al., 1995).

Acknowledgments

This study was funded by the Israel Ministry of Energy and Infrastructure, under contract no. 92-05-002/92-1-1 and by the Hydraulic and Structural Research Center of ENEL Spa. The material presented in this paper reports parts of M. Priven's D.Sc. thesis. M. Priven was supported by Nate H. and Beatrice G. Sherman Fellowship. J. Atkinson was supported by the Lady Davis Fellowship Trust Fund.

References

Browand, F. K., and Winant, C. D., 1971, "Upstream Growing Shear Layer in Stratified Flow," *Physics of Fluids,* Vol. 14, No. 5, pp. 1025–1027.

Browand, F. K., and Winant, C. D., 1972, "Blocking Ahead of a Cylinder Miving in Stratified Fluid: An Experiment," *Geophysical Fluid Dynamics,* Vol. 4, pp. 29–53.

Imberger, J., 1980, "Selective Withdrawal: A Review," *Proc. 2nd Int. Symp. Stratified Flows,* Int. Ass. Hydr. Res., 1, Trondheim, Norway.

Jirka, G. H., and Akar, P. J., 1991, Hydrodynamic classification of submerged multiport-diffusers, *Journal of Hydraulic Engineering,* Vol. 117(9), pp. 1113–1128.

Johnstone, H. W., and Zangrando, F., 1988, "Mixing Depth of a Submerged Buoyant Jet," ASME *Journal of Solar Energy Engineering,* Vol. 110, pp. 125–131.

Kaghazchi, T., 1988, "Use of Laminar Jet in Determining the Overall Rate of Liquid-Liquid Reactions," Conference of the Division of Petroleum Chemestry, American Chemical Society, Vol. 33, N. 3. Washington, DC.

Kaplan, R. E., 1964, "The Stability of Laminar Incompressible Boundary Layers in the Presence of Compliant Boundaries," M.I.T. Aereo-Elastic and Structure Research Laboratory, ASRL-TR 116-1.

Keren, Y., Bemporad, G. A., and Rubin, H., 1991, "Basic Experiments Related to the Advanced Solar Pond (ASP) Performance," ASME JOURNAL OF FLUIDS ENGINEERING, Vol. 113, pp. 116–123.

Keren, Y., Priven, M., Atkinson, J., Bemporad, G. A., and Hillel, R., 1993, "Theoretical and Experimental Comparison of Conventional and Advanced Solar Pond Performance," *Solar Energy,* Vol. 51(4), pp. 255–270.

Manins, P. C., 1976, "Intrusion into a Stratified Fluid," *Journal of Fluid Mechanics,* Vol. 74, N. 3, pp. 547–560.

Maxworthy, T., 1972, "Experimental and Theoretical Studies of Horizontal Jets in a Stratified Fluid," *International Symposium on Stratified Flows,* Novosibirsk.

Miles, J. W., 1961, "On the Stability of Heterogeneous Shear Flows," *Journal of Fluid Mechanics,* Vol. 10, pp. 496–508.

Pao, Y., 1968, "Laminar Flow of a Stably Stratified Fluid Past a Flat Plate," *Journal of Fluid Mechanics,* Vol. 34, pp. 795–808.

Priven, M., Atkinson, J., Bemporad, G. A., and Rubin, H., 1995, "Experimental study of the injection of a single layer into a stratified environment," ASME JOURNAL OF FLUIDS ENGINEERING, published in this issue pp. 000–000.

Roberts, P. J. W., and Matthews, P. R., 1987, "Behavior of Low Buoyancy Jets in a Linearly Stratified Fluid," *Journal of Hydraulic Research,* Vol. 25(4), pp. 503–519.

Schlichting, H., 1933, "Laminar Spread of a Jet," *Z. Angew. Math. Mech.,* 13, pp. 260–263.

Shames, I. H., 1962, *Mechanics of Fluids,* McGraw-Hill, p. 361.

Sherman, B. S., and Imberger, J., 1991, "Control of Solar Pond," *Solar Energy,* Vol. 46, pp. 71–81.

Tatsumi, T., and Kakutani, T., 1958, "The Stability of a Two-Dimensional Jet," *Journal of Fluid Mechanics,* Vol. 4, pp. 261–275.

Zangrando, F., and Fernando, H. J. S., 1991, "A Predictive Model For the Migration of Double Diffusive Interfaces," ASME *Journal of Solar Energy Engineering,* Vol. 113, pp. 59–65.

M. Priven
CAMERI-Coastal and Marine Engineering Research Institute, Technion City, Haifa 32000, Israel

G. A. Bemporad
ISMES Spa, V.le G. Cesare 29, 24100 Bergamo, Italy (deceased)

J. Atkinson
Department of Civil Engineering, State University of New York at Buffalo, Amherst, NY 14260

H. Rubin
CAMERI-Coastal and Marine Engineering Research Institute, Technion City, Haifa 32000, Israel

Experimental Study of a Laminar Jet in a Double-Diffusion Environment*

An experimental analysis of the flow development caused by the simultaneous injection and withdrawal of a buoyant fluid layer with low Reynolds number in a double-diffusion environment is presented. The injection of positively, neutrally, and negatively buoyant fluid layers was simulated in the experimental setup. Innovative procedures were developed to efficiently create the desired density distributions in the laboratory flume. Results presented in this paper concern the injection of fluid into environments stratified by temperature, salinity or both. Basic features of the flow patterns are described, in particular, intrusion rate, effect on ambient stratification and vertical displacement. The experimental data on the fluid vertical displacement were compared with results from a numerical model and good agreement was found.

1 Introduction

In a companion paper (Priven et al., 1995), hereafter termed paper I, we discussed basic theoretical aspects relevant to the simultaneous injection and withdrawal of a buoyant fluid layer in a single-diffusion or double-diffusion stratified environment. A major objective of that analysis and of the present experimental investigations was to understand the flow patterns associated with injection of single jets under laminar conditions in a doubly stratified environment. Moreover, experimental results presented here are used to validate the numerical model developed in paper I.

An experimental setup was prepared in order to study the injection and withdrawal of a buoyant fluid layer in a double-diffusion stratified environment. Three series of tests were performed: (1) temperature-stratified system (designated by T); (2) salinity-stratified system (designated by S); and (3) double-diffusive system (designated by TS).

The following sections describe the experimental work as well as the calibration of numerical tools for the prediction of the major flow characteristics associated with the fluid injection and withdrawal.

2 Laboratory Setup

The laboratory setup consists of a flume whose length, width and depth are 320 cm, 60 cm, and 100 cm, respectively, as shown in Fig. 1. It is made of concrete, with one side made of glass for flow visualization. The entrance unit consists of several outlet ports, or slots. The middle outlets inject the various fluid sublayers to be studied, while the upper and lower outlets are used to inject fluid to maintain boundary conditions for the gradient region. Each slot is 56.0 cm wide and 2.0 cm high, and is connected with the mixing unit where fluids of different salinity and temperature are mixed to obtain the desired fluid properties. Three outlets are positioned at the downstream end of the flume. The upper and the lower outlets withdraw water which is recirculated through the heat-exchangers (or through the tank with hot brine) to maintain boundary conditions. The middle outlet removes fluid from the gradient zone at the level of the injection slots. This arrangement was designed to create a homogeneous bottom layer of thickness 20 cm, a gradient zone of thickness 50 cm and a surface layer of 10–15 cm. Within the gradient zone it was possible to inject one to three sublayers, each of 2 cm height. In the present study, however, we examine only results for injection of a single layer.

The constant temperature and salinity gradients of the gradient zone are set up with the filling procedure described in Appendix A. The density gradients were measured by slowly withdrawing fluid at a given height and measuring its specific gravity with a hydrometer. The experimental uncertainty in the density measurements was ± 1.0 kgm^{-3}. Uncertainty in the vertical position was ± 0.5 mm. An initial analysis was performed to determine the character of the fluid withdrawal during the density measurements. Fluid in the vicinity of the salinity probe was colored with crystals of potassium permanganate to provide a visualization of the withdrawal process. No disturbances were observed above or below the probe, so that it may be assumed that the measured brine was withdrawn exactly at the level of the probe. The injection and filling discharges were measured by flowmeters, with an accuracy estimated as two percent. A calibration of the flowmeters with salt water did not show any significant influence of salt on the discharge measurements.

Temperature profiles were measured by using 16 thermocouples fastened on a fiberglass bar at different intervals and connected to a data unit. A detailed calibration of the temperature measurement procedure showed that these data had a maximum expected accuracy of ± 0.3°C. In the zone of fluid injection the distance between the thermocouples was 1.0 cm. Temperature measurements were taken before injection and during injection at a distance of 15.0 cm from the injection slot and at a distance of 20.0 cm from the exit port. Dye was added to the fluid to visualize the resulting flow patterns. Photographs taken during the fluid propagation were used to estimate the layer velocity.

Different combinations of salinity and temperature can provide the same density and may strongly affect the initial jet behavior (depending on ambient stratification), as shown in paper I. The injection of fluid of neutral buoyancy with the desired salinity concentration and temperature could be performed through the procedure described in Appendix A.

* Parts of this study were presented at the 3rd International Conference on Progress in Solar Ponds, El Paso, Texas, May 1993 and at the 2nd International Conference on Water Pollution, Milan, Italy, June 1993.

Contributed by the Fluids Engineering Division for publication in the JOURNAL OF FLUIDS ENGINEERING. Manuscript received by the Fluids Engineering Division October 2, 1993; revised manuscript received August 31, 1994. Associate Technical Editor: M. Gharib.

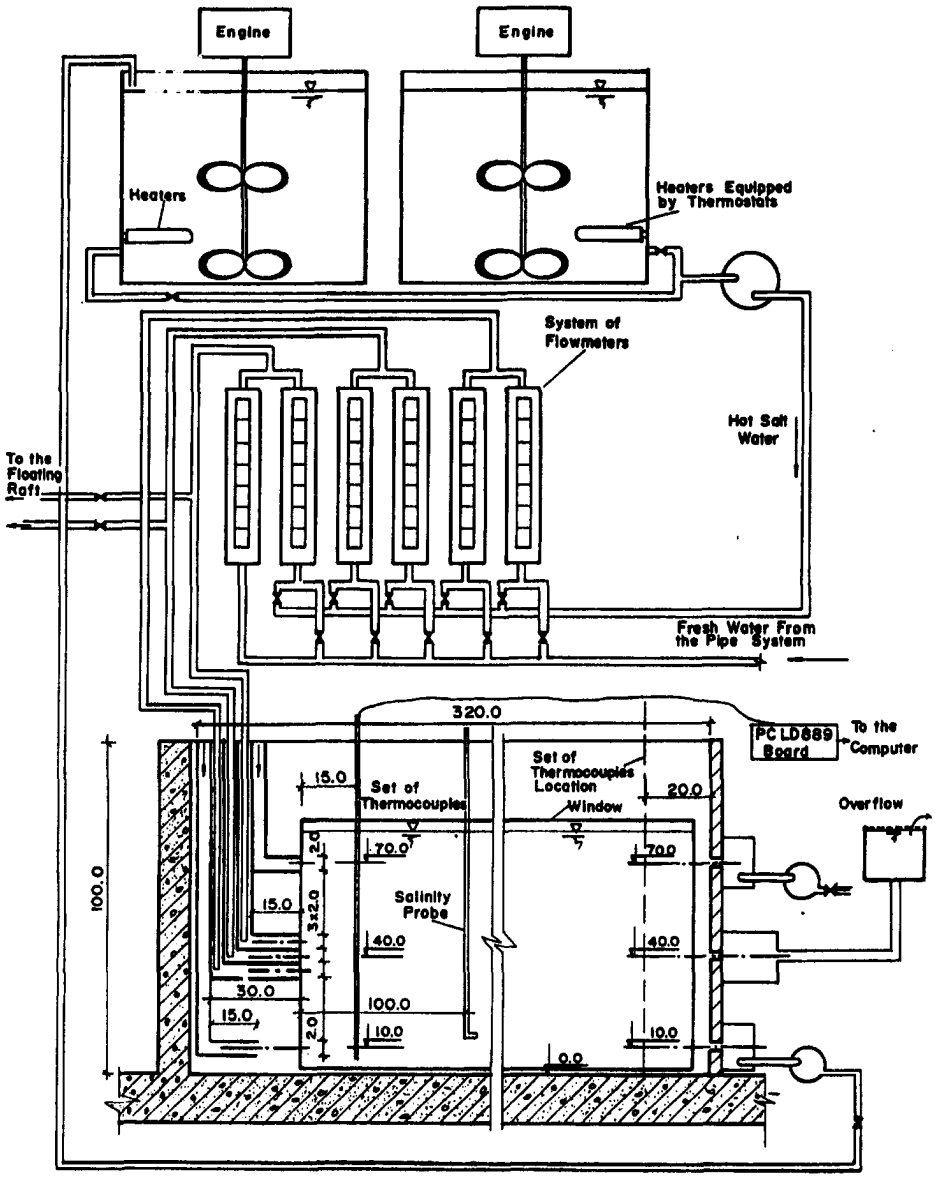

Fig. 1 Schematic view of the experimental setup

3 Experimental Work

Table 1 shows data for the experiments of type T. This table reports the fluid layer injection temperature T_j, the ambient temperature at the level of the injection port $T_{a,j}$, the temperature gradient G_T, the initial velocity v_j, the Froude and the Reynolds numbers Fr and Re, respectively, defined as

$$\mathrm{Fr} = v_j \left(d_j g \frac{(\varrho_j - \varrho_{a,j})}{\varrho_{a,j}} \right)^{-1/2} \qquad \mathrm{Re} = \frac{d_j v_j}{\nu} \qquad (1a, b)$$

and the layer vertical deviation ΔY (the net vertical movement, relative to the level of the injection slot—see paper I). In Eq. ($1a$, b) g is the gravitational acceleration, ϱ_j is the fluid layer injection density, $\varrho_{a,j}$ is the ambient density at the level of the injection port, d_j is the initial jet thickness, and ν is the kinematic viscosity.

A summary of the experimental data for tests of type S is presented in Table 2. In this table G_ϱ is the density gradient. Finally, Table 3 presents the main characteristics of the TS type experiments; in this table $\Delta\varrho = \varrho_{a,j} - \varrho_j$, and the rest of parameters are the same as in Tables 1 and 2.

Flow Visualization. The flow patterns for buoyant and nonbuoyant fluid layers in a stratified environment were found to be very similar for all three series of experiments, with only minor differences found with different stratifications. Only the most important features, common for all experiments, will be described here. The simultaneous injection and withdrawal of a neutral jet was characterized by zero vertical deviation of the jet axis, i.e., $\Delta Y = 0$. Flow visualization for experiment T5, which refers to the injection of an almost neutral jet (see Table 1), is shown in Fig. 2. The fluid intruded into the stratified environment as a slug, with a smooth pointed nose. The slug thickness did not change significantly and was constantly around 2.0 cm until it reached the vicinity of the withdrawal port.

In this experiment, red dye was initially added to the injected fluid; after the slug nose reached the withdrawal port, blue dye was added. As shown in Fig. 2, the dark trace repeated exactly the same trace of the (earlier) lighter one its thickness was almost the same. This means that the jet vertical spreading observed is in fact the result of the dye and heat diffusion, while the "real" jet thickness was not changed significantly.

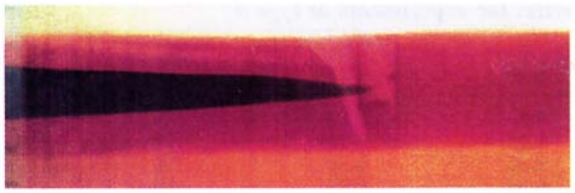

Fig. 2 Side view of the fluid slug in the vicinity of the exit port (experiment T5)

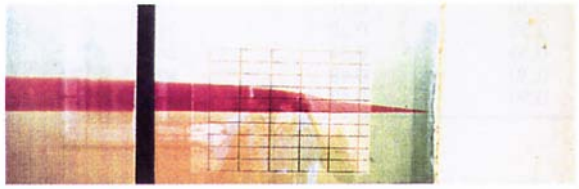

Fig. 3 Side view of the fluid slug in the vicinity of the exit port (experiment T8)

Experiments performed with slightly buoyant fluid layers showed a stronger increase of the fluid layer thickness with respect to neutrally buoyant layers in the region close to the injection port, where some degree of turbulence due to buoyancy was observed. Figure 3 shows the flow development for experiment T8, which had a slight buoyancy. In this experiment the density difference at the injection level was $\varrho_{a,j} - \varrho_j = 0.95$ kgm^{-3} and the density gradient was $\Delta\varrho/\Delta h = 21.5$ kgm^{-4} (see Table 1 for other characteristics). In the vicinity of the withdrawal port, the lower edge of the slug advanced in the horizontal direction, while the upper edge had an evident curvature, which appeared to be a function of the location of the withdrawal port. It appears that the lower slug edge accelerated, whereas the upper edge slowed down. Similar phenomena were observed, for instance, in experiment T15, which had a slight negative buoyancy. For this experiment, $\varrho_{a,j} - \varrho_j = -1.2$ kgm^{-3} and $\Delta\varrho/\Delta h = 37.3$ kgm^{-4}.

These last two experiments clearly showed that the withdrawal procedure significantly influenced the flow. The withdrawal port did not force the fluid layer either to drop or to rise with respect to its equilibrium level. Instead, it withdrew fluid only from a small region located at the same level.

Figure 4 shows the movement of vertical dye traces recorded during experiment S14 (see also Table 2). The jet was not colored initially in order to make the trace movement more visible. As shown in Fig. 4, the slug intrusion generated a back-flow above and below its body. In experiment S14 these back-flows were located inside the gradient zone, because above and below the slug they were bounded on one side by the fluid slug and on the other side by the interfaces located at both ends of the gradient zone. However, measurements of the density profiles before and immediately after the fluid injection did not show any evidence of a density transfer. Therefore, the back-flow or convection-like currents must occur in the horizontal plane.

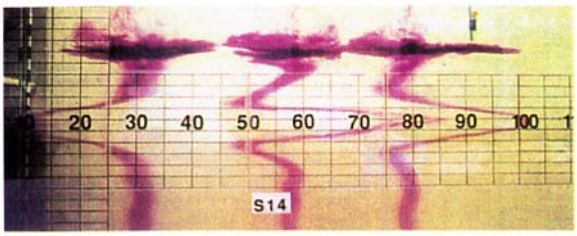

Fig. 4 Flow visualization of experiment S14

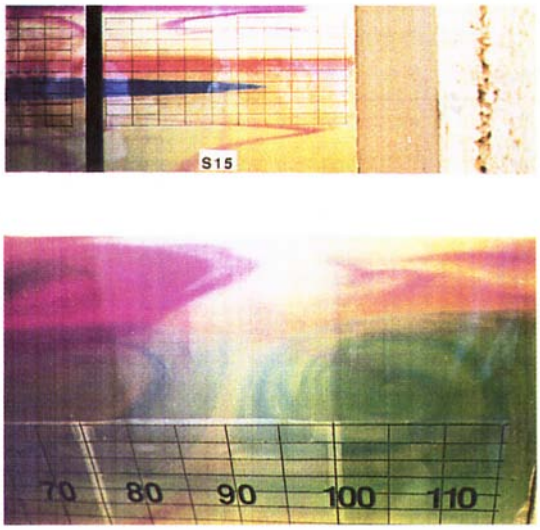

Fig. 5 Propagation of a negatively buoyant fluid layer into a salinity-stratified environment (experiment S15): (*a*) Slug propagation; (*b*) convective forms at the levels of the buoyant layer

The propagation of a negatively buoyant fluid layer is shown in Fig. 5(*a*). This figure refers to experiment S15, characterized by a density difference of 10.0 kgm^{-3}. In this experiment the fluid layer sinks immediately after its injection to reach an equilibrium level. Once the injected fluid reached this equilibrium level, it propagated as a neutrally buoyant jet. Near the downstream wall the horizontal velocity decreased while the layer thickness increased. In about 5 min the jet thickness increased from 4.0 to 6.0 cm.

Because of entrainment, there must be some return flow in the test section. In a two-dimensional framework (vertical plane) the return flow must be associated with recirculation in the vertical plane, generated above and below the discharge level. However, with a three-dimensional setup there is also the possibility of recirculation in a horizontal plane. In fact, this latter possibility is preferred when stratification limits vertical motions, as in the present tests. Evidence for horizontal recirculation comes from the above-mentioned observation of a lack of significant changes in the density profile, and also from pictures taken after an experiment was concluded, showing horizontal "ring" structures. These rings were observed at the slug level and also near the top of the gradient zone (Fig. 5(*b*)). For double-diffusive conditions the faster diffusion of heat may induce buoyancy as the injected fluid moves into the stratified region (see paper I).

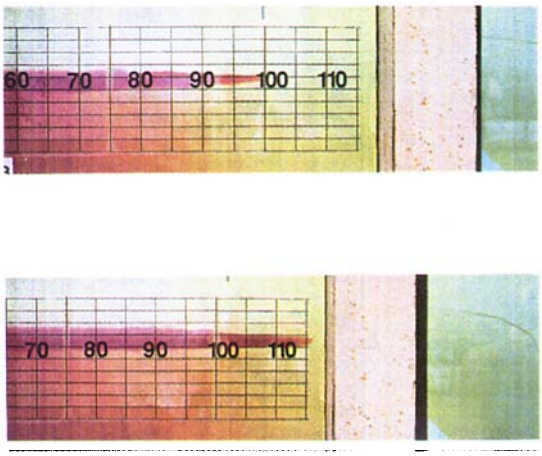

Fig. 6 Visualization of double-diffusive effects after jet injection

Table 1 Fluid layer and ambient properties for experiments of type T

Run	T_j °C	$T_{a,j}$ °C	G_T °C/m	v_j cm/s	Fr —	Re —	ΔY cm
T3	29.7	28.9	25.0	0.53	0.84	130	0.0
T4	35.0	28.9	21.4	0.27	0.13	73	5.0
T5	30.5	28.9	60.0	0.32	0.30	98	0.0
T6	31.0	28.8	53.3	0.32	0.26	60	2.3
T8	33.6	30.9	51.5	0.32	0.23	90	4.0
T9	28.0	34.3	120.0	0.32	0.15	62	−0.5
T11	30.0	32.6	54.2	0.30	0.22	75	−1.0
T12	48.0	35.5	61.7	0.30	0.08	86	3.0
T13	34.0	36.5	60.0	0.30	0.21	83	−4.5
T14	29.5	32.4	85.9	0.30	0.21	75	−2.5
T15	28.0	31.5	100.7	0.30	0.20	71	−1.0
T16	33.5	32.4	84.1	0.30	0.34	86	0.0
T17	35.3	35.7	140.2	0.30	0.48	82	−2.0
T18	34.0	35.6	87.3	0.50	0.43	143	−1.6

For example, in Test TS13 $\Delta C = -0.34$ percent and $\Delta T = -5.8$°C. This is an almost neutral jet, though significant effects of double-diffusion were observed. In this test the jet was observed to propagate horizontally at 0.6 cm sec^{-1} during the first 81 s. Gradually the jet fluid was heated and the fluid rose about 2 cm (see Fig. 6(*a*), (*b*)). The interesting feature of this test, related to double-diffusive phenomena, is that this rise occurred very quickly and that the entire slug rose almost simultaneously. After this action the jet continued to flow horizontally at its new position.

Influence of the Fluid Injection on the Density Profile. Typical density distributions before and after injection for neutral and buoyant fluid injection are shown in Fig. 7, which refers to experiments S9, S8, and S15. Figure 7(*a*) shows the development of the density profile for a neutral jet, run S9. Minor modifications of the density profile are present above and below the injection level, however, the density was constant at the injection level. These results are similar to results reported by Browand and Winant (1972) for a cylinder moving slowly through a stratified fluid. However, density gradient distortions reported by Manins (1976) differ from Fig. 7(*a*), especially in the region above the jet. This difference is believed to be due to the withdrawal procedure used in the present tests, which maintains total depth (there was no withdrawal in Manins' experiment).

Figures 7(*b*, *c*) show the density profile development for positively (experiment S8) and negatively (experiment S15) buoyant jets, respectively. In both cases strong asymmetrical distortions of the density profile are evident above (below) the jet level for positively (negatively) buoyant jet. However, the density gradient is not affected by the fluid intrusion near the bottom or the top of the gradient zone and again it appears that the withdrawal procedure is responsible.

Jet Propagation. Tests by Maxworthy (1972) showed that the slug length should grow as $t^{5/6}$ and the slug width as $t^{1/6}$. To check this relationship the experimental data from all runs were plotted in the same form as done by Maxworthy (1972) and by Manins (1976). However, there is a major difference between the present experiments and these previous studies, namely the presence of a withdrawal procedure operating simultaneously with the fluid injection. Because of this difference, results from each series were analyzed separately for neutrally buoyant and buoyant fluid layers. Nonbuoyant jets demonstrate a linear dependence on elapsed time or show the $t^{5/6}$ behavior for the S and TS series, while nonbuoyant jet from the T series propagate more slowly. This phenomena was also recorded by Manins (1976) for jets with Re numbers less than 100 (T series experiments were characterized by Re < 100). Probably quick heat diffusion is responsible for this phenomena. Figure 8(*a*) show the slug length growth in time for nonbuoyant jets of type TS.

The buoyant jets show $t^{5/6}$ behavior as long as the slug length is less than about $\frac{2}{3}$ of the tank length. After that point the behavior is quite different and experimental data started to differ significantly from the theoretical predictions as shown, for in-

Table 2 Fluid layer and ambient properties for experiments of type S

Run	ϱ_j kg/m^3	$\varrho_{a,j}$ kg/m^3	G_ϱ kg/m^4	v_j cm/s	Fr —	Re —	ΔY cm
S3	1011.2	1011.8	75.7	0.5	0.46	28	1.0
S4	1009.3	1011.1	68.9	1.0	0.54	112	1.0
S5	1012.2	1011.3	85.7	0.6	0.45	40	−0.5
S6	1016.8	1011.0	84.5	0.5	0.15	28	−5.0
S7	1009.9	1010.0	94.7	0.7	1.12	55	0.0
S8	1004.5	1008.8	81.1	0.6	0.21	40	3.0
S9	1010.5	1010.0	79.6	0.8	0.81	72	0.0
S10	1024.1	1011.0	75.6	0.6	0.12	40	−5.0
S11	1008.3	1008.3	84.6	0.9	—	91	0.0
S12	1008.3	1008.5	82.0	0.8	1.25	68	0.0
S13	1002.6	1008.0	83.4	0.6	0.18	40	6.0
S14	1009.4	1009.5	88.0	1.0	—	112	0.0
S15	1019.5	1009.5	83.0	0.6	0.13	40	−4.0
S16	1005.2	1010.8	98.5	0.6	0.18	40	3.5
S17	1008.0	1008.0	89.3	0.6	—	40	0.4
S18	1008.6	1008.8	92.2	1.3	2.40	189	1.0
S19	1056.0	1014.0	172.1	0.6	0.07	40	−8.0
S20	1018.0	1018.0	202.3	1.3	—	189	0.0

Table 3 Fluid layer and ambient properties for experiments of type TS

Run	$\Delta\varrho$ kg/m^3	G_ϱ kg/m^4	G_T °C/m	v_j m/s	Fr —	Re —	ΔY cm
TS1	0.20	80.5	57.0	0.5	0.80	151	−2.0
TS2	14.65	81.8	67.6	0.5	0.09	151	6.0
TS3	0.0	73.8	55.9	0.7	—	212	0.5
TS5	−14.0	79.2	49.1	0.6	0.12	182	−6.0
TS6	8.0	132.3	72.1	0.6	0.15	182	2.0
TS7	0.0	76.5	57.1	0.8	—	242	0.0
TS8	−20.7	77.0	42.0	0.6	0.10	182	−6.0
TS9	0.1	82.6	56.5	1.0	2.26	303	1.0
TS10	−10.4	85.7	39.7	0.6	0.14	182	−4.0
TS11	−0.4	72.9	63.1	0.6	0.68	182	0.0
TS12	−4.75	80.9	43.9	0.6	0.20	182	−3.0
TS13	−0.05	85.1	57.1	0.6	1.92	182	2.0
TS14	0.25	76.3	49.2	1.3	1.86	393	0.0
TS15	−18.25	86.1	48.1	0.6	0.10	182	6.0
TS16	0.0	84.6	—	0.6	—	182	−2.0

stance, in Fig. 8(b). The buoyant jets are apparently subject to a wall effect. This phenomenon is not noticeable for the neutral jets since they do not deviate from the injection/withdrawal level (i.e., the neutral jets "see" the exit, while the buoyant jets encounter the end wall).

4 Double-Diffusive Effects

The theoretical analysis performed in paper I shows that double-diffusive jet behavior may be described by the jet stability ratio $R_{\varrho,j}$. All experimental runs of type TS were subdivided into neutral and slightly buoyant fluid injection (Table 4) and buoyant fluid injection (Table 5). Tables 4 and 5 show the salinity and temperature differences between the jet and the respective ambient fluid properties, as well as the jet stability ratio $R_{\varrho,j}$. The initial jet behavior as a function of temperature and salinity differences may be obtained from Table 1 of paper I. In experiments of type TS the density profile development was basically the same as described before for fluid injection into a single-diffusive ambient. Experiment TS7 represents a nonbuoyant jet injection as long as the density difference between the jet and the ambient fluid is equal to zero (see Table 3). Definite temperature and salinity differences were recorded in experiment TS7, but the jet did not deviate from its initial level. We have to consider, however, that the experimental tank

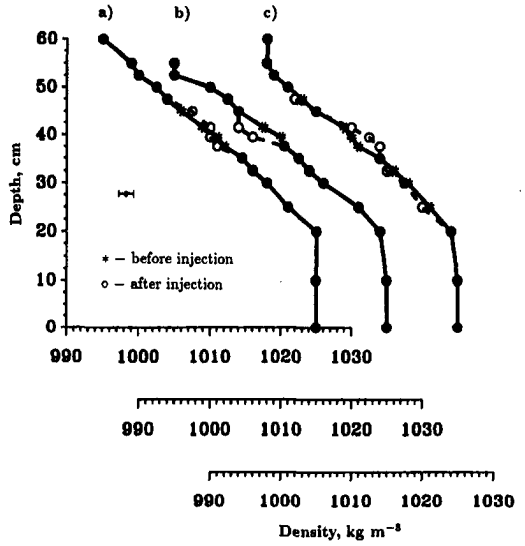

Fig. 7 Measured density profiles before and after injection of a: (a) Neutrally buoyant layer; (b) positively buoyant layer; (c) negatively buoyant layer

was of finite length may not have been sufficient for the appearance of double-diffusive effects. Near the entrance unit the jet influences the temperature distribution and strong temperature gradient distortion was apparent at the jet level. In this case the ambient fluid gained heat (and buoyancy) from the jet, apparently in the region above the jet, while the region below the jet was not affected. Different temperature profile developments were observed in the cases when the jet fluid temperature was smaller than the respective ambient temperature. For instance, experiment TS10 represents the case of a negatively buoyant jet (see also Tables 3 and 5). A strong deformation of the temperature field was recorded over the whole tank length in the region below the injection level, whereas it was not changed significantly above the slug level.

Results from experiment TS13 described above proved the influence of double-diffusive effects on the jet flow (see also Fig. 6(a, b)). Basic jet characteristics for this experiment appear in Tables 3 and 4. It is apparent from Fig. 6(b) that the jet deviated from the initial horizontal direction after approximately 100 s. Unfortunately, we have no detailed temperature and density measurements during this interval of time and we can only speculate about what happened with the ΔT and ΔS values. However, the jet behavior is in agreement with the description provided in paper I.

Atkinson et al. (1988) examined the role of double-diffusive convection on interfacial heat and salt fluxes at the upper and lower boundaries of the gradient zone. A criterion for determining the importance of double-diffusive mixing was defined as $t_c < t_*$, where t_c is the boundary layer instability time scale and t_* is the eddy time scale in the mixed layer. The values of t_c and t_* according to Atkinson et al. (1988) may be calculated as

$$t_c = \left\{\frac{1}{\pi k_T}\left[\frac{\nu \mathrm{Ra}_c}{g\alpha\Delta T(1-\tau^{1/2})^3}\right]^2\right\}^{1/3} \qquad t_* = \frac{h}{u_*} \quad (2a, b)$$

where $\tau = k_S/k_T$ is diffusivity ratio, k_T and k_S are molecular heat and salt diffusivities, respectively, $\mathrm{Ra}_c = g\delta\varrho d_T^3/\varrho_0\nu k_T$ is critical value of Rayleigh number, h is mixed layer depth, and u_* is friction velocity. Using representative values of $k_T = 1.4\cdot10^{-3}$ cm^2 s^{-1}, $\nu = 10^{-2}$ cm^2 s^{-1}, $\alpha = 2\cdot10^{-4}$°C^{-1}, and considering that the critical value of Ra_c is in the range 1000–1600, it was shown that for $\Delta T = 5 - 30$°C values of t_c are between 15–100 sec. Although the flow configurations considered by Atkinson et al. (1988) and in the present case are different, it is possible to compare t_c directly with experimental observations. For experiment TS13 the jet rose on 2.0 cm presumably due to heat diffusion after about 80 sec. This result correlates with Atkinson et al. (1988) prediction quite well.

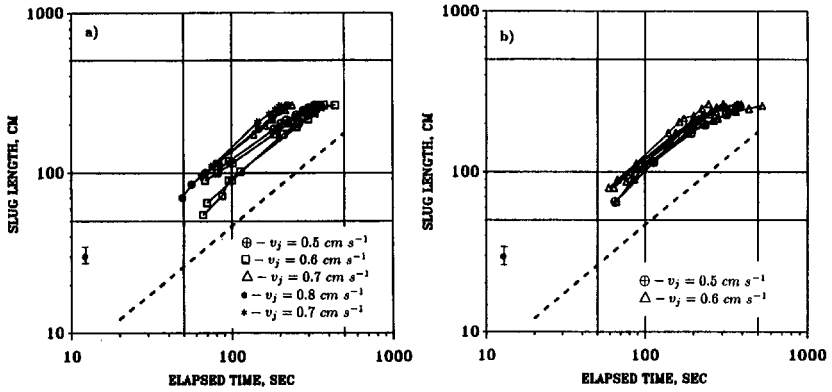

Fig. 8 Slug length versus elapsed time for experiments of type TS: (*a*) Neutrally buoyant layers; (*b*) negatively and positively buoyant layers

5 Jet Deviation

In paper I it was determined that the buoyant layer deviation from the horizontal axis ΔY could be expressed in terms of characteristic length scales in the following form

$$\frac{\Delta Y}{l_N} = f\left(\frac{l_Q}{l_N}, \frac{l_M}{l_N}\right) \tag{3}$$

where l_Q characterizes the distance from the origin over which the source volume flux exerts a dynamic influence on the flow field, (this length scale is essentially the nozzle diameter); l_M characterizes the distance from the origin over which the momentum flux is important relative to the buoyancy flux; and l_N is a length scale which characterizes the strength of the source momentum flux relative to stratification.

In the present experimental runs the l_Q/l_N ratio was in the range 3.0–5.0; however, no influence of the ratio l_Q/l_N on the vertical deviation could be observed. Instead, the l_M/l_N ratio has a certain effect on the vertical deviation. For increasing l_M/l_N we could observe a decreasing value of $\Delta Y/l_N$. This phenomenon was already observed by investigators in the analysis of turbulent jets (e.g., Johnstone and Zangrando, 1988), but this has never been confirmed experimentally for jets of small momentum flux. The present set of experiments showed that for laminar or transition to laminar flow conditions the buoyancy forces are the main factor defining the behavior of the buoyant fluid layer. Volume flux and momentum flux had only a limited influence on the buoyant layer.

The specific form of (3) was found by regression of the experimental data,

$$\frac{\Delta Y}{l_N} = 0.3 \cdot \left((\varrho_{a,j} - \varrho_j)\left(\frac{d\varrho_a}{dy}\right)^{-1} v_j^{-1} N \right)^{0.61} \tag{4}$$

Figure 9 shows the experimental data together with the regression curve for the T, S, and TS series. It is obvious from Fig. 9 that experimental points for single and double-diffusive buoyant jets are located in the same field. Therefore, the mechanism driving buoyant jet deviations in single or double-diffusive environment is the same. This approximation should give better results when double-diffusive jets are influenced by strong buoyancy forces and double-diffusive effects are not important. Results provided by Eq. (4) may not be correct if the jet has initially the same density as the receiving fluid, but different temperature and salinity. In this case, as shown previously, the jet deviates from the initial horizontal level mainly due to double-diffusive effects.

The numerical model developed in paper I was calibrated with the present experimental results in order to determine the optimal values of the drag coefficient C_D and the entrainment coefficient α (see paper I). It was found that the parameters which produce the best agreement between experimental deviations and numerical predictions are $C_D = 2.0$ and $\alpha = 0.1$. This last parameter is valid only before the point of jet collapse, as explained in paper I. After this point the value of α was reduced by two orders of magnitude to correspond with the reduction in turbulence. Figure 10 shows the measured and the computed vertical deplacement for experiments of type T, S, and TS. Very good agreement is seen. Minor differences can be found between predicted and experimental data for strongly negative buoyant layers.

6 Concluding Comments

The present set of experiments was performed to analyze the behavior of neutral and buoyant jets in single and double-diffusive environments. These experiments proved the practical possibility of creating and maintaining a stable layer flowing in a stratified environment without significant mixing between the layer and the ambient environment. Observations of the flow patterns in the experimental tank showed that the flow in the stratified environment is quite complicated and basically three dimensional.

Simultaneous injection and withdrawal of neutral buoyant fluid layers under laminar conditions creates circulation patterns in the horizontal plane which however could not cause convec-

Table 4 Injected and ambient fluid properties for neutrally buoyant fluid layers

Run	ΔC (%)	ΔT (°C)	$R_{\varrho,j}$	Case
TS1	0.30	4.8	0.90	5*b* → 5*a*
TS3	−0.38	−6.3	0.87	9*b* → 9*a*
TS7	0.37	5.4	0.99	5*b*
TS9	0.09	1.6	0.81	5*c*
TS11	−0.18	−3.8	0.68	9*b* → 9*a*
TS13	−0.34	−5.8	0.84	9*a*
TS14	0.40	6.5	0.89	5*b*

Table 5 Injected and ambient fluid properties for buoyant fluid layers

Run	ΔC (%)	ΔT (°C)	$R_{\varrho,j}$	Case
TS5	3.5	19.3	2.62	5*a*
TS6	−1.03	1.3	11.46	8
TS8	2.38	−8.5	4.05	6
TS10	1.10	−5.8	2.74	6
TS12	0.44	−3.8	1.67	6
TS15	2.30	−4.5	7.40	6
TS16	0.83	15.3	0.78	5*c* → 5*a*

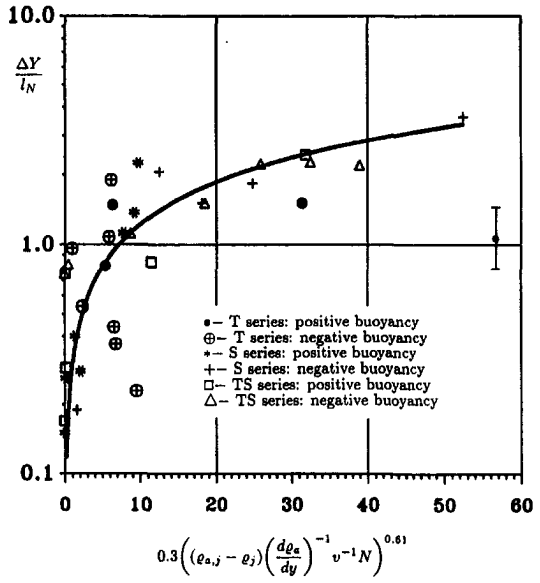

Fig. 9 Measured vertical deviations versus the nondimensional parameter of Eq. (4) for experiments of type T, S, and TS

tive transport in the gradient zone. This is not the case during injection of buoyant layers, which deviate from the injection-withdrawal ports level and as a result strong density profile deformation appears immediately above (below) that level. The regions close to the top and bottom of the gradient zone are not affected by the jet injection presumably due to the selective nature of the withdrawal procedure and convective currents in the horizontal planes which can not lead to vertical density transport.

The injection of buoyant fluid into a stratified environment leads to a certain layer deviation from the horizontal level. This phenomenon occurs immediately after injection starts, until the fluid reaches an equilibrium level. At this level the ambient density is equal to the density of the mixed fluid layer. After that moment the fluid propagates as a nonbuoyant fluid layer for a certain distance from the downstream wall. In our experiments we found this distance to be approximatively 1.0 m, consistent with the predictions of Browand and Winant (1972).

The experimental data were used to calibrate a numerical model which is able to simulate fluid injection into a stratified ambient fluid. Comparison of numerical and experimental results proved the capability of the numerical model to correctly simulate the fluid development. The validation of the present mathematical model offers an alternative approach for jet simulations in stratified flows. The intrinsic simplicity of this approach should be of some appeal for practical uses in engineering practice, mainly as a tool for the engineering solution of a wide class of environmental and industrial problems.

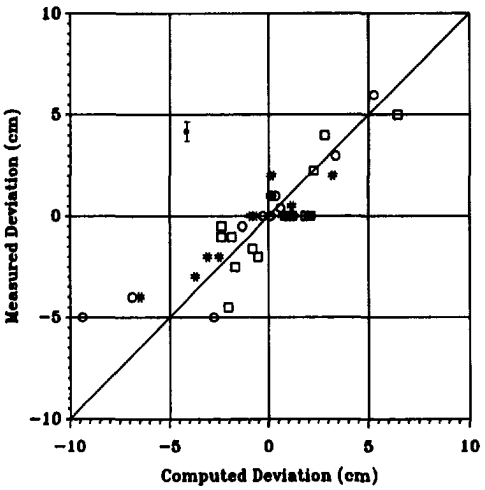

Fig. 10 Measured and computed vertical deviations

Acknowledgments

This study was funded by the Israel Ministry of Energy and Infrastructure, under contract no. 92-05-002/92-1-1 and by the Hydraulic and Structural Research Center of ENEL Spa. The material presented in this paper reports parts of M. Priven's D.Sc. thesis. M. Priven was supported by Nate H. and Beatrice G. Sherman Fellowship. J. Atkinson was supported by the Lady Davis Fellowship Trust Fund.

References

Atkinson, J. F., Adams, E. E., and Harleman, D. R., 1988, "Double-Diffusive Fluxes In a Salt Gradient Solar Pond," ASME *Journal of Solar Energy Engineering,* Vol. 34, No. 110, pp. 17–22.

Browand, F. K., and Winant, C. D., 1972, "Blocking Ahead of a Cylinder Miving in Stratified Fluid: An Experiment," *Geophysical Fluid Dynamics,* Vol. 4, pp. 29–53.

Johnstone, H. W., and Zangrando, F., 1988, "Mixing Depth of a Submerged Buoyant Jet," ASME *Journal of Solar Energy Engineering,* Vol. 110, pp. 125–131.

Manins, P. C., 1976, Intrusion Into a Stratified Fluid, *Journal of Fluid Mechanics,* Vol. 74, N. 3, pp. 547–560.

Maxworthy, T., 1972, Experimental and Theoretical Studies of Horizontal Jets in a Stratified Fluid, *International Symposium on Stratified Flows,* Novosibirsk.

Oster, G., 1965, "Density gradients," *Sci. Am.,* No. 213(2), pp. 70–79.

Priven, M., Atkinson, J., Bemporad, G. A., and Rubin, H., 1995, "Theoretical study of a laminar jet in a double-diffusion environment," ASME JOURNAL OF FLUIDS ENGINEERING, published in this issue, pp. XXX.

APPENDIX A

Construction of the Density Gradient

Different filling procedures were developed to establish the required gradients. The first procedure essentially adopts the Oster (1965) approach, where less dense fluid from a first tank is mixed with fluid of higher density in a second tank. The gradient zone is built by discharging one above the other layers of decreasing density from the second tank. These two tanks, named Tank 1 and Tank 2, were located above the flume. This first procedure was applied for experiments of type S, where only salinity concentration varies along the flume depth. For experiments of type T, where only temperature varies along the flume depth, this procedure was not applicable, and a different flume filling technique had to be implemented (see below).

A mathematical model was developed to set the main parameters which characterize the gradient zone filling as a function of time. We consider experiments of type S, but the analysis is identical when temperature variations are included to create a double-diffusion ambient fluid. At the beginning of each experiment Tank 1 and Tank 2 are filled with water of different salt concentrations C_1 and C_2, respectively. The salt concentrations in each tank are set according to the relationship

$$C_2 = C_1 - G_C Y_G \qquad (A.1)$$

where $G_C < 0$ is the required salinity gradient and Y_G is the required stratified zone depth. The flume is initially filled until a given level with water at concentration C_2. From this moment, say $t = 0$, fluid quantities from both Tank 1 and Tank 2 are mixed in tank M and then diverted to the water flume. The mass and solute conservation equations for tank M are

$$Q_M = Q_1 + Q_2$$

$$C_M = \frac{Q_1 C_1 + Q_2 C_2}{Q_M} \qquad (A.2a\text{-}b)$$

where Q_1 and Q_2 are the outflows from Tank 1 and Tank 2, respectively; Q_M is the outflow from tank M at concentration C_M. The infinitesimal level variations in the flume, caused by the water discharge Q_M, is

$$dy_F = \frac{Q_M}{A_F}\,dt \tag{A.3}$$

The concentration variation in time, required to set the given density gradient G_C, is therefore

$$\frac{dC_M}{dt} = \frac{G_C dy_F}{dt} = G_C \frac{Q_M}{A_F} \tag{A.4}$$

The flume is of rectangular shape, so that A_F is constant. In addition, we assume that the filling is done in such a manner that Q_M does not vary in time. Integration of the differential Eq. (A.4), subject to the initial condition $C_M = C_2$ for $t = 0$, leads to the following expression for the concentration variation in tank M.

$$C_M(t) = C_2 + G_C \frac{Q_M}{A_F}\,t \tag{A.5}$$

Introducing the mass and solute conservation equations (A.2) we obtain, after some algebric manipulations, the following explicit expressions for the discharges Q_1 and Q_2, diverted at time t into tank M from Tank 1 and Tank 2, respectively:

$$Q_1 = \frac{G_C}{C_1 - C_2}\frac{Q_M^2}{A_F}\,t$$

$$Q_2 = \left(1 - \frac{G_C}{C_1 - C_2}\frac{Q_M}{A_F}\,t\right)Q_M \tag{A.6a-b}$$

where

$$Q_M = \frac{V_G}{\tau} = \frac{A_F Y_G}{\tau}$$

V_G is the volume of water needed to fill the gradient zone, τ is the time required for filling the stratified zone; it is usually set according to operational considerations, and eventually determine the velocity of the gradient zone filling process. It should be noted that, according to Eq. (A.6), $Q_1 = 0$, $Q_M = Q_2$ for $t = 0$ and $Q_1 = Q_M$, $Q_2 = 0$ for $t = \tau$. The minimum volume content of tank 1 and 2, required for the filling of the gradient zone, may be determined by integrating Q_1 and Q_2 from $t = 0$ to $t = \tau$. Simple mathematical manipulation leads to

$$V_1 = V_2 = \tfrac{1}{2}V_G \tag{A.7}$$

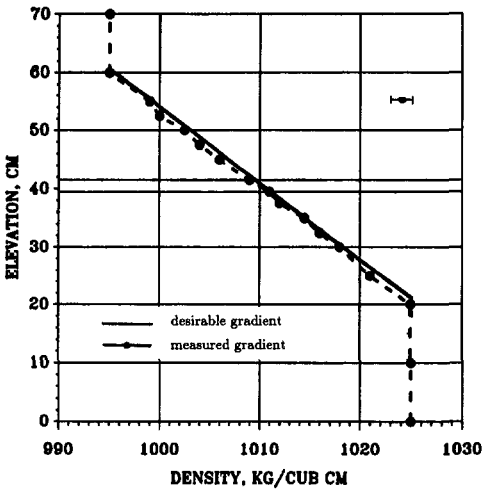

Fig. A.1 Desirable and measured densities in a salinity-stratified gradient zone after the flume filling

During the flume filling, to avoid turbulence water was discharged from the mixing tank to the flume through a floating raft. The filling time was usually kept equal to 3 hours. After every flume filling operation good agreement was recorded between the required and the measured density gradients. In Fig. A.1 both the required and measured density gradient are compared; this figure shows that density variations are well within the accuracy of the density measurement. The same procedure was applied to create a double-diffusive stratification, characterized by negative gradients of temperature and salinity.

The temperature gradient required for experiments of type T could be prepared by filling the laboratory flume with water of constant temperature up to a given level. Then, increasingly warmer water was diverted, mixing fluid from Tank 1 and Tank 2, to the flume through a floating raft. Because of the high heat diffusivity, heat diffuses rapidly downward creating a certain temperature gradient. Then, the required temperature gradient could be obtained by continuously discharging warm water and letting it overflow past a specified threshold. Temperature profiles were measured every 30 minutes until the central part of the stratified zone was located at the level of the jet exit.

The Vortical Structure of Parasitic Capillary Waves

(Data Bank Contribution)*

R. C. Y. Mui

D. G. Dommermuth

Naval Hydrodynamics Division,
Science Applications
International Corporation,
San Diego, CA 92121

A two-dimensional numerical simulation of the parasitic capillary waves that form on a 5 cm gravity-capillary wave is performed. A robust numerical algorithm is developed to simulate flows with complex boundary conditions and topologies. The free-surface boundary layer is resolved at the full-scale Reynolds, Froude, and Weber numbers. Seventeen million grid points are used to resolve the flow to within 6×10^{-4} cm. The numerical method is used to investigate the formation of parasitic capillary waves on the front face of a gravity-capillary wave. The parasitic capillary waves shed vorticity that induces surface currents that exceed twenty-five percent of the phase velocity of the gravity-capillary wave when the steepness of the parasitic capillary waves is approximately 0.8 and the total wave steepness is 1.1. A mean surface current develops in the direction of the wave's propagation and is concentrated on the front face of the gravity-capillary wave. This current enhances mixing, and remnants of this surface current are probably present in post-breaking waves. Regions of high vorticity occur on the back sides of the troughs of the parasitic capillary waves. The vorticity separates from the free surface in regions where the wave-induced velocities exceed the vorticity-induced velocities. The rate of energy dissipation of the gravity-capillary wave with parasitic capillaries riding on top is twenty-two times greater than that of the gravity-capillary wave alone.

1 Introduction

The formation of parasitic capillary waves was first measured by Cox (1958). Longuet-Higgins (1963) developed a theory based on the assumption that the parasitic capillary waves are steady in a frame of reference moving with the carrier wave. The potential-flow simulations of Dommermuth (1994b) show that the ripples are not steady and actually undergo a nonlinear recurrence. Perlin et al. (1993) also observe nonlinear recurrence in their experiments. In addition, nonlinear recurrence is observed in the model equation that Ferguson et al. (1978) use to study parasitic capillary waves.

Okuda et al. (1977) and Ebuchi et al. (1987) observe that a strong vortical region forms in the crest of steep wind-generated waves in the neighborhood of the parasitic capillary waves. Based on a boundary-layer theory, Longuet-Higgins (1992) argues that the source of the vortical region, which he calls a vortical roller, is the parasitic capillary waves. Longuet-Higgins shows that the peak vorticity values occur slightly aft of a capillary wave's trough and that a mean flux of vorticity is induced by the capillary waves. Based on momentum arguments, he determines that the resulting surface currents that would form beneath steep parasitic capillary waves can approach the phase speed of a gravity-capillary wave.

Based on an earlier investigation of vortex tubes interacting with a free surface (see Dommermuth, 1993), we make extensions to our method that enable us to resolve the free-surface boundary layer beneath very steep gravity-capillary waves. The new numerical algorithm is capable of imposing complex boundary conditions on a curved boundary. We use this new numerical capability to investigate the vortical structure of a 5 cm near-breaking gravity-capillary wave. This wavelength is shorter than the wave-lengths that Duncan et al. (1994) measure (≈80 cm) and Longuet-Higgins (1994) and Longuet-Higgins et al. (1993 and 1994) model (>40 cm). Our numerical simulations show that parasitic capillary waves are primarily responsible for the production of vorticity, whereas in the experiments of Duncan et al. (1994) and the analysis of Longuet-Higgins (1994), the formation of a cusp leads to flow separation.

Our numerical simulations of the formation of parasitic capillary waves on the front face of the 5 cm carrier wave is qualitatively similar to the experiments of Cox (1958), Chang et al. (1978), Perlin et al. (1993), and Lin and Rockwell (1995). Regions of high vorticity form in the troughs of the parasitic capillary waves. The vorticity induces strong surface currents down the face of the gravity-capillary wave. These surface currents may be an important mechanism for mixing of the upper few centimeters of the free surface.

2 Mathematical Formulation

2.1 Field Equations. Let $\mathbf{u} = \mathbf{u}(x, z, t) = (u, w)$ represent the two-dimensional velocity field as a function of time. Applying Helmholtz's theorem gives:

$$\mathbf{u} = \nabla\phi + \mathbf{U}, \tag{1}$$

where $\phi(x, z, t)$ is a velocity potential which describes the irrotational flow and $\mathbf{U}(x, z, t) = (U, W)$ is a solenoidal field which describes the vortical flow such that:

$$\nabla^2\phi = 0 \tag{2}$$

$$\nabla \cdot \vec{U} = 0. \tag{3}$$

Since ϕ satisfies Laplace's equation and the divergence of the rotational field ($\mathbf{U}$) is chosen to equal zero, the total velocity field ($\vec{u}$) conserves mass. Note that $\mathbf{U}$ may contain a portion

* Data have been deposited to the JFE Data Bank. To access the file for this paper, see instructions on p. 544 of this issue.

Contributed by the Fluids Engineering Division for publication in the JOURNAL OF FLUIDS ENGINEERING. Manuscript received by the Fluids Engineering Division May 31, 1994; revised manuscript received October 7, 1994. Associate Technical Editor: D. P. Telionis.

of the irrotational field depending on how the boundary conditions are defined.

Based on this Helmholtz decomposition of the velocity field, the total pressure Π is defined in terms of a rotational pressure P and an irrotational pressure as follows:

$$\Pi = P - \frac{\partial \phi}{\partial t} - \frac{1}{2}\nabla\phi\cdot\nabla\phi - \frac{1}{F_r^2}z. \quad (4)$$

Here, the pressure terms are normalized by ρU_c^2 where U_c is the characteristic velocity and ρ is the density. $F_r^2 = U_c^2/gL_c$ is the Froude number and L_c is the characteristic length. The vertical coordinate z is positive upward, and the origin is located at the mean free surface. Substituting these decompositions (1 and 4) into the Navier-Stokes equations gives:

$$\frac{D\mathbf{U}}{Dt} + ((\vec{U} - \vec{V} + \nabla\phi)\cdot\nabla)\mathbf{U} + (\mathbf{U}\cdot\nabla)\nabla\phi = -\nabla P + \frac{1}{R_e}\nabla^2\mathbf{U}, \quad (5)$$

where $D/Dt = \partial/\partial t + \mathbf{V}\cdot\nabla$ is a substantial time derivative, $\mathbf{V} = (X_t, Z_t)$ accounts for the motion of the interior flow due to the surface waves, $R_e = U_cL_c/\nu$ is the Reynolds number, and ν is the kinematic viscosity. The $\mathbf{V}$ terms are equivalent to the D'Alembert terms that occur in the equations of Dimas and Triantafyllou (1994).

The field equations and the boundary conditions for the velocity field are used to deduce the rotational pressure in the fluid and the behavior of the rotational pressure near the boundaries. The divergence of the momentum equations (5) used in combination with the mass-conservation equations (2 and 3) are used to derive a Poisson equation for the rotational pressure. This Poisson equation is subject to a solvability condition (see Dommermuth, 1994a).

2.2 Exact Free-Surface Boundary Conditions. Let the free-surface elevation be given by $z = \eta(x, y, t)$. The unit normal to the free surface is then given by

$$\vec{n} = \frac{(-\eta_x, 1)}{\sqrt{\eta_x^2 + \eta_y^2 + 1}}. \quad (6)$$

The Helmholtz decomposition of the velocity field requires an additional boundary condition to be prescribed on the free surface. We impose that the rotational velocity is zero on the free surface:

$$\mathbf{U}\cdot\mathbf{n} = 0. \quad (7)$$

This constraint means that the evolution of the free-surface elevation is entirely prescribed in terms of the free-surface elevation and the velocity potential as follows:

$$\frac{\partial\eta}{\partial t} + \eta_x\phi_x - \phi_z = 0, \quad (8)$$

where each term is evaluated on the free surface, $z = \eta$.

In addition to the two kinematic conditions (7 and 8), the normal and tangential stress conditions must also be satisfied on the free surface. The normal stress condition is

$$\frac{d\phi}{dt} + \frac{1}{2}(\phi_x^2 - \phi_z^2) + \eta_x\phi_x\phi_z + \frac{1}{F_r^2}\eta - P + \frac{2}{R_e}(n_zn_z(W_z + \phi_{zz}) + n_xn_z(W_x + U_z + 2\phi_{xz}) + n_xn_x(U_x + \phi_{xx})) = -P_a + \frac{1}{W_e}\frac{\eta_{xx}}{(1+\eta_x^2)^{3/2}}, \quad (9)$$

where $d/dt = \partial/\partial t + \eta_t\phi_z$ is a substantial time derivative, P_a is the atmospheric pressure, $W_e = \rho U_c^2L_c/T$ is the Weber number, T is the surface tension, and (n_x, n_z) are the xz-components of the unit normal.

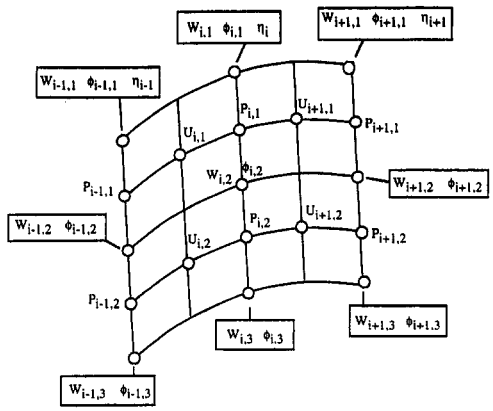

Fig. 1 The fully-staggered grid

For a clean free surface, the tangential stress condition is

$$(U_z + W_x + 2\phi_{xz})(n_zn_z - n_xn_x) + 2(U_x - W_z + \phi_{xx} - \phi_{zz})n_xn_z = 0. \quad (10)$$

The tangential stress boundary conditions can be modified to account for surfactants as shown by Dommermuth (1993).

3 Numerical Formulation

The momentum Eqs. (5), kinematic condition (8), and the normal stress condition (9) are integrated with respect to time using a third-order Runge-Kutta scheme. Each stage of the Runge-Kutta scheme is formulated to inhibit the accumulation of errors in the divergence of the rotational flow field. The rotational pressure is used to project the rotational velocity onto a solenoidal field with zero normal velocity on the free surface (7). Laplace's equation for the potential (2) and Poisson's equation for the rotational pressure are solved at each stage of the Runge-Kutta scheme, and a solvability condition is enforced for the rotational pressure. A multigrid solution scheme is used to solve the three-dimensional elliptic equations. Periodic boundary conditions are used on the sides of the domain and a free-slip boundary condition is used on the bottom.

3.1 Gridding. Figure 1 illustrates the fully-staggered grid that is used in the numerical simulations. The solenoidal velocities (U, W) and the rotational pressure (P) are staggered relative to each other. The grid spacing is evenly spaced along the horizontal (x) and vertical (z) directions. As a reference point, the position of the grid points for the velocity potential are provided below:

$$x_{i,k} = i\Delta x$$
$$z_{i,k} = \eta_i - \Delta z_i(k-1), \quad (11)$$

where $i = 1, I_{max}$ and $k = 1, K_{max}$ are the indices along the x- and z-axes, respectively. η_i is the free-surface elevation at $x = i\Delta x$. The grid spacings are $\Delta x = L/I_{max}$ and $\Delta z_i = (\eta_i + D)/(K_{max} - 1)$, where L is the length and D is the depth.

3.2 The TAME Algorithm. The numerical simulation of near-breaking waves at full scale is difficult because the wave steepness is order one, and the various length and time scales are disparate. The free-surface boundary layer is difficult to resolve since it is very thin relative to the wave-length and the wave amplitude. The free-surface boundary conditions are also difficult to impose on the exact position of the free surface, especially the tangential-stress condition (10).

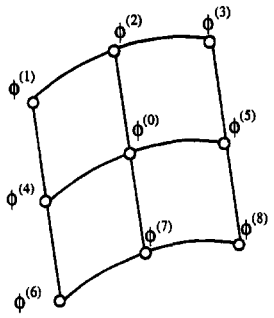

Fig. 2 Nine-point stencil for the evaluation of the Laplacian

The numerical simulation of near-breaking waves required the development of a new numerical algorithm named **T**aylor's **A**ccurate **M**ethod of **E**valuation (TAME). TAME uses Taylor series expansions to evaluate functions and their derivatives directly in physical space. The TAME algorithm can have second- or higher-order accuracy, even on unstructured grids. The accuracy of the TAME algorithm is not sensitive to grid irregularities, grid stretching, or grid coarsening. TAME permits the evaluation of nonanalytic functions, and it can incorporate boundary conditions that are arbitrarily complex. TAME can be used to calculate derivatives, to perform interpolation, extrapolation, and smoothing, to provide upwind biasing, and to enforce boundary conditions. TAME applies equally well to two- and three-dimensional problems.

3.3 A TAME Laplacian. The stencil that is used to evaluate a TAME Laplacian is illustrated in Fig. 2. The Laplacian operator is required in the Laplace equation for the velocity potential (2), the viscous diffusion terms (5), and the Poisson equation for the vortical pressure.

As an example of TAME's implementation, consider the Taylor-series expansion of the velocity potential:

$$\phi^{(i)} = \phi^{(0)} + \Delta x_i \phi_x^{(0)} + \Delta z_i \phi_z^{(0)} + \frac{\Delta x_i^2}{2}\phi_{xx}^{(0)} + \Delta x_i \Delta z_i \phi_{xz}^{(0)} + \frac{\Delta z_i^2}{2}\phi_{zz}^{(0)} + \frac{\Delta x_i^3}{6}\phi_{xxx}^{(0)} + \frac{\Delta x_i^2 \Delta z_i}{2}\phi_{xxz}^{(0)} + \frac{\Delta x_i \Delta z_i^2}{2}\phi_{xzz}^{(0)} + \frac{\Delta z_i^3}{6}\phi_{zzz}^{(0)} + \frac{\Delta x_i^4}{24}\phi_{xxxx}^{(0)} + \frac{\Delta x_i^3 \Delta z_i}{6}\phi_{xxxz}^{(0)} + \frac{\Delta x_i^2 \Delta z_i^2}{4}\phi_{xxzz}^{(0)} + \frac{\Delta x_i \Delta z_i^3}{6}\phi_{xzzz}^{(0)} + \frac{\Delta z_i^4}{24}\phi_{zzzz}^{(0)}, \quad (12)$$

where $\phi^{(0)}$ is the value of ϕ at the Taylor-expansion point, $\phi^{(i)}$ are the values at neighboring points, and $\Delta x_i = x^{(i)} - x^{(0)}$ and $\Delta z_i = z^{(i)} - z^{(0)}$ are offsets in the horizontal and vertical directions, respectively.

On the nine-point stencil that is illustrated in Figure 2, second-order approximations to $\phi_x^{(0)}$, $\phi_z^{(0)}$, $\phi_{xx}^{(0)}$, $\phi_{xz}^{(0)}$, and $\phi_{zz}^{(0)}$ are obtained by selectively solving for terms ($\phi_x^{(0)}$, $\phi_z^{(0)}$, $\phi_{xx}^{(0)}$, $\phi_{xz}^{(0)}$, $\phi_{zz}^{(0)}$, $\phi_{xxz}^{(0)}$, $\phi_{xzz}^{(0)}$, and $\phi_{xxzz}^{(0)}$) in the Taylor-series expansion as illustrated below:

$$\begin{vmatrix} \Delta x_1 & \cdots & \frac{\Delta x_1^2 \Delta z_1^2}{4} \\ \vdots & & \vdots \\ \Delta x_8 & \cdots & \frac{\Delta x_8^2 \Delta z_8^2}{4} \end{vmatrix} \begin{vmatrix} \frac{\partial \phi^{(0)}}{\partial x} \\ \vdots \\ \frac{\partial^4 \phi^{(0)}}{\partial x^2 \partial z^2} \end{vmatrix} = \begin{vmatrix} \phi^{(1)} - \phi^{(0)} \\ \vdots \\ \phi^{(8)} - \phi^{(0)} \end{vmatrix} \quad (13)$$

If the velocity potential, i.e., $\phi^{(i)}$, is known, this procedure provides its derivatives, including the Laplacian, at all of the grid points. If, however, the solution to a boundary-value problem is required, then the Laplace operator must be expressed in terms of the neighbors of $\phi^{(0)}$:

$$\phi_{xx}^{(0)} + \phi_{zz}^{(0)} = \sum_{i=1}^{8} c_i (\phi^{(i)} - \phi^{(0)}), \quad (14)$$

where the coefficients, c_i, are derived by inverting the equations in Eq. (13). This stencil for the interior points of the velocity potential is supplemented with other stencils near the boundaries to impose either Dirichlet, Neumann, or mixed boundary conditions. The resulting boundary-value problem is amenable to iterative solution procedures because the diagonal and the off-diagonal terms are multiplied by the same coefficients, which promotes diagonal dominance.

The TAME algorithm requires Gaussian elimination with partial pivoting to be performed at each grid point. This operation is performed in parallel on the CM-5 computer. As noted by Dr. Edwin P. Rood in a private communication, an additional gain in efficiency could be realized by building a special computer chip to solve the TAME low-order systems-of-equations.

3.4 A TAME Treatment of the Free Surface. The TAME algorithm has been developed primarily to treat the tangential-stress boundary condition on the free surface (see Eq. 10). Figure 3 illustrates the stencil that is required to evaluate the viscous diffusion terms with the tangential-stress condition imposed. Ten samples of the U-velocity grid and eleven samples of the W-velocity grid are required for second-order accuracy on a curved free surface. (Note that $U^{(1)}$, which appears in the stress condition, is not on the U-velocity grid.) $U^{(2)}, U^{(3)}, \ldots, U^{(10)}$ and $W^{(1)}, W^{(2)}, \ldots, W^{(10)}$ are expanded about the locations of the points $U^{(0)}$ and $W^{(0)}$, respectively, as shown in Eq. (12). The tangential-stress boundary condition is also expanded in a Taylor series about the same two points:

$$(U_z^{(0)} + \Delta x_1 U_{xz}^{(0)} + \Delta z_1 U_{zz}^{(0)} + \ldots + W_x^{(0)})(n_z^2 - n_x^2) + 2(U_x^{(0)} + \Delta x_1 U_{xx}^{(0)} + \Delta z_1 U_{xz}^{(0)} + \ldots - W_z^{(0)}) n_x n_z = -2\phi_{xz}^{(o)}(n_z^2 - n_x^2) - 2(\phi_{xx}^{(o)} - \phi_{zz}^{(o)}) n_x n_z.$$

The Taylor-series terms that are eliminated for both $U^{(0)}$ and $W^{(0)}$ include the x-, z-, xx-, xz-, zz-, xxx-, xxz-, xzz-, zzz-, and $xxzz$-derivatives. This leads to twenty independent equations for derivatives of $U^{(0)}$ and $W^{(0)}$ near the free surface. The diffusion terms are evaluated as $(U_{xx}^{(0)} + U_{zz}^{(0)})/\mathrm{R_e}$ and $(W_{xx}^{(0)} + W_{zz}^{(0)})/\mathrm{R_e}$ and they are then inserted into the Navier-Stokes equations (5). The points that are in the interior of the fluid

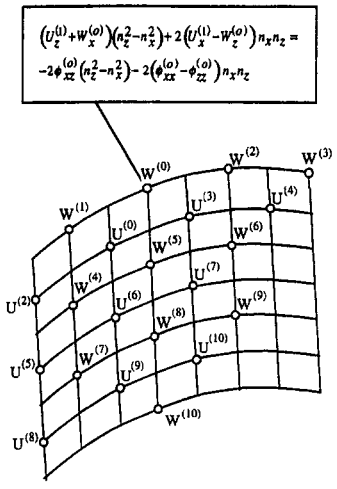

Fig. 3 Stencil for viscous diffusion terms with tangential-stress condition imposed

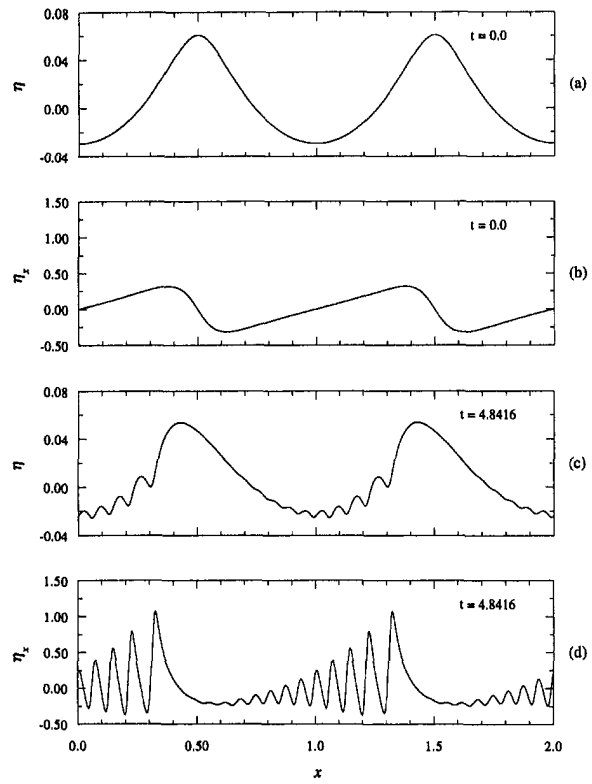

Fig. 4 Formation of ripples on a 5 cm gravity-capillary wave. Parts (a) and (b) plot the initial free-surface elevation and slope. Parts (c) and (d) plot the same quantities at time $t = 4.8416$. The x-axis has been periodically extended.

are evaluated using the nine-point stencil that we have discussed in the previous section.

3.5 Numerical Accuracy and Computations. The second-order accuracy of every TAME subroutine is tested by prescribing as input a quantity that has a known solution. The accuracy and the convergence rates of the elliptic solvers are also tested using known solutions. For a 4096×4097 grid, the elliptic solvers converge to machine accuracy using only sixteen iterations of V-cycle multigrid and ten iterations of a damped Jacobi smoother per V-cycle. The validated TAME tools are combined to simulate free-surface waves. The final assembled code is tested using exact Stokes waves as initial conditions. Convergence and validation studies are available in the JFE Data Bank.

4 Numerical Results

4.1 The Initial Conditions. We examine the formation of parasitic capillary waves on the front face of a 5 cm gravity-capillary wave. Let the characteristic length and velocity be denoted by $L_c = \lambda$ and $U_c = \sqrt{g\lambda}$, respectively, where λ is the length of the gravity-capillary wave and g is gravity. Then the Froude, Weber, and Reynolds numbers are $F_r = 1$, $W_e = \rho g \lambda^2 / T$, and $R_e = g^{1/2}\lambda^{3/2}/\nu$, where ρ is the fluid density, T is the surface tension, and ν is the kinematic viscosity. For our numerical simulation of a 5 cm wave, $F_r = 1$, $W_e = 331$, and $R_e = 35{,}000$.

The two-dimensional numerical simulation is initialized using an exact solution for a gravity wave. The exact solution for the gravity wave is based on a numerical procedure that is similar to Schwartz's (1974) algorithm. The parasitic capillaries are generated from rest due to a parametric resonance. Figure 4 illustrates the formation of ripples on a 5 cm gravity-capillary wave. The wave profile is initially smooth, but ripples naturally form as a result of nonlinearities in the governing equations. Longuet-Higgins (1963) shows that this phenomenon is irrotational.

The initial steepness of the gravity wave is 0.2827, and the mean depth is equal to one quarter of a wave length. In our simulation, we initially use an inviscid boundary-layer formulation (see Dommermuth, 1994b). After the parasitic capillary waves have reached their maximum steepness at time $t = 4.5$, we switch to full Navier-Stokes solutions. The free-surface elevation and the velocity potential from the inviscid formulation are used as initial conditions for the Navier-Stokes formulation. At first, we use a moderate resolution Navier-Stokes solution. Later, we switch to high resolution Navier-Stokes solutions to establish convergence. The inviscid formulation enabled us to take larger time steps with a lower resolution than is possible with the fully-resolved Navier-Stokes formulation. We use 512×129 grid points for the inviscid simulation and 2048×513, 4096×1025, and 8192×2049 grid points for the viscous simulations. The time step of the inviscid simulation is $\Delta t = 3.75 \times 10^{-3}$, and the time steps of the viscous simulations are $\Delta t = 8.0 \times 10^{-4}$, $\Delta t = 1.0 \times 10^{-4}$, and $\Delta t = 4.0 \times 10^{-5}$, respectively. Low-pass filtering of the free-surface elevation and the velocity potential permits larger time steps to be taken than is possible without low-pass filtering.

Surface vorticity will form whenever there is flow near a curved free surface (Longuet-Higgins, 1992). This creation of surface vorticity is used to check the accuracy of our Navier-Stokes simulation as described in the next section. The free-surface boundary-layer develops from rest as the surface vorticity diffuses into the bulk of the flow.

Based on a boundary-layer thickness $\delta^2 = 2/(R_e\sigma)$, where $\sigma^2 = 2\pi$ is the wave frequency, the resolutions of the boundary layer used in the Navier-Stokes simulations are ten, twenty, and forty grid points. We are currently developing a capability that would permit even higher resolution of the free-surface boundary layer by using grid stretching. However, the present capability, with no grid stretching, is useful for investigating the effects of turbulence on the formation of parasitic capillary waves.

The calculation of sixteen hundred time steps of the inviscid boundary-layer formulation with 512×129 grid points required three hours on the 256-node partition on the CM-5 at the University of Minnesota Army High Performance Computing Research Center. The calculation of four hundred time steps of the Navier-Stokes formulation with 2048×513 grid points required six hours, two hundred time steps of the 4096×1025 simulation required eight hours, and forty time steps of the 8192×2049 simulation required four hours.

4.2 The Vortical Structure. Figure 4 illustrates the formation of ripples on a 5 cm gravity-capillary wave. Parts (a) and (b) show the initial free-surface elevation and slope. Parts (c) and (d) show the same quantities at time $t = 4.8416$. The x-axis has been periodically extended to double the horizontal extent of the computational domain. The wave is propagating from right to left. The numerically-predicted train of parasitic waves appears similar to the laboratory measurements of Cox (1958), Chang et al. (1978), Perlin et al. (1993), and Lin and Rockwell (1995) who measure wavelengths of about 5, 6–12, 6–10, and 8.8 cm, respectively.

The initial wave steepness is approximately $\epsilon \approx 0.3$. When the parasitic capillary waves form, the steepness increases to $\epsilon \approx 1.2$. The formation of parasitic capillary waves leads to a significant increase in the rate of wave energy dissipation. The rate of wave energy dissipation is

$$\frac{dE_w}{dt} = \frac{dE_{\phi\phi}}{dt} + \frac{dE_{\eta\eta}}{dt} + \frac{dE_s}{dt},$$

where E_w is the total wave energy, $E_{\phi\phi}$ is the wave kinetic energy, $E_{\eta\eta}$ is the wave potential energy, and E_s is the wave superficial energy.

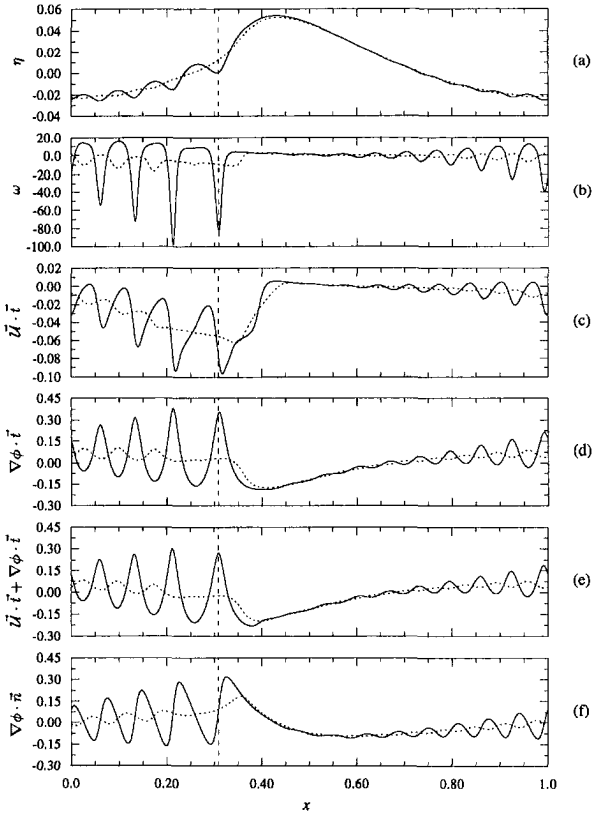

Fig. 5 Free-surface quantities. (a) Free-surface elevation. (b) Vorticity. (c) Tangential component of the solenoidal velocity field. (d) Tangential component of the potential velocity field. (e) Tangential component of the total velocity field. (f) Normal component of the total velocity field.

According to the linearized theory of Lamb (1932),

$$\frac{dE_w}{dt} = -4\,\frac{k^2}{\mathrm{R_e}}\,E_w(t=0),$$

where $k = 2\pi$ is the wavenumber of the gravity-capillary wave. Based on the present numerical results, dE_w/dt is twenty-two times greater with parasitic capillary waves than without them. This result agrees with that of Longuet-Higgins (1962), who estimated an order of magnitude increase for a 6 cm carrier wave.

Figure 5 shows the following quantities on the free surface at time $t = 4.8416$: (a) the free-surface elevation, (b) the vorticity, (c) the tangential component of the solenoidal velocity field, (d) the tangential component of the potential velocity field, (e) the tangential component of the total velocity field, and (f) the normal component of the total velocity field. The normal component of the total velocity field is equal to the normal component of the potential velocity field because the normal component of the solenoidal velocity field is zero. The dashed horizontal curves are 401-point moving averages along the x-axis. The dashed vertical lines indicate the locations of the minima of the surface vorticity. The direction of the tangent ($\mathbf{t}$) is in the direction of wave propagation.

The extrema of the vorticity occur slightly aft of the wave troughs of the parasitic capillary waves, which agrees with the capillary-wave boundary-layer theory of Longuet-Higgins (1992). The extreme minima in vorticity occur behind the troughs because the wavy portion ($\nabla\phi$) of the flow sweeps the vorticity back and up against the troughs. Figure 5d shows that the wave-induced tangential velocities are positive in the troughs, in the opposite direction of wave propagation. Figure 5f shows that normal velocity is positive behind the troughs, i.e., upward on the right-hand sides of the troughs. These two components of velocity push the vorticity back and up against the troughs of the parasitic capillary waves.

Longuet-Higgins (1992) argues that a vortical roller forms at the wave crest due to vorticity diffusing from beneath the parasitic capillary waves. According to Longuet-Higgins, the surface currents that are induced by this type of vortical roller are in the direction of wave propagation. In Fig. 5c, our numerical simulations show that the surface currents induced by the vorticity are down the face of the wave. At the crest of the gravity-capillary wave (see Fig. 5c) for $0.40 \le x \le 0.50$), our numerical simulations show that the vorticity induces a very weak current that is in the opposite direction of wave propagation, which disagrees with Fig. 12 in Longuet-Higgins' paper. Compared to the magnitude of the vorticity that occurs near the troughs of the parasitic capillary waves, the vorticity in the crest of the gravity-capillary wave is very weak, and its sign is the opposite of what Longuet-Higgins (1992) indicates in his Fig. 12. We conjecture that a strong vortical roller with a sign that corresponds to the results of Longuet-Higgins (1992) and the wind-wave experiments of Ebuchi et al. (1987), could form under the action of wind or when flow separation occurs, but without wind or flow separation there is no strong vortical roller at the crest of a gravity-capillary wave. The mere diffusion of vorticity from beneath the parasitic capillary waves does not appear to be a strong mechanism for generating a vortical roller.

Longuet-Higgins et al. (1993, 1994) show that an inviscid instability could lead to the formation of a cusp-like feature near the crest of a steep gravity wave. (The gravity waves that Longuet-Higgins et al. (1993, 1994) analyze are longer (>40 cm) than the 5 cm wave that we have simulated.) If the flow separates beneath the cusp, as Duncan et al. (1994) observe in their experiments, then Duncan et al. (1994) and Longuet-Higgins (1994) argue that a shear-layer instability could lead to the formation of long capillary waves and spilling. This type of mechanism for spilling breaking is different from the mechanism that appears in our numerical simulations. In our numerical simulations, there is no cusp and no flow separation. However, the formation of steeper parasitic capillary waves than we simulate in this paper could lead to flow separation. Longuet-Higgins, in a private communication, suggests that another type of spilling may be caused by parasitic capillary waves becoming so steep that they pinch off a bubble of air and the flow separates. Our numerical simulations appear to show the early stages of this type of spilling event.

The mean vorticity on the front face of the wave is negative as illustrated by the dashed curve in Fig. 5b. The negative mean vorticity gives a mean tangential velocity that is down the face of the gravity-capillary wave. The mean surface current down the face is observed in Fig. 5c. We conjecture that as the wave steepens and the vorticity becomes stronger, the tangential velocity that is induced by the vortical portion ($\mathbf{U}\cdot\mathbf{t}$) of the flow may cancel the tangential velocity that is induced by the wavy portion of the flow ($\nabla\phi\cdot\mathbf{t}$). We observe that $\mathbf{U}\cdot\mathbf{t}$ is ninety degrees out-of-phase with $\nabla\phi\cdot\mathbf{t}$. Although $\mathbf{U}\cdot\mathbf{t}$ oscillates, it is almost completely negative and has a mean negative value. $\nabla\phi\cdot\mathbf{t}$ oscillates positive and negative about the positive mean value that is induced by the gravity-capillary wave.

Figure 5c shows that the tangential velocity induced by the vortical portion of the flow is negative, in the direction of wave propagation. For very steep waves, $\mathbf{U}\cdot\mathbf{t}$ will be directly downward in the troughs of the parasitic capillary waves and $\nabla\phi\cdot\mathbf{t}$ will be upward. If the magnitude of $\mathbf{U}\cdot\mathbf{t}$ exceeds $\nabla\phi\cdot\mathbf{t}$, a vortex will be swept down into the fluid. Figure 5e shows that $\mathbf{U}\cdot\mathbf{t}$ reduces $\nabla\phi\cdot\mathbf{t}$ at the troughs and increases it at the crests of the parasitic capillary waves. Once the vortex is outside the boundary layer, the potential portion of the flow will sweep it back toward the crest of the gravity-capillary wave.

The mean surface currents that are induced by vorticity are represented by the dashed lines in Fig. 5c. Remnants of the surface currents are probably present even after the wave spills.

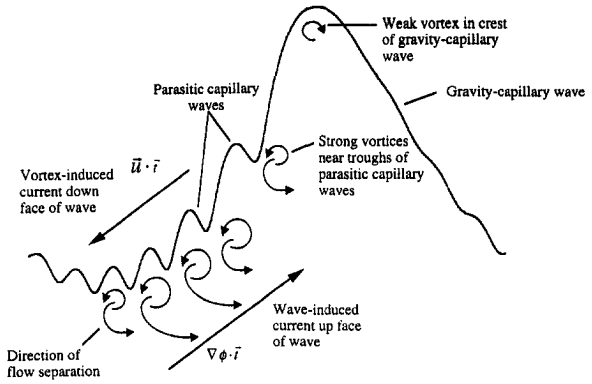

Fig. 6 The vortical structure and the velocity field of a near-breaking gravity-capillary wave with no wind effects

Since $\mathbf{U}\cdot\mathbf{t}$ is down into the fluid when the parasitic capillary waves are very steep, it contributes to the transfer of energy, momentum, heat, and gases into the bulk of the fluid and the mixing of the upper few centimeters of the boundary-layer.

Duncan et al. (1994) conjecture that an instability occurs on a shear layer that is located between two layers of fluid, one immediately below the capillary waves, and one slightly deeper. In the layer immediately below the capillary waves, the flow appears to be moving down the face in their experiments. This layer of fluid would correspond to $\mathbf{U}\cdot\mathbf{t}$ in our numerical simulations. In the slightly deeper layer, the flow is moving up the face of the wave. This deeper layer of fluid corresponds to $\nabla\phi\cdot\mathbf{t}$. We differ with Duncan et al., however, in that our numerical simulation of a 5 cm wave shows that the flow separates near the troughs of the parasitic capillary waves. This mechanism differs from the shear-layer instability of Duncan, et al., who observe flow separation at the cusp of a 80 cm wave. Figure 6 summarizes our results.

Figure 7 compares the free-surface vorticity as predicted by numerics to theory. The theory is based on the analyses of Longuet-Higgins (1992) and Wu (1995). According to theory, the surface vorticity (ω^s) is a function of the total normal velocity (u_n), the total tangential velocity (u_t), and the surface curvature (κ):

$$\omega^s = -2\left(\frac{\partial u_n}{\partial t} + \kappa u_t\right), \qquad (15)$$

In this theory, the surface vorticity is dominated by the potential portion of the flow because the solenoidal portion is small. The surface vorticity can be calculated using two different methods: first, using Eq. (15) and second, using the definition of vorticity ($\omega^s = \nabla \times U$ evaluated on $z = \eta$). As a result, Eq. (15) can be used to check how well the free-surface boundary-layer is

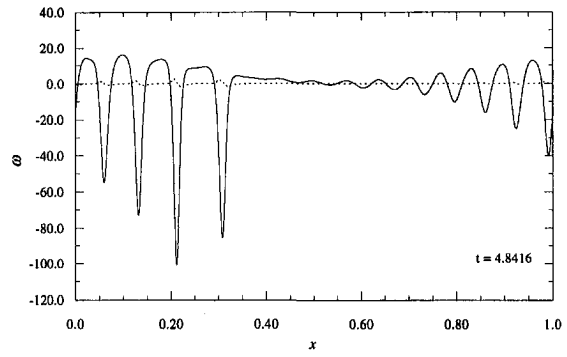

Fig. 7 Free-surface vorticity. Numerical predictions are denoted by a solid line and the difference between numerical and theoretical predictions is denoted by a dashed line.

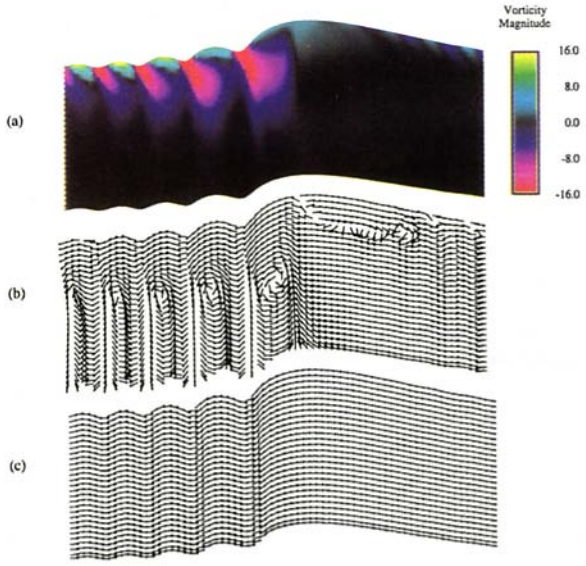

Fig. 8 The subsurface structure of parasitic capillary waves. (a) Vorticity. (b) Solenoidal velocity field. (c) Potential velocity field.

resolved in a numerical simulation. As shown in Fig. 7, the numerical predictions of the surface vorticity agree very well with theory. The relative error between numerical and theoretical predictions is less three percent for our highest resolution simulation.

Figure 8 shows the vorticity and velocity fields at time $t = 4.84$. Figure 8a shows the vorticity field, Fig. 8b shows the solenoidal velocity field in a fixed frame of reference, and Fig. 8c shows the potential velocity field in a frame of reference moving with the wave. The wave is propagating from right to left. The tops of the figures correspond to the free surface, and the figures are four boundary-layer thicknesses deep based on a boundary-layer thickness $\delta^2 = 2/(\mathrm{R}_e\sigma)$. In real physical units the figures are about 1 mm deep. About three-quarters of a wavelength is shown in Fig. 8. The maximum vector magnitudes in Figs. 8b and 8c are 0.80 and 0.096, respectively. The streamlines are parallel to the free surface in Fig. 8c because the flow is nearly steady. As shown in Fig. 8b, the streamlines are parallel to the free surface because the component of the vortical flow that is normal to the free surface is zero by construction.

As shown in Fig. 8a, there are strong vortices beneath the troughs of the parasitic capillary waves and a weak separation zone in the crest of the gravity-capillary wave, which is clearly visible in Fig. 8b. For a longer wave than we simulate, Professor Longuet-Higgins (1992) predicts that vorticity diffusing from beneath the parasitic capillary waves would lead to the formation of a vortical roller in the crest of gravity-capillary wave with a different sign than what is observed in Fig. 8b. Longuet-Higgins (1992) predictions are based on laminar-flow analysis with no flow separation. We conjecture that wind stress or flow separation from beneath parasitics or a cusp could lead to the formation of a vortical roller that would have the same sign as what is observed in laboratory studies of wind-wave generation. However, in the absence of wind and if the flow has not separated, the sign of the vorticity is as illustrated in Figs. 8a and 8b. These numerical results agree qualitatively with the experimental results of Lin and Rockwell (1995), who used Digital Particle Image Velocimetry to calculate the vorticity beneath the parasitic capillary waves. The signs of the vorticity that Lin and Rockwell (1995) measure agree with our numerical predictions.

Figure 8b clearly shows the circulation zones that exist beneath parasitic capillary waves. The circulation zones may be

an important mechanism for mixing the upper few centimeters of the free-surface boundary layer.

5 Conclusions

Parasitic capillary waves form on the front face of steep gravity-capillary waves. Regions of high vorticity are located near the troughs of the parasitic capillary waves. The vorticity induces strong surface currents. For very steep parasitic capillary waves ($\epsilon > 2$), the surface currents can become so strong that the flow separates and injects vorticity into the fluid below the troughs of the parasitic capillary waves. This injection of vorticity convects energy, momentum, heat, and air bubbles below the free surface. The parasitic capillary waves can become so steep that the flow separates beneath them and they pinch off a bubble of air.

JFE Data Bank Contribution

The convergence properties of the TAME numerical algorithm have been deposited in the JFE Data Bank. The numerical convergence is illustrated using a combination of energy and enstrophy conservation laws, experimental and analytic results, and enforcement of selected free-surface boundary conditions.

Acknowledgments

The development of our free-surface capability is financially supported by ONR under contract number N00014-93-C-0046 with Dr. Edwin P. Rood as program manager. This work is also supported in part by the Army Research Office contract number DAALO3-89-C0038 with the University of Minnesota Army High Performance Computing Research Center (AHPCRC) and the DoD Shared Resource Center at the AH-PCRC. The numerical simulations have been performed on the CM-5 computers at Naval Research Laboratory and the AHPCRC.

References

Chang, J. H., Wagner, R. N., and Yuen, H. C., 1978, "Measurement of High Frequency Capillary Waves on Steep Gravity Waves," *Journal of Fluid Mechanics,* Vol. 86, pp. 401–413.

Cox, C. S., 1958, "Measurements of Slopes of High-Frequency Wind Waves," *Journal of Marine Research,* Vol. 16, pp. 199–225.

Dimas, A. A., and Triantafyllou, G. S., 1994, "Non-linear Interaction of Shear Flow with a Free Surface," *Journal of Fluid Mechanics,* Vol. 260, pp. 211–246.

Dommermuth, D. G., 1993, "The Laminar Interactions of a Pair of Vortex Tubes with a Free Surface," *Journal of Fluid Mechanics,* Vol. 246, pp. 91–115.

Dommermuth, D. G., 1994a, "The Initialization of Vortical Free-Surface Flows," ASME JOURNAL OF FLUIDS ENGINEERING, Vol. 116, pp. 95–102.

Dommermuth, D. G., 1994b, "Efficient Simulation of Short- and Long-Wave Interactions with Applications to Capillary Waves," ASME JOURNAL OF FLUIDS ENGINEERING, Vol. 116, pp. 77–82.

Dommermuth, D. G., and Novikov, E. A., 1993, "Direct-Numerical and Large-Eddy Simulations of Turbulent Free-Surface Flows," *Proceedings of the 6th International Conference on Numerical Ship Hydrodynamics,* Iowa City, to appear.

Dommermuth, D. G., Novikov, E. A., and Mui, R. C. Y., 1994, "The Interaction of Surface Waves with Turbulence," *Proceedings of the ASME Symposium on Free-Surface Turbulence,* Lake Tahoe, to appear.

Duncan, J. H., Philomin, V., Behres, M., and Kimmel, J., 1994, "The Formation of Spilling Breaking Waves," *Physics of Fluids,* Vol. 6, pp. 2558–2560.

Ebuchi, N., Kawamura, H., and Toba, Y., 1987, "Fine Structure of Laboratory Wind-Wave Surfaces Studied Using an Optical Method," *Boundary-Layer Methods,* Vol. 39, pp. 133–151.

Ferguson, W., Saffman, P., and Yuen, H., 1978, "A Model Equation to Study the Effects of Nonlinearity, Surface Tension, and Viscosity in Water Waves," *Studies in Applied Mathematics,* Vol. 58, pp. 165–185.

Lamb, H., 1932, *Hydrodynamics,* Dover.

Lin, J. C., and Rockwell, D., 1994, "Evolution of a Quasi-Steady Breaking Wave," Submitted for publication.

Longuet-Higgins, M. S., 1963, "The Generation of Capillary Waves by Steep Gravity Waves," *Journal of Fluid Mechanics,* Vol. 16, pp. 138–159.

Longuet-Higgins, M. S., 1992, "Capillary Rollers and Bores," *Journal of Fluid Mechanics,* Vol. 240, pp. 659–679.

Longuet-Higgins, M. S., 1994, "Shear Instability in Spilling Breakers," *Proceedings of the Royal Society of London Series A,* Vol. 446, pp. 399–409.

Longuet-Higgins, M. S., and Cleaver, R. P., 1993, "Crest Instabilities of Gravity Waves, 1. The Almost Highest Wave," *Journal of Fluid Mechanics,* Vol. 258, pp. 115–130.

Longuet-Higgins, M. S., Cleaver, R. P., and Fox, M. J. H., 1994, "Crest Instabilities of Gravity Waves, 2. Matching and Asymptotic Analysis," *Journal of Fluid Mechanics,* Vol. 259, pp. 333–344.

Okuda, K., Kawai, S., and Toba, Y., 1977, "Measurements of Skin Friction Distribution Along the Surface of Wind Waves," *Journal of the Oceanography Society of Japan,* Vol. 33, pp. 190–198.

Perlin, M., Lin, H., and Ting, C.-L., 1993, "On Parasitic Capillary Waves Generated by Steep Gravity Waves: an Experimental Investigation with Spatial and Temporal Measurements," *Journal of Fluid Mechanics,* Vol. 255, pp. 597–620.

Schwartz, L. W., 1974, "Computer Extension and Analytic Continuation of Stokes' Expansion for Gravity Waves," *Journal of Fluid Mechanics,* Vol. 62, pp. 553–578.

Wu, J. Z., 1995, "A Theory of Three-Dimensional Interfacial Vorticity Dynamics," The University of Tennessee Space Institute, Report No. 95-01.

J. Y. Kim*

M.-C. Lai
Associate Professor.
Mem. ASME

Mechanical Engineering Department,
Wayne State University,
Detroit, MI 48202

P. Li

G. K. Chui

Ford Motor Company,
Scientific Research Laboratory,
Dearborn, MI 48121

Flow Distribution and Pressure Drop in Diffuser-Monolith Flows

Most current automotive catalytic converters use diffusers to distribute the flow field inside the monolithic bricks where catalysis takes place. While the characteristics and performance of a simple diffuser flow are well documented, the influence of downstream brick resistance is not clear. In this paper, the trade-off between flow-uniformity and pressure drop of an axisymmetric automotive catalytic converters is studied numerically and experimentally for selected cases. The monolithic brick resistance is formulated from the pressure gradient of fully developed laminar duct-flow and corrected for the entrance effect. The monolithic brick downstream stabilizes the diffuser flows both physically and computationally. A distribution index was formulated to quantify the degree of nonuniformity in selected test cases. The test matrix covers a range of different diffuser angles and flow resistance (brick types). For simplicity, an axisymmetric geometry is chosen. Flow distribution within the monolith was found to depend strongly on diffuser performance, which is modified strongly by brick resistance. Pressure drop due to the headers and brick resistance and their relative roles is also identified. The implications of these data for converter design are discussed in terms of the trade-off between flow-uniformity and pressure drop.

Introduction

Monolithic catalytic converters have been used extensively in automobiles to comply with the limits imposed on pollutant emissions. Much effort has been devoted to design and development to improve the catalyst-gas conversion efficiency of catalytic converters. This efficiency, from a fluid dynamics point of view, depends strictly on the mass transfer rate between gas and catalysts, which is dominated by the influence of the gas flow field at the monolith inlet section, including inlet diffuser, which most current automotive catalytic converters use to distribute the flow field inside the monolithic bricks where catalysis takes place. While the characteristics and performance of a simple diffuser flow are well studied and documented, the influence of downstream brick resistance is not clear. The resultant flow uniformity strongly affects the light-off condition and the lifetime of converters (Oh et al., 1985; Bella et al., 1991; Lai et al., 1992). Also, a significant portion of the exhaust-system pressure loss is attributed to the catalytic converters. Thus, there is a need to study the trade-off between pressure-drop and flow uniformity as affected by different flow (engine operating conditions) and geometric (packaging constrains) parameters.

An earlier analysis (Lai et al., 1992) applied finite difference techniques simulate the 3-D internal flow field of non-reacting dual-monolith automotive catalytic converters. Monolithic brick resistance was formulated from the pressure gradient of fully developed laminar duct-flow and corrected for the entrance effect. This correlation was found to agree with experimental pressure drop data, and was introduced as an additional source term into the nondimensional momentum equation within the brick. Flow distribution within the monolith was found to depend strongly on diffuser performance, which is a complex function of flow Reynolds number, brick resistance, and inlet pipe length and bending angles. In general, flow distribution inside the brick is found to be more uniform with smaller Reynolds number and larger brick resistance, with a straight inlet pipe rather than a bent one, and with a shorter pipe rather than a longer one. The predictions were in very good agreement with the velocity measurement using laser Doppler anemometry for a few selected cases (Lai et al., 1992). This paper presents a parametric study of the trade-off between flow-uniformity and pressure drop of an axisymmetric diffuser-bricks-nozzle configuration, i.e., dual monolith bricks with tapered inlet- and outlet-headers.

Diffusers are widely used in flow systems to convert kinetic energy to potential energy. There are many experimental studies of diffuser performance. For example, Kline and his co-workers (e.g., Chui and Kline, 1967; Reneau et al., 1967; Ghose and Kline, 1976, 1978; Bardina et al., 1981) at Stanford University have conducted a great deal of experimental and analytical research on two-dimensional (2-D) planar diffusers. Different operating regimes (no stall, transitory stall, bistable stall and jet flow) have been identified and data on pressure losses have been compiled (e.g., Cockrell and Markland, 1963; White, 1986) for 2-D planar diffusers. However, similar regimes for conical diffusers are less well defined. Although simple in geometry, 2-D diffuser flows actually present one of the most complicated type of flows because they are rotational, three-dimensional, and subject to an extremely high streamwise pressure gradient. Consequently, diffuser flows are difficult to investigate, not only experimentally but also computationally. Most of the earlier analyses of 2-D turbulent planar and conical diffuser flows were based on boundary layer approximations, and the solutions were obtained by solving the integral equations (Ghose and Kline, 1976, 1978; Senoo and Nishi, 1977; Bardina et al., 1981). For uniform inlet flows and small diffuser angles, therefore, the effect of geometry on overall performance has been fairly well established. However, since parabolic calculation ignores downstream effects, the complicated adverse pressure gradient effects cannot be properly accounted for. In addition, integral solution is incapable of providing detailed flow distribution information.

Only recently have there appeared a few applications of multidimensional CFD techniques to diffuser flows. Hah (1983) used a second-order skew-upwind scheme with the algebraic Reynolds-stress turbulence model to calculate the effects of inlet swirl and distortion in conical diffuser flows. However,

* Currently, Product Design Engineer, Ford Motor Company, Electrical and Fuel Handling Division, Ypsilanti, MI 48197.

Contributed by the Fluids Engineering Division for publication in the JOURNAL OF FLUIDS ENGINEERING. Manuscript received by the Fluids Engineering Division January 4, 1993; revised manuscript received February 1, 1994. Associate Technical Editor: Ho, Chih-Ming.

the comparison with experimental data was quite limited, and only for swirl inlet flow. Yuan et al. (1991) used a McCormack's predictor-corrector scheme with subgrid scale turbulence model to analyze a 2-D non-symmetric planar diffuser flow. Comparison with data is limited to only one non-symmetric planar geometry with no-stall condition. Lai et al. (1989) used a SIMPLE algorithm with standard and low-Re models to compute 1.3-degree (half-angle) planar and 4-degree (half-angle) conical diffuser flows, both limited to no-stall conditions. They found that the standard model can predict the behavior of the pressure coefficients and centerline velocity correctly, but overpredicts in the near wall region. The low-Re model with a coarse grid or without correction for pressure gradient effects fails even worse. The results show that a modified low-Re model with a fine grid is capable of better performance. Most of these recent analyses, however, are all limited to the unstalled region and are very specific concerning the test geometries. This demonstrates the difficulties involved in predicting the complicated diffuser flows, even the unstalled ones.

Even though the ability of the standard $k - \epsilon$ model and wall function to account for strong pressure gradient and streamline curvature effects in complicated diffuser flows may be limited, they are used in the present analysis because they are relatively insensitive to grid density and easy to implement. These considerations are particularly important in the present study, since a large number of flow geometries and conditions must be computed. The shortfall of the standard $k - \epsilon$ model and wall function is also less severe for diffuser flows with large angles, since the separation point is fixed, as in flow over a backward-facing step. In addition, downstream block resistance helps to stabilize the flow and the computation, as will be discussed later. Therefore current approach is a feasible and presently available solution to the engineering design problem. For simplicity, an axisymmetric geometry is chosen for the current study. Although this may impose a severe limitation, since separated diffuser flows in the transitory or stable stalled regimes are known to be quite three-dimensional, the experimental results for selected cases show good agreement with predictions. Our main focus is on how the brick resistance modifies diffuser performance, and its implications for engineering design in terms of flow uniformity and pressure loss.

Numerical Approach

The brick resistance formulation of the monolithic square-cell flow passage can be reduced by empirical experimental pressure drop data (Yamamoto et al., 1990) or derived from the Darcy equation for steady, incompressible, fully developed laminar flow in a constant-area duct (White, 1986) as

$$f_r \, \mathrm{Re}_{\mathrm{cell}} = 56.91 \tag{1}$$

By choosing the diameter and mean velocity at the inlet pipe as the reference length and velocity scales, the formulation for the nondimensional pressure gradient within the duct is then

$$BR = E \frac{28.488}{\mathrm{Re}_i} \frac{V_c}{D_{hc}^2} \tag{2}$$

where Re_i is the Reynolds number at the inlet pipe, V_c is the flow velocity inside the cell of the brick, D_{hc} is the hydraulic diameter of the cell, and E is a correction factor for the entrance effect similar to the treatment of Johnson and Chang (1974):

$$E = \left(1 + \frac{0.0445}{\bar{x}}\right)^{1/2} \tag{3}$$

where $\bar{x} = L/D_{hc}\,\mathrm{Re}_c$ is the nondimensional brick length and $\mathrm{Re}_c = V_c D_{hc}/\nu$ is the Reynolds number inside the monolith cell.

Simulated local flow velocity with high accuracy inside the monolith is required to prescribe the pressure gradient indicated in Eq (2). To achieve this aim, the flow inside the monolith is treated as one-dimensional. Convection and diffusion transports in the other two directions are disabled. The effect of the porosity of the brick is included by partially blocking the streamwise convective and diffusive fluxes across the discretized cell surface.

Local flow velocity inside the monolith V_c is solved together with the rest of the converter in the multidimensional simulation of momentum transport. This formulation has been validated with experimental pressure drop data across bricks of different cell densities and at different flow rates up to a cell Reynolds number of 2000 when transition to turbulence occurs. Since the cell Reynolds number seldom exceeds 2000 in practical operation, there is no need to correct for turbulence effects.

The analysis considers a stationary, incompressible, three-dimensional turbulent flow. The nondimensional time-averaged equations of motion are:

Conservation of mass (continuity):

$$\frac{\partial U_j}{\partial X_j} = 0 \tag{4}$$

Conservation of momentum:

$$U_j \frac{\partial U_i}{\partial X_j} = -2 \frac{\partial P}{\partial X_i} + \frac{\partial}{\partial X_j}\left(\frac{1}{\mathrm{Re}} + \nu_t\right)\left(\frac{\partial U_i}{\partial X_j} + \frac{\partial U_j}{\partial X_i}\right) + BR \tag{5}$$

where P is the normalized pressure, nondimensionalized with respect to the dynamic head at the inlet pipe, $\frac{1}{2}\rho V_i^2$; BR is the brick resistance formulated by Eq. (2), which is only turned

Nomenclature

BR = nondimensional pressure gradient due to the monolithic brick resistance, in Eq. (2)
C_p = pressure recovery coefficient,
C_1, C_2, C_μ = model constants, in Eq. (10)
D_{hc} = hydraulic diameter of the cell inside the monolithic brick
E = correction factor for the entrance effect, in Eq. (3)
G_k = generation term of, in Eq. (9)
k = turbulent kinetic energy
M_d = maldistribution index, in Eq. (11)
P = normalized pressure, $P/\frac{1}{2}\rho V_i^2$
P = pressure
Re = Reynolds number
V_c = flow velocity inside the cell of the brick
V_i = average flow velocity at the inlet pipe
U_i = mean velocity in the i-direction
x_i = body-fitted coordinate system
X_i = normalized coordinate system, x_i/D_i
ϵ = dissipation rate of turbulent kinetic energy, k
μ = dynamic viscosity
ν = kinematic viscosity
ν_t = turbulent kinematic viscosity, Eq. (6)
ρ = density of the fluid
σ_k, σ_ϵ = turbulent Prandtl/Schmidt numbers, Eq. (10)

Subscript

i = at inlet pipe
c = inside the cell of the monolithic brick
1 = at the inlet of diffuser
2 = at the exit of diffuser

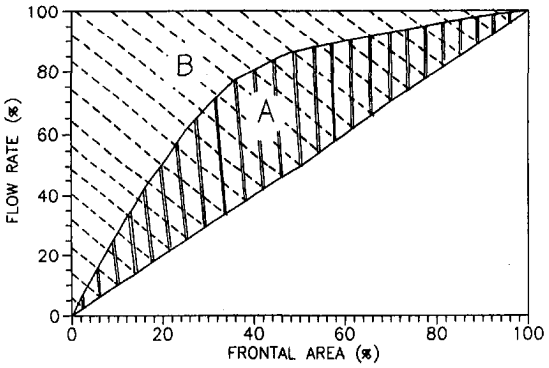

Fig. 1 Definition of maldistribution index

on inside the brick along the streamwise direction. The standard $k - \epsilon$ model is used to calculate the turbulent eddy viscosity as

$$\nu_t = C_\mu \frac{k^2}{\epsilon} \tag{6}$$

The model equations for turbulent kinetic energy k and turbulent dissipation rate ϵ are

$$\frac{\partial U_j k}{\partial X_j} = \frac{\partial}{\partial X_j}\left(\frac{\nu_t}{\sigma_k}\frac{\partial k}{\partial X_j}\right) + G_k - \epsilon \tag{7}$$

$$\frac{\partial U_j \epsilon}{\partial X_j} = \frac{\partial}{\partial X_j}\left(\frac{\nu_t}{\sigma_\epsilon}\frac{\partial \epsilon}{\partial X_j}\right) + C_1 \frac{\epsilon}{k} G_k - C_2 \frac{\epsilon^2}{k} \tag{8}$$

where G_k is the generation term of k:

$$G_k = \nu_t\left(\frac{\partial U_i}{\partial X_j} + \frac{\partial U_j}{\partial X_i}\right)\frac{\partial U_i}{\partial X_j} \tag{9}$$

The dimensionless empirical constants recommended for plane shear layers and plane jet (Launder and Spalding, 1974) are used here without alteration:

$$C_\mu = 0.09, \quad C_1 = 1.44, \quad C_2 = 1.92, \quad \sigma_k = 1, \quad \sigma_\epsilon = 1.3 \tag{10}$$

In order to quantify the degree of flow uniformity, an index must be devised to evaluate the design performance. This is done by first sorting the individual velocities across the monolith according to their magnitude and then integrating the mass flux, in reducing order, with respect to the frontal area. An ideal uniform distribution curve is linear. Referring to Fig. 1, the area **A** between the distribution curve and the linear curve represents the degree of maldistribution. A maldistribution index, M_d, is taken to be the normalized area with respect to the worst possible distribution, area **B**; i.e.,

$$M_d = \frac{\text{area } \mathbf{A}}{\text{area } \mathbf{B}} \tag{11}$$

Experimental Apparatus and Procedures

The experimental setup is shown in Fig. 2. Axial mean velocities were measured using Laser Doppler Anemometry (LDA) at 1 mm upstream from the leading face of the first monolith. The flow Reynolds numbers investigated were 25,000 and 135,000 based on inlet pipe diameter for 10, 30, and 50 deg diffuser half-angles. The LDA system used in this experiment is a single-channel, dual-beam system, in backscatter mode. One of the split laser beam is displaced to the optical axis in order to make measurement close to the brick surface (Lai et al., 1986). A 4-watt argon ion laser at 488 nm wavelength is used as the light source. The LDA system is mounted on an optical base which is traversed at various points along the optical axis to measure velocities along the brick surface. A TSI counter processor (model 1980B) is used for signal conditioning and processing; the data are then acquired and analyzed using a personal computer through an A/D converter (Data Translation 2828).

The air flow is generated by suction using a vortex blower downstream. The air flowrate is carefully metered using a laminar flow meter consisting of a calibrated monolith brick and a differential pressure transducer (MKS 220CA). Fine water droplets generated by a humidifier are introduced well upstream of the inlet as seeding particles for the LDA system. Static pressure data are also taken at selected locations along the air gap, rear nozzle and exit pipe.

Results and Discussion

Brickless Diffuser Flows. First of all, the performance of the current approach on brickless diffusers is examined. In this study, the characteristic length and velocity scales used to nondimensionalized geometry and flow quantities are taken to be the diameter and the averaged velocity at the inlet pipe. Conical diffusers with a fixed diffuser length of $2.2D_i$ but different diffuser angles are considered for analysis. All the diffuser angles referred to in this paper are the half-angles of the diffuser. The inlet pipe length is fixed at $1.66D_i$. A uniform velocity profile is prescribed at the inlet with a Reynolds number of 135,000, corresponding to fully turbulent diffuser flows with thin inlet boundary layers. It is well known that for brickless diffusers, the addition of even a short uniform duct downstream augments both the maximum value of the pressure recovery coefficient and the area ratio at which it occurs. Therefore, a $1.66D_i$-long uniform pipe was added to the diffuser section. A coarse grid of $2 \times 13 \times 54$ is used for the computation.

A comparison of the computed pressure recovery coefficient, C_p, with those mapped by McDonald and Fox (1966) is shown in Fig. 3. Owing to the limited information available for their experimental conditions, the comparison is only preliminary. In general, the predicted response of C_p with respect to the diffuser angle is delayed compared with the experimental data, although the maximum C_p value, ca. 0.54, is predicted accurately for the configuration considered. The predicted C_p is lower at smaller diffuser angles. Therefore, the maximum C_p point (where the flow begins to separate) is postponed until a larger angle. This is due to the three-dimensionality of the separated flow during inside a conical diffuser and the underprediction of friction

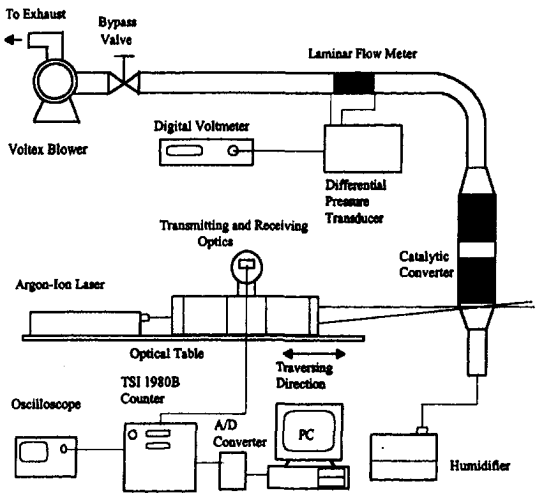

Fig. 2 Experimental setup for the velocity measurements

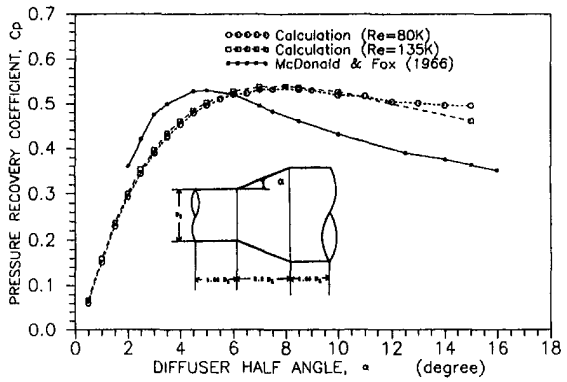

Fig. 3 Predicted and measured pressure recovery coefficients for conical diffusers

velocity for the unstalled regimes by the standard $k - \epsilon$ model, similar to the result of Lai et al. (1989). After the flow separates, however, the measured C_p seems to drop faster than the predicted trend. For diffuser angles larger than 30 degrees, when the flows become highly unsteady and rotational, the computation also becomes relatively unstable, reflecting the shortcomings of the turbulence model and the limitations of the current numerical approach, which is limited to two-dimensional and steady-state solution. This can be monitored by looking at the residual convergence history. As the diffuser angle increases past bulk separation, convergence of the solution also deteriorates. However, when block resistance is added at the diffuser exit, the computation and flow are stabilized tremendously; the convergence history is obviously improved. This is because the presence of the brick constrains the size of the separation bubble, forcing the separated flow to reattach within the diffuser and making the flow field to be more axisymmetric. With the improved physical and numerical stability, and the availability of some limited experimental validations (Lai et al., 1992), the current numerical approach should be applicable to design analysis of the diffuser-brick flows. Applications to brickless diffusers, however, are less well validated, especially for large diffuser angles. These results are included only for comparison.

Diffuser-Monolith-Nozzle Flows. For the analysis of diffuser-brick flows, the following geometries were considered, with applications to automotive catalytic converters in mind: The diameter of the cylindrical monolithic brick section was taken to be $2.23D_i$, resulting in an area-expansion-ratio of 5. The length of the inlet pipe was fixed at $3.6D_i$. The diffuser/nozzle angle and the brick resistance were varied. The Reynolds number at the inlet, Re_i, was also fixed at 135,000. A plug flow velocity profile was used for the initial boundary condition at the inlet. Figure 4 shows the typical grid geometries used in the computations. Two $1.65D_i$-thick monolithic bricks separated by a $0.55D_i$ air gap were placed between the diffuser and the nozzle. A coarse grid system of $2 \times 13 \times 86$ was used to carry out the parametric study. Care was taken to insure that the first grid from the wall lies within the log law-of-wall layer. A grid sensitivity test was performed by increasing the grid densities 80 and 150 percent more. The results show that the coarse grid is sufficient for the present analysis, with less than one percent variation in pressure drop including total, 1st brick and 2nd brick and less than two percent in the maldistribution index. Four brick resistance values were chosen for the computation: 0, $0.38V_c$, $0.48V_c$, and $0.70V_c$. These four cases are denoted as brick types **N**, **L**, **M**, and **H**, corresponding to **N**o brick, **L**ow, **M**edium, and **H**igh brick resistance. With an inlet pipe diameter of 46 mm, the three resistance values correspond to the conditions of 0.465, 0.62, and 0.93 cell-per-square-mm (or 300, 400, and 600 cell-per-square-inch) bricks having the same wall-thickness of 0.152 mm.

Figure 5 shows numerical results of the flow distributions inside the first monolith for type **M** brick, with different diffuser angles. As the diffuser angle increases, flow is concentrated more to the center of the brick because flow separation inside the diffuser leads to jet impingement on the brick surface. Porosity of the brick in effect reduces the flow area; therefore, the averaged velocity is around 0.26, rather than 0.2 as expected from the area-expansion ratio of 5. Since the monolith constrains the flow to be one-dimensional, one maldistribution index describes the flow distribution for the entire brick. Figure 6 shows numerical results of the maldistribution index for the entire test matrix. The flow inside the second brick is much more uniform as a result of the flow redistribution inside the air gap. To study the flow uniformity issues, therefore, only the index of the first brick needs to be shown. For the no-brick case (case **N**), the flow separation bubble extends well into the constant-area casing; therefore, the maldistribution index continues to change after the diffuser. The rapid rise of the index values at about 5 degrees indicates the onset of diffuser separation for all cases. Compared with the no-brick case, brick resistance greatly dampens the effect of bulk flow separation but does not seem to delay its onset. As expected, brick resistance makes the flow distribution more uniform. The higher the brick resistance, the better the distribution. The smallest index values are obtained when the diffusers are not stalled. However, from the practical point of view, the diffuser length is always limited by the packaging constraints. A small increase in the diffuser length when it is short, shows a great improvement in flow distribution initially. In this region, an increase in the brick resistance also improves the flow distribution significantly. However, these benefits quickly become marginal as the diffuser becomes longer. Because of packaging constraints, a very long diffuser is usually not practical. Therefore, realistic diffuser angles are in the range from 20 to 50 degrees, corresponding to diffuser lengths of 3.5 to 0.5 times the inlet pipe diameter.

Figure 7 shows numerical results of the variation of static pressure in the axial direction for a type **M** brick with a 30 degree diffuser. Note that the pressure data are surface-averaged and relative to the pressure at the exit pipe. The static pressure variation (solid line) is quite plausible; it shows a large increase (pressure recovery) at the diffuser, an almost constant-gradient decrease within the bricks (with some pressure recovery within the air gap), then a sharp drop at the nozzle. The total pressure (including the dynamic head) variation is also shown as dash line in Fig. 8. Excluding the variations within the diffuser and the nozzle, it shows a monotonic decrease. Similar to the findings of Wendland et al. (1991), the total pressure drop is primarily due to the brick resistance and the headers, with only minor contributions from the air gap.

The breakdown of pressure loss due to the first and second bricks and the headers (including the nozzle and the diffuser) for a type **M** brick at different diffuser angles is shown in Fig. 8. It is observed that pressure losses due to headers alone are quite significant and are comparable to those due to the bricks. For type **M** brick, the header loss roughly amounts to between one-third and one-half of the total pressure drop. The pressure loss due to the headers is the same using either static or total pressure data, although the static pressure loss due to the headers is actually the difference between the larger pressure drop at the nozzle and the smaller pressure recovery of the diffuser.

Figure 9 also shows numerical results of the total pressure drop data compiled for the test matrix. The fact that the pressure drop penalty rises faster when the diffuser half-angle is larger than 50 degree also suggests that these geometries should be avoided. Compared with Figure 6, pressure variation does not show the change of slope in the maldistribution index around 10 degrees. Therefore, a very long diffuser which operates in the unstalled region does not really improve the pressure penalty, in spite of the fact that it has the most uniform flow distribution.

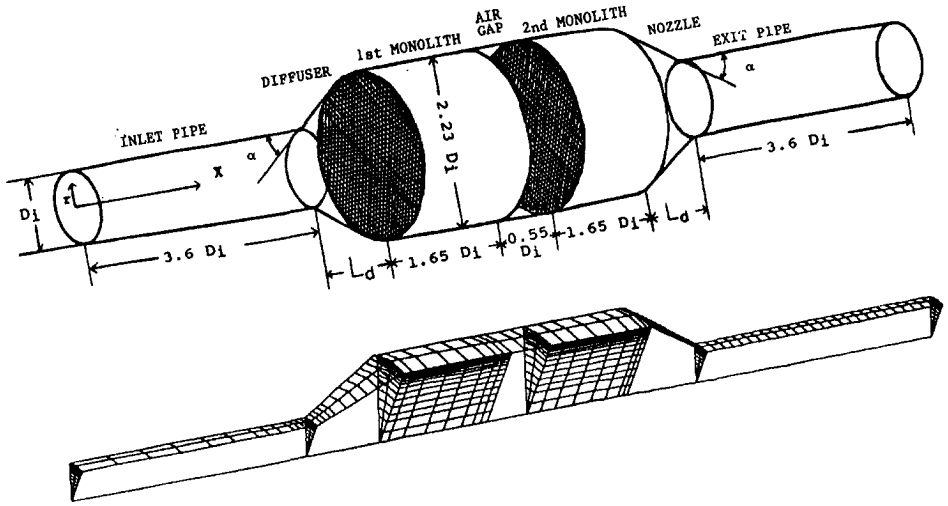

Fig. 4 Physical geometry and typical grid used in the computation

This further confirms that practical diffuser angle should be in the range of 20 to 50 degrees.

Some headers are foreshortened or truncated (i.e., feature sudden expansion from the inlet pipe to the monolith brick), since they can be made more easily than tapered headers. Figure 10 shows the performance comparison between converters with truncated and tapered headers, both having type **M** bricks. Truncated headers introduce larger pressure loss and maldistribution index. Although there is room between the monolith and the sudden expansion for flow to redistribute through the vena contracta, turbulence mixing causes significant loss of flow potential. The loss in the truncated header will decrease if the expansion volume is enlarged (i.e., increasing L_d/D_i). Also shown in the figure is one case with oval cross-section (three-dimensional) headers from an earlier analysis (Lai et al., 1992); this has the same area-expansion ratio, Reynolds number, and brick type. Compared to axisymmetric header cases, three-dimen-

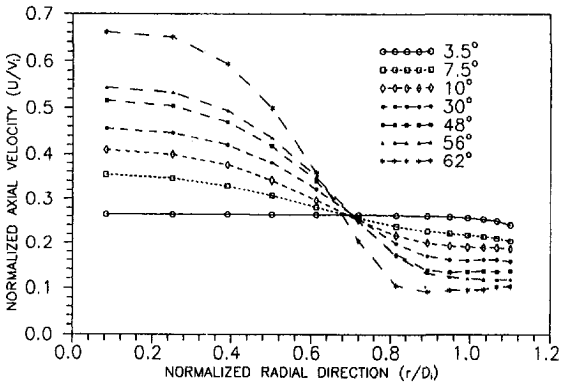

Fig. 5 Axial flow distribution inside the first monolith for type M brick

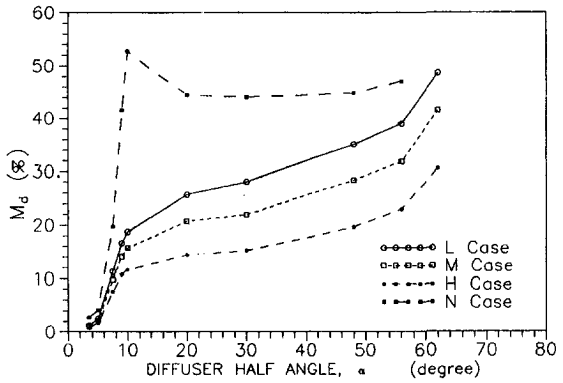

Fig. 6 Maldistribution index results for different bricks as a function of diffuser angle

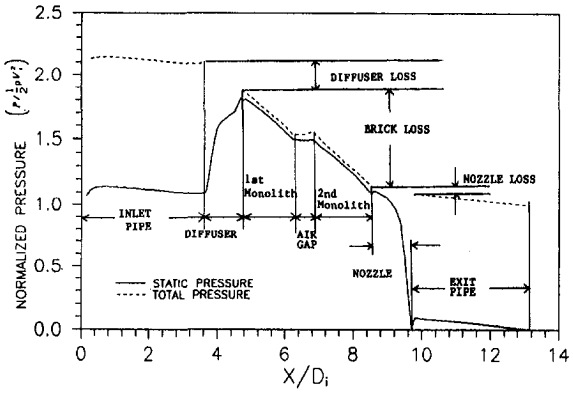

Fig. 7 Static and total Pressure variation in the streamwise direction for type M brick with 30-degree diffuser

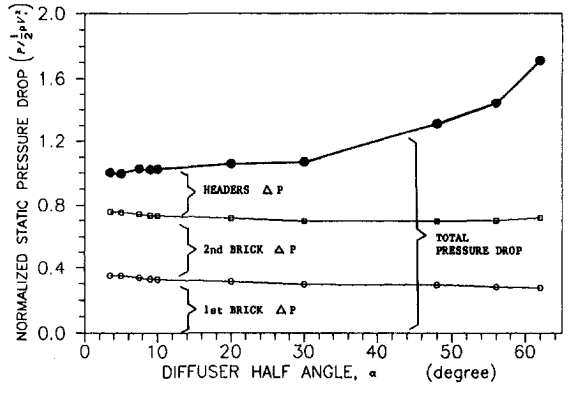

Fig. 8 Contribution to pressure loss by the bricks and headers for type M brick. The pressure loss across the outlet header includes contribution from the nozzle and exit pipe.

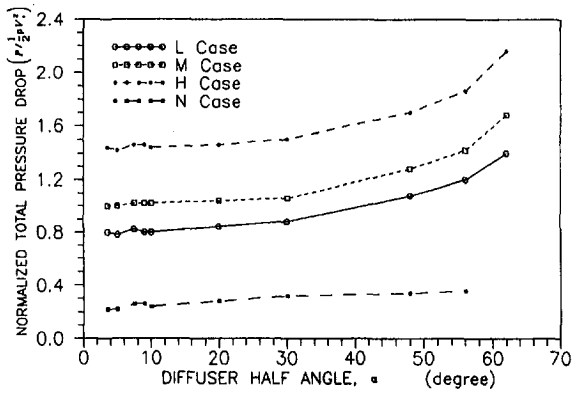

Fig. 9 Total pressure drop for different bricks as a function of diffuser angle

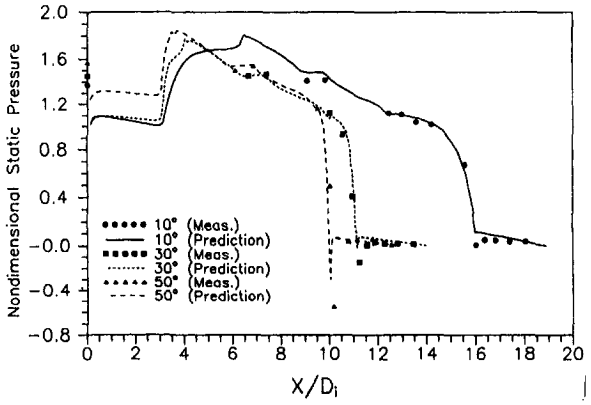

Fig. 12 Simulated and measured static pressure profiles for Re = 135,000. Brick type: 0.62 cpsmm with 0.165 mm thickness

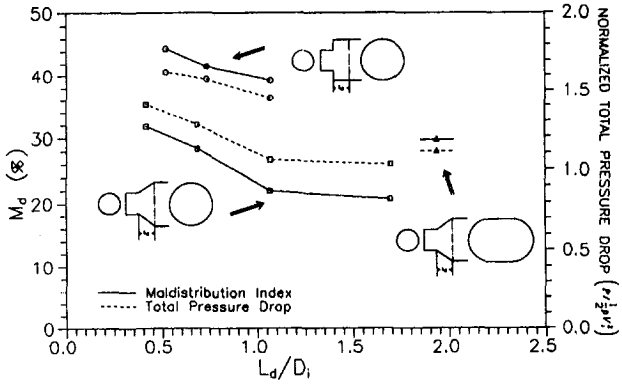

Fig. 10 Comparison of performance for truncated, tapered, and oval-shape cross-sectioned headers for type M brick

sional headers also have a larger pressure loss and maldistribution index.

Comparison With Experimental Results. Figure 11 shows the comparisons of the predicted and measured axial velocity profiles at the leading face of the first monolith. The Reynolds number is 25,000 and 135,000 based on inlet condition for 30 deg diffuser half-angle. It is found that the simulated and the experimental results are in very good agreement, validating the current numerical approach. High-Reynolds-number flows have less uniform velocity profiles. It is interesting to note that the peak velocity tends to move away from the centerline with increasing diffuser angles; this is more obvious for the low Reynolds number (25,000) case. In the high Reynolds number cases, however, the results show that the momentum near the centerline is large enough to overcome the brick resistance and the impinging-jet-like profile persists further. Figure 12 also shows the good agreement between the computed static pressure profiles with the measurements at selected locations for 10, 30 and 50 deg diffuser half-angles with different brick properties under the high Reynolds number flow conditions. All the values of pressure were normalized based on the exit conditions (atmospheric pressure).

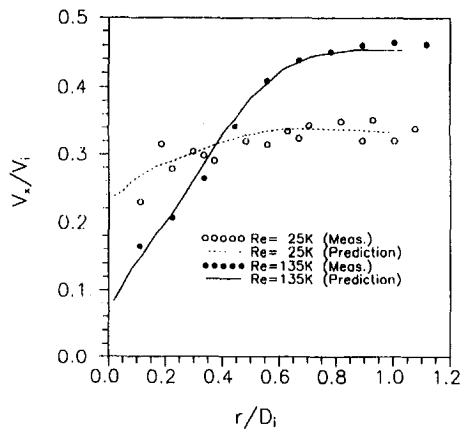

Fig. 11 Simulated and measured velocity profiles at the leading face of the first monolith. 0.62 cpsmm with 0.165 mm thickness

The standard procedures for uncertainty analysis recommended by Kline and McClintock (1953) and Kline (1985), were performed to estimate the appropriate uncertainty bands for the velocity and pressure measurements. The estimated uncertainty for measured velocity is less than 2.5 percent at Re = 25,000, and 2.8 percent at Re = 135,000. The measured pressure data P were converted to the nondimensional P. The accuracy for the pressure transducer (± 0.2 percent reading) was obtained from the manufacturer's specification and the uncertainty for the property was derived using the ideal gas equation of state for the ambient air, and the uncertainty in air density ρ turned out to be 1 percent on the average. The resulting uncertainty is 1.1 percent for pressure measurements.

Summary and Conclusions

In this paper the flow fields of dual-monolith automotive catalytic converters are studied numerically; an axisymmetric geometry was used. Limited experiments at low Reynolds number validate the numerical approach. The implications of these data to the converter design are discussed in terms of the trade-off between flow-uniformity and pressure drop. Flow distribution within the monolith was found to depend on the diffuser performance, which is modified strongly by the brick resistance. Realistic diffuser angles are in the range of 20 to 50 degrees, corresponding to diffuser lengths of 3.5 to 0.5 times the inlet pipe diameter. Truncation of both the inlet and outlet headers will introduce a larger pressure loss, but the effect could be reduced by providing enough room between the sudden expansion and the monolith for more thorough mixing. Also, the monolithic brick downstream stabilizes the diffuser flows both physically and computationally.

The influence of the headers and brick resistance on pressure drop is also identified. Pressure loss due to the outlet header remains relatively constant, while the diffuser pressure recovery decreases significantly with increasing diffuser angles. Hence, a longer inlet header combined with a shorter outlet header is more desirable than symmetric headers if the total length of the converter is fixed.

Compared with axisymmetric tapered header cases, both truncated and three-dimensional headers have larger pressure loss and maldistribution index. Increasing the pipe diameter relative to the monolith size not only decreases pressure drop significantly, but also decreases the maldistribution index and improves the overall converter efficiency.

The trade-off relationship between the pressure drop and flow uniformity implies that one can utilize brick resistance or different diffuser angle to optimize the converter efficiency. However, for practical design optimization, the trade-off must include the catalysis conversion efficiency, which also is a strong function of flow uniformity.

Based on the results of the flow distributions presented in this study, the CFD (*C*omputational *F*luid *D*ynamics) model at the current stage is seen to give fairly accurate predictions of flow field of diffuser-monolith flows. Thus the numerical model can be used extensively in the routine converter design process.

Acknowledgment

This work is supported by Ford Motor Company and the Institute for Manufacturing Research at Wayne State University.

References

Bardina, J., Lyrio, A., Kline, S. J., Ferziger, J. H., and Johnston, J. P., 1981, "A Prediction Method for Planar Diffuser Flows," ASME JOURNAL OF FLUIDS ENGINEERING, Vol. 103, pp. 315–321.

Bella, G., Rocco, V., and Maggiore, M., 1991, "A Study of Inlet Flow Distortion Effects on Automotive Catalytic Converters," ASME paper 91-ICE-13.

Chui, G., and Kline, S. J., 1967, "Investigation of a Two-Dimensional Fully Stalled Turbulent Flow Field," Report MD-19, Dept. of Mechanical Engineering, Stanford University.

Cockrell, D. J., and Markland, E., 1963, "A Review of Incompressible Diffuser Flows," *Aircraft Engineering,* Vol. 35, pp. 286–292.

Ghose, S., and Kline, S. J., 1976, "Prediction of Transitory Stall in Two-Dimensional Diffusers," Report MD-36, Dept. of Mechanical Engineering, Stanford University.

Ghose, S., and Kline, S. J., 1978, "The computation of Optimum Pressure Recovery in Two-Dimensional Diffusers," ASME JOURNAL OF FLUIDS ENGINEERING, Vol. 100, pp. 419–426.

Hah, C., 1983, "Calculation of Various Diffuser Flows with Inlet Swirl and Inlet Distortion Effects," *AIAA Journal,* Vol. 21, No. 8, pp. 1127–1133.

Johnson, W. C., Chang, J. C., 1974, "Analytical Investigation of the Performance of Catalytic Monoliths of Varying Channel Geometries based on Mass Transfer Controlling Conditions," Society of Automotive Engineering, SAE paper 740196.

Kline, S. J., 1985, "1983 Simposium on Uncertainty Analysis Closure," ASME JOURNAL OF FLUIDS ENGINEERING, Vol. 107, pp. 181–182.

Kline, S. J., and McClintock, F. A., 1953, "Describing Uncertainties in Single-Sample Experiments," *Mechanical Engineering,* Vol. 75, pp. 3–8.

Lai, M.-C., Jeng, S. M., and Faeth, G. M., 1986, "Structure of Turbulent Adiabatic Wall Plumes," ASME *Journal of Heat Transfer,* Vol. 108, pp. 827–834.

Lai, M.-C., Lee, T., Kim, J.-Y., Cheng, C.-Y., Li, P., and Chui, G., 1992, "Numerical and Experimental Characterization of Automotive Catalytic Converter Internal Flows," *Journal of Fluids & Structures,* Vol. 6, No. 4, pp. 451–470.

Lai, Y. G., So, R. M. C., and Hwang, B. C., 1989, "Calculation of Planar and Conical Diffuser Flows," *AIAA Journal,* Vol. 27, No. 5, pp. 542–548.

Launder, B. E., and Spalding, D. B., 1974, "The Numerical Computation of Turbulent Flows," *Computer Methods in Applied Mechanics and Engineering,* Vol. 3, pp. 269–289.

McDonald, A. T., and Fox, R. W., 1966, "An Experimental Investigation of Incompressible Flow in Conical Diffusers," *International Journal of Mechanical Science,* Vol. 9, pp. 125–139.

Oh, S. H., and Cavendish, J. C., 1985, "Mathematical Modeling of Catalytic Converter Lightoff, Part III: Predication of Vehicle Emissions and Parametric Analysis" *AIChE Journal,* Vol. 31, No. 6, pp. 943–949.

Patankar, S. V., and Spalding, D. B., 1972, "A Calculation Procedure for Heat, Mass and Momentum Transfer in Three-Dimensional Parabolic Flows," *International Journal of Heat and Mass Transfer,* Vol. 15, pp. 1787–1806.

Reneau, L. R., Johnston, J. P., and Kline, S. J., 1967, "Performance and Design of Straight Two-Dimensional Diffusers," ASME *Journal of Basic Engineering,* Vol. 89, No. 1, pp. 141–150.

Senoo, Y., and Nishi, M., 1977, "Prediction of Flow Separation in a Diffuser by a Boundary Layer Calculation," ASME JOURNAL OF FLUIDS ENGINEERING, pp. 379–389.

Wendland, D. W., Sorrell, P. L., and Kreucher, J. E., 1991, "Sources of Monolith Catalytic Converter Pressure Loss," Society of Automotive Engineering, SAE paper 912372.

White, F. M., 1986, *Fluid Mechanics,* p. 331, 2nd ed. McGraw-Hill, New York.

Yamamoto, H., Horie, H., Kitagawa, J., and Machida, M., 1990, "Reduction of Wall Thickness of Ceramic Substrates for Automotive Catalysts," Society of Automotive Engineering, SAE paper 900164.

Yuan, M., Song, C. C. S., and He, J., 1991, "Numerical Analysis of Turbulent Flow in a Two-Dimensional Nonsymmetric Plane-Wall Diffuser," ASME JOURNAL OF FLUIDS ENGINEERING, Vol. 113, pp. 210–215.

Quantitative Visualization of a Submerged Pseudoplastic Jet Using Particle Image Velocimetry

A. Shekarriz

J. R. Phillips

T. D. Weir†

Fluid Dynamics Laboratory,
Pacific Northwest Laboratory,*
Richland, WA 99352

A preliminary experimental study of a pseudoplastic jet flow is reported in this paper. The velocity field was measured using Particle Image Velocimetry. Unlike a Newtonian jet, the pseudoplastic jet was observed to experience a sudden drop in its velocity at a reproducible position downstream of the nozzle for the range of velocities examined. This position moved downstream with an increase in the nozzle exit velocity. The center-line streamwise velocity decayed as X^{-15} to X^{-30} within the terminating region of the jet for three different nozzle exit velocities of 2.43, 3.17, and 5.42 m/s. This decay is in contrast to X^{-1} decay for a turbulent or laminar Newtonian jet. The location of the terminating region did not appear to scale with Reynolds number, Plasticity number, or Hedstrom number. At Reynolds numbers of 3000 and 6400, the instantaneous streamwise velocity maps indicated that the flow was fairly laminar, with a sinuous instability appearing at the higher Reynolds number condition. Close observation of the jet indicated that local turbulence could exist within regions of high shear rate. Further detailed study is required to confirm this observation.

1 Introduction

Flows of submerged pseudoplastic jets have received limited attention in the literature. There is, however, considerable interest in understanding the behavior of these jets, which are proposed to be used for resuspension of settled slurries and colloidal dispersions in waste tanks located at various DOE sites. The wastes in some of these tanks have been shown to be rheologically complex fluids, many exhibiting pseudoplastic behavior, with and without yield strength. For design of waste mobilization and uniformity processes, several state-of-the-art computational tools are currently being used. In most cases, the codes assume that turbulence within non-Newtonian fluids is similar to its Newtonian counterpart (Trent and Michener, 1993). It is also commonly assumed that the jet spread rate is identical to a turbulent Newtonian jet (Terrones and Eyler, 1993). Because of the lack of experimental data in this area, most of the computational tools used for modeling the flow of purely viscous non-Newtonian jets are neither validated nor verified.

The studies performed on purely viscous non-Newtonian jets have focused on laminar pseudoplastic jets (Gutfinger and Shinnar, 1964; Serth, 1972; Mitwally, 1978; Kumar et al., 1984; and Jordan et al., 1992). In most of these studies, the authors have attempted to develop similarity solutions for the laminar flow region. Studies of turbulent non-Newtonian jets are limited to viscoelastic fluids. In the late 60's and early 70's, there was some interest in understanding the effect of drag reducing polymers (i.e., the effect of viscoelasticity) on the structure of turbulence in free-shear flows. There is disagreement on how the addition of long chain drag reducing polymers affect the dissipation and inertial scales of turbulence (White, 1969; Baker, 1973). Koziol and Glowacki (1989) provide an excellent review of the literature on this subject.

The objective of the current study is to investigate how a pseudoplastic (shear-thinning) rheology influences the flow topology, turbulent structures, and decay of the center-line velocity in a transitional/turbulent round jet submerged in the same fluid. A particle image velocimeter (PIV) is used for qualitative and quantitative visualization of the flow field. The instantaneous velocity, shear-rate, and cross-stream vorticity within a longitudinal plane inclusive of jet center-line have been measured. The main features of the flow have been compared to a Newtonian jet at the same "Reynolds Number"[1] and streamwise location. Also the changes in the flow structures in the non-Newtonian jet are observed for two different Reynolds numbers.

2 Experimental Apparatus and Procedure

2.1 Flow System. Figure 1 is a schematic diagram of the experimental setup. The tank dimensions are 30 cm × 60 cm × 40 cm. The jet is injected into the tank through a 3.57 mm diameter nozzle. A straight tube section more than 20 nozzle diameters in length was used prior to the exit of the nozzle to ensure suppression of any secondary flow generated at the tube bend. The jet was driven by a $\frac{1}{3}$ hp flexible impeller pump. Two ball valves were used to control the jet flow rate. The nozzle exit velocity was measured during each run using a Laser Doppler Velocimeter system. Care was taken to align the nozzle discharge in the horizontal and vertical directions. The uncertainty in geometric alignment of the jet in the YZ-plane is $\Delta(Y/D) = \pm 1.5$ and $\Delta(Z/D) = \pm 1.5$ at $X/D = 80$.

The fluid used was an aqueous solution of Carbopol®[2] 980. The solution consists of 0.12 percent wt. of the resin dispersed in water. The mixture is slightly acidic at this point and has a viscosity very close to that of water. In order to obtain a pseu-

† Graduate student at Washington State University, Pullman, WA.

* Pacific Northwest Laboratory is operated for the U.S. Department of Energy by Battelle Memorial Institute under Contract DE-AC06-76RL01830.

Contributed by the Fluids Engineering Division for publication in the JOURNAL OF FLUIDS ENGINEERING. Manuscript received by the Fluids Engineering Division March 30, 1994; revised manuscript received October 31, 1994. Associate Technical Editor: M. Gharib.

[1] $\mathrm{Re}_D = \rho U_0^{2-n} D^n / 8^{n-1} K$, where ρ is the fluid density, U_0 is the jet exit velocity, D is the nozzle diameter, n is the behavior index, and K is the consistency factor as defined in the rheological model of the fluid in this paper.

[2] ®BF Goodrich Company, Cleveland, Ohio.

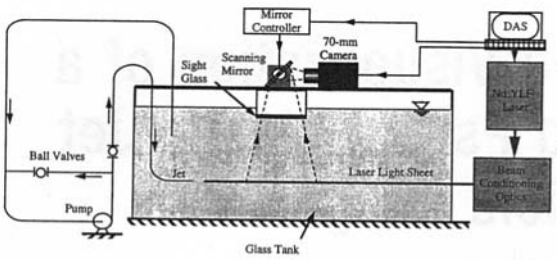

Fig. 1 Schematic diagram of the experimental setup

doplastic rheology, we neutralized the solution using Sodium Hydroxide (NaOH). The rheology of the solution is a strong function of pH. Special care was taken to ensure that the final mixture was stabilized at pH = 7.0. All of the data were collected with the same batch of fluid to eliminate variability in the properties of the fluid from one experiment to the next. A small sample of the fluid was collected following each experiment and immediately characterized using a standard controlled shear rate rheometer. The resulting rheogram is shown in Fig. 2. An Ostwald model of the form $\tau = K|\dot{\gamma}|^{n-1}\dot{\gamma}$ appears to be the most appropriate simple constitutive relation which describes the rheology of the fluid. In the above relation, τ (Pa) is the shear stress, $\dot{\gamma}$ (1/s) is the shear rate, K is the consistency factor, and n is the behavior index. Using $K = 3.41$ and $n = 0.32$ gives the best fit in the 0 to 5 sec^{-1} range of shear rate and $K = 2.552$ and $n = 0.4066$ in the 0 to 300 sec^{-1} range.

2.2 PIV System. The experimental technique used in this study for measurement of the velocity is a multiple pulsed photographic Particle Image Velocimetry (PIV) system. A simplified diagram of the PIV setup is shown in Fig. 1. A Q-switched, frequency doubled Nd:YLF laser was used as the light source. A light sheet, approximately 0.5 mm thick, was formed using a cylindrical lens and it was centered along the centerline of the jet with an uncertainty in its position being less than 0.5 nozzle diameter. The illuminated section was imaged using a 70 mm Hasselblad camera with a magnification of 0.475 ± 0.001. A galvanometric scanning mirror was used to add a velocity shift to the image in order to eliminate the directional ambiguity. After analysis of the data, the shift velocity was subtracted from the velocity field (see Adrian, 1991). The uncertainty in the mirror scan rate was found to be less than 0.5 percent. A 15 cm × 15 cm fused silica window was used as an observation window through the liquid surface interface. The images were recorded on Kodak TMAX-400 film, with a resolution better than 150 lines/mm. Images were printed on polycontrast Kodak paper to a net image magnification of 2.5. The prints were scanned on a flat-bed scanner with a gray scale resolution of 24 pixels/mm (60 pixels/mm in real space dimension). The original gray scale images were analyzed on a workstation, without image enhancement or thresholding.

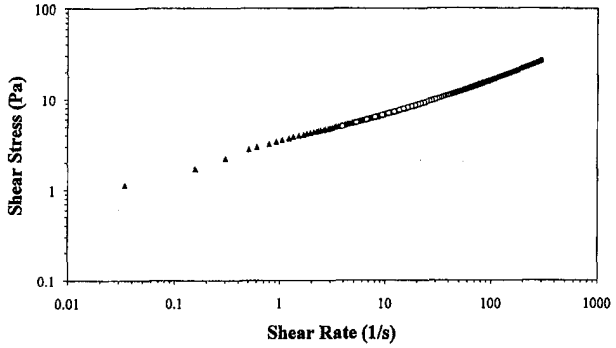

Fig. 2 Rheogram of 0.12% aqueous Carbopol solution used in this study

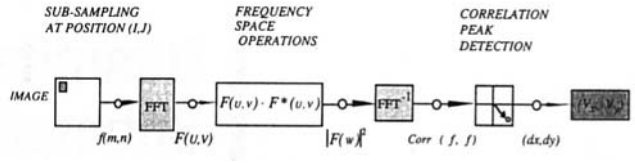

Fig. 3 Flow diagram of the analysis software for finding velocity distribution using the spatial auto-correlation method

2.3 Image Analysis. The analysis approach used in this study is based on the method of spatial autocorrelation, which is commonly used for analyzing PIV images (Cenedese and Paglialunga, 1990; Adrian, 1991; Willert and Gharib, 1991). Figure 3 shows the algorithm used in the analysis software. The function $f(m, n)$ represents the gray scale (8-bit) information in an image. The local displacement of the particles within the image is found by using the autocorrelation analysis. The average velocity within this sampling window is the ratio of the displacement to the time-step size between two consecutive laser pulses. In the current study, 256 pixel × 256 pixel sampling window was used. This translates to an averaging area of 4 mm × 4 mm in the real space. The sampling window was incremented in both X and Y directions in 1 mm increments. The actual resolution, however, was limited by the size of the interrogation window. This resolution was deemed adequate to achieve accurate measurements since the Taylor microscale at the interrogation window was estimated to be 2.5 mm for the high Reynolds number Newtonian jet flow. The smallest flow scale in the pseudoplastic fluid is difficult to estimate but is generally larger than found in Newtonian fluid at the same Reynolds number (Boger and Walters, 1993). The accuracy of the analysis software was tested using several computer simulated images. These images simulated actual images of a particle-laden flow field, where particles of various sizes were randomly distributed in the image. Statistical analysis on the autocorrelation of these images show an uncertainty of less than 0.5 percent in the average of the magnitudes and angles of the displacement vectors with standard deviation of less than 0.5 percent.

3 Results and Discussion

3.1 Qualitative Observations. Qualitative observations were made using streak photography of the flow within a plane containing the jet center-line. In the interest of clarity the different regions observed in the pseudoplastic jet are shown schematically in Fig. 4. The nozzle diameter used in this study was 3.57 mm and the nozzle exit velocities ranged from 2.43 to 8.54 m/s. Under these conditions, the jet consisted of a laminar core terminating in a stationary vortex ring followed by a creeping flow region. At the higher end of the nozzle exit velocity range there was also an annular region of flow instability and traveling vortex rings as shown in the figure.

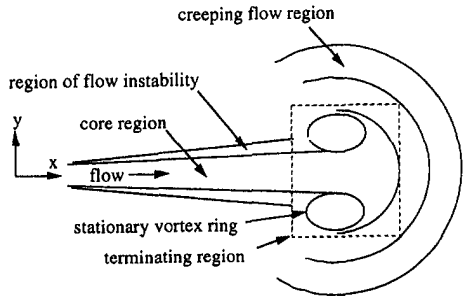

Fig. 4 Schematic diagram showing the various flow regions within the pseudoplastic jet

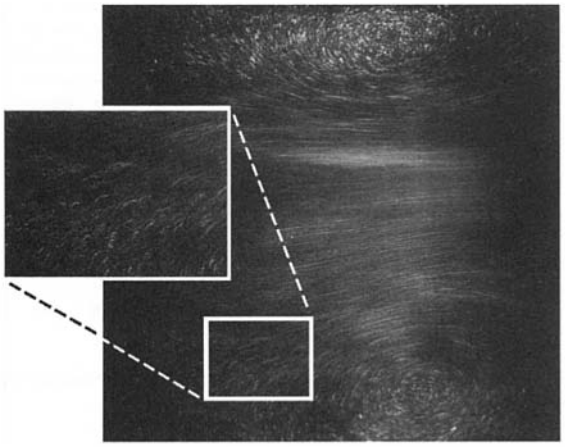

Fig. 5 Streak photograph of a jet prior to the terminating region. Flow is from left to right; $Re_D = 5300$; $X/D = 60$ at the center of the photograph.

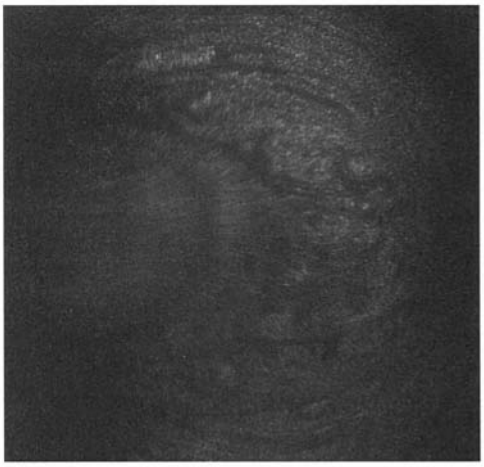

Fig. 6 Streak photograph of the terminating region. $Re_D \sim 2500$; $X/D = 60$ at the center of the photograph.

In order to ensure that the terminating region of the pseudoplastic jet is not a consequence of the tank geometry (e.g., recirculation or stagnation flow), several qualitative experiments were performed. Initially, experiments were performed for a submerged water jet. Independent of the Reynolds number, the water jet did not terminate until it reached the end of the tank where a stagnation flow was observed. The submerged pseudoplastic jet terminated before reaching the end of the tank for nozzle exit velocities ranging from less than 1 m/s up to 8.45 m/s. In fact, at ~1 m/s velocity, the jet terminated within 10 diameters downstream of the nozzle and well over 150 diameters before reaching the end of the tank. Based on these observations it appears that tank geometry is not responsible for existence of the terminating region.

Figure 5 shows a photograph of the laminar core and the region of flow instability and traveling vortex rings. This photograph is centered 60 diameters downstream of the nozzle and the jet exit velocity was 7.61 m/s. In the core the streak lines are nearly parallel and smooth indicating laminar flow. Traveling vortex rings are captured in this photograph, identifiable by the coherent elliptic structures on either side of the laminar core. It also appears that some higher frequency waves may be traveling in the same region with the vortex rings as evidenced by the wavy streak lines. Although the laminar core is modulated by the traveling vortex rings, they do not penetrate fully into the laminar core or destabilize it. Traveling vortex rings seem to be confined to an annular region defined by higher shear rates. The persistence of a stable vortex ring at 60 diameters downstream of the nozzle and at a relatively high Reynolds number of ~5300 is surprising (the definition of Re_D is given in the following section).

Figure 6 is a photograph of the region containing the stationary vortex ring and the origin of the creeping flow region. Henceforth this region will be referred to as the "terminating region." The photograph is centered at 60 diameters downstream of the nozzle and the initial velocity was about 5 m/s. The creeping flow region has a layered structure as evidenced by the particle number density distribution in the photograph, and the layers appear to be nearly spherical. The folding structures at the origin of the creeping flow region are noteworthy. These stretching and folding patterns suggest the existence of an instability which is not well understood at this point. However, as will be discussed below, the effective viscosity changes dramatically in the terminating region.

3.2 PIV Measurements. Using the PIV instrumentation, we obtained velocity data sets for the terminating region of the jet. Figure 7(*a*) shows the dimensionless magnitude of the velocity in the visualized plane for an initial velocity of 2.43 m/s. Note that the geometric centerline of the jet and the position of the maximum axial velocity do not coincide due to both position uncertainty, as discussed earlier, as well as the fact that an instantaneous map captures meandering of a jet in the cross-stream direction. The meandering can occur for both a laminar as well as a turbulent jet and it is both a consequence of large scale convection in the tank as well as instability in the jet. In this case, the flow appears to be laminar and the jet reaches a point at which the velocity drops very quickly. As the speed drops, the constant speed surfaces become more spherical.

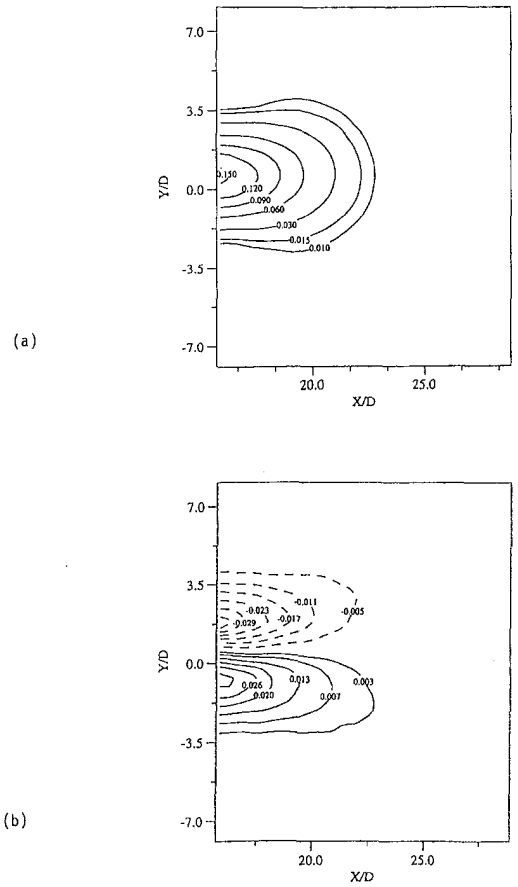

Fig. 7 (*a*) Contour map of the instantaneous speed in a plane along the center-line of the jet within the terminating region; (*b*) contour map of shear-rate for the same flow condition ($U_0 = 2.43$ m/s)

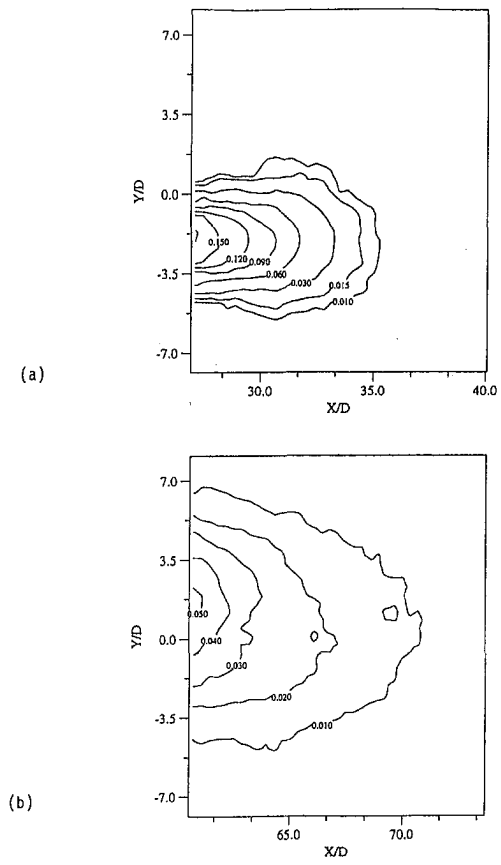

Fig. 8 Contour map of the instantaneous speed in a plane along the center-line of the jet within the terminating region; (*a*) U_0 = 3.17 m/s; (*b*) U_0 = 5.42 m/s

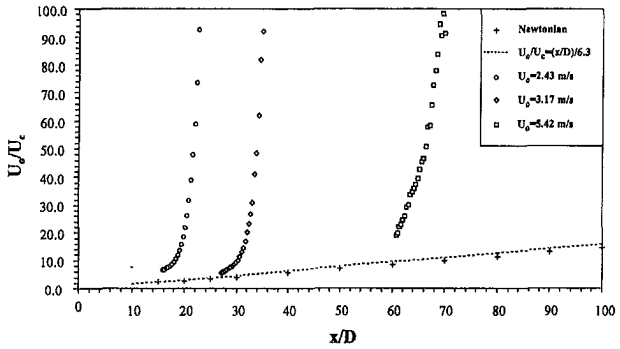

Fig. 9 Instantaneous center-line velocity within the terminating regions shown in Figs. 7 and 8

Figure 7(*b*) shows the dimensionless shearing rate for the same case as Fig. 7(*a*). By multiplying the dimensionless shear rate by the ratio of nozzle exit velocity and diameter we obtain the shear rate in units of s^{-1}. The resulting dimensional shear rate places the terminating region at a shear rate less than 2 s^{-1} which is the region with the largest change in slope of the curve, as shown in Fig. 2. The rapid increase in the slope of the shear stress versus shear rate curve (local viscosity) shifts the dominance in the momentum equation from the inertia terms to the diffusion terms, resulting in a creeping flow.

Two cases at higher velocities are shown in Figs. 8(*a*) and 8(*b*). Increasing the nozzle exit velocity implies that the jet starts out with a higher maximum shear rate and may travel further before reaching the point in its rheological behavior where the slope of the $\tau - \dot{\gamma}$ curve rapidly changes (see Fig. 2). Indeed, as the nozzle exit velocity is increased from 2.43 m/s to 3.17 m/s to 5.42 m/s the terminating region is observed to move further downstream—to 23, 35, and 70 diameters away from the nozzle, respectively.

Figure 9 is the plot of inverse of the centerline velocity for both Newtonian and shear-thinning fluids. Although the shear-thinning data is instantaneous, the centerline plots can be used as typical samples of a statistically steady flow with small variance. It should be noted that all the time-averaged data for high Reynolds number turbulent Newtonian jets would fall on a single line with a slope ranging between 5.75 and 7.3 (Rajaratnam, 1976). The data points shown in Fig. 9 which are represented as "+" are time-averaged data for a Newtonian jet in the same facility, collected using a LDV system. The dashed line is a typical correlation used to model the center-line decay in turbulent Newtonian jets. In addition, laminar Newtonian jets do not collapse on a single curve (since they depend on Reynolds number) but every curve is linear. The shear-thinning jets, however, do not collapse under this normalization and their terminal decay rate, U_c/U_0, has a log slope somewhere between -15 and -30! That is, rather than decaying as $1/X$ (as in the case of Newtonian jets), these flows decay as X^{-15} or X^{-30} in the terminating region of the jet. We compared the velocity decay in the terminating region with a simple spherical source flow model (with a virtual origin) but did not obtain satisfactory agreement.

We attempted to collapse the pseudoplastic jet data in Fig. 9 using Reynolds number, $\mathrm{Re}_D = \rho U_0^{2-n} D^n / 8^{n-1} K$, Plasticity number, $\mathrm{Pl} = \tau_0/\rho U_0^2$, and Hedstrom number, $\mathrm{He} = \tau_0/K(U_0/D)^n$ (with a reference stress, τ_0 = 1 Pa) by scaling the X/D axis (definition of these parameters are obtained from Hanks, 1986). None of these scaling parameters captures the majority of the physics from the nozzle exit to the terminating region. Appropriate scaling for this problem may be difficult and involve two or more dimensionless groups.

Figures 10(*a–c*) show instantaneous streamwise velocity contour maps for a Newtonian jet at Re_D = 3000, a pseudoplas-

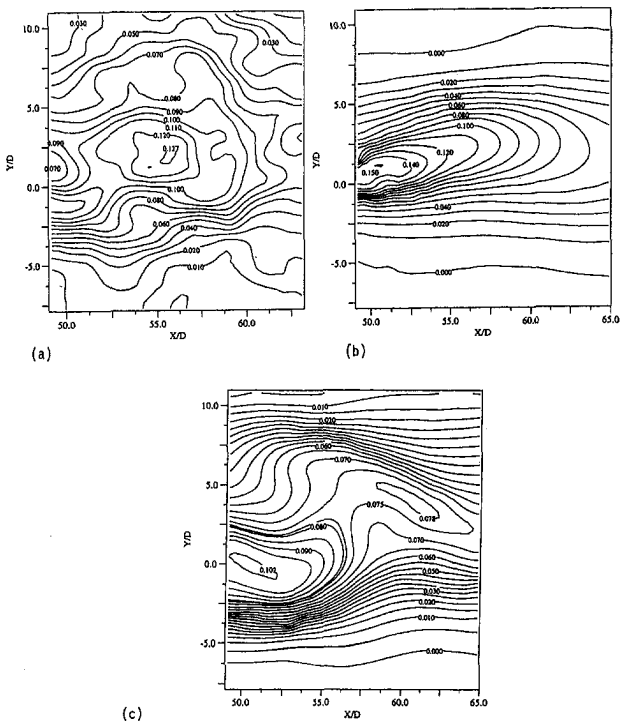

Fig. 10 Instantaneous streamwise velocity contour maps in a plane along the center-line of the jet: (*a*) Newtonian jet at Re_D = 3000; (*b*) pseudoplastic jet at Re_D = 3000; (*c*) pseudoplastic jet at Re_D = 6400

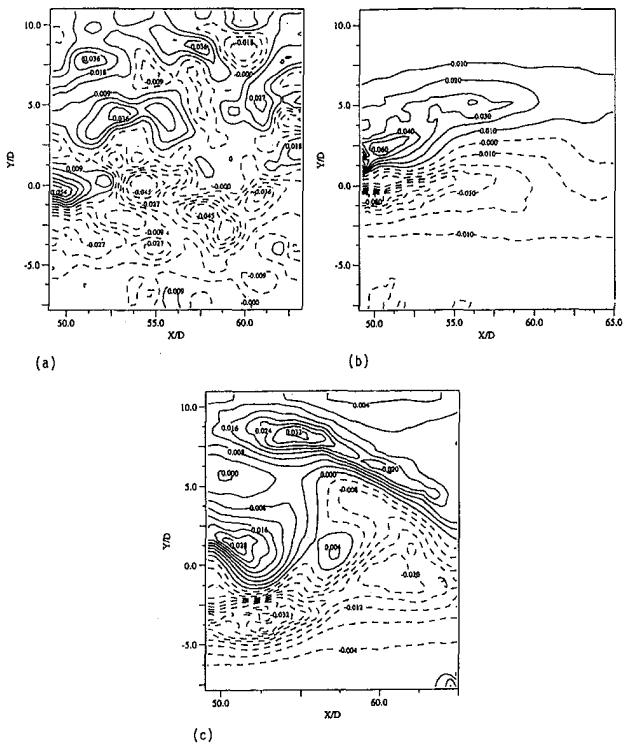

Fig. 11 Instantaneous cross-stream vorticity maps in a plane along the center-line of the jet: (*a*) Newtonian jet at Re_D = 3000; (*b*) pseudoplastic jet at Re_D = 3000; (*c*) pseudoplastic jet at Re_D = 6400

tic jet at Re_D = 3000, and a pseudoplastic jet at Re_D = 6400, respectively. The Reynolds number is defined in the usual manner for the Newtonian jet and as $Re_D = \rho U_0^{2-n} D^n / 8^{n-1} K$ for the pseudoplastic jet. Note that the terminating region for the non-Newtonian conditions are farther downstream and are not shown in these maps. The difference between the Newtonian and non-Newtonian jet is remarkable. The most evident difference is the laminar appearance of the non-Newtonian jet at the higher Reynolds number Re_D = 6400. The instantaneous centerline velocity appears to be lower in the case of the Newtonian jet. The lower magnitude of velocity is consistent with the radial distribution of velocity, which shows a larger growth of the Newtonian jet. Indeed, the radial location at which point the streamwise velocity drops below say 4 percent of the nozzle exit velocity is further away from the center-line for the Newtonian jet at Re_D = 3000, even when compared to the non-Newtonian jet at Re_D = 6400.

When the Reynolds number increases from 3000 to 6400, the non-Newtonian jet exhibits a very interesting behavior. In addition to having a lower centerline velocity, the core of the jet appears to be experiencing a sinuous type instability. When referring to the z-component of vorticity (Figs. 11(b)), we observe that at the low Reynolds number flow condition two distinctly separated regions of negative and positive vorticity exist. This is in contrast to a Newtonian jet in which pockets of negative and positive vorticity are distributed throughout the jet (Fig. 11(a). At the higher Reynolds number condition (Fig. 11(c)), the flow is no longer as symmetric as a result of the presence of the sinuous instability. Recall from Figs. 5(a) and 5(b) that at a velocity of 7.61 m/s, ring vortices traveled downstream along the shear layer. One could observe that the 0.03 and −0.03 peaks in the vorticity map at Re_D = 6400 might correspond to a ring vortex.

It is clear that a pseudoplastic jet cannot be adequately described using a single parameter such as a Reynolds number. In fact, it is problematic to make any general comparison between Newtonian and pseudoplastic jets. Although the issue of pseudoplastic jet scaling remains unresolved, it is clear that many types of flow behavior occur and more than one scaling parameter will be required to describe the jet.

4 Conclusions

Throughout this paper we have reported the results of pseudoplastic jet experiments. Several interesting features of a pseudoplastic jet seem noteworthy. An annular region of high frequency waves and traveling vortex rings may indicate existence of local turbulence, and a terminating region throughout which the jet undergoes a sudden growth are some of the qualitative features observed in this study. The center-line velocity within the terminating region decays rapidly as X^{-15} to X^{-30} and the results for various nozzle exit velocities do not seem similar when scaled with Reynolds, Plasticity, and Hedstrom numbers. The jet streamwise velocity was nearly symmetric at Re_D = 3000 and was sinuously unstable and asymmetric at Re_D = 6400.

These results have come from a preliminary study and we have raised many questions that need to be addressed in future studies. Future studies will rely on the use of Laser Doppler Velocimetry for a more careful examination of the transition region and the temporal nature of turbulence at various locations within a pseudoplastic jet. More comprehensive studies need to be performed to examine the scaling of a pseudoplastic jet as a function of rheology.

Acknowledgments

This project was supported by PNL under discretionary funding provided to the Fluid Dynamics Laboratory. The authors would like to thank Mr. Nick Lombardo from the Applied Physics Center and Dr. Fadel E. Erian from the Fluid Dynamics Laboratory of PNL for their continuing support.

References

Adrian, R. J., 1991, "Particle-Imaging Techniques for Experimental Fluid Mechanics," *Annual Review of Fluid Mechanics,* Vol. 23, pp. 261–304.

Barker, S. J., 1973, "Laser-Doppler Measurements on a Round Turbulent Jet in Dilute Polymer Solutions," *Journal of Fluid Mechanics,* Vol. 60, part 4, pp. 721–731.

Boger, D. V., and Walters, K., 1993, *Rheological Phenomena in Focus,* Elsevier Publishing, pp. 101–108.

Cenedese, A., and Paglialunga, A., 1990, "Digital Direct Analysis of a Multiexposed Photograph in PIV," *Experiments in Fluids,* Vol. 8, pp. 272–280.

Gutfinger, C., and Shinnar, R., 1964, "Velocity Distributions in Two-Dimensional Laminar Liquid-into-Liquid Jets in Power-Law Fluids," *AIChE Journal,* Vol. 10, No. 5, pp. 631–639.

Hanks, R. W., 1986, "Principles of Slurry Pipeline Hydraulics," *Encyclopedia of Fluid Mechanics,* N. P. Cheremisinoff, ed., Vol. 5, pp. 213–276.

Jordan, C., Rankin, G. W., and Sridhar, K., 1992, "A Study of Submerged Pseudoplastic Laminar Jets," *Journal of Non-Newtonian Fluid Mechanics,* Vol. 41, pp. 323–337.

Koziol, K., and Glowacki, P., 1989, "Turbulent Jets of Dilute Polymer Solutions," *Journal of Non-Newtonian Fluid Mechanics,* Vol. 32, pp. 311–328.

Kumar, K. R., Rankin, G. W., and Sridhar, K., 1984, "Laminar Length of a Non-Newtonian Fluid Jet," *Journal of Non-Newtonian Fluid Mechanics,* 15, pp. 13–27.

Mitwally, E. M., 1978, "Solutions of Laminar Jet Flow Problems for Non-Newtonian Power-Law Fluids," ASME JOURNAL OF FLUIDS ENGINEERING, Vol. 100, pp. 363–366.

Rajaratnam, N., 1976, *Turbulent Jets,* Elsevier Science Publishing Co., pp. 27–50.

Serth, R. W., 1972, "The Axisymmetric Free Laminar Jet of a Power-Law Fluid," *Journal of Applied Mathematics and Physics,* Vol. 23, pp. 131–138.

Terrones, G., and Eyler, L. L., 1993, "Computer Modeling of ORNL Storage Tank Sludge Mobilization and Mixing," PNL-8855/UC-510 Report, Pacific Northwest Laboratory, Richland, WA, pp. 5.12–5.23.

Trent, D. S., and Michener, T., 1993, "Numerical Simulation of Jet Mixing Concepts in Tank 241-SY-101," PNL-8559 Report, Pacific Northwest Laboratory, Richland, WA.

White, A., 1969, *Viscous Drag Reduction,* C. S. Wells, ed., Plenum Press, pp. 297–311.

Willert, C. E., and Gharib, M., 1991, "Digital Particle Image Velocimetry," *Experiments in Fluids,* Vol. 10, pp. 181–193.

Turbulent Vortex Ring/Free Surface Interaction

A. Weigand

M. Gharib

Graduate Aeronautical Laboratories,
California Institute of Technology,
Pasadena, CA 91125

The interaction of turbulent vortex rings that approach a clean water surface under various angles is experimentally investigated. The temporal evolution of the vortex rings with an initial Reynolds number of $Re_0 = 7500$ is characterized by the laminar/turbulent transition and asymptotic relaminarization of the flow. Using the shadowgraph technique, two major flow cases were identified as a result of the vortex-ring/free-surface interaction: a trifurcation case that results from the interaction during the transition stage, and a bifurcation case that evolves during the fully-developed turbulent stage. In contrast to the laminar interaction, the turbulent bifurcation pattern is characterized by the reconnection and mutual interaction of many small-scale structures. Simultaneous digital particle image velocimetry (DPIV) and shadowgraph measurements reveal that the evolution of the small-scale structures at the free surface is strongly dominated by the bifurcation pattern, which in turn is a consequence of the persisting laminar sublayer in the core regions of the reconnected turbulent vortex loops.

I Introduction

The interaction of complex shear flows (e.g., ship wakes) with a free surface is a very intriguing problem in fluid dynamics. Since full simulations of such complex flows are difficult to perform in the laboratory, free-surface interactions of elementary shear flows such as vortex rings and vortex couples have received much attention in the past. In this regard, the free-surface interaction of vortex rings and vortex couples was investigated mainly in the laminar flow regime. Bernal and Kwon (1989), Bernal et al. (1989), and Gharib et al. (1992) experimentally investigated the laminar vortex-ring/free-surface interaction. Bernal and Kwon showed that as a vortex ring approaches the free surface at an oblique angle, the upper part of the vortex ring deforms and opens its ends to reconnect to the surface. Additionally, Kwon (1989) observed that the lower part of the vortex ring can also interact with the free surface which results in the bifurcation of the vortex ring. Gharib et al. developed a physical flow model of the laminar vortex-ring reconnection including the effect of secondary vorticity that results from the local surface deformation and surface-tension differences.

In this paper, we mainly focus on the oblique interaction of turbulent vortex-rings with a free surface. Similar to experimental investigations of turbulent vortex/free-surface interactions (e.g., Sarpkaya et al., 1994), the major motivation for this study was to investigate the reconnection behavior of coexisting small- and large-scale structures in the presence of a highly three-dimensional flow field in the bulk. Additionally, in terms of the reconnection of closed vortex loops, turbulent vortex-rings can be regarded as elemental flow structures that are part of more complex free-surface flows such as high Reynolds and Froude number ship wakes.

There is relatively little knowledge about the physical properties of turbulent vortex rings (see, e.g., Maxworthy, 1974 and Glezer and Coles, 1990). Therefore, we extensively utilized flow visualization and digital particle image velocimetry (DPIV) to map the initial conditions and the flow field of the vortex rings in the fully-submerged case (Weigand and Gharib, 1994). The interaction of the turbulent vortex rings with the free surface was visualized with the shadowgraph technique. Using combined shadowgraph and DPIV, simultaneous measurements of the deformation field and velocity-vector field at the water surface were performed.

II Experimental Setup and Procedures

Experiments were conducted in a water tank filled with deionized water (D.I. water). Figure 1 shows a general schematic of the experimental setup. Vortex rings of diameter D, circulation Γ, and propagation velocity U_V were generated by a piston that pushes fluid out of a sharp-edged cylindrical nozzle with an inner orifice diameter of $D_0 = 2.0$ cm. The nondeformed water surface coincides with the x, z-plane, where the positive z-axis points toward the reader. The centerline of the vortex-ring generator (i.e., the x'-axis) is inclined with respect to the water surface at an angle α, and the origin $x' = 0$ is located at $x = 0$ and $y = -h$, where h designates the submergence depth.

Several different procedures were applied to keep the water and its surface clean, and to minimize surface contamination and surface-tension differences between the water in the bulk and at the surface. Besides working in a clean environment (i.e., wearing non-contaminating gloves, cleaning all parts in contact with water using ethyl alcohol, operating a UV filter to prevent bacterial growth in the water, and exchanging the D.I. water every second or third day), a constantly operating skimmer and a vacuum operated suction device were used to remove the aging water surface. Surface-tension measurements were performed before and after each experimental run using a ring tensiometer. An IBM PC provides precise timing and synchronization of different events in the experiment (time resolution better than 10^{-3} s). These events include vortex-ring generation, dye injection for flow visualization, and initialization of measurement processes.

Regarding DPIV, only those aspects of the measurement technique that are relevant to the present work are described in the following. For more details, the reader is referred to Willert and Gharib (1991). DPIV measures the two-dimensional displacement-vector field of particles that are suspended in the flow. As the schematic in Fig. 2 shows, the measurement plane is illuminated by a thin, pulsed sheet of laser light. In contrast to conventional particle image velocimetry, DPIV employs a video camera (RS 170 video standard) that records a sequence of images of the particle field. The camera is positioned normal to the illuminated measurement plane, while the exposure times

Contributed by the Fluids Engineering Division for publication in the JOURNAL OF FLUIDS ENGINEERING. Manuscript received by the Fluids Engineering Division October 17, 1994; revised manuscript received December 19, 1994. Associate Technical Editor: D. P. Telionis.

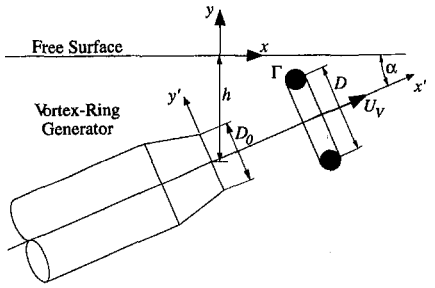

Fig. 1 General schematic of the experimental setup

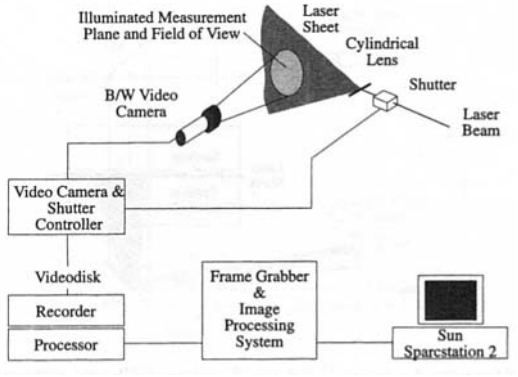

Fig. 2 Digital particle image velocimetry (DPIV) system

and the time difference between two successive image exposures are synchronized and controlled by a camera controller and a shutter. The latter prevents streaking particle images and limits the maximum displacement of particles in the imaging plane. The recorded image sequence is stored on an analog video disk and subsequently digitized by a frame grabber. By cross-correlating spatial sub-samples (windows) of two successive video images, the average local displacement vector of the particles contained in the correlation window is estimated. Moving the correlation window over the entire image (moving average), the displacement-vector field is obtained. The latter is divided by the time difference of two successive image exposures yielding the velocity-vector field.

In Fig. 3, the experimental setup of the simultaneous DPIV and shadowgraph measurement technique is shown. Regarding the shadowgraph setup, a high power light source (Mercury arc-lamp, 1000 W) is used in combination with a 20 cm (8 in) diameter spherical mirror (F# = 3) to generate a parallel beam of white light. The beam is reflected through the water surface by a front surface mirror (M2). A second front surface mirror (M3) projects the refracted light beam on a diffusive screen, where the shadowgraph images are recorded by a shuttered video camera. With respect to the velocity-field measurements, the DPIV camera focuses via mirror M2 through the bottom of the water tank onto the measurement plane. Therefore, refractive distortions of the particle-scatter light caused by the deformation of the water surface are eliminated. The measurement plane is illuminated by a 0.1 cm thick sheet of laser light that is positioned parallel and 0.1 cm below the water surface. A narrow band-pass filter (bandwidth: ±5 nm) centered on the green Argon-Ion laser line (514.5 nm) prevents the DPIV camera from recording scatter light of the shadowgraph illumination. To obtain a large overlapping field of view of both cameras, the parallax angle of $\Theta \approx 3.5°$ was kept small by positioning the spherical mirror M1 and the DPIV camera close to each other and at a relatively large distance of 2.5 m (8 ft) from mirror M2. As Fig. 4 shows, the exposure of the shuttered shadowgraph camera is centered between the two successive illumination peaks of the DPIV measurement. Therefore, the shadowgraph and DPIV measurements are truly simultaneous.

In the present experiments, neutrally buoyant, silver-coated glass spheres with an average diameter of 14 ± 5 μm were used as seeding particles. The DPIV images were digitized with a resolution of 768 × 480 pixels, and processed with a window size of 32 × 32 pixels and a step size for the moving average of 8 × 8 pixels (75 percent window overlap). The data processing results in a field measurement of 96 × 60 velocity vectors and, for a typical field of view of 11 × 8 cm, in a spatial wavelength resolution of 0.46 × 0.53 cm. In the fully-submerged flow case, the exposure times and time difference between exposures were chosen to be $t_{e1} = t_{e2} = 2 \cdot 10^{-3}$ s and $\Delta t = 6 \cdot 10^{-3}$ s. The simultaneous DPIV and shadowgraph measurements required a different illumination setting with $t_{e1} = t_{e2} = 11 \cdot 10^{-3}$ s, $\Delta t = 17 \cdot 10^{-3}$ s, and $t_{eS} = 4 \cdot 10^{-3}$ s. The resulting displacement-vector fields were geometrically corrected for the parallax error, while the relatively large exposure times of the DPIV camera were chosen in order to compensate for the loss of particle-scatter light in the bandpass filter. In the present results, the maximum surface velocities are smaller than 5 cm/s. Therefore, the maximum particle displacement was approximately 6 to 8 pixels, and the size of streaking particle images was limited to less than 4 pixels. Since the location of the cross-correlation peak can be resolved with a sub-pixel accuracy of better than 0.01 pixel (Willert and Gharib, 1991), the maximum uncertainty based on the local velocity and vorticity magnitude is ±1 and ±3 percent, respectively.

III Properties of Turbulent Vortex Rings

Prior to the investigation of the vortex-ring/free-surface interaction, the evolution of the vortex rings was investigated in

Nomenclature

D = diameter of vortex-ring
D_0 = inner diameter of cylindrical nozzle
Fr = Froude number; $\mathrm{Fr} = \Gamma/(gD^3)^{1/2}$
g = gravitational acceleration; g = 9.81 m/s^2
h = submergence depth of vortex-ring generator
n = wavenumber of bending instability
Re = Reynolds number of vortex ring; $\mathrm{Re} = \Gamma/\nu$
Re_0 = initial Reynolds number of vortex ring
t = time; $t = 0$: initiation of piston motion
t_e = frame-exposure time
Δt = time difference between exposures of DPIV measurements
U_V = propagation velocity of vortex ring
We = Weber number; $\mathrm{We} = \rho\Gamma^2/(\sigma D)$
x,y,z = Cartesian coordinate system; $y = 0$: location of non-deformed water surface
x',y',z' = Cartesian coordinate system fixed to vortex-ring generator; $x' = 0$: location of nozzle center
α = angle between centerline of vortex-ring generator and free surface
Γ = circulation of vortex ring
Γ_0 = initial circulation of vortex ring
ν = kinematic viscosity of water; $\nu = 10^{-2}$ cm^2/s
ρ = density of water; $\rho = 1000$ kg/m^3
σ = surface tension of water; $\sigma = 72.1 \pm 0.5$ dyn/cm (1 dyn = 10^{-5} N)
ω = vorticity component (indices x,y,z indicate direction)
Θ = parallax angle between DPIV and shadowgraph camera

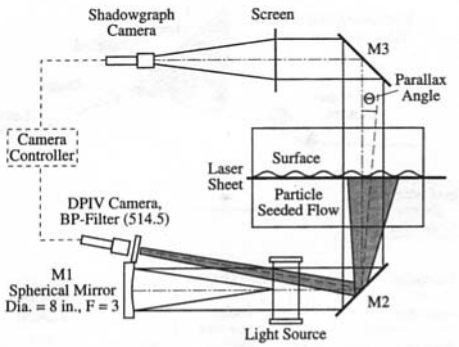

Fig. 3 Experimental setup of the simultaneous DPIV and shadowgraph technique

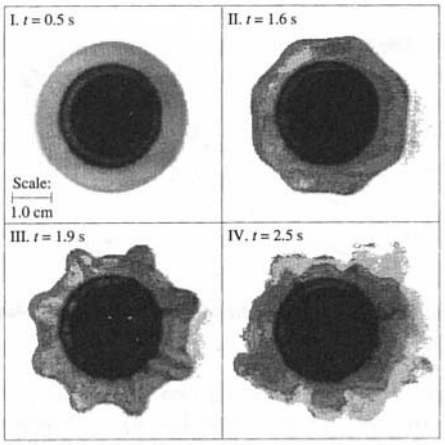

Fig. 5 Sequence of front views (along the negative x'-axis) of the evolution of a turbulent vortex ring with $Re_0 = 7500$

the fully-submerged case by means of flow-visualization and digital particle image velocimetry (DPIV). In the following, some major results of this study are reported for a flow case with initial Reynolds number of $Re_0 = 7500$ (for a more detailed discussion, see Weigand and Gharib, 1994). The Reynolds number is defined by the ratio of the circulation Γ to the kinematic viscosity ν, i.e., $Re = \Gamma/\nu$.

The image sequence shown in Fig. 5 indicates the important stages of the temporal evolution of the vortex ring. The images are front views (along the negative x'-axis) and were realized by using dye-flow visualization. Time $t = 0$ corresponds to the initiation of the piston motion. As Fig. 5-I shows, during the generation and for an initial period of $t \approx 1.3$ s, the vortex ring is characterized by a laminar flow behavior. After $t \approx 1.3$ s, azimuthal bending instabilities similar to those observed by Krutzsch (1936, 1939), Widnall and Sullivan (1973), and Widnall et al. (1974) start to develop which marks the beginning of the transition stage. In Fig. 5-II and III, the azimuthal bending instability with a wave number of $n = 8$ leads to a strong and symmetric growth of the ring deformation within a short period of approximately 0.3 s. As Fig. 5-IV shows, the latter causes a sudden break up of the vortex ring at $t \approx 2.5$ s which marks the beginning of the turbulent stage. As the side-view (along the negative z-axis) in Fig. 6 indicates, the turbulent stage is characterized by a strong dye-shedding process into the wake of the vortex ring.

In Fig. 7, DPIV measurements of the temporal evolution of the vortex ring are presented. The measurement plane coincides with the plane $z = 0$. Figure 7(a) shows the evolution of the magnitude of the circulation that was computed from the line integral of the velocity data along the vorticity contour $\omega_z = \pm 2.5\ s^{-1}$. As the experimental investigations of Willert and Gharib (1991) show, the uncertainty in the circulation measurement is better than ± 1 percent of the local circulation value. The vorticity contour $\omega_z = \pm 2.5\ s^{-1}$ separates the upper- and lower-core regions from the ambient flow field and the wake region. In order to cover the spatial extension of the flow, the evolution of the flow field was measured in seven consecutive and partially overlapping downstream regions. The circulation data is averaged over four independent realizations and was found to be repeatable within ± 2 percent of the presented average values. The solid line represents the mean value of the magnitude of the upper and lower core circulation. In Fig. 7(b)-I to IV, equi-vorticity contours of instantaneous flow fields that correspond to the major stages of the evolution of the vortex ring are shown. The vorticity field with $\omega_z = \partial v/\partial x - \partial u/\partial y$ was computed by using a second order finite differencing scheme and smoothed with a 3×3 radially weighting smoothing kernel.

During the initial stage, the nearly circular shape and dense distribution of vorticity contours at $t = 0.5$ s indicate the laminar and highly concentrated core structure of the vortex ring with peak vorticities of $\omega_z \approx \pm 80\ s^{-1}$. Shortly after the transition stage, the core structure in Fig. 7(b)-II shows first signs of the turbulent break up leading to a relatively mild reduction in the circulation of approximately 8 percent between 1.6 s $< t <$ 2.5 s. Additionally, the shape of the upper and lower core is symmetrically deformed, and its size has increased which is indicated by a 25 percent reduction of the peak vorticities. At $t \approx 3$ s, the on-going break up leads to a further reduction of the circulation due to the shedding of vorticity into the wake of the vortex ring.

Figure 7(a) shows that the circulation does not decrease monotonically, but in periodic stages with intermittent and nearly constant levels of circulation. In combination with the vorticity-contours in Fig. 7(b)-III, the latter is a remarkable indication of the periodic shedding process of small-scale struc-

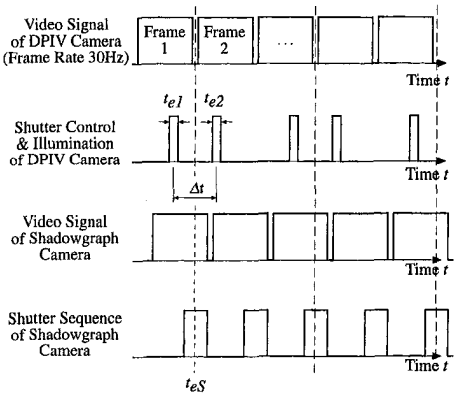

Fig. 4 Illumination and exposure sequence of the synchronized DPIV and shadowgraph cameras

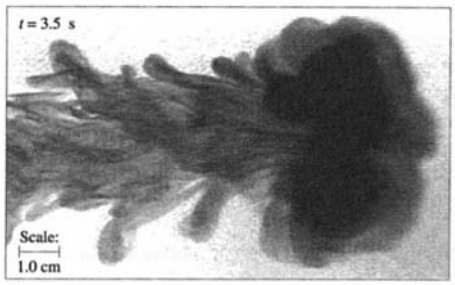

Fig. 6 Side view (along the negative z'-axis) of a turbulent vortex ring with $Re_0 = 7500$ after the transition stage

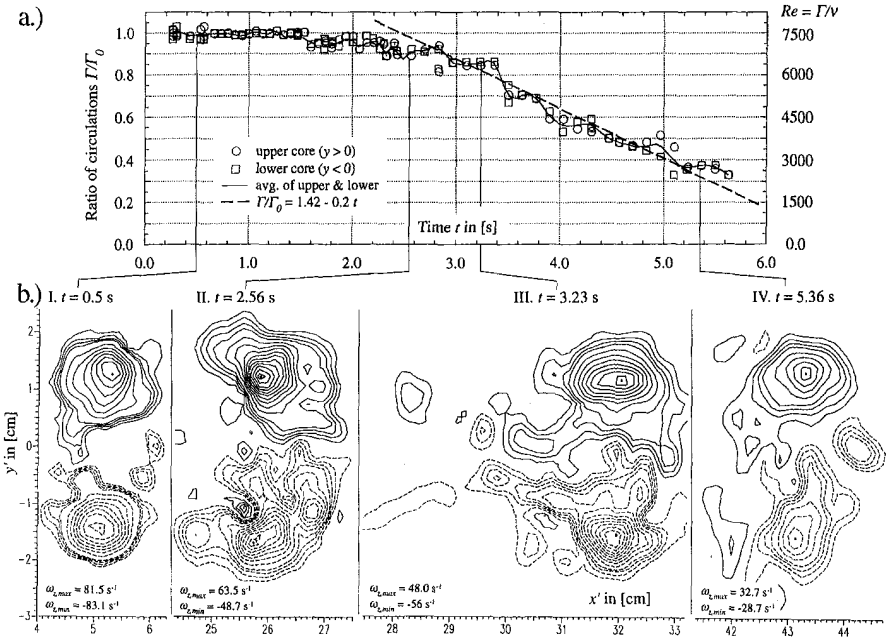

Fig. 7 Temporal evolution of a turbulent vortex ring with $Re_0 = 7500$: (*a*) circulation; (*b*) sequence of vorticity fields; frame I: $\Delta\omega_z = \pm 2.5\ s^{-1}$ for $2.5\ s^{-1} \leq |\omega_z| \leq 10\ s^{-1}$, $\Delta\omega_z = \pm 10\ s^{-1}$ for $|\omega_z| > 10\ s^{-1}$; frames II to IV: $\Delta\omega_z = \pm 2.5\ s^{-1}$ for $2.5\ s^{-1} \leq |\omega_z| \leq 10\ s^{-1}$, $\Delta\omega_z = \pm 5\ s^{-1}$ for $|\omega_z| > 10\ s^{-1}$

tures that contain a finite amount of circulation. Between 2.6 s $\leq t \leq$ 5.6 s, the time averaged decrease of the vortex-ring circulation is best described by the linear function $\Gamma/\Gamma_0 = 1.42 - 0.2t$. Figure 7(*b*)-III indicates that, even though the vortex ring is in the break-up stage, the vorticity distribution in the core regions remains relatively concentrated. After the vortex ring lost approximately 65 percent of its initial circulation to the wake, Fig. 7(*b*)-IV shows at $t = 5.4$ s, that the core structures are still persistent and regularly shaped. This indicates a fourth and asymptotic stage of the temporal evolution of the vortex ring, namely the relaminarization of the flow. In general, the loss of circulation is equivalent to a reduction of the Reynolds number of the vortex ring. In the case presented here, the Reynolds number decreases from the initial value of $Re_0 = 7500$ to $Re \approx 2300$ at $t = 5.6$ s.

IV Turbulent Vortex-Ring/Free-Surface Interaction

Overview. As the results of Section 3 indicate, the vortex ring can start to interact with the water surface at different stages, namely during the laminar, transition or fully turbulent stage. By varying the angle α and the submergence depth h of the vortex-ring generator in a range of $7 \leq \alpha \leq 20$ deg and $2D_0 \leq h \leq 3D_0$, the three interaction cases were investigated using a vortex ring with an initial Reynolds number of $Re_0 = 7500$. The Froude and Weber number based on the initial conditions are $Fr = \Gamma/(gD^3)^{1/2} = 0.46$ and $We = \rho\Gamma^2/(\sigma D) = 26$, with the initial diameter of the vortex ring $D = 3.0$ cm, the measured surface tension of D.I.-water $\sigma = 72.1 \pm 0.5$ dyn/cm, the density of water $\rho = 1000$ kg/m^3, and the gravitational acceleration $g = 9.81$ m/s^2.[1]

[1] The surface tension measurements with a ring tensiometer (nominal accuracy of ±0.1 dyn/cm and experimentally determined repeatability of ±0.5 dyn/cm) revealed that the efforts to keep the water surface clean practically prevented surface contamination. The latter is also indicated by the presented shadowgraph images, where the formation of Reynolds ridges due to surface-tension differences was not observed. Regarding DPIV measurements, the particle seeding with silver-coated glass spheres and a concentration in the order of 10^3 to 10^4 cm^{-3} had no measurable effect on the magnitude of the surface tension.

Interaction During the Transition Stage. The sequence of shadowgraph images in Fig. 8(*a*) shows the temporal evolution of the flow at the free surface for a vortex ring that starts to interact with the free surface during the transition stage. This case with $h = 3.8$ cm and $\alpha = 7$ deg leads initially to the bifurcation of the vortex ring. The bifurcation pattern is very similar to the results reported by Kwon (1989) who investigated the free-surface interaction of laminar vortex rings with a Reynolds number of $Re = 5000$ and an incidence angle of $\alpha = 20$ deg. The schematic in Fig. 9(*a*) shows the major stages of the vortex-ring bifurcation. Initially, the interaction with the free surface leads to the reconnection of the upper part of the vortex ring and the formation of a single, U-shaped vortex loop. Due to the impulse of the ring and the oblique angle with the free surface, the lower part of the vortex loop moves upward and, in the case of a clean surface, reconnects too. The latter leads to the splitting of the lower part of the vortex ring and the symmetric formation of two separate, U-shaped vortex loops. As frame I in Fig. 8(*a*) shows, the bifurcation process evolves in a regular fashion without the superposed reconnection of small-scale structures. Additionally, downstream of the bifurcation, a very distinct and regular wave pattern becomes visible that is not a result of imperfections in the initial conditions (e.g., mechanical vibrations or wave reflections caused by the tank walls). This pattern is very similar to a wave-field that is generated by the superposition of two closely aligned point sources. Upstream of the bifurcation, the surface-deformation field is characterized by waves that are aligned parallel to the x-axis. The latter is also observed during the interaction of vortex pairs with a free surface (see, e.g., Sarpkaya, 1992). As the reconnection of small-scale structures in frame II at $t = 3.2$ s indicates, the bifurcated and separated vortex loops break up simultaneously and leave behind a strong and elongated signature of their wake at the free surface. The latter is caused by longitudinal vortices that form during the initial stage of the vortex-ring break-up due to the strong growth of the bending deformations. The evolution of these longitudinal vortices in the wake of the bifurcated vortex loops leads to their simultaneous and symmetric reconnection at the free surface. Therefore,

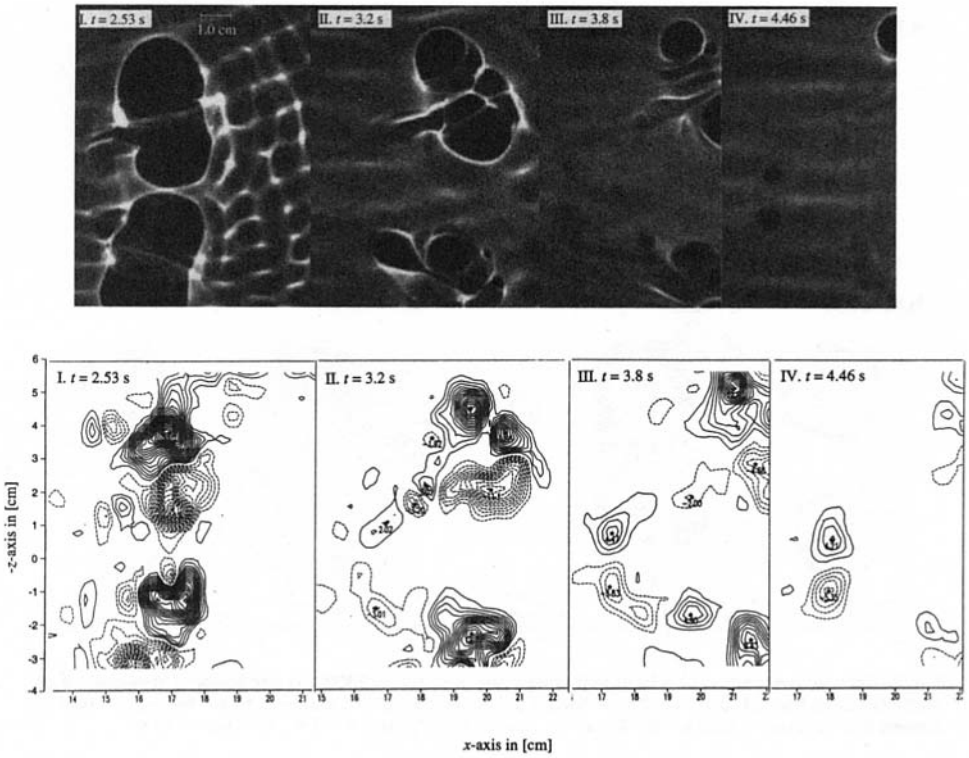

Fig. 8 Simultaneous DPIV and shadowgraph measurements of the reconnection of a vortex ring during the transition stage with $Re_0 = 7500$, $h = 3.8$ cm and $\alpha = 7°$: (*a*) sequence of shadowgraph images; (*b*) corresponding sequence of vorticity-fields; first vorticity contour $\omega_y = \pm 1\ s^{-1}$, step size $\Delta\omega_y = \pm 1\ s^{-1}$

as frames III and IV indicate, a third vortex pair appears upstream and centered between the bifurcated vortex loops which leads to a trifurcation pattern at the surface (see the schematic in Fig. 9(b)). This process was observed to be very typical and also repeatable for the vortex-ring/free-surface interaction during the transition stage.

Figure 8(b) shows DPIV measurements of the flow field close to the free surface in the plane $y = -0.1$ cm that are simultaneous with the shadowgraph images of Fig. 8(a). Since the spatial scale of Figs. 8(a) and 8(b) is the same, the vorticity (ω_y-component) and deformation field can be easily compared by superposing both image sequences. As frame I in Fig. 8(b) shows, the initial bifurcation pattern is clearly marked by two concentrated and reconnected vortex pairs. The spatial location and the size of the vortex pairs agrees very well with the deformation pattern shown in the corresponding shadowgraph image of Fig. 8(a)-I. In Fig. 8(b)-II, elongated vorticity regions upstream of the vortex pairs indicate the initial interaction of the longitudinal wake vortices with the free surface. Additionally, in partial agreement with the deformation field, the turbulent break up of the reconnected vortex loops is characterized by the formation and reconnection of small-scale vortices at the free surface. The reason for deviations between the deformation and the vorticity field in terms of the signature of small-scales at the free surface is twofold: first, the structures that are visible, for example, upstream of the bifurcated vortex pair in the lower part of the shadowgraph image of Fig. 8(a)-II are partially too small to be resolved by the DPIV measurements. Instead, the vorticity field in Fig. 8(b)-II indicates a comparatively large, negative vorticity region. Second, and more important in a physical sense, the deformation field is not only affected by the vortical regions, but also by the irrotational velocity field at the surface (see, e.g., Dommermuth, 1992). The latter is visible, for example, in frame I of Figs. 8(a) and 8(b), where the wave field upstream of the bifurcation pattern does not leave any signature in the vorticity field.

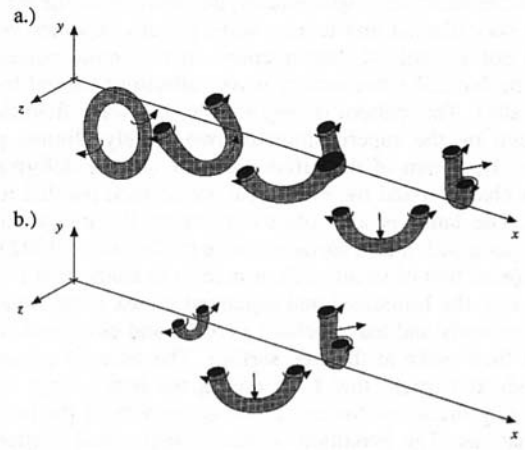

Fig. 9 Schematics of the major stages of (*a*) vortex-ring bifurcation and (*b*) transitional vortex-ring trifurcation

In frame III of Fig. 8(b), the vorticity field clearly shows the concentrated and symmetric reconnection of the wake vortices which leads to the formation of a third vortex pair and the eventual trifurcation pattern at the free surface. In contrast to the vorticity field, the shadowgraph image in Fig. 8(a)-III shows only a faint signature of the initial stage of the trifurcation pattern. The latter is marked by the curl-like shape of the surface deformation at the upstream end of the strongly elongated wake vortices. In good agreement with the deformation field, Fig. 8(b)-IV shows the further separation and concentration of the third vortex pair upstream of the bifurcated vortex loops.

Interaction During the Fully-Developed Turbulent Stage. In Fig. 10, the sequence of shadowgraph images shows the typical evolution of a fully-developed, turbulent vortex-ring/

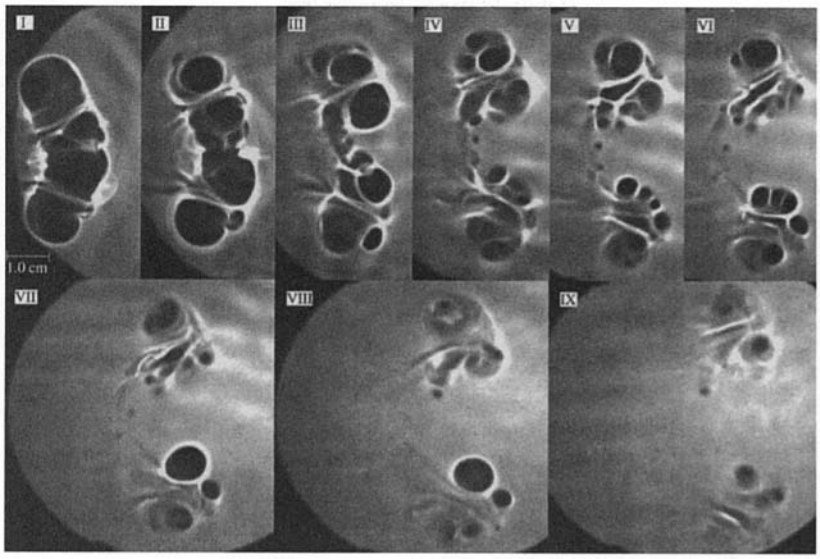

Fig. 10 Shadowgraph sequence of the reconnection of a fully-developed turbulent vortex ring with $Re_0 = 7500$, $h = 5.4$ cm and $\alpha = 7°$; frame I: $t = 3.3$ s, time difference between successive frames: 0.33 s

free-surface interaction with $h = 5.4$ cm and $\alpha = 7$ deg. The single frames are separated by a time difference of $\Delta t = 0.33$ s. As Frame I at time $t = 3.3$ s shows, the initial stage of the interaction is marked by a strong surface deformation that is caused by the reconnection of the upper part and the simultaneous upward motion of the lower part of the vortex ring. Between frame II and IV, the reconnection of the lower part leads to the bifurcation of the vortex ring into two separate and perpendicularly reconnected vortex loops at the free surface. However, in contrast to the transition case, the shadowgraph images indicate the early and multiple reconnection of smaller-scale structures as a consequence of the shedding process of the fully-developed turbulent vortex ring. The dynamics of the small-scale structures at the free surface appears to be dominated by the bifurcation pattern. However, as many observable pairing processes show, the small-scale structures interact strongly with each other within that bifurcation pattern. For example, in the lower part of the shadowgraph images between frame III and VII, four distinct small-scale structures reconnect to the free surface, of which at least three are subject to a very rapid pairing process. The triple pairing evolves in less than 0.33 s between frame VI and VII and leads to a concentrated and relatively large-scale single vortex. The latter is indicated by the strong and circular surface deformation in the lower part of frames VII and VIII.

Figures 11(a) to 11(c) show a typical example of simultaneous DPIV and shadowgraph measurements of the vortex-ring/free-surface interaction during the fully-developed turbulent stage. The figure shows the evolution of the turbulent bifurcation at the free surface in the half plane $z \leq 0$. The initial conditions are the same as in the flow case presented in Fig. 10. In order to compare the spatial correspondence, the resulting vorticity and deformation fields are superposed to each other (the gray scale of the shadowgraph images was slightly modified to enhance the visibility of the vorticity contours).

Figure 11(a) shows the initial and distinct deformation pattern at the surface consisting of the bifurcated vortex pair superposed by several small-scale structures. For example, in the center and the upper part of the vortex pair, the separated small-scale dark regions of the shadowgraph image are in excellent spatial agreement with small-scale vortical regions. In the lower part of Fig. 11(a) the large circular deformation corresponds to a relatively large and concentrated vortex. Additionally, in the wake of the vortex pair, the flow field at the surface consists of several small-scale vortical structures that are not visible as single structures in the deformation field. Following the temporal evolution of the vorticity and deformation field, Fig. 11(b) indicates that the small-scale structures spatially align according to the flow field that is induced by the bifurcated and relatively strong vortex pair. In comparison to Fig. 11(a), the vortex pair still leads to a visible but weaker surface deformation. The latter is also indicated in the vorticity field, where the scale of the major vortex pair increases and the magnitude of the peak vorticity decreases.

Figure 11(c) shows that the upper vortex re-concentrates its vorticity distribution which is indicated by the dense distribution of equi-vorticity contours, a relatively high peak vorticity, and a strong surface deformation. In contrast to that, the size of the lower vortex is increased and its peak vorticity reduced yielding a relatively weak surface deformation. In comparison to the earlier stages, Fig. 11(c) shows that the number of reconnected small-scale structures has considerably reduced. The latter is a result of the combined action of different mechanisms, e.g., the loss of structures to the wake and the underlying three-dimensional flow, and pairing processes at the free surface similar to those shown in Fig. 10.

In comparison to the development of the fully-submerged turbulent vortex ring, Fig. 12 shows the temporal evolution of the total positive and negative circulation Γ_+ and Γ_- that reconnects to the free surface within the boundaries of the measurement region (i.e., in the half-plane $z \leq 0$). Within the regarded time interval, the flow behavior at the surface is symmetric with respect to the magnitudes of the total circulations, i.e., $|\Gamma_+| = |\Gamma_-|$. The latter indicates that all reconnection and disconnection events within the measurement region are accounted for. As Fig. 12 shows, the magnitude of the reconnected total circulation in the half plane $z \leq 0$ is approximately 70 percent of the vortex-ring circulation in the fully-submerged case. As is evident from the schematics in Fig. 9(a), in the case of a laminar vortex-ring bifurcation, the reconnected vortex pair can be expected to have the same amount of circulation as the fully-submerged vortex ring. In the case of a turbulent bifurcation, however, it is not clear at this point, why only 70 percent of the vortex-ring circulation are detected at the free surface. One can conjecture that the three dimensional flow field in the bulk prevents part of the small-scale structures from reconnecting to the surface. On the other hand, the underlaying flow field might cause multiple folding, bending, and reconnection processes of single vortex tubes leading to an increase

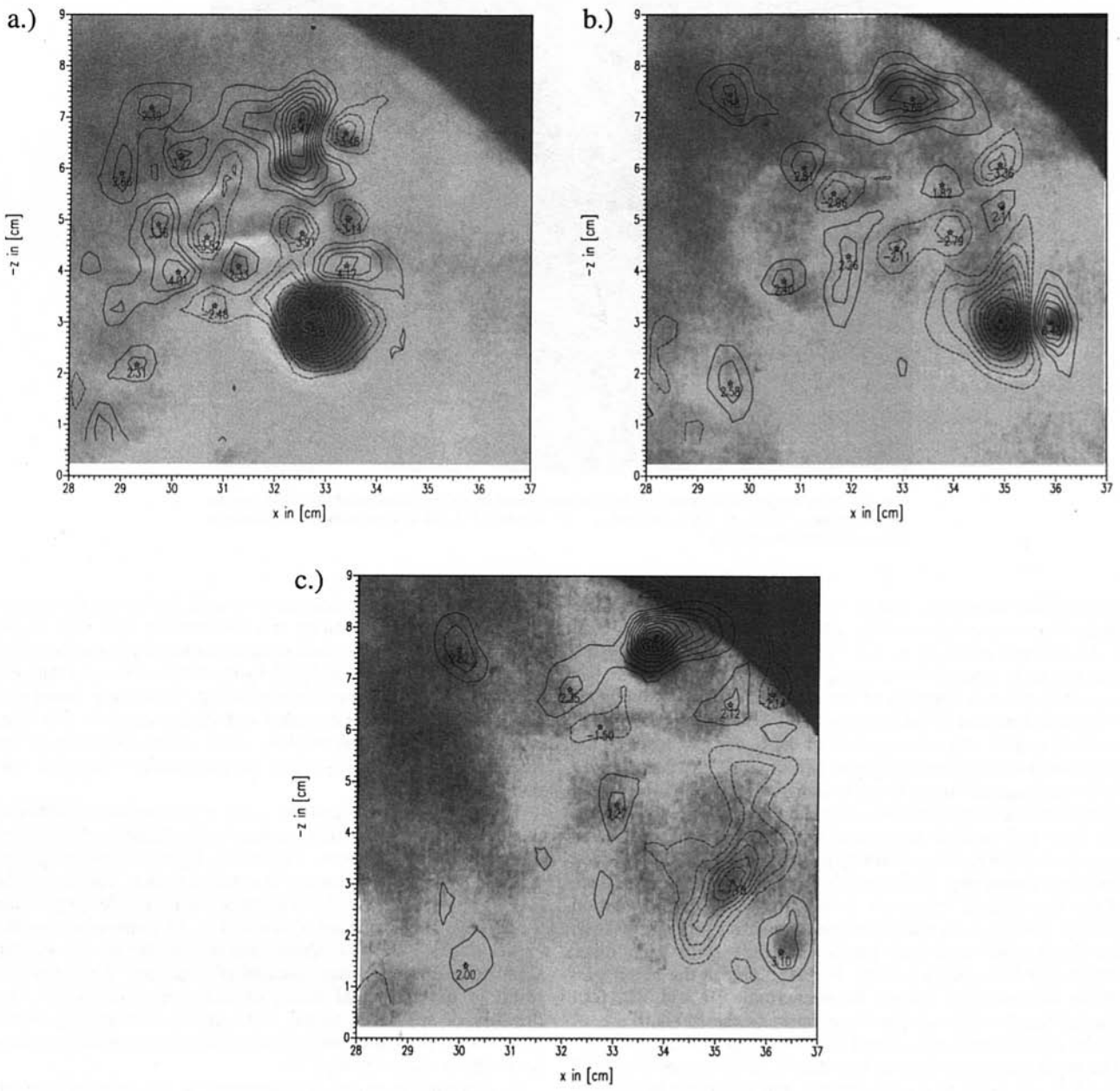

Fig. 11 Overlay sequence of simultaneous DPIV and shadowgraph measurements for the reconnection of a fully-developed turbulent vortex ring with $Re_0 = 7500$, $h = 5.4$ cm and $\alpha = 7°$; first vorticity contour $\omega_y = \pm 1\ s^{-1}$, step size $\Delta\omega_y = \pm 1\ s^{-1}$; (*a*) $t = 5.2$ s, (*b*) $t = 6.2$ s, and (*c*) $t = 6.9$ s

of the circulation at the surface. However, the limited spatial resolution of the measurement technique makes it experimentally difficult to detect and separate the effects of the bulk flow on the reconnection behavior of smaller-scale structures.

To gain more information about the mechanisms that are of importance for the flow behavior at the free surface, the measurement sequence in Fig. 11 was used to track the development of the small-scale structures and their associated circulations. In Fig. 13, splitting and pairing as well as reconnection and disconnection events are marked by different symbols. At time $t \approx 4.7$ s, the regarded flow field contains four separate structures, while at $t \approx 5.2$ s, three additional small-scale vortices reconnect to the surface. For example, at $t \approx 5.5$ s, the structure with a circulation of $\Gamma \approx 19\ cm^2/s$ was formed by a triple pairing event and separates into three new structures due to a splitting event. During the regarded time interval, a total of ten pairing and ten splitting events were observed, which also includes the pairing of opposite sign vorticity, i.e. the cancellation of vorticity at the free surface. As Fig. 13 shows, pairing and splitting events can be observed on all measured scales. Between 5.5 s $\leq t \leq$ 6.9 s, the number of small-scale structures is reduced from seven to four, while the number of large-scale structures (major vortex pair) remains constant.

V Conclusions

Regarding the vortex-ring/free-surface interaction, two distinct flow cases were observed. During the interaction in the transition stage, the vortex ring initially bifurcates into two separate vortex pairs at the free surface, while the longitudinal wake vortices of the bifurcated vortex loops simultaneously reconnect and form a third vortex pair at the free surface. During the evolution of this trifurcation case, the bifurcated and reconnected vortex loops break up at the free surface which leads to the subsequent reconnection of small-scale structures. Similar to the transition case, the interaction in the fully-developed

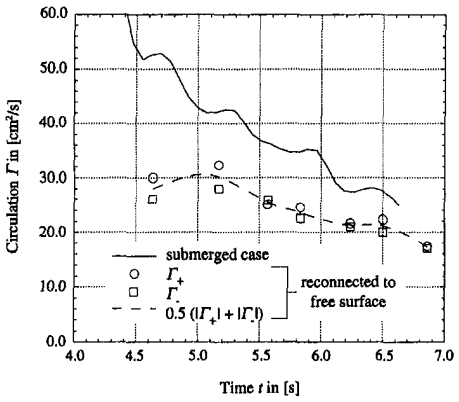

Fig. 12 Comparison of the vortex-ring circulation in the submerged case with the evolution of the total circulation that reconnects to the free surface in the half-plane $z \leq 0$ during the fully-developed turbulent interaction case presented in Fig. 11

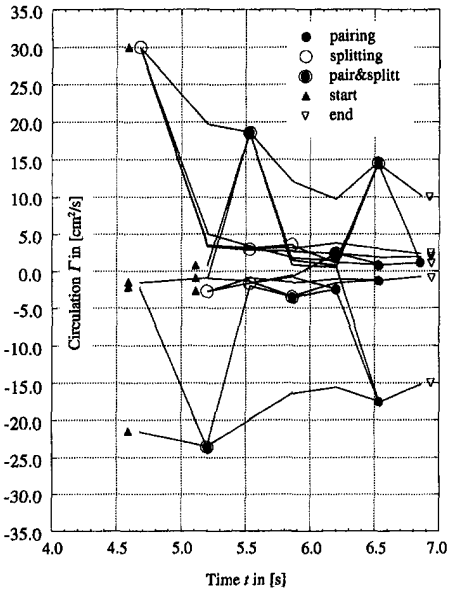

Fig. 13 Temporal evolution of the circulation of individual structures that are reconnected to the free surface in the half-plane $z \leq 0$ during the fully-developed turbulent interaction case presented in Fig. 11

turbulent stage leads also to the bifurcation of the vortex ring. However, from the beginning of the interaction, the bifurcation pattern is superposed by multiple reconnections of small-scale structures. It is interesting to note that the formation of a regular flow pattern at the free surface during the transition and the fully-developed turbulent stage is not affected by the mutual interaction of small-scale structures that are present in the bulk and reconnected to the surface. In combination with relatively high Reynolds numbers, the bifurcation or trifurcation patterns are observed for considerably smaller angles of incidence as compared to the case of laminar vortex-ring/free-surface interactions.

Shadowgraph visualization and simultaneous DPIV measurements of the fully turbulent interaction show that the small-scale structures mutually interact with each other in form of pairing processes that evolve at the surface within the bifurcated vortex-pair pattern. The vorticity field at the free surface is characterized by many pairing and splitting events that evolve on all measured scales. In the case of concentrated and spatially separated vortical structures, the vorticity field is in excellent spatial agreement with the corresponding shadowgraph images.

In addition to the mutual interaction of the small-scale structures, the bifurcated vortex loops strongly align and partially engulf the small-scale structures according to the induced velocity field at the free surface. The latter is dominated by the vortex-pair pattern that contains a relatively high concentration of vorticity and results from the persisting laminar sublayer in the core structure of the turbulent vortex ring.

The dominance of large-scale and highly-concentrated vorticity regions over the small-scale structures at the free surface is similarly observed for the case of turbulent vortex/free surface interactions (see, e.g., Sarpkaya et al., 1994). This behavior can also be expected in higher Reynolds and Froude number flows such as ship wakes, where large-scale structures coexist with small-scale turbulence in the background. Therefore, in terms of modeling turbulent free-surface flows, it is imperative to include the effect of large-scale vortices.

Acknowledgments

This work has been sponsored by the Office of Naval Research under the ONR-URI grant N00014-92-J-1610.

References

Bernal, L. P., and Kwon, J. T., 1989, "Vortex Ring Dynamics at a Free Surface," *Physics of Fluids* A, Vol. 1, pp. 449–451.

Bernal, L. P., Hirsa, A., Kwon, J. T., and Willmarth, W. W., 1989, "On the Interaction of Vortex Rings and Pairs with a Free Surface for Varying Amounts of Surface Active Agents," *Physics of Fluids* A, Vol. 1, pp. 2001–2004.

Dommermuth, D. G., 1994, "The initialization of vortical free-surface flows," ASME JOURNAL OF FLUIDS ENGINEERING, Vol. 116, pp. 95–102.

Gharib, M., Weigand, A., Willert, C., and Liepmann, D., 1992, "Experimental Studies of Vortex Reconnection to a Free Surface: A Physical Flow Model," Preprints, *19th. Symposium on Naval Hydrodynamics,* Seoul, Korea, Vol. 2, pp. 189–201.

Glezer, A., and Coles, D., 1990, "An Experimental Study of a Turbulent Vortex Ring," *Journal of Fluid Mech.,* Vol. 211, pp. 243.

Krutzsch, C. H., 1936, "Über ein instabiles Gebiet bei Wirbelringer," *Zeitschrift für angewandte Mathematik und Mechanik,* Vol. 16, pp. 352–353.

Krutzsch, C. H., 1939, "Über eine experimentell beobachtete Erscheinung an Wirbelringen bei ihrer translatorischen Bewegung in wirklichen Flüssigkeiten," *Annalen der Physik,* Vol. 35, pp. 497–523.

Kwon, J. T., 1989, "Experimental Study of Vortex Ring Interaction with a Free Surface," Technical Report No. 89-06, University of Michigan, Dept. of Aerospace Engineering, Ann Arbor, MI.

Maxworthy, T., 1974, "Turbulent Vortex Rings," *Journal of Fluid Mechanics,* Vol. 64, pp. 227–239.

Sarpkaya, 1992, "Three-Dimensional Interactions of Vortices with a Free Surface," AIAA 92-0059, *Proceedings of the 30th AIAA Aerospace Sciences Meeting,* Reno, NV.

Sarpkaya, T., Magee, M., and Merrill, C., 1994, "Vortices, Free Surface and Turbulence," *1994 ASME Symposium on Free-Surface Turbulence,* Lake Tahoe, CA.

Weigand, A., and Gharib, M., 1994, "On the Decay of a Turbulent Vortex Ring," *Physics of Fluids,* Vol. 6, pp. 3806–3808.

Widnall, S. E., and Sullivan, J. P., 1973, "On the Stability of Vortex Rings," *Proceedings of the Royal Society of London,* A, Vol. 332, pp. 335–353.

Widnall, S. E., Bliss, D. B., and Tsai, C.-Y., 1974, "The Instability of Short Waves on a Vortex Ring," *Journal of Fluid Mechanics,* Vol. 66, pp. 35–47.

Willert, C. E., and Gharib, M., 1991, "Digital Particle Image Velocimetry," *Experiments in Fluids,* Vol. 10, pp. 181–193.

Xing Yu
Graduate Student Researcher.

Ronald W. Yeung
Professor and Department Chair.

Department of Naval Architecture and Offshore Engineering,
University of California at Berkeley, CA 94720

Interaction of Transient Waves With a Circular Surface-Piercing Body*

A pseudo-spectral formulation for solving unsteady, three-dimensional fluid motion with a free surface in cylindrical coordinates is presented. An effective method for treating the Laplace equation, as a special application of a generalized Poisson solver, is developed. This approach is demonstrated by studying the evolution of transient surface waves near a vertical circular cylinder enclosed in open or closed domains. Results are observed to have a high degree of precision and spatial resolution even at large time. Potential applications of this method to other problems are discussed.

1 Introduction

In many marine-related engineering problems, one is faced with the task of estimating the unsteady wave loads on a fixed body, or the unsteady motion of the body if it were not rigidly mounted. The hydrodynamic interaction of waves and bodies is therefore a subject of much recent and continuing interest.

While much of the classical literature on this subject area has been directed toward frequency-domain analyses, it has become increasingly popular to attack the problem directly in the time domain. If one is restricted to the case of inviscid-fluid motion, boundary-integral formulation remains the most attractive approach. Under this category, there are two basic approaches, one is based on the availability of a time-dependent free-surface Green function, whose numerical evaluation is non-trivial (Wehausen, 1967; Yeung, 1981; Beck and Liapis, 1987; Korsmeyer et al., 1988). The other is based on the so-called "simple-source" or Rankine-source formulation, in which case the free-space source is distributed on the free-surface (Bai and Yeung, 1974; Gadd, 1976; Isaacson and Cheung, 1990; Nakos and Sclavounos, 1990). This latter approach normally leads to a larger number of unknowns and requires the use of an approximate open-boundary condition.

If only relatively simple geometries are under consideration, such as circular or elliptical cylindrical structures, which occur frequently in ocean-related applications, it would be worthwhile to pursue a pseudo-spectral formulation. This is the thematic approach being investigated and demonstrated here.

During the past two decades, spectral methods in one form or another have been extensively studied and applied to the numerical solution of several fluid dynamics problems (Yeung, 1975; Gottlieb and Orszag, 1977; Korczak and Patera, 1986; Hussaini and Zang, 1987; Tan, 1989, among others). Although the methods are restrictive in their ability to handle general geometry, their efficiency and accuracy are outstanding. In the present paper, a pseudo-spectral formulation is developed for the solution of unsteady three-dimensional free-surface flow around circular structures. Specifically, a Poisson-equation solver is first examined on the basis of a spectral formulation. Although a Laplace-equation solver would have sufficed for the particular types of problem considered here, successful treatment of the Poisson equation would allow one to handle the solution of the pressure equation in a viscous fluid in future work (see Yeung and Yu, 1994).

In Section 2, we review the formulation of such hydrodynamic problems within the framework of unsteady linearized flows. Section 3 describes the pseudo-spectral method of solution for free-surface flow. Analytical validation and accuracy assessment of the numerical algorithm are addressed in Section 4. Section 5 details the application of this new method to obtain the solutions of two unsteady three-dimensional problems. Future potential and extension of this method is discussed in a concluding section.

2 Formulation of the Problem

In this section the theoretical background for solving transient three-dimensional free-surface flow is briefly reviewed. Consider a fixed cylindrical coordinate system (r, θ, z) chosen so that the z-axis points vertically upwards and the undisturbed free-surface is at $z = 0$ (see Fig. 1). The fluid region Ω is enclosed by the cylindrical body boundary $\mathcal{S}$ located at $r = r_i$, free-surface $\mathcal{F}$ at $z = 0$, far-field boundary Σ at $r = r_0$, and a bottom $\mathcal{B}$ located at $z = -d$.

Under the assumptions that the flow is irrotational and the fluid incompressible, it can be established that there exists a velocity potential of the flow ϕ, which satisfies the Laplace equation,

$$\nabla^2\phi = 0 \tag{1}$$

in the domain Ω, with the following boundary conditions (see, e.g., Wehausen and Laitone, 1960):

On $\mathcal{F}$, a Dirichlet condition for ϕ can be obtained by a time-stepping of the potential using the linearized dynamic condition:

$$\frac{\partial\phi}{\partial t} = -g\eta, \tag{2}$$

where g is the gravitational acceleration, and $\eta(r, \theta, t)$ is the free-surface elevation. The latter satisfies the following linearized kinematic condition:

$$\frac{\partial\eta}{\partial t} = \frac{\partial\phi}{\partial z}. \tag{3}$$

The exact or nonlinear conditions on the free surface can be found in Yeung (1982). The above linearized conditions, which are based on a small wave-amplitude assumption, are used for demonstrative purposes. On $\mathcal{S}$, which may be considered to have

* Preliminary version of this work received the 1993 Best Graduate Student Paper Award of ASME-Ocean Engineering Division. Revised version submitted to ASME JOURNAL OF FLUIDS ENGINEERING.

Contributed by the Fluids Engineering Division for publication in the JOURNAL OF FLUIDS ENGINEERING. Manuscript received by the Fluids Engineering Division January 29, 1994; revised manuscript received August 10, 1994. Associate Technical Editor: M. Gharib.

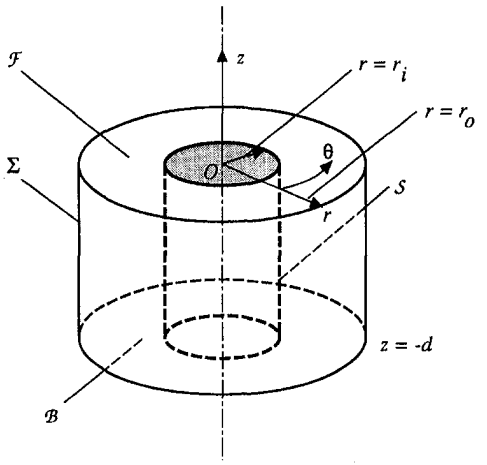

Fig. 1 Notation and coordinate system

a prescribed velocity **V**, the appropriate normal derivative for ϕ is

$$\phi_n = \mathbf{V}\cdot\mathbf{n}, \tag{4}$$

where **n** is a normal on the body surface pointing outwards of Ω. On $\mathcal{B}$, the following no-flux condition is applicable:

$$\phi_z = 0. \tag{5}$$

On the surface Σ, if it is a solid boundary,

$$\phi_n = 0. \tag{6}$$

If Σ is taken as a far-field boundary, we may impose

$$\phi = 0 \tag{7}$$

as an approximation for an open boundary, provided that Σ is taken to be sufficiently large so that no wave disturbances reach Σ. Alternatively, one might consider a time-dependent Sommerfeld type radiation condition as carried out in Yeung and Vaidhyanathan (1992). This latter case is treatable within the present framework of solution.

To complete the problem, initial conditions for ϕ and its derivatives on $\mathcal{F}$ should be specified.

3 Pseudo-Spectral Method of Solution

3.1 A Poisson-Equation Solver. The solution of Eq. (1) may be considered as a special application of a Poisson solver which is also needed in a number of closely related fluid-mechanics problems (see, e.g., Yeung and Ananthakrishnan, 1992). Here we will develop a pseudo-spectral formulation using ideas similar to Tan (1985). For the present problem in cylindrical coordinates, we will exploit Chebyshev polynomials in the vertical direction and Fourier modes in the circumferential direction. The resulting finite-difference equations for the radial direction are treated by a diagonalization technique. The method developed can treat both homogeneous and inhomogeneous boundary conditions of the Dirichlet, Neumann, or mixed type, which encompass the class of boundary conditions stated in Section 2.

For the right-handed cylindrical coordinate system (r, θ, z) shown in Fig. 1, the independent variables are defined in the following ranges:

$$\begin{aligned} r_i \le r \le r_0 \\ 0 \le \theta \le 2\pi \\ -d \le z \le 0 \end{aligned} \tag{8}$$

where r_i and r_0 are the radii of the inner and outer cylindrical boundaries, respectively. It is convenient to map the above domain into a normalized computational domain (R, Φ, Z) such that

$$\begin{aligned} -1 \le R \le 1 \\ -1 \le \Phi \le 1 \\ -1 \le Z \le 1 \end{aligned} \tag{9}$$

by using the following relations:

$$\begin{aligned} r &= \zeta R + \xi \\ \theta &= (1 + \Phi)\pi \\ z &= \kappa(-1 + Z) \end{aligned} \tag{10}$$

where $\zeta = \frac{1}{2}(r_0 - r_i)$, $\xi = \frac{1}{2}(r_0 + r_i)$, and $\kappa = d/2$ are scale and translational factors.

In (R, Φ, Z), the Poisson equation $\nabla^2 U = S(R, \Phi, Z)$, as a generalization of (1), can be written as:

$$\left[\mathcal{L} + \frac{1}{(\zeta R + \xi)^2\pi^2}\frac{\partial^2}{\partial\Phi^2} + \frac{\partial^2}{\kappa^2\partial Z^2}\right]U(R, \Phi, Z) = S(R, \Phi, Z) \tag{11}$$

where

$$\mathcal{L} \equiv \frac{1}{\zeta^2}\frac{\partial^2}{\partial R^2} + \frac{1}{\zeta(\zeta R + \xi)}\frac{\partial}{\partial R}. \tag{12}$$

Here we use U to designate the more general case of an un-

Nomenclature

a = amplitude of body motion
$\mathcal{B}$ = bottom of the fluid domain (at $z = -d$)
d = fluid depth
$\mathcal{F}$ = free surface (at $z = 0$)
F_x = horizontal force acting on the body
g = gravitational acceleration
h = grid spacing in the radial (R) direction
K.E. = kinetic energy in the fluid domain
L = number of grids in the radial (R) direction
M = number of grids in the circumferential (Φ) direction, an even integer
$\mathbf{n}$ = (n_x, n_y, n_z) unit outward normal to fluid
N = number of grids in the vertical (Z) direction
p = pressure in the fluid
P.E. = potential energy in the fluid domain
(r, θ, z) = cylindrical coordinates in physical space
(R, Φ, Z) = normalized cylindrical coordinates in computational space
$\mathcal{S}$ = body surface (at $r = r_i$)
T.E. = total energy in the fluid domain
ϵ = error tolerance value
η = free-surface elevation
λ_{xx} = damping coefficient in x-direction due to body motion in the x-direction
μ_{xx} = added mass in x-direction due to body motion in the x-direction
Σ = outer boundary (at $r = r_0$)
ϕ = velocity potential
ω = angular frequency of oscillatory motion of body
Ω = fluid domain

known function where the Poisson instead of the Laplace equation is satisfied. Clearly, for inviscid-fluid applications, one would simply take $S = 0$.

The boundary conditions in Eqs. (2), (3), (5), (6), or (7) can be treated as special cases of the following generalized types:

$$\alpha_{\pm}U(\Phi, Z) + \beta_{\pm}\frac{\partial U(\Phi, Z)}{\partial R} = F_{\pm}(\Phi, Z), \quad \text{at} \quad R = \pm 1 \tag{13}$$

$$A_{\pm}U(R, \Phi) + B_{\pm}\frac{\partial U(R, \Phi)}{\partial Z} = H_{\pm}(R, \Phi), \quad \text{at} \quad Z = \pm 1 \tag{14}$$

with all $\alpha_{\pm}$, $\beta_{\pm}$, $A_{\pm}$, and $B_{\pm}$ considered given constants.

In our spectral approach to the solution of Eq. (11), the functions U, S, $F_{\pm}$, and $H_{\pm}$ are approximated by truncated Chebyshev-Fourier series of the form:

$$\begin{Bmatrix} U(R, \Phi, Z) \\ S(R, \Phi, Z) \\ F_{\pm}(\Phi, Z) \end{Bmatrix} = \sum_{m=-M/2}^{(M/2)-1}\sum_{n=0}^{N}\begin{Bmatrix} U_{mn}(R) \\ S_{mn}(R) \\ f_{\pm mn} \end{Bmatrix} e^{im\pi\Phi}T_n(Z), \quad i = \sqrt{-1} \tag{15}$$

and

$$H_{\pm}(R, \Phi) = \sum_{m=-M/2}^{(M/2)-1} h_{\pm mn}(R)e^{im\pi\Phi} \tag{16}$$

where the Chebyshev polynomials $T_n(Z)$ are given by $\cos [n \cos^{-1} Z]$. Note that by assumption, we consider S_{mn}, $f_{\pm mn}$, and $h_{\pm mn}$ as given, while the sequence U_{mn} are unknown functions to be solved.

By introducing a Chebyshev-Tau representation (Gottlieb and Orszag, 1977) to incorporate the boundary conditions (14) at $Z = \pm 1$, and by applying the recurrence relations for the derivatives of Chebyshev polynomials, we can rewrite:

$$\frac{\partial^2 U}{\partial Z^2} = \sum_{m=-M/2}^{(M/2)-1}\sum_{n=1}^{N-1} U_{mn}^{(0,2)}(R)e^{im\pi\Phi}T_n(Z), \tag{17}$$

where

$$U_{mn}^{(0,2)}(R) = \sum_{q=0}^{N-2}\gamma_{nq}U_{mq}(R) + D_{mn}(R). \tag{18}$$

Expressions for γ_{nq} and $D_{mn}(R)$ can be derived after some effort and form the crux of the present numerical development. The lengthy expressions for γ_{nq} and $D_{mn}(R)$, in terms of known quantities, are omitted here for clarity of exposition. Substitution of the above results (Eqs. (17) and (18)) into the Poisson Eq. (11) yields:

$$\left[\mathcal{L} - \frac{m^2}{(\zeta R + \xi)^2}\right]U_{mn}(R) + \frac{1}{\kappa^2}\sum_{q=0}^{N-2}\gamma_{nq}U_{mq}(R) = S_{mn}(R) - \frac{1}{\kappa^2}D_{mn}(R) \equiv \sigma_{mn}(R) \tag{19}$$

for $m = -M/2$ to $(M/2) - 1$, and $n = 1$ to $N - 1$.

To avoid solving Eq. (19) with full coupling between m and n, we first proceed to diagonalize a matrix $\mathbf{\Gamma}$ with elements γ_{nq}. $\mathbf{\Gamma}$ is of dimension $N - 1$. Thus we assume

$$\boldsymbol{\epsilon}^{-1}\mathbf{\Gamma}\boldsymbol{\epsilon} = \mathbf{\Lambda}, \tag{20}$$

where $\mathbf{\Lambda}$ is a *diagonal* matrix of dimension $N - 1$ with diagonal elements λ_n, $n = 1, \ldots, N - 1$, as the eigenvalues. $\boldsymbol{\epsilon}$ is the associate eigenvector matrix, and $\boldsymbol{\epsilon}^{-1}$ its inverse. Next, if we consider the matrices $\mathbf{U}$ and $\mathbf{\Sigma}$ to be defined by elements U_{mn} and σ_{mn}, we may define correspondingly a matrix $\hat{\mathbf{U}}$ with elements $\hat{U}_{mn}$ and $\hat{\mathbf{\Sigma}}$ with elements $\hat{\sigma}_{mn}$ by the following relations:

$$\mathbf{U} = \hat{\mathbf{U}}\boldsymbol{\epsilon}^T, \qquad \mathbf{\Sigma} = \hat{\mathbf{\Sigma}}\epsilon^T, \tag{21}$$

where the superscript T denotes transpose.

Thus by Eqs. (20) and (21), Eq. (19) reduces to:

$$\left[\mathcal{L} - \frac{m^2}{(\zeta R + \xi)^2}\right]\hat{U}_{mn}(R) + \frac{1}{\kappa^2}\lambda_n\hat{U}_{mn}(R) = \hat{\sigma}_{mn}(R) \tag{22}$$

for $m = -M/2$ to $(M/2) - 1$, and $n = 1$ to $N - 1$. The significance of Eq. (22), in comparison with Eq. (19), is that the system of ordinary differential equations in (22) is uncoupled in m and n. Had we not made this transformation, we would have to face with the insurmountable task of solving $m \times n$ coupled differential equations.

To solve the system of ODEs defined in Eq. (22), we may employ a second-order differencing algorithm over a uniform grid of spacing h in R-direction to represent $\mathcal{L}$. This can be shown to yield

$$\left[\frac{1}{h^2\zeta^2} + \frac{1}{2h\zeta(\zeta R_l + \xi)}\right]\hat{U}_{mn}^{l+1} + \left[-\frac{2}{h^2\zeta^2} + \frac{\lambda_n}{\kappa^2} - \frac{m^2}{(\zeta R_l + \xi)^2}\right]\hat{U}_{mn}^{l} + \left[\frac{1}{h^2\zeta^2} - \frac{1}{2h\zeta(\zeta R_l + \xi)}\right]\hat{U}_{mn}^{l-1} = \hat{\sigma}_{mn}^{l} \tag{23}$$

where $\hat{U}_{mn}^{l}$, $l = 2, \ldots, L - 2$, represent the discrete values of $\hat{U}_{mn}(R)$ at $R = R_l$ with $R_l \equiv -1 + 2l/L$. The boundary conditions at $R = \pm 1$ are also discretized, according to (13), as

$$\left[\alpha_{-} - \frac{3\beta_{-}}{2h}\right]\hat{U}_{mn}^{0} + \frac{2\beta_{-}}{h}\hat{U}_{mn}^{1} - \frac{\beta_{-}}{2h}\hat{U}_{mn}^{2} = \hat{f}_{-mn} \tag{24}$$

$$\frac{\beta_{+}}{2h}\hat{U}_{mn}^{L-2} - \frac{2\beta_{+}}{h}\hat{U}_{mn}^{L-1} + \left[\alpha_{+} + \frac{3\beta_{+}}{2h}\right]\hat{U}_{mn}^{L} = \hat{f}_{+mn}, \tag{25}$$

where $\hat{f}_{\pm mn}$ are elements of matrix $\hat{\mathbf{F}}_{\pm} = \mathbf{F}_{\pm}(\boldsymbol{\epsilon}^T)^{-1}$, with $\mathbf{F}_{\pm}$ being the matrix containing elements $f_{\pm mn}$.

The systems (Eqs. (23) to (25)) yield a set of linear equations with a tridiagonal matrix, which can be solved very efficiently by Thomas' algorithm (Press et al., 1989).

As another alternative to a finite-difference solution of the ODEs in Eq. (22), a spectral collocation method can be used (Hussani et al., 1989). The linear systems will however result in a full matrix, which needs to be solved by either a direct or an iterative method (Orszag, 1980).

3.2 Treatment of the Free-Surface Conditions. As pointed out earlier, the potential ϕ and wave elevation η on the free surface $\mathcal{F}$ are obtained by integrating Eqs. (2) and (3), respectively. Implicit difference schemes are used here because of their excellent stability properties (Yeung, 1982). To implement such schemes, the following iterative procedure is employed

$$\eta_{(p+1)}^{k+1} = \eta^k + \frac{\Delta t}{2}(\phi_{z(p)}^{k+1} + \phi_z^k) \tag{26}$$

$$\phi_{(p+1)}^{k+1} = \phi^k - g\frac{\Delta t}{2}(\eta_{(p)}^{k+1} + \eta^k). \tag{27}$$

Here the superscript k denotes an index of the time step and p

denotes the index of iterations within a given time step. The iteration process is halted after the pth iteration when

$$|\phi^{k+1}_{z(p)} - \phi^{k+1}_{z(p-1)}| \leq \epsilon, \tag{28}$$

where ϵ is a prescribed tolerance value. An absolute accuracy of $\epsilon = 10^{-10}$ was used for all cases of results presented.

It is worthwhile to point out that the particular implicit free-surface conditions in Eqs. (26) and (27) can also be implemented without iterations. The two equations can be shown to yield a mixed boundary condition for the velocity potential ϕ^{k+1}, similar in form to Eq. (14). The above iterative schemes were selected because they will provide greater flexibility in the treatment of free-surface conditions in moving coordinates, which normally involve tangential derivatives.

4 Analytical Validation

Before proceeding to some general and more complex problems, it is essential to establish the accuracy and convergence characteristics of the procedure presented in Sections 2 and 3. For this purpose, we test the procedure against two analytical solutions that can be worked out relatively easily.

In the first case, we wish to verify that the Poisson solver for Eqs. (11) to (14) can treat any arbitrary function of S. Here we assume an analytical form of $U(r, \theta, z)$ defined below (in Eq. (29)), and evaluate $S(r, \theta, z)$ corresponding to Eq. (11) accordingly. The boundary conditions (13) and (14) can be imposed by taking the left-hand side as given and the right-hand side computed. Then the numerical algorithm for the solution of U is applied with S, F, and H as given. The numerical solution can then be compared with the exact solution for different types of boundary conditions.

For this test, we take $U(r, \theta, z)$ as

$$U(r, \theta, z) = \left[\cos\left\{\frac{\pi}{2}\left[\frac{1}{\eta}(r-\xi)-1\right]\right\} + \sin\left\{\frac{\pi}{2}\left[\frac{1}{\eta}(r-\xi)-1\right]\right\}\right] \times \left[\cos\left\{\pi\left(\frac{\theta}{2\pi}-1\right)\right\} + \sin\left\{\pi\left(\frac{\theta}{2\pi}-1\right)\right\}\right] \times \left[\cos\left\{\frac{\pi}{2}(Z-1)\right\} + \sin\left\{\frac{\pi}{2}(Z-1)\right\}\right] \tag{29}$$

with $r_i = 1$, $r_0 = 10$. The boundary conditions considered are taken to be one of the following three types:

$$\begin{aligned} &\text{Dirichlet Conditions:} && \alpha_\pm = A_\pm = 1, \quad \beta_\pm = B_\pm = 0, \\ &\text{Neumann Conditions:} && \alpha_\pm = A_\pm = 0, \quad \beta_\pm = B_\pm = 1, \\ &\text{Mixed Conditions:} && \alpha_\pm = A_\pm = 1, \quad \beta_\pm = B_\pm = 1. \end{aligned} \tag{30}$$

Once the solution for U has been obtained, its pointwise error can be computed over the entire domain Ω. In Fig. 2, the maximum pointwise error of the numerical solution in Ω, relative to the exact analytical solution, is shown for a range of grid resolution. In these and later computations, the grid resolution is measured by the number of radial grids, L, and the number of spectral terms in the circumferential direction, M, and the number of spectral terms in the vertical direction, N. For the specific case in question, we take $L = M = N$, with N ranging from 8 to 32. Fig. 2 shows that the value of the error, Er decreases exponentially as the grid resolution N increases for each of the above three types of boundary conditions. Specifically, we observe that

$$Er \sim 10^{-N/N_0}, \tag{31}$$

where N_0 is of the order of 20 when a second-order finite-difference scheme is used, and is of order 1 when a spectral collocation method is used. Figure 2 also shows that primary source of error comes from the discrete approximation in the radial direction. The spectral collocation scheme for solving Eq. (22) (see, e.g., Yeung and Yu, 1994) yields errors so small that machine accuracy (14 digits) is reached by using merely $L = M = N = 16$.

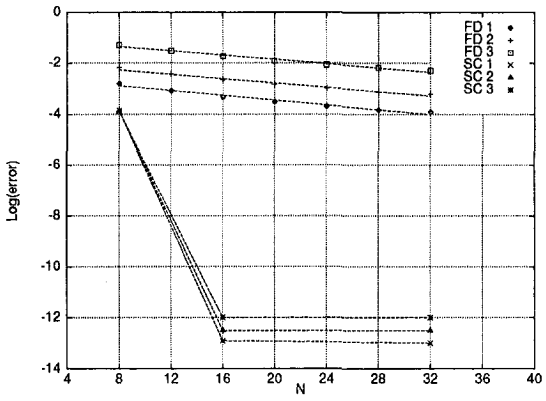

Fig. 2 Logarithmic maximum pointwise errors versus grid resolution for various boundary conditions (Case 1: Dirichlet Conditions on *R* and *Z* directions; Case 2: Neumann Conditions on *R* and Dirichlet on *Z*; Case 3: Mixed Conditions on *R* and *Z*. FD: Finite difference method; SC: Spectral collocation method).

For these computations, a particular run, based on an IBM 320H workstation, consumes approximately 0.07 seconds for a grid of $8 \times 8 \times 8$, and increases to 5.35 seconds for $32 \times 32 \times 32$, in the case of finite difference method. If a spectral collocation method is used, the time requirement is about 0.17 seconds for a grid of $8 \times 8 \times 8$ and 35.47 seconds for $32 \times 32 \times 32$.

To demonstrate the flexibility of the procedure, as well as to test the accuracy of our algorithm in the handling of wave-related problems, we solve, as the second test case, an axisymmetric Cauchy-Poisson wave problem (Lamb, 1932). Problems of this type usually consist of specifying an initial elevation or velocity of the surface wave, and one is faced with the prediction of the wave evolution at subsequent time. The governing equations are given in Section 2, with the initial conditions to be specified. Here we assume the initial conditions to be of an axisymmetric wave form that occurs between two concentric impermeable vertical cylinders located at $r = r_i(S)$, and at $r = r_0(\Sigma)$:

$$\frac{\partial \phi}{\partial t} = \exp\{-[r - (r_i + r_0)/2]^2\} \equiv f(r), \quad \text{at} \quad t = 0 \tag{32}$$

$$\phi = 0, \quad \text{at} \quad t = 0 \tag{33}$$

An analytical solution of the above problem can be derived by the use of Laplace transform and separation of variables. The details are omitted here. The final result for the wave elevation is

$$\eta(r, t) = g_0 + \sum_{n=1}^{\infty} g_n \left[J_0(k_n r) - \frac{J_1(k_n r_i)}{N_1(k_n r_i)} N_0(k_n r)\right] \cos \omega_n t \tag{34}$$

where J_ν and N_ν are the Bessel functions of the first and the second kind of order ν. k_n is the nth zero of the following equation for k

$$J_1(kr_i)N_1(kr_0) - J_1(kr_0)N_1(kr_i) = 0. \tag{35}$$

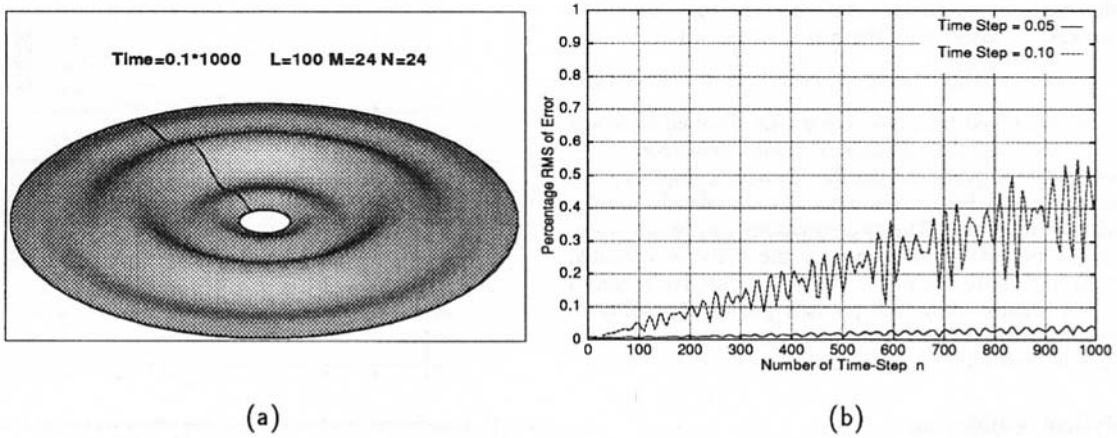

Fig. 3 Free-surface elevation at $t(g/r_i)^{1/2} = 100.0$ (left) and the root mean square of errors of free-surface elevation as a function of time-steps (right) in an axisymmetric Cauchy-Poisson wave problem

The "natural" frequencies ω_n satisfy a finite-depth "dispersion relation":

$$\omega_n^2 = gk_n \tanh k_n d. \tag{36}$$

The coefficients g_n in Eq. (34) are given analytically in terms of $f(r)$:

$$g_m = \begin{cases} \dfrac{\int_{r_i}^{r_0} rf(r)dr}{\int_{r_i}^{r_0} rdr} & \text{for} \quad m = 0 \\ \dfrac{\int_{r_i}^{r_0} rf(r)\left[J_0(k_m r) - \dfrac{J_1(k_m r_i)}{N_1(k_m r_i)} N_0(k_m r)\right] dr}{\int_{r_i}^{r_0} r\left[J_0(k_m r) - \dfrac{J_1(k_m r_i)}{N_1(k_m r_i)} N_0(k_m r)\right]^2 dr} & \text{for} \quad m = 1, 2, 3. \ldots \end{cases} \tag{37}$$

The numerical solution of this problem was obtained using the spectral method described in Section 3. The results of the computed wave elevation $\eta_c(r, t)$ were compared with the corresponding analytical solution $\eta_a(r, t)$ given by Eq. (34). Excellent agreement was found at every value of t. Figure 3(*a*) shows the free-surface elevation for one such simulation at nondimensional time $t\sqrt{g/r_i} = 100.0$. The RMS error in free-surface elevation as a function of time is defined as

$$E_{\text{RMS}}(t) = \sqrt{\frac{\int_S \{[\eta_c(r, t) - \eta_a(r, t)]/\eta_0\}^2 dS}{S}} \tag{38}$$

where η_0 is the elevation for the initial free-surface pulse, and S the planform area of the free surface. A plot of $E_{\text{RMS}}(t)$ versus time-step index n is given in Fig. 3(*b*). For $L = 100$, $M = 24$ and $N = 24$, the error is found to be bounded by 0.5 percent when a nondimensional time step $\Delta t\sqrt{g/r_i}$ of 0.1 is used, but reduced drastically to a mere 0.05 percent if the time step is halved. These results lend credence to the potential and effectiveness of the method.

5 Results and Discussion

Two problems of significant practical interests are treated in this section. These are chosen in the first place to illustrate the ability of the method to handle a (laterally infinite) open domain by employing a large size Σ, as opposed to the case of a relatively small outer radius. Aside from the contrasting extent of the domain, one would observe in these solutions, in one case, the approach to a steady-state behavior under periodic excitation, while in the other case, a continuously evolving state even at very large time.

5.1 A Swaying Cylinder Undergoing Periodical Motion. Consider a vertical cylinder with given periodic velocity $U(t)$, along the x-axis, starting from $t = 0$ in otherwise still water of depth d. This is a well-known problem in hydrodynamics for which a closed form solution for the case of a laterally unbounded fluid can be obtained (Yeung, 1981). The hydrodynamic properties of the circular cylinder is characterized by force coefficients that are dependent on the frequency of the oscillation.

Specifically, we let $\mathbf{V}(t)$ on the right-hand side of Eq. (4) be given by a magnitude of:

$$V(t) = \begin{cases} 0 & \text{when} \quad t < 0 \\ a\omega \sin(\omega t) & \text{when} \quad t \geq 0 \end{cases} \tag{39}$$

where a denotes the amplitude of the body motion, and ω the angular frequency. If the hydrodynamic problem for ϕ in Section 2 is solved, the force on the cylinder can be obtained by integrating the hydrodynamic pressure using the linearized Euler integral:

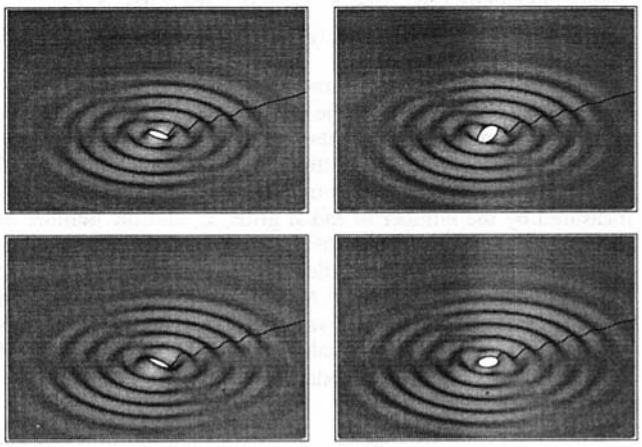

Fig. 4 Instantaneous free-surface elevation plots for the swaying cylinder problem in one cycle of motion with $\omega(r_i/g)^{1/2} = \pi/2$, and $t(g/r_i)^{1/2} = 32.5, 35.0, 37.5,$ and 40.0

Table 1 Comparison of added mass and damping coefficient computed by the present method and those in Yeung (1981)

Computational Methods	$\omega(r_i/g)^{1/2} = \pi/4$		$\omega(r_i/g)^{1/2} = \pi/2$	
	$\mu_{zz}/\rho\pi r_i^2 d$	$\lambda_{zz}/\omega\rho\pi r_i^2 d$	$\mu_{zz}/\rho\pi r_i^2 d$	$\lambda_{zz}/\omega\rho\pi r_i^2 d$
Yeung (1981)	0.40159	0.45051	0.46771	0.04650
Present Method	0.41047	0.44689	0.47149	0.04198

$$F_x = \int_S pn_x dS \approx -\int_S \rho\phi_t n_x dS. \tag{40}$$

If a steady-state solution is reached, the force can be simply expressed in terms of an added mass coefficient μ_{xx} and a damping coefficient λ_{xx} defined below (Wehausen and Laitone, 1960):

$$F_x(t) = -\mu_{xx}\frac{dU(t)}{dt} - \lambda_{xx}U(t) \tag{41}$$

The solution of this problem is sought by using the method described in this paper with $r_0/r_i = 30$ for two frequencies of oscillation, $\omega\sqrt{r_i/g} = \pi/2$ and $\pi/4$. Figure 4 shows the free-surface elevation for a complete cycle of body motion at one-quarter period intervals for $a/r_i = 0.055$ and $\omega\sqrt{r_i/g} = \pi/2$ after the body has oscillated for 9 periods. The dark line on the surface is a reference curve for $\theta = -\pi/2$, having no physical significance. The hydrodynamic force acting on the cylinder for this case is shown in Fig. 5 as a function of time. It is evident that a harmonic steady state is reached after the body has undergone only 2 or 3 periods.

From the force time history, it is possible to evaluate the added-mass and damping coefficients and compare them with known analytical results (Yeung, 1981). Table 1 shows such a comparison for a grid density of $L = 150$, $M = 48$, and $N = 24$, when solved as a transient three-dimensional problem. The agreement is seen to be excellent since no symmetry assumptions are made. The envelope of the force curve in Fig. 5 confirms the method has excellent stability characteristics.

5.2 A Nonaxisymmetric Cauchy-Poisson Problem. We solve here a Cauchy-Poisson problem with a nonaxisymmetric initial wave elevation (see Fig. 6(*a*)) located between two cylindrical walls. This initial wave form is taken to be the following:

$$\eta(r, \theta, t = 0) = \exp\{-[r\cos\theta - (r_i + r_0)/2]^2 - [r\sin\theta]^2\}. \tag{42}$$

Because of the reflection of waves from the outer wall and their interference with the inner cylinder, the wave surface evolves in a complicated manner. Figures 6(*b*) to 6(*d*) reveal some of these interaction features at four instants of time. The outward-moving "ring waves" of the pulse (Fig. 6(*b*)) first hit the outer cylinder and rebound, interestingly, almost as a plane wave system (Fig. 6(*c*)). The inward-moving ring waves are diffracted around the inner cylinder and eventually bounce off the far side of the outer cylinder to interact with the "plane waves" which somewhat encircle around the inner cylinder to reach the far side. When all these waves meet at the far end, they evolve into waves of much shorter lengths, moving at much lower spatial velocities. All these flow features are well captured by a radial grid dimension of merely 48 points. A video animation of the solution is available on a VHS tape from the authors for interested readers.

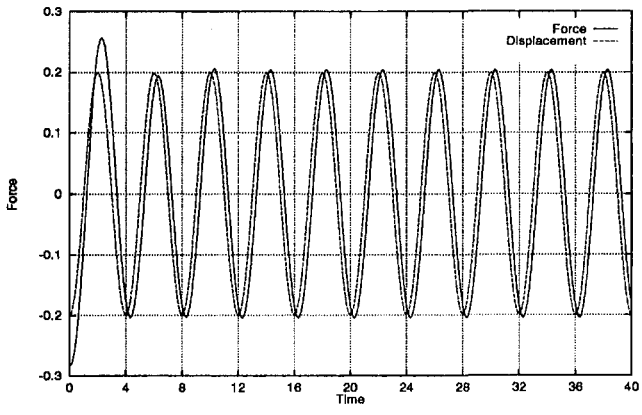

Fig. 5 Horizontal force on the cylinder as function of time

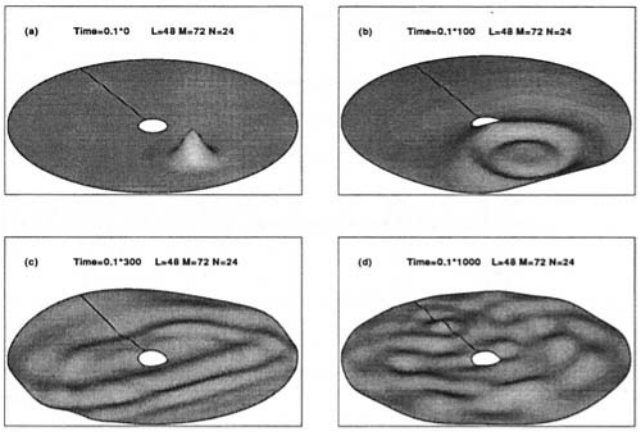

Fig. 6 Instantaneous free-surface elevation plots for the Cauchy-Poisson wave problem, *L*, *M*, *N* representing resolution in the radial, circumferential, and vertical directions

It is important to validate the accuracy of the solution. As a measure of the accuracy of this type of computation, we will demonstrate that the flow retains the same total energy as the initial wave pulse. We define the following energy quantities following Yeung (1982): the total energy (T.E.) in the fluid domain as the sum of its kinetic and potential parts

$$\text{T.E.}(t) = \text{K.E.}(t) + \text{P.E.}(t) = \int_{S\cup\mathcal{T}\cup\Sigma\cup\mathcal{B}} \tfrac{1}{2}\phi\phi_n dS + \int_{\mathcal{F}} \tfrac{1}{2}\eta^2 dS \tag{43}$$

where the contributions to the first integral from $\mathcal{S}$, Σ, and $\mathcal{B}$ vanish because $\phi_n = 0$. Clearly, in the absence of any energy source, T.E. must stay constant. Figure 7 shows that the error in the total energy is no more than 2 percent of the initial potential energy of the wave form even after a thousand steps of simulation. Of course, by the principle of equal energy distribution, one observes that P.E. and K.E. each hovers around and converges to the value of 0.5. This confirms that the wave motion would never vanish completely, which is to be expected in the absence of viscosity.

6 Conclusions

A very effective pseudo-spectral Poisson solver has been developed and applied to several transient free-surface wave problems associated with wave-body interaction. The method is found capable of providing three-dimensional results with high accuracy. Excellent convergence characteristics and relatively low computational requirements are also attractive properties of this method. These features are well demonstrated by the results shown in this paper. The limitation is that only relatively simple geometry can be studied at this point. However, by introducing a hybrid formulation and numerical mapping, treatment of more complicated body geometry is believed to be possible. Future extension of this

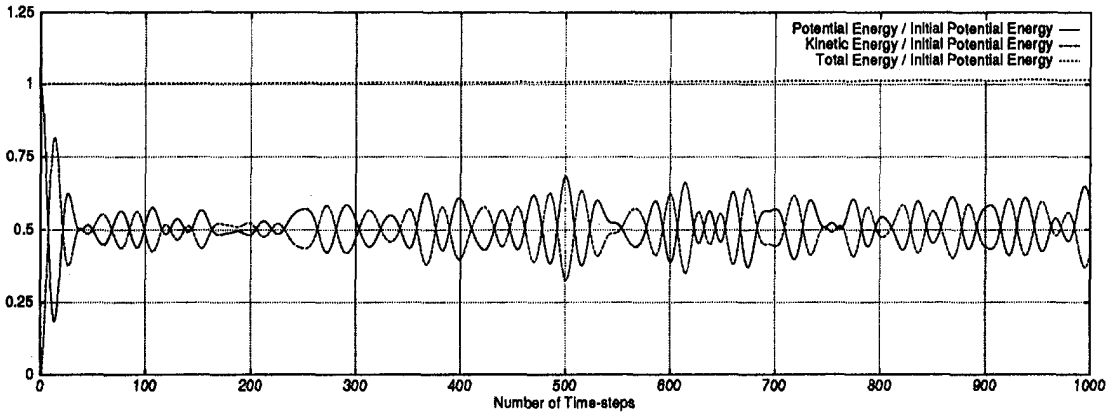

Fig. 7 Energy balance in the Cauchy-Poisson wave problem of Fig. 6

work to consider nonlinear boundary conditions and to account for effects of fluid viscosity also appears promising.

Acknowledgments

Research reported here has been supported by the Office of Naval Research under grant N00014-91-J1155. Partial support from two other grants, Chevron Oil and Mitsubishi Heavy Industries, are also acknowledged. The authors are grateful to Dr. P. Ananthakrishnan for many useful discussions.

References

Bai, K. J., and Yeung, R. W., 1974, "Numerical Solution to Free-Surface Flow Problems," *Proceedings of 10th Symposium on Naval Hydrodynamics,* Cambridge, MA.

Beck, R. F., and Liapis, S. J., 1987, "Transient Motion of Floating Bodies at Zero Forward Speed," *Journal of Ship Research,* Vol. 31, pp. 164–176.

Gadd, G. E., 1976, "A Method for Computing the Flow and Surface Wave Pattern Around Full Forms," *Transactions of the Royal Institution of Naval Architects,* Vol. 113, pp. 207–219.

Gottlieb, D., and Orszag, S. A., 1977, "Numerical Analysis of Spectral Methods: Theory, and Application," *Society for Industrial and Applied Mathematics,* Philadelphia, PA.

Hussaini, M. Y., and Zang, T. A., 1987, "Spectral Methods in Fluid Dynamics," *Annual Review of Fluid Mechanics,* Vol. 19, pp. 339–367.

Hussaini, M. Y., Kopriva, D. A., and Patera, A. T., 1989, "Spectral Collocation Methods," *Applied Numerical Mathematics,* Vol. 5, pp. 177–208.

Isaacson, M., and Cheung, K. F., 1990, "Time-Domain Solution for 2nd-Order Wave Diffraction," *Journal of Waterway, Port, Coastal and Ocean Engineering,* Vol. 116, pp. 191–210.

Korczak, K. Z., and Patera, A. T., 1986, "An Isoparametric Spectral Element Method for Solution of the Navier-Stokes Equations in Complex Geometry," *Journal of Computational Physics,* Vol. 62, pp. 361–382.

Korsmeyer, F. T., Lee, C. H., Newman, J. N., and Sclavounos, P. D., 1988, "The Analysis of Wave Effects on Tension-Leg Platforms," *Offshore Mechanics and Arctic Engineering Conference* The Hague, The Netherlands.

Lamb, H., 1932, *Hydrodynamics,* 6th edition, Dover, New York.

Nakos, D. E., and Sclavounos, P. D., 1990, "Ship Motions by a Three-Dimensional Rankine Panel Method," *Proceedings of the 18th Symposium on Naval Hydrodynamics,* Ann Arbor, MI.

Orszag, S. A., 1980, "Spectral Methods for Problems in Complex Geometries," *Journal of Computational Physics,* Vol. 37, pp. 70–92.

Press, W. H., Flannery, B. P., Teukolsky, S. A., and Vetterling, W. T., 1989, *Numerical Recipes,* 1st edition, Cambridge University Press, Cambridge, England.

Tan, C. S., 1985, "Accurate Solution of Three-Dimensional Poisson Equation in Cylindrical Coordinate by Expansion in Chebyshev Polynomials," *Journal of Computational Physics,* Vol. 59, pp. 81–95.

Tan, C. S., 1989, "A Muti-Domain Spectral Computation of Three-Dimensional Laminar Horseshoe Vortex Flow Using Incompressible Navier-Stokes Equations," *Journal Computational Physics,* Vol. 85, pp. 130–158.

Wehausen, J. V., and Laitone, E. V., 1960, "Surface Waves," *Handbuch der Physik,* Vol. 9, Springer, Berlin.

Wehausen, J. V., 1967, "Initial Value Problem for the Motion in an Undulating Sea of a Body with Fixed Equilibrium Position," *Journal of Engineering Mathematics,* Vol. 1, pp. 1–19.

Yeung, R. W., 1975, "A Hybrid Integral-Equation Method for Time-Harmonic Free-Surface Flow," *Proceedings of the 1st. International Conference on Numerical Ship Hydrodynamics,* Bethesda, MD.

Yeung, R. W., 1981, "Added Mass and Damping of a Vertical Cylinder in Finite-Depth Waters," *Applied Ocean Research,* Vol. 3, pp. 119–133.

Yeung, R. W., 1982, "Numerical Methods in Free Surface Flows," *Annual Review of Fluid Mechanics,* Vol. 14, pp. 395–442.

Yeung, R. W., and Ananthakrishnan, P., 1992, "Oscillation of a Floating Body in a Viscous Fluid," *Journal of Engineering Mathematics,* Vol. 26, pp. 211–230.

Yeung, R. W., and Vaidhyanathan, M., 1992, "Non-linear Interaction of Water Waves With Submerged Obstacles," *International Journal for Numerical Methods in Fluids,* Vol. 14, pp. 1111–1130.

Yeung, R. W., and Yu, X., 1994, "Three-Dimensional Flow Around A Surface-Piercing Body," *Proceedings of the 20th Symposium on Naval Hydrodynamics,* Santa Barbara, CA.

Eugene Kordyban

Abdul Hakim Okleh

Department of Mechanical Engineering,
University of Detroit Mercy,
4001 W. McNichols Road,
Detroit, MI 48219-0900

The Effect of Surfactants on the Wave Growth and Transition to Slug Flow

In this work the effect of the surfactants on the wave growth is investigated analytically and experimentally. It is found that short waves are damped by surfactants quite effectively and since the natural wave growth begins with short waves, the transition to slug is shifted to higher gas velocities by a substantial amount. Slugs, in fact, form on level liquid surface. However, when long waves are produced by a wave maker, the slugs form in the usual manner.

Introduction

In the field of two-phase flow the slug flow is well known, perhaps, mainly due to its nuisance value, because of its pressure and flow-rate fluctuations. It occurs when the fast moving gas raises the crests of liquid waves to the top covering the whole cross section; these liquid slugs are then driven piston like by gas. In some cases conduits were damaged by fast moving slugs. Over the last 20 years a number of investigations have appeared in the literature concerned with the transition to slug flow in horizontal ducts. While most agree that the formation of slugs is a consequence of Kelvin-Helmholtz instability of the liquid waves, this in itself is not sufficient to predict the transition to slug flow and a number of hypothesis, such as those of Wallis and Dobson (1973), Taitel and Dukler (1976), Gardner (1973), Minato et al. (1981) have been proposed. These hypotheses agree quite well with each other and with experimental data, but most of the data have been obtained for air and water at roughly atmospheric conditions.

More recently, Kordyban (1991) has proposed that the transition depends only on the distance of the crest of the highest wave to the top of the channel for a given gas velocity. It is thus tied to the wave growth and is necessary to study the wave growth to fully predict the transition to slug flow. This proposition agrees well with experiment and its strength is in the fact that it can account for various fluid properties, if they affect the wave growth.

In further work to test this proposition Kordyban and Okleh (1993) performed experiments in which syrup was added to water to increase its viscosity and alcohol with its lower surface tension was used as the liquid phase. It was found that, within the range of values used in the experiments, neither the viscosity nor surface tension had any noticeable effect on the transition to slug flow. When a surfactant in the form of liquid soap, however, was added to water, its effects became immediately apparent; the wave growth was suppressed to a considerable degree and the transition to slug flow began at much higher gas velocities. Still, when the highest waves were measured, the transitions could be predicted from Kordyban's hypothesis while being in conflict with other theories. Thus a strong support was given to Kordyban's hypothesis.

The fact that the surfactants can delay the formation of slugs has also important practical implications, since there are many industrial processes in which such delay is desirable and, at least in some of them, it may be possible to use the surfactants.

Contributed by the Fluids Engineering Division for publication in the Journal of Fluids Engineering. Manuscript received by the Fluids Engineering Division January 7, 1994; revised manuscript received February 9, 1995. Associate Technical Editor: M. Gharib.

Because of this, an analytical and experimental program was undertaken to understand the mechanism by which the waves are damped and how the slugs form in such cases. The results of this work are presented in this paper.

Theoretical Background

The calming of the sea by oil films has been known to sailors since antiquity. Actually the effect of damping of long waves is quite small, since they are so lightly damped in clean water but the surfactants are effective in diminishing the ripples. This delays the breaking of the high waves which is dangerous to sea-going vessels.

Only since the last century an attempt has been made to explain this phenomenon. Initially it was thought that the apparent damping was the result of the reduced surface tension but, with the growth of science of surface physics and chemistry, a more logical explanation was advanced, namely, that there exists a surface tension gradient on the wavy surface. The damping occurs due to stretching and compression of the surfactant layer and exists with or without the air flow over the surface, but the air flow inputs the energy into the liquid waves counteracting the damping. Thus the effective growth of waves is diminished, or it may become negative. This damping is most effective in capillary waves where the length may be one millimeter or less and most of the experimental studies have been conducted on such waves.

A number of somewhat differing theories is available at the present time and the one selected for this study is that due to Levich (1962). Levich, however, does not consider the effect of gas flow on the waves and this is taken into account in the development that follows.

The gas flow affects the waves both by shear and variation of surface pressure. Following Miles (1957) we neglect the former and assume the pressure variation to be

$$p_a = \alpha^1 \eta + \beta^1 \frac{\partial \eta}{\partial x} \tag{1}$$

The usual equations for linearized waves are

$$v_x = (ikAe^{kz} - lCe^{lz})e^{ikx+\alpha t} \tag{2}$$

$$v_z = (kAe^{kz} + ikCe^{lz})e^{ikx+\alpha t} \tag{3}$$

$$p = -\rho_l \alpha\, Ae^{kz} e^{ikx+\alpha t} - \rho_l g z \tag{4}$$

The values of the quantity α and the amplitude ratio A/C are determined from the boundary conditions and these differ from the boundary conditions for pure liquid.

The normal and tangential components of the surface force per unit area are

$$p_n = -p + 2\mu \frac{\partial v_z}{\partial z} \tag{5}$$

and

$$p_t = \mu\left(\frac{\partial v_x}{\partial z} + \frac{\partial v_z}{\partial x}\right)$$

The normal force on deformed liquid surface is

$$p_n = \sigma(\Gamma)\frac{\partial^2 \eta}{\partial x^2} + \alpha^1 \eta + \beta^1 \frac{\partial \eta}{\partial x} \tag{6}$$

these equations are now solved for wave growth coefficient β_r.

For the case of pure water, $\epsilon/\sigma = 0$ and solution for the real part of the wave growth coefficient is in the form

$$\beta_r = \frac{-\frac{8m}{\omega_o} + \frac{2\beta^1 k^2}{\rho_l \omega_o^3}}{\frac{4}{\omega_o^2}} = -2\nu k^2 + \frac{\beta^1 k^2}{\rho_l \omega_o} \tag{7}$$

The first term in Eq. (7) represents the usual damping of the wave by viscosity while the second term represents the counteracting wave growth due to gas flow. It should be noted here that the coefficient of the pressure component 180 deg out of phase with the wave surface α^1 has also some effect on the wave growth, since it is included in ω_o.

Turning now to the other limiting case i.e., $\epsilon/\sigma = 1$ we obtain for β

$$\beta = \frac{-1 + 4m^2\frac{l}{k} - 4m^2 + i\left(-4m\frac{l}{k} - \frac{\beta^1 k^2}{\omega_o^2} - 4m - \frac{\beta^1 k^2}{\omega_o^2}\right)}{\frac{8m}{\omega_o} + \frac{2}{\omega_o}\frac{\beta^1 k^2}{\rho_l \omega_o^2} + i\left(\frac{2}{\omega_o} + 2\frac{l}{k}\frac{1}{\omega_o}\right)}$$

Neglecting terms of the order of m^2 and, following Levich, taking $l/k = \sqrt{i/m}$ we have for the real part of β

$$\beta_r = -\frac{\sqrt{2}}{4}\nu^{1/2} k \omega_o^{1/2} + \frac{\beta^1 k^2}{\rho_l \omega_o} \tag{8}$$

Comparison between Eqs. (7) and (8) shows that for relatively short waves the damping is considerably greater, as demonstrated by Levich, while the growth coefficient due to gas flow remains unchanged. It should be noted that the limiting case of $\epsilon/\sigma = 1$ represents the surface as completely elastic which neither expands nor contracts, but bends.

The coefficient β^1 is, of course, a function of gas density and velocity, but its numerical value is not well established in literature. It is related to Jeffreys' (1925) sheltering coefficient and he proposes some numerical values for it based on observations, while Miles (1957) obtains numerical values by the solution of air flow equations, but the latter appear to be too small compared to measured wave growth by Bole and Hsu (1967). With increasing gas velocity it would appear that, eventually, the second term in Eq. (8) will become greater than the first and the waves will grow, but there is a possibility of the onset of Kelvin-Helmholtz instability which may lead to the formation of slugs in closed channels. In the experimental portion of this work, which is described in greater detail in later sections of this paper, we observed the formation of slugs from essentially level surface and we examine now this possibility analytically.

For small linearized waves we shall use the wave equation in the form presented by Miles (1962).

$$\frac{\rho_l}{k}\frac{\partial^2 \eta}{\partial t^2} + (\rho_l g + \sigma k^2)\eta = -p_a \tag{9}$$

The pressure at the wave surface p_a with gas flowing over the wave may be found from one-dimensional Bernoulli equation

$$p_a = -\frac{V_c^2 - V^2}{2}\rho_g = -\frac{V^2 \rho_g}{2}\left(\frac{h^2}{(h-\eta)^2} - 1\right) \tag{10}$$

For a fixed value of x Eq. (9) may be considered an ordinary differential equation and, substituting from Eq. (10) we have

$$\frac{\rho_l}{k}\frac{d^2\eta}{dt^2} + (\rho_l g + \sigma k^2)\eta = \frac{V^2 \rho_g}{2}\left[\frac{h^2}{(h-\eta)^2} - 1\right] \tag{11}$$

This equation may be integrated to obtain

$$\left(\frac{d\eta}{dt}\right)^2 = -\frac{\rho_l g k + \sigma k^3}{\rho_l}\eta^2 + \frac{V^2 \rho_g k}{\rho_l}\left[\frac{h^2}{h-\eta} - \eta\right] + D \tag{12}$$

The constant is determined by establishing an initial condition. If it is assumed that initially we have a simple sinusoidal wave

$$\eta = \eta_o \sin \omega_o t$$

then, at

$$t = 0 \quad \eta = 0, \quad \frac{d\eta}{dt} = \eta_o \omega_o.$$

Nomenclature

A = constant in wave equation
C = constant in wave equation
c = wave speed
D = constant in wave equation
g = acceleration of gravity
h = height of gas channel
H = height of channel
J = superficial gas velocity
$J^* = J\,[\rho_g/(\rho_l - \rho_g)\cdot(1/gH)]^{1/2}$
k = wave number
L = length
$l = \sqrt{k^2 + \alpha/v}$
$m = vk^2/\omega_o$
p = pressure
p_a = pressure at wave surface
p_n = normal force per unit area
p_t = tangential force per unit area
v_x = horizontal liquid velocity
v_z = vertical liquid velocity
V_c = gas velocity at wave crest
V = gas velocity
α = coefficient of temporal term in wave equation
α^1 = coefficient of pressure component 180 deg out of phase with wave surface
α_v = void fraction
β = wave growth factor
β^1 = coefficient of pressure component in phase with wave slope
γ = defined in text
$\bar{\gamma}$ = defined in text
Γ = concentration of surfactant at surface of liquid
Γ_o = average concentration of surfactant at the surface of liquid
$\epsilon = (\partial\sigma/\partial\Gamma)\Gamma_o$
η = surface elevation
η_o = amplitude
η_{ox} = amplitude at distance x
$\bar{\eta}_o$ = nondimensional amplitude
μ = liquid absolute viscosity
ν = liquid kinematic viscosity
ρ_l = liquid density
ρ_g = gas density
σ = surface tension
ω_o = wave frequency

For deep-water waves

$$\omega_o = \sqrt{gk + \frac{\sigma}{\rho_L} k^3}$$

Solving for D and substituting in Eq. (12) we have

$$\frac{d\eta}{dt} = \left[\frac{\rho_l g k + \sigma k^3}{\rho_l} (\eta_o^2 - \eta^2) + \frac{V^2 \rho_g k}{\rho_l} \left(\frac{h^2}{h - \eta} - h - \eta \right) \right]^{1/2} \quad (13)$$

In examining the radical in Eq. (13) for $o < \eta < h$ we find that it has one minimum there. If this minimum is positive the wave will grow and thus the neutral stability occurs where the minimum is equal to zero. Designating the radical as $R(\eta)$ and setting it equal to zero, we have

$$R_{(\eta)} = \eta_o^2 - \eta^2 + \frac{V^2 \rho_g k}{\rho_l g k + \sigma k^3} \left(\frac{\eta^2}{h - \eta} \right) = 0 \quad (14)$$

To find the minimum we differentiate the radical with respect to η and set the result equal to zero,

$$\frac{dR(\eta)}{d\eta} = -2 \frac{\rho_l g k + \sigma k^3}{\rho_l} \eta + \frac{V^2 \rho_g k}{\rho_l} \left[\frac{2(h - \eta)\eta + \eta^2}{(h - \eta)^2} \right] = 0$$

Letting $V^2 \rho_g k / (\rho_l g k + \sigma k^3) = \gamma$ and solving for η we have

$$\eta = h - \frac{\gamma}{H} - \sqrt{\frac{\gamma h}{2} + \frac{\gamma^2}{16}} \quad (15)$$

and substituting into Eq. (14)

$$\eta_o^2 - \left(h - \frac{\gamma}{4} - \sqrt{\frac{\gamma h}{2} + \frac{\gamma^2}{16}} \right)^2 + \gamma \frac{\left(h - \frac{\gamma}{4} - \sqrt{\frac{\gamma h}{4} - \frac{\gamma^2}{16}} \right)^2}{\frac{\gamma}{4} + \sqrt{\frac{\gamma h}{2} + \frac{\gamma^2}{16}}} = 0$$

Nondimensionalizing above equation by letting

$$\bar{\eta}_o = \frac{\eta_o}{h} \quad \text{and} \quad \bar{\gamma} = \frac{\gamma}{4h}$$

we have

$$\bar{\eta}_o^2 = (1 - \bar{\gamma} - \sqrt{2\bar{\gamma} + \bar{\gamma}^2})^2 + 4\bar{\gamma} \frac{(1 - \bar{\gamma} - \sqrt{2\bar{\gamma} + \bar{\gamma}^2})^2}{\bar{\gamma} + \sqrt{2\bar{\gamma} + \bar{\gamma}^2}} \quad (16)$$

It may be concluded from Eq. (16) that for a given value of parameter $\bar{\gamma}$ there is a value of $\bar{\eta}_o$ at which the wave will become unstable and the exponential growth will begin.

For a plane surface which corresponds to the experimental case using the surfactant, $\bar{\eta}_o \to 0$ and Eq. (16) reduces to

$$1 - \bar{\gamma} - \sqrt{2\bar{\gamma} + \bar{\gamma}^2} = 0$$

or

$$\bar{\gamma} = \tfrac{1}{4}$$

Substituting the original values for $\bar{\gamma}$ we have

$$\frac{V^2 \rho_g}{h(\rho_l g + \sigma k^2)} = 1$$

If surface tension is neglected the above expression reduces to a form of Froude number

$$\frac{V^2}{hg} \cdot \frac{\rho_g}{\rho_l} = 1 \quad (17)$$

As will be shown later, for water with soap, the slugs were formed from practically-level liquid surface and Eq. (17) is used to compare the predicted values with experimental results.

Experimental Work

The experiments were conducted in a channel which was 10 cm deep, 15 cm wide, and approximately 5 m long made of acrylic plastic. The downstream end was equipped with a sloping beach to minimize the reflection of the waves, while the air inlet was placed at the upstream end. A plate extended form the air inlet into the channel and it could be adjusted so it would just touch the liquid surface tangentially. The upstream end was also equipped with an oscillating plate wave maker with adjustable stroke and frequency. The channel was mounted on adjustable supports which permitted setting the slope to desired value.

The wave height was measured by electrical conductivity gages which consisted of two parallel platinum wires 0.127 mm in diameter and about 3 mm apart set in a vertical plane perpendicular to flow. Three wave height gages were placed in the channel at various locations.

The gages were frequently calibrated statically by varying the liquid level in the channel and then comparing the readings with those of a hook gage. The output of the gages was read on a strip chart recorder.

The instantaneous values of the liquid level were recorded to obtain the wave characteristics. The mean level was also recorded by the use of low pass band pass filter.

Air at essentially atmospheric pressure was used as the gaseous phase and its flowrate was measured by a laminar flowmeter. The liquid phase was tap water with surfactant added. The surfactant was commercially available dishwashing liquid and was added to produce a concentration of 2.8 percent by volume. The solution was thoroughly mixed before the tests began, but it was found that the full effect in the surfactant did not develop until the soap remained in the water for approximately four days. Tests with both fresh and aged solution were conducted. In both cases the static surface tension was 0.039 N/m.

The tests were conducted as follows. For a particular liquid level, the air velocity was increased in steps and at each step the slope of the channel was adjusted to produce approximately constant liquid level throughout the channel. Once it was judged that the transition to slug flow was impending, the air velocity was increased in small steps, while the recorder was run continuously. When the first slugs appeared, the values of maximum wave height, of air velocity and of mean liquid level were recorded.

Auxiliary tests during which the liquid surface was photographed by a still camera and where the wave generator was used were also conducted.

Results

The measured values of mean liquid level as a function of mean air velocity at transition to slug flow are shown in Table 1 for aged solution.

The results for both the fresh and aged solutions as well as those for air and water are shown in Fig. 1. In this figure the coordinates suggested by Wallis and Dobson (1973) are used, the α_v represents the void fraction while the ordinate is the nondimensional superficial gas velocity. The void fraction is

Table 1 Measured values for transition to slug flow for water-soap mixture, aged solutions

Superficial air velocity, m/s	Mean liquid level at transition, cm
5.72	6.11
5.12	6.45
4.66	6.53
4.56	6.84
4.05	6.77
3.97	7.05
3.88	7.43
3.54	7.43
3.31	7.71
3.08	7.76
2.44	8.14
2.39	8.05

calculated on the basis of mean liquid level, while J^* is found from

$$J^* = J\left[\frac{\rho_g}{\rho_l - \rho_g}\cdot\frac{1}{gH}\right]^{1/2}$$

and J is found from measured gas flow rate. The curve shown in this figure is from Eq. (17). As may be seen from this figure there are two distinct groups of data. The fresh solution exhibits some damping which was consistent from test to test. The aged solution exhibits much higher damping of waves. Reason for the difference is not clear at this point, but it is apparent that we are dealing with some definite transition.

In order to illustrate the waves under discussion several photographs are presented. In Fig. 2 the wave growth on pure water is shown. The first photograph was taken at a distance of 20 cm from the air inlet, the second at 1.5 m and the third at 3.4 m. The growth of the waves both in height and in length is apparent in these pictures.

Figure 3 shows the growth of waves on aged soap solution, with the first one 20 cm from air inlet and the second at 3.4 m.

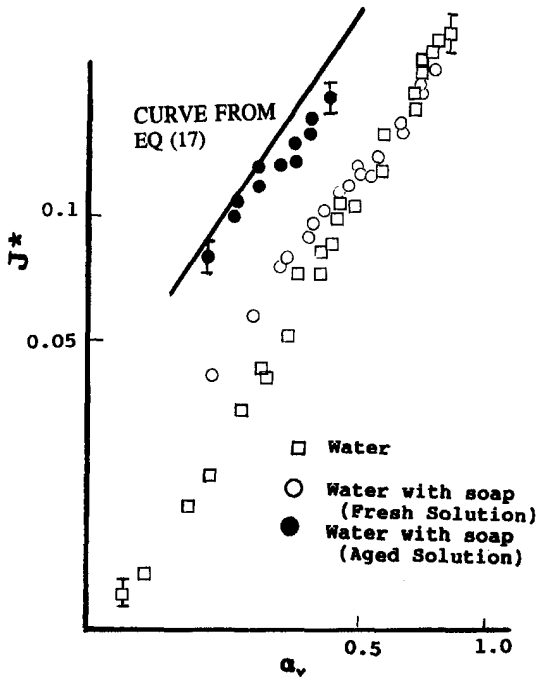

Fig. 1 Transition to slug flow for water with soap [Uncertainty estimate, J^* less than 3 percent, α less than 4 percent]. Uncertainty estimates as shown by bars apply to all points in the proportion shown.

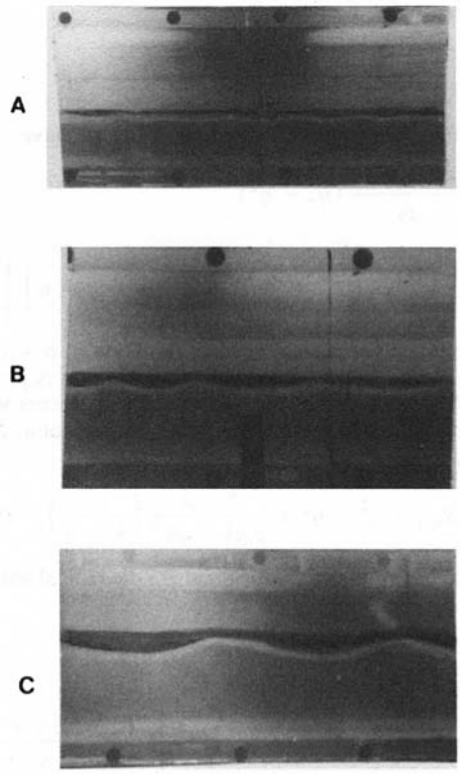

Fig. 2 Wave growth on pure water (*a*) 20 cm, (*b*) 1.5 m, and (*c*) 3.4 m from air inlet

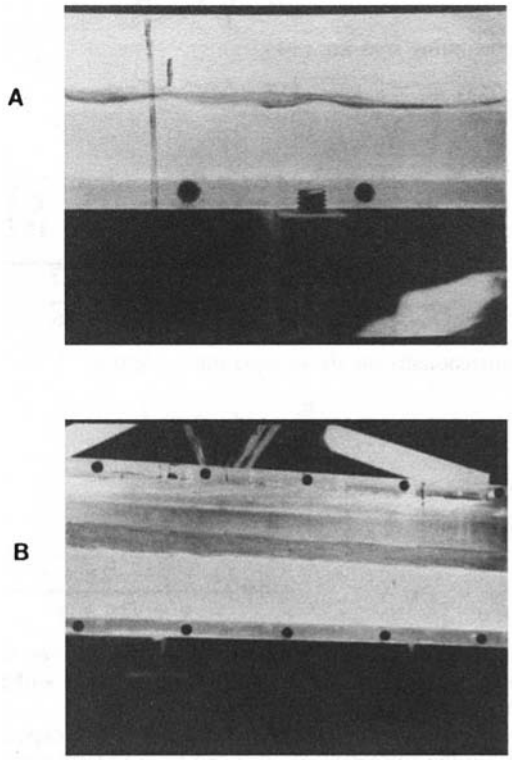

Fig. 3 Waves on aged solutions (*a*) 20 cm and (*b*) 3.4 m from air inlet

It is of interest to note that visible waves are produced near the inlet. They are damped to about 10 percent of their initial height in 1.2 m and disappear almost completely at a distance of 3.4 m, as may be seen from the photograph.

The wave growth factor β_r as found from observations agrees reasonably well with that found from Eq. (8) indicating that the experiments were conducted with ϵ/σ close to unity.

Uncertainty Estimates

The following estimates are based on maximum uncertainty.

The primary quantities measured in this work are liquid level and gas flow rate.

The superficial gas velocity was determined by dividing the gas flow rate by the total channel cross section. Since the cross section area is found with negligible uncertainty, the maximum uncertainty for the superficial gas velocity is the same as for the flow rate. It is estimated to be

$$3\% \text{ at } J = 2 \text{ m/s}$$

$$1\% \text{ at } J = 6 \text{ m/s}$$

The liquid level measured by electrical conductivity gages is judged to be accurate within ± 1 mm, but if statistical fluctuations are included in determining the void fractions α_v, the uncertainty is estimated to be

$$2\% \text{ at } \alpha_v = 0.7$$

$$5\% \text{ at } \alpha_v = 0.2$$

The actual gas velocity is found by dividing the gas flowrate by the actual gas flow cross section. The uncertainty is estimated to be

$$2.5\% \text{ at } V = 6 \text{ m/s}$$

$$6\% \text{ at } V = 3 \text{ m/s}$$

Discussion of Results

This work was started as a test whether the transition to slug flow can be predicted in every case by knowing the wave height. The results of this work reinforce the supposition in that even in this unusual case the transition to slug flow can be so predicted.

Previous work (Kordyban and Okleh, 1993) has shown that the variation of viscosity or surface tension has no effect on the transition to slug flow. Here it is shown that addition of the surfactants can substantially shift the transition to higher gas velocities. Thus the relationships of Taitel and Dukler (1976), Wallis and Dobson (1973), Gardner (1979) and others are not applicable to this case. This shift in the transition is definitely due to the damping of short waves near the air inlet in the channel. This was proven by producing waves by the wave maker which were sufficiently long not to be effectively damped by the surfactant. In this case the waves grew and the transition to slug flow occurred in normal fashion. This happened even in the absence of wave maker waves. When a long wave disturbance was inadvertently introduced in the course of the experiment, slugs formed unexpectedly.

The analysis carried out on damping of waves followed closely the steps of Levich (1962) except that the energy input due to gas flow was introduced. It should be noted that both the damping and energy input terms were assumed to be small and under that assumption there are no cross effects between these terms in the final equation; they are simply additive.

This is the only case known to the authors where the slugs form from practically level interface. The results of analysis of such conditions agree reasonably well with experimental results as may be seen in Fig. 1. The curve of Eq. (17) falls slightly above the experimental points indicating perhaps that the surface is not entirely smooth.

It should be noted here that other work with surfactants (Weisman et al., 1979) shows no effect an the transition to slug flow. While there is no reason to doubt these results, we are quite certain of our data, since the lack of wave growth and the shift of transition to higher gas velocities could be easily observed visually. This discrepancy deserves further study.

The difference between the fresh and aged solutions in their damping effectiveness appears to be due to some kind of physical or chemical transition which occurs when the solution is between 3 and 5 days old. This is a rather sudden transition with a very substantial change in the damping characteristics and no intermediate values were observed. To illustrate this change, at $\alpha_v = 0.3$ the superficial critical gas velocity is 1.55 m/s for pure water, 2.14 m/s for fresh solution, and 4.36 m/s for aged solution.

The fact that the surfactants delay the formation of slugs could have important practical implications, since there are many cases in two-phase flow where avoiding the slug flow may be desirable and in a number of these cases there exists a possibility of using the surfactants. Thus further study of the basic nature of wave damping and the effectiveness of various surfactants is indicated.

Conclusions

In this work it has been found both experimentally and analytically that at least certain types of surfactants impede the growth of interfacial waves in two-phase flow. It appears, in fact, that for proper surfactant, the growth of waves may be stopped all together.

The analysis similar to Levich, but which includes the energy input of the faster flowing gas to the interfacial waves predicts the behavior of the interfacial waves rather well.

In the absence of waves the slugs will eventually form on the level liquid surface, but this occurs at much higher gas velocities than predicted from the usual correlations. The formation of slugs can be predicted reasonably well by the linear theory presented in this work.

References

Bole, J. B. and Hsu, E. Y., 1967, Technical Report No. 79, Department, of Civil Engineering, Stanford, University, CA.

Gardner, C. C., 1979, "Onset of Slugging in Horizontal Ducts," *International Journal of Multiphase Flow,* V6, p. 201.

Jeffreys, H., 1925, "On the Formation of Water Waves by Wind," *Proceedings of Royal Society,* Series A 107, p. 189.

Kordyban, E., 1978, "Growth of Interfacial Waves in Closed Horizontal Channels," ASME Paper 78-WA/FE8.

Kordyban, E., 1991, "The Effect of Wave Growth on the Transition to Slug Flow," *Multiphase Flow Forum,* ASME Publication.

Kordyban, E. and Okleh, A. H., 1994, "The Effect of Interfacial Waves on the Transition to Slug Flow," ASME JOURNAL OF FLUIDS ENGINEERING, Vol. 116, p. 583.

Levich, V. G., 1962, *Physicochemical Hydrodynamics,* Prentice-Hall.

Miles, J. W., 1957, "On the Generation of Surface Waves by Shear Flows," *Journal of Fluid Mechanics,* Vol. 3, p. 185.

Miles, J. W., 1962, "On the Generation of Surface Wave by Shear Flows, Part 4," *Journal of Fluid Mechanics,* Vol. 13, p. 433.

Minato, A., Ikeda, T., and Naifeh, M., 1981, "Mechanistic Model of Slugging Onset in Horizontal Circular Tubes," *Journal of Nuclear Science and Technology,* Vol. 23, p. 761.

Taitel, N. and Dukler, A. E., 1976, "A Model for Predicting Flow Regime Transitions in Horizontal and Near Horizontal Gas-Liquid Flow," *American Institute of Chemical Engineers Journal,* Vol. 22, p. 46.

Wallis, G. B., and Dobson, J. E., 1973, "The Onset of Slugging in Horizontal Stratified Air-Water Flow," *International Journal of Multiphase Flow,* Vol. 1, p. 173.

Weisman, J., Duncan, D., Gibson, J. and Crawford, J., 1979, "Effect of Fluid Properties and Pipe Diameters on Two-Phase Flow Patterns in Horizontal Lines," *International Journal Multiphase Flow,* Vol. 5, p. 437.

Deformation Process of a Water Droplet Impinging on a Solid Surface

Natsuo Hatta
Professor.

Hitoshi Fujimoto
Research Associate.

Hirohiko Takuda
Lecturer.

Department of Mineral Science and Technology,
Kyoto University,
Kyoto 606,
Japan

This paper is concerned with numerical simulations of the deformation behavior of a liquid droplet impinging on a flat solid surface, as well as the flow field inside the droplet. In the present situation, the case where a droplet impinges on the surface at room temperature with a speed in the order of a few [m/s], is treated. These simulations were performed using the MAC-type solution method to solve a finite-differencing approximation of the Navier-Stokes equations governing an axisymmetric and incompressible fluid flow. For the first case where the liquid is water, the liquid film formed by the droplet impinging on the solid surface flows radially along it and expands in a fairly thin discoid-like shape. Thereafter, the liquid flow shows a tendency to stagnate at the periphery of the circular film, with the result that water is concentrated there is a doughnut-like shape. Subsequently, the water begins to flow backwards toward the center where it accumulates in the central region. For the second case where a n-heptane droplet impinges the surface, the film continues to spread monotonically up to a maximum diameter and there is no recoiling process to cause a backwards flow towards the central region. In this study the whole deformation process was investigated from numerical as well as experimental points of view. We find that the results obtained by the present mathematical model give fairly good agreement with the experimental observations. The effects of the viscous stresses and the surface tension on the deformation process of the droplets are estimated and discussed from a practical standpoint.

1 Introduction

The process of cooling a high temperature surface with a water spray is widely used in iron and steel-making industries. Specifically, the spray cooling method is applied to the secondary cooling zone in a continuous casting process. Also, the hot strip passing through the last finishing roll is cooled on a runout table, from the austenitic finishing temperature to the coiling temperature. In this case, the upper strip surface is cooled by a laminar flow cooling method, while the lower surface is cooled by a water spray. Hence, the numerical analysis of the flow field of subsonic free jets of gas-particle mixtures composed of air and water droplets, was performed (Hatta et al., 1992). Again, the problem of flow structures of the two-phase subsonic jets impinging on a flat plate normal to the flow, corresponding to the mist/spray cooling situation, was solved on the assumption that the droplets were reflected perfectly elastically from a surface by the present authors (1993). However, we cannot shed further light on the mist/spray cooling mechanism without understanding the deformation process of individual water droplets impinging on a plate surface.

Practically speaking, in spite of the widespread use of this cooling method, there seems to be a conspicuous lack of knowledge concerning the spray cooling mechanism. Therefore, many experimental studies have been performed focusing upon the collision and deformation processes of a water droplet impinging on a hot plate surface (Wachters and Westerling, 1966; Ueda et al., 1979; Akao et al., 1980; and Chandra and Avedisian, 1992). However, the diameters of spherical water droplets adopted in those experiments were relatively large, ranging from 1 mm to 3 mm. This was because the high speed deformation process of the droplet must be observable from a photographic point of view. Actually, the droplet diameters in spray cooling are believed to range from 100 μm to 500 μm. In this regard, Pederson (1970) treated relatively small droplets, from 200 μm to 400 μm, but the photographs of the impact process were not sharp enough to allow an understanding of the detailed behavior of the droplet deformation process. In passing, we note that it is currently impossible to experimentally measure the inner flow field of a droplet during and subsequent to the collision with a solid surface.

Again, there are a few reports concerning the numerical analyses of the collision and deformation processes of a liquid droplet impinging on a surface. Harlow and Shannon (1967) analyzed numerically the deformation process of a droplet impinging on a flat plate and compared the result obtained with experimental data. Although the effect of surface tension on the deformation process was neglected in their analysis, a fairly good agreement between the numerical and experimental results was found. Turutani et al. (1989) studied the deformation process of the droplet using the SMAC method (Amsden and Harlow, 1970) and discussed the effect of surface tension by comparing the numerical results with experimental values. The two results were found quantitatively to show a similar tendency on the whole. However, in the above-mentioned analytical studies, the surface configurations were not so sharp, due to following the free surface by the so-called marker particles. Moreover, these numerical analyses were restricted to an earlier deformation process.

The deformation process of a n-heptane droplet on a stainless steel surface at room temperature was studied using a flash photography method by Chandra and Avedisian (1991). They found that a liquid film formed by the droplet impinging on a surface, continued to spread monotonically in a fairly thin discoid-like shape and reached a maximum diameter of four times the initial droplet diameter. In the present experiment, where a water droplet impinges on an Inconel 625 alloy surface, it was found that the liquid showed a tendency to be stagnant at the

Contributed by the Fluids Engineering Division for publication in the JOURNAL OF FLUIDS ENGINEERING. Manuscript received by the Fluids Engineering Division March 14, 1994; revised manuscript received September 28, 1994. Associate Technical Editor: J. A. C. Humphrey.

periphery of the circular film and concentrated there in a doughnut-like shape, and that, thereafter, the liquid began to flow backwards towards the center until it reached an equilibrium configuration and was concentrated at the central region rather than at the periphery.

In the present paper, both the radially expanding process of the liquid film formed by a droplet impinging on a solid surface at room temperature and the subsequent process of flow reversal from the periphery of the circular liquid film towards the central region, have been investigated from numerical and experimental points of view. Concretely, the experimental results obtained by the present authors and Chandra and Avedisian (1991), were analyzed from a numerical point of view. The inner velocity vector fields, as well as the above characteristic parameters, were calculated using an axisymmetric coordinate system. The surface tension effect was taken into consideration. The calculation approach was based on the MAC-type solution method. This did not need to introduce the so-called marker particles, which will be mentioned later. A comparison had been made between the calculated time histories of droplet diameter and height during the deformation with corresponding experimental observations. In the present experiments, the time variation of the droplet diameter and its impinging velocity, were determined by direct measurement from multiple-exposure images using micro flash units. The computations were performed on the Fujitsu supercomputer VP2600 at the Data Processing Center of Kyoto University.

2 Conservation Equation

The conservation equations to be solved are expressed nondimensionally in terms of the following dimensionless variables:

$$\left.\begin{aligned} t = \bar{t}/(\bar{D}_p/\bar{u}_0), \quad x = \bar{x}/\bar{D}_p, \quad y = \bar{y}/\bar{D}_p \\ u = \bar{u}/\bar{u}_0, \quad v = \bar{v}/\bar{u}_0, \quad p = \bar{p}/(\bar{\rho}\bar{u}_0^2) \end{aligned}\right\} \tag{1}$$

in which t is the time; (x, y) denote the coordinates in the radial and axial directions respectively; (u, v) denote the velocity components in the x and y-directions respectively and p is the pressure. $\bar{D}_p$, $\bar{u}_0$ and $\bar{\rho}$ denote the initial droplet diameter, the impinging velocity and the material density of the droplet, respectively. Here overbars denote the dimensional quantities.

The system of equations governing the motion of fluid in the deforming droplet is given by:

$$\frac{\partial u}{\partial x} + \frac{\partial v}{\partial y} + \frac{u}{x} = 0 \tag{2}$$

$$\frac{\partial u}{\partial t} + \frac{\partial u^2}{\partial x} + \frac{\partial uv}{\partial y} + \frac{u^2}{x} = -\frac{\partial p}{\partial x} + \frac{1}{\mathrm{Re}}\left[\frac{\partial^2 u}{\partial x^2} + \frac{\partial^2 u}{\partial y^2} + \frac{\partial}{\partial x}\left(\frac{u}{x}\right)\right] \tag{3}$$

$$\frac{\partial v}{\partial t} + \frac{\partial uv}{\partial x} + \frac{\partial v^2}{\partial y} + \frac{uv}{x} = -\frac{\partial p}{\partial y} - \frac{1}{\mathrm{Fr}^2} + \frac{1}{\mathrm{Re}}\left[\frac{\partial^2 v}{\partial x^2} + \frac{\partial^2 v}{\partial y^2} + \frac{1}{x}\frac{\partial v}{\partial x}\right] \tag{4}$$

in which Re and Fr are the Reynolds number and the Froude number, respectively, defined as:

$$\mathrm{Re} = \bar{u}_0 \cdot \bar{D}_p/\bar{\nu}, \quad \mathrm{Fr} = \bar{u}_0/\sqrt{\bar{g}\cdot\bar{D}_p} \tag{5}$$

Here, $\bar{\nu}$ and $\bar{g}$ denote the kinematic viscosity and the gravitational acceleration, respectively.

Next, the pressure balance condition on the free surface yields:

$$p_s - p_\infty + \frac{1}{\mathrm{Re}}\frac{\partial U_\eta}{\partial \eta} = \frac{1}{\mathrm{We}}\left(\frac{1}{R_1} + \frac{1}{R_2}\right) \tag{6}$$

in which:

$$\mathrm{We} = \frac{\bar{\rho}\bar{u}_0^2\bar{D}_p}{\bar{\sigma}} \tag{7}$$

where p_s and p_∞ are the surface and atmospheric pressures, respectively. R_1 and R_2 are the principal radii of curvature at a given point on a free surface, respectively. η is the coordinate normal to the surface and U_η is the component of velocity in the η-direction. $\bar{\sigma}$ is the surface tension. Obviously, the sign on the left-hand side of Eq. (6) depends upon the sign of R_1 and R_2, that is, whether a concave or convex surface.

3 Numerical Procedure

The numerical techniques suitable for solving free-boundary problems of fluid mechanics, can be divided roughly into two kinds of methods. One method is to track the free surface on a fixed coordinate system in a Lagrangian manner, based upon the MAC technique developed by Harlow and Welch (1965). The other, is to renew the curvilinear coordinate system so that the coordinates of the free surface boundary are fitted at every new time step (Ryskin and Leal, 1984). The use of the boundary-fitted curvilinear coordinate system is considered to be of advantage in treating the boundary condition at the free surface easily and strictly, and in maintaining the conservation law of mass and momentum at the free boundary. However, computational cost is appreciably expensive in comparison with the fixed coordinate system, because the adjustment must always be made so as to fit the current boundary shape. On the other hand, the numerical technique based on the MAC-type solution method is capable of catching the overturning of a free surface wave, the mixing of bubbles in liquid, etc. In the present investigation, the calculation of the deformation process of a droplet was performed using the fixed coordinate system because of numerical instability when using the boundary-fitted approach due to the strongly curved shape of the droplet just after collision with the surface.

Nomenclature

$\bar{D}_p$ = initial droplet diameter, m
$\bar{g}$ = gravitational acceleration, m/s^2
Fr = $\bar{u}_0/\sqrt{\bar{g}\cdot\bar{D}_p}$ Froude number
f = CFL number
p = dimensionless pressure
R_1, R_2 = principal radii of curvature at a point on free surface
Re = $(\bar{u}_0\bar{D}_p/\bar{\nu})$ Reynolds number
t = time
U_η = velocity component in η direction
u, v = velocity components
u_s, v_s = velocity components on free surface
$\bar{u}_0$ = impinging velocity, m/s
We = $\bar{\rho}\bar{u}_0^2\bar{D}_p/\bar{\sigma}$ Weber number
x, y = coordinates
x_s, y_s = surface position
Δx, Δy = mesh size
η = coordinate normal to surface
$\bar{\rho}$ = material density of droplet, kg/m^3
$\bar{\nu}$ = kinematic viscosity, m^2/s
$\bar{\sigma}$ = surface tension, Newton/m
$(\bar{\ })$ = dimensioned quantities

The system of conservation equations has been solved numerically using finite-difference approximation of the Navier-Stokes equations for an axisymmetric incompressible flow. The staggered mesh system has been adopted in the numerical simulation. The second-order upwind scheme, which is commonly called the donor cell method, has been applied to the convection terms, and the second-order central differencing scheme has been applied to the viscous terms. Also, the explicit Euler scheme has been adopted for time integrations. First, the velocity vector field was determined by the finite-differencing approximations to the momentum Eqs. (3) and (4). Next, the pressure field was determined by solving the finite-difference approximation of the Poisson equation on the basis of an iterative procedure. The calculation approach which has been mentioned so far, basically follows the MAC-type solution method (Harlow and Welch, 1965), except that it uses no marker particles and applies the donor cell method to the convection terms.

Now, we can briefly describe the calculation procedure of the free surface configuration. It is assumed that the free surface consists of a large number of segments and that the two end-points of each segment are located on the underlying lines of the rectangular cell system. According to Miyata (1986), the time evolution of the free surface is followed by the Lagrangian movement of the segments that form the free surface configuration. The end points (x_s^n, y_s^n) of the segments at a time step n, are moved to the new points (x_s^{n+1}, y_s^{n+1}) at the next time step in the Lagrangian manner:

$$\left.\begin{aligned} x_s^{n+1} &= x_s^n + \Delta t \cdot u_s \\ y_s^{n+1} &= y_s^n + \Delta t \cdot v_s \end{aligned}\right\} \tag{8}$$

where u_s and v_s denote the velocity components in the radial and axial directions, respectively and Δt is the time increment per calculation cycle. The new segments are temporarily determined by (x_s^{n+1}, y_s^{n+1}). Then, the new formal end-points are given by the intersecting points between the temporary segments and the underlying mesh lines. The submesh system, whose mesh size is half that of the main system, is introduced in the present calculation. Because the free surface configuration is represented by a succession of line segments, it becomes smoother due to the fact that the number of intersecting points increases to twice that of the main mesh system alone. It should be borne in mind that the calculation of the velocity vector and pressure fields is performed only on the main mesh system. Again, the radial position of the contact line of the free surface on the plate is determined by a linear extrapolation from the two end-points close to the solid surface.

In addition, the velocity components of the new segments are determined by extrapolation of the velocity vector field in the nearest neighboring sites inside the fluid. Also, it is noted that the radii R_1 and R_2 required to estimate the surface pressure p_s (see Eq. (6)), are calculable by first and second-order differential terms and these are obtained by a second-order accurate difference approximation. There are some cases where it is impossible to calculate exactly the third term on the left hand side of Eq. (6), particularly at a sharply convex or concave region where the grid points are too few in number. However, the term is considered to be negligibly small compared with the other terms in Eq. (6) and is neglected.

In the present calculation, the moment of impingement of a droplet on a horizontally fixed flat surface was set at $t = 0$. It was assumed that the droplet was perfectly spherical in shape and had no velocity distribution within it at $t = 0$.

Next, we considered the effect of selecting the mesh size on numerical accuracy. A regular square mesh ($\Delta x = \Delta y$) was adopted in this calculation. For various mesh sizes, numerical experiments were performed and the results were compared with each other.

Figure 1 gives the time variation of the radial distance $x_{s,y=0}$ of the contact line of a droplet for $\Delta x = 1/30$, $1/60$, $1/100$ and $1/120$ respectively, for the case with Re = 1500, We = 62.5 and Fr = 42.9. The numerical error was found to be at most 1 percent between $\Delta x = 1/100$ and $\Delta x = 1/120$. Accordingly, $\Delta x = 1/100$ was selected in the present calculation for the sake of saving computer memory and CPU time.

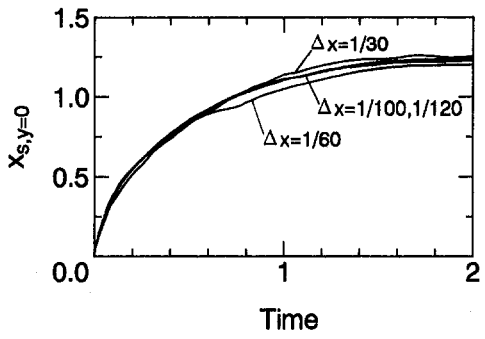

Fig. 1 Preliminary check on the effect of mesh size on numerical accuracy

Again, the computational time interval Δt, was determined by the CFL (Courant-Friedrichs-Lewy) condition as follows:

$$\Delta t = f \times \text{Min}\left(\frac{\Delta x}{\sqrt{u^2 + v^2}}\right) \tag{9}$$

where f is the CFL number. The condition of $f \leq 0.5$ had to be satisfied because the submesh system was introduced in the present numerical model, as mentioned above. The same numerical experiments, as in the above case, were performed for $f = 0.07$, 0.05 and 0.04 respectively. As a result, almost no significant numerical error was recognized between $f = 0.05$ and 0.04. Accordingly, we selected $f = 0.05$ throughout the present simulations.

In the calculations the no-slip condition was adopted ($u = v = 0$ at the wall) and the pressure condition at the solid/liquid interface was given by:

$$p' = p_{1/2} - \frac{1}{2} v_1 |v_1| + \frac{\Delta y}{\text{Fr}^2} - \frac{2v_1}{\text{Re} \cdot \Delta y} \tag{10}$$

in which p' and $p_{1/2}$ denote the pressure at the external and the interior cells of the wall, respectively, and v_1 is the velocity component normal to the wall.

4 Experimental Procedure

The experimental study was undertaken to understand the deformation process of an impinging droplet on a plate surface. It was desired to calculate the deformation process of a droplet for which experimental data are available, so that a direct comparison with the calculations could be made.

Figure 2 shows a schematic diagram of the experimental apparatus. Water stored in a leakproof tank was introduced into a needle and a droplet was formed at its tip. The water was pressurized statically by high pressure air to ensure repeatability of droplet formation and release of droplets at the needle tip with a 0.2 mm inner diameter. A needle oscillator using a speaker coil which vibrated at a particular frequency was attached to the needle tip so that droplets with a uniform diameter and a constant velocity were produced. An 18 cm diameter disk, which had a long and narrow rectangular hole (hence for the referred to as the slit hole), rotated horizontally between the needle tip and the solid surface. Accordingly, a large number of droplets appearing from the needle tip were blocked by the rotating disk, but one droplet per revolution passed through the slit hole of the rotating disk and reached the flat surface.

The video camera recorder, which was equipped with a macro filter, was horizontally fixed at the same level as the solid sur-

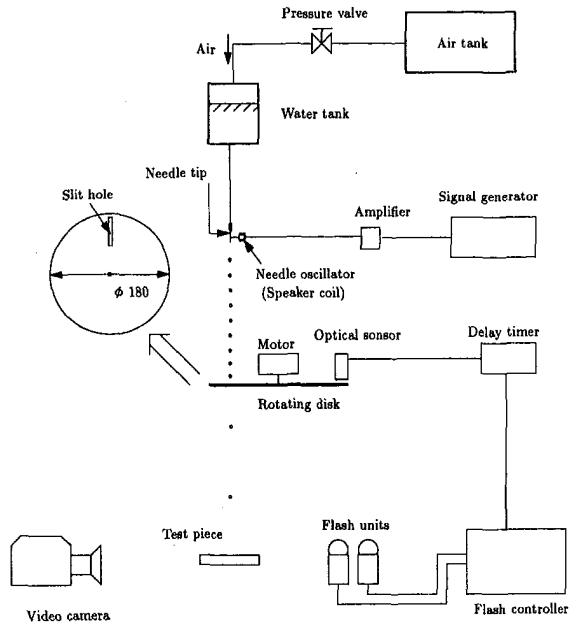

Fig. 2 Experimental apparatus

face. The closeup image of the droplet on the video screen was taken by the back light method using micro flash units. The video camera recorder, the solid surface on which the droplet impinged and the micro flash lights were arranged in a straight line. Upon registering the position of the slit hole on the disk, the optical sensor unit sent a signal to the delay timer when a droplet passed through the disk hole. The delay timer transmitted a signal to the flash controller units (Sugawara SG303A, MP102A) with a delay time. The two micro flash units (Sugawara MP230) providing a 1.6 μs or shorter duration flash, were triggered in scheduled time intervals of 60 $\sim$ 500 μs, when signals were sent from the flash controller units. Again, the error of the time interval was kept below 1 μs. The video image was set to be exposed only by the flash light. The moving distance of a droplet during a flash, was smaller than the measurement accuracy mentioned below.

The droplet size was measured directly from a video still image using a personal computer. Again, because the measurement accuracy of the video still image depended upon the resolution of the video system and the image magnitude, it could not be bettered than 0.008 mm with the present measurement system. The impinging velocity was easily estimated by the moving distance of the droplet in the time interval from one flash to another. The time history of the droplet deformation was measured from a large number of multi-exposure images of the droplet before the collision with the surface at the first flash and after the collision at the second flash. The period from the moment of impact to the second flash was calculated from three factors; the impinging velocity, the distance between the bottom/top of the droplet at the first flash and the surface, and the time interval between the two flashes.

Strictly speaking, it is difficult to regularly produce droplets with the same diameter and the same velocity. Therefore, the diameter of all the droplets on the video image, has been measured to obtain exact experimental data. Again, the impinging velocity can be regarded as constant, on condition that the delay timer is set at the same delay time, because droplets with different velocities were not caught on a small video frame area. The velocity of a droplet could be varied within the range 1.3 m/s to 4.0 m/s with the present experimental apparatus.

5 Results and Discussion

First, we considered the effect of the physical properties of the plate surface on the deformation process of droplets. The surface material was Inconel 625 alloy. In order to examine whether or not the surface conditions were significant the deformation process of a droplet impinging on the waxed plate surface was compared with the case of the non-waxed (bare) plate surface on condition that $\bar{D}_p = 0.4$ [mm] and $\bar{u}_0 = 3.75$ [m/s] (Re = 1500 and We = 78). Figure 3(a) demonstrates the comparison between the two cases. We note that the height $\bar{h}$ and the radius $\bar{r}$ were normalized by the initial droplet diameter $\bar{D}_p$ and that the dimensionless height h ($=\bar{h}/\bar{D}_p$) and the dimensionless radius r ($=\bar{r}/\bar{D}_p$) obey the definition shown in Fig. 3(b). There was no observed difference in the time history of the height and the radius, at least during the early period of impact. The deformation processes were similar to each other. The evolution of the wetted area and spreading rate, both of a droplet on a stainless steel surface and of a droplet spreading over a thin film created by the deposition of a prior droplet, were compared to each other using a n-heptane droplet by Chandra and Avedisian (1991). The experimental results show that the deformation process of the droplet spreading on a thin liquid film, is essentially the same as on a solid surface during the early period. Again, they found that the radius of the n-heptane film on the surface at an ambient temperature of 24°C increased monotonically until it reached a maximum.

However, it was found in the present experiment using water droplets, that the film began to recoil towards the center after the radius reached a maximum on the solid surface at the ambient temperature, as described below. Practically, we believe that the wettability between the surface and the liquid should be taken into consideration. In other words, the deformation process of a liquid droplet on a solid surface in the later stage after impact is considered to depend strongly upon the wettability at the solid/liquid interface, although the deformation process may be regarded as independent of the surface condition during the early period of impact, as pointed out by Chandra and Avedisian.

However, the above interaction effect was not taken into account in the present numerical simulations, even when the whole deformation process, from the moment of impact to reaching the final configuration, was not able to give appreciable agreement with experimental data. Nevertheless, we compare the numerical results obtained by the present model with the experimental ones for the case where a water droplet impinges on an Inconel 625 alloy surface. Figure 4(a) shows the comparison between the calculated and experimental time histories of

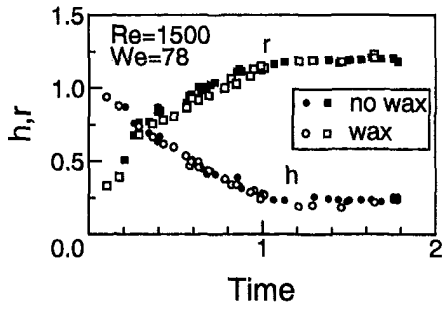

Fig. 3(a)

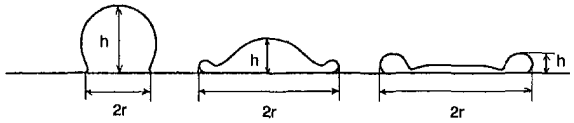

Fig. 3(b)

Fig. 3(a) and 3(b) Effect of physical properties of plate surface on deformation process (a) and definition of droplet height h and radius r (b). Note that the experimental uncertainties in both the droplet radius r and height h are kept within ±0.041 on a nondimensional scale.

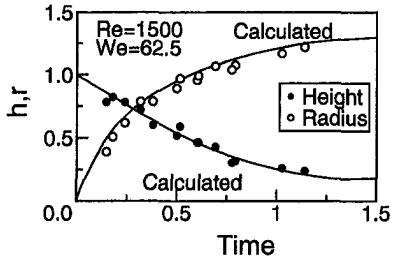

Fig. 4(*a*)

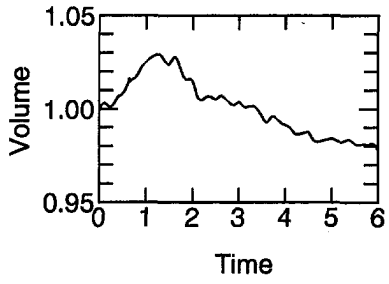

Fig. 4(*b*)

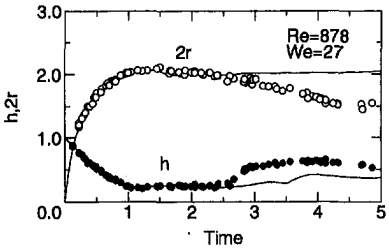

Fig. 4(*c*)

Fig. 4(*a*)–4(*c*) Comparison of numerical time histories of droplet height *h* and radius *r* with experimental values and time history of numerical droplet volume during deformation (*b*) for Re = 1500 and We = 62.5. And comparison of numerical result and experimental ones for Re = 878 and We = 27 (*c*). Note that the experimental uncertainties in both the droplet radius *r* and height *h* are kept ±0.041 on nondimensional scale in Fig. 4(*a*) and Fig. 4(*c*), and that the numerical error of the droplet volume during deformation is at most 3 percent in Fig. 4(*b*).

the height h and the radius r for the case with $\bar{D}_p = 0.5$ [mm] and $\bar{u}_0 = 3.0$ [m/s] (Re = 1500 and We = 62.5). It can be seen from this figure, that the calculated time history of the reduction process of h $(=\bar{h}/\bar{D}_p)$ shown by the solid line gives a fairly good fit to the experimental data corresponding to the solid circles. Also, the calculated time history of the spreading process of r $(=\bar{r}/\bar{D}_p)$ shown by the solid line, is roughly in agreement with the experimental data corresponding to the empty circles. While the calculated values of r are a little larger than the experimental, the difference is at most 4% for $t > 0.5$. Figure 4(b) shows the time variation of the calculated liquid volume during the deformation due to numerical error. Here, the initial spherical volume was fixed at unity. The numerical error of the liquid volume was at most three percent. As mentioned above, it has been clarified that the calculated deformation process of the droplet was in agreement with the experimental in the early period of impact ($t < 1.5$). Then, the subsequent process was investigated. Figure 4(c) indicates the comparison between the calculated and experimental results in the period of $t < 5.0$ just after impact for the case with $\bar{D}_p = 0.39$ [mm] and $\bar{u}_0 = 2.25$ [m/s] (Re = 878 and We = 27). The calculated and experimental time variations of h and r were found to agree well with each other in the time range of $t \leq 2.5$. However, a significant difference between the calculated and experimental results appeared in the subsequent deformation process. The experimental r-value decreased because of the recoiling process in the time range of $t \geq 2.5$, while the calculated value remained almost constant. This may have occurred due to the fact that the no-slip condition was adopted at the liquid/solid interface as the boundary condition and thereby the contact line around the circular wetted area could not be made movable toward the center.

We now consider the deformation process and the flow field after the droplet impinges on the plate. Figure 5(a) shows the evolution of the free surface and the velocity vector field for

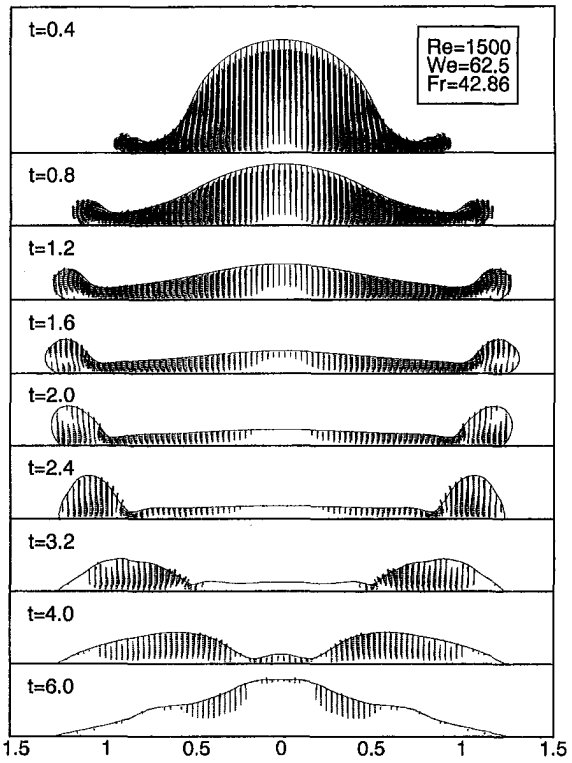

Fig. 5(*a*)

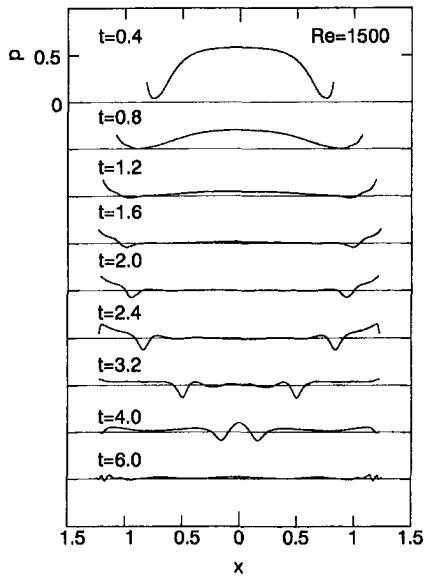

Fig. 5(*b*)

Fig. 5(*a*) and 5(*b*) Numerical free surface configuration and velocity vector field of a droplet impinging on a flat plate (*a*) and pressure distribution along the surface (*b*) with Re = 1500, We = 62.5 and Fr = 42.86

the case with Re = 1500, We = 62.5 and Fr = 42.86. Figure 5(*b*) shows the corresponding distribution of pressure p on the solid surface. Here, $p = 0$ corresponds to the ambient pressure and the negative pressure corresponds to a lower than ambient pressure. It is noted that the magnitude of the velocity vector in this figure is common at every time stage. The water film expands radially during the early period of impact because the pressure at the impinging region is higher than that at the periphery. The edge part in the neighborhood of the contact line, was observed to be roundish owing to the surface tension effect. A velocity boundary layer formed in the water film adjacent to the surface due to the no-slip condition imposed. The calculated results show that liquid flows radially from the center to the relatively stagnant edge zone of the water film, and that the roundish edge zone expands in the early period of impact ($t < 1.6$). As a result, the central part of the liquid film became lower than the height of the edge zone between $t = 1.2$ and 1.6.

The film radius reached a maximum value at $t \simeq 1.6$ owing to the decrease in the radial velocity component, associated with the fluid friction with the solid surface and the reversal of the pressure gradient in the radial direction. Thereafter, the liquid flowed radially backwards from the edge to the center. The phenomenon of flow reversed was strongly affected by the vortical structure appearing at the rounded edge zone. The center of the vortical structure formed first near the contact line, and then moved upwards. As a result, the edge zone moved in the radial direction ($t = 1.2 \sim 1.6$). On the other hand, upon formation the flow towards the center on the underside of the edge zone came into collision with the flow from the center towards the periphery. The collision of the two flows led to a rising flow and thereby the rounded edge zone grew in both thickness and width ($t = 2.0 \sim 2.4$). At even later time, the flow towards the center overcame the flow from the center towards the periphery with the result that the position where the flow towards the central part collided with the opposite flow, shifted towards the center with time. Thus, the position where the liquid film thickened was shifted from the peripheral region to the center. In contrast, the central liquid film with a smaller and almost uniform thickness, was seen to be in an almost stagnant state ($t = 2.0 \sim 3.2$). Thereafter, the flow from the periphery to the center became dominant and again, the central part of the liquid film was elevated. As a whole, the configuration of the water film in this state was high in the central zone and lower with increasing water film radius ($t = 6.0$).

Figure 6 shows a time-sequence for the time variation of the deformation process for the same conditions as in the case of Fig. 5. The images were made from a video printer output taken from the video image. The droplets were photographed from a slightly oblique angle with respect to the plate surface. For this a flash light source was triggered once per droplet. Therefore, it should be noted that the droplets are different in each of the instantaneous photographs. That is to say, the same droplet was not followed, but the various instantaneous behaviors of different droplets were photographed and arranged in a regular sequence. Also, the time elapsed after the collision of each droplet with the surface could not be measured accurately due to the shortness of this event. At any rate, it has been visually observed that droplets impinging on the solid surface form a radial liquid film and spread with time (see Fig. 6(*a*), (*b*), and (*c*)). Again, when the liquid film expands in a discoid-like form, the thickness of the central region, is seen to be smaller than that of the peripheral one, as shown in Fig. 6(*d*). Furthermore, it can be observed from Fig. 6(*e*) that thereafter flow reversal occurred from the peripheral region toward the center. The last photograph is observed to be very similar to the shape of $t = 3.2$ in Fig. 5(*a*). On the whole, it may be justifiable to consider that these photographs indicate a qualitative agreement with the results obtained by the present numerical model, even

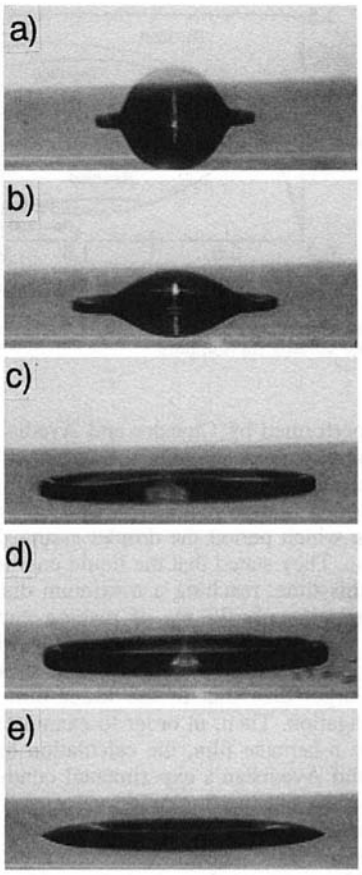

Fig. 6 Photographic time-sequence showing the deformation process of droplet impinging on a flat plate with $\bar{D}_p$ = 0.5 ± 0.02 mm and u_0 = 3.0 ± 0.02 m/s

if the values of t at which the pictures were taken could not be measured.

It should be noted that there was a slight recoiling effect revealed in the photographs. In the experiments performed using the n-heptane droplet (Chandra and Avedisian, 1991) there was no recoiling process on the stainless steel surface at the ambient temperature, while the recoiling process apparently exists in Fig. 5(*a*). However, a surface wetted by a liquid once cannot be regarded as being in a non-wetting state, due to the fact that the no-slip condition exists at the liquid/solid interface. In fact, the diameters of the circular contact lines were seen to be constant after reaching a maximum, as shown in Fig. 5(*a*). Here, it should be noted that the maximum diameter of the liquid film was different from that of the circular wetted area.

Figure 7 indicates the influence of the impinging velocity on the time history of both the height h and the radius r during the deformation. We found that the height was reduced along the same time history curve up to $t \simeq 1.0$ in the present range of the Re number. Also, the height changed at the same rate in the range of $t < 0.5$ regardless of the Re number and the decreasing rate was almost the same as the impinging velocity. After that, the decreasing rate became lower, but the droplet height began to increase slightly at $t = 1.0$, 1.2 and 1.3 for Re = 1050, 1300, and 1500, respectively. This suggests that the height of the central region was lower than that of the peripheral zone (see Fig. 5(*a*)). As the We number is reduced, the effect of the surface tension became more remarkable. Specifically, the attainable radius was reduced and the time required to reach it decreased with a decrease in the We number.

Next, we discuss an experimental case where a n-heptane droplet of 1.5 mm diameter impinged a stainless steel surface at an ambient temperature of 24°C. This corresponds to the

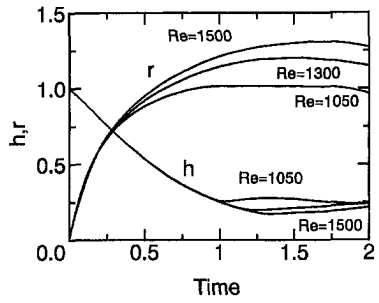

Fig. 7 Time history of numerical droplet height h and radius r impinging on a flat plate for various Re numbers

experiments performed by Chandra and Avedisian (1991). A sequence of photographs showing the deformation process of the droplet during and subsequent to the collision with the solid surface is reported in their paper. The first 2.6 ms of impact is shown, during which period the droplet assumed the shape of a flattened disc. They stated that the liquid continued to further spread after this time, reaching a maximum diameter of 6.04 mm after approximately 20 ms of making contact with the surface. This was four times the initial droplet diameter.

The ratio of the maximum radius of the n-heptane film is significantly larger than that of the water film shown in the present investigation. Then, in order to examine the spreading process of the n-heptane film, the calculation had been made on Chandra and Avedisian's experimental conditions that We = 43. Re = 2300 and the impinging velocity $\bar{u}_0$ = 0.93 m/s. Figure 8 indicates the comparison between experimental and calculated results. Here, solid circles denote the experimental data and solid lines denote the calculations. Also, d denotes the diameter of the circular wetted area according to Chandra and Avedisian (1991). The calculations were made both accounting for and neglecting surface tension. Comparing the predicted values with the experimental data given by Chandra and Avedisian, the numerical results obtained by neglecting surface tension obviously gave better agreement with the measurements for the time variations of the height and diameter of liquid film during the deformation. In their experiment, the n-heptane film continued to spread monotonically until it reached a maximum and the recoiling process was not observed. Therefore, we believe that the surface tension effect is very small not only during the early stage of impact but also subsequently, at least at the surface temperature of 24°C. In reality, the advancing liquid-solid contact angle at the contact line was measured to be 32 deg at 24°C. Although the pictures in Fig. 6 show an evolution of the droplet very similar to that observed in Chandra and Avedisian's pictures for the case where a n-heptane droplet impinged on a steel plate at room temperature, the contact angle at the contact line of the former case was observed to be relatively large in comparison to that of the latter case. At any rate, the n-heptane liquid seems to easily wet a stainless steel surface at the ambient temperature.

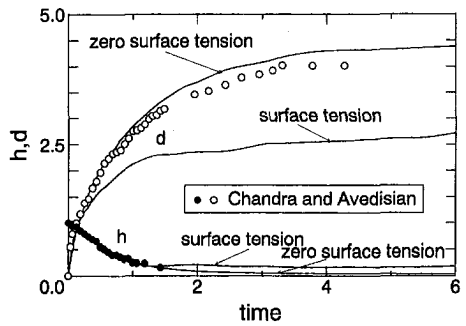

Fig. 8 Comparison between numerical and experimental results with Re = 2300 and We = 43. Note that solid circles give deformation process of n-heptane droplet observed by Chandra and Avedisian.

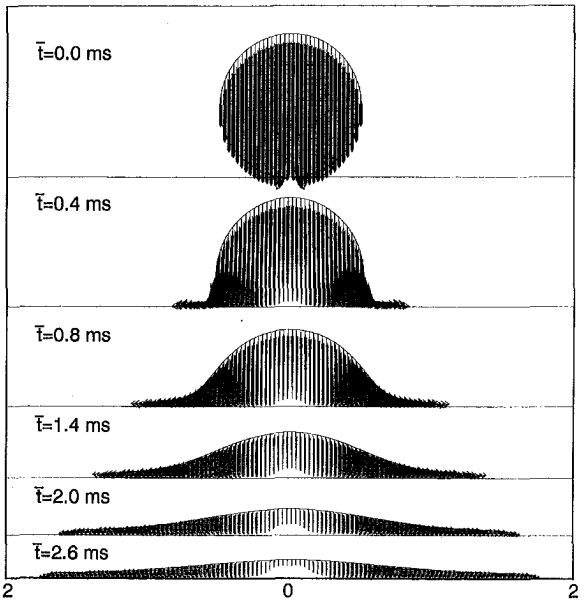

Fig. 9 A sequence of calculated surface configurations and velocity vector fields showing the impact of a droplet of n-heptane on a stainless steel surface

Figure 9 is a sequence of calculated surface configurations, including the velocity vector field, during the impact of a droplet of n-heptane on a stainless steel surface at 24°C. Although the calculation was made neglecting the surface tension effect, the surface configurations in this figure are very similar to those observed in the photographs of Chandra and Avedisian (1991). The value of the time $\bar{t}$ shown in each figure corresponds to that of $\bar{t}$ at which each picture was taken.

Akao et al. (1980) have showed that the spreading of the drop over the surface is basically independent of thermal effects since the maximum diameter correlates well with the initial kinetic energy of the falling droplet. They proposed an empirical formula capable of predicting the value of the maximum dimensionless diameter for a case where a liquid droplet of 0.2 to 0.3 cm impinges on a copper surface heated to 400°C. According to the formula, the value of the maximum dimensionless diameter must be 2.65 for the case where a value of 4.0 or more was given in the work by Chandra and Avedisian. Again, the value should be 3.0 for a case where the result shown in Fig. 4(a) is approximately 2.6 in the present calculation. In short, the experimental results of d given by Chandra and Avedisian are too large on the basis of this formula and the present results too small by 13 percent or so.

In summary, the deformation process of a liquid droplet on a solid surface is considered to depend not only upon the Weber and the Reynolds numbers, but also upon other parameters such as the initial kinetic energy of a droplet, the interaction of the physical properties of a liquid with those of a solid surface and the affinity at the solid/liquid interface.

6 Conclusions

The collision dynamics of a water droplet impinging on a rigid surface at room temperature have been described from numerical and experimental points of view. Emphasis is placed upon the analysis of the whole deformation process of a liquid droplet after collision with the surface. The effects of viscous stresses and surface tension have been taken into consideration and a numerical model capable of predicting

the deformation process has been developed. The results obtained by the model have been compared with experimental data. First, the impingement of a water droplet on an Inconel 625 alloy surface at room temperature was considered. It was found that the water film formed by a droplet impinging on the surface began to recoil from the peripheral region towards the center after the radius reached a maximum. It was found that the calculated deformation process of the droplet is in agreement with the experimental results in the early period of impact, but that a significant difference between the calculated and experimental results appears in the subsequent deformation process. This is attributed to the no-slip condition adopted at the liquid/solid interface. The impingement of a n-heptane droplet on a stainless-steel surface at room temperature has also been studied by other researchers. These investigations confirm experimentally that the n-heptane film formed by impingement continues to spread monotonically up to the attainable radius with no recoiling process. Calculations were made here for two cases where the surface tension effect is accounted for and neglected. The numerical results obtained by neglecting the surface tension effect were found to give fairly good agreement with the experimental data and the surface configurations were found to be very similar to photographs obtained during the deformation at each time step.

From various points of view, it may be concluded that the deformation process of a liquid droplet on a solid surface cannot be determined using only the Weber and Reynolds numbers, but that other parameters have to be considered. The problem concerning such parameters will be treated in the near future. The present investigation contributes to the physical understanding of the collision dynamics of a liquid droplet impinging on a solid surface as well as the dynamics of free surface bodies.

Acknowledgment

The authors note that this study was supported through a Grant in Aid for Scientific Research (07455287) of the Ministry of Education, Science and Culture in Japan and the Kawakami Memorial Foundation.

References

Amsden, A. A., and Harlow, F. H., 1970, "The SMAC Method: A Numerical Technique for Calculating Incompressible Fluid Flows," Los Alamos Scientific Report LA-4370.

Akao, F., Araki, K., Mori, S., and Moriyama, A., 1980, "Deformation Behaviors of a Liquid Droplet Impinging Onto Hot Metal Surface," *Transaction of ISIJ,* Vol. 20, pp. 737–743.

Chandra, S., and Avedisian, C. T., 1991, "On the Collision of a Droplet with a Solid Surface," *Proceedings of the Royal Society* (London) Series A, Vol. 432, pp. 13–41.

Chandra, S., and Avedisian, C. T., 1992, "Observations of Droplet Impingement on a Ceramic Porous Surface," *International Journal of Heat Mass Transfer,* Vol. 35, No. 10, pp. 2377–2388.

Harlow, F. H., and Welch, J. E., 1965, "Numerical Calculation of Time Dependent Viscous Incompressible Flow of Fluid with Free Surface," *Physics of Fluids,* Vol. 8, pp. 2182–2189.

Harlow, F. H., and Shannon, J. P., 1967, "The Splash of a Liquid Drop," *Journal of Applied Physics,* Vol. 38, pp. 3855–3866.

Hatta, N., Ishii, R., and Fujimoto, H., 1992, "Numerical Analysis of Gas-Particle Two-Phase Subsonic Freejets," ASME JOURNAL OF FLUIDS ENGINEERING, Vol. 114, pp. 420–429.

Hatta, N., Fujimoto, H., and Takuda, H., 1993, "Numerical Analysis of Flow Pattern of Impinging Liquid Sprays in a Cold Model for Cooling a Hot Flat Plate," *Applied Scientific Research,* Vol. 50, pp. 129–147.

Miyata, H., 1986, "Finite-Difference Simulation of Breaking Waves," *Journal of Computational Physics,* Vol. 65, pp. 179–214.

Pedersen, C. O., 1970, "An Experimental Study of the Dynamic Behavior and Heat Transfer Characteristics of Water Droplets Impinging Upon a Heated Surface," *Int. Heat Mass Transfer,* Vol. 13, pp. 369–381.

Ryskin, G., and Leal L. G., 1984, "Numerical Solution of Free-Boundary Problems in Fluid Mechanics. Part 1. The Finite-Difference Technique," *Journal of Fluid Mechanics,* Vol. 148, pp. 1–17.

Turutani, K., Yao, M., Senda, J., and Fujimoto, H., 1989, "Numerical Analysis of the Deformation Process of a Droplet Impinging Upon a Surface (in Japanese)," *Transactions of the JSME-B,* Vol. 55, pp. 814–819.

Ueda, T., Enomoto, T., and Kanetsuki, M., 1979, "Heat Transfer Characteristics and Dynamic Behavior of Saturated Droplets Impinging on a Heated Vertical Surface," *Bulletin of the JSME,* Vol. 22, pp. 724–732.

Wachters, L. H. J., and Westerling, N. A., 1966, "The Heat Transfer From a Hot Wall to Impinging Water Drops in the Spheroidal State," *Chemical Engineering Science,* Vol. 21, pp. 1047–1056.

Effect of Reynolds Number on Isotropic Turbulent Dispersion

Renwei Mei
Department of Aerospace Engineering, Mechanics & Engineering Science, University of Florida, Gainesville, FL 32611

Ronald J. Adrian
Department of Theoretical & Applied Mechanics, University of Illinois, Urbana, IL 61801

The influence of the spatio-temporal structure of isotropic turbulence on the dispersion of fluid and particles with inertia is investigated. The spatial structure is represented by an extended von Kármán energy spectrum model which includes an inertial sub-range and allows evaluation of the effect of the turbulence Reynolds number, Re_λ. *Dispersion of fluid is analyzed using four different models for the Eulerian temporal auto-correlation function* $D(\tau)$. *The fluid diffusivity, normalized by the integral length scale* L_{11} *and the root-mean-square turbulent velocity* u_0, *depends on* Re_λ. *The parameter* $c^E = T_0 u_0 / L_{11}$, *in which* T_0 *is the Eulerian integral time scale, has commonly been assumed to be constant. It is shown that* c^E *strongly affects the value of the fluid diffusivity. The dispersion of a particle with finite inertia and finite settling velocity is analyzed for a large range of particle inertia and settling velocity. Particle turbulence intensity and diffusivity are influenced strongly by turbulence structure.*

Introduction

Background. The principal difficulty in predicting the dispersion of a fluid element or a particle by turbulence is the essential nonlinearity (Lumley, 1957), wherein the statistics of the fluid turbulence must be specified along the unknown trajectory of the fluid particles. Theoretical treatments of the subject can be found, among others, in the works of Taylor (1922), Tchen (1947), Corrsin (1959), Yudine (1959), Csanady (1963), Chao (1964), Kraichnan (1970), Phythian (1975), Lundgren and Pointin (1976), Reeks (1977), Pismen and Nir (1978), Nir and Pismen (1979), Wang and Stock (1988 and 1993), and Mei et al. (1991). Most analyses of particle dispersion focus on the effects of the particle inertia and the settling velocity in a specific model of turbulence. Dispersion of fluid is characterized by the mean square displacement tensor

$$Y_{ij}(\tau) = \langle y_i(t) y_j(t+\tau) \rangle, \tag{1a}$$

where $\langle\ \rangle$ stands for an ensemble average, and $y_i(t)$ denotes the ith component of the fluid displacement. $Y_{ij}(\tau)$ is related to the Lagrangian correlation tensor along the fluid trajectory,

$$R^L_{u_i u_j}(\tau) = \langle u_i(t) u_j(t+\tau) \rangle, \tag{1b}$$

as

$$Y_{ij}(\tau) = 2 \int_0^\tau \int_0^{t'} R^L_{u_i u_j}(t'' - t') dt'' dt' \tag{1c}$$

where $u_i(t)$ is the ith component of the turbulent velocity on the fluid trajectory.

Reeks (1977) and Pismen and Nir (1978) have shown for a particle with settling velocity V_T in an isotropic turbulence that the fluid velocity correlation tensor, $R^p_{u_i u_j}(\tau)$, evaluated on the particle trajectory can be expressed, using the independence approximation (Corrsin, 1959), in terms of the turbulence energy spectrum tensor $\Phi_{ij}(\mathbf{k}, \tau)$ as

$$\bar{R}^p_{u_\alpha u_\alpha}(\bar{\tau}) = \int_{-\infty}^{\infty} \cos\left(\frac{V_T}{u_0} \bar{k}_1 \bar{\tau}\right) \Phi_{\alpha\alpha}(\bar{\mathbf{k}}, \bar{\tau}) \times \exp[-\tfrac{1}{2} k_n k_n \bar{Y}_{nn}(\bar{\tau})] d^3\bar{\mathbf{k}}, \tag{2a}$$

$$\bar{R}^p_{u_\alpha u_\gamma}(\bar{\tau}) = 0, \quad \text{for} \quad \alpha \neq \gamma, \tag{2b}$$

(no summation over the repeated Greek indices). Here, $\bar{\mathbf{k}}$ and $\bar{\tau}$ are scaled by a typical wave number k_0 and $1/(k_0 u_0)$, and $\bar{R}^p_{u_\alpha u_\alpha}$ and $\bar{Y}_{\alpha\alpha}$ are scaled by u_0^2 and $1/k_0^2$. The dimensionless mean square displacement is

$$\bar{Y}_{\alpha\alpha}(\bar{\tau}) = 2 \int_0^{\bar{\tau}} (\bar{\tau} - t') \bar{R}^p_{u_\alpha u_\alpha}(t') dt'. \tag{3}$$

Averaging over $\alpha = 1$ to 3 and denoting $\bar{Y}$ for $\bar{Y}_{\alpha\alpha}$ for fluid dispersion, Eq. (2a) gives

$$\bar{R}^p_{uu}(\bar{\tau}) \equiv \tfrac{1}{3} \bar{R}^p_{u_i u_i}(\bar{\tau}) = \tfrac{2}{3} D(\bar{\tau}) \int_0^\infty E(\bar{k}) \exp[-\tfrac{1}{2} k^2 \bar{Y}(\bar{\tau})]\, d\bar{k}. \tag{4}$$

In the above, $\Phi_{\alpha\alpha}(\mathbf{k}, \tau)$ has been assumed to be separable in $\mathbf{k}$ and τ, $E(k)$ is the energy spectrum, and $D(\bar{\tau})$ is the Eulerian auto-correlation that accounts for the eddy self-decay.

Most theoretical investigations of dispersion have adopted Kraichnan's (1970) model

$$E(k) = E_I(k) = u_0^2 \frac{32}{(2\pi)^{1/2}} \frac{k^4}{k_0^5} \exp(-2k^2/k_0^2). \tag{5}$$

It lacks the $k^{-5/3}$ power law that is characteristic of the inertial subrange of high Re_λ turbulence. The Kolmogorov length scale implied by $E_I(k)$ is $\eta \sim k_0^{-1} \sim L_{11}$ which is realistic only if Re_λ is very low. At high Re_λ, the longitudinal Eulerian correlation $f(r)$ is often approximated by $f(r) = \exp(-|r|/L_{11})$. However, it cannot represent finite Re_λ because of the discontinuous first derivative at $r = 0$. The corresponding $E(k)$ is (Hinze, 1975, p. 245)

$$E_{II}(k) = \frac{8}{\pi} u_0^2 L_{11} \frac{(kL_{11})^4}{[1 + (kL_{11})^2]^3}, \tag{6}$$

which is correct only for $k/k_0 \ll 1$. It contains neither $k^{-5/3}$ law of the inertial subrange nor the viscous dissipation range. Thus $E_{II}(k)$ will not be used.

For low Re_λ turbulence, the Eulerian auto-correlation $D(\tau)$ is typically represented by a Gaussian function

$$D(\tau) = D_I(\tau) = \exp(-\tfrac{1}{2} \omega_0^2 \tau^2) \tag{7}$$

where ω_0 is related to the integral time scale T_0 (in a frame moving with the mean flow) by $\omega_0 = \sqrt{\pi/2}/T_0$. However, $D_I(\tau)$

Contributed by the Fluids Engineering Division for publication in the JOURNAL OF FLUIDS ENGINEERING. Manuscript received by the Fluids Engineering Division May 5, 1994; revised manuscript received January 24, 1995. Associate Technical Editor: M. W. Reeks.

only describes the behavior of $D(\tau)$ correctly near $\tau = 0$ if Re_λ is not low. For high Re_λ turbulence, an exponential form

$$D_{II}(\tau) = \exp(-|\tau|/T_0). \quad (8)$$

was often adopted (e.g., Wang and Stock, 1988 and 1993) to study fluid dispersion in isotropic turbulence. However, the infinite curvature of $D_{II}(\tau)$ at $\tau = 0$ implies more energy in the high frequency range than there should be.

Energy Spectrum and Eddy Self-Decay Functions

Wavenumber Spectra. This study focuses on the effects of the structure of the space-time correlation function on the dispersion of fluid and particles with finite settling velocity and inertia in isotropic turbulence. For assumed $E(k)$ and $D(\tau)$, $R^p_{u_iu_j}(\tau)$ is obtained via numerical integration of (2). The following energy spectrum will be used,

$$E_{III}(k) = \frac{3}{2} u_0^2 \alpha \frac{k^4}{k_0^5} \frac{1}{[1 + (k/k_0)^2]^{17/6}} \exp(-\eta_0^2 k^2). \quad (9)$$

The parameter $\bar{\eta}_0 = \eta_0 k_0$ is related to Re_λ. $E_{III}(k)$ describes the large scale behavior correctly at $k/k_0 \ll 1$ because $E_{III}(k) \propto k^4$. For $\bar{\eta}_0 \ll 1$ it has an inertial subrange for $1 \ll \bar{k} \ll \bar{\eta}_0^{-1}$. The Gaussian cut-off term in E_{III} models the high wavenumber viscous dissipation; so E_{III} is referred to as the viscous von Kármán model. Although an exponential cut-off for $E(k)$ in the viscous dissipation range has been observed at finite Re_λ (Combte-Bellot and Corrsin, 1971; Yeung and Pope, 1989; Domaradzki, 1992, and Wang and Maxey, 1993), the Gaussian decay is adopted because it allows for a direct comparison of the dispersion result with those based Kraichnan's model. Using $0.8u_0^3/L_{11}$ for the dissipation rate $\bar{\epsilon}$ (Batchelor, 1953) and the relationship between $\bar{\epsilon}$ and the Taylor micro-length scale, we obtain $\mathrm{Re}_\lambda \sim 5.237\bar{\eta}_0^{-2/3} + 5.151$ for $\bar{\eta}_0 \ll 1$ (Mei and Adrian, 1994). For lower Re_λ, $\bar{\epsilon}L_{11}/u_0^3$ increases with decreasing Re_λ for $\mathrm{Re}_\lambda < 100$ (Sreenivasan, 1984). Assuming $\bar{\epsilon} = 0.8u_0^3/L_{11}$ as an extrapolation, a relationship between Re_λ and $\bar{\eta}_0$ can be obtained by numerical integration. Some typical values of Re_λ ($\bar{\eta}_0$) can be found in Table 1 for finite $\bar{\eta}_0$. The coefficient α in E_{III} is determined as

$$\alpha^{-1}(\bar{\eta}_0) = \int_0^\infty \frac{\bar{k}^4}{(1 + \bar{k}^2)^{17/6}} \exp(-\bar{\eta}_0^2 \bar{k}^2)\, d\bar{k}. \quad (10)$$

Asymptotic properties for the integral, micro-, and Kolmogorov length scales, and the turbulence Reynolds number Re_λ defined by $E_{III}(k)$ for $\bar{\eta}_0 \ll 1$ can be found in Mei (1990).

Consistent with the construction of $E_{III}(k)$, the following form of the eddy self-decay function will be used

$$D_{III}(\tau) = \frac{1}{2[1 - \mathrm{erf}\,(\eta_1/T)]} \left\{ e^{-\tau/T}\left[1 + \mathrm{erf}\left(\frac{\tau}{2\eta_1} - \frac{\eta_1}{T}\right)\right] + e^{\tau/T}\left[1 - \mathrm{erf}\left(\frac{\tau}{2\eta_1} + \frac{\eta_1}{T}\right)\right]\right\}, \quad (11)$$

(See Mei, 1990.) It recovers $D_I(\tau)$ for $\eta_1/T \gg 1$ and $D_{II}(\tau)$ for $\eta_1/T \ll 1$.

Another model of the wavenumber-frequency energy spectrum has been proposed by Hunt et al. (1987) based on the direct numerical simulation (DNS) of forced turbulence at $\mathrm{Re}_\lambda \sim 48$ and the random sweeping hypothesis,

$$\epsilon(k, \omega) = E(k) \exp\left(- \frac{\omega^2}{2(aku_0)^2}\right) \Big/ [\sqrt{2\pi}\,(aku_0)] \quad (12)$$

where $a \approx 0.51$ for $kL_{11} \leq 10$, and $a \approx 0.4$ for $kL_{11} \geq 15$. The eddy self-decay function $D_{IV}(k, \tau)$ can be obtained by Fourier transforming (12),

$$\epsilon(k, \tau) = E(k) \exp[-\tfrac{1}{2}\tau^2 (aku_0)^2] = E(k)\, D_{IV}(k, \tau). \quad (13)$$

Hunt et al. (1987) have suggested extrapolating this $k - \omega$ energy spectrum to high Re_λ.

Time Scales. The relationship between T_0 and L_{11} is not known in general but on dimensional grounds it is taken to have the form

$$T_0 = c^E L_{11}/u_0, \quad (14)$$

where c^E is an unknown coefficient. The value $c^E = 0.5$ was set in Kraichnan (1970). Reeks (1977) treated c^E as a parameter. Hunt's model gives $c^E = 1.043$ for $a = 0.51$. There seems to exist a large range of possible values for c^E (Wang and Stock, 1993). It is likely a function of Re_λ and may also depend on the specific type of the turbulent flow. By analogy, we also assume that η_0 and η_1 are related by

Nomenclature

$D(\tau)$ = Eulerian auto-correlation function
D_f = fluid turbulent diffusivity
D_{ij} = particle turbulent diffusivity tensor
$E(k)$ = energy spectrum in the wavenumber space
$f(r)$ = longitudinal Eulerian correlation function
$\mathbf{k}$ = wavenumber vector
L_{11} = integral length scale of the turbulence
Re_λ = turbulence Reynolds number
$R^L_{u_iu_j}(\tau)$ = fluid Lagrangian correlation function tensor
$R^p_{u_iu_j}(\tau)$ = fluid Lagrangian correlation tensor on particle trajectory
$R^p_{uu}(\tau)$ = fluid Lagrangian correlation in isotropic turbulence
$R_{v_\alpha v_\alpha}$ = particle velocity correlation
$S^p_{u_\alpha u_\alpha}(\omega)$ = power spectrum of the fluid velocity on particle trajectory
$S_{v_\alpha v_\alpha}(\omega)$ = power spectrum of the particle velocity
T_0 = Eulerian integral time scale of turbulence
T^L = Lagrangian integral time scale of turbulence
u_i = ith component of the fluid turbulence
u_0 = rms turbulent velocity
$\langle v_1^2 \rangle$ and $\langle v_2^2 \rangle$ = particle turbulence intensity
V_T = particle settling velocity
$\Phi_{ij}(\mathbf{k}, \tau)$ = turbulence energy spectrum tensor
$y_i(t)$ = ith component of the particle displacement
$Y_{ij}(\tau)$ = mean square displacement tensor
α = coefficient associated with $E(k)$
β = reciprocals of time constants
$\bar{\epsilon}$ = dissipation rate of turbulence
$\epsilon(k, \omega)$ = wavenumber-frequency energy spectrum
η = Kolmogorov length scale
η_0 = a parameter characterizing the viscous dissipation in $E_{III}(k)$
η_1 = time-scale in the viscous dissipation range
λ = particle settling rate = V_T/u_0
τ = time delay
ω = frequency

Overhead

$\hat{}$ = scaling using L_{11} and u_0
$\bar{}$ = scaling using $1/k_0$ and u_0

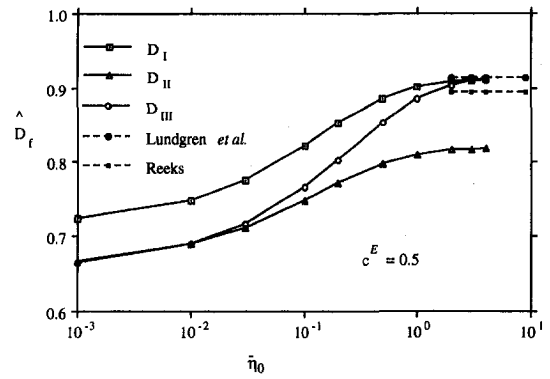

Fig. 1 Influence of $\bar{\eta}_0$ on the fluid diffusivities evaluated using models $D_I(\tau)$, $D_{II}(\tau)$ and $D_{III}(\tau)$ with $c^E = 0.5$

$$\eta_1 = c_1^E \eta_0 / u_0. \tag{15}$$

As shown in Mei (1990), $c_1^E \sim c^E$ for $D_{III}(\tau)$ to be consistent with $E_{III}(k)$ at low Re_λ. For finite η_1/T or $\bar{\eta}_0$, c_1^E/c^E may be different from unity. As an extrapolation, we set

$$c_1^E = c^E. \tag{16}$$

The uncertainty in η_1 is thus combined with that in c^E.

The effect of c^E on fluid dispersion will first be studied parametrically. An approximate expression for c^E as a function of Re_λ will then be obtained using $E_{III}(k)$ and $D_{III}(\tau)$ by matching the predicted fluid diffusivity with: i) accurate experimental measurements in a grid turbulence by Sato and Yamamoto (hereinafter referred as SY, 1987) at low Re_λ; and ii) the predicted fluid diffusivity at high Re_λ using the renormalization group (RNG) analysis by Yakhot and Orszag (hereinafter referred as YO, 1986) or the experimentally determined turbulent diffusivity at high Re_λ. This more specific relation for c^E is then used to investigate the effect of the turbulence structure on particles dispersion.

Analysis of Fluid Dispersion

Formulation for the Dispersion of Fluid Elements. From Eq. (2*a*), one can easily obtain, for the dispersion of fluid,

$$\bar{R}_{uu}^p(\bar{\tau}) = \frac{\alpha(\bar{\eta}_0) D(\bar{\tau})}{\alpha\{[\bar{\eta}_0^2 + \frac{1}{2}\bar{Y}(\bar{\tau})]^{1/2}\}} \quad \text{if} \quad D(\bar{\tau}) \neq D_{IV}(\bar{\tau}), \tag{17a}$$

or

$$\bar{R}_{uu}^p(\bar{\tau}) = \frac{\alpha(\bar{\eta}_0)}{\alpha\{[\bar{\eta}_0^2 + \frac{1}{2}\bar{Y}(\bar{\tau}) + \frac{1}{2}(a\bar{\tau})^2]^{1/2}\}} \quad \text{if} \quad D(\bar{\tau}) = D_{IV}(\bar{\tau}), \tag{17b}$$

where $D_{IV}(\bar{\tau})$ is defined by Eq. (13). Equations (3) and (17) can be solved iteratively. After the solutions converge, the dimensional diffusivity is obtained as

$$D_f = u_0/k_0 \bar{D}_f = u_0/k_0 \int_0^\infty \bar{R}_{uu}^p(\bar{\tau})\, d\bar{\tau}. \tag{18}$$

In Mei et al. (1991), $u_0/k_0 = u_0 L_{11}/\sqrt{2\pi}$ was used to scale the diffusivities when $E_I(k)$ was used. For $E_{III}(k)$, we should use L_{11} rather than k_0 to characterize the dispersion, because it is a more commonly used characteristic of the large scale turbulence. The dimensionless diffusivity is thus

$$\hat{D}_f = D_f \sqrt{2\pi}/(u_0 L_{11}) = \bar{D}_f \sqrt{2\pi}/\bar{L}_{11} \tag{19a}$$

where the overbar denotes the quantity scaled using $1/k_0$, and the carat denotes scaling with L_{11}. The corresponding dimensionless time $\hat{\tau}$ is

$$\hat{\tau} = \tau u_0 \sqrt{2\pi}/L_{11} = \bar{\tau}\sqrt{2\pi}/\bar{L}_{11}. \tag{19b}$$

Results and Discussion of Fluid Dispersion

Dependence of Fluid Diffusivity On Turbulence Structure. Figure 1 shows $\hat{D}_f$ as a function of $\bar{\eta}_0$ using $D_I(\bar{\tau})$, $D_{II}(\bar{\tau})$, and $D_{III}(\bar{\tau})$ with $c^E = 0.5$. The corresponding Re_λ ranges from 23.54 ($\bar{\eta}_0 = 4.5$) to 528.8 ($\bar{\eta}_0 = 0.001$). For $\bar{\eta}_0 \geq 2$, the result based on $D_{III}(\bar{\tau})$ is very close to that based on $D_I(\bar{\tau})$, both approaching 0.913 which can be obtained from the analysis of Lundgren and Pointin (1976). The result of Reeks (1977), $\hat{D}_f = 0.893$, is also shown for comparison. The result based on $D_{III}(\bar{\tau})$ approaches that based on $D_{II}(\bar{\tau})$ as $\bar{\eta}_0 \to 0$. Such behavior of $\hat{D}_f$ is expected since $D_{III}(\bar{\tau})$ approaches $D_I(\bar{\tau})$ and $D_{II}(\bar{\tau})$ in the respective limits of $\bar{\eta}_0$. For the selected value of $c^E = 0.5$, $\hat{D}_f$ changes from 0.664 at $\bar{\eta}_0 = 0.001$ to 0.911 at $\bar{\eta}_0 = 4.5$, about a 37 percent variation. This relatively large difference in the diffusivity, which is already scaled by L_{11}, is due to the change in Re_λ influencing the shape of $E(k)$. It is generally accepted that the turbulent dispersion is controlled by the large scale motion and that the small scale motion contributes little to the diffusivity. Present results suggest that while the fluid diffusivity is indeed mainly characterized by u_0 and L_{11}, it is also influenced by the shape of $E(k)$, i.e., the energy distribution among various scales. The increase in $\hat{D}_f$ with decreasing Re_λ is due to the fact that there is more energy associated with the large-scale motion at small Re_λ than at large Re_λ.

The normalized fluid Lagrangian correlation increases with decreasing Re_λ as shown in Fig. 2 for $\bar{R}_{uu}^p(\hat{\tau})$ at $\mathrm{Re}_\lambda = 23.55$, 40.56, 124.4 and 528.8. The correlation exhibits quite different behavior near $\hat{\tau} = 0$ for low and high values of Re_λ. For $\mathrm{Re}_\lambda = 23.55$, it overall resembles a Gaussian function. For $\mathrm{Re}_\lambda = 528.8$, it has a vanishingly small radius of curvature at $\hat{\tau} = 0$ and can be represented by an exponential function.

The results discussed above are for $c^E = 0.5$. However, its exact value and its dependence on $\bar{\eta}_0$ or Re_λ are not generally known. To examine its effect on dispersion, $\hat{D}_f$ is shown in Fig. 3(*a*) as a function of $\bar{\eta}_0$ for c^E varying from 0.3 to 3.0 with an interval of 0.1. $\hat{D}_f$ increases with c^E because $\hat{D}_f$ is scaled by L_{11}. For a fixed L_{11}, a large c^E implies a slower decay of eddy structure resulting in an increase in the diffusivity. However, this trend does not go on indefinitely. For very large c^E, $\hat{D}_f$ starts leveling off as shown in Fig. 3(*b*) for $\mathrm{Re}_\lambda = 528.8$. In general, c^E is order-one valued, and its value is impossible to determine within the framework of dispersion analysis. It is clear that c^E is critical to the determination of fluid diffusivity.

Dispersion of Fluid According to the Energy Spectrum of Hunt et al. Consider the fluid dispersion modeled from the $k - \omega$ energy spectrum of Hunt et al. (1987), equation (12). Since $\int_0^\infty \epsilon(k, \tau = 0)dk = \frac{3}{2}u_0^2$, we have

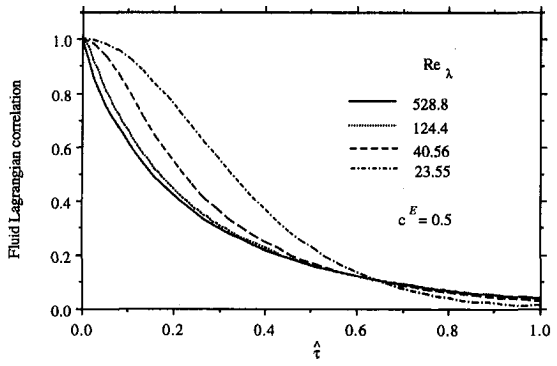

Fig. 2 Lagrangian fluid velocity correlation function at various Re_λ

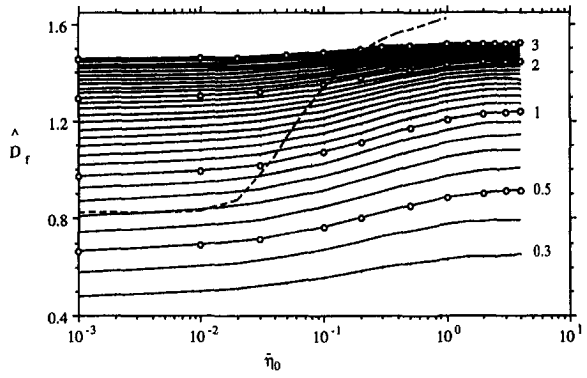

Fig. 3(*a*)

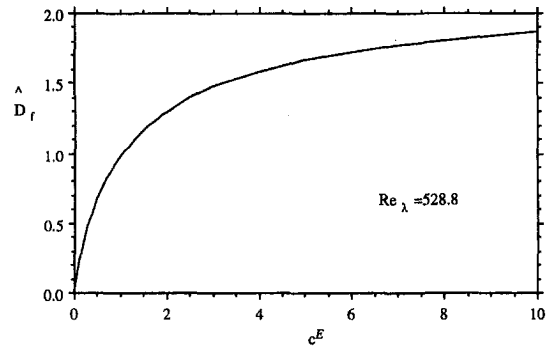

Fig. 3(*b*)

Fig. 3 Influence of c^E on the fluid diffusivity. (*a*) $\bar{\eta}_0$ ranging from 0.001 to 4.0 for c^E from 0.3 to 3.0; (*b*) $Re_\lambda = 528.8$, c^E from 0 to 10.

$$\int_0^\infty \int_0^\infty \epsilon(k, \tau) dk d\tau = \tfrac{3}{2} u_0^2 T_0, \tag{20}$$

which results in

$$T_0 = \tfrac{2}{3} \frac{\pi}{u_0^2} \int_0^\infty \epsilon(k, \omega = 0)\, dk = \tfrac{2}{3} \frac{\pi}{u_0^2} \int_0^\infty E(k) /$$

$$[\sqrt{2\pi}\,(aku_0)]\, dk = \tfrac{2}{3}(2/\pi)^{1/2} \frac{L_{11}}{au_0} \sim 1.043 \frac{L_{11}}{u_0}. \tag{21}$$

In Eq. (21), $a \sim 0.51$ (which is applicable only for small k) is used for the entire range of k for simplicity. Using $E(k) = E_{III}(k)$ with $\bar{\eta}_0 = 0.0655$ ($Re_\lambda \sim 48$) and $D_{IV}(\bar{\tau})$, we obtain $\hat{D}_f \approx 1.466$. For the same value of $\bar{\eta}_0$ and $c^E \approx 1.043$, the model based on E_{III} and D_{III} gives $\hat{D}_f \approx 1.067$ which is 27% lower than the prediction using $D_{IV}(\bar{\tau})$. Unfortunately, the Lagrangian

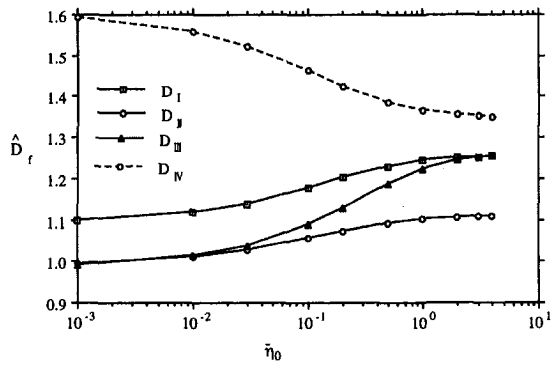

Fig. 4 Comparison of the fluid diffusivities evaluated using $D_I(\tau)$, $D_{II}(\tau)$, $D_{III}(\tau)$ and $D_{IV}(\tau)$ (Hunt's model) with $c^E = 1.043$

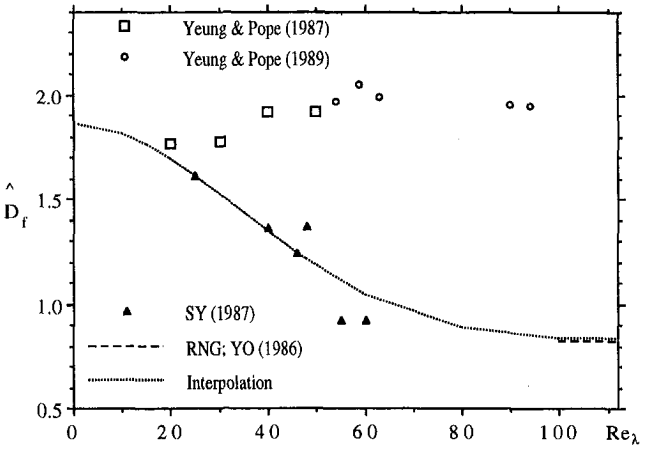

Fig. 5 Fluid diffusivity as a function of Re_λ

information is not available in Hunt et al. (1987), and definitive assessments of either model cannot be made.

Hunt et al. (1987) suggested that this low Re_λ result with $c^E \approx 1.043$ may be extrapolated to higher Re_λ. In Fig. 4, the dimensionless diffusivity $\hat{D}_f$ is shown as a function of $\bar{\eta}_0$ based on $E(k) = E_{III}(k)$ and four different models for the self-decay function, $D_I(\bar{\tau})$, $D_{II}(\bar{\tau})$, $D_{III}(\bar{\tau})$, and $D_{IV}(\bar{\tau})$ with $c^E \approx 1.043$. It is noted that the first three models for $D(\bar{\tau})$ give a consistent trend for $\hat{D}_f(\bar{\eta}_0)$ as $\bar{\eta}_0$ varies from 0.001 to 4 while $D_{IV}(\bar{\tau})$ based on the random sweeping hypothesis gives an opposite trend. The same behavior is observed at $c^E = 0.5$ and $a = 1$. As Re_λ increases, the model of Hunt et al. suggests that the dimensionless diffusivity increases, rather than decreases, contradictory to intuition. The reason for this trend lies in the decay behavior of $\epsilon(k, \tau)$ (Mei and Adrian, 1994) and fixed value of c^E as Re_λ varies.

Approximate Variation of C^E With Re_λ Using SY's Data and RNG Prediction

In SY (1987), accurate measurements of $\bar{R}^p_{uu}(\hat{\tau})$ in a grid turbulence were obtained for $Re_\lambda \sim 25$ to 66. The ratio of the Lagrangian integral length scale, $u_0 T^L$, to the Eulerian integral length scale L_{11} was given at various Re_λ. It can be readily shown that the fluid diffusivity is given by

$$\hat{D}_f(\bar{\eta}_0, c^E) = \sqrt{2\pi}\, u_0 T^L / L_{11}. \tag{22}$$

The integral time scale data of SY (1987) has been used to obtain the diffusivity plotted in Fig. 5 (solid symbols). Unfortunately, T_0 was not given, which precludes a direct determination of c^E as a function of Re_λ from this measurement.

YO (1986) derived the diffusivity of a passive scalar in isotropic turbulence at high Re_λ using RNG analysis. The diffusivity D_f is found to be 1.3929 times of fluid turbulent viscosity; the inverse of 1.3929 is close to the measured turbulent Prandtl number in the boundary layer flows at high Re_λ (Kays and Crawford, 1980, p. 226–227). For high Re_λ, it can be shown for the RNG result, based on the present definition for $\hat{D}_f$ given by Eq. (22), that

$$\hat{D}_f(\bar{\eta}_0 \to 0, c^E) \sim 0.822 \quad \text{as} \quad Re_\lambda \to \infty. \tag{23}$$

This asymptotic limit seems to join the experimental data of SY well. The following curve fit to these two results,

$$\hat{D}_f(Re_\lambda) \sim 0.822[1 + \exp(-0.000368 Re_\lambda^2)], \tag{24}$$

is plotted in Fig. 5. Two sets of data for $\hat{D}_f$ from the DNS studies of Yeung and Pope (1987, 1989) are also shown. They differ significantly from the experimental data and do not approach the asymptotic value at high Re_λ. Thus, the results for

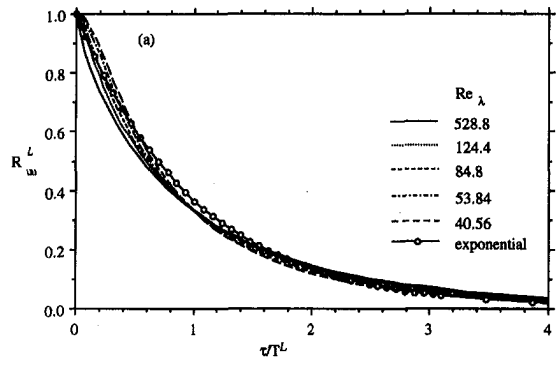

Fig. 6(*a*)

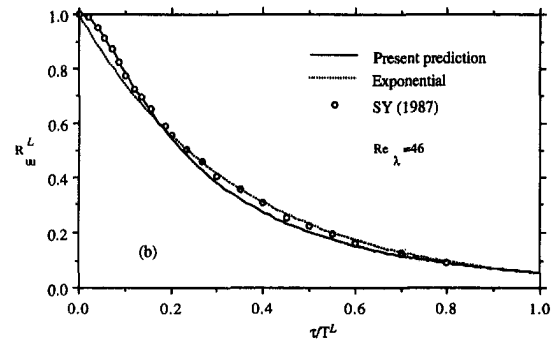

Fig. 6(*b*)

Fig. 6 Fluid Lagrangian correlation function. (*a*) for various Re_λ; (*b*) comparison with the data of Sato and Yamamoto (1987) at $Re_\lambda = 46$.

particle diffusivity, as well as other large scale Eulerian statistics such as T_0 and L_{11} obtained from DNS using artificial forcing on the large scale cannot be used. Based on the relation between $\hat{D}_f$ and $(\overline{\eta}_0, c^E)$ from $E_{III}(k)$ and $D_{III}(\tau)$ given in Fig. 3*a*, and the approximate relation between Re_λ and $\overline{\eta}_0$, the following interpolation is obtained by fitting the data of SY and the RNG prediction of YO (or measured turbulent Prandtl number),

$$c^E \sim 0.73 + 17.875 \exp(-0.0665 Re_\lambda). \quad (25)$$

It is interesting to note that $c^E \sim 0.73$ at high Re_λ given by (25) is quite close to the value $c^E \sim 0.8$ used by Fung et al. (1992). The present result is based on the models of $E_{III}(k)$ and $D_{III}(\tau)$ and the scalar diffusivity at high Re_λ; their result is based on the random sweeping hypothesis and the measured Eulerian frequency spectrum.

For lower Re_λ, c^E given by (25) appears to be too large to be realistic. The reason is that the inviscid approximation for the dissipation rate, $\bar{\epsilon} = 0.8u_0^3/L_{11}$, is no longer accurate at lower Re_λ. In the analysis of particle dispersion, Table 1 relating c^E and $\overline{\eta}_0$ is used. For $\overline{\eta}_0 \geq 0.3$, $c^E \sim 3$ is set. Since $c^E \sim 3$ may be a little too large, the results should be interpreted as for the frozen turbulence limit, rather than a realistic low Re_λ turbulence. The above relation at large Re_λ should be more accurate.

Figure 6(*a*) shows $R^L_{u_iu_j}(\tau/T^L)$ for $Re_\lambda = 40.56$, 53.84, 84.75, 124.4, and 528.8. The Lagrangian correlation is not similar for different values of Re_λ (from 41 to 529) when the details of $R^L_{u_iu_j}(\tau/T^L)$ are examined. Figure 6(*b*) compares the predicted Lagrangian correlation with that measured experimentally at $Re_\lambda = 46$. The prediction for $R^L_{u_iu_j}(\tau/T^L)$ is quite close to the measured values, especially for $\tau/T^L < 0.2$. Based on limited comparisons, the present model for turbulence structure described by $E_{III}(k)$ and $D_{III}(\tau)$ with proper value of c^E given in Table 1 can give quite reliable prediction for $R^L_{u_iu_j}(\tau/T^L)$.

Dispersion of Particles With Finite Inertia and Settling Velocity

In unsteady, nonuniform flow a variety of forces are acting on particles. Since the main goal of this work is to evaluate the influence of spectral structure on particle dispersion, the particle dynamics will be assumed to have a simplified form by retaining only the quasi-steady drag and the body force. Constant inertial parameters will be used in the equation governing the fluctuating particle velocity while the anisotropy in the time constants that is caused by the drag non-linearity and finite settling (Mei et al., 1993) will be incorporated in the present formulation since it causes little complication. The dynamic equation governing the fluctuating particle motion may be written as (see Mei et al., 1993)

$$\frac{dv_\alpha}{dt} = \beta_\alpha(u_\alpha - v_\alpha), \quad \alpha = 1, 2, 3 \quad (26)$$

The parameters β_α are determined from the quasi-steady drag. The assumption of constant values for each β_α is consistent with Stokesian drag or a non-Stokesian drag law linearized about a mean slip velocity.

Applying Fourier transformation to (26) and taking ensemble average, one obtains the power spectrum of the particle velocity

$$S_{v_\alpha v_\alpha}(\omega) = S^p_{u_\alpha u_\alpha}(\omega)/[1 + (\omega/\beta_\alpha)^2] \quad (27)$$

in terms of $S^p_{u_\alpha u_\alpha}(\omega)$, the power spectrum of the fluid velocity on the particle trajectory. The ratio of V_T to the root mean square value of the turbulence fluctuations, u_0,

$$\lambda = V_T/u_0 \quad (28a)$$

is an important parameter appearing in Eq. (2*a*). Similar to (19*b*), we define

$$\hat{\beta}_\alpha = \beta_\alpha L_{11}/(u_0\sqrt{2\pi}). \quad (28b)$$

There are several different regions in the $(\hat{\beta}, \lambda)$ parameter space, in which asymptotic results for particle dispersion can be obtained (Mei, 1990). They are: i) $\lambda \gg 1$; ii) $\hat{\beta} \gg 1$ and $\lambda \ll 1$; iii) $\hat{\beta} \ll 1$ and $\lambda \ll 1$. The fourth region with order-one values of $\hat{\beta}$ and λ must be dealt with numerically.

Formulation for Particle Dispersion With Arbitrary Settling Rate. Following the analysis in Mei et al. (1991), a closed system of equations for $\bar{Y}_{\alpha\alpha}$, $\bar{R}^p_{u_\alpha u_\alpha}$ and $\bar{R}_{v_\alpha v_\alpha}$, and $S_{v_\alpha v_\alpha}$ and $S^p_{u_\alpha u_\alpha}$ can be obtained. It consists of (2), (3), (27) and pertinent Fourier transformations. The system is solved numerically. The numerical integration in the wavenumber space is computationally intensive for $\lambda > 0$. An efficient approach is described in Mei (1990). The appropriate dimensionless particle diffusivity $\hat{D}_{\alpha\alpha}$ is defined following (19*a*).

Results and Discussion of Particle Dispersion

Since the main focus is to examine the effect of Reynolds-number-dependent turbulence structure on the dispersion, we

Table 1 Relation between Re_λ, c^E and $\overline{\eta}_0$

$\overline{\eta}_0$	0.001	0.01	0.02	0.03	0.04	0.05	0.08	0.1	0.2	0.3	0.5	1.0
Re_λ	528.8	124.4	84.75	68.67	59.68	53.84	44.15	40.56	32.54	29.48	26.83	24.76
c^E	0.73	0.73	0.79	0.92	1.07	1.23	1.68	1.93	2.78	3.0	3.0	3.0

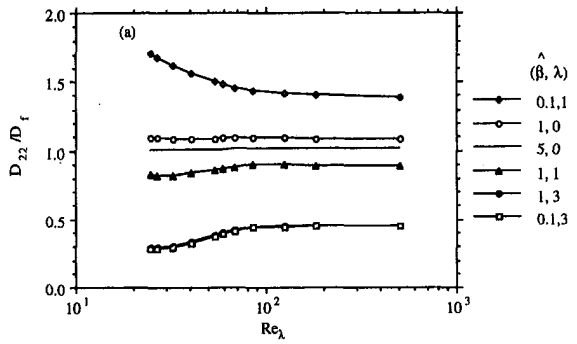

Fig. 7(*a*) D_{22}/D_f as a function of Re_λ at various $(\hat{\beta}, \lambda)$

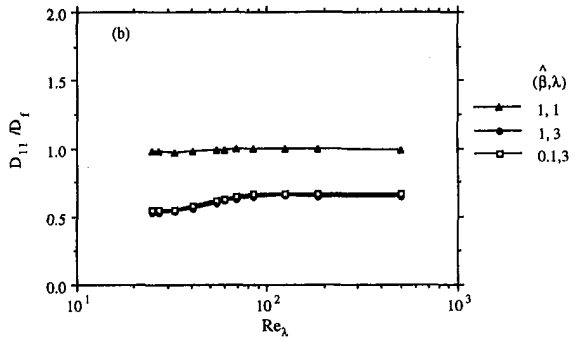

Fig. 7(*b*) D_{11}/D_f as a function of Re_λ at various $(\hat{\beta}, \lambda)$

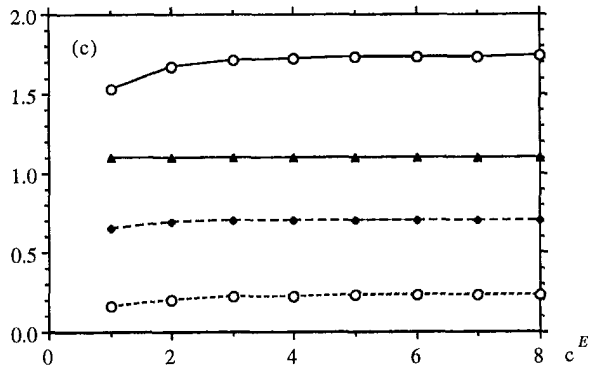

Fig. 7(*c*) Effect of c^E on D_{22}/D_f and $\langle v_2^2\rangle/u_0^2$ for low Re_λ turbulence, Re_λ = 24.76. Solid line, D_{22}/D_f; dash lines $\langle v_2^2\rangle/u_{p0}^2$; solid symbol: $(\hat{\beta}, \lambda)$ = (0.1, 0); open symbol: $(\hat{\beta}, \lambda)$ = (1, 0).

shall compare the results at fixed $(\hat{\beta}, \lambda)$ with varying Re_λ. For simplicity, discussions are limited to $\hat{\beta}_1 = \hat{\beta}_2 = \hat{\beta}$.

Dependence of Particle Diffusivity. Figures 7(*a–b*) show the dependence of $\hat{D}_{\alpha\alpha}/\hat{D}_f$ on Re_λ for $\alpha = 1$ and 2 and various values of inertia $\hat{\beta}$ and settling rate λ. $\hat{D}_f$ is recomputed using c^E given by Table 1. The selected parameters are representative of typical regions in the $(\hat{\beta}, \lambda)$ space. The maximum diffusivity ratio of the particle to fluid is simply T_0/T^L which is attained in the limit as $\hat{\beta} \to 0$ at $\lambda = 0$ (Reeks, 1977; Mei, 1990; Wang and Stock, 1993; Mei and Adrian, 1994). The diffusivity ratios $\hat{D}_{11}/\hat{D}_f$ and $\hat{D}_{22}/\hat{D}_f$ depend weakly on Re_λ for small λ and $\hat{\beta} \sim O(1)$ or larger, although $\hat{D}_f$ itself is strongly influenced by Re_λ as seen from Fig. 8. For $(\hat{\beta}, \lambda) = (0.1, 0)$, particle diffusivity is significantly larger than the fluid diffusivity at low Re_λ because a large c^E is used which implies a slower eddy self-decay. A parametric study performed by varying c^E for a given $\hat{\beta}$ at Re_λ = 24.76, $(\hat{\beta}, \lambda) = (0.1, 0)$ and $(1, 0)$, indicates that at low Re_λ the diffusivity ratio as well as the particle turbulence intensity ratio are not sensitive to the actual value of c^E for $c^E > 1$,

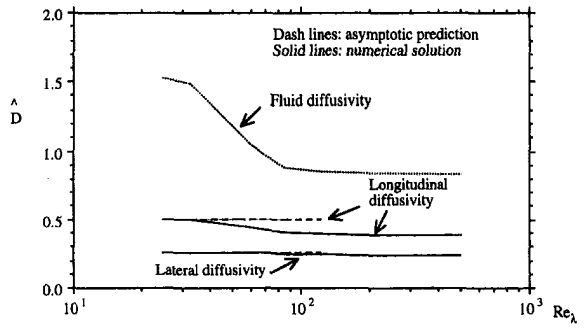

Fig. 8 Asymptotic behavior of particle diffusivities at large settling

$\hat{\beta} > 0.1$ as shown in Fig. 7(*c*). Thus for low Re_λ, the present model predicts $\hat{D}_{22}/\hat{D}_f$ and the intensity ratio quite well, even without adequate knowledge of c^E. It is interesting to note that $\hat{D}_{22}/\hat{D}_f = 1.70$ and 2.97 in the low Re_λ limit for $(\hat{\beta}, \lambda) = (0.1, 0)$ and $(0.01, 0)$, respectively. These values may be considered high. In fact, the diffusivity ratio at $\hat{\beta} = 0.0001$ is still 6 percent lower than the asymptotic limit $T_0/T^L = 2.215$ at $Re_\lambda = 528.8$. If $c^E = 0.5$ is used for $Re_\lambda = 528.8$, one obtains $\hat{D}_{22}(\hat{\beta} = 0)/\hat{D}_f = 1.887$, which is still higher than $\hat{D}_{22}(\hat{\beta} = 0)/\hat{D}_f = 1.373$ using $c^E = 0.5$ in a low Re_λ model $E_1(k)$ and $D_1(t)$. The difference in the diffusivity ratio is mainly caused by the difference in the spatio-temporal structure.

The effect of crossing trajectories at large settling velocity (represented by $\lambda = 3$ in Figs. 7(*a*)–(*b*) is known to reduce the diffusivity. It is more pronounced at low Re_λ because the turbulence at high Re_λ evolves more rapidly in time, offsetting the effect of crossing trajectories. Figure 8 compares the numerically obtained diffusivity with the asymptotic values for $(\hat{\beta}, \lambda) = (0.1, 5)$. The asymptotic prediction for $\hat{D}_{22} = \sqrt{\pi/2}/\lambda$ is quite accurate for $\lambda = 5$. As Re_λ increases the eddy self-decay becomes important at large but finite λ so that the actual diffusivity is less than the asymptotic value for $\hat{D}_{11} = \sqrt{2\pi}/\lambda$. The fluid continuity effect on particle diffusivity is also evident at large λ. The ratio $\hat{D}_{11}/\hat{D}_{22}$ is around 2 at low Re_λ. At large Re_λ, $\hat{D}_{11}$ is only slightly larger than the asymptotic value of $\hat{D}_{22}$ for the same $(\hat{\beta}, \lambda)$. Thus the effect of fluid continuity in further reducing the lateral component $\hat{D}_{22}$ is not as obvious in high Re_λ as in low Re_λ for a given large but finite settling rate.

Dependence of Particle Turbulence Intensity. Figure 9 shows the dependence of the particle turbulence intensity $\langle v_2^2\rangle/u_0^2$ on Re_λ at $\lambda = 0$ and $\hat{\beta} = 0.1$, 1, 5 and 20 for c^E given by Table 1. The dependence of $\langle v_2^2\rangle$ on turbulence structure is clear. For large $\hat{\beta}$, $\langle v_2^2\rangle/u_0^2$ is expected to approach one. However, at $\hat{\beta} = 20$, $\langle v_2^2\rangle/u_0^2 = 0.9979$ and 0.9032, respectively, for $Re_\lambda = 23.55$ and 528.8; the asymptotic behavior is not the same in low and high Re_λ turbulence. The difference in $\langle v_2^2\rangle/u_0^2$ re-

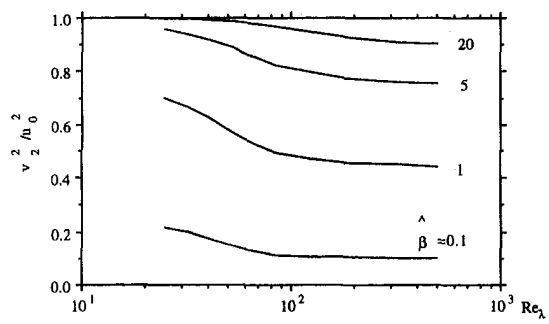

Fig. 9 Influence of Re_λ on particle intensity v_2^2/u_0^2 at zero settling for $\hat{\beta}$ = 0.1, 1, 5, and 20

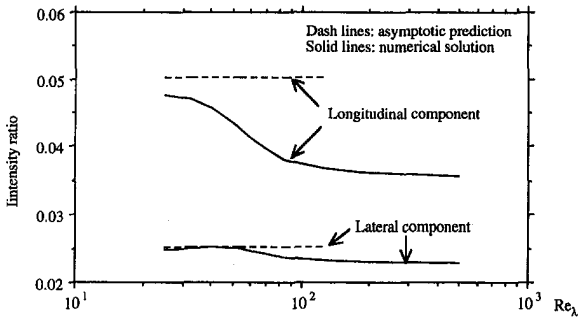

Fig. 10 Comparison of the asymptotic values of particle intensity v_α^2/u_0^2 at large settling and large inertia with the numerical solution at $(\hat{\beta}, \lambda) = (0.1, 5)$

flects the influence of Re_λ on $\bar{R}^p_{uu}(\hat{\tau})$ especially near $\hat{\tau} = 0$ as shown in Fig. 2. Near $\hat{\tau} = 0$, $\bar{R}^p_{uu}(\hat{\tau}, Re_\lambda = 23.55) \sim 1 - q_2\hat{\tau}^2 + O(\hat{\tau}^4)$. For $Re_\lambda = 528.8$, $\bar{R}^p_{uu}(\hat{\tau})$ may be approximated as $\exp(-\tau/T^L)$ for $\hat{\beta} \leq 100$ and most of τ/T^L. The asymptotic behavior for the intensity (Mei et al., 1993) is thus quite different,

$$\langle v_2^2\rangle/u_0^2 \sim \hat{\beta}\int_0^\infty \exp(\hat{\beta}\hat{\tau})\bar{R}^p_{uu}(\hat{\tau})d\hat{\tau} \sim \begin{cases} 1 - O(\hat{\beta}^{-1}) & \text{for large } Re_\lambda \\ 1 - 2q_2/\hat{\beta}^2 & \text{for low } Re_\lambda. \end{cases} \quad (29)$$

Figure 10 shows the particle turbulence intensities for $\hat{\beta} \ll 1$ and $\lambda \gg 1$. At $(\hat{\beta}, \lambda) = (0.1, 5)$, $\langle v_\alpha^2\rangle/u_0^2$ is close to the asymptotic value $\sqrt{2\pi/(\lambda\alpha)}$ at low Re_λ, while the longitudinal intensity depends more strongly on Re_λ than the lateral component, a similar trend observed for the particle diffusivities $\hat{D}_{\alpha\alpha}$ under the same condition. The effect of fluid continuity on the particle turbulence intensities is obvious. For $(\hat{\beta}, \lambda) = (0.1, 5)$ at low Re_λ, $\langle v_1^2\rangle/\langle v_2^2\rangle = 1.92$ which is close to 2; but it is not so strong, $\langle v_1^2\rangle/\langle v_2^2\rangle \sim 1.58$, at high Re_λ.

Validation of the Analysis Using Monte-Carlo Simulations

The foregoing analyses rely on independence approximation being valid. Monte Carlo simulations of particle motions are performed in an isotropic, Gaussian pseudo-turbulence to examine the validity of that approximation. Details of the simulations can be found in Mei (1990, 1994) except that the random wavenumber $\mathbf{k}$ and frequency ω are generated using an algebraically probability density function (Wang, 1990). The simulation results are based on the ensemble average over 4,000–10,000 particles. The rms statistical error ϵ_v for $\langle v_1^2\rangle$ is estimated using the following (Bendet and Piersol, 1986): $\epsilon_v = \{2\langle v_1^2\rangle T_v/[N_p\Delta T]\}^{1/2}$, in which T_v is the integral time scale of v_1, and ΔT is the duration of time averaging. Only the results at $\lambda = 0$ are presented; hence ϵ_v is further reduced by a factor of $\sqrt{3}$. Table 2 compares $\hat{D}_{11}$ and $\langle v_1^2\rangle/u_0^2$ at $(\hat{\beta}, \lambda) = (2, 0)$ for Re_λ ranging from 32.54 to 528.8 between the simulation and analysis. The rms statistical errors for $\langle v_1^2\rangle/u_0^2$ are estimated to range from 0.3% to 0.5% for the simulation results in Table 2. The prediction for $\langle v_1^2\rangle/u_0^2$ agrees well with the simulation results. The difference in $\hat{D}_{11}$ ranges from 2% to 6%. Although the simulation results are larger than analytical results, the independence approximation seems to give reliable results for the dispersion of particles.

Table 2 Comparisons of $\hat{D}_{11}$ and $\langle v_1^2\rangle/u_0^2$ between Monte-Carlo simulation and analysis at $\hat{\beta} = 2$, $\lambda = 0$

	Simulation		Analysis	
Re_λ	$\hat{D}_{11}$	$\langle v_1^2\rangle/u_0^2$	$\hat{D}_{11}$	$\langle v_1^2\rangle/u_0^2$
32.54	1.6360	0.8289	1.5309	0.8093
40.56	1.4378	0.7844	1.3855	0.7751
53.84	1.1941	0.7413	1.1756	0.7224
124.4	0.9083	0.6234	0.8890	0.6207
528.8	0.8880	0.5895	0.8589	0.5876

Conclusions

The influence of turbulence structure on the dispersion of fluid and particles has been investigated. The fluid diffusivity, normalized by the integral length scale and the root-mean-square turbulent velocity, depends on Re_λ and strongly on the parameter $c^E = T_0u_0/L_{11}$. The experimental data of Sato and Yamamoto (1987) and the prediction for the scalar diffusivity by Yakhot and Orszag (1986) based on RNG analysis are used to approximate the dependence of c^E on Re_λ. In the high Re_λ limit, $c^E = 0.73$ is obtained. The prediction for $R^L_{uu}(t)$ at $Re_\lambda = 46$ agrees very well with the experimental measurements of SY. In general, the diffusivity ratio of the particle to fluid depends on Re_λ, as well as on $(\hat{\beta}, \lambda)$. For $\hat{\beta} \to 0$, $\lambda = 0$, $Re_\lambda \to \infty$, this diffusivity ratio can be as high as 2.22. At large λ, the crossing-trajectory effect significantly reduces the particle diffusivity for low Re_λ turbulence; the effect is not as strong at high Re_λ. The uncertainty in c^E as a function of Re_λ at low Re_λ does not affect the diffusivity ratio. Particle turbulence intensity depend strongly on Re_λ for $\lambda \sim 1$ or less. It approaches one in the large $\hat{\beta}$ limit much faster for low Re_λ than for higher Re_λ due to the difference in the turbulence spatio-temporal structure.

References

Batchelor, G. K., 1953, *The Theory of Homogeneous Turbulence,* Cambridge University Press.

Bendat, J. S. and Piersol, A. G., 1986, *Random Data: Analysis and Measurement Procedures,* Wiley-Interscience Publication, 2nd ed.

Chao, B. T., 1964, "Turbulent Behavior of Small Particles in Dilute Suspension," *Osterreichisches Ingenieur-Archiv,* Vol. 18, pp. 7–21.

Comte-Bellot, G., and Corrsin, S., 1971, "Simple Eulerian Time Correlation of Full- and Narrow-Band Velocity Signals in Grid-Generated, 'Isotropic' Turbulence," *Journal of Fluid Mechanics,* Vol. 48, pp. 273–337.

Corrsin, S., 1959, "Progress Report on Some Turbulent Diffusion Research," *Adv. in Geophys.,* Vol. 6, New York, Academic Press, pp. 161–184.

Csanady, G. T., 1963, "Turbulent Diffusion of Heavy Particles in the Atmosphere," *Journal Atmospheric Science,* Vol. 20, pp. 201–208.

Domaradzki, J. A., 1992, "Nonlocal Triad Interactions and the Dissipation Range of Isotropic Turbulence," *Physics of Fluids A,* Vol. 4(9), pp. 2037–2045.

Fung, J. C. H., Hunt, J. C. R., Malik, N. A., and Perkins, R. J., 1992, "Kinematic Simulation of Homogeneous Turbulence by Unsteady Random Fourier Modes," *Journal of Fluid Mechanics,* Vol. 236, pp. 281–318.

Hinze, J. O., 1975, *Turbulence,* McGraw-Hill Book, New York.

Hunt, J. C. R., Buell, J. C., and Wray, A. A., 1987, "Big Whorls Carries Little Whorls," *Proceedings of the Summer Program,* Center for Turbulence Research, Stanford University.

Kays, W. M., and Crawford, M. E., 1980, *Convective Heat and Mass Transfer.* McGraw-Hill, New York.

Kraichnan, R. H., 1970, "Diffusion by a Random Velocity Field," *Physics of Fluids,* Vol. 13, pp. 22–31.

Lumley, J. L., 1957, "*Some Problems Connected with the Motion of Small Particles in Turbulent Fluid.*" Ph.D. thesis, The Johns Hopkins University, Baltimore, MD.

Lundgren, T. S., and Pointin, Y. B., 1976, "Turbulent Self-diffusion," *Physics of Fluids,* Vol. 19, pp. 355–358.

Mei, R., 1990, "Particle Dispersion in Isotropic Turbulence and Unsteady Particle Dynamics at Finite Reynolds Number," Ph.D. thesis, University of Illinois at Urbana-Champaign, Urbana, IL.

Mei, R., 1994, "Effect of Turbulence on Particle Settling Velocity in Nonlinear Drag Range," *International Journal of Multiphase Flow,* Vol. 20(2), pp. 273–284.

Mei, R., and Adrian, R. J., 1994, "Effect of Reynolds-Number-Dependent Turbulence Structure on the Dispersion of Fluid and Particles," TAM Report. No. 747, Department of Theoretical and Applied Mechanics, University of Illinois, Urbana, IL.

Mei, R., Adrian, R. J., and Hanratty, T. J., 1991, "Particle Dispersion in Isotropic Turbulence under Stokes Drag and Basset Force with Gravitational Settling," *Journal of Fluid Mechanics,* Vol. 225, pp. 481–495.

Mei, R., Adrian, R. J., and Hanratty, T. J., 1993, "Particle Dispersion in Isotropic Turbulence under the Influence of Non-Stokesian Drag and Gravitational

Settling," TAM Report. No. 735, Department of Theoretical and Applied Mechanics, University of Illinois, Urbana, Illinois.

Nir, A., and Pismen, L. M., 1979, "The Effect of a Steady Drift on the Dispersion of a Particle in Turbulent Fluid," *Journal of Fluid Mechanics,* Vol. 94, pp. 369–381.

Phythian, R., 1975, "Dispersion of Random Velocity Fields," *Journal of Fluid Mechanics,* Vol. 67, pp. 145–153.

Pismen, L. M., and Nir, A., 1978, "On the Motion of Suspended Particles in a Stationary Homogeneous Turbulence," *Journal of Fluid Mechanics,* Vol. 84, pp. 193–206.

Reeks, M. W., 1977, "On the Dispersion of Small Particles Suspended in an Isotropic Turbulent Fluid," *Journal of Fluid Mechanics,* Vol. 83, pp. 529–546.

Sato, Y., and Yamamoto, K., 1987, "Lagrangian Measurement of Fluid-Particle Motion in an Isotropic Turbulent Field," *Journal of Fluid Mechanics,* Vol. 175, pp. 183–199.

Sreenivasan, K. R., 1984, "On the Scaling of the Turbulence Energy Dissipation Rate," *Physics of Fluids,* Vol. 27(5), pp. 1048–1051.

Taylor, G. I., 1921, "Diffusion by Continuous Movement," *Proceeding London Mathematical Society,* Ser. 2, Vol. 20, pp. 196–211.

Tchen, C. M., 1947, "Mean Value and Correlation Problems Connected with the Motion of Small Particles Suspended in a Turbulent Fluid," Ph.D. thesis, Delft University, Netherlands.

Wang, L. P., 1990, "On the Dispersion of Heavy Particles by Turbulent Motion," Ph.D. thesis, Washington State University.

Wang, L. P., and Maxey, M. R., 1993, "Settling Velocity and Concentration Distribution of Heavy Particles in Homogeneous Isotropic Turbulence," *Journal of Fluid Mechanics,* Vol. 256, pp. 27–68.

Wang, L. P., and Stock, D. E., 1988, "A Theoretical Method of Obtaining Lagrangian Statistics from Measurable Eulerian Statistics for Homogeneous Turbulence," *Eleventh Symposium on Turbulence.* Oct. 17–19, X. B. Reed, ed., University of Missouri-Rolla.

Wang, L. P., and Stock, D. E., 1993, "Dispersion of Heavy Particles by Turbulence Motion," *Journal of Atmospherical Science,* Vol. 50(3), pp. 1897–1913.

Yakhot, V., and Orszag, S. A., 1986, "Renormalization Group Analysis for Turbulence. I. Basic Theory," *Journal of Scientific Computing,* Vol. 1(1), pp. 3–51.

Yeung, P. K., and Pope, S. B., 1987, "Lagrangian Velocity Statistics Obtained from Direct Numerical Simulations of Homogeneous Turbulence," *Proc. Sixth Symposium on Turbulent Shear Flows,* Toulouse, France.

Yeung, P. K., and Pope, S. B., 1989, "Lagrangian Statistics from Direct Numerical Simulations of Isotropic Turbulence," *Journal of Fluid Mechanics,* Vol. 207, pp. 531–586.

Yudine, M. I., 1959, "Physical Consideration on Heavy Particle Diffusion," *Advances in Geophysics,* Vol. 6, New York, Academic Press, pp. 185–191.

J. J. Gorski
Aerospace Engineer,
Carderock Division,
Naval Surface Warfare Center,
Bethesda, MD 20084-5000

P. S. Bernard
Professor,
Department of Mechanical Engineering,
University of Maryland,
College Park, MD 20742

Vorticity Transport Analysis of Turbulent Flows

Turbulence closure for the Reynolds averaged Navier-Stokes equations based on vorticity transport theory is investigated. General expressions for the vorticity transport correlation terms in arbitrary two-dimensional mean flows are derived. Direct numerical simulation data for flow in a channel is used to evaluate the modeled terms and set unknown scales. Results are presented for a channel, flat plate boundary layer, and flow over a hill. The computed mean flow and kinetic energy compares well with numerical and physical experiments. The vorticity transport model appears to perform better than conventional Boussinesq eddy viscosity Reynolds stress models near the separated flow region on the leeward side of the hill.

Introduction

Vorticity transport theory constitutes the principal alternative to eddy viscosity momentum transport models in effecting closure of the Reynolds averaged Navier-Stokes equations (Speziale, 1991). As first derived by Taylor (1915, 1932) using Lagrangian variables, the vorticity flux is modeled by a gradient transport law. This later proved to be incapable of accommodating the dominant role of vortex stretching in causing countergradient transport adjacent to fixed boundaries (Taylor, 1935, 1937). More recently, an alternative Lagrangian framework has been shown (Bernard, 1990a) to lead to a useful means of accommodating vortex stretching effects in a transport law. In test calculations for channel flow, the additional terms were found to be remarkably accurate in capturing the near wall behavior of all four non-zero fluxes. A detailed analysis of vorticity transport using fluid particle paths computed in a direct numerical simulation (DNS) of channel flow (Rovelstad, 1991) has further elucidated the physics behind the vorticity fluxes including the role of viscous effects close to the wall.

An analysis of the Reynolds stress correlation comparable to that just cited for the vorticity flux must attempt to incorporate the effects of pressure and viscous forces on momentum transport. While such factors have been shown to be significant near walls (Bernard and Handler, 1990; Handler et al., 1992), unlike the case of vorticity transport they are not responsible for a countergradient flux near the boundary. Thus, for typical boundary layer flows the commonly assumed eddy viscosity gradient models cannot be a priori disqualified. This represents a clear advantage of momentum transport models in comparison to gradient vorticity transport models, but not necessarily for the more general vorticity flux model. It is also known that eddy viscosity models are inappropriate for such flows as a wall jet (Hinze, 1975) or channel flow with transpiration (Piomelli et al., 1989) as well as being inadequate in predicting complex fluid phenomena associated with separation, strong vortices, and curvature (Lakshminarayana, 1986). This represents an additional incentive to explore the properties of vorticity transport theory in predicting turbulent flows.

The isotropy assumption inherent in the Boussinesq model for the Reynolds stress tensor is also partly to blame for its poor performance. While full Reynolds stress equation models avoid this assumption and preserve anisotropic effects, such higher order models have additional complex modeling requirements besides needing a great investment in computational resources. Algebraic Reynolds stress models, in the form of corrections to the basic Boussinesq assumption, have also been developed as a more economically viable means of retaining information about anisotropic conditions. A variety of flows have been calculated with these models, and the results are often better than those obtained with the standard $k - \epsilon$ model. Many of the approximations used to obtain the algebraic relations have been designed to predict only particular flows, though some recently developed models are more generic in nature, e.g., Speziale (1987), and may prove to be more generally applicable. Another intent of the present study is to show that the vorticity transport approach provides a natural way for modeling some significant anisotropic effects without recourse to either high order closures or the assumptions entailed in algebraic models.

For the present work, the relative merits of the vorticity transport closure versus traditional gradient momentum models are explored within the context of the $k - \epsilon$ closure. As part of this, we develop a systematic means for determining time scales appearing in the closure and calibrate them for a series of canonical flows. After this development, the model can be consistently applied to a wide range of applications. Here we investigate its performance in the complex flow over a hill at high Reynolds number where significant flow separation takes place. Previous applications of the method to engineering flows by Bernard (1990b) and Raul and Bernard (1992) have been in the context of a vorticity covariance closure scheme which does not permit examination of the potential merits of the vorticity transport model in isolation from other effects.

Vorticity Transport Model

A natural starting point for the implementation of a vorticity transport closure is the Reynolds averaged Navier-Stokes equations given by

$$\frac{\partial \bar{U}_i}{\partial t} + \bar{U}_j \frac{\partial \bar{U}_i}{\partial x_j} = -\frac{\partial \bar{P}}{\partial x_i} + \nu \frac{\partial^2 \bar{U}_i}{\partial x_j^2} + \epsilon_{ijk}\overline{u_j \omega_k} \qquad (1)$$

where $\bar{U}_i$ is the mean velocity, u_i and ω_i are the velocity and vorticity fluctuations, respectively, $\overline{u_i\omega_j}$ is the vorticity flux tensor, $\bar{P} = \bar{p}/\rho + k$, $\bar{p}$ is the mean pressure and $k = u_i^2/2$ is the turbulent kinetic energy. In contrast to Reynolds stress closures based on the standard Boussinesq eddy viscosity model

$$\overline{u_i u_j} = \frac{2}{3} k\delta_{ij} - \nu_t\left(\frac{\partial \bar{U}_i}{\partial x_j} + \frac{\partial \bar{U}_j}{\partial x_i}\right), \qquad (2)$$

where $\nu_t = C_\mu k^2/\epsilon$ and C_μ is a constant, we must consider models for the flux tensor $\overline{u_i\omega_j}$ in order to close (1).

Contributed by the Fluids Engineering Division for publication in the JOURNAL OF FLUIDS ENGINEERING. Manuscript received by the Fluids Engineering Division March 11, 1994; revised manuscript received September 12, 1994. Associate Technical Editor: G. Karniadakis.

By previous analysis (Bernard, 1990a), the following approximation to the vorticity flux at a point $\mathbf{x}$ at time t may be derived

$$\overline{u_i\omega_j} = -\int_{t-\tau}^{t} \overline{u_i(t)u_k(s)}\,ds\,\frac{\partial\bar{\Omega}_j}{\partial x_k} + \int_{t-\tau}^{t} \overline{u_i(t)\frac{\partial u_j(s)}{\partial x_k}}\,ds\bar{\Omega}_k \tag{3}$$

where $\Omega_i = \epsilon_{ijk}\partial U_k/\partial x_j$ is the vorticity, the overbars refer to ensemble averages, and $\tau > 0$ is a time interval. The notation $f(s)$ indicates a quantity f evaluated at the position occupied by a fluid particle at time s which is known to arrive at $\mathbf{x}$ at time t, so that the integrands in the time integrals are Lagrangian correlation functions. In the derivation of (3) it is assumed that $\tau > \tau_m$ where τ_m, a mixing time, is large enough so that the integrands are zero for $\tau > \tau_m$. In this case the integrals are independent of τ. For convenience, Lagrangian integral scales T and Q may be introduced to simplify (3) to the form

$$\overline{u_i\omega_j} = -T\overline{u_iu_k}\frac{\partial\bar{\Omega}_j}{\partial x_k} + Q\overline{u_i\frac{\partial u_j}{\partial x_k}}\bar{\Omega}_k \tag{4}$$

where it must be recognized that T and Q harbor a dependence on the indices so that in the most general case one may identify nine T scales and 27 Q scales. Moreover, if such dependence on index is permitted, then the scales will clearly be coordinate system dependent. Thus, some care must be taken to insure that the scale values used in calculations transform properly under rotations of the coordinate system.

In addition to the multiplicity of time scales, the implementation of the vorticity transport model in (4) is made difficult by the presence of the Reynolds stresses and the velocity/velocity derivative correlations, $\overline{u_iu_{j,k}}$ where $u_{j,k} \equiv \partial u_j/\partial x_k$. Hence, (4) needs to be considerably modified to be of practical use. In the case of the Reynolds stresses appearing in the gradient term it is not feasible to make the simplification

$$-T\overline{u_iu_k}\frac{\partial\bar{\Omega}_j}{\partial x_k} = -\nu_t\frac{\partial\bar{\Omega}_j}{\partial x_i}, \tag{5}$$

such as is done with momentum transport modeling, since it was shown by Bernard (1990a) that the part of the gradient term in (4) associated with the shear stresses can be significant. To accommodate the shear terms, while making use of (5) for the normal terms, we introduce two T scales, one associated with each of these terms. Specifically, for the normal terms we take $T_1\overline{u_iu_i} = \tau_1\nu_t$ for $i = 1, 2, 3$ where τ_1 is a constant. This is equivalent to taking $u_i^2 = \frac{2}{3}k$, $i = 1, 2, 3$ and $T_1 = \frac{3}{2}C_\mu\tau_1(k/\nu\zeta)$ which is essentially the standard scaling of Lagrangian integral scales. Here, $\zeta = \omega_i^2$ is the enstrophy. In practice, since a $k-\epsilon$ model is used, ζ is replaced with ϵ/ν which is an exact relation for isotropic flows and a very good approximation for the present channel flow simulation as shown by Gorski et al. (1994). For the shear terms we use the expression $T_2\overline{u_iu_j}$, $i \neq j$ where $T_2 = \tau_2(k/\nu\zeta)$ is the time scale for the shear terms and $\overline{u_iu_j}$ is computed from (2). With the introduction of two T scales in this way, invariance under an arbitrary change of coordinates is maintained. Values for τ_1 and τ_2 are determined by calibration of the model.

Modeling the nongradient terms in (4) requires an expression for $\overline{u_iu_{j,k}}$ and consideration of up to 27 different Q scales. Bernard (1990a) introduced an algebraic formalism which resulted in expressions for $\overline{u_iu_{j,k}}$ in terms of the Reynolds stresses, mean vorticity, and time scales. Ainane (1989) developed expressions for arbitrary three-dimensional mean fields containing all 9 T scales and 27 Q scales. These formulas are extremely complicated and there is little basis for setting the various Q scales. In the present work only two-dimensional mean flows are considered, and in this case just four Q scales remain.

In the following analysis, it is assumed that the flow is two-dimensional so that $\bar{\Omega}_1 = \bar{\Omega}_2 = 0$ and $\bar{\Omega}_3 = \bar{\Omega}$. According to (4), the three helicity correlations, $\overline{u_i\omega_i}$, $i = 1, 2, 3$ are identically zero in this case, a result which agrees with the DNS channel flow data. It can also be shown (Gorski, 1993) that the six correlations $\overline{u_iu_{j,k}}$ for which $i \neq j \neq k$ are zero, implying that the fluxes $\overline{u_1\omega_2} = \overline{u_2\omega_1} = 0$ for two-dimensional mean flows.

The expressions for the four remaining vorticity fluxes given by (4) lead to a coupled system of equations for the unknowns $\overline{u_1u_{2,1}}$, $\overline{u_3u_{1,3}}$, $\overline{u_3u_{2,3}}$, and $\overline{u_2u_{1,2}}$ whose solution implies that

$$\overline{u\omega_3} = -\frac{Q_1}{2D}\left(\frac{\partial\overline{w^2}}{\partial x}\bar{\Omega} + \frac{\partial\overline{w^2}}{\partial y}Q_4\bar{\Omega}^2\right) - \tau_1\nu_t\frac{\partial\bar{\Omega}}{\partial x} - T_2\overline{uv}\frac{\partial\bar{\Omega}}{\partial y} \tag{6}$$

$$\overline{w\omega_2} = \frac{Q_4}{2D}\left(\frac{\partial\overline{w^2}}{\partial y}\bar{\Omega} - \frac{\partial\overline{w^2}}{\partial x}Q_3\bar{\Omega}^2\right) \tag{7}$$

$$\overline{w\omega_1} = \frac{Q_3}{2D}\left(\frac{\partial\overline{w^2}}{\partial x}\bar{\Omega} + \frac{\partial\overline{w^2}}{\partial y}Q_4\bar{\Omega}^2\right) \tag{8}$$

$$\overline{v\omega_3} = -\frac{Q_2}{2D}\left(\frac{\partial\overline{w^2}}{\partial y}\bar{\Omega} - \frac{\partial\overline{w^2}}{\partial x}Q_3\bar{\Omega}^2\right) - \tau_1\nu_t\frac{\partial\bar{\Omega}}{\partial y} - T_2\overline{uv}\frac{\partial\bar{\Omega}}{\partial x} \tag{9}$$

where $D = 1 + Q_3Q_4\bar{\Omega}^2$ and for convenience we have made the definitions $Q_1 = Q_{133}$, $Q_2 = Q_{233}$, $Q_3 = Q_{313}$, and $Q_4 = Q_{323}$. It is interesting to note that these relations for two-dimensional mean flows depend only on $\overline{w^2}$ and $\overline{uv}$. The two T and four Q Lagrangian integral time scales must still be set. For this purpose the flow in a two-dimensional channel is utilized, as discussed in the next section.

Channel Flow Approximation

For fully developed channel flow (6)–(9) simplify to

$$\overline{u\omega_3} = -\frac{d\overline{w^2}}{dy}\frac{Q_1Q_4\bar{\Omega}^2}{2D} - T_2\overline{uv}\frac{d\bar{\Omega}}{dy} \tag{10}$$

$$\overline{w\omega_2} = \frac{d\overline{w^2}}{dy}\frac{Q_4\bar{\Omega}}{2D} \tag{11}$$

$$\overline{w\omega_1} = \frac{d\overline{w^2}}{dy}\frac{Q_3Q_4\bar{\Omega}^2}{2D} \tag{12}$$

$$\overline{v\omega_3} = -\frac{d\overline{w^2}}{dy}\frac{Q_2\bar{\Omega}}{2D} - \tau_1\nu_t\frac{d\bar{\Omega}}{dy} \tag{13}$$

where x is the streamwise and y the wall-normal direction, $\bar{U}(y)$ is the mean streamwise velocity, and $\bar{\Omega} = -d\bar{U}/dy$ is the vorticity. Bernard (1990a) showed that good predictions of the vorticity transport correlations computed in a DNS of channel flow could be obtained from the above expressions by using constant T and Q scales. The same simulation is used here to assist in the calibration of the model. In this we have $R_\tau = 145$ based on half-channel height and friction velocity. The simulation incorporates a mesh with $96 \times 97 \times 96$ points in the streamwise, wall-normal, and spanwise directions, respectively, and a computational box of dimensions $1822 \times 290 \times 683$, expressed in wall units.

Since the present work addresses general applications of the model, the Reynolds stress correlations in (10)–(13) must be computable from available quantities. The shear stress $\overline{uv}$ is

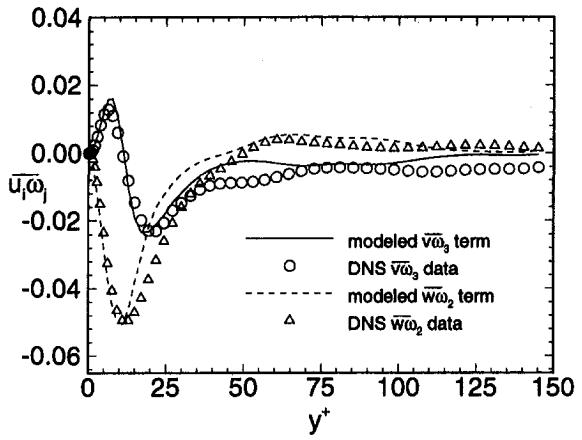

Fig. 1 Modeled $\overline{v\omega_3}$ and $\overline{w\omega_2}$ correlations for channel

modeled quite well with the Boussinesq eddy viscosity model. However, the approximation $w^2 \approx \frac{2}{3}k$ from (2) is quite poor near boundaries, so it is assumed that $\overline{w^2} = (1.0 - e^{-0.02y^+})k$ which gives a very good estimate of $\overline{w^2}$ for the channel as shown by Gorski (1993).

Since the Q scales reflect the vortex stretching and shearing processes, it may be surmised that they scale most appropriately with the time scale $1/\sqrt{\zeta}$. In this case we take

$$Q_i = \frac{C_i}{\sqrt{\zeta}} \quad i = 1, \ldots, 4. \tag{14}$$

The Q_3 and Q_4 scales are set first using the DNS channel flow data for $\overline{w\omega_2}$ and $\overline{w\omega_1}$. The remaining Q and T scales are set using the data for $\overline{v\omega_3}$ and $\overline{u\omega_3}$. Because the gradient and nongradient contributions to $\overline{v\omega_3}$ and $\overline{u\omega_3}$ are of opposite sign, the choice of Q_1, Q_2, τ_1, and τ_2 are very much limited once Q_3 and Q_4 are chosen. In the present work the following values were found for the constants employed in the Lagrangian scales: $C_1 = 4.5$, $C_2 = 0.75$, $C_3 = 0.3$, $C_4 = 2.25$, $\tau_1 = 0.175$, and $\tau_2 = 0.09$. These yield the values for the vorticity transport correlations $\overline{v\omega_3}$ and $\overline{w\omega_2}$ shown in Fig. 1. Here the DNS channel data for kinetic energy, enstrophy, and vorticity are used. The comparisons are quite good, suggesting that the modeled equations and Lagrangian time scales are a reasonable representation of the actual terms, at least for the channel flow. Comparable agreement is also found for the other fluxes given by (10) and (12).

General Two-Dimensional Relations

For two-dimensional mean flows, the x and y momentum equations according to (1), (6)–(9) take the form

$$\frac{\partial \bar{U}}{\partial t} + \bar{U}\frac{\partial \bar{U}}{\partial x} + \bar{V}\frac{\partial \bar{U}}{\partial y} = -\frac{\partial \bar{P}}{\partial x} + (\nu + \tau_1\nu_t)\nabla^2\bar{U} - T_2\overline{uv}\nabla^2\bar{V} + \frac{[Q_2 + Q_4]}{2D}\left(-\frac{\partial \overline{w^2}}{\partial y}\bar{\Omega} + \frac{\partial \overline{w^2}}{\partial x}\bar{\Omega}^2 Q_3\right) \tag{15}$$

$$\frac{\partial \bar{V}}{\partial t} + \bar{U}\frac{\partial \bar{V}}{\partial x} + \bar{V}\frac{\partial \bar{V}}{\partial y} = -\frac{\partial \bar{P}}{\partial y} + (\nu + \tau_1\nu_t)\nabla^2\bar{V} - T_2\overline{uv}\nabla^2\bar{U} + \frac{[Q_1 + Q_3]}{2D}\left(\frac{\partial \overline{w^2}}{\partial x}\bar{\Omega} + \frac{\partial \overline{w^2}}{\partial y}\bar{\Omega}^2 Q_4\right) \tag{16}$$

respectively, where $\nabla^2 = \partial^2/\partial x^2 + \partial^2/\partial y^2$ and the mean continuity equation $\partial\bar{U}/\partial x + \partial\bar{V}/\partial y = 0$ has been used to write $\partial\bar{\Omega}/\partial y = -\nabla^2\bar{U}$ and so forth. To apply the scale information derived from our analysis of channel flow to (15) and (16), some care must be taken with regards to the unavoidable coordinate dependence of the scales stemming from the simplification of (3) to (4). For example, the vortex stretching term

$$-\frac{\partial \overline{w^2}}{\partial y}\bar{\Omega}\frac{[Q_2 + Q_4]}{2D}$$

in (15), after a 90 degree rotation of the coordinate axis becomes

$$\frac{\partial \overline{w^2}}{\partial x}\bar{\Omega}\frac{[Q_1^* + Q_3^*]}{2D}$$

which must be formally equivalent to the appropriate term in (16). In this case it is evident that we must have

$$Q_2 + Q_4 = Q_1^* + Q_3^*. \tag{17}$$

By repeating this analysis for the cross stream momentum equation, the following relation is obtained

$$Q_4[Q_1 + Q_3] = Q_3^*[Q_2^* + Q_4^*]. \tag{18}$$

From (17) and (18) it may be concluded that in setting time scales for the rotated coordinate system one should insist that $Q_3^* = Q_4$ and $Q_1^* = Q_2$.

A simple means of setting the time scales independently of coordinate rotations for general two-dimensional mean flows is to assume relations of the form

$$Q_1 = \frac{C_1\bar{U}^2 + C_2\bar{V}^2}{\bar{U}^2 + \bar{V}^2}\frac{1}{\sqrt{\zeta}} \tag{19}$$

$$Q_2 = \frac{C_2\bar{U}^2 + C_1\bar{V}^2}{\bar{U}^2 + \bar{V}^2}\frac{1}{\sqrt{\zeta}} \tag{20}$$

$$Q_3 = \frac{C_3\bar{U}^2 + C_4\bar{V}^2}{\bar{U}^2 + \bar{V}^2}\frac{1}{\sqrt{\zeta}} \tag{21}$$

$$Q_4 = \frac{C_4\bar{U}^2 + C_3\bar{V}^2}{\bar{U}^2 + \bar{V}^2}\frac{1}{\sqrt{\zeta}}. \tag{22}$$

With the use of (19)–(22), Eqs. (15) and (16) are now invariant under a rotation of coordinates.

It may also be observed in (2) that only a single time scale is implicit in the Boussinesq approximation. This is one of the reasons why it models only some of the stresses well. Thus, by its incorporation of a greater number of independent scales, the current approach is able to encompass more of the transport physics than is possible with isotropic models.

Equations (15) and (16) must be solved in conjunction with a closure scheme supplying values of k and ϵ. For this purpose the two-equation $k - \epsilon$ model of Speziale et al. (1992) is used. Calculations are also done using this $k - \epsilon$ model together with the low Reynolds number form of (2) proposed by Speziale et al. (1992) in order to assess the effectiveness of (6)–(9) in comparison to (2). While it is possible that these results are sensitive to the particular model used for the k and ϵ equations, it is unlikely that our general conclusions would be affected by such modifications.

Solution Procedure

Only a brief description of the solution procedure is given here as details can be found elsewhere (Gorski, 1988). The Navier-Stokes equations as well as the $k - \epsilon$ equations contain both first derivative convective terms and second derivative viscous terms. The viscous terms are discretized using standard central differences. Third order upwind differencing is used for the convective part of the equations. The Jacobian matrices of the convective terms are used to generate eigenvectors and eigenvalues for the system of equations. The convective terms

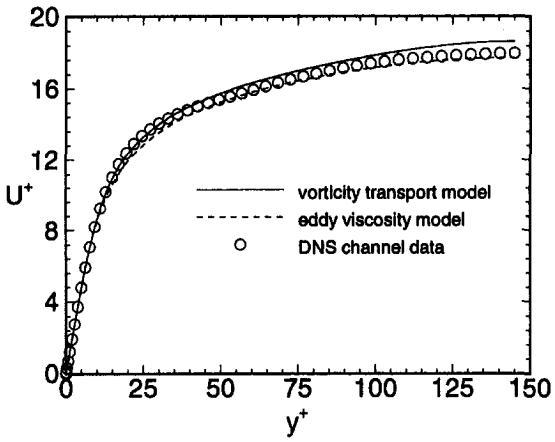

Fig. 2 Mean velocity for channel

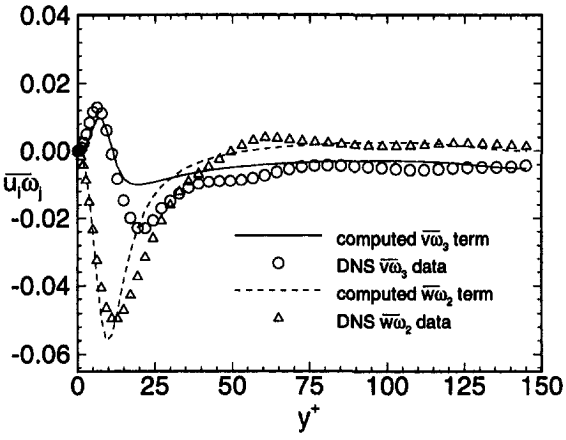

Fig. 4 Computed $\overline{v\omega_3}$ and $\overline{w\omega_2}$ correlations for channel

are then forward or backward differenced based on the sign of the eigenvalues. With this approach no artificial dissipation terms are added to the equations for stability. The equations are transformed to a body fitted coordinate system and solved using a finite volume procedure. The artificial compressibility technique of Chorin (1967) is used to add a time derivative term for pressure to the continuity equation. This allows the system of equations to be marched in time in an implicit coupled manner using approximate factorization which requires the inversion of block tri-diagonal matrices. The implicit side of the equations are only first order accurate, but the final converged solution has the third order accuracy of the explicit part of the equations.

Results and Discussion

We now apply Eqs. (15) and (16) in concert with the $k - \epsilon$ closure of Speziale et al. (1992) to the prediction of several flows in order to explore the capabilities of vorticity transport modeling. Previously we used DNS data of channel flow to fix the Q scales through (10) – (13). Now we calculate the channel flow using the complete closure scheme as a test of the method. This will highlight the performance of (10) – (13) in the context of a closure scheme where DNS data is not used to supply values for k and ϵ. In the calculation, a stretched grid with 57 points across one-half the channel and 5 points in the streamwise direction is used. This grid is sufficient for grid independent solutions. The first grid point away from the wall is at $y^+ \approx 0.1$, and symmetry boundary conditions are applied at the centerline. The inlet and outlet pressures are set to match the DNS data, and periodic boundary conditions are used for the velocities and turbulent quantities in the streamwise direction. The centerline velocity evolves as part of the solution thus providing another test of the model.

Figure 2 shows that the mean velocity computed with both models is quite good, and that the wall profile shape has the correct characteristics. This is especially significant for the vorticity transport model, since apart from the model used in computing w^2, no near-wall damping functions are added analogously to the f_μ function used in eddy viscosity models. In the case of kinetic energy, Fig. 3 indicates some differences between the two closures, but neither is necessarily better than the other. A similar result is found in the case of ϵ.

As seen in Fig. 4, inaccuracies in predicting k and ϵ degrade the prediction of the $\overline{v\omega_3}$ and $\overline{w\omega_2}$ correlations. However, the total contribution to the streamwise momentum equation is still quite good as shown in Fig. 5. The computed $\overline{w\omega_1}$ and $\overline{u\omega_3}$ correlations are also found to have the correct shapes and tend to go to zero where appropriate. Overall, the predictions are quite good for all of the vorticity fluxes.

To test the model further, the boundary layer flow developing on a flat plate with zero pressure gradient is computed. The predicted fields are compared with two different data sets. One comes from the low Reynolds number simulations of Spalart (1988) at Reynolds numbers R_θ = 300, 670, and 1410 where R_θ is based on the momentum thickness. The other data set is that measured experimentally by Weighardt (1968) at a Reynolds number of 2.2×10^6. To calculate these boundary layer flows, a grid with 41 points in the streamwise and 57 points in the wall-normal direction is used. Points are highly clustered at the leading edge of the flat plate and at the wall. At the inlet,

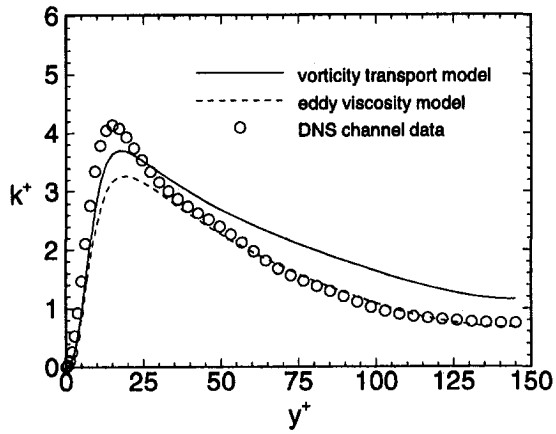

Fig. 3 Kinetic energy for channel

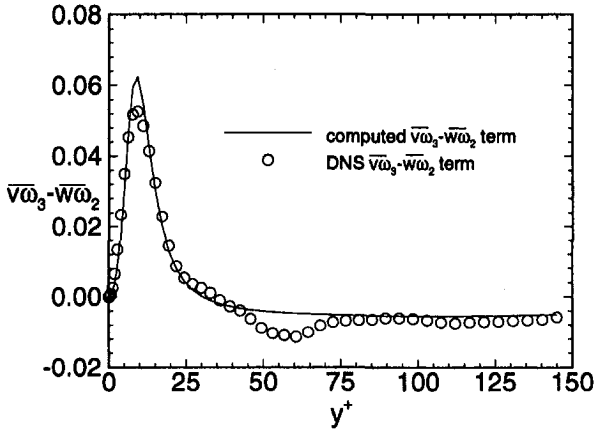

Fig. 5 Total $\overline{v\omega_3} - \overline{w\omega_2}$ term for channel

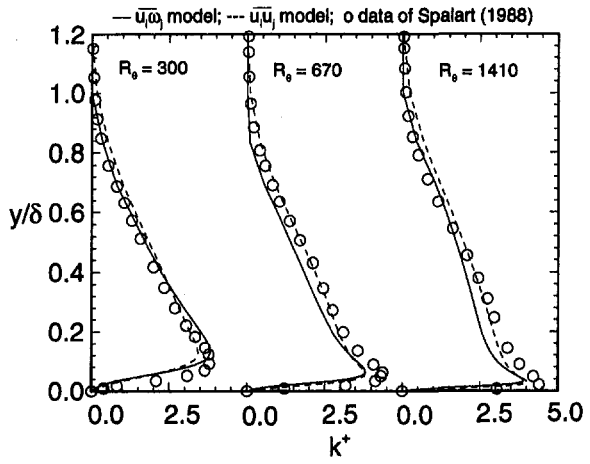

Fig. 6 Flat plate kinetic energy

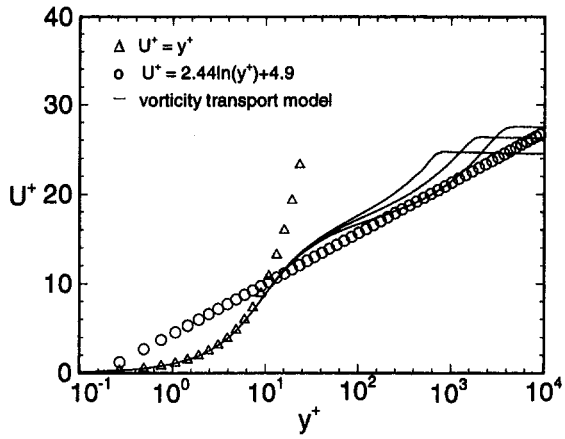

Fig. 8 Law of the wall comparison for the vorticity transport model.

the streamwise velocity is set to a constant, the wall-normal velocity is set to zero, and the pressure is extrapolated from the interior of the computational domain. In addition, the kinetic energy and enstrophy are set to small values. At the downstream boundary, all quantities are extrapolated from the interior, while at the freestream boundary the pressure is set to a constant and all other values are extrapolated from the interior. No-slip boundary conditions are set at the wall. Although the Spalart (1988) data has no leading edge effects, the boundary layers we calculate for these Reynolds numbers are far enough downstream that the computed leading edge effects are minimized.

For the low Reynolds number flat plate flow of Spalart (1988) there is no significant difference between the mean velocity computed with the two closure models or with the data. For kinetic energy, it is seen in Fig. 6 that the predictions are also comparable. Some differences become apparent when the results are compared with the Weighardt (1968) flat plate data. Here the skin friction is slightly higher and has a flatter profile with the vorticity transport correlations as shown in Fig. 7. However, the velocities predicted with the two closures are comparable and agree well with the experimental data.

A comparison with the law of the wall is shown in Fig. 8. The agreement with the linear law is excellent, and at the lower Reynolds numbers the profile is flat in the law of the wall region. However, the profiles start to develop a waviness at large y^+ values for the thicker boundary layer profiles. The problem is likely due to setting the constants based on DNS channel flow data which only extends to $y^+ = 145$ at the centerline, much less than the $y^+ \approx 10{,}000$ for the high Reynolds number boundary layer flow. Since the vortex stretching terms depending on the Q scales are only significant near the wall, it is likely that the selection of the T scales is in need of improvement. By examining the equations, it appears that τ_1 should ≈ 1.0 away from the wall for the vorticity transport model to be approximately the same as the Boussinesq approximation in this location. However, τ_1 of this magnitude would be inappropriate for the near wall. Thus, it may be necessary for τ_1 to vary across the boundary layer to get better results for the high Reynolds number boundary layer profiles. Overall though, the results are quite encouraging considering that no special functions are added to the Lagrangian time scales to better fit the data, and that all of the constants are set from low Reynolds number channel flow data.

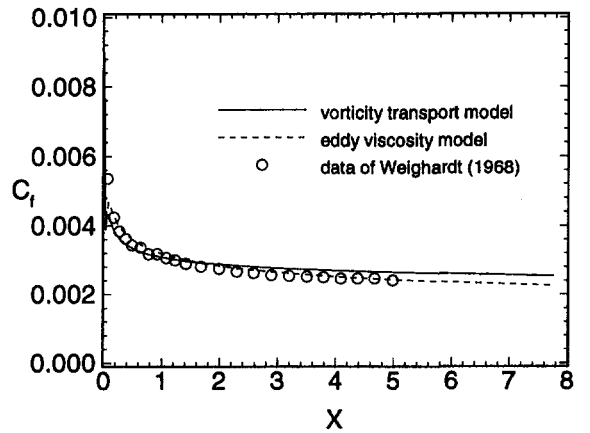

Fig. 7 Flat plate C_f

The hill flow considered here is that measured experimentally by Baskaran et al. (1987) in which a boundary layer developing on one wall of a duct flow encounters a hill. The alternating regions of concave and convex curvature lead to an adverse pressure gradient at the rear of the hill leading to flow separation. The Reynolds number based on free stream velocity and arclength of the hill is 1.33×10^6, and the leading edge of the hill in the experiment is 1.0 meters from the leading edge of the flat plate on which it rests. The flow is tripped 0.15 meters downstream from the leading edge of the flat plate, making it difficult to compute numerically because of the transition region in front of the hill. Hence, the mean velocity and turbulence quantities in the calculation are set from the experimental data 0.596 meters downstream from the leading edge of the flat plate. The proximity of this location to the hill rules out the use of a fully developed flat plate boundary layer profile as the inlet boundary condition. Tests showed that the results are somewhat sensitive to the inlet boundary conditions which may account for some of the discrepancies between the computed results and experiment. At the downstream boundary all quantities are extrapolated from the interior, and reflection boundary condition are used at $y = 2.0$. The grid used for the calculations is 111×121 in the streamwise and wall-normal directions, respectively. Grid independence of the solution was established by doing a second calculation with a mesh of 171×181 points which produced no significant differences from the coarse grid solution.

The improvements possible with the use of the vorticity transport relations in comparison to gradient momentum transport modeling are illustrated in Fig. 9 giving the wall static pressure, C_p. Here the horizontal axis is given in arclengths, X, from the leading edge of the flat plate. The hill is located between $X = 1.0$ and $X = 2.35$. The minimum C_p is somewhat high at the top of the hill for both models which may be partly due to the inlet boundary conditions. At the trailing edge of the hill, C_p is significantly overpredicted for the momentum model and does

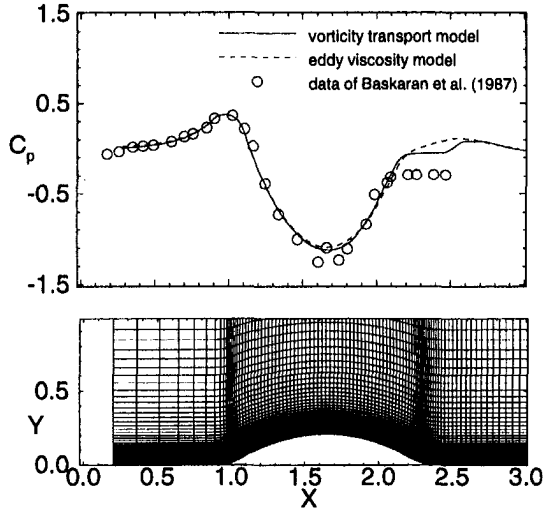

Fig. 9 C_p on hill surface

not have the characteristically flat profile associated with separated flows. In contrast, C_p computed using the vorticity transport correlations is significantly more accurate. In particular, the profile is much flatter near the trailing edge of the hill since the vorticity transport solution provides a larger separated flow region—significantly closer to that seen experimentally—than does the eddy viscosity model.

The experimental data shows that the hill flow separates at $X = 2.1$ meters and reattaches at $X = 2.7$ meters. For the Boussinesq model the predicted separation occurs at $X = 2.15$ and reattachment at 2.46. The skin friction obtained with the vorticity transport correlations is considerably different than the Boussinesq model, as shown in Fig. 10. C_f is higher at the front of the hill and has a much steeper drop to zero along the back of the hill. The skin friction profile is also less rounded with the vorticity transport approach, a feature which is more consistent with the experimental data. With the vorticity transport correlations the flow separates at $X = 2.1$, agreeing well with the data, and reattaches at $X = 2.56$, which is still somewhat underpredicted. The computations using the Boussinesq eddy viscosity assumption predict a separation area about $\frac{1}{2}$ the size of the actual data, consistent with the $k - \epsilon$ calculations of Michelassi and Shih (1991) for this flow. The vorticity transport correlation predicts a separation area about $\frac{3}{4}$ the size of the actual data and the mean flow prediction has definitely improved in the separated region. This may be due to the introduction of

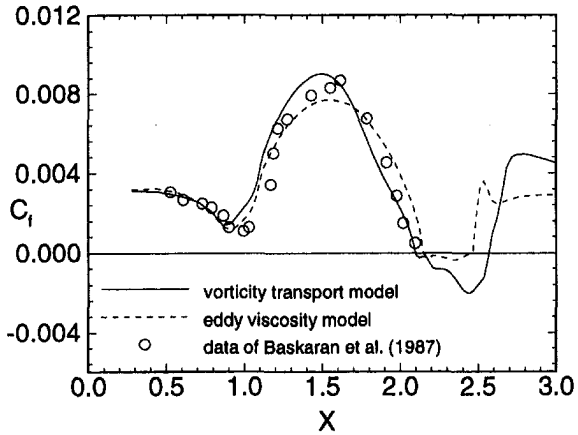

Fig. 10 C_f on hill surface

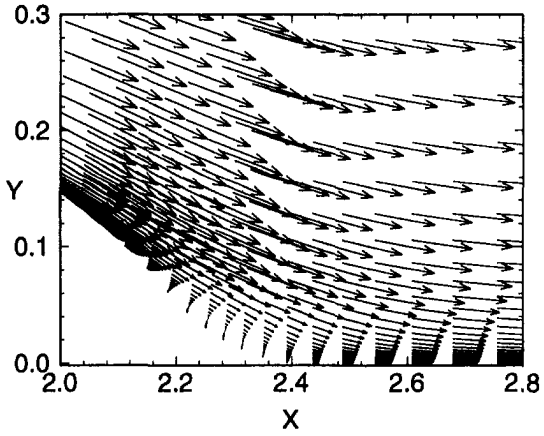

Fig. 11 Velocity vectors computed using the Reynolds stresses

nonisotropic affects. As shown in Figs. 11 and 12, the separation bubble predicted using the Reynolds stresses is barely discernable while that predicted with the vorticity transport correlations is much wider as well as longer. The larger separation area predicted by the vorticity transport approach also produces much larger negative values of skin friction which are more consistent with experiments.

Conclusions

This work has investigated the properties of a vorticity transport closure as an alternative to the Reynolds stresses for closing the primitive variable form of the Navier-Stokes equations. Previous results (Bernard, 1990a, Rovelstad, 1991) have shown the general compatibility of the vorticity transport model with DNS data. The present study is the first practical application of the approach in which all terms are modeled based on the computed velocities, kinetic energy, and dissipation. A methodology for determining a minimum set of time scales appropriate to the vorticity flux model was derived. Although there may be some problem with the way the present model transitions between near and far wall effects governed by the vortex stretching and gradient terms, respectively—as seen from law of the wall comparisons—the results are encouraging and indicate that the vorticity transport based model may be a viable alternative to Boussinesq eddy viscosity models. This is particularly true in complex flow regimes, such as the wall flows considered here, where nonisotropic affects are important.

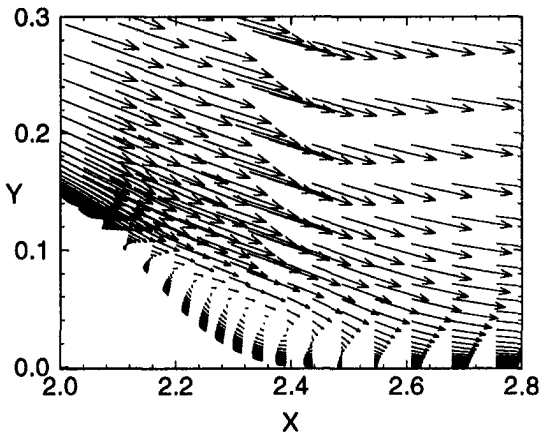

Fig. 12 Velocity vectors computed using the vorticity transport correlations

Acknowledgments

J. J. Gorski was supported by the NSWC Independent Research Program in this study. Support of P. S. Bernard was provided through ONR grant no. N00014-93-10184.

References

Ainane, S., 1989, "A Numerical Investigation of Turbulent Channel Flow Using a Second Order Turbulence Closure," Ph.D. dissertation, University of Maryland, College Park, MD.

Baskaran, V., Smits, A. J., and Joubert, P. N., 1987, "A Turbulent Flow Over a Curved Hill Part 1. Growth of an Internal Boundary Layer," *Journal of Fluid Mechanics,* Vol. 182, pp. 47–83.

Bernard, P. S., 1990a, "Turbulent Vorticity Transport in Three Dimensions," *Theoretical and Computational Fluid Dynamics,* Vol. 2, pp. 165–183.

Bernard, P. S., 1990b, "Turbulence Effects in the Edgetone Flow Field," *Journal of Fluids and Structures,* Vol. 4, pp. 449–470.

Bernard, P. S., and Handler, R. A., 1990, "Reynolds Stress and the Physics of Turbulent Momentum Transport," *Journal of Fluid Mechanics,* Vol. 220, pp. 99–124.

Chorin, A. J., 1967, "A Numerical Method for Solving Incompressible Viscous Flow Problems," *Journal of Computational Physics,* Vol. 2, pp. 12–26.

Gorski, J. J., 1988, "TVD Solutions of the Incompressible Navier-Stokes Equations With an Implicit Multigrid Scheme," *Proceedings of the 1st National Fluid Dynamics Congress,* Vol. 1, pp. 394–401.

Gorski, J. J., 1993, "Application of Vorticity Transport Analysis to the Development of Physically Accurate Turbulence Models," Ph.D. dissertation, University of Maryland, College Park, Maryland.

Gorski, J. J., Wallace, J. M., and Bernard, P. S., 1994, "The Enstrophy Equation Budget of Bounded Turbulent Shear Flows," *The Physics of Fluids,* Vol. 6, pp. 3197–3199.

Handler, R. A., Bernard, P. S., Rovelstad, A., and Swearingen, J., 1992, "On the Role of Accelerating Particles in the Generation of Reynolds Stress," *The Physics of Fluids A,* Vol. 4, pp. 1317–1319.

Hinze, J. O., 1975, *Turbulence,* 2nd Ed. McGraw-Hill, New York, p. 580.

Lakshminarayana, B., 1986, "Turbulence Modeling for Complex Shear Flows," *AIAA Journal,* Vol. 24, pp. 1900–1916.

Michelassi, V., and Shih, T.-H., 1991, "Elliptic Flow Computation by Low Reynolds Number Two-Equation Turbulence Models," NASA TM 105376.

Piomelli, U., Moin, P., and Ferziger, J., 1989, "Large Eddy Simulation of the Flow in a Transpired Channel," AIAA Paper No. 89-0375.

Raul, R., and Bernard, P. S., 1992, "A Numerical Investigation of the Turbulent Flow Field Generated by a Stationary Cube," ASME JOURNAL OF FLUIDS ENGINEERING, Vol. 113, pp. 216–222.

Rovelstad, A., 1991, "Lagrangian Analysis of Vorticity Transport in a Numerically Simulated Turbulent Channel Flow" Ph.D. dissertation, University of Maryland, College Park, Maryland.

Spalart, P. R., 1988, "Direct Simulation of a Turbulent Boundary Layer up to $R_\theta = 1410$," *Journal of Fluid Mechanics,* Vol. 187, pp. 61–98.

Speziale, C. G., 1987, "On Nonlinear $k - l$ and $k - \epsilon$ Models of Turbulence," *Journal of Fluid Mechanics,* Vol. 178, pp. 459–475.

Speziale, C. G., 1991, "Analytical Methods for the Development of Reynolds-Stress Closures in Turbulence," *Annual Review of Fluid Mechanics,* Vol. 23, pp. 107–157.

Speziale, C. G., Abid, R., and Anderson, E. C., 1992, "Critical Evaluation of Two-Equation Models for Near-Wall Turbulence," *AIAA Journal,* Vol. 30, pp. 324–331.

Taylor, G. I., 1915, "Eddy Motion in the Atmosphere," *Philosophical Transactions of the Royal Society of London,* Vol. 215, pp. 1–26.

Taylor, G. I., 1932, "The Transport of Vorticity and Heat Through Fluids in Turbulent Motion," *Proceedings of the Royal Society,* Vol. 135A, pp. 685–705.

Taylor, G. I., 1935, "Distribution of Velocity and Temperature Between Concentric Rotating Cylinders," *Proceedings of the Royal Society* (London) Series A, Vol. 151, p. 494.

Taylor, G. I., 1937, "Flow in Pipes and Between Parallel Plates," *Proceedings of the Royal Society* (London) Series A, Vol. 159, p. 496.

Weighardt, K., 1968, "Flat Plate Flow," *Proceedings of the Computation of Turbulent Boundary Layers,* 1968 AFOSR-IFP-STANFORD Conference, Vol. 2, pp. 98–123.

K. C. Chang
Professor. Assoc. Mem. ASME

W. D. Hsieh
Research Assistant.

C. S. Chen
Research Assistant.

Institute of Aeronautics and Astronautics,
National Cheng-Kung University,
Tainan, Taiwan

A Modified Low-Reynolds-Number Turbulence Model Applicable to Recirculating Flow in Pipe Expansion

A modified low-Reynolds-number k-ϵ turbulence model is developed in this work. The performance of the proposed model is assessed through testing with fully developed pipe flows and recirculating flow in pipe expansion. Attention is specifically focused on the flow region around the reattachment point. It is shown that the proposed model is capable of correctly predicting the near-wall limiting flow behavior while avoiding occurrence of the singular difficulty near the reattachment point as applying to the recirculating flow in sudden-expansion pipe.

Introduction

Turbulence closure models are the most feasible and economical approaches for the analysis of practical turbulent flows so far (Nallasamy, 1987). Most conventional closure models are only applicable to high-Reynolds-number flow regimes. They link the conditions at the wall, which are low-Reynolds-number flow regimes, to the first calculation point through use of the wall functions. However, many simulations do not suit the wall function approach. Such examples include turbulent boundary layer at low Reynolds number, separated flows, the flow over surfaces with heat and/or mass transfer, etc. It is therefore necessary to have a way to extend the application of the existing closure models to the rather thin sublayer affected by molecular viscosity.

Among turbulence closure models, the second-order closure models such as Reynolds stress models (RSM) have been used in the simulation of complex turbulent flows (Farhanieh et al., 1993; Nikjooy and Mongia, 1991). However, it is generally agreed that second-order closure models require more computational time and complexity than first-order closure models such as the two-equation models. The scope of this work is restricted to recirculating flows in a sudden-expansion pipe without the swirl effect. The two-equation models are reportedly able to describe, to some extent, the turbulent motion in this kind of flow (Nallasamy, 1987). However, since the conventional two-equation models assume isotropic eddy diffusivity in modeling the Reynolds stress tensor, they usually lead to less accurate predictions for normal Reynolds stresses (Speziale, 1991). As a result, the two-equation models cannot be fully successful in application to certain flow phenomena such as the secondary flow in noncircular duct and the recirculating flow in sudden-expansion pipe, where the anisotropic normal Reynolds stresses play an important role. To remedy these defects, considerable research efforts have been directed toward the development of nonlinear (or anisotropic) generalizations of eddy-viscosity models (Speziale, 1991). In this work, our interest focuses on the flow region near the reattachment point. For the sake of simplicity, the conventional two-equation models, instead of the ones with anisotropic representations of the eddy viscosity, are to be discussed here.

The k-ϵ model is the most popular two-equation turbulence model in use today. When utilized in conjunction with wall functions, the k-ϵ model performs reasonably well. It has been applied to a variety of engineering problems with a moderate amount of success. Over the past two decades, many modifications (see Table 1) have been made to extend the k-ϵ model for use at low Reynolds numbers and to describe accurately the flow behaviors close to a solid wall. Patel et al. (1985) made a detailed review of the low-Reynolds-number k-ϵ models developed before 1985 and concluded that none of the existing low-Reynolds-number k-ϵ models were capable of accurately predicting the wall limiting behavior.

A few low-Reynolds-number k-ϵ turbulence models (Myong and Kasagi, 1990; Nagano and Tagawa, 1990) have recently taken near-wall limiting behavior into account and yielded satisfactory predictions in the entire region of straight-pipe flow. However, application of these low-Reynolds-number k-ϵ models to recirculating flows in the sudden-expansion pipe was subject to a singularity occurring near the reattachment points. The objective of this work is to develop a modified low-Reynolds-number k-ϵ model which can eliminate the aforementioned deficiencies. The proposed model will be applied first to the fully developed pipe flows and then to the pipe flows in sudden expansion. The performance of the proposed model will be assessed through a comparison to the experimental data available in open literature and to predictions obtained with some widely used low-Reynolds-number k-ϵ models.

Development of a Modified Low-Reynolds-Number k-ϵ Model

Modeling. The wall limiting conditions of turbulence quantities possess the following asymptotic relations:

$$-\overline{u'v'} \propto y^3,\ k \propto y^2,\quad \mu_t \propto y^3,\quad \epsilon \to \epsilon_w \text{ as } y \to 0 \qquad (1)$$

With the Prandtl-Kolmogorov description of eddy viscosity given by:

$$\mu_t = \rho C_\mu f_\mu k^2/\epsilon \qquad (2)$$

(noting that the model coefficient C_μ is a constant value of 0.09), we can conclude that the model function f_μ must satisfy $f_\mu \propto y^{-1}$. As noted by Chapman and Kuhn (1986), none of the low-Reynolds-number k-ϵ models discussed by Patel et al. (1985) meet this requirement.

Shih and Mansour (1990) currently proposed the following f_μ function which is similar to the one used in Chien's model (1982, hereafter referred as the CH model).

$$f_\mu = [1 - \exp(-a_1 y^+ - a_2 y^{+^2} - a_3 y^{+^3} - a_4 y^{+^4})] \qquad (3)$$

where a_1, a_2, a_3, and a_4 are empirical constants. Very recently,

Contributed by the Fluids Engineering Division for publication in the JOURNAL OF FLUIDS ENGINEERING. Manuscript received by the Fluids Engineering Division June 14, 1993; revised manuscript received April 17, 1995. Associate Technical Editor: G. Karniadakis.

Table 1 Summary of model functions

Model	f_μ	f_1	f_2
Standard	1.0	1.0	1.0
Launder-Sharma (1974)	$\exp[-3.4/(1 + R_t/50)^2]$	1.0	$1.0 - 0.3\exp(-R_t^2)$
Lam-Bremhorst (1981)	$[1.0 - \exp(-0.0165R_k)]^2(1 + 20.5/R_t)$	$1.0 + (0.05/f_\mu)^3$	$1 - 0.3\exp(-R_t^2)$
Chien (1982)	$1.0 - \exp(-0.0115y^+)$	1.0	$1.0 - 0.22\exp(-R_t^2/36)$
Nagano-Hishida (1987)	$[1.0 - \exp(-y^+/26)]^2$	1.0	$1.0 - 0.3\exp(-R_t^2)$
Myong-Kasagi (1990)	$[1.0 - \exp(-y^+/70)](1 + 3.45/R_t^{1/2})$	1.0	$\{1.0 - 2/9\exp[-(R_t/6)^2]\}[1 - \exp(-y^+/5)]^2$
Nagano-Tagawa (1990)	$[1.0 - \exp(-y^+/26)]^2(1 + 4.1/R_t^{3/4})$	1.0	$\{1.0 - 0.3\exp[-(R_t/6.5)^2]\}[1 - \exp(-y^+/6)]^2$
Present work	$[1.0 - \exp(-0.0215R_k)]^2(1 + 31.66/R_t^{5/4})$	1.0	$[1 - 0.01\exp(-R_t^2)][1 - \exp(-0.0631R_k)]$

Shih and Lumley (1993) proposed another representation of the f_μ function:

$$f_\mu = [1 - \exp(b_1R_k + b_2R_k^3 + b_3R_k^5)]^{1/2} \quad (4)$$

where

$$R_k = \sqrt{k}y/\nu \quad (5)$$

b_1, b_2 and b_3 are empirical constants. Note that f_μ functions shown in Eqs. (3) and (4) do not exhibit the limiting behavior of $f_\mu \propto y^{-1}$. Nevertheless, a few low-Reynolds-number models developed lately have taken this requirement into account. For instance, Myong and Kasagi (1990) proposed the f_μ function in the form of

$$f_\mu = [1 - \exp(-y^+/70)](1 + 3.45/R_t^{1/2}) \quad (6)$$

where

$$y^+ = u_\tau y/\nu \quad (7)$$

$$u_\tau = \sqrt{\tau_w/\rho} \quad (8)$$

$$R_t = k^2/\nu\epsilon \quad (9)$$

Working with the model developed previously by Nagano and Hishida (1987) as a base, Nagano and Tagawa (1990, the NT model) improved the f_μ function:

$$f_\mu = [1 - \exp(-y^+/26)]^2(1 + 4.1/R_t^{3/4}) \quad (10)$$

The low-Reynolds-number turbulence models expressed above, except for those developed by Shih and Mansour (1990) and Shih and Lumley (1993), have improved f_μ functions which allow them to meet the limiting behavior requirement of $f_\mu \propto y^{-1}$. However, these models still have a singular problem related to the simulation of recirculating flows in a sudden-expansion pipe. This is because these low-Reynolds-number models formulated the f_μ model functions in terms of the friction velocity u_τ which itself includes the wall shear stress τ_w in its definition as shown in Eq. (8). As we know, the wall shear stress approaches zero value in the neighborhood of the reattachment positions occurring in the recirculating flow fields of sudden-expansion pipe. This, in turn, results in a singularity problem; that is, f_μ and/or f_2 become zero regardless of y's value. According to Eq. (2), all μ_t values, even those located in the fully turbulent region, drop to zero. This is physically impossible.

In order to remedy this singularity difficulty, the new model functions of f_μ and f_2 are developed with proper parameters. To comply with the required limiting behavior of $f_\mu \propto y^{-1}$, the f_μ function is given by

$$f_\mu = [1 - \exp(-A_\mu R_k)]^2(1 + B_\mu/R_t^{5/4}) \quad (11)$$

Note that both parameters R_k and R_t which appeared in Eq. (14) are not expressed in terms of y^+ (or τ_w implicitly) and, therefore, do not induce the aforementioned singularity problem when applied to the recirculating flow in pipe expansion. The asymptotic relation of these two parameters are

$$R_k \propto y^2, \quad R_t \propto y^4, \quad \text{as } y \to 0 \quad (12)$$

Also near the wall, the ϵ equation (see Table 2) is reduced to

$$\mu\frac{\partial^2\epsilon}{\partial y^2} = C_2f_2\rho\epsilon_w^2/k = \text{finite value} \quad (13)$$

Thus, one can conclude that the f_2 function must be proportional to y^2 in the regions near the wall by introducing the asymptotic relations shown in Eq. (1) into Eq. (13). Although the low-Reynolds-number k-ϵ models developed lately such as by Myong and Kasagi (1990) and Nagano and Tagawa (1990) have f_2 functions designed to account for limiting behavior, the inclusion of y^+ parameter in their modeling works leads to the similar singularity problems in regard to the f_μ function near the reattachment point in application to recirculating flow in the sudden-expansion pipe. To account for these two concerns, a new, modified design of the f_2 function is proposed:

$$f_2 = [1 - \exp(-A_2R_k)][1 - B_2\exp(-R_t^2)] \quad (14)$$

Based upon a comparison with data available in open literature on straight pipe flows, the optimal values of the coefficients A_μ, B_μ, A_2, and B_2 which appeared in Eqs. (11) and (14) are determined using the least-squares algorithm (Marquardt, 1963):

Nomenclature

C_μ, C_1, C_2 = turbulence model constants
d = diameter of pipe upstream of expansion
D = diameter of pipe downstream of expansion and extra source term in k equation, respectively
E = extra source term in ϵ equation
f_μ, f_1, f_2 = turbulence model functions
G_k = production term of k
k = turbulent kinetic energy
p = mean pressure
R = radius of pipe
Re = Reynolds number
r = radial ordinate
S_ϕ = general source term
u, u' = mean and fluctuating axial velocity, respectively
u_c = mean axial velocity in centerline
v, v' = mean and fluctuating radial velocity, respectively
x = axial ordinate
Γ_ϕ = turbulent diffusion coefficient
ϵ = dissipation rate of turbulent kinetic energy
μ, μ_t = molecular and eddy viscosities, respectively
ρ = density
σ_k = turbulent Prandtl number for diffusion of k
σ_ϵ = turbulent Prandtl number for diffusion of ϵ
ϕ = dependent variable

Table 2 Governing equations

ϕ	Γ_ϕ	S_ϕ
1	0	0
u	μ_{eff}	$-\frac{\partial p}{\partial x}+\frac{\partial}{\partial x}\left(\mu_{eff}\frac{\partial u}{\partial x}\right)+\frac{1}{r}\frac{\partial}{\partial r}\left(r\mu_{eff}\frac{\partial v}{\partial x}\right)$
v	μ_{eff}	$-\frac{\partial p}{\partial r}+\frac{\partial}{\partial x}\left(\mu_{eff}\frac{\partial u}{\partial r}\right)+\frac{1}{r}\frac{\partial}{\partial r}\left(r\mu_{eff}\frac{\partial v}{\partial r}\right)$ $-2\mu_{eff}\ v\ /r^2$
k	$\mu+\mu_t/\sigma_k$	$G_k-\rho\epsilon+D$
ϵ	$\mu+\mu_t/\sigma_\epsilon$	$(C_1 f_1 G_k - C_2 f_2 \rho\epsilon)\epsilon/k+E$

$$G_K=\mu_t\left\{2\left[\left(\frac{\partial u}{\partial x}\right)^2+\left(\frac{\partial v}{\partial r}\right)^2+\left(\frac{v}{r}\right)^2\right]+\left(\frac{\partial v}{\partial x}+\frac{\partial u}{\partial r}\right)^2\right\}$$

$\mu_t=\rho C_\mu f_\mu k^2/\epsilon$
$\mu_{eff}=\mu+\mu_t$

$$A_\mu=0.0215,\quad B_\mu=31.66,\quad A_2=0.0631,\quad B_2=0.01$$

Governing Equations. The present study deals with the steady-state, axisymmetrical, Reynolds-averaged equations for conservation of momentum, turbulent kinetic energy, and its dissipation rate. These governing equations are cast into the following general form which permits a single algorithm to be used:

$$\frac{1}{r}\left[\frac{\partial}{\partial x}(r\rho u\phi)+\frac{\partial}{\partial r}(r\rho v\phi)\right]=\frac{1}{r}\left[\frac{\partial}{\partial x}\left(r\Gamma_\phi\frac{\partial\phi}{\partial x}\right)+\frac{\partial}{\partial r}\left(r\Gamma_\phi\frac{\partial\phi}{\partial r}\right)\right]+S_\phi \quad (15)$$

The parameters ϕ, Γ_ϕ and S_ϕ appearing in Eq. (15) are summarized in Table 2. The corresponding model constants and functions shown in Table 2 for each tested turbulence model are listed in Table 3 for the reader's convenience.

Numerical Analysis

Numerical calculations of Eq. (15) are performed using the finite-volume method via integration of the differential equations over control volume to deduce the corresponding algebraic equations of conservation of fluxes. The implementation of these algebraic conservation equations is facilitated by the power-law scheme (Patankar, 1980) for the estimation of convective and diffusive fluxes over the surface of the control volume. The SIMPLER algorithm (Patankar, 1980) is used to treat the velocity-pressure coupling in the momentum equations.

Grid meshes used for the computational domains of tested flows in both straight pipe and sudden-expansion pipe consist of 60×90 non-uniformly distributed nodes. In order to reduce false diffusion in the investigation of recirculating flow by use of the power-law scheme, care must be taken in establishing the grid mesh. Distribution of grid nodes is arranged to ensure that small regions that exert a large influence on the flow field are adequately resolved. Numerical tests disclosed that the employed grid meshes yielded nearly grid-independent solutions for all investigated flow cases. The convergence criterion adopted in the present work is that the summation of the absolute mass residuals normalized by the inlet mass, in the entire computational domain, is less than 10^{-5}.

Results and Discussion

The validity of the proposed low-Reynolds-number k-ϵ model was first tested with two fully developed pipe flows. This model was next applied to the simulation of the flow in sudden-expansion pipe to demonstrate its usefulness particularly in the region near the reattachment point.

Straight Pipe Flow. The experimental work on a turbulent, fully-developed pipe flow conducted by Laufer (1954) was selected as the first test problem in this work. The test pipe was 12.4966 m long which is equivalent to 50.62 D (the diameter of the pipe, 0.24688 m). The Reynolds number based on the diameter of the pipe and the mean velocity (2.438 m/s) equaled 40,000. No measurements in the inlet region were provided in this experiment. Thus, uniform velocity profile was assumed at the inlet. The inlet profiles of k and ϵ were given in the following empirical manner (Nallasamy, 1987):

$$k=0.003u^2 \quad (16)$$

$$\epsilon=C_\mu k^{1.5}/0.03R \quad (17)$$

The outflow boundary condition was assumed to be fully developed in the calculation by using adequately long computational domain. At the bounded wall, all quantities vanished except ϵ_w, which had given in Table 3. At the symmetric axis, the zero gradient condition, $\partial\phi/\partial r=0$, was made except in the radial velocity component which is naturally zero.

Table 3 Summary of model constants and functions appearing in Table 2

Model	D	E	ϵ_w – B.C.	C_μ	C_1	C_2	σ_k	σ_ϵ
Standard	0	0	wall function	0.09	1.44	1.92	1.0	1.3
Launder-Sharma (1974)	$-\frac{\mu}{2k}\left(\frac{\partial k}{\partial y}\right)^2$	$2\mu\nu_t\left(\frac{\partial^2 u}{\partial y^2}\right)^2$	0	0.09	1.44	1.92	1.0	1.3
Lam-Bremhorst (1981)	0	0	$\frac{\partial\epsilon}{\partial y}=0$	0.09	1.44	1.92	1.0	1.3
Chien (1982)	$-2\mu k/y^2$	$-2\mu\epsilon e^{-0.5y^+}/y^2$	0	0.09	1.44	1.92	1.0	1.3
Nagano-Hishida (1987)	$-\frac{\mu}{2k}\left(\frac{\partial k}{\partial y}\right)^2$	$(1-f_\mu)\mu\nu_t\left(\frac{\partial^2 u}{\partial y^2}\right)^2$	0	0.09	1.44	1.92	1.0	1.3
Myong-Kasagi (1990)	0	0	$\epsilon_w=\nu\left(\frac{\partial^2 k}{\partial y^2}\right)$	0.09	1.4	1.8	1.4	1.3
Nagano-Tagawa (1990)	0	0	$\epsilon_w=\nu\left(\frac{\partial^2 k}{\partial y^2}\right)$	0.09	1.45	1.9	1.4	1.3
Present work	0	0	$\epsilon_w=\nu\left(\frac{\partial^2 k}{\partial y^2}\right)$	0.09	1.44	1.92	1.0	1.3

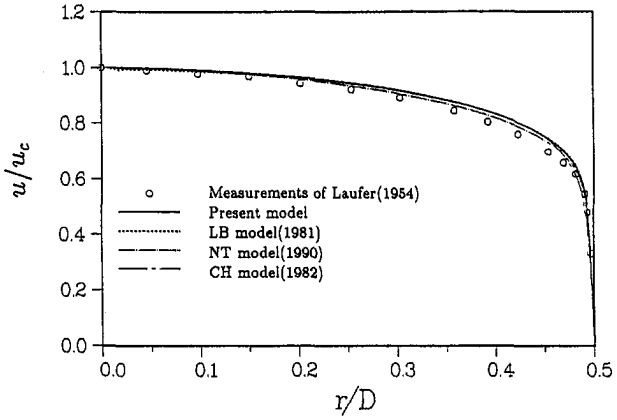

Fig. 1 Comparison of predicted and measured fully developed profiles of mean axial velocity component in straight pipe flow (Re = 40,000)

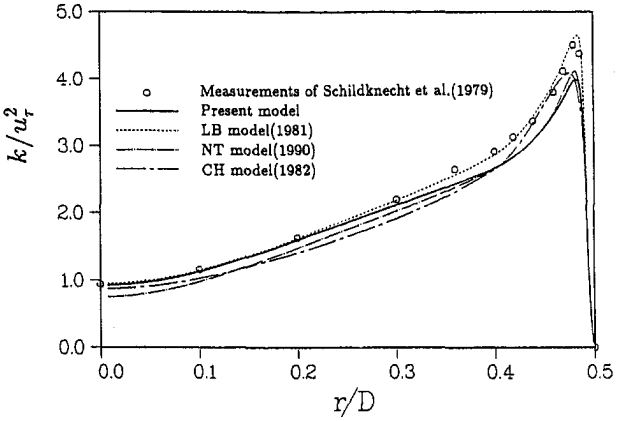

Fig. 3 Comparison of predicted and measured fully developed profiles of turbulent kinetic energy in straight pipe flow (Re = 17,250)

Figures 1 and 2 compare the predicted and measured fully developed profiles of mean axial velocity component and turbulent kinetic energy, respectively. Table 1 summarizes the low-Reynolds-number k-ϵ model developed in this work and another six models found in open literature. Patel et al. (1985) and Myong and Kasagi (1990) commented that the model developed by Launder and Sharma (1974) did not perform satisfactorily in the simulation of pipe flow. Our study also corroborates this comment. Therefore, the results obtained with this model are not included in Figs. 1 and 2. Since the model of Nagano and Tagawa (1990) performed better than its predecessor (Nagano and Hishida, 1987, the NH model), only the results obtained through the NT model are presented in Figs. 1 and 2. Also, our study reveals that the performance of the model of Myong and Kasagi (1990) resembles that of the NT model because both models adopt similar expressions of f_μ and f_2, as shown in Table 1. For the sake of brevity, the results obtained through the model of Myong and Kasagi (1990) are not included in Figs. 1 and 2. Thus, Figs. 1 and 2 present four sets of predictions, including the one obtained through the presently developed model. In terms of velocity profile, all of the predictions are in good agreement with the measurements, as is shown in Fig. 1. The comparison shown in Fig. 2 indicates that all four models are capable of capturing the peak location of turbulent-kinetic-energy profile. Generally speaking, the model of Lam and Bremhorst (1981, the LB model) seems to slightly overpredict the distribution of turbulent kinetic energy. The present model agrees well with the measurements in the near-wall region, while also overpredicts the distribution of turbulent kinetic energy in the core region. The performances of the CH and NT models agree satisfactorily with actual measurements.

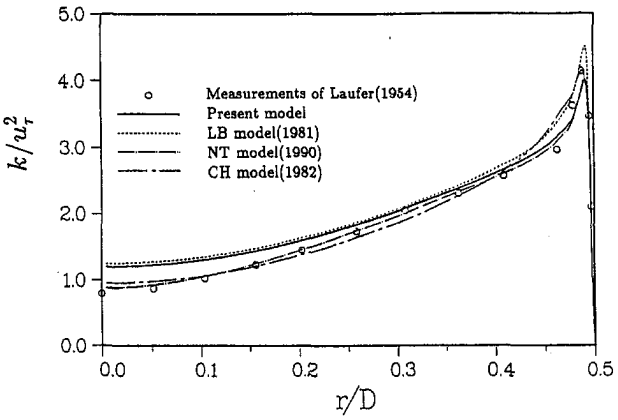

Fig. 2 Comparison of predicted and measured fully developed profiles of turbulent kinetic energy in straight pipe flow (Re = 40,000)

One more straight-pipe flow problem was tested in order to examine the generality of the developed low-Reynolds-number k-ϵ model. The work of other fully-developed pipe flow experiments conducted by Schildknecht, et al. (1979), was selected as the second test problem. The test pipe was 9 m long which was equivalent to 180 D (D = 0.05 m). Since no measurements in the inlet region were provided in this experiment, the same assumed inlet conditions which were used in the previous test problem were adopted. The case with Re = 17,250 investigated by Schildknecht et al. (1979) was run using the four different low-Reynolds-number k-ϵ models mentioned previously in this work. Again, all predictions of the mean axial velocity component using the four different models agree well with the measurements. For the sake of brevity, these results do not present here. Figure 3 compares the predicted and measured fully developed profiles of turbulent kinetic energy. A comparison of Figs. 2 and 3 reveals that the predicted profiles of turbulent kinetic energy in the previous and the present fully-developed-flow cases exhibit similar trends in all four investigated models. However, the LB model now has the best performance among the four investigated models. Both the CH and NT models exhibit slight underpredictions in Fig. 3. The performance of the present model falls between the other two.

A comparison of predicted f_μ values obtained through the four different models and the experimental f_μ values calculated by Patel et al. (1985) using the Laufer's data (1954) is made in Fig. 4. Clearly, the LB and CH models which were developed before 1985 are incapable of yielding correct predictions of the wall limiting behavior, i.e. $f_\mu \propto y^{-1}$, as is discussed in the review paper of Patel et al. (1985). Furthermore, the CH model gives poor f_μ predictions in the near wall region as displayed in Fig. 4. In general, f_μ distributions (including wall limiting behavior) obtained through the present model and the NT model are in favorable agreement with the experimental data taken from Patel et al. (1985).

In summary, the modified low-Reynolds-number k-ϵ model has been shown to work correctly in the two tests on fully developed flow in straight pipe.

Sudden-Expansion Pipe Flow. The experimental study of an axisymmetrical sudden-expansion flow conducted by Durret et al. (1988) was selected as the third test problem. The diameters of upstream (d) and downstream expansion (D) tubes were 50 mm and 95.2 mm, respectively, to achieve expansion ratio of 1.904. The test chamber was 660.8 mm long. The Reynolds number based upon the inlet diameter (D) and the mean velocity was 84,000. Durret et al. (1988) reported that the mean velocity profile at the inlet plane was very flat, and no other measured

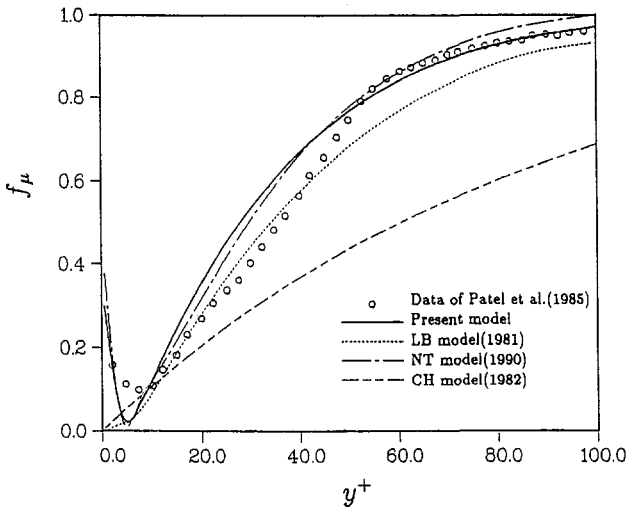

Fig. 4 Comparison of predicted f_μ profiles with the results of Patel et al. (1985) in near-wall region in straight pipe flow (Re = 40,000)

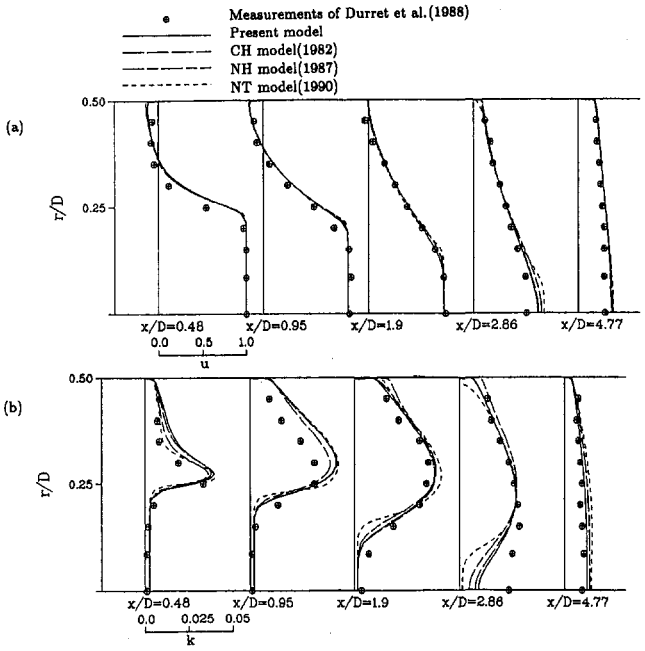

Fig. 5 Comparison of predicted and measured sectional profiles of (a) mean axial velocity component and (b) turbulent kinetic energy at five axial stations in pipe-expansion flow (Re = 84,000)

inlet information was provided. Therefore, the same assumed inlet profiles of k and ϵ described in Eqs. (16) and (17) were used for the calculation of the third test problem. Note that the radius R appearing in Eq. (17) denotes the radius of the upstream tube now.

Figures 5a and 5b compare the predicted and measured sectional profiles of mean axial velocity component and turbulent kinetic energy, respectively, at five axial stations. Of the four investigated low-Reynolds-number k-ϵ models, the LB model

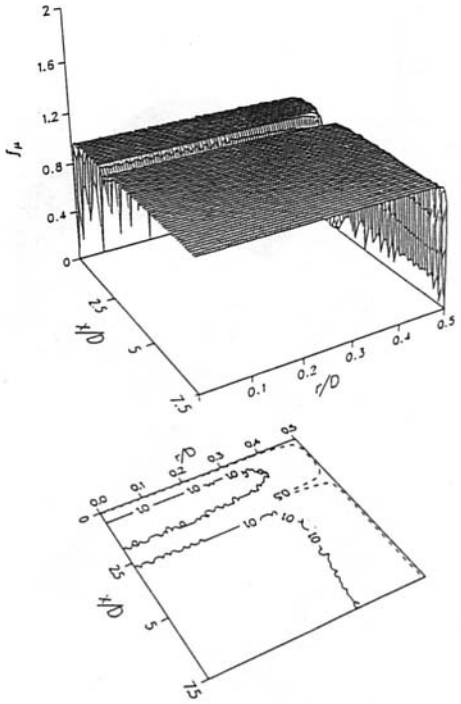

Fig. 6 Stereographic distribution of f_μ function obtained with the low-Reynolds-number k-ϵ model of Nagano and Hishida (1987)

lacks the capability to predict wall limiting behavior but does not encounter the singularity problem in applications on the recirculating flow in a pipe expansion (see Table 1). In contrast, the NT model is capable of predicting wall limiting behavior but faces the singularity problem in applications on the recirculating flow in a pipe expansion. The CH model, based upon the model functions listed in Table 1, possesses above deficiencies mentioned above. The results shown in Figs. 5a and 5b were obtained with the presently developed model, the CH model, the NT model, and the NH model. As Table 3 shows, the NT model adjusted the values of the turbulence model constants such as C_1, C_2, and σ_k best for experimental data in a straight-pipe flow (Nagano and Tagawa, 1990) in comparison to those conventionally used for the standard k-ϵ model. Nevertheless, the NH model adopts the same values of turbulence model constants as those used for the standard k-ϵ model and it exhibits similar performance characteristics as that of the NT model in application to the flows in straight pipe. Therefore, the results obtained through the NH model are included in Figs. 5a and 5b to demonstrate the influence of the values of the turbulence model constants on flowfield calculations in sudden expansion pipe. Generally speaking, the performances of the present model and the CH model are similar. These models take first place in terms of agreement with the measured data, as is shown in Figs. 5a and 5b. They are followed by the NH model, which takes second place, and the NT model, which gives somewhat unsatisfactory results in the downstream inner regions. This may be attributed to the adjustment of the turbulence model constants in the NT model (see Table 3). Thus, a comparison of the results in Figs. 5a and 5b shows less generality in the application of the NT model. The reattachment lengths predicted by using these mod-

Table 4 Comparison of reattachment lengths

Experiment (Durret et al., 1988)	Standard k-ϵ model	Present model	CH model (1982)	NH model (1987)	NT model (1990)	MK model (1990)
1.97 D	2.10 D	1.94 D	1.95 D	2.30 D	2.44 D	2.53 D

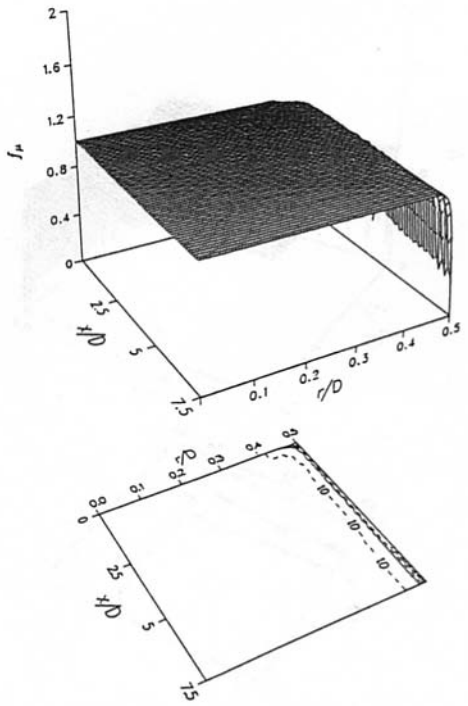

Fig. 7 Stereographic distribution of f_μ function obtained with the present model

els are summarized in Table 4 and compared with the measurement of Durret et al. (1988). Of the four investigated low-Reynolds-number k-ϵ models, the present and the CH models can give better predictions.

As mentioned in the previous discussion, singularity occurs in the neighborhood of the flow reattachment for some low-Reynolds-number k-ϵ models and is expressed in terms of the y^+ parameter. For example, Fig. 6 shows the stereographic distribution of the f_μ function obtained with the NH model. It is clearly shown that there a gap exists around the flow reattachment point. According to a concept adopted in construction of the low-Reynolds-number turbulence model, the model function f_μ plays a damping role when moving from the fully turbulent (high Reynolds number) region to the wall adjacent (low Reynolds number) region, as is demonstrated in Fig. 4. This requirement is equally valid even for the flow field over the reattachment point; that is, away from the viscosity-affected (boundary) layer, the f_μ function should approach unity value. However, the projected plot displayed in Fig. 6 shows f_μ contours that differ from this due to the singularity difficulty encountered in

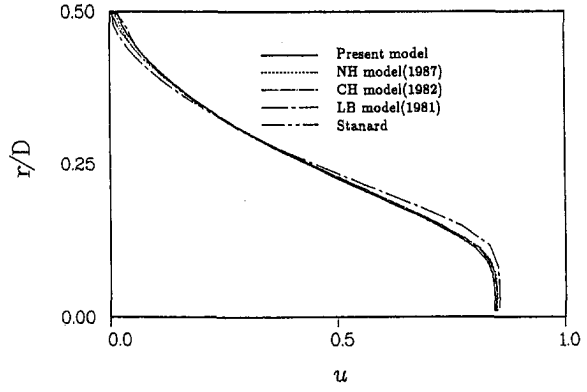

Fig. 8 Comparison of predicted profiles of mean axial velocity component using various models at reattachment point of pipe-expansion flow

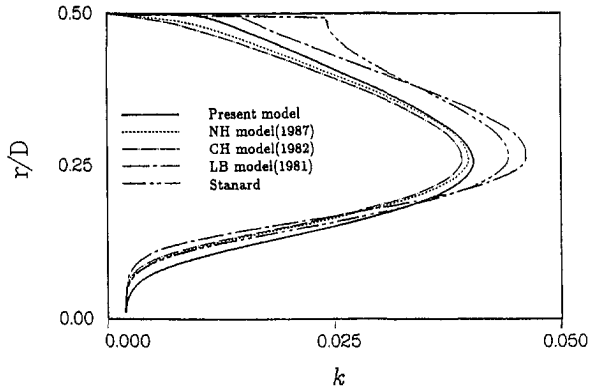

Fig. 9 Comparison of predicted profiles of turbulent kinetic energy using various models at reattachment point of pipe-expansion flow

the NH model. In contrast, implementation of the flow field calculation using the present model yields a f_μ distribution consistent with the physical state as displayed in Fig. 7. This corroborates the statement that the presently proposed functions of f_μ and f_2, in terms of the proper parameters, do not encounter singularity problems in applications on the recirculating flow in a pipe expansion.

Figures 8 and 9 compare the profiles of the mean axial velocity component and turbulent kinetic energy, respectively, predicted with the five models at each corresponding reattachment points. The predictions in Figs. 8 and 9 using various models do not differ significantly. This is because the influences of the existence of singularity on the governing equations for u and k were mainly calculated through the diffusion term, i.e. $(\mu + \mu_t)\nabla^2\phi$ (see Table 2). In formulation of the discrete conservation equations at a given grid node, the total flux crossing the surface of the control volume is composed of convection and diffusion terms. This means that the diffusion term just provides a partial contribution to the determination of total flux. Thus, the existence of singularity may result in some prediction errors for u and k but only to a limited extent. However, eddy viscosity defined by Eq. (2) is directly proportional to f_μ. Unlike the flow properties of u and k in which impact due to the influence of singularity is caused by the diffusion term in the governing equations, the impact of f_μ on μ_t due to the existence of singularity is direct and is further aggravated by the prediction errors conveyed from k and ϵ. Eddy viscosity is an important transport property in modeling turbulent transfers of momentum, heat, and mass. Moreover, the accurate prediction of f_μ distribution in the near-wall region is a prerequisite for attainment of correct solutions of wall heat/mass transfers.

Conclusions

A modified low-Reynolds-number k-ϵ model, which is capable of correctly yielding the near-wall limiting flow behavior (for the straight-pipe flow case) while avoiding occurrence of the singular problem near the reattachment point (for the pipe-expansion flow case), has been successfully developed. The performance of this model was assessed through the testing of two fully developed pipe flows and one recirculating flow in a pipe expansion. A comparison of the simulation and actual measurements reveals that this model gives flowfield predictions which are in good agreement with the measurements. It has been shown that significant improvements in predictions of flow properties particularly in the near-wall region of the reattachment point can be achieved through use of this model. Application of this model to recirculating flows in pipe expansion with wall heat transfer is now underway.

Acknowledgment

The authors gratefully acknowledge the grant support from the National Science Council of the Republic of China for this work under the contract NSC82-0401-E006-197.

References

Chapman, D. R., and Kuhn, G. D., 1986, "The Limiting Behavior of Turbulence Near a Wall," *Journal of Fluid Mechanics,* Vol. 170, pp. 265–292.

Chien, K. Y., 1982, "Predictions of Channel and Boundary-Layer Flows with a Low-Reynolds-Number Turbulence Model," *AIAA Journal,* Vol. 20, pp. 33–38.

Durret, R. P., Stevenson, W. H., and Thompson, H. D., 1988, "Radial and Axial Turbulent Flow Measurements with an LDV in an Axisymmetrical Sudden Expansion Air Flow," ASME JOURNAL OF FLUIDS ENGINEERING, Vol. 110, pp. 367–372.

Farhanieh, B., Davidson, L., and Sudén, B., 1993, "Employment of Second-Moment Closure for Calculation of Turbulent Recirculating Flows in Complex Geometries with Collocated Variable Arrangement," *International Journal of Numerical Methods for Fluids,* Vol. 16, pp. 525–544.

Lam, C. K. G., and Bremhorst, K. A., 1981, "A Modified Form of the k-ϵ Model for Predicting Wall Turbulence," ASME JOURNAL OF FLUIDS ENGINEERING, Vol. 103, pp. 456–460.

Laufer, J., 1954, "The Structure of Turbulence in Fully Developed Pipe Flow," NACA Report 1174.

Launder, B. E., and Sharma, B. I., 1974, "Application of the Energy-Dissipation Model of Turbulence to the Calculation of Flow Near a Spinning Disc," *Letters in Heat and Mass Transfer,* Vol. 1, pp. 131–138.

Marquardt, D. M., 1963, "An Algorithm for Least-Squares Estimation of Nonlinear Parameters," *Society for Industrial and Applied Mathematics, Journal,* Vol. 11, pp. 431–441.

Myong, H. K., and Kasagi, N., 1990, "A New Approach to Improved k-ϵ Turbulence Model for Wall-Bounded Shear Flows," *JSME International Journal, Series II,* Vol. 33, pp. 63–72.

Nagano, Y., and Hishida, M., 1987, "Improved Form of the k-ϵ Model for Wall Turublent Shear Flows," ASME JOURNAL OF FLUIDS ENGINEERING, Vol. 109, pp. 156–160.

Nagano, Y., and Tagawa, M., 1990, "An Improved k-ϵ Model for Boundary Layer Flows," ASME JOURNAL OF FLUIDS ENGINEERING, Vol. 112, pp. 33–39.

Nallasamy, M., 1987, "Turbulence Models and Their Applications to the Prediction of Internal Flows: a Review," *Computers and Fluids,* Vol. 3, pp. 151–194.

Nikjooy, M., and Mongia, H. C., 1991, "A Second-Order Modeling Study of Confined Swirling Flow," *International Journal of Heat and Fluid Flow,* Vol. 12, pp. 12–18.

Patankar, S. V., 1980, *Numerical Heat Transfer and Fluid Flow,* Hemisphere, Washington, D.C.

Patel, V. C., Rodi, W., and Scheuerer, G., 1985, "Turbulence Models for Near-Wall and Low-Reynolds-Number Flows: a Review," *AIAA Journal,* Vol. 23, pp. 1308–1319.

Schildknecht, M., Miller, J. A., and Meier, G. E. A., 1979, "The Influence of Suction on the Structure of Turbulence in Fully Developed Pipe Flow," *Journal of Fluid Mechanics,* Vol. 90, pp. 67–107.

Shih, T. H., and Lumley, J. L., 1993, "Kolmogorov Behavior of Near-Wall Turbulence and Its Application in Turbulence Modeling," *International Journal of Computational Fluid Dynamics,* Vol. 1, pp. 43–56.

Shih, T. H., and Mansour, N. N., 1990, "Modeling of Near-Wall Turbulence," NASA TM-103222.

Speziale, C. G., 1991, "Analytical Methods for the Development of Reynolds-Stress Closures in Turbulence," *Annual Review of Fluid Mechanics,* Vol. 23, pp. 107–157.

Structural Parameters and Prediction of Adverse Pressure Gradient Turbulent Flows: An Improved k-ϵ Model

G. Chukkapalli[1]

Ö. F. Turan[2]

Mechanical Engineering Department
Middle East Technical University,
Ankara 06531 Turkey

A modified k-ϵ model is proposed to predict complex, adverse pressure gradient, turbulent diffuser flows. The need for an eddy viscosity is eliminated by using three structural parameters. A fuller treatment of the rate of kinetic diffusion terms is incorporated with a Reynolds stress model representation. A thorough evaluation is given of the three structural parameters in three decreasing and one increasing adverse pressure gradient diffuser flows leading to a three-layer representation. The results indicate the need for better modeling of the ϵ-equation.

I Introduction

Prediction of adverse pressure gradient (APG) turbulent internal flows finds practical applications in designing turbomachinery passages, wind tunnels, and diffusers, in general. Such flows are complex according to the definition of Bradshaw (1976), and as a result, numerical prediction is difficult. The main reasons for this complexity are wall effects and the effects due to adverse pressure gradients. The effect of wall on turbulence structure is two-fold. First, viscous effects surface due to reduced local turbulence Reynolds number. Second, transverse normal Reynolds stresses are preferentially suppressed, and turbulent eddies are distorted in wall vicinity, thus making turbulence structure anisotropic. As a result of APG, the assumption of self-preservation in the longitudinal direction becomes questionable. Turbulence activity is greatly enhanced; in other words, additional mechanisms of production, dissipation, and transport of turbulence, such as through lateral vortex stretching, appear. Most prominent physical phenomena responsible for this additional activity are irrotational strains and lateral divergence. The presence of additional strain rates causes the interaction between mean flow field and turbulent eddies to be more complex. Contribution of normal stresses to kinetic energy production can no longer be neglected as in the case of simple flows.

The present study is a step toward practical numerical prediction of turbulent diffuser flows. Three decreasing and one increasing APG flows are examined. In the representation of Reynolds stresses, the concept of structural parameters is compared with the Boussinesq formulation. A modified k-ϵ model is proposed with structural parameters, and the triple correlation model of Hanjalič and Launder (1972, hereafter referred to as HL72) is incorporated into the exact kinetic diffusion of turbulence kinetic energy, k. The prediction of k, and of its rate of dissipation, ϵ, with the modified model are compared with the prediction using the conventional scalar gradient diffusion representation.

II Modeling Difficulties

Turbulent diffuser flows with the complexities mentioned above are still impractical for direct numerical simulation or large eddy simulation, due to their wide range of time and length scales. As a result, the prediction of these common turbulent flows have to depend on the averaged, unclosed Navier-Stokes (N-S) equations and closure modeling. In order for the closure models to predict complex flows with sufficient accuracy, they should incorporate various terms representing the physical mechanisms occurring. Hence, zero and one-equation models are generally not sophisticated enough for such flows. On the other hand, Reynolds stress equation models require modeling of more terms than two-equation models, such as pressure re-distribution and individual Reynolds stress dissipation rates. Since not all these modeled terms have been assessed experimentally, additional uncertainties arise.

A popular closure approach is to solve the transport equations for turbulence kinetic energy, k, and its rate of dissipation, ϵ, along with the averaged N-S equations. The unmodeled transport equations for k and ϵ in tensor form are given below:

$$Dk/Dt = \underbrace{-\partial/\partial x_i[\overline{u_i(p/\rho + k)}]}_{D} \underbrace{- \overline{u_i u_j}.\partial U_j/\partial x_i}_{P_k} + \underbrace{\nu.\partial/\partial x_i[\overline{u_j(\partial u_i/\partial x_j + \partial u_j/\partial x_i)}]}_{D_\nu} \underbrace{-\nu.\overline{(\partial u_i/\partial x_j + \partial u_j/dx_i)\partial u_j/\partial x_i}}_{\epsilon} \quad (1)$$

$$D\epsilon/Dt = \underbrace{-2.\nu.\partial U_i/\partial x_k(\overline{\partial u_i/\partial x_l.\partial u_k/\partial x_l} + \overline{\partial u_l/\partial x_i.\partial u_l/\partial x_k})}_{P_\epsilon} \underbrace{- 2.\overline{(\nu.\partial^2 u_i/\partial x_k/\partial x_l)^2}}_{\epsilon_\epsilon} \underbrace{- (\nu/\rho).\partial/\partial x_i(\overline{\partial p/\partial x_i \partial u_i/\partial x_l})}_{D_p} \underbrace{- 2.\nu.\overline{\partial u_i/\partial x_k \partial u_i/\partial x_l \partial u_k/\partial x_l}}_{P_{\epsilon T}} \underbrace{- \partial/\partial x_k(\overline{u_k \epsilon})}_{D_\epsilon} \quad (2)$$

where D, P_k, D_ν, and ϵ of Eq. (1) represent the rates of kinetic (turbulent) diffusion, production, viscous diffusion, and anisotropic rate of dissipation, respectively, of turbulence kinetic energy, k. Similarly, P_ϵ, ϵ_ϵ, D_p, $P_{\epsilon T}$, and D_ϵ of Eq. (2) represent the rates of production due to mean field, destruction, pressure diffusion, production due to turbulence, and turbulent diffusion, respectively, of ϵ. The kinetic diffusion and dissipation terms of the k-equation and most of the ϵ-equation terms, have to be modeled in terms of k, ϵ, and mean gradients in order to obtain a closed form. The pressure diffusion is neglected here based on the available experimental data for the k-equation (Turan and Azad, 1993).

[1] Now with the Mechanical Engineering Department, University of Toronto, Toronto, Ontario, Canada.

[2] Address correspondence to this author.

Contributed by the Fluids Engineering Division for publication in the JOURNAL OF FLUIDS ENGINEERING. Manuscript received by the Fluids Engineering Division September 3, 1992; revised manuscript received March 21, 1994. Associate Technical Editor: R. E. A. Arndt.

Basic k-ϵ Model. In the basic model, the kinetic diffusion is given by, $D = \partial/\partial x_i(\nu_T \partial k/\partial x_i)$, where $\nu_T = C_\mu k^2/\epsilon$ is the turbulence eddy viscosity. Reynolds stresses are modeled using the Boussinesq formulation as, $\overline{u_i u_j} = \nu_T.(\partial U_i/\partial x_j + \partial U_j/\partial x_i) + 2/3.\delta_{ij}k$. Thus, the rate of production becomes, $P_k = [\nu_T.(\partial U_i/\partial x_j + \partial U_j/\partial x_i) + 2/3.\delta_{ij}k].\partial U_i/\partial x_j$. The following isotropic form is used for the rate of dissipation: $\epsilon = \nu.(\partial u_i/\partial x_j)^2$. Similarly, the terms of the ϵ-equation are modeled as follows: $P_\epsilon = C_{\epsilon 1}.P_k.\epsilon/k$; $\epsilon_\epsilon = C_{\epsilon 2}.\epsilon^2/k$; $D_\epsilon = \partial/\partial x_i(\nu_T \partial\epsilon/\partial x_i)$; where $C_{\epsilon 1}$ and $C_{\epsilon 2}$ are model constants.

The basic two-equation model, i.e., the high Reynolds number k-ϵ transport equation model, fails to produce correct trends and most important, the correct limiting behavior, as the wall is approached. The main reasons for this discrepancy are, the assumption of isotropy in representing the individual Reynolds stresses and the rate of dissipation, ϵ, the asymptotic modeling for high turbulence Reynolds numbers, which neglects viscous effects, and incorrect near wall behavior of modeled Reynolds stresses. Since the first two assumptions break down as the wall is approached, these three points are linked.

A number of modified two-equation models has appeared in the literature to remedy the drawbacks of the basic k-ϵ model. Earlier models use high Reynolds number forms with wall functions. In more recent models, high Reynolds number models are modified for low Reynolds number applications using wall damping functions. In order to obtain the correct near wall behavior, P_ϵ and ϵ_ϵ of the ϵ-equation and ν_T are multiplied by wall damping functions f_1, f_2, and f_μ, respectively. A transport equation for $\tilde{\epsilon}$ rather than the isotropic dissipation ϵ, is solved in some cases, where $\tilde{\epsilon} = \epsilon - 2\nu(\partial k^{1/2}/\partial x)^2$. A comprehensive review of near wall models is given by Patel et al. (1985), and more recently by So et al. (1991) and Speziale et al. (1992). In addition, anisotropic k-ϵ models are proposed in which Reynolds stresses are linked to the mean gradients of higher order (Speziale, 1991). With these corrections to the basic k-ϵ model, most wall bounded flows, especially their mean flow fields, can be predicted with accuracy (Lai et al., 1989). Still, these modified models fall short of predicting the turbulence fields of arbitrary APG flows. This shortfall is due to the following three reasons:

1 *Representation of Reynolds Stresses.* In complex APG flows, local equilibrium between mean and turbulence structures does not exists. The response and recovery rates of the mean and turbulence fields to disturbances are quite different. Such history effects are not taken into account when the Boussinesq approximation is used. History effects are clearly demonstrated by Saddoughi and Joubert (1991) through their experimental evaluation of eddy viscosity. They indicate that Reynolds stresses cannot respond instantaneously to the rapid change of strain rates as modeled by an eddy viscosity model. In addition, normal Reynolds stresses, along with the shear stress $\overline{uv}$, take part in turbulence-mean flow interaction. Thus, any model which neglects or poorly models these additional stresses cannot be expected to predict the turbulence characteristics.

2 *Kinetic Diffusion Modeling.* Of the two commonly used kinetic diffusion models, namely, scalar gradient diffusion and bulk convection type of diffusion, most k-ϵ models use the isotropic gradient diffusion. Hence, the rate of kinetic diffusion of k is assumed proportional to scalar gradients of k. This modeling is based on the assumption that diffusion by turbulence fluctuations is similar to molecular diffusion. Scalar gradient diffusion is expected to yield poor results when turbulent transport is dominated by large eddies. Another disadvantage of this model is the assumption of isotropic diffusion such that diffusion of all normal Reynolds stresses in all three directions is taken to be similar. Thus, in complex APG flows, where kinetic diffusion is a major contributor toward the balance of both k and ϵ budgets, predictions of both of these scalars are expected to be poor. Noncoincidence of the peak production of these scalars with their peak values and shifting of peaks away from the wall also indicate the importance of the transport terms in APG flows.

3 *Representation of the Rate of Dissipation.* Almost all k-ϵ models use the isotropic ϵ-equation, because of the complexity of the anisotropic one. In addition, various terms, such as production, transport and destruction, of the isotropic ϵ-equation are modeled similar to that of the k-equation, even though there is not experimental evidence of both of these scalars being governed by identical mechanisms. Rate of dissipation obtained by solving the isotropic ϵ-transport equation grossly underestimates the true dissipation. Enhancement of dissipation especially near the wall by anisotropic mechanisms is being overlooked in the case of isotropic formulations. In addition, contribution to the dissipation or enhancement of dissipation by vortex stretching mechanisms is ignored in general in the ϵ-equation modeling. As a result, the rate of dissipation is underpredicted in turbulent diffuser flows because of the prominence of vortex stretching due to lateral streamline divergence. The problems associated with the ϵ-equation modeling leading to over-prediction of Reynolds stresses was first recognized by Pope (Hanjalič and Launder, 1980, hereafter referred to as HL80) who added an additional production term due to stretching of mean vorticity to the ϵ-equation for this purpose. Later, the under prediction of ϵ in APG flows was attributed by HL80 to poor representation of energy transfer mechanisms from energy containing eddies to dissipative eddies by irrotational strains. Thus, a coefficient, $C_{\epsilon 3}$, was proposed to enhance the production of ϵ by irrotational strains. This addition was proved successful later by Rodi and Scheuerer (1986) and more recently by Henau et al. (1990).

III Present Model

Structural Parameters. The importance of structural coefficients in relating Reynolds stresses to turbulence kinetic energy is evident from the experimental results of Cutler and Johnston (1989) and Fernholtz and Vagt (1981). This relationship is especially apparent in the case of complex flows with extra strain rates. Saddoughi and Joubert (1991) experimentally showed that deviation from the simple flow trend of the structural parameter which relates the turbulence shear stress to its kinetic energy is minimal in flows with streamline divergence. A similar pattern was also shown to be true in the case of weak APG flows (Bradshaw, 1967). In the present study, the relationship between Reynolds stresses and kinetic energy is analyzed from the available experimental data from APG diffuser flows. The detailed results are presented in Section IV. The eddy viscosity concept is replaced by structural parameters to relate various Reynolds stresses to the turbulence kinetic energy as follows: $\overline{uv} = a_1.k$; $\overline{u^2} - \overline{v^2} = a_2.k$; and $\overline{w^2} - \overline{v^2} = a_3.k$. From $k = (\overline{u^2} + \overline{v^2} + \overline{w^2})/2$, the following relationships between the normal Reynolds stress components and k can be obtained: $\overline{u^2} = b_1.k$; $\overline{v^2} = b_2.k$; $\overline{w^2} = b_3.k$; where $b_1 = (2 + 2.a_2 - a_3)/3$; $b_2 = (2 - a_2 - a_3)/3$; $b_3 = (2 - a_2 + 2.a_3)/3$.

Bradshaw et al. (1967) converted the kinetic energy equation into an equation for Reynolds shear stress by defining a_1 for thin shear flows in which case other stresses are negligible. Later, HL80 introduced a_2, still using the eddy viscosity concept in the case of APG flows. In both of these cases, a_1 and a_2 were assumed to be constants throughout the flow field. As it is shown in Section IV, the structural parameters a_1, a_2, and a_3 are not constants. The parameter a_3 is proposed in the present study, since both a_2 and a_3 are necessary to represent flow anisotropy in transverse and span-wise directions, respectively.

The Kinetic Diffusion and Production Terms of the k-Equation. The original diffusion term, D, of the k-equation, Eq. (1) contains triple velocity correlations which have to be

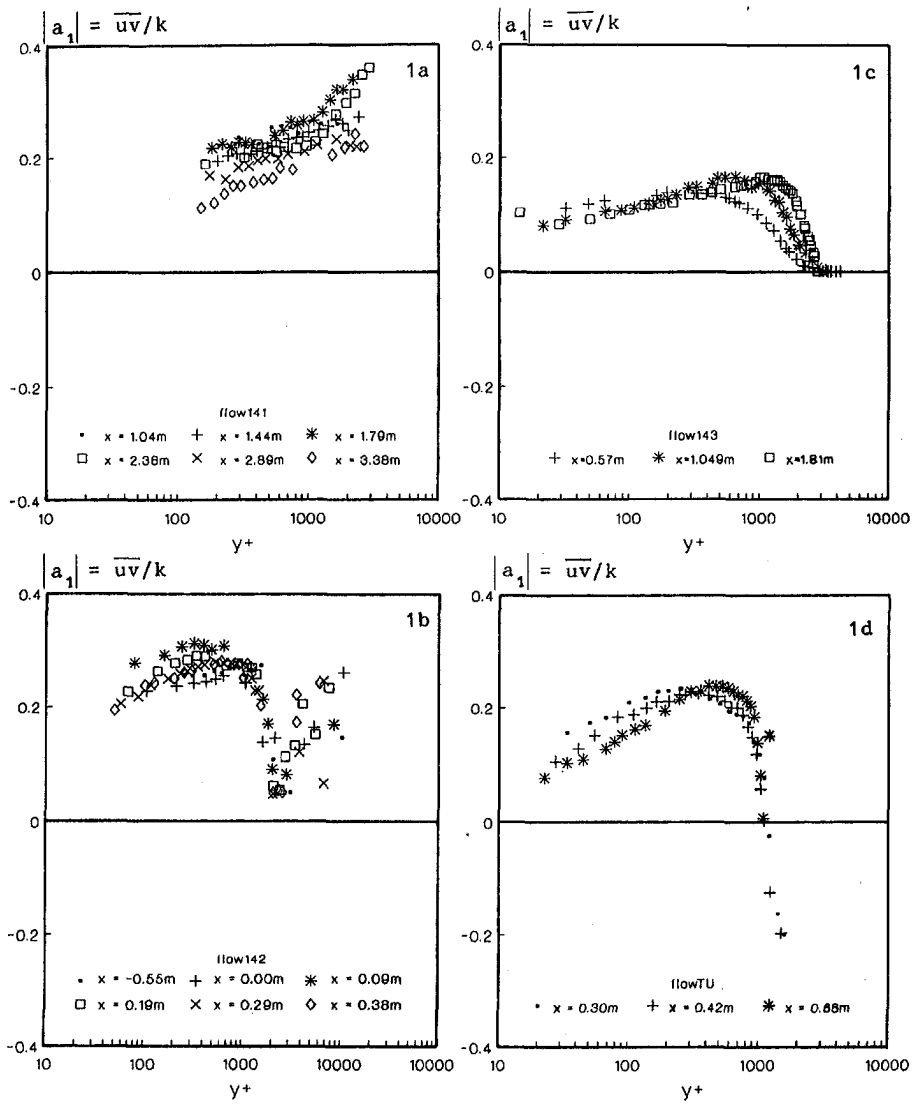

Fig. 1 Transverse variation of the structural parameter $|a_1|$ $(=\overline{uv}/k)$ at different longitudinal measuring stations in the four APG diffuser flows. In Figs. 1(*a*), 1(*b*), 1(c), and 1(*d*), Stations in FLOW 141, FLOW 142, FLOW 143 and FLOW TU, respectively, are shown.

modeled in terms of Reynolds stresses. Amano and Goel (1987) tested four triple correlation models against the experimental data from a backward facing step. This work indicates that HL72's symmetric expansion into gradients of Reynolds stresses yields the best results. Thus, their model is selected here: $\overline{u_iu_ju_k} = -C_sk/\epsilon(\overline{u_iu_l}\partial\overline{u_ju_k}/\partial x_l + u_ju_l\partial\overline{u_iu_k}/\partial x_l + \overline{u_ku_l}\partial\overline{u_iu_j}/\partial x_l)$. This model replaces the isotropic gradient diffusion form of the k-ϵ models found in the literature. Throughout the model development, the flow is assumed two dimensional for simplicity, and hence, the mean velocity and gradients in the third direction are neglected. When expanded in $r - \theta$ coordinates the turbulent diffusion term becomes,

$$-\partial/\partial x_i(\overline{u_ik}) = \partial/\partial x\{C_sk/\epsilon[\overline{u^2}(\partial k/\partial x + \partial\overline{u^2}/dx) + \overline{uv}(\partial k/\partial r + \partial\overline{u^2}/\partial r + \partial\overline{uv}/\partial x) + \overline{v^2}\partial\overline{uv}/\partial r]\} + 1/r\,.\,\partial/\partial r\{rC_sk/\epsilon[u^2\partial\overline{uv}/\partial x + \overline{uv}(\partial k/\partial x + \partial\overline{uv}/\partial r + \partial\overline{v^2}/\partial r) + \overline{v^2}(\partial k/\partial r + \partial\overline{v^2}/\partial r)]\}. \quad (3)$$

This expansion is similar to Henau et al.'s (1990). The Reynolds stresses in Eq. (3) are then expressed in terms of k using the structural parameters. The isotropic gradient diffusion model, $-\partial/\partial x_i(\overline{u_ik}) = \partial/\partial x(\nu_T/\sigma_k\,.\,\partial k/\partial x) + 1/r\,.\,\partial/\partial r(r\nu_T/\sigma_k\,.\,\partial k/\partial r)$, where $\nu_T = C_\mu k^2/\epsilon$, can be obtained from Eq. (3) by invoking isotropy. With the assumption of isotropy, the relationship between C_μ, σ_k, and C_s can be obtained as, $C_\mu/\sigma_k = (10/9)C_s$. The model constants of the present study are given in Section VI.

The production term, P_k, is incorporated without neglecting any normal stresses as the axial mean gradients and additional strains are not negligible for a conical diffuser. Thus, the rate of production of k, P_k is:

$$\overline{u_iu_j}.\partial U_j/\partial x_i = [\underbrace{\overline{uv}.(\partial U/\partial r + \partial V/\partial x)}_{\text{I}} + \underbrace{(\overline{u^2} - \overline{v^2}).\partial U/\partial x}_{\text{II}} + \underbrace{(\overline{w^2} - \overline{v^2}).V/r}_{\text{III}}]. \quad (4)$$

Here, Terms I, II, and III, respectively, represent the production due to basic shear, due to irrotational strain and due to lateral divergence specific to conical geometry. By using structural parameters, Eq. (4) becomes,

$$\overline{u_iu_j}\,.\,\partial U_j/\partial x_i = k.[a_1.(\partial U/\partial r + \partial V/\partial x) + a_2.\partial U/\partial x + a_3.V/r]. \quad (5)$$

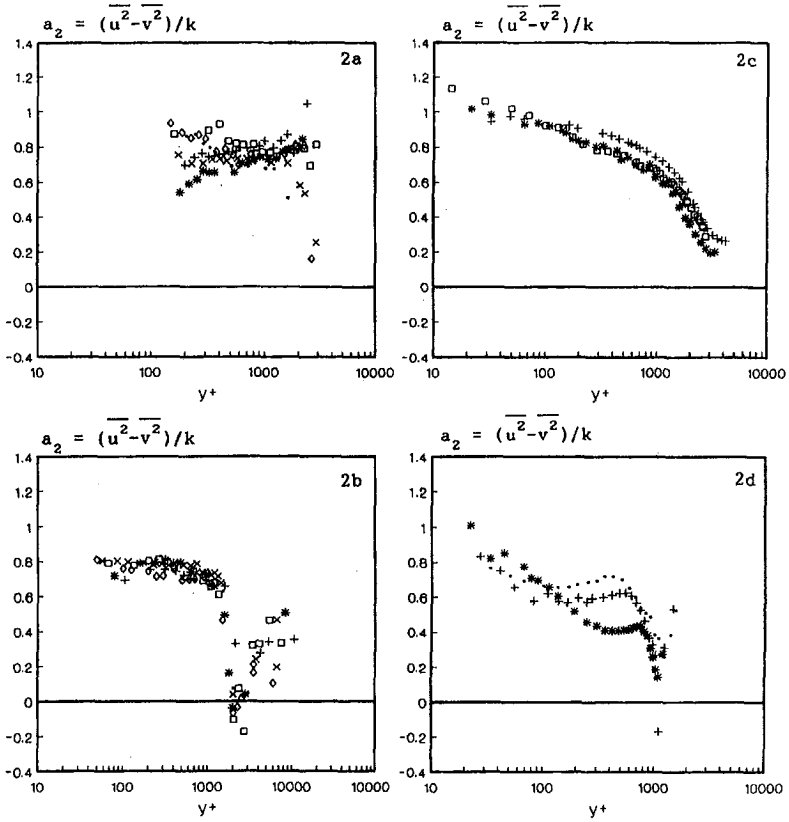

Fig. 2 Transverse variation of the structural parameter $a_2 (=\overline{u^2} - \overline{v^2})/k$ at different longitudinal measuring stations in the four APG diffuser flows. In Figs. 2(*a*), 2(*b*), 2(*c*), and 2(*d*), stations in FLOW 141, FLOW 142, FLOW 143, and FLOW TU, respectively, are shown. The legend is the same as in Fig. 1.

The ϵ-equation. The terms of the ϵ-equation, Eq. (2), are modeled similar to the basic k-ϵ model given in Section II, except for the rate of turbulent diffusion, D_ϵ, and the rate production, P_ϵ. The turbulent diffusion of the dissipation rate is modeled according to the HL72 model: $\partial/\partial x_k(\overline{u_k\epsilon}) = \partial/\partial x_k[-C_\epsilon k/\epsilon\overline{u_k u_l}\partial\epsilon/\partial x_l)]$. In cylindrical-polar coordinates, this model leads to the following:

$$D_\epsilon = -\partial/\partial x[C_\epsilon k/\epsilon(\overline{u^2}\partial\epsilon/\partial x + \overline{uv}\partial\epsilon/\partial r)] + 1/r\,.\,\partial/\partial r[rC_\epsilon k/\epsilon(\overline{uv}\partial\epsilon/\partial x + \overline{v^2}\partial\epsilon/\partial r)]. \quad (6)$$

The production of ϵ is taken as similar to that of k-production except that the generation due to irrotational strains are multiplied by a coefficient $C_{\epsilon 3}$ such that $C_{\epsilon 3} > C_{\epsilon 1}$ (HL80). Thus, the generation of ϵ is given by,

$$P_\epsilon = -\epsilon/k[[C_{\epsilon 1}\,.\,a_1\,.\,(\partial U/\partial r + \partial V/\partial x) + C_{\epsilon 3}a_2\,.\,\partial U/\partial x + C_{\epsilon 1}\,.\,a_3\,.\,V/r]. \quad (7)$$

IV Model Evaluation

Structural Parameters. Four adverse pressure gradient diffuser flows were selected for the evaluation of structural parameters and their behavior. These four flows are, FLOW 141, FLOW 142, and FLOW 143 of the 1981 AFOSR-HTTM conference (Kline et al., 1981) and an eight degree conical diffuser (Turan, 1988, referred as FLOW TU hereafter). In addition to having almost complete sets of experimental turbulence data, these flows have different enough APG characteristics to help assess generality of the structural parameter concept. FLOW 141 is an increasingly APG planar diffuser flow; whereas the others are decreasing APG conical diffuser flows. FLOW 143 has high core turbulence. FLOW TU has a fully developed inlet; whereas the others are boundary layer flows.

In Figs. 1 to 3, plots of the structural parameters, a_1, a_2, and a_3, respectively, are given as a function of y^+. In Figs. 1(a), 2(a), and 3(a), the structural parameter development is given at Stations $x = 2.38$ m and $x = 2.89$ m of FLOW 141 in steeply increasing APG; whereas Station $x = 3.38$ m is in decreasing APG ($x = 0$ indicates diffuser inlet). In Figs. 1(b), 2(b), and 3(b), the first 6 stations of FLOW 142 are presented. Of these, the last 3 stations are in steeply decreasing APG; whereas the first 3 are in the pipe and at the entrance to the diffuser. In Figs. 1(c), 2(c) and 3(c) the development of the three structural parameters in high core turbulence caused by a highly disturbed inlet is shown in FLOW 143. The variation of the structural parameters in FLOW TU, an 8 degree conical diffuser, are presented in Figs. 1(d), 2(d), and 3(d). The three stations shown are in mildly decreasing APG. Due to the experimental difficulties, a_1, a_2, and a_3 cannot be obtained for $y^+ < 20$.

Four zones are identified in the transverse direction in Figs. 1 to 3 for the structural parameters, a_1, a_2, and a_3:

1 *The Wall Region.* $y^+ < 10$. In this region, the asymptotic near wall behavior of the structural parameters is estimated from the asymptotic behavior of Reynolds stresses: $u^2 = a_u^2\,.\,y^{+2} + O(y^{+3})$; $v^2 = a_v^2\,.\,y^{+4} + O(y^{+5})$; $w^2 = a_w^2\,.\,y^{+2} + O(y^{+3})$; $|\overline{uv}| = a_{uv}\,.\,y^{+3} + O(y^{+4})$; $k = a_k\,.\,y^{+2} + O(y^{+3})$; where $a_u = 0.36$; $a_v = 0.009$; $a_w = 0.19$; $a_{uv} = 0.00072$; $a_k = 0.083$. The coefficients are taken from Kim et al.'s (1987) channel flow simulation data at Re = 6,500.

2 *The Logarithmic Region.* $20 < y^+ < 250$. In this region, parameters a_1, a_2, and a_3 follow a logarithmic variation with respect to y^+.

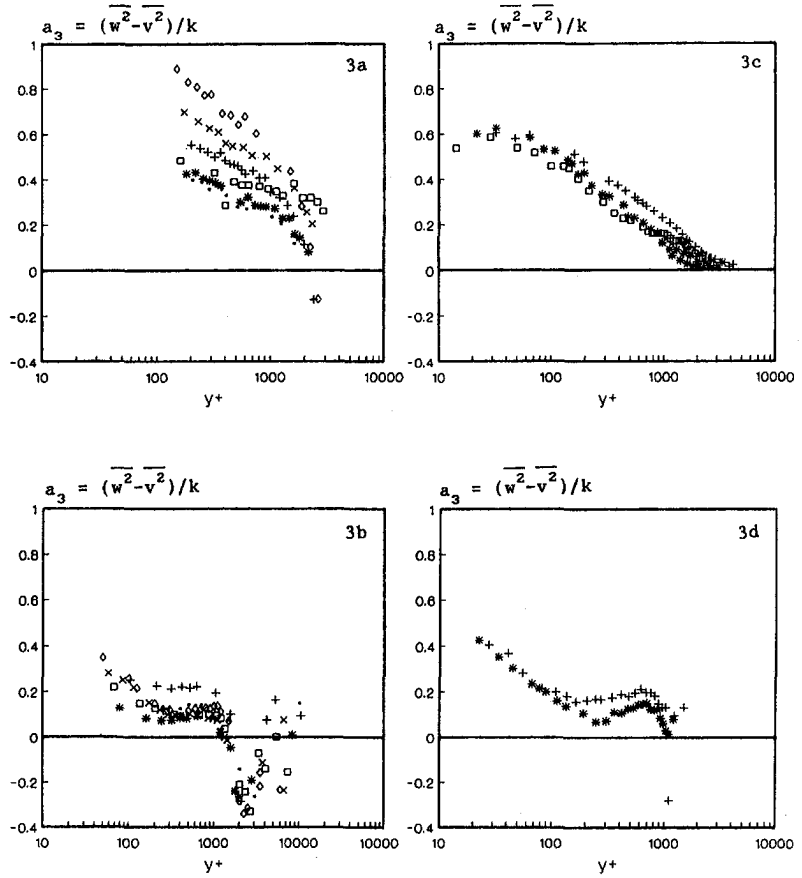

Fig. 3 Transverse variation of the structural parameter $a_3 (=\overline{w^2} - \overline{v^2})/k$ at different longitudinal measuring stations in the four APG diffuser flows. In Figs. 3(*a*), 3(*b*), 3(c), and 3(*d*), stations in FLOW 141, FLOW 142, FLOW 143, and FLOW TU, respectively, are shown. The legend is the same as in Fig. 1.

3 *The Constant Region.* Here, all the structural parameters are approximately constant, $y^+ > 250$.

4 *The Core Region.* Here, large scatter is observed due to division by small experimental values used in calculating the structural parameters. The uncertainty in the calculations due to experimental error is high in this region. Constant structural parameters may be assumed in the core without causing large errors due to weak turbulence and mean gradients.

The extent of the constant region depends on core turbulence and on increasing or decreasing APG. The constant region expands when the flow approaches equilibrium; whereas the logarithmic region is observed in all three decreasingly APG flows tested. In increasing APG, given in Figs. $1(a)$, $2(a)$, and $3(a)$ only two of the four regions identified above in decreasing APG, are present, namely, the constant region and the core region. The reason for this observation can be due to lack of experimental data for $y^+ < 100$ in this flow, where the logarithmic region is expected. Each of the structural parameters is modeled below according to the four regions identified above.

1 *Parameter* $a_1 = \overline{uv}/k$. This parameter represents the relationship between the energy transferring ($\overline{uv}$) and energy containing eddies (k). A flow disturbance which maximizes the momentum transport, increases a_1, and a flow disturbance which increases the turbulence kinetic energy without contributing to the momentum transport, reduces a_1. Thus, in APG flows, due to production of k by irrotational strain, lower values exist than in ZPG flows. The originally proposed value of constant $|a_1|$ is 0.30. $|a_1| = 0.22$ has been found to fit the constant a_1 region here.

In all the flows examined, the extend of the constant a_1 region increases as the flow becomes more and more developed, as seen in Fig. $1(d)$ for the fully developed case of FLOW TU. A similar pattern exists in the last stations of the FLOW 142, and hence, these stations are not shown here. This result is in agreement with previous observations of constant a_1 in equilibrium boundary layers. The value of the constant changes with the pressure gradient. For example, stations which are in a steep adverse pressure gradient such as $x = 2.89$ m in FLOW 141 and $x = 0.57$ m in FLOW 143, assume smaller values as seen in Figs. $1(a)$ and $1(c)$. At these stations, the extent of the flat region of a_1 versus y^+ can be attributed to the direct production of $\overline{v^2}$.

High core turbulence is expected to reduce a_1, as can be seen in Fig. $1(c)$ from the values calculated for FLOW 143. Close to the wall, all flows show smaller values which can be attributed to the wall effect (preferential damping of the normal component) leading to poor correlation.

2 *Parameter* $a_2 = (\overline{u^2} - \overline{v^2})/k$. As seen in Figs. $2(c)$ to $2(d)$, in all the flows examined, higher values of a_2 are calculated near the wall. This effect can be attributed to large production of $\overline{u^2}$ close to the wall due to high mean shear, and the wall damping effect on $\overline{v^2}$. The value of a_2 decreases steeply away from the wall as soon as the APG effects are felt. These effects, as discussed previously, increase v^2 and decrease u^2 making a_2 small. After this region, a_2 becomes nearly constant and approximately equal to 0.5, the extent of which once again depends on the status of equilibrium in the flow. In addition, the APG effects are much more pronounced in distorting the a_2

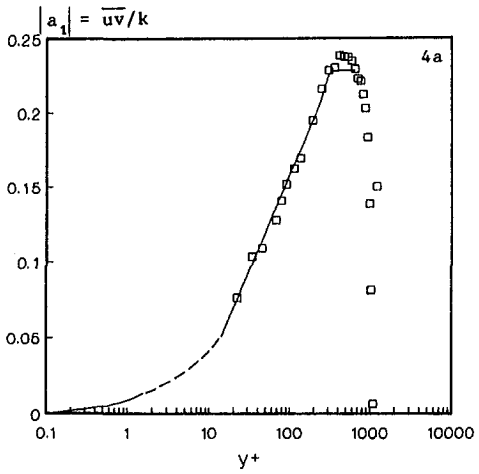

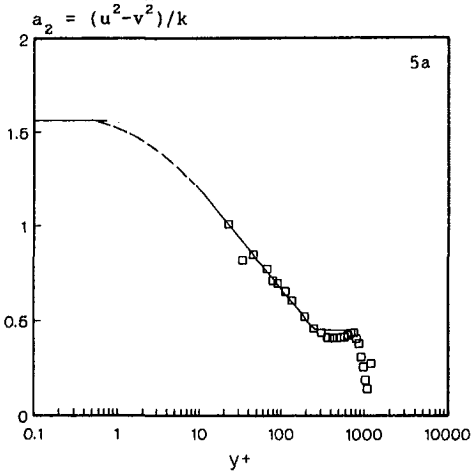

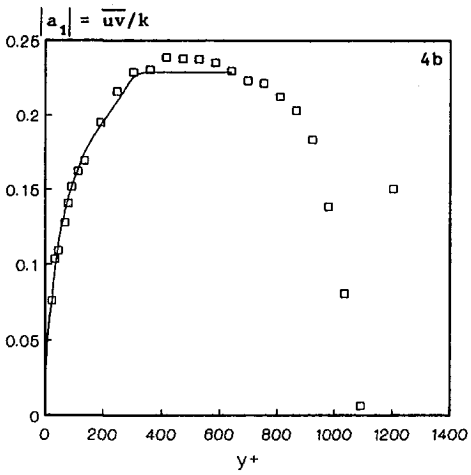

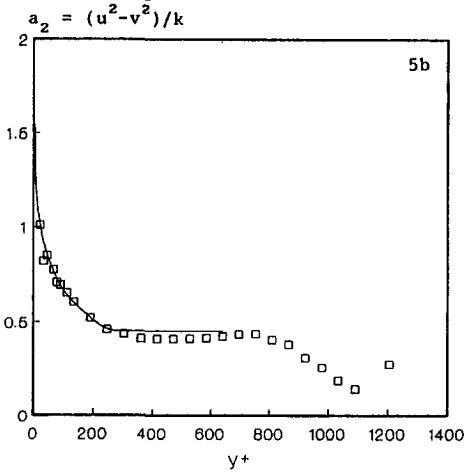

Fig. 4 The four region representation of the structural parameter $|a_1|$, given by Eq. (8*a*). Semi-logarithmic and linear plots are presented in Figs. 4(*a*) and 4(*b*), respectively, to highlight the logarithmic and constant regions. □, experimental data from the last station of FLOW TU (x = 66 cm), shown as an example.

Fig. 5 The four region representation of the structural parameter a_2, given by Eq. 8(*b*). Semi-logarithmic and linear plots are presented in Figs. 5(*a*) and 5(*b*), respectively. The legend is the same as in Fig. 4.

curve at a particular station than the a_1 curve. a_2 reaches a nonzero value of 1.56 asymptotically as the wall is approached; and hence, it represents large anisotropy close to the wall.

3 *Parameter* $a_3 = (\overline{w^2} - \overline{v^2})/k$. As seen in Figs. 3(*b*) to 3(*d*), due to the wall damping effect on v^2, a_3 is high near the wall, and falls off sharply away from the wall. This behavior of a_3 is similar to that of a_2 in the APG flows examined. The constant value of a_3 is approximately 0.1. In the case of FLOW 142, a_3 becomes negative at the inlet of the diffuser approximately half way between the wall and the center line, as shown in Fig. 3(*b*), similar to the behavior of a_2 in the same region in this flow shown in Fig. 2(*b*). Both of these patterns can be attributed to the direct production of v^2 at the edge of the shear layer.

As a result of these observations, it can be concluded that the structural parameters can be expressed as follows at any station:

$$a_1 = (\beta_1.y^+) + (a_{L1} + b_{L1}.\log y^+) + (a_{c1}), \qquad (8a)$$

$$a_2 = (\alpha_2 - \beta_2.y^{+2}) + (a_{L2} + b_{L2}.\log y^+) + (a_{c2}), \qquad (8b)$$

$$a_3 = \underbrace{(\alpha_3 - \beta_2.y^{+2})}_{y^+ < 10} + \underbrace{(a_{L3} + b_{L3}.\log y^+)}_{20 < y^+ < 250} + \underbrace{(a_{c3})}_{y^+ > 250}, \qquad (8c)$$

The wall region behaviors are given by the following: $a_1 = f(y^+) = \beta_1.y^+$; $a_2 = f(y^{+2}) = \alpha_2 - \beta_2.y^{+2}$; $a_3 = f(y^{+2}) = \alpha_3 - \beta_2 \cdot y^{+2}$; where $\beta_1 = a_{uv}/a_k$; $\alpha_2 = a_u^2/a_k$; $\beta_2 = a_v^2/a_k$ and $\alpha_3 = a_w^2/a_k$. The modeled behavior of a_1, a_2, and a_3 is illustrated in Figs. 4 to 6, respectively, in semi-log and linear plots. Hence, along with the correct near wall behavior of the predicted Reynolds stresses without requiring a wall damping function, such as f_μ, only the averaged turbulence quantities are required to be similar, instead of requiring similarity of the mean and turbulence fields, as would be the case with the eddy viscosity model (in that case, the near wall behavior would be, $\overline{u^2} \sim O(y^{+2})$, $\overline{v^2} \sim O(y^{+2})$ and $\overline{uv} \sim O(y^{+2})$).

Evaluation of the Kinetic Diffusion Term. FLOW TU has been used for evaluating the modeled triple correlations and diffusion term, since triple velocity correlation measurements are not available for the other three APG flows examined here. In Figs. 7(*a*) to 7(*f*), respectively, comparison is presented of experimental and modeled $\overline{u^3}$, $\overline{uv^2}$, $\overline{uw^2}$, $\overline{u^2v}$, $\overline{v^3}$, and $\overline{vw^2}$ correlations at station x = 66 cm (from the inlet of the 72-cm diffuser). Similar predictions are obtained at the remaining stations of this flow. In general, agreement is obtained within experimental error, except in the cases of $\overline{v^3}$ and $\overline{vw^2}$, as seen in Figs. 7(*e*) and 7(*f*).

Comparison of the total diffusion term, Eq. (3) (the HL72 model), with experimental data and the scalar gradient representation, is shown in Fig. 8 with C_s = 0.11. Agreement with

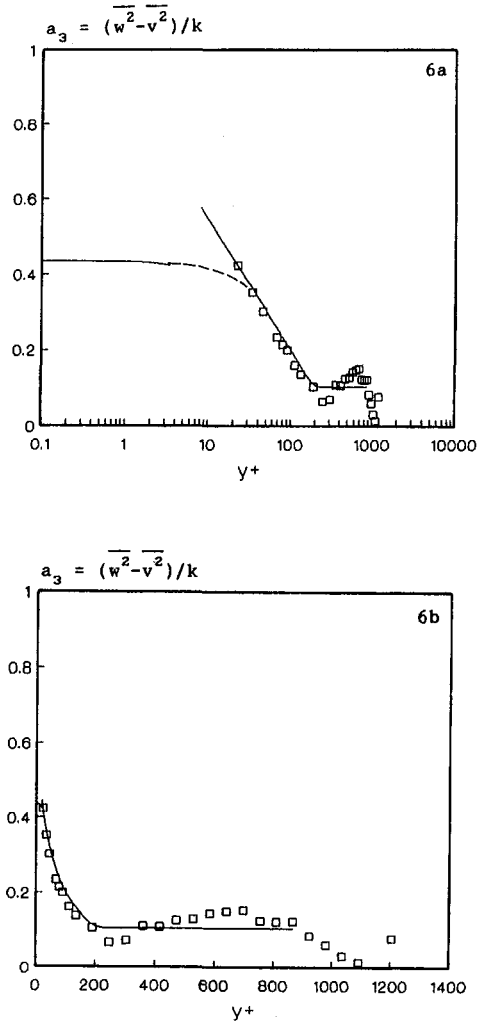

Fig. 6 The four region representation of the structural parameter a_2, given by Eq. 8(c). Semi-logarithmic and linear plots are presented in Figs. 6(a) and 6(b), respectively. The legend is the same as in Fig. 4.

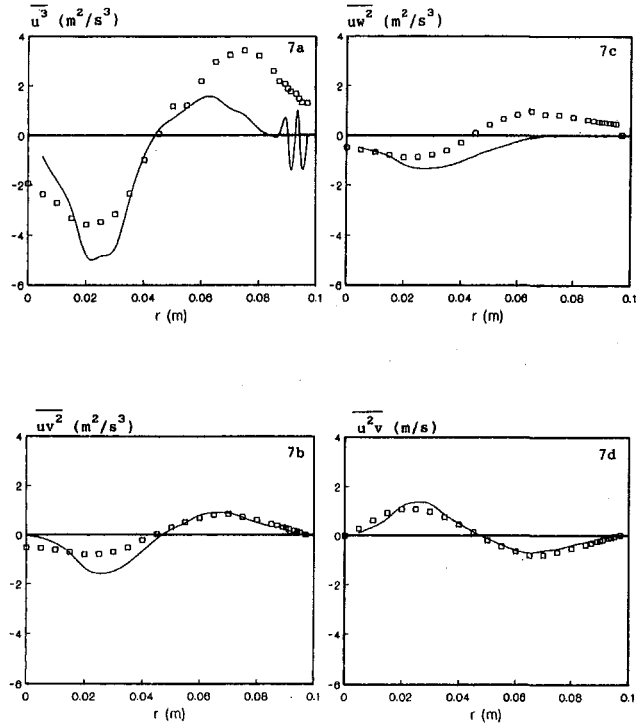

Fig. 7 Comparison of the HL72 modeled (solid line) and experimental (□) triple velocity correlations $\overline{u_i u_j u_k}$ in the last station, x = 66 cm, of FLOW TU. Hot-wire measurements were corrected for yaw and high turbulence intensity (Turan, 1988). In Figs. 7(a) to 7(f), respectively, transverse variations of u^3, uv^2, uw^2, u^2v, v^3, and vw^2 are given.

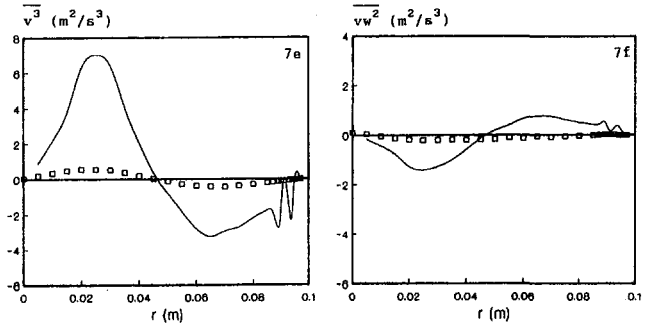

Fig. 7 (Cont.)

experimental data is observed except for the oscillations in modeled terms around the centerline and close to the wall. These oscillations are due to differentiation of discrete experimental values. The near wall behaviors of both the scalar gradient diffusion and the HL72 model are incorrect with respect to the expected asymptotic behavior of the unmodeled diffusion term, $O(y^{+3})$. The scalar gradient and HL72 modeled diffusion terms have $O(y^{+2})$ and $O(y^{+4})$ variations, respectively. Since the rate of turbulent diffusion close to the wall is negligible compared to the rate of viscous diffusion and dissipation, the incorrect near-wall behavior has been found not to affect k and ϵ predictions here.

V Numerical Procedure

Only the k and ϵ transport equations are solved here by inputting the necessary mean flow data. FLOW TU is used for this purpose. The equations are solved radially for four stations by inputting the axial gradients. Control volume approach is used to obtain the algebraic equations with Patankar's power law scheme for approximating the control volume face values (Patankar 1980). The additional nongradient diffusion terms of the present model are integrated according to the control volume approach. This additional kinetic diffusion cannot be used in calculating the Peclet number. Errors due to the power law scheme are not investigated here, although the power law scheme is known to give large errors at a Peclet number of 2. The first experimental data point is given as the wall boundary condition. The results are shown with a grid equivalent to that of experimental data although grid independence has been checked. Initial guess independence has also been verified. A residual of 10^{-5} is kept as the convergence criterion for all cases presented. Further details are given by Chukkapalli (1993).

VI Comparison of Predicted k and ϵ With Experimental Data

While scrutinizing the results, two points should be kept in mind. First, experimental errors affect the predicted results. Second, errors due to differentiating discrete experimental points lead to oscillations. These two effects are expected to be prominent close to the wall.

The computations were carried out first for a fully developed pipe flow. The Reynolds number based on the centerline velocity was 139,000 ± 3000 (Turan, 1988). This flow at the inlet of FLOW TU was chosen as a simple test case. For comparison

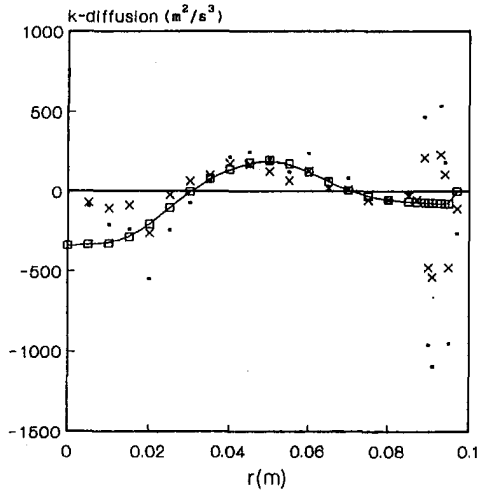

Fig. 8 Comparison of the modeled rate of kinetic energy diffusion of k (Eq. (3), ·) with experimental data (□) and isotropic scalar gradient diffusion model (x) of the eddy viscosity k-ϵ model. The experimental data are from the last station, x = 66 cm, of FLOW TU.

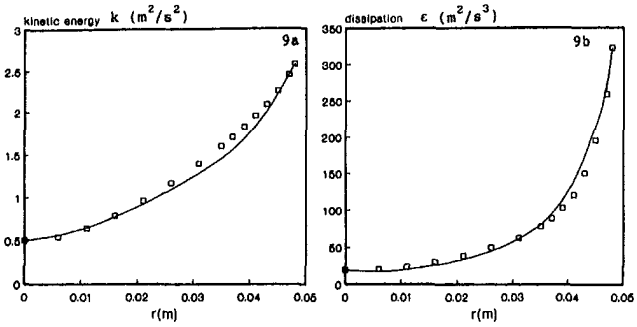

Fig. 9 Comparison of the predicted k and ϵ with experimental data (□) from a fully developed pipe flow (inlet of FLOW TU, Re = 139,000, ±3000). The eddy viscosity k-ϵ model was used in the prediction with the unmodified Y-O constants.

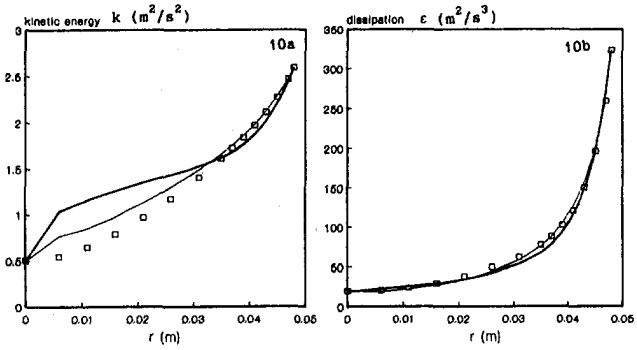

Fig. 10 Comparison of the k and ϵ variations predicted with the eddy viscosity k-ϵ model using the modified Y-O constants (light line) with the present model (dark line) and with experimental data (□) from the same fully developed pipe flow as in Fig. 9.

with the present model, the eddy viscosity k-ϵ model was also used. Out of the several model constants tried, the constants derived from the renormalization group (RNG) methods by Yakhot and Orszag (referred to as Y-O hereafter, Speziale, 1991) gave the best results. These model constants are, σ_k = 0.7179; σ_ϵ = 0.7179; C_μ = 0.0837; $C_{\epsilon 1}$ = 1.42; $C_{\epsilon 2}$ = 1.7215. The pipe results are presented in Figs. 9(a) and 9(b). As can be seen from these plots, both k and ϵ predictions are within

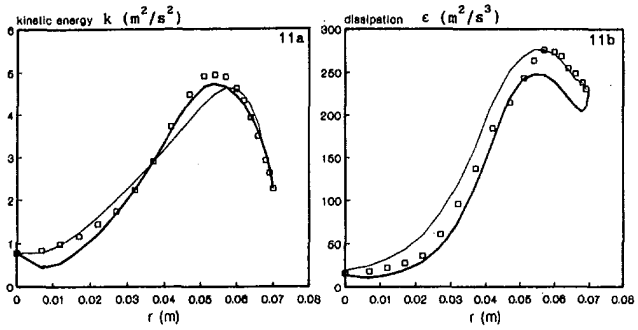

Fig. 11 Comparison of the k and ϵ variations predicted with the eddy viscosity k-ϵ model using the modified Y-O constants with the present model and with experimental data from x = 30 cm of FLOW TU. The legend is the same as in Fig. 10.

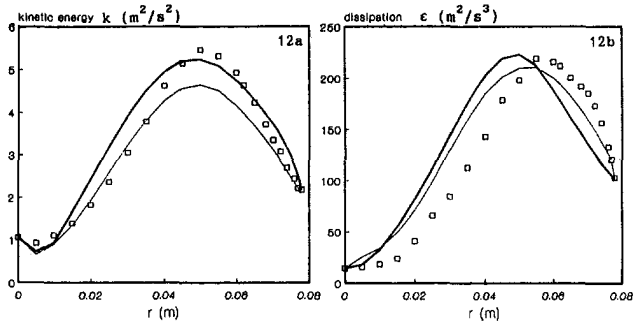

Fig. 12 Comparison of the k and ϵ variations predicted with the eddy viscosity k-ϵ model using the modified Y-O constants with the present model and with experimental data from x = 42 cm of FLOW TU. The legend is the same as in Fig. 10.

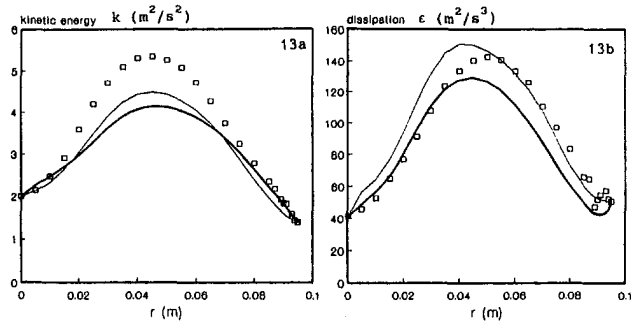

Fig. 13 Comparison of the k and ϵ variations predicted with the eddy viscosity k-ϵ model using the modified Y-O constants with the present model and with experimental data from x = 66 cm of FLOW TU. The legend is the same as in Fig. 10.

experimental uncertainty which is given by Turan and Azad (1993) to be ±20 percent in ϵ obtained as the closing term of Eq. (1), based on repeatability.

The computations failed to converge when the eddy viscosity k-ϵ model is used with the same constants in the diffuser flow, FLOW TU, along with $C_{\epsilon 3}$ in the ϵ-equation. Slight modifications to these coefficients gave good prediction of experimental results both in the pipe and diffuser flows, as can be seen in Figs. 10(a) to 13(b). In these figures, the k and ϵ predicted with the present modified k-ϵ model and with the eddy viscosity k-ϵ model using the modified Y-O constants are compared with the experimental data. The modified Y-O constants are as follows: σ_k = 0.7319; σ_ϵ = 0.7319; C_μ = 0.0730; $C_{\epsilon 1}$ = 1.42; $C_{\epsilon 2}$ = 1.7235. $C_{\epsilon 3}$ = 4.44 (Rodi and Scheuerer, 1986) was used in the diffuser flow predictions. These modified constants were

calculated with a minimum nodal residual criterion for all four stations examined.

The constants of the present model are as follows: $C_s = 0.11$; $C_\epsilon = 0.15$; $C_{\epsilon 1} = 1.395$; $C_{\epsilon 2} = 1.92$. These coefficients are similar to Hanjalič and Launder's (1976). Here, $C_{\epsilon 1}$ is derived from $C_{\epsilon 2}$ and C_ϵ using the following expression: $C_{\epsilon 1} = C_{\epsilon 2} - 3.5C_\epsilon$, as derived by HL72 for a constant shear layer. A $C_{\epsilon 3}$ of 2.5 was used by HL80. This value was modified to 4.44 and 5.6, respectively, by Rodi and Scheuerer (1986) and Henau et al. (1990). In the present study, $C_{\epsilon 3} = 3.49$, 6.42 and 4.74, respectively, are calculated as the optimum values for the results given in Figs. 11, 12, and 13.

From a comparison of Figs. 9(*a*) and 9(*b*) with Figs. 10(*a*) and 10(*b*), it can be seen that the eddy viscosity k-ϵ model with the unmodified Y-O constants gives better prediction of both k and ϵ in the fully developed pipe flow. This result is expected, since the eddy viscosity k-ϵ model and the Y-O constants were developed for simpler (zero or favorable pressure gradient) turbulent flows. In the APG diffuser flow as seen from Figs. 11(*a*) to 13(*b*), an improvement can be observed in the predicted k and ϵ when the present modified model is used, in comparison with the predictions obtained with the eddy viscosity k-ϵ model with the modified Y-O constants. The improvement is in that the predicted slopes are closer to the experimental ones when the present model is used. Since the gradients of Reynolds stresses calculated using structural parameters are needed in the averaged mean equations, the present model is expected to give better prediction of the mean flow field for engineering applications.

The improvement obtained in predicting k and ϵ with the present model is less than expected with the improved representation of Reynolds stresses and kinetic diffusion. This discrepancy can be attributed to the poor modeling of the terms of the ϵ-equation, as also indicated by the lack of generality of the model constant $C_{\epsilon 3}$. As mentioned before, various terms of the ϵ-equation should be modeled by logical approximation of the exact terms rather than adopting the k-equation modeling. Therefore, experimental results from complex cases, or direct numerical simulation data of simple flows, are needed of the terms of the exact ϵ-equation for testing the modeled terms.

VII Conclusions

The development of structural parameters a_1, a_2, and a_3 is examined in four APG plane and conical diffuser flows. A third structural parameter, a_3, is introduced in addition to a_2 of HL72 and a_1 of Bradshaw et al., to account for the production of k due to lateral strain for conical cases. It is shown that the structural parameters are not constant in these flows. A four-region description is proposed for each structural parameter, which includes the near wall limiting behavior for $y_+ < 10$ followed by a logarithmic region and a constant region.

A modified k-ϵ model is developed which uses structural parameters instead of the Boussinesq approximation in estimating Reynolds stresses. The rate of kinetic diffusion of k is derived from the expansion of triple correlations using the HL72 modeling which reduces to the conventional scalar gradient diffusion form if isotropy is assumed. Similarly, the rate of kinetic diffusion of ϵ of the full Reynolds stress model of HL72 is introduced in conjunction with the structural parameters into the ϵ-equation. With these changes, the modified model enables better prediction of k and ϵ in an APG turbulent diffuser flow.

Acknowledgments

This work was supported financially by NSERC (Natural Sciences and Engineering Research Council) Canada. The authors are grateful to S. Tomaçoğlu of METU for revising the figures.

References

Amano, R. S., and Goel, P., 1987, "Investigation of Third-Order Closure Model of Turbulence for the Computation of Incompressible Flows in a Channel With a Backward-Facing Step," ASME JOURNAL OF FLUIDS ENGINEERING, Vol. 109, pp. 424–428.

Bradshaw, P., 1967, "The Structure of Equilibrium Boundary Layers," *Journal of Fluid Mechanics,* Vol. 29, pp. 624–645.

Bradshaw, P., 1976, "Complex Turbulent Flows," *Theoretical and Applied Mechanics,* W. T. Koiler, ed., North Holland Publishing Co., pp. 103–113.

Bradshaw, P., Ferris, D. H., and Atwell, N. P., 1967, "Calculation of Boundary-Layer Development Using the Turbulent Energy Equation," *Journal of Fluid Mechanics,* Vol. 28, pp. 593–616.

Chukkapalli, G., 1993, "An Experimental and Numerical Investigation of an Increasing Adverse Pressure Gradient Turbulent Boundary Layer," M. Eng. thesis, Mechanical Engineering Department, McMaster University.

Cutler, A. D., and Johnston, J. P., 1989, "The Relaxation of a Turbulent Boundary Layer in Adverse Pressure Gradient," *Journal of Fluid Mechanics,* Vol. 200, pp. 367–387.

Fernholtz, H. H., and Vagt, J.-D., 1981, "Turbulence Measurements in an Adverse Pressure Gradient Three-Dimensional Turbulent Boundary Layer Along a Circular Cylinder," *Journal of Fluid Mechanics,* Vol. 111, pp. 233–269.

Hanjalič, K., and Launder, B. E., 1972, "A Reynolds Stress Model of Turbulence and Its Application to Thin Shear Flows," *Journal of Fluid Mechanics,* Vol. 52, pp. 609–638.

Hanjalič, K., and Launder, B. E., 1976, "Contribution Towards a Reynolds-Stress Closure for Low-Reynolds-Number Turbulence," *Journal of Fluid Mechanics,* Vol. 74, pp. 593–610.

Hanjalič, K., and Launder, B. E., 1980, "Sensitization the Dissipation Equation to Irrotational Strains," ASME JOURNAL OF FLUIDS ENGINEERING, Vol. 102, pp. 34–40.

Kim, J., Moin, P., and Moser, R. D., 1987, "Turbulence Statistics in Fully Developed Channel Flow at Low Reynolds Number," *Journal of Fluid Mechanics,* Vol. 177, pp. 133–186.

Kline, S. J., Kantwell, B. J., and Lilly, G. M., 1980–81, AFOSOR-HTTM-Stanford Conference on Complex Turbulent Flows: Comparison of Computation and Experiment.

Lai, Y. G., So, R. M. C., and Hwang, B. C., 1989, "Calculation of Planar and Conical Diffuser Flows," *AIAA Journal,* Vol. 27, pp. 542–548.

Patankar, S. V., 1980, *Numerical Heat Transfer and Fluid Flow,* Hemisphere Publications.

Patel, V. C., Rodi, W., and Scheuerer, G., 1985, "Turbulence Models for Near-Wall and Low Reynolds Number Flows: A Review," *AIAA Journal,* Vol. 23, pp. 1308–1319.

Rodi, W., and Scheuerer, G., 1986, "Scrutinizing the k-ϵ Turbulence Model Under Adverse Pressure Gradient Conditions," ASME JOURNAL OF FLUIDS ENGINEERING, Vol. 108, pp. 174–179.

Saddoughi, S. G., and Joubert, P. N., 19XX, "Lateral Straining of Turbulent Boundary Layers Part I: Streamline Divergence," *Journal of Fluid Mechanics,* Vol. 229, pp. 173–204.

So, R. M. C., Lai, Y. G., Zhang, H. S., and Hwang, B. C., 1991, "Second Order Near-Wall Closures: A Review," *AIAA Journal,* Vol. 29, No. 11, pp. 1819–1835.

Speziale, C. G., 1991, "Analytical Methods for the Development of Reynolds Stress Closures in Turbulence," *Annual Review of Fluid Mechanics,* Vol. 23, pp. 107–157.

Speziale, S. P., Abid, R., and Anderson, E. C., 1992, "Critical Evaluation of Two-Equation Models for Near-Wall Turbulence," *AIAA Journal,* Vol. 30, pp. 324–331.

Turan, Ö. F., 1988, "Further Study of a New Method of Evaluating Turbulence Dissipation," Ph.D. Thesis, Mechanical Engineering, Department, University of Manitoba.

Turan, Ö. F., and Azad, R. S., 1993, "Comparison of the Zero-Wire-Length Dissipation Technique with Spectral Corrections and the Effect of High Turbulence Intensity," *Experimental Thermal Fluid Science,* Vol. 6, pp. 292–308.

Structure of Turbulence in an Incipient-Separating Axisymmetric Flow

(Data Bank Contribution)*

Rakesh K. Singh

Ram S. Azad

Department of Mechanical and Industrial Engineering, University of Manitoba, Winnipeg, Manitoba, Canada R3T 2N2

The relative intensity, skewness, and flatness of fluctuating streamwise velocity along the centerline of an 8 deg included angle conical diffuser show dramatic rapid growth in the final stages of the flow under the increasing influence of growing instantaneous reversals in the wall-layer. Pulsed-wire anemometry was effectively used for the measurement of quantitative instantaneous reversals and the turbulent flow field. In the severe adverse pressure gradient of the diffuser flow, the maxima of the streamwise and transverse fluctuating velocities, Reynolds shear stress, and turbulent energy production coincide and move away from their near-wall position in the pipe, also the velocity triple products show completely opposite nature as compared to the pipe flow. These measurements reveal the strong influence of instantaneous backflow on the structure of turbulence. The present results further corroborate the ability of the "structural" turbulence model of Nagano and Tagawa (1990) to predict velocity triple products in an axisymmetric diffuser flow.

Introduction

The efficient performance of conical diffusers is very important in practice as these are critical elements in turbomachinery and commonly used in many other flow devices to increase pressure and reduce kinetic energy of the flows. This has led to a significant number of experimental and computational investigations. The flow in a conical diffuser is one of the complex turbulent flows reviewed by Bradshaw (1975). In the initial region of a conical diffuser the flow is subjected to sudden perturbations of severe adverse pressure gradient, streamline curvature, lateral divergence, and extra strain rates, resulting in the initiation and growth of instantaneous backflow in the wall layer. Smits and Wood (1985) have reviewed the behavior of turbulent boundary layers subjected to sudden perturbations and highlighted the limitations of modeling multiple perturbations as we do not know a priori how their nonlinear interaction may proceed. This makes conical diffuser flows nearly intractable for accurate prediction of the turbulence flow field employing most of the present turbulence models (Lai et al., 1989; Cho and Fletcher, 1991). Therefore, to validate prediction models and to enhance our understanding of the complicated axisymmetric separating flows, extensive experimental investigations must be conducted using new measurement techniques (e.g., Dengel and Fernholz, 1990) to obtain some accurate information about the turbulent quantities and quantitative instantaneous backflow.

An eight-degree total angle conical diffuser with an area ratio 4:1 has highest effectiveness of all the conical diffusers (Sovran and Klomp, 1967). This optimum geometry was selected for the present study. The local turbulence intensity level (over 80 percent in the wall region) in this diffuser was much higher than most of the other complex shear flows (Ruderich and Fernholz, 1986). Most of the earlier studies in the near-optimum-geometry conical diffuser flows used conventional pressure measurements or hot-wire anemometry, which were unable to detect and take into account the presence of instantaneous backflow. In the present study the pulsed-wire anemometry (Bradbury and Castro, 1971; Castro, 1992) has been used to measure turbulent flow field. The results are presented for Reynolds number ($\equiv U_{bi}D_i/\nu$) of 6.9×10^4, based on the mean bulk velocity, U_{bi} (=10.5 m/s), and diameter, D_i, of the pipe. The main objective of this research was to study the behavior of turbulence in a strong adverse pressure gradient conical diffuser flow to increase our understanding of highly turbulent axisymmetric separating flows. Another objective was to provide a more accurate and reliable data set for turbulence model development. A comparison of the measured triple velocity correlations with the predicted results of a structural turbulence model according to Nagano and Tagawa (1990) is also presented.

Experimental Equipment and Procedure

The wind tunnel facility used for the present measurements has been described previously by Okwuobi and Azad (1973) and Singh and Azad (1993). Briefly, the air from a 25-hp variable speed centrifugal fan is blown through a 2.20 m long settling chamber containing three sets of fine mesh double screens before it enters a circular contraction nozzle of nominal area ratio 87:1 and a 74 diameter long smooth steel pipe of inside diameter, D_i = 0.1016 m. To obtain a fully developed turbulent flow at pipe exit, one diameter length of pipe at the inlet end is pasted with no. 16 floor-sanding paper. The fully developed pipe flow is fed to an eight-degree nominal total angle conical diffuser which discharges free to the atmosphere. The plexiglas diffuser has inlet and outlet diameters of 0.1016 m and 0.202 m, respectively, thus having a nominal area ratio of 4:1 over its length of 0.745 m. Figure 1 presents the conical diffuser geometry and position of the stations for measurements. Most of the measurements were made at the nine x-stations, where x is the axial distance from the diffuser inlet measured towards diffuser exit. Each station has eight drilled holes uniformly spaced in the circumferential direction, and two plugs for each hole. The plugs have central holes suitable for position-

* Data have been deposited to the JFE Data Bank. To access the file for this paper, see instructions on p. 544 of this issue.

Contributed by the Fluids Engineering Division for publication in the JOURNAL OF FLUIDS ENGINEERING. Manuscript received by the Fluids Engineering Division December 26, 1993; revised manuscript received October 21, 1994. Associate Technical Editor: W. S. Saric.

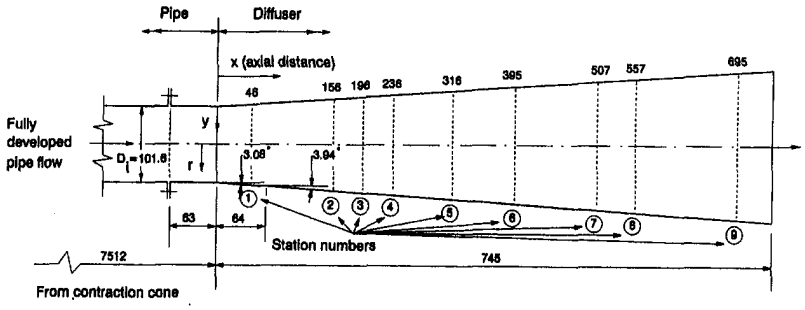

Fig. 1 Conical diffuser geometry. All dimensions in mm.

ing wall static pressure tap tubing and pulsed-wire wall shear stress probes. The inside surfaces of these plastic plugs were aligned and curved flush with the inner surface of the diffuser wall.

The symmetry and fully developed flow condition in the pipe were checked by Okwuobi and Azad (1973). In addition, the axisymmetry of the conical diffuser flow was verified by spanwise wall shear stress measurements and comparing long time mean values of turbulence quantities up to fourth moments as well as mean velocity at equal distances from diffuser axis. The wall static pressures P_{sw} were measured with wall static taps consisting of 0.70 mm inside diameter square ended steel tubing flush mounted in the plugs at the diffuser stations. A static pressure probe was traversed along the diffuser wall to obtain static pressures at intermediate locations. Hot-wire data were obtained with Dantec 55P05 boundary layer probes and Dantec 55P51 x-wire probes using Dantec 55M01 constant temperature anemometers with standard accessories. The usual calibration and measurement procedures were followed. Hot-wire measurements were corrected for yaw and high intensity of turbulence. The x-wire data were checked for their reliability in a fully developed turbulent pipe flow, in which the wall shear stress could be obtained from the streamwise pressure gradient measurements.

The presence of appreciable instantaneous reversals in the present diffuser indicated that the only reliable technique for the measurement of mean and fluctuating velocities and skin-friction in this flow would be the pulsed-wire anemometry (Castro, 1992). The pulsed-wire measurements were obtained using PELA Flow Instruments pulsed-wire probes and anemometer interfaced to a microcomputer so that on-line calibration and measurements could be made. For skin-friction measurements, 3000 to 5000 samples of time of flight were taken at a sampling rate of 10 to 50 Hz. For velocity measurements, 4000 to 10000 samples of time of flight were recorded at each location, depending on the local turbulence intensity and instantaneous backflow level, using a sampling rate of 50 to 100 Hz. The mean and fluctuating velocities, and the higher moments were calculated from the probability distributions obtained by pulsed-wire velocity probe. The instantaneous backflow was measured in terms of the reverse-flow parameter χ (Ruderich and Fernholz, 1986), defined as the fraction of the time flow moves in an upstream direction. Table 1 presents the estimated experimental uncertainties of the measured quantities. The hot-wire and pulsed-wire calibrations were repeated before and after each profile measurement and the data were rejected if the calibration changed by more than 1.5 percent. The measurements were obtained using a hot-wire anemometer wherever possible and pulsed-wire technique where essential, based on local instantaneous reversals and turbulence intensity values.

Results and Discussion

Figure 2 presents the distribution of nondimensional wall static pressure recovery coefficient, $C_p \equiv \{P_{sw}(x) - P_{sw}(\text{pipe})\}/(0.5\rho U_{bi}^2)$, where $P_{sw}(x)$ and $P_{sw}(\text{pipe})$ are wall static pressures at x location in the diffuser and at $x = -0.025$ m in the pipe, respectively, and ρ is the mass density of fluid. Figure 2 also shows the distribution of friction velocity u_*. Both C_p and u_* have the usual trend expected in a severe adverse pressure gradient flow. The wall value of reverse-flow parameter, χ_w, was obtained by pulsed-wire wall shear stress probe at 0.05 mm above the wall surface. Figure 2 shows that χ_w increases rapidly in the first half of the conical diffuser, whereas its rate of increase slows down in the latter half of the diffuser. The instantaneous flow reversals begin in the wall-layer near $x = 0.14$ m and grow as the flow moves in a downstream direction. At station 2, $x = 0.156$ m, $\chi_w \approx 0.01$, i.e. instantaneous backflow was detected about 1 percent of the time. This is the position of incipient detachment (ID) according to classification of Simpson et al. (1981). Similarly, parameter χ_w was 0.20 near $x = 0.38$ m, close to station 6, indicating it to be the position of intermittent transitory detachment (ITD). The locations of ID and ITD for the present diffuser flow are shown in Fig. 2.

Castro and Haque (1987) pointed out that the growth of the shear layer can be measured in terms of the increase in vorticity thickness, $\Lambda = U_{cL}/|dU/dr|_{\max}$, where U_{cL} is the centerline streamwise mean velocity, U is the local streamwise (or axial) mean velocity, and r is the radial distance from the diffuser axis. In the present conical diffuser, the distribution of vorticity thickness was found to increase continuously at an increasing rate, indicating the rapid growth of the wall-layer as the flow moves in a downstream direction. In a similar geometry conical diffuser, Azad and Kassab (1989) have presented the distribution of the relative strength of large eddies, $S_L = [(\overline{q^2 v})_{\max} - (\overline{q^2 v})_{\min}]/(\overline{q^2}_{\max})^{3/2}$, where $q^2 (\equiv \overline{u^2} + \overline{v^2} + \overline{w^2})$ is the turbulent kinetic energy, and u, v, w are the streamwise, transverse and spanwise fluctuating velocities, respectively. In the present flow, S_L and χ_w were found to have a linear relationship, within exper-

Table 1 Estimated experimental uncertainties of the measured quantities. All uncertainties are quoted at 95 percent confidence level.

Measured quantity	Measurement technique	Uncertainty
Distance from the wall	Mechanical dial guage	± 0.2 mm
Mean pressure	Combustion instruments micromanometer	± 0.01 mm H_2O
U	Hot-wire anemometer	± 2%
$\overline{u^2}$	(in the region without	± 5%
$\overline{v^2}$, $\overline{w^2}$	instantaneous reverse	± 8%
$\overline{uv}$	flow)	± 15%
S_u, S_v, $\overline{vu^2}$, $\overline{vuv}$, F_u		± 15%
U	Pulsed-wire	± 5%
$\overline{u^2}$, τ_w, τ'_{wx}	anemometer	± 10%
S_u, F_u		± 20%
χ, χ_w		higher of ± 0.005 or 5% of the measured value

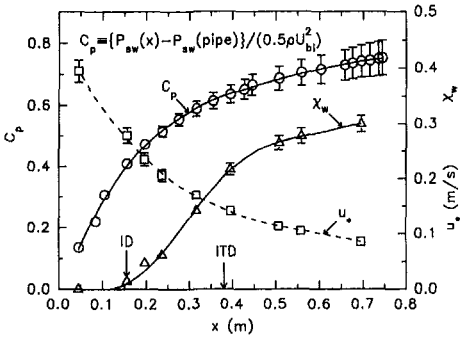

Fig. 2 Wall static pressure recovery coefficient C_p, friction velocity u_*, and wall value of reverse-flow parameter χ_w in conical diffuser. Error bars represent estimated uncertainty in experimental data at 95 percent confidence level. Lines for visual aid only.

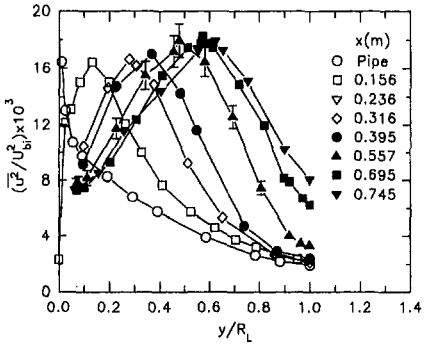

Fig. 4 Profiles of nondimensional streamwise Reynolds normal stress in the pipe and conical diffuser. R_L is the local radius at x-station and y is the distance from the wall measured in the direction perpendicular to the diffuser axis.

imental error, indicating that the relative strength of large eddies increases with the growth of instantaneous backflow in a conical diffuser.

Figure 3 shows that in the latter half of the conical diffuser along diffuser centerline, the relative intensity, u'/U_{cL} (where u' is the rms value of u), the skewness factor, S_u, and the flatness factor, F_u, of the streamwise velocity fluctuations, change rapidly and achieve very high magnitudes, under the increasing influence of the growing wall-region. The complexity of the latter part of a conical diffuser flow is well illustrated by this dramatic distribution of turbulent quantities. These results also suggest that the growth of instantaneous reversals is retarded in the latter half of the conical diffuse under the influence of the highly turbulent central region.

Okwuobi and Azad (1973) detected the presence of an axisymmetric surface in a similar geometry conical diffuser flow along which the Reynolds shear stress, $|\overline{uv}|$, is maximum and the skewness S_u is zero. This local peak $|\overline{uv}|$ position is also the location of maximum kinetic energy production and the maximum Reynolds normal stresses. In the present diffuser, the region of instantaneous reversals grows consistently as the flow moves downstream but remains confined to the wall region, away from the core region and bounded on the top by the energy peak line. Hence, the outer extremities of the instantaneous reversals region nearly coincides with the location of the local $|\overline{uv}|$ maxima. These results obtained in a conical diffuser corroborate the observation of Simpson (1991) in a separating boundary layer that the instantaneous backflow occurs as far away from the wall as the maximum Reynolds shear stress location. The $|\overline{uv}|$ maxima increase as the flow moves downstream and instantaneous reversals grow in the wall layer. These results would suggest that Reynolds shear stress receives a positive contribution from the local instantaneous reversals. In the present diffuser the reverse-flow parameter χ is not a linear function of local axial mean velocity gradient, indicating that eddy-viscosity assumptions may not be true in the instantaneous backflow regions. The present study thus supports the conclusions of Thompson and Whitelaw (1985) and Moser and Moin (1987). Further, this is the cause of failure of the boundary layer approximations in predicting Reynolds shear stress and skin-friction in severe adverse pressure gradient axisymmetric flows.

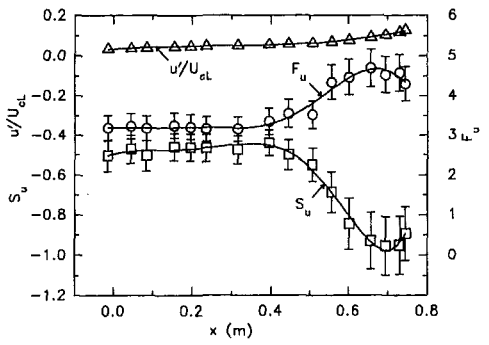

Fig. 3 Distribution of relative intensity u'/U_{cL}, skewness factor S_u, and flatness factor F_u of the streamwise velocity fluctuations along conical diffuser centerline. Lines merely indicate the interpreted trend.

The distribution of the nondimensional pressure gradient parameter, $P^+ = (\nu/u_*^3)(1/\rho)(dP_{sw}/dx)$, where ν is the kinematic viscosity of the fluid, was found to have very high values and a consistently rising trend in the present conical diffuser (Singh and Azad, 1993). This flow also has very high relative intensities of streamwise fluctuating wall shear stress, τ'_{wx}/τ_w, where τ_w is the streamwise mean wall shear stress and τ'_{wx} is the rms value of the streamwise fluctuating wall shear stress (τ_{wx}). The intensity τ'_{wx}/τ_w was found to have a linear relationship with parameter P^+ in a conical diffuser. This is an important relation as it relates a mean flow parameter P^+ with a turbulent flow parameter τ'_{wx}/τ_w. This shows the ability of P^+ to illustrate the nature of wall layer turbulence in strong adverse pressure gradient flows. This also indicates that with the increase of P^+, the wall region becomes more and more turbulent. Further, with the increase of P^+, the streamwise fluctuating velocity in the wall region decreases as a result of the reduction in turbulence production rate, as will be discussed later.

Figure 4 presents profiles of streamwise Reynolds normal stress $\overline{u^2}$, in a nondimensional form. It can be seen that the peak of the Reynolds normal stress profiles moves away from the wall as the flow moves downstream. However, the peak level increases only slightly. Figure 5 shows the profiles of the Reynolds shear stress $|\overline{uv}|$. The profiles obtained by x-wire traverses are extrapolated to the wall skin-friction data obtained by the pulsed-wire wall shear probe and show a consistent trend. Similar to the maxima of the Reynolds normal stress, the peaks of the Reynolds shear stress profiles also move away from the wall and as the flow proceeds in a downstream direction. In the present diffuser flow, the streamwise distribution of the maxima of $\overline{u^2}$, $\overline{v^2}$, and $|\overline{uv}|$ indicated that the peak values of the streamwise Reynolds normal stress increase by a maximum of about 15 percent as the flow moves from the diffuser inlet to diffuser exit. The overall growth in the level of the $\overline{v^2}$ maxima as well as $|\overline{uv}|$ maxima is nearly two-fold, within experimental error, as compared to the entry level. The similarity in the development of the maxima of the $\overline{v^2}$ and $|\overline{uv}|$ can be used for the modeling of the Reynolds shear stress.

Regarding the accuracy of the present measurements in the region of instantaneous reversals and high turbulence intensities only u' can be considered as accurate, since they were measured using a pulsed-wire anemometer. In these regions the rms values

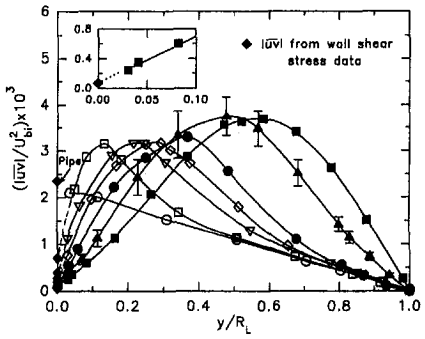

Fig. 5 Profiles of nondimensional Reynolds shear stress in the pipe and conical diffuser. Symbols as in Fig. 4.

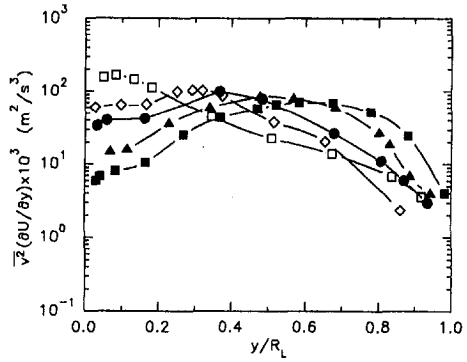

Fig. 7 Distribution of production term $\overline{v^2}(\partial U/\partial y)$ in conical diffuser. Symbols as in Fig. 4.

of transverse fluctuating velocity, v', and Reynolds shear stress, $\overline{uv}$, data obtained using a hot-wire may be too low due to rectification error. However, the extrapolation of $|\overline{uv}|$ profiles measured away from the wall with an x-wire were not inconsistent with the wall values of the independent wall shear stress measurements obtained using a pulsed-wire skin-friction probe (Fig. 5). Due to the higher uncertainties in the pulsed-wire measurements of v' in the wall region and the small instantaneous backflow in the outer region of the conical diffuser, the hot-wire measurements of v' and $\overline{uv}$ are assumed to give correct qualitative behavior and therefore presented here.

The loci of the maxima of the Reynolds normal stress and Reynolds shear stress move away from the wall as the flow moves downstream in the conical diffuser. This behavior of the maxima can be quantitatively presented by considering the production terms of the partial differential transport equations for the streamwise Reynolds normal stress and the Reynolds shear stress. The distribution of the two production terms $|\overline{uv}|(\partial U/\partial y)$ and $\overline{v^2}(\partial U/\partial y)$, where y is the distance from the wall measured in the direction perpendicular to the diffuser axis, are shown in Figs. 6 and 7, respectively, in a dimensional form. Here, it should be noted that these production terms are approximated without considering other second order terms, which may become important near separation, as pointed out by Simpson et al. (1981). It can also be seen that under severe adverse pressure gradient in the present diffuser the production peak quickly moves away from its near-wall position in the pipe flow. It can be noted that both the production terms are slightly suppressed near the wall and the peak moves towards the central region of the radius as the flow proceeds in a downstream direction. Integration of the curves from the wall to the diffuser centerline, $\int_0^{R_L} |\overline{uv}|(\partial U/\partial y)dy$ and $\int_0^{R_L} \overline{v^2}(\partial U/\partial y)dy$, indicates that production remains nearly constant, within experimental uncertainties, at x-stations. The loci of the maximum values of the streamwise Reynolds normal stress, Reynolds shear stress, and their production terms are illustrated in Fig. 8. It can be seen that the loci of the maxima move away from the wall consistently for the above two Reynolds stresses and their production terms in a similar manner. The rate of growth is faster in the initial stages, whereas it slows down slightly in the second half of the conical diffuser, especially near the diffuser exit.

Figure 9 shows the profiles of skewness factor S_u in the pipe and conical diffuser. It can be seen that in the wall region of the final stages of diffuser, where appreciable instantaneous backflow is present, the skewness profiles are flat and positive, and have a decreasing trend as the wall is approached. Whereas, in the initial stages of the diffuser, where no appreciable instantaneous reversals were present, skewness profiles have a rising trend in the wall region, similar to the other adverse pressure gradient flows. In the initial stages of the diffuser the skewness profiles in the central region are qualitatively similar to that of pipe flow. However, in the final stages their profile is distinctly

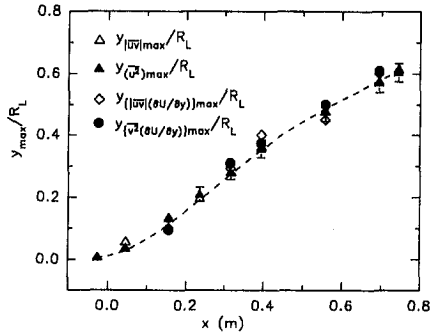

Fig. 8 Loci of the maximum values of $\overline{u^2}$ and $|\overline{uv}|$ and their production terms. Line merely indicates the interpreted trend.

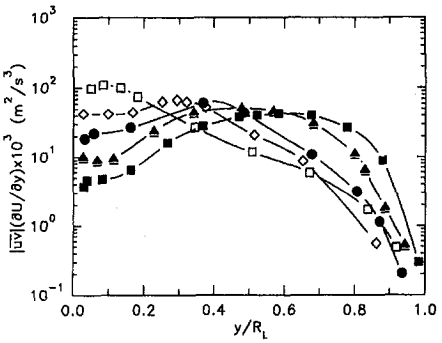

Fig. 6 Distribution of production term $|\overline{uv}|(\partial U/\partial y)$ in conical diffuser. Symbols as in Fig. 4.

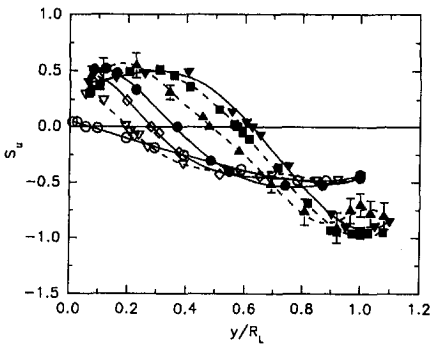

Fig. 9 Skewness factor of streamwise velocity fluctuations in the pipe and conical diffuser. Symbols as in Fig. 4.

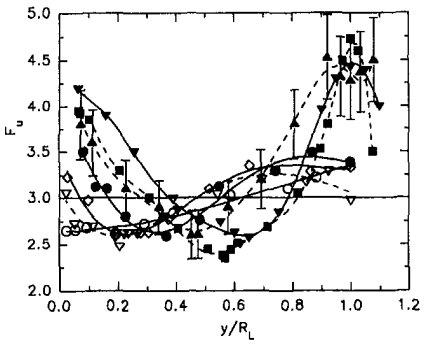

Fig. 10 Flatness factor of streamwise velocity fluctuations in the pipe and conical diffuser. A flatness of 3 corresponding to a Gaussian distribution is also included for a reference. Symbols as in Fig. 4.

different as compared to the initial region. For each profile skewness changes sign from positive to negative at the radial location of the maxima of Reynolds shear stress and the production term, and reaches a minimum value at the centerline of the diffuser. In the second half of the diffuser the magnitude of the negative skewness of the central region profile increases faster than the skewness at the diffuser centerline. Further downstream the centerline region of the diffuser has consistently increasing negative skewness.

Figure 10 presents the profiles of flatness factor F_u in the pipe and conical diffuser. Due to appreciable instantaneous backflow, F_u profiles are flat with lower flatness values in the wall region of the final stages of the diffuser. In the wall regions of the initial stages of the diffuser flow the flatness factor has a rising trend similar to the other adverse pressure gradient flows. The F_u profiles at x-stations have minima corresponding to the position of zero skewness S_u and positions of the maxima of the Reynolds shear stress and production. The central region flatness in the initial stages of the conical diffuser has profiles similar to the pipe flow. However, as the flow proceeds downstream, the centerline flatness value increases rapidly especially in the latter half of the diffuser, indicating an approach to the increasingly intermittent core region.

The important role of the Reynolds shear stress in the analysis and modeling of turbulent flows has stimulated attempts at finding a physical explanation for its production and transport mechanism. It is now widely accepted that the turbulent transport process of second-order moments is governed almost completely by the coherent structures in a turbulent shear flow. Nagano and Tagawa (1990) utilized this experimental fact for the development of a structural turbulence model for triple velocity correlations $\overline{vuv}$ and $\overline{vu^2}$ considering their physical behavior, on the basis that the triple products of velocity and scalar are determined by the dynamical fluid motions such as the ejections (Q2-motions) and sweeps ($Q4$-motions). According to this model the nondimensional turbulent transport velocity triple correlations $\overline{\hat{v}\hat{u}\hat{v}}$ and $\overline{\hat{v}\hat{u}^2}$ can be represented as

$$\overline{\hat{v}\hat{u}\hat{v}} = C[S_u + \sigma_{\overline{uv}}(\pi/2)S_v] \tag{1}$$

$$\overline{\hat{v}\hat{u}^2} = C[\sigma_{\overline{uv}}(\pi/2)S_u + S_v] \tag{2}$$

where, $\overline{\hat{v}\hat{u}\hat{v}} = (\overline{vuv})/(u'v'^2)$ and $\overline{\hat{v}\hat{u}^2} = (\overline{vu^2})/(v'u'^2)$; S_u and S_v are the skewness factors of the streamwise and transverse fluctuating velocities, respectively; $C = 1/[3\{(\pi/2)^2 - 1\}]$; $\sigma_{\overline{uv}}$ is a sign function introduced to make a model independent of a coordinate system, $\sigma_{\overline{uv}} = 1$ for $\overline{uv} \geq 0$, $\sigma_{\overline{uv}} = -1$ for $\overline{uv} < 0$; and $\pi = 22/7$.

The turbulent diffusion is determined by dynamic phenomenon associated with organized motions of ejections and sweep, and due to this reason the static model, such as gradient-type diffusion of second-order moments, are unable to adequately describing the third-order moments. The mixed moments $\overline{\hat{v}\hat{u}\hat{v}}$ and $\overline{\hat{v}\hat{u}^2}$ at x-stations were measured and compared with the computed values obtained using Eqs. (1)–(2) and the results are shown in Fig. 11. It can be seen that the structure of turbulence is strongly affected by the severe adverse pressure gradient in this diffuser and the velocity triple correlations $\overline{vuv}$ and $\overline{vu^2}$ show opposite sign compared to the pipe flow, indicating remarkable structural changes taking place in the axisymmetric separating flows.

The distribution of turbulent transport $\overline{vuv}$, or the normal transport of the $\overline{uv}$ shear stress in Fig. 11 shows that as the flow moves downstream, the negative values of $\overline{vuv}$ as found in the wall region of the pipe flow increasingly disappear, indicating that in the diffuser flow more and more turbulent diffusion of Reynolds shear stress, $-\overline{uv}$, occurs toward the wall from the outer region, i.e., in a direction opposite to the pipe flow. The significant regions of positive $\overline{vuv}$ indicate a downward transport of $-\overline{uv}$. Similarly the positive $\overline{vu^2}$ observed in the wall region of the pipe disappears partly as the flow reaches station 4, x = 0.236 m. In the wall region at the downstream stations of the conical diffuser, the increasing negative values of the moment $\overline{vu^2}$ indicate the existence of increasing turbulence energy trans-

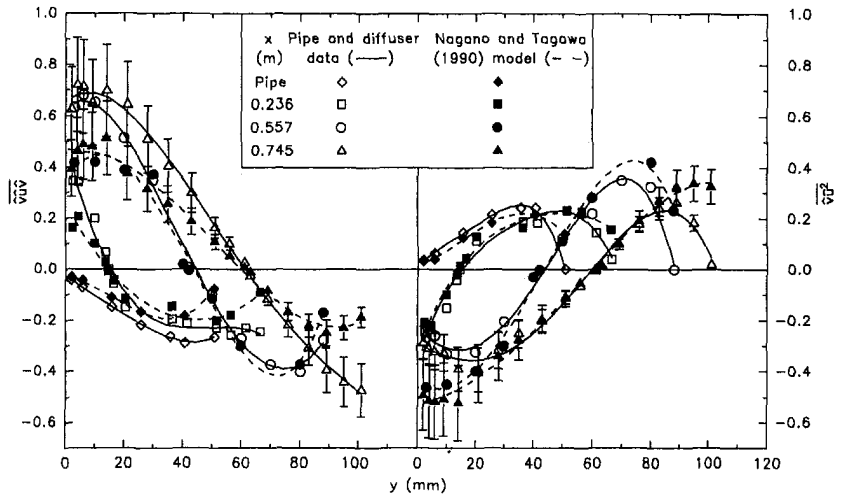

Fig. 11 Distribution of velocity triple products in the pipe and conical diffuser. Present data and Nagano and Tagawa (1990) structural model prediction results. Error bars represent estimated uncertainty in experimental data at 95 percent confidence level. Lines for visual aid only.

port towards the wall from the outer regions, similar to the observations in the adverse pressure gradient boundary layer flows (Nagano et al., 1993). Similar results were found also at the other x-stations. The present results corroborate that in general the mixed triple products can be successfully predicted at various stations of a conical diffuser by the 'structural' model reported by Nagano and Tagawa (1990), however, some deviations are found in the core region and in the wall region. These deviations can be attributed to the higher experimental uncertainties associated with the measurement of the triple velocity products in the wall region due to the presence of appreciable instantaneous flow reversals and very high turbulence intensities. Also, they can be partially attributed to the limitation of the model to predict in the outer region and near the boundary conditions.

Concluding Remarks

In the near-wall regions of the final stages of an incipient-separating conical diffuser, the streamwise velocity fluctuations were found to be as large as the mean velocities. Under the strong adverse pressure gradient in this diffuser, the maxima of Reynolds stresses, $\overline{u^2}$, $\overline{v^2}$, and $|\overline{uv}|$, and turbulent energy production terms coincide and rapidly move away from their near-wall position in the pipe flow. In a conical diffuser, the instantaneous backflow region is limited to the wall layer and bounded on the top by the region of the Reynolds shear stress maxima. The peak value of $\overline{u^2}$ increase by about 15 percent, whereas the growth in $\overline{v^2}$ maxima as well as $|\overline{uv}|$ maxima is nearly two-fold, as the flow moves from the diffuser inlet to the diffuser exit. The present results suggest that the Reynolds shear stress receives positive contribution from the growing instantaneous flow reversals in the wall layer. Hence, for the prediction of Reynolds shear stress in complex axisymmetric flows the turbulence models should explicitly account for the presence of instantaneous flow reversals. In the final stages of the conical diffuser flow, along the diffuser centerline, the relative intensity u'/U_{cL} skewness factor S_u and flatness factor F_u show dramatic rapid rise under the increasing influence of the growing wall layer. Some features of pipe flow, such as coinciding locations for $\overline{u^2}$ maxima with F_u minima and $S_u = 0$ are also preserved in the diffuser flow. In the regions of appreciable instantaneous backflow the S_u profiles are flat and reducing towards the wall. Under the severe adverse pressure gradient in a conical diffuser flow the velocity triple products $\overline{vuv}$ and $\overline{vu^2}$ have opposite sign as compared to the pipe flow, indicating the existence of totally different coherent motions and dynamical flow structures. In general, the structural turbulence model of Nagano and Tagawa (1990) was able to predict mixed velocity triple correlations at various stations of the conical diffuser.

Data Bank Contribution

The data files provided on a disk contain the results presented in this paper and the axial mean velocity profiles data obtained at stations 2, 5, 6, 8, and 9 in the conical diffuser.

Acknowledgment

The financial assistance provided by the Natural Sciences and Engineering Research Council of Canada is gratefully acknowledged.

References

Azad, R. S., and Kassab, S. Z., 1989, "Turbulent Flow in a Conical Diffuser: Overview and Implications," *Physics of Fluids A*, Vol. 1 (3), pp. 564–573.

Bradbury, L. J. S., and Castro, I. P., 1971, "A Pulsed-Wire Technique for Velocity Measurements in Highly Turbulent Flows," *Journal of Fluid Mechanics*, Vol. 49, pp. 657–691.

Bradshaw, P., 1975, "Complex Turbulent Flows," ASME JOURNAL OF FLUIDS ENGINEERING, Vol. 97, pp. 146–154.

Castro, I. P., and Haque, A., 1987, "The Structure of a Turbulent Shear Layer Bounding a Separation Region," *Journal of Fluid Mechanics*, Vol. 179, pp. 439–468.

Castro, I. P., 1992, "Pulsed Wire Anemometry," *Exp. Thermal Fluid Science*, Vol. 5, pp. 770–780.

Cho, N.-H., and Fletcher, C. A. J., 1991, "Computation of Turbulent Conical Diffuser Flows Using a Non-orthogonal Grid System," *Computers & Fluids*, Vol. 19 (3/4), pp. 347–361.

Dengel, P., and Fernholz, H. H., 1990, "An Experimental Investigation of an Incompressible Turbulent Boundary Layer in the Vicinity of Separation," *Journal of Fluid Mechanics*, Vol. 212, pp. 615–636.

Lai, Y. G., So, R. M. C., and Hwang, B. C., 1989, "Calculation of Planar and Conical Diffuser Flows," *AIAA Journal*, Vol. 27 (5), pp. 542–548.

Moser, R. D., and Moin, P., 1987, "The Effects of Curvature in Wall-Bounded Turbulent Flows," *Journal of Fluid Mechanics*, Vol. 175, pp. 479–510.

Nagano, Y., and Tagawa, M., 1990, "A Structural Model for Triple Products of Velocity and Scalar," *Journal of Fluid Mechanics*, Vol. 215, pp. 639–657.

Nagano, Y., Tagawa, M., and Tsuji, T., 1993, "Effects of Adverse Pressure Gradients on Mean Flows and Turbulence Statistics in a Boundary Layer," *Turbulent Shear Flows 8*, F. Durst, R. Friedrich, B. E. Launder, F. W. Schmidt, U. Schumann and J. H. Whitelaw, eds., Springer-Verlag, Berlin, pp. 7–21.

Okwuobi, P. A. C., and Azad, R. S., 1973, "Turbulence in a Conical Diffuser with Fully Developed Flow at Entry," *Journal of Fluid Mechanics*, Vol. 57, pp. 603–622.

Ruderich, R., and Fernholz, H. H., 1986, "An Experimental Investigation of a Turbulent Shear Flow with Separation, Reverse Flow, and Reattachment," *Journal of Fluid Mechanics*, Vol. 163, pp. 283–322.

Simpson, R. L., Chew, Y.-T., and Shivaprasad, B. G., 1981, "The Structure of a Separating Turbulent Boundary Layer. Part 1. Mean Flow and Reynolds Stresses," *Journal of Fluid Mechanics*, Vol. 113, pp. 23–51.

Simpson, R. L., 1991, "The Structure of the Near-Wall Region of Two-Dimensional Turbulent Separated Flow," *Phil. Trans. R. Soc. Lond.*, Vol. A 336, pp. 5–17.

Singh, R. K., and Azad, R. S., 1993, "Effects of Incipient Separation on the Mean and Turbulent Fluctuating Velocities in a Conical Diffuser Flow," *Proceedings of the Third World Conference on Experimental Heat Transfer, Fluid Mechanics and Thermodynamics*, M. D. Kelleher, R. K. Shah, K. R. Sreenivasan, and Y. Joshi, eds., Elsevier, New York, pp. 977–984.

Smits, A. J., and Wood, D. H., 1985, "The Response of Turbulent Boundary Layers to Sudden Perturbations," *Ann. Rev. Fluid Mech.*, Vol. 17, pp. 321–358.

Sovran, G., and Klomp, E. D., 1967, "Experimentally Determined Optimum Geometries for Rectilinear Diffusers with Rectangular, Conical or Annular Cross-Section," *Fluid Mechanics of Internal Flow*, G. Sovran, ed., Elsevier, New York, pp. 270–319.

Thompson, B. E., and Whitelaw, J. H., 1985, "Characteristics of a Trailing-Edge Flow with Turbulent Boundary-Layer Separation," *Journal of Fluid Mechanics*, Vol. 157, pp. 305–326.

Calculation of Numerical Uncertainty Using Richardson Extrapolation: Application to Some Simple Turbulent Flow Calculations

Ismail Celik

Wei-Ming Zhang

Department of Mechanical and Aerospace Engineering, West Virginia University, Morgantown, WV 26506-6101

Richardson extrapolation has been applied to turbulent pipe flow and turbulent flow past a backward facing step. A commercial CFD code is used for this purpose. It is found that the application of the method is not straightforward and some aspects need careful consideration. Some of the problems are elucidated. The particular code used for the present application employs a hybrid scheme, and it does not give monotonic convergence for all the variables in all regions as the grid is refined. The flow regions and the variables which converge monotonically in these regions should be identified first before the method is applied. When this is done Richardson extrapolation gives good results in calculating the apparent order of the numerical procedure used, as well as obtaining grid independent results with which discretization error bounds can be calculated as measures of numerical uncertainty. Even in cases where it does not work, the method can be used as an error indicator for some obscured user mistakes. This paper also demonstrates several shortcomings of using commercial CFD codes. The present findings should help the users of CFD software in general, to quantify discretization errors in their calculations.

Introduction

Computational fluid dynamics (CFD) is being used extensively as a viable research and engineering tool to study physics of complex flow phenomenon and to improve design of engineering equipment. However, it is not always used correctly, and the degree to which the CFD results are being accepted is still largely dependent on confidence building measures via comparison of "predictions" with experiments. In order to use CFD as an independent engineering tool it is necessary to provide some quantitative measures of the numerical uncertainty when the predictions are presented alone.

In the past, the nuclear industry has been concerned with numerical uncertainty (see e.g., Ronen, 1988), but their effort and findings have, somehow, not propagated to the CFD community. In the field of nuclear reactor analysis a combined sensitivity-uncertainty analysis (see e.g., Lewins and Becker, 1982) is carried out for determining uncertainties due to input parameters. The theoretical basis for sensitivity analysis can be found in the book edited by Ronen (1988). The NATO Advisory Group for Aerospace Research (AGARD) has also been concerned with a related topic of validation (see AGARD Proc. No. 437, 1988). In recent years, some activities such as forums and panel discussions relevant to this topic have been coordinated by the Fluids Engineering Division and the Heat Transfer Division of ASME. Most of the relevant references in this area are cited by Celik (1992) and Celik et al. (1993). As the use of CFD has increased rapidly, the concern over the degree of computational uncertainty involved in these computations has also caught the attention of more and more researchers (see e.g., Roache et al., 1986; Ferziger, 1988, 1993; Celik, 1989, 1992, and 1993; Roache, 1990; Blottner, 1990; Mehta, 1991, and Freitas, 1993). Because of the relatively new nature of this area there is not much coherence, nor consensus about the definition, the nature, the sources, and the remedies for computational uncertainty.

The overall uncertainty (or the global error) involved in CFD results can be due to several sources of errors such as modeling error (the inaccuracy inherent to the mathematical model of a certain physical phenomenon), domain dependency errors (i.e., errors arising from finite representation of a domain of influence such as that of flow past bluff bodies), errors due to inaccurate implementation of the boundary and initial conditions, iterative convergence errors (e.g., incomplete convergence), truncation convergence error (errors due to insufficient grid refinement, i.e., discretization error). Truncation convergence error should be distinguished from truncation error which describes how well the differential equations are approximated by the discretization and is the residual (or remainder) terms when the numerical solution is inserted into the exact continuous equations. (See Ferziger (1993) for the relations between these two types of errors.) One should also mention the multiple solution errors where the assumption of a unique exact solution does not apply but a unique numerical solution is still sought. Another commonly encountered uncertainty is multiple steady-state solutions, which can be obtained by using different relaxation factors in iterative schemes or different initial conditions.

It is beyond the scope of this paper to address all sources of the errors mentioned above. Here, the concern is restricted to the truncation convergence error. One can define a so-called "solution error" as the difference between the exact solution of the discretized equations and the numerical solution which is obtained after full iterative convergence (Ferziger, 1993). This error is a combination of discretization and grid generation errors, but when rectangular Cartesian grids are used as is the case in the present study, it is believed that the latter should be negligible. Some researchers disagree in separation of discretization and grid generation errors and take the latter as part of

Contributed by the Fluids Engineering Division for publication in the JOURNAL OF FLUIDS ENGINEERING. Manuscript received by the Fluids Engineering Division November 8, 1993; revised manuscript received September 8, 1994. Associate Technical Editor: O. Baysal.

discretization error. Any numerical solution obtained using a convergent and consistent scheme with complete iterative convergence and sufficient grid refinement should give the exact solution of the continuum problem represented by a certain mathematical model, provided that there is no obscure human error in the implementation of the overall numerical scheme. If there are multiple solutions to the given problem one should further assume that these solutions are well-separated so that a sufficiently accurate initial guess should allow the method to converge to the desired solution.

Richardson extrapolation (Richardson, 1910) is a relatively simple technique for obtaining quantitative measures of truncation convergence errors (or incomplete grid refinement errors) (see Roache, 1972; Churchill et al., 1981; deVahl, 1983; Caruso et al. 1985; Ferziger, 1988, 1993; Dang et al., 1989; and Patankar, 1988). The successful applications presented by Kessler et al. (1988) and Demuren and Wilson (1994) showed that this method can indeed be used as a quantitative error indicator for CFD calculations.

In spite of the positive indications from the above-mentioned studies, some problems concerning the application of Richardson extrapolation, particularly in prediction of turbulent flows, remain unresolved. Some of these problems are related to specifying a single mesh parameter characterizing the grid fineness, identifying regions of monotonic convergence, the implications of the use of wall functions, and achieving numerical solutions in the asymptotic range. In this paper, applications of Richardson extrapolation to a developing turbulent pipe flow and turbulent flow over a backward facing step are presented, and the results relevant to the above mentioned problems are discussed.

2 Richardson Extrapolation

For a first order method the error, ϵ, in a numerical solution can be expressed as (Richardson, 1910; Roache, 1972; Ferziger, 1988 and 1993):

$$\epsilon_h = \phi - \phi_h = a_1 h + a_2 h^2 + a_3 h^3 + \ldots \tag{1}$$

where ϕ is the exact numerical solution to the discretized equations, ϕ_h is the approximate numerical solution, h is a characteristic discretization parameter, and a_i, $i = 1, 2, 3, \ldots$ are coefficients which can be functions of the coordinates but do not depend on h in the asymptotic range. For sufficiently small h where the leading term dominates (i.e., in the asymptotic range) Eq. (1) can be written as

$$\epsilon_{\alpha h} = \phi - \phi_{\alpha h} = C(\alpha h)^n \tag{2}$$

where n is the order of the method, α is the grid refinement factor, and C is a coefficient which can be a function of the coordinates. If the solution with the grid size h is taken as the base case and two more solutions are obtained for coarser grids with $\alpha = 2$ and $\alpha = 4$ (note that α values need not be an integer, fractional values such as $\alpha = 0.5$, 0.75, or 1.25 should work as well), using Eq. (2) the following three equations can be derived (see Celik and Zhang, 1993) from Eq. (2) for the three unknowns, namely, n, ϕ_{ext}, and C:

$$n = \ln\left[(\phi_{2h} - \phi_{4h})/(\phi_h - \phi_{2h})\right]/\ln 2 \tag{3}$$

$$\phi_{\text{ext}} = (2^n\phi_h - \phi_{2h})/(2^n - 1) \tag{4}$$

$$C = (\phi_{\text{ext}} - \phi_h)/h^n \tag{5}$$

In the above equations, ϕ is replaced by ϕ_{ext} to denote an extrapolated value. If h is not sufficiently small higher order terms must be included, but this brings in the extra unknowns a_2, a_4 etc. However, for large h, the estimates, although inaccurate, are large and indicate that the solution is not acceptable. Hence the coarse grid solutions can also be used as error indicators. From Eqs. (3) and (5) it is seen that the order of the method, n, and the extrapolated numerical solution, ϕ_{ext}, are independent of the discretization parameter h; but C is not (Eq. (5)). Using the extrapolated value one can define an approximate, relative grid refinement error by

$$e_r = \left|(\phi_{\text{ext}} - \phi_h)/\phi_{\text{ext}}\right| \tag{6}$$

Equations (1) and (2) can be used to derive (Celik and Zhang, 1993) the following relations for the error ϵ_h for sufficiently small h:

$$\epsilon_h = (\phi_h - \phi_{\alpha h})/(\alpha - 1); \quad a_1 \neq 0 \tag{7a}$$

$$\epsilon_h = (\phi_h - \phi_{\alpha h})/(\alpha^2 - 1); \quad a_1 = 0 \tag{7b}$$

Equation (3) is meaningful only in case of monotonic convergence of the solution to the exact numerical solution as the grid is refined. If this convergence is oscillatory (i.e., $\epsilon_{\alpha h}$ is equal to Ch^n, $-C(2h)^n$, and $C(4h)^n$ for $\alpha = 1$, 2, and 4, respectively) it is tempting to replace the argument of the logarithm function in Eq. (3) by its absolute value, but there is no theoretical basis for this. Richardson extrapolation for cases with oscillatory truncation convergence needs further investigation.

Computational Details

About the Computer Codes. Simulations were performed using two different codes with the same turbulence model and the same solution procedure. The first (Code #1) is a commercial code, PHOENICS (Ludwig et al., 1989). This code uses the well-known SIMPLE (or SIMPLEST) algorithm (see e.g., Patankar, 1980) and the control volume approach with a hybrid of upwind and central differencing schemes. Two-dimensional Navier-Stokes equations or their time averaged forms with a turbulence closure model are solved for the primitive flow variables, namely the two velocity components, the pressure, and in the case of turbulent flows, the turbulent kinetic energy, k, and its dissipation rate, ε. From the several options available for turbulence modeling, the standard k-ε model (Rodi, 1980) was selected for this study. The turbulence model constants used were $\kappa = 0.435$, EWALL = 9, $C_d = 0.1643$, $C'_\mu = 0.5478$

Nomenclature

C_P = pressure coefficient; $\Delta P/(0.5\rho U^2)$
C_f = friction coefficient; $\tau_w/(0.5\rho U^2)$
C_d = turbulence model constant
C_μ = turbulence model constant
D = pipe diameter
e_r = relative error
k = turbulent kinetic energy
H = step height
h = grid size
L = total length of pipe
l_t = turbulence length scale
n = apparent order of the method
P = pressure
u_* = friction velocity
U_{in} = inlet velocity
U = velocity in axial direction
V = velocity in transverse direction
X = axial coordinate
Y = coordinate in the transverse direction
y_w = distance from the wall
y^+ = dimensionless length in transverse direction ($= u_* y/\nu$)
α = grid refinement parameter
κ = Von Karman constant
ϕ = general dependent variable
ϕ_{ext} = numerical, extrapolated value
ν = kinematic viscosity
ν_t = turbulent eddy viscosity
ε_h = absolute trunction error
ε = dissipation rate of turbulent kinetic energy

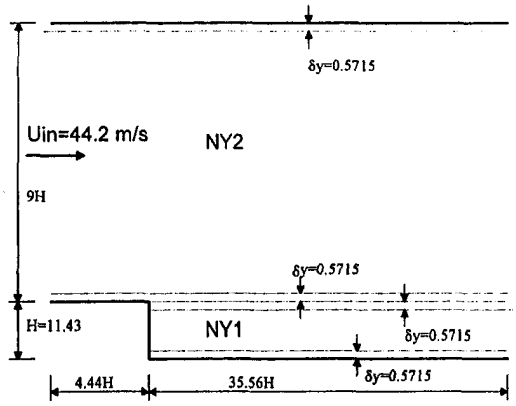

Fig. 1 Geometry for the backward facing-step flow showing the calculation domain along with some grid parameters

($C_\mu = C_d C'_\mu = 0.09$), $C_{1\varepsilon} = 1.44$, $C_{2\varepsilon} = 1.92$, $\sigma_k = 1.0$, and $\sigma_\varepsilon = 1.314$; the notation for these constants is the standard notation used in the literature (see e.g., Rodi, 1980). The turbulence length scale is calculated from $l_t = C_d k^{3/2}/\epsilon$ and the turbulent eddy viscosity is calculated from $v_t = C'_\mu l_t k^{1/2}$.

The second code (Code #2) is a readily available working version of the well-known TEACH code (Gosman and Pun, 1973; Durst and Loy, 1984). This code has essentially the same solution procedure as in PHOENICS. The turbulence model constants in TEACH were slightly different from those used in PHOENICS but when the same constants were used later on, the results did not show any difference.

In both of these codes a hybrid of the first order upwind differing scheme and the second order central differencing scheme is used for the convective terms, and the latter is used for the diffusion terms. Hence, the formal order of accuracy should be such that $1 \leq n \leq 2$ for truncation error.

Boundary Conditions. At the inlet, uniform profiles were specified for all variables; the transverse component of the velocity was set to zero. Since the present results are not compared to measurements no attempt was made to match the measured inlet profiles. At the outlet, convective outflow boundary conditions were imposed on all variables except pressure. This amounts to imposing zero first derivatives. At the wall boundaries, the wall function approach was used (see e.g., Rodi, 1980) where the shear stress was calculated from the log-law velocity profile. The near wall values of k and ϵ were fixed at the first grid node inside the calculations domain according to

$$k = u_*^2/(C_\mu)^{1/2}; \quad \varepsilon = (C_d k^{3/2})/(\kappa y_w) = u_*^3/(\kappa y_w) \quad (8)$$

where $u_* = (\tau_w/\rho)^{1/2}$ is the friction velocity, and y_w is the normal distance from the wall. Since the log-law is valid only in a certain region of the boundary layer such that $y^+ = (u_* y)/\nu > 30$ this becomes a problem in grid refinement.

Description of the Cases Studied. The first case studied was turbulent developing flow in the entrance region of a pipe at Reynolds number, Re = 2700 and 2425, with the fluid density, $\rho = 877.84$ kg/m^3, the pipe diameter, $D = 0.01905$ m, and the pipe length, $L = 5.0$ m. These flow parameters were selected because there were some measurements available which were used as a guide to avoid mistakes.

The second case was two-dimensional, turbulent flow over a backward facing step with a step height $H = 11.43$ mm, $\nu = 1.56 \times 10^{-5}$ m^2/s, and Re $= U_{in}H/\nu = 32400$, where $U_{in} = 44.2$ m/s is the average flow velocity at the inlet. The geometry and the relevant dimensions for this case is shown in Fig. 1.

Grid Distribution. For the pipe flow, the first set of calculations were performed by distributing the grid uniformly in both coordinate directions; Δx and Δy were not necessarily equal. A second set of calculations were performed by fixing the first grid node near the wall and then sequentially increasing the number of points in the remaining region by a factor of two. As explained later the first grid node near the wall needed to be fixed to keep y^+ sufficiently large.

The grid distribution for the backward-facing step flow was uniform in the axial direction. The grid nodes near the wall boundaries were fixed for all calculations as shown in Fig. 1 again to keep y^+ at these nodes sufficiently large. The grid lines marked in Fig. 1 pass through the cell faces. The number of grid nodes in the regions marked as NY1 and NY2 were distributed uniformly with some reasonable values at first, then they were doubled sequentially for finer grids. The grid spacing in these two regions were not equal.

Table 1 Grid-dependence of turbulent pipe flow calculations (Code #1)

Re = 2700; $D = 0.02$ m; $U_{ave} = 1$ m/s; $\rho = 877.84$ kg/m^3

Case	Grid	$\Delta P/0.5\rho U_{ave}^2$	U_{max}/U_{ave}	u_*/U_{ave}
TPL1	10*10	16.4	1.343	0.06
TPL2	20*20	21.7	1.395	0.06
TPL3	40*40	23.5	1.402	0.06
TPL4	80*80	23.0	1.389	0.10

Results and Discussion

Turbulent Flow in the Entrance Region of a Pipe. The relevant mean flow quantities are listed in Tables 1 and 2. The maximum residuals (not normalized) for P, U, V, k, and ε were 7.0E-6, 9.1E-5, 7.0E-3, 6.6E-6, and 2.0E-3, respectively, for PHOENICS calculations; for TEACH calculations those were 9.5E-3, 5.5E-2, 1.5E-1, 5.6E-6, and 3.8E+5. The large residuals were most of the time for the case of finest grids. It is not clear why the residuals from the two codes are so different, but it is most probably due to implementation of pressure boundary conditions at the outlet. The cases with large residuals were run for thousands of more iterations and no significant change was observed in the flow variables which are presented here.

Tables 1 and 2 show that, there are significant differences between the two sets of calculations using two different codes which use essentially the same methodology. For example, Code #1 gives a dimensionless pressure drop of 23 whereas Code #2 gives a value of 37 for the same parameter. As the grid is refined uniformly, the calculations from Code #2 converge monotonically, but those from Code #1 converge in an oscillatory manner. Hence, Richardson's extrapolation can be applied to Code #2 but not to Code #1 results.

If we let ϕ represent the dimensionless pressure drop for our problem, and use the results from the first three set and the last three set of grids given in Table 2, the method gave $\phi_{ext} = 53.2$, and $n = 0.4$; and $\phi_{ext} = 42.3$ and $n = 0.8$ for the first and last three sets of grids, respectively. The theoretical (or formal) order of the method should be at least equal to one, if the boundary conditions are implemented correctly, because the

Table 2 Grid-dependence of turbulent pipe flow calculations (Code #2)

Re = 2700; $D = 0.02$ m; $U_{ave} = 1$ m/s; $\rho = 877.84$ kg/m^3

Case	Grid	$\Delta P/0.5\rho U_{ave}^2$	U_{max}/U_{ave}	u_*/U_{ave}
TPL1	10*10	19.5	1.276	0.10
TPL2	20*20	27.6	1.335	0.11
TPL3	40*40	33.8	1.37	0.13
TPL4	80*80	37.4	1.387	0.14

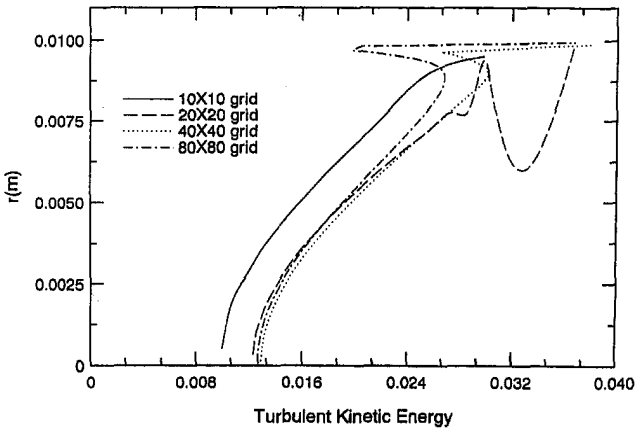

Fig. 2(*a*) Variation of turbulent kinetic energy in the radial direction (Code #1)

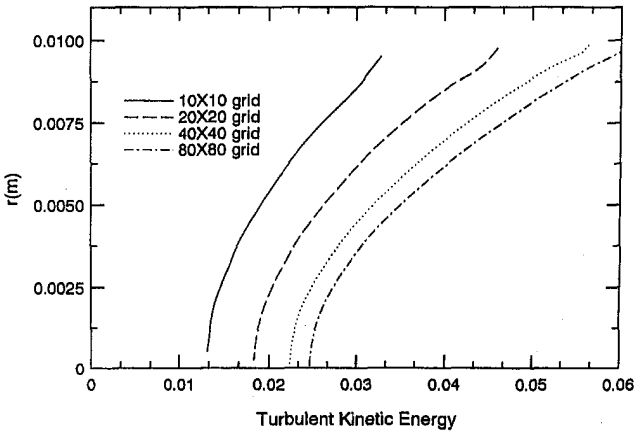

Fig. 2(*b*) Variation of turbulent kinetic energy in the radial direction (Code #2)

scheme used is the hybrid scheme. One can conclude from here that either there is something wrong with the calculations or the 10×10 and 20×20 grids are too coarse and solutions are not in the asymptotic range. To find out more details about the numerical solution the turbulent kinetic energy profiles are investigated next.

Kinetic energy profiles presented in Figs. 2(*a*) and 2(*b*) show an unrealistic behavior near the wall for Code #1; for Code #2 there is no apparent improper behavior. The calculated y^+ values at the first grid node ranged approximately from 12 for the 10×10 grid to 1.0 for the 80×80 grid for both codes. Evidently, the way that the wall functions were implemented in Code #1 must be different than that in Code #2. The calculated k-profiles signal a misuse on part of the user, that is, the y^+ values are too small and the log-law is not applicable in this region. This may also explain the large residuals obtained for the ε-equation.

A second set of calculations was performed for the pipe flow with Code #1. This time the first grid node near the wall was fixed so that y^+ was approximately 20 for Re = 2,425 and 32 for Re = 10,000. The results were almost the same for uniformly distributed grids of 7×40, 12×20, 12×40, and 22×40; the calculated mean flow parameters had the following values: $2\Delta P/\rho U\text{in}^2 = 12.8$, $U\text{max}/U\text{in} = 1.176$, and $u_*/U\text{in} = 0.079$. For Re = 10,000 these values were: $2\Delta P/\rho U\text{in}^2 = 4.96$, $U\text{max}/U\text{in} = 1.2$, and $u_*/U\text{in} = 0.065$. In the above calculations the friction velocity, u_*, was calculated from $u_* = (C_\mu^{0.5} k)^{0.5}$ which follows from Eq. (8).

The above results constitute a good example of how Richardson extrapolation can be used together with physics to identify sources of errors and mistakes.

Turbulent Flow Over a Backward Facing Step. This flow situation was approximately the same as one of the cases (the undeflected wall case) investigated experimentally by Driver and Seegmiller (1985) which is also a test case for the Collaborative Testing of Turbulence Models (Bradshaw et al., 1991). Since in this paper, the objective is not to compare the results with experiments, not much effort was made to match the simulation conditions exactly to those of the experiments. Only Code #1, PHOENICS, was used for this case with four sets of grids, namely, 20×18, 36×36, 68×72, 132×144 in the y- and x-directions.

Observation of the y^+ values at the first grid node inside the calculation domain along the wall has shown that the condition for being in the log-law region (i.e., $y^+ > 3.0$) is not satisfied in most of the recirculating flow region behind the step. This is of course the case in many other calculations where the wall function approach is used. Due to the presence of at least two singular points in this region, namely the corner stagnation point and the reattachment point, the log-law region is restricted to very narrow regions, if it exists at all. This situation can not be avoided as long as the wall function approach is used. Nevertheless, log-wall functions were applied anyway, because, other alternatives are not so attractive and also this is the most commonly used procedure in practice. Along the wall which is opposite to the step the calculated y^+ values (not shown here) were between 30 and 60 which does meet the required criteria for the log-law.

In Fig. 3 the variation of the friction coefficient, C_f, is depicted as a function of the axial distance for different grids. It is seen that the solution does seem to converge as the grid is refined. A similar behavior was observed in case of the pressure coefficient, C_p, however the convergence was not monotonic beyond approximately $x/H = 8.9$, whereas for C_f values it is monotonic everywhere. Driver and Seegmiller (1985) mention that their calculations performed using a modified version of the TEACH code with the standard k-ε model were grid independent for a grid size of 42×42. The present calculations show grid dependence even at grid sizes of 132×144 using PHOENICS (Fig. 3). The predicted reattachment length changes from 5.82 to 4.89 as the grid is refined from 20×18 to 132×144 but not monotonically. The final value of 4.89 agree well with the numerical predictions of Driver and Seegmiller, and with other calculations using the standard k-ε model.

Richardson extrapolation is applied to C_p values at x/H of 4.4 and 6.7 and C_f values at x/H of 6.7 and 11.1. The calculated values for the apparent order, n, of the method are listed in

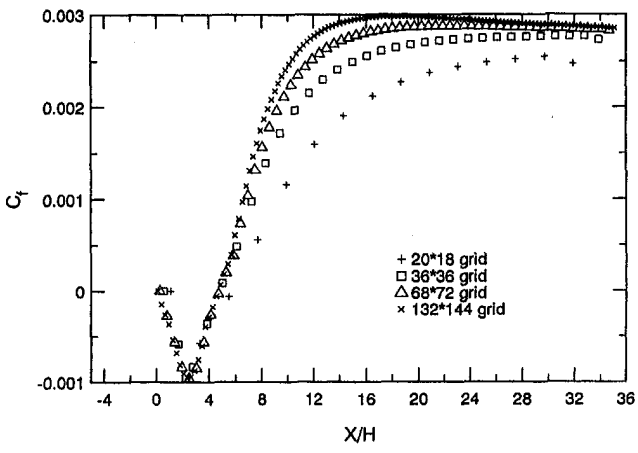

Fig. 3 Variation of friction coefficient along the south wall (step side)

Table 3 Calculated n values from C_p and C_f profiles

Using the first 3 grid distributions:					
x/H	n from C_p	(C_p)ext (% error)	x/H	n from C_f	(C_f)ext (% error)
4.4	1.22	0.898 (38.0)	6.7	1.41	0.00123 (10.7)
6.7	1.34	0.219 (10.3)	11.1	1.15	0.0026 (9.0)

Using the last 3 grid distributions:			
x/H	n from C_p	x/H	n from C_f
4.4	0.36	6.7	0.22
6.7	1.10		

Table 3. These calculations were done by using graphical interpolation in the regions where there is a monotonic convergence pattern. The first thing to observe in Table 3 is that there is most probably something wrong with the 132 × 144 grid solution, because the order of the method calculated using this grid is unacceptable. It is not clear what went wrong other than may be incomplete iterative convergence. The residuals were significantly large for this fine grid solution. The calculations were continued for thousands of more iterations but no significant changes were observed in the flow variables. This, however, is not sufficient to consider the results to be fully converged. Many other ways were tried to reduce the residuals without any success. This may be due to large scale unsteadiness induced by the unstable reattachment phenomenon. Unfortunately, iterative convergence seems to be one of the serious problems that the users of commercial codes have to cope with painfully. Nevertheless, the solutions with the 132 × 144 grid was discarded and the analysis was continued with the first three grid distributions.

The order of the method calculated using the first three sets of calculations is found to be between 1.15 and 1.41 (see Table 3). These numbers include interpolation errors and they do seem to be sensitive to small changes in the ϕ values. The values calculated at different locations and different flow variables are not exactly the same but they are close. It should be noted that Eq. (6) remains valid when ϕ is replaced by any other variable which is a linear combination of ϕ; C_p is a linear function of P, and C_f is a linear function of k as calculated in this analysis.

Now that the apparent order of the method is determined one can place error bounds on the computed variables at least in the regions where the method is applicable. The calculated relative errors using $n = 1.35$, Eq. (4) and Eq. (6), are also listed in Table 3.

Next Richardson extrapolation was applied to the axial velocity component. Sample results are tabulated in Table 4. At $x/H = 2.2$ (within the recirculation region), and $x/H = 4.4$ (close to reattachment point) the method does not work well; at $x/H = 2.2$ it gives some reasonable values between 1.3 to 2.6, but near the reattachment point the results are very inconsistent. However, away from the recirculation region (see Table 4) it seemed to work alright. At $x/H = 8.9$ the calculated values of n are between 0.96 and 1.65, which is in agreement with the previously calculated order of the method. The variation of the order n might partly be due to the zonal variability of the actual scheme used during the calculations; the hybrid scheme degenerates to the first order upwind scheme in convection dominated zones, and to the 2nd order central scheme in diffusion dominated zones.

The extrapolated values of the velocity are used with $n = 1.35$ (an average value) to calculate the truncation errors and these are included in Table 4. This is precisely what needs to be done to quantify numerical uncertainty in a given set of calculations. It should be noted that the errors can not be calculated using Eq. (7) unless the apparent order of the method is calculated in a reasonable manner. That is, the order should be calculated first and problematic regions should be identified as it was done above. Only then Eq. (6) or (7) can be used as an error estimator in those regions. In situations where n is not known the lowest value, which is one, can be used for conservative error estimates.

The variation of the axial velocity profiles at $h/H = 8.9$ with grid refinement are shown in Fig. 4. The three plots are the blown up sections of the profiles in the transverse direction. This was done to be able to depict the small variation as the grid is refined. Section (a) is close to the wall on the step side. Here the velocity decreases monotonically as the grid is refined. There is a crossover point near $y = 0.01$ m. In the mid-section of the channel (Fig. 4(b)) the velocity increases monotonically, and then the trend changes again near the opposite wall (Fig. 4(c)). Such a variation must occur with any conservative scheme; if the axial velocity increases in one region it must decrease in another so that the equation of continuity is satisfied.

There are two types of problems in the application of Richardson extrapolation to such variations: (1) near the crossover points the variations are so small that Eq. (6) gives erroneous results; of course, at the crossover point it is singular, hence a limiting procedure must be applied; (2) in regions with sharp gradients, e.g., near $y = 0.111$ in Fig. 4(c), the interpolation errors are large; some type of interpolation is needed to obtain values of the variable at the coarse grid nodes using the fine grid nodes. In Table 4, grid nodes 15 and 16 correspond to type 1, and type 2 problematic areas, respectively. Note that Eq. (4) can be used if n is known a priori. But it is recommended that

Table 4 Richardson extrapolation: velocity at $X/H = 8.9$ downstream from step (68*72, 36*36 and 20*18 grid)

Grid no.	Y (m)	Calculated velocity (68*72 grid)	Extrapolated velocity	Calculated exponent (n)	Extrapolated velocity ($n = 1.35$)	Error %
1	0.00229	19.650	21.131	1.444	21.296	7.729
2	0.00571	26.050	27.749	1.252	27.566	5.502
3	0.00914	34.700	35.718	1.217	35.571	2.449
4	0.01591	40.150	39.997	1.400	39.988	0.403
5	0.02374	40.450	40.258	1.359	40.256	0.481
6	0.03156	40.700	40.495	1.302	40.506	0.478
7	0.03939	40.950	40.713	1.180	40.756	0.475
8	0.04721	41.200	41.035	1.333	41.038	0.393
9	0.05504	41.400	41.204	1.189	41.238	0.391
10	0.06286	41.600	41.478	1.405	41.470	0.311
11	0.07069	41.750	41.607	1.263	41.620	0.310
12	0.07852	41.900	41.829	1.647	41.803	0.231
13	0.08634	42.000	41.789	0.963	41.870	0.308
14	0.09417	42.150	42.042	1.263	42.053	0.230
15	0.10200	42.300	—	—	42.300	0.000
16	0.10980	41.450	—	—	41.837	0.925

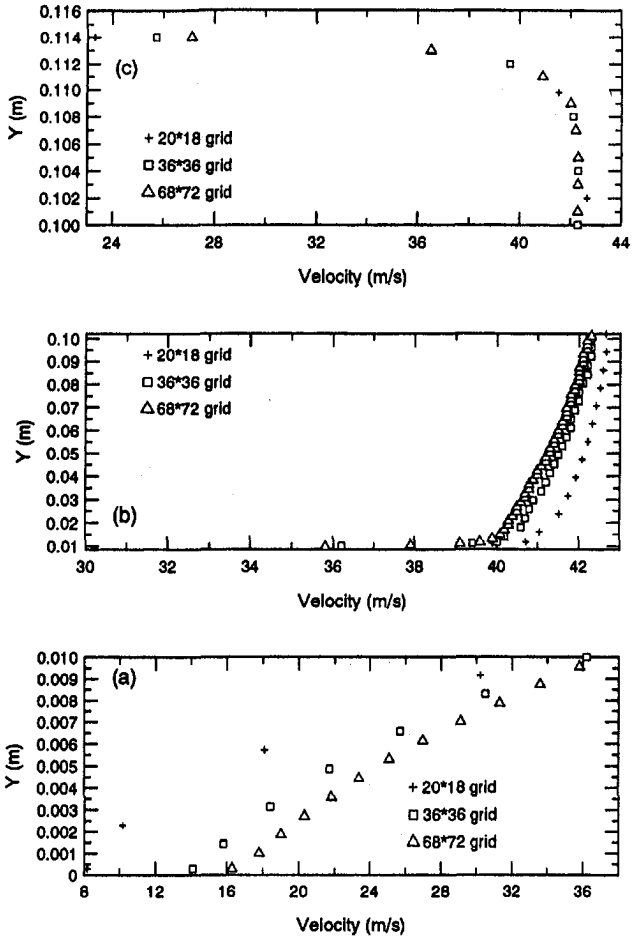

Fig. 4 Variation of axial velocity profile at $X/H = 8.9$ with grid refinement

the apparent order should still be calculated via Eq. (3), because its unreasonable values can be used as an error indicator.

Conclusions

The Richardson extrapolation method (REM) is applied to numerical simulations of turbulent developing pipe flow and turbulent recirculating flow over a backward facing-step. A commercial code, PHOENICS (Code #1), and a readily available code, TEACH (Code #2), were used for the simulations. The application of the method to turbulent pipe flow was not successful for either of the codes. The unreasonable values calculated for the order of the method indicated a user mistake, which was found to be the use of log-law boundary conditions in the sublayer where y^+ was less than 5. In this case the calculated turbulent kinetic energy profiles from Code #1 were unacceptable. It can be concluded from this that even in cases where it does not work, REM can be used as an error indicator.

Application of the method to turbulent recirculating flows is restricted by the presence of singular points, such as, separation and reattachment points. The use of wall function approach introduces further restriction in that the placement of some grid points in the sublayer can not be avoided. When this is the case the variation of flow parameters with grid refinement is not smooth, hence REM can not be applied in the whole flow domain. Furthermore, the grid refinement cannot be extended to the immediate vicinity of the wall. However, such problematic regions can be identified by using REM. In the remaining regions the method gives good results provided that the particular computational procedure being used give monotonic convergence with grid refinement.

For the present application, the apparent order of the computational method is calculated to be in the range $1.0 < n < 1.6$, using the simulations performed with Code #1. This result is quite reasonable since the hybrid scheme used in Code #1 has a theoretical order between 1 and 2. Approximately, the same values of n were calculated using three different flow variables, namely the pressure coefficient, friction coefficient and the axial velocity component. For some flow parameters, e.g., the reattachment length, the grid convergence was oscillatory, hence REM could not be applied.

In general, applications of REM the apparent order of the method should be calculated first to check the theoretical order; for hybrid schemes it must be calculated in any case, because the order of these schemes are domain dependent. Then, the fine grid results can be extrapolated, and with this and the apparent order of the code, truncation-convergence error bounds can be placed on the fine grid solution. For conservative error estimates, the lowest order of unity can be used.

References

Blottner, F. G., 1990, "Accurate Navier-Stokes Results for the Hypersonic Flow over a Spherical Nosetip," *J. Spacecraft and Rockets,* Vol. 27, No. 2, pp. 113–122.

Bradshaw, P., Launder, B. E., and Lumley, J. L., 1991, "Collaborative Testing of Turbulence Models," AIAA 91-0215, 29th Aerospace Science Meeting, Reno, NV, Jan. 7–10.

Celik, I., 1989, "Numerical Uncertainty in Fluid Flow Calculations: A Survey of Ideas and Opinions," Paper presented at the forum on *Methods for Estimating Uncertainty Limits in Fluid Flow Calculations,* ASME Winter Annual Meeting, San Francisco, CA, Dec. 10–15.

Celik, I., 1992, "Numerical Uncertainty in Fluid Flow Calculations: An Assessment of Current Status and Basic Needs for Future Research," *Proceedings of the Symposium on Future Research Needs in Fluid Mechanics,* ASME Fluids Engineering Division, Fluids Engineering Conference, Los Angeles, CA, June 21–26, pp. 27–30.

Celik, I., 1993, "Numerical Uncertainty in Fluid Flow Calculations: Needs for Future Research," ASME JOURNAL OF FLUIDS ENGINEERING, Vol. 115, pp. 194–195.

Celik, I., Chen, C. J., Roache, P. J., and Scheuerer, G., 1993, "Quantification of Uncertainty in Computational Fluid Dynamics," ASME Publication FED-Vol. 158, New York, NY.

Celik, I., and Zhang, W-M., 1993, "Application of Richardson Extrapolation to Some Simple Turbulent Flow Calculations," *Proceedings of the Symposium on Quantification of Uncertainty in Computational Fluid Dynamics,* I. Celik et al. eds., ASME Fluids Engineering Division Spring Meeting, Washington, D.C., June 20–24, pp. 29–38.

Caruso, S. C., Ferziger, J. H., and Oliger, J., 1985, "Adaptive Grid Techniques for Elliptic Flow Problems," Rept. No. TF-23, Thermosciences Div., Stanford University, Stanford, CA.

Churchill, S. W., Chao, P., and Ozoe, H., 1981, "Extrapolation of Finite-Difference Calculations of Laminar Natural Convection in Enclosures to Zero Grid Size," *Numerical Heat Transfer,* Vol. 4, pp. 39–51.

Dang, A. L., Kehtarnavaz, H., and Coats, D. E., 1989, "The Use of Richardson Extrapolation in PNS Solutions of Rocket Nozzle Flow," AIAA Paper No. 89-2895, AIAA/ASME/SAE/ASEE 25th Joint Propulsion Conference, Monterey, CA, July 10–12.

deVahl Davis, G., 1983, "Natural Convection of Air in a Square Cavity: A Bench Mark Numerical Solution," *International Journal of Numerical Methods in Fluids,* Vol. 3, pp. 249–264.

Demuren, A. O., and Wilson, R. V., 1994, "Estimating Uncertainty in Computations of Two-Dimensional Separated Flows," ASME JOURNAL OF FLUIDS ENGINEERING, Vol. 116, No. 2, pp. 216–220.

Driver, D. M., and Seegmiller, H. L., 1985, "Features of a Reattaching Turbulent Shear Layer in Divergent Channel Flow," *AIAA Journal,* Vol. 23, No. 2, Feb., pp. 163–171.

Durst, F., and Loy, T., 1984, "TEACH: Ein Berechnungsverfahren fuer Zweidimensionale Laminare und Turbulente Stroemungen," Report, Institute fuer Universitaet Hydromechanik, Universitaet Karlsruhe, Germany.

Ferziger, J. H., 1988, "A Note on Numerical Accuracy," Special Note, *International Journal for Numerical Methods in Fluids,* Vol. 8, pp. 995–996.

Ferziger, J. H., 1993, "Estimation and Reduction of Numerical Error," *Proceedings of the Symposium on Quantification of Uncertainty in Computational Fluid Dynamics,* I. Celik, C. J. Chen, P. J. Roache, G. Sheuerer, eds., ASME Fluids Engineering Division Spring Meeting, Washington DC. June 20–24, pp. 1–8.

Freitas, C. J., 1993, "JFE Editorial Policy statement on the Control of Numerical Accuracy," ASME JOURNAL OF FLUIDS ENGINEERING, Vol. 115, pp. 339–340.

Gossman, A. D., and Pun, W. M., 1973, TEACH: Lecture Notes for the Course entitled "Calculation of Recirculating Flows," Imperial College, London.

Kessler, R., Peric, M., and Scheuerer, G., 1988, "Solution Error Estimation in the Numerical Predictions for Turbulent Recirculating Flows," NATO AGARD

Conference Proc. No. 437 on *Validation of Computational Fluid Dynamics,* Lizbon, Portugal.

Lewins, J., and Becker, M., 1982, Eds., "Sensitivity and Uncertainty Analysis of Reactor Performance Parameters," *Advances in Nuclear Science and Technology,* Vol. 14, Plenum Press, New York.

Ludwig, J. C., Qin, H. Q., and Spalding, D. B., 1989, *The PHOENICS Reference Manual,* Cham TR/200, CHAM Limited, Bakery House, 40 High Street, Wimbledon Village, London SW19 5AU, England.

Mehta, U. B., 1991, "Some Aspects of Uncertainty in Computational Fluid Dynamics Results," ASME JOURNAL OF FLUIDS ENGINEERING, Vol. 113, pp. 538–543.

NATO (North Atlantic Treaty Organization)—Advisory Group for Aerospace Research and Development (AGARD), *Proceedings of the Conference on Validation of Computational Fluid Dynamics,* Proc. No. 437, Lisbon, Portugal, 1988.

Patankar, S. V., 1980, *Heat Transfer and Fluid Flow,* Hemisphere, NY.

Patankar, S. V., 1988, "Numerical Uncertainty in Fluid Flow Calculations," presented at the Panel Discussion on "Numerical Uncertainty in Fluid Flow Calculations," ASME Winter Annual Meeting, Chicago, Ill., Nov. 30–Dec. 2.

Richardson, L. F., 1910, "The Approximate Arithmetical Solution by Finite Differences of Physical Problems Involving Differential Equations, with an Application to the Stresses In a Masonary Dam," *Transactions of the Royal Society of London,* Ser. A, Vol. 210, pp. 307–357.

Roache, P. J., 1972, *Computational Fluid Dynamics,* Hermosa Publishers, Albuquerque, NM.

Roache, P. J., 1990, "Need for Control of Numerical Accuracy," *Journal of Spacecraft and Rockets,* Vol. 27, No. 2, Mar.–Apr., pp. 98–102.

Roache, P. J., Ghia, K. N., and White, F. M., 1986, "Editorial Policy Statement on the Control of Numerical Accuracy," ASME JOURNAL OF FLUIDS ENGINEERING, Vol. 108, p. 2.

Ronen, Y., 1988, *Uncertainty Analysis,* CRC Press Inc, Boca Raton, FL.

Rodi, W., 1980, *Turbulence Models and Their Application in Hydraulics,* Book Publication of Int. Association for Hydraulic Research, Delft, The Netherlands.

Ronen, Y., 1988, Ed., *Uncertainty Analysis,* CRC Press, Boca Raton, FL.

D. D. Joseph

R. Bai

T. Y. Liao

A. Huang

Department of Aerospace Engineering
and Mechanics,
University of Minnesota,
Minneapolis, MN 55455

H. H. Hu

Department of Mechanical Engineering
and Applied Mechanics,
University of Pennsylvania,
Philadelphia, PA 19104-6315

Parallel Pipelining

In this paper we introduce the idea of parallel pipelining for water lubricated transportation of oil (or other viscous material). A parallel system can have major advantages over a single pipe with respect to the cost of maintenance and continuous operation of the system, to the pressure gradients required to restart a stopped system and to the reduction and even elimination of the fouling of pipe walls in continuous operation. We show that the action of capillarity in small pipes is more favorable for restart than in large pipes. In a parallel pipeline system, we estimate the number of small pipes needed to deliver the same oil flux as in one larger pipe as $N = (R/r)^{\alpha}$, where r and R are the radii of the small and large pipes, respectively, and $\alpha = 4$ or 19/7 when the lubricating water flow is laminar or turbulent.

1 Introduction

The use of water as a lubricant to reduce friction in pipelining of heavy crude oil is an old idea which has been used sporadically over the past half century (Joseph and Renardy, 1992). The essence of lubrication is that water forms an annulus around oil so that oil does not touch the pipe wall, thus reducing the drag. A surprising but robust feature of fluid dynamics is that such a flow configuration is achieved more often than a stratified configuration, even when the densities of the viscous oil and the less viscous water are different. The levitation of the oil core against gravity appears to involve lift forces which are not yet perfectly understood. However, the fluids in a stopped pipeline are bound to stratify, leaving oil on the wall. The restart of a stopped pipeline is a major obstacle to be overcome before any water lubrication system becomes operational. Different ideas have been brought forth to prevent oil from sticking to the pipe wall and to make startup easier. For instance, hydrophilic walls, like the wall of a cement-lined pipe, have been proposed and are under investigation currently. In this work we shall discuss the possible effects of the size of the pipe upon the startup problem of a lubricated pipeline. We shall show that small pipes promote the action of capillarity and lead to configurations which are better for restart. In a parallel system we seek to determine the number of small pipes that will deliver the same flux as in one larger pipe with the same pressure gradient. The solution of this problem depends on the nature of the flow, laminar or turbulent, and other factors. It takes many more small pipes to deliver the same fluxes as in one larger pipe. A parallel system can have major advantages over a single pipe with respect to the cost of maintenance and continuous operation of the system, to the pressure gradients required to restart a stopped system and to the reduction and even elimination of the fouling of pipe walls in continuous operation. The engineering decision about whether many small pipes are better than a large one depends on the conditions of application in which the underlying fluid mechanics is a major player.

Contributed by the Fluids Engineering Division for publication in the JOURNAL OF FLUIDS ENGINEERING. Manuscript received by the Fluids Engineering Division October 30, 1993; revised manuscript received June 29, 1994. Associate Technical Editor: O. C. Jones.

2 Number of Small Pipes Which Are Equivalent to One Larger Pipe

We are going to calculate the number of small pipes of radius r needed to get the same flux of oil as in one larger pipe of radius R, provided that the pressure gradient and input ratio of volume flow rates are the same in each and every pipe.

First, consider the case when the lubricating water flow is laminar, and no secondary motion is present. The velocity field has one component, the axial component W, which can be solved analytically or numerically (see Bentwich, 1965 and Huang et al., 1995). The total fluid flux can be calculated from

$$Q = \int_{\Omega} W d\Omega, \tag{2.1}$$

where the integral is over the cross section of the pipe. Since the velocity W is linearly proportional to R^2 and the pressure gradient along the axis of the pipe, and $d\Omega$ scales as R^2, it is readily seen that

$$Q = R^4 q, \tag{2.2}$$

where the function q does not depend on R. Hence if a set of smaller pipes of radius r is to be used to deliver the same flux as one single larger pipe of radius R, $N = (R/r)^4$ of them will be needed.

For turbulent flow, a more realistic calculation of the number of small pipes can be performed based on empirical relations put forward by Arney, et al. (1993). A theoretical justification for these relations based on $k - \epsilon$ modeling of turbulence in the lubricating water flow has been given by Huang, Christodoulou and Joseph (1995).

Define an average velocity

$$V = \frac{Q}{\pi R^2}, \tag{2.3}$$

and a Reynolds number

$$\mathrm{Re} = \frac{2\rho_c RV}{\mu_w}(1 + \eta^2(m - 1)), \tag{2.4}$$

where Q is the total flux, η (≤ 1) is the radius ratio of the concentric oil core to the pipe, m is the viscosity ratio of water

to oil, and $\rho_c = (1 - \eta^2)\rho_w + \eta^2\rho_o$ is a composite density of water (ρ_w) and oil (ρ_o). The friction factor is defined as

$$\lambda = \frac{4Rf}{\rho_c V^2} \tag{2.5}$$

where f is the pressure gradient along the pipe.

A number of authors have attempted to correlate the friction factor λ with the Reynolds number Re, for example, Sinclair (1970) and Brauner (1991). For our purpose here we shall take a simple empirical relation put forward by Arney et al. (1993), which is

$$\mathrm{Re}^{1/4}\lambda = 0.316. \tag{2.6}$$

Substituting (2.3), (2.4), and (2.5) into the above correlation, we get

$$Q = R^{19/7}q$$

where q again is a function independent of R. Hence in turbulent flow, $N = (R/r)^{19/7}$ small pipes with radius r will be needed to deliver the same flux as in a single pipe of radius R.

Therefore, in general, the number of smaller pipes needed to deliver the same amount of total flux can be written as

$$N = (R/r)^{\alpha}, \tag{2.7}$$

where $\alpha = 4$ when the lubricating water flow is laminar, and $\alpha = 19/7$ when the water flow is turbulent. For example, the total flux in five pipes of radius 1 in. is the same as in one pipe of radius 1.495 in. in laminar flow, and the same as in one pipe of radius 1.809 in. in turbulent flow. This shows that a rather large number of small pipes are required to deliver the same flux as a single larger one.

However, if it is possible to get a more efficient lubrication with smaller water fractions in small pipes than in large pipes, then the number of small pipes needed would decrease. We can also decrease the number of small pipes by paying a penalty in the pressure gradient required for the parallel pipes. If the small pipes are efficiently lubricated, an increase in the oil flux can be achieved at a small cost.

3 Cost, Maintenance, and Continuous Operation of a Parallel Pipeline System

One of the major advantages of parallel pipelining is that the system can be kept in continuous operation without failures. It is unlikely that all of the parallel pipes in a system would fail at the same time. The repair of a single pipe in the system need not interfere with the continued operation of the others. It could be useful to have a water-filled pipe in the parallel system to press into service if one of the pipes in the parallel system fails. It is also easier to handle small pipes rather than large ones.

Another advantage of parallel pipelines is the possible reduction of the total cost in the pipeline system: initial, maintenance and operational costs. A rough quotation of cost of cement-lined pipe in 1993 is: \$5/ft for 2-in. pipe; \$8/ft for 3-in. pipe; and \$12/ft for 4-in. pipe. The initial cost of a parallel pipeline may be higher than a single one. However, the savings in the maintenance and operational costs may outweigh the initial cost. The engineering decision about whether many small pipes are better than a large one depends on the conditions of application and the required reliability of the system.

4 Effects of Capillarity in Lubrication and Restart of a Lubricated Pipeline

In a stopped lubricated pipeline, initially centered and continuous oil core may break up into drops or slugs under the action of capillarity, contact the pipe wall and spread. In this and the next two sections we are going to examine the effect of capillary force on the breakup and the spreading of the core.

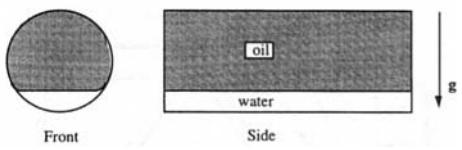

Fig. 1 Oil rises up in the pipe and sticks to the wall. We have a perfect vertical stratification. This situation is promoted by a large density difference, small interfacial tension, hydrophobic walls and large pipe radius. This configuration is not good for restart or continuous operation because the oil is sticking to the wall and water wedging between oil and wall is not possible.

Fig. 2 Water-wedged rest configuration of oil slugs in water. This is promoted by small pipes, small density differences, large interfacial tension and hydrophilic walls (water-wet concrete walls, for example). Restart of this configuration is much easier than the restart of the completely stratified configuration shown in Fig. 1.

Capillarity works more strongly in small than large pipes. Another way to say this is that gravity is more important in large pipes. The capillary force can be used to keep oil from sticking to the wall. To fix the idea, let us suppose that there is about 20 percent water and 80 percent oil in the pipe, and there is no motion. The oil can be distributed in the pipe in many ways. In Fig. 1 we show a bad distribution. In Fig. 2 we show a good distribution in which water is wedged between the pipe wall and the oil. In Fig. 3 slugs developed in an actual experiment in which capillarity is sufficiently strong relative to gravity. In this experiment the ratio of the effects of gravity to those of surface tension is not large enough for oil to ball up to plug the pipe. If the pipe were larger or the surface tension were smaller, we would get a picture more like Fig. 1.

It is apparent that strong effects of capillarity, especially when combined with the antisticking effects of hydrophilic walls, like wet cement, are advantageous for the startup of a stopped line.

Hu and Joseph (1992) computed the size of slugs like those shown in Fig. 3 from an idealized problem, in which a motionless oil core of uniform radius is centrally located in a pipe filled with water and gravity is neglected. They then studied the linearized stability of this problem to disturbances proportional to $\exp(\sigma t)\exp(i\alpha x)$, where t is the time, x is the coordinate along the axis of the pipe, α is the wave number of the disturbance in the x direction and σ is the growth rate of the disturbance. The analysis is framed in Bessel functions and is essentially the same as one given previously in a Ph.D. thesis by Hammond (1982). The growth rate σ is real valued. They found that the presence of the pipe wall has an important role in determining the wavelength corresponding to the maximum instability and the maximum growth rate of the disturbances. As the fraction of the fluid in the annulus becomes smaller and smaller, the wave number of maximum instability increases and tends to a limiting value of $0.7/R_1$ where R_1 is the radius of the

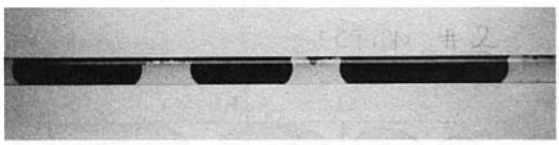

Fig. 3 Oil slugs are in water. The inner diameter of the pipe is 0.625 in. The ratio of the viscosity of water to the oil is 3.7×10^{-4}. The average size of a slug is predicted by linear stability theory using Rayleigh's idea of a maximum growth rate, taking into account of viscous forces, surface tension, volume fraction and pipe radius but neglecting gravity.

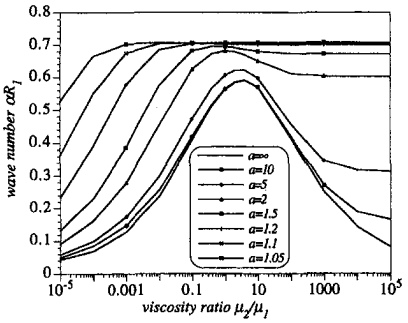

Fig. 4 Variation of the wave number corresponding to the maximum instability with the viscosity ratio (μ_2/μ_1) at different radius ratios ($a = R_2/R_1$), where μ_1 and μ_2 are the viscosities of the fluid in the core and in the annulus, R_1 and R_2 are the radii of the core and the pipe

core, see Fig. 4. The presence of the pipe wall reduces the growth rate of the disturbances (Fig. 5). The reduction is especially large when the more viscous fluid is in the annulus. When the annulus is very thin, the core may not break up during the time interval of interest since the growth rate is so small. Hu and Joseph (1992) reported that satisfactory agreement was exhibited between the theory and an experiment.

We get small slugs in small pipes; they scale with the pipe radius. Since gravity is neglected, the slugs will not flatten. In practice, the spreading property of the sessile drop, which is discussed in the next section, will spread the drop laterally in the pipe. Hence, for large pipes we can expect a stopped pipeline to look like Fig. 1, whereas for small pipes we might expect configuration shown in Fig. 2 and Fig. 3, which are good for restart.

5 Maximum Height of Sessile Drops

Once the lubricated pipeline stops, the drops or slugs of oil will float to the top section of the pipe, contact the pipe wall, spread and form the configuration shown in Fig. 2. Here we review the spreading property of a sessile drop on a planar surface.

Suppose a sessile drop is placed on a plane as in Fig. 6. The volume of the drop is increased holding the contact angle fixed. There is a volume when $h = h_{max}$ such that further increase of

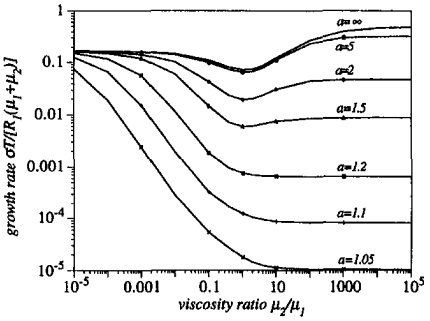

Fig. 5 Variation of the growth rate versus viscosity ratio at various radius ratios, where T is the interfacial tension

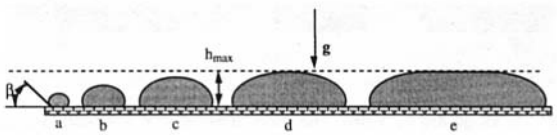

Fig. 6 If the volume of a sessile drop is increased while holding the contact angle fixed, a condition will be reached where the height of drop does not increase and the drop just spreads laterally

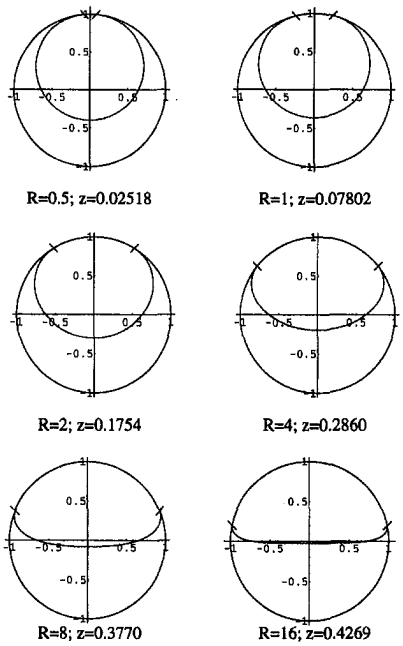

Fig. 7 Shapes of the oil core in different sizes of pipeline, where R is the pipe radius and z is the ratio of the arc length of contact between the oil and pipe wall to the circumference of the pipe. The pipeline is normalized by its radius. Density of water is 1.0 gm/cm^3, oil is 0.995 gm/cm^3. The value of the interfacial tension is 26.3 dyne/cm. The volume ratio is one to one. The contact angle of oil to the pipe wall is zero.

volume leads to lateral spreading rather than to an increase in the height of the drop. We can say that gravity prevents the drop height from increasing past h_{max}. Finn (1986, p. 63) has shown that the maximum height of an axisymmetric sessile drop is

$$h_{max} = \sqrt{\frac{2(1 + \cos\beta)T}{g\Delta\rho}} \tag{5.1}$$

where T is the interfacial tension, g is the gravitational acceleration, $\Delta\rho$ is the density difference of the fluids inside and outside the drop, and β is the contact angle of the drop with the solid surface as shown in Fig. 6. The maximum height h_{max} is a limiting value of the highest point on a drop of zero contact angle ($\beta = 0$) as the volume of the drop is increased to large values. The same Eq. (5.1) holds for a two dimensional sessile drop. The top of the drop will get flatter and flatter as the volume of the drop is increased. We call this a spreading property of sessile drops. Obviously we can put a sessile drop in a pipe.

6 Effect of Pipe Size on the Shape of Oil Core

In this section we examine the shape of a two dimensional sessile drop inside a pipe. Consider the case where the oil is lighter than the water and the volume ratio of oil to water is 1 to 1. Obviously increasing the diameter of the pipe increases the volume of the sessile drop and brings the spreading property into play. The effects of surface tension get less and less important. In Fig. 7 we have plotted the shape of the core in pipes of different diameter. The contact angle of the oil with the pipe wall is taken to be zero, which is appropriate for a hydrophilic wall, like the wall of a cement-lined pipe which absorbs water. There is an arc of contact of the oil bubble with the top wall. The length of the contacting arc increases with pipe radius because the buoyant weight of a larger bubble must be balanced by a bigger reaction force resulted from integrating the pressure inside the oil core over the contacting arc length.

It is obvious that the pressure gradient required to restart a stopped pipe will be greater when the arc of contact is larger. So small pipes are advantageous.

7 Effects of Capillarity on the Friction Factor and Holdup of Stratified Flow

When oil touches the pipe wall there will be a huge decrease in the oil flux due to the large viscosity of oil. If the oil-water interface is known, the velocity profile can be obtained by solving the governing equations of fluid dynamics. With the velocity profile, we can calculate the average velocity. Then a correlation between the friction factor λ (2.5) and the Reynolds number (2.6) can be obtained. In the perfect concentric core-annular laminar flow case this correlation is simply

$$\lambda = \frac{64}{\mathrm{Re}}.$$

In the case of stratified flow, this correlation depends on the viscosity ratio, the arc length of the contact between the oil and the wall and the holdup ratio H_w, which is defined as (see Arney et al., 1993)

$$\frac{V_w}{V_w + V_o}$$

where V_o and V_w are the volumes of oil and water in the pipe, respectively. A related quantity is the so-called input ratio of water

$$C_w = \frac{Q_w}{Q_w + Q_o}$$

where Q_o and Q_w are the oil and water flux, respectively. From Section 6 we know that we get shorter arc length of contact in smaller pipes. This in turn will give a higher value of oil flux as shown in Fig. 8, where the dimensionless oil flux q_o is plotted as a function of parameter $A = [(\rho_w - \rho_o)gR^2/T]$ for a viscosity ratio of 50, contact angle of zero degree and holdup ratio of 0.5. However, oil barely moves in the pipe when its viscosity is large. Thus the oil flux is much smaller than that of the water, which results in a value of input ratio of water C_w very close to one, as shown in Fig. 9. In the figure C_w is computed for different values of holdup ratio H_w and the length of contact. Therefore the total flux does not change dramatically as the contact length gets smaller. This means that the averaged velocity or the friction factor is not sensitive to the change of the pipe radius.

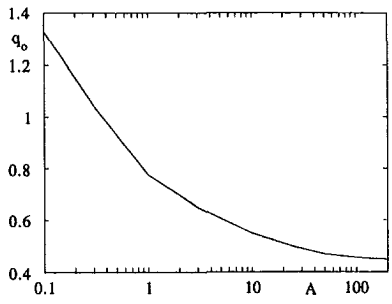

Fig. 8 The (dimensionless) oil flux as a function of parameter A, which is proportional to R^2. The viscosity ratio is 50, the contact angle is zero degree and $H_w = 0.5$.

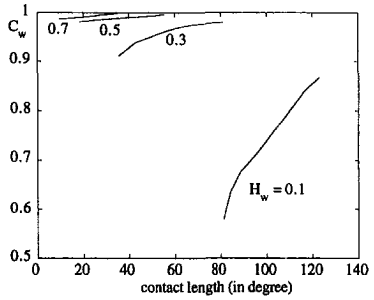

Fig. 9 The input ratio of water C_w as a function of the contact length for different values of H_w. The viscosity ratio is 50.

8 Conclusions

In a parallel pipeline system, we calculated that $N = (R/r)^\alpha$ small pipes are needed to deliver the same oil flux as in one larger pipe, where r and R are the radii of the small and large pipes respectively, and $\alpha = 4$ or $19/7$ when the lubricating water flow is laminar or turbulent. In practice, it is possible to get a more efficient lubrication with small pipes than in large pipes, thus the number of small pipes needed would decrease.

We show that strong effects of capillarity, especially when combined with the anti-sticking effects of hydrophilic walls, create a good configuration in which water is wedged between the pipe wall and the oil, and are advantageous for the startup of a stopped pipeline.

We calculated the shape of an oil core in pipes of different diameter. The relative arc length of contact increases with pipe radius, requiring a larger pressure gradient to restart a stopped line. So again small pipes are advantageous.

Therefore, a parallel system can have major advantages over a single pipe with respect to the cost of maintenance and continuous operation of the system, to the pressure gradients required to restart a stopped system and to the reduction and even elimination of the fouling of pipe walls in continuous operation.

Acknowledgments

This work was supported by the NSF, by the U.S. Army, Mathematics and AHPCRC, by the DOE, and by the Minnesota Supercomputer Institute. HHH acknowledges supports from NSF DMR91-20668 through the Laboratory for Research on the Structure of Matter at the University of Pennsylvania and from the Research Foundation of the University of Pennsylvania.

References

Arney, M. S., Bai, R., Guevara, E., Joseph, D. D., and Liu, K., 1993, "Friction Factor and Holdup Studies for Lubricated Pipelining I: Experiments and Correlations," *International Journal of Multiphase Flow,* Vol. 19, No. 6, pp. 1061–1076.

Bentwich, Michael, 1964, "Two-Phase Viscous Axial Flow in a Pipe," ASME *Journal of Basic Engineering,* pp. 669–672.

Brauner, N., 1991, "Two-Phase Liquid-Liquid Annular Flow," *International Journal of Multiphase Flow,* Vol. 17, pp. 59–76.

Finn, R., 1986, *Equilibrium Capillary Surfaces,* Springer-Verlag, New York.

Hammond, P. S., 1982, "Flows Driven by Surface Tension with Nearly Rigid Boundaries," Ph.D. thesis, University of Cambridge, U.K.

Huang, A., Christodoulou, C., and Joseph, D. D., 1995, "Friction Factor and Holdup Studies for Lubricated Pipelining II: Laminar and $k - \epsilon$ Models of Eccentric Core Flow," to appear in *International Journal of Multiphase Flow.*

Hu, H., and Joseph, D. D., 1992, "Capillary Instability of a Liquid Thread in a Circular Pipe," Army High Performance Computing Research Center, preprint 92-059.

Joseph, D. D., and Renardy, Y., 1992, "Fundamentals of Two-Fluid Dynamics, Vol. I: Mathematical Theory and Applications, Vol. II: Lubricated Transport, Drops and Miscible Liquids," *Springer Interdisciplinary Applied Mathematics,* Vols. 3 and 4.

Sinclair, A. R., 1970, "Rheology of Viscous Fracturing Fluids," *Journal of Petroleum Technology,* June, pp. 711–719.

Experimental Investigation of the Flow Inside a Water Model of a Gas Turbine Combustor: Part 1—Mean and Turbulent Flowfield

J. J. McGuirk[1]
Professor of Aerodynamics.

J. M. L. M. Palma[2]
Assistant Professor.

Imperial College of Science, Technology and Medicine,
Mechanical Engineering Department,
Exhibition Road,
London SW7 2BX
England

The present study examines the flow inside the water model of a gas turbine combustor, with the two main objectives of increasing the understanding of this type of flow and providing experimental data to assist the development of mathematical models. The main features of the geometry are the interaction between two rows of radially opposed jets penetrating a cross-flowing axial stream with and without swirl, providing a set of data of relevance to all flows containing these features. The results, obtained by laser Doppler velocimetry, showed that under the present flow conditions, the first row of jets penetrate almost radially into the combustor and split after impingement, giving rise to a region of high turbulence intensity and a toroidal recirculation zone in the head of the combustor. Part 1 discusses the mean and turbulent flowfield, and the detailed study of the region near the impingement of the first row of jets is presented in Part 2 of this paper.

1 Introduction

Until very recently, a rather simple methodology has been followed in the study of gas-turbine combustors, whereby its flow components were studied separately. Emphasis has been given to swirl (e.g., Vu and Gouldin 1982; Rhode et al., 1983; La Rue et al., 1984) and to the mixing of either a single jet or a row of jets with a crossflow (e.g., Chleboun et al., 1982; Atkinson et al., 1982; Andreopoulos and Rodi, 1984; Holdeman et al., 1984). These studies, although of great interest, were not fully representative, since the flow inside a gas-turbine combustor is not simply set up by one of its flow components, but by their relative strengths. Thus, experiments of increased practical relevance (e.g., Noyce et al., 1981; Green and Whitelaw, 1983; Heitor and Whitelaw, 1986; Bicen and Jones, 1986; Koutmos and McGuirk, 1989; Cameron et al., 1988) have begun to be performed in geometries similar to real combustors, and under experimental conditions such that realistic gas turbine combustor flowfields prevail inside these laboratory models (Bicen et al., 1989).

The works above underlined the multiplicity of fluid mechanics phenomena observed in gas turbine combustor flows, for instance the injection of jets into either swirling or non-swirling crossflow, the presence of curved shear layers, the formation of counter-rotating vortex systems, vortex shedding, etc. All of these features pose a formidable challenge for developers of mathematical models. It has, however, not to date proven easy to deduce the source of errors in comparison between current combustor models and data taken in reacting flow systems. Separation of errors between numerical, combustion, and turbulence models has been difficult if not impossible. However, many aspects of combustion depend strongly on mixing, controlled mainly by turbulent diffusion, and isothermal models then become of particular interest since the flow inside the combustor can be studied without the additional complexities implied by, for instance, variable gas densities, turbulence/combustion interaction and spray/droplet dynamics. In the present work, attention has been given to aerodynamics phenomena under isothermal conditions only.

A small scale perspex model of a can-type gas-turbine combustor (Lefebvre, 1983) is used in the experiments, however information gathered will be of general validity in all flows containing jet/jet and jet/swirl interactions. The work had the two main objectives of increasing our understanding of the dominant phenomena in this type of flow and providing experimental data to assist the development and validation of mathematical models, hopefully leading to improved combustor design and satisfying the highly demanding requirements of future combustors (Bahr, 1987).

The present paper contains three major sections: Section 2 describes the experimental set-up and geometry, whereas the bulk of the results are included in Section 3 and the most important conclusions are summarized in Section 4.

2 Experimental Procedures

2.1 Experimental Setup and Model Geometry. The combustor model, constructed from perspex, is shown in Fig. 1. The swirler, fuel injector, primary jets, and dilution jets, were all fed from constant head tanks through concentrically arranged independent circuits. The fuel injector was a cone with 10 equally spaced holes of 1.7 mm diameter. Two swirlers were used, both with 18 curved vanes but of different angles, 30 and 45, with swirl numbers of 0.46 and 0.56, respectively. These values were evaluated from velocity measurements taken in a separate experiment inside a downstream tube with a diameter identical to the swirlers diameter. The cylindrical barrel, terminated by a circular to rectangular nozzle, contained six primary

[1] Present address: Loughborough University of Technology, Department of Aeronautical and Automotive Engineering and Transport Studies, Loughborough, Leicestershire LE11 3TU, England.

[2] To whom all correspondence should be addressed. Present address: Faculdade de Engenharia da Universidade do Porto, Departamento de Engenharia Mecânica e Gestão Industrial, Rua dos Bragas, 4099 Porto Codex, Portugal.

Contributed by the Fluids Engineering Division for publication in the JOURNAL OF FLUIDS ENGINEERING. Manuscript received by the Fluids Engineering Division February 15, 1993; revised manuscript received February 23, 1995. Associate Technical Editor: Wing-Fai Ng.

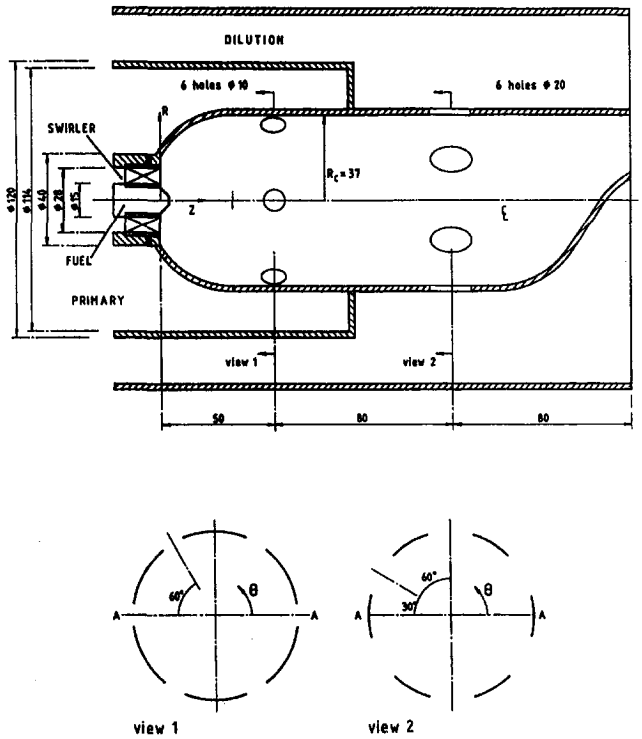

Fig. 1 Combustor model

and six dilution jets, 80 mm apart and staggered by half a pitch with respect to each other.

The present model is a replica of a metal model used for combusting studies by Tse (1988) and Bicen et al. (1990), and differs from that used by Heitor and Whitelaw (1986) and Koutmos and McGuirk (1989) in number and size of dilution holes and swirler size. These changes have been made to simulate more closely the primary zone characteristics of modern can-type combustors.

2.2 Measurement Technique and Error Analysis. The single-component laser Doppler velocimeter (LDV) system was operated in differential forward scatter mode (Durst et al., 1981). The emitting part of the optics consisted of a 6 mW He-Ne laser (Spectra Physics, model 120S), an imaging lens, a grating disk (model type R-H, manufactured by Technisch Physische Dienst TNO-TH, Delft, The Netherlands) and two collimating lenses. The rotating grating module (the grating disc and its motor) and the last two lenses were all part of an integrated optical unit, which enabled the alternate measurements of two perpendicular components of velocity without realignment. The main characteristics of the LDV system are summarised in Table 1.

Table 1 Characteristics of the laser-doppler velocimeter

Characteristics of the beam originating from the He-Ne laser:	
Nominal power	6 mW
Wavelength in vacuum	632.8 nm
Diameter of $1/e^2$ intensity region	0.8 mm
Characteristics of the lenses (nominal focal lengths):	
Imaging lens from laser to grating	150 mm
Collimating lens after grating	300 mm
Imaging lens to form measuring volume	300 mm
Imaging lens to collect scattered light	200 mm
Characteristics of the measuring volume:	
Half-angle of intersection in air (measured)	5.82° (±0.01°)
Half-angle of intersection in water (calculated)	4.37°
Minor axis of region within $1/e^2$ intensity in water (calculated)	0.152 mm
Major axis of region within $1/e^2$ intensity in water (calculated)	1.981 mm
Number of fringes (calculated)	48
Fringe spacing (calculated)	3.120 μm
Velocimeter transfer constant	0.321 MHz/(m/s)
Shift frequency	0.944 MHz; 2.411 MHz

The optical set up was attached to a traversing table, positionable within ±0.1 mm. However, the reference location was found by positioning the measuring volume on the wall and a displacement error of 1 mm can occur. Figure 1 indicates the coordinate system and its orientation with respect to the vertical. Measurements at different angular locations (Θ) were made by rotation of the whole combustor. Parallelism between the test section and the laser beam could only be guaranteed when a jet hole edge interrupted the beam (i.e., at Θ = 0 deg and 30 deg; but not at Θ = 15 deg location). Positioning errors can also occur due to refraction phenomena; because of this, measurements of radial velocity close to the walls were deleted on the grounds of unreliability and corrections were made to the location of the measuring volume and, in the case of the swirl component, also to the velocimeter transfer constant. These corrections, made according to Bicen (1982), did not exceed 1 percent in the case of profiles along the barrel and 2 percent for the combustor head. The low magnitude of these corrections, corresponding to the worst situation (close to the walls), is a consequence of the small thickness of the model wall compared to its diameter.

The photomultiplier tube (E.M.I. 9558) was powered by a Brandenburg power supply (model 2475R), and its electric signal, after being high-pass filtered (Khron-Hite filter model 3200), was analysed via a digital counter processing system. The counter (Heitor et al., 1984) was able to perform measurements of frequencies from 31.25 kHz up to 15 MHz at a sampling frequency of 25 kHz. The remote control of the counter

Nomenclature

k = turbulence kinetic energy
$\dot{m}$ = mass flow rate
u = turbulent velocity scale
U_b = bulk velocity in the combustor
r = radial coordinate
R_C = combustor radius
R_λ = Reynolds number based on Taylor microscale
Re_{bulk} = Reynolds number based on bulk velocity and combustor diameter
U, V, W = time-averaged axial, radial and circumferential velocities
$\sqrt{u^2}, \sqrt{v^2}, \sqrt{w^2}$, = rms turbulence intensities in axial, radial, and circumferential directions
z = axial coordinate
λ = Taylor microscale
θ = swirler vane angle
Θ = azimuthal coordinate
η = Kolmogorov microscale
ν = kinematic fluid viscosity
ϵ = turbulence energy dissipation rate

Subscripts

sw = swirler flow
pr = primary jet flow
dil = dilution jet flow
tot = total flow rate (i.e., sw + pr + dil)
cross = crossflow (i.e., sw + pr)

Table 2 Experimental conditions

N.	θ	$\dot{m}_{sw}$ [kg/s]	$\dot{m}_{pr}$ [kg/s]	$\dot{m}_{dil}$ [kg/s]	$\dot{m}_{tot}$ [kg/s]	U_b [m/s]	Re_{bulk}	$\dot{m}_{pr}/\dot{m}_{sw}$	$\dot{m}_d/\dot{m}_{cross}$
1	45°	0.543 [17]	1.04 [33]	1.60 [50]	3.19	0.741	4.9×10^4	1.92	1.01
2	30°	0.797 [23]	1.04 [30]	1.60 [47]	3.44	0.800	5.3×10^4	1.31	0.87
			higher swirler flow						
3	—	—	1.04 [40]	1.60 [60]	2.64	0.615	4.1×10^4	∞	1.53
			without swirler flow						
4	30°	0.543 [100]	—	—	0.543	0.126	8.3×10^3	0	0
			swirler flow only						

NOTE. — mass flow rate as percentage of the total within brackets.

and pre-processing of the data were carried out by a microcomputer which set the minimum measurable frequency and the time resolution of the system; this digitisation error was always less than 0.1 percent of the measured frequency and varied from 30 Hz up to 4 kHz. The spatial resolution of the system is set by the largest dimension of the measuring volume (George and Lumley, 1972) and an estimate of the Kolmogorov microscale length ($\eta = (\nu^3/\epsilon)^{1/4}$, from Tennekes and Lumley, 1972) assuming $u = U_b$ ($\epsilon = u^3/2R_C$) shows that its measurement is beyond the capabilities of the present system; the Taylor microscale, λ ($\lambda/\eta = 15^{1/4}\, R_\lambda^{1/2}$), is just within the limitations of the system.

Because of the low Doppler frequency characteristics of the flow and the low frequency limitations of the counter system, frequency shifting was always required. The minimum shift frequency available was 0.944 MHz and this centered the signal in a range of frequencies where the resolution of the counter was 0.49 kHz (0.0015 m/s) and the accuracy was 0.025 percent. Careful determination of the frequency shift was required due to its high magnitude compared with the Doppler frequency, which was particularly critical when measuring in regions of low velocities. Two values of shift frequency were used: 0.944 MHz and 2.41 MHz. The latter was restricted to high turbulence locations which, unfortunately, were also locations of nearly zero velocity; nevertheless the resolution of the counter was always only 1.9 kHz and the accuracy 0.1 percent. At some stage, an attempt was made to use a frequency tracker (Cambridge Consultants CC08 Processor) but the needs of higher dynamic response led to the use of the highest frequency range of the instrument, 16 MHz, with an inherent accuracy of 0.5 percent, 8 kHz (i.e., 0.25 m/s), and it was abandoned; similar problems have been reported by Founti et al. (1985).

Statistical quantities were found from direct ensemble averaging over a maximum block size of 8064 individual samples. Post-processing included the refraction corrections mentioned above and the increase of the block size, by merging the statistics of various data blocks corresponding to a single location, especially in regions with a high energy content at low frequencies. Although samples of any size could then be obtained in practice, no more than four sets of 8064 samples were taken, restricted to the region around the primary jet impingement. Due to the finite sample size, a statistical error analysis of the mean and rms measurements has been performed, based on Yanta and Smith (1973). Assuming a 99 percent confidence level, the resulting error bars were smaller than the symbols used for plotting. It is important to note that this analysis is valid only under the assumption of Gaussian turbulence; in Part 2 of the present study (McGuirk and Palma, 1995), the measurements of skewness and flatness provide a point by point check on the validity of this assumption.

Gradient broadening (Durst et al., 1981) is also a possible source of errors. This can lead to overestimation of the rms values by up to 5 percent in regions of very steep gradients, but in most parts of the combustor the maximum error in the rms values was less than 2 percent for the size of measuring volume used in the experiments. Velocity bias error (McLaughlin and Tiedermann, 1973; Edwards, 1987) was neglected; a simple unweighted average was used.

2.3 Experimental Conditions. The experimental conditions under which the rig was used are shown in Table 2. The swirler flow rate was monitored by a rotameter accurate to within 2 percent. The primary and dilution jet flows were found by integration of measured velocity profiles in the annular region of the corresponding supply tubes; no better than 10 per-

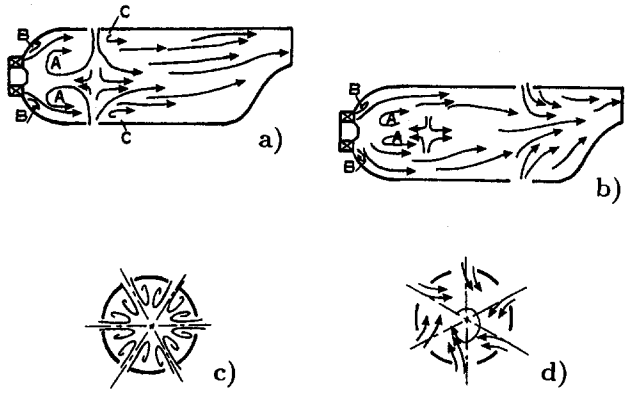

Fig. 2 Schematic longitudinal and cross-sectional views of the flow pattern inside the combustor: (a) primary holes plane (Θ = 0 deg, center longitudinal plane); (b) dilution holes plane (Θ = 30 deg, mid longitudinal plane); (c) primary holes plane; (d) dilution holes plane (as viewed from the nozzle towards the swirler)

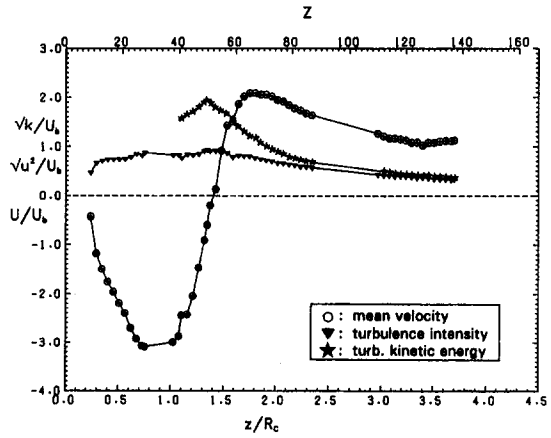

Fig. 3 Centreline values of mean axial velocity, turbulence intensity and turbulence kinetic energy (case 1)

cent accuracy could be achieved due to the uncertainty associated with the exact dimensions of the tubes. Case 1, the standard case, simulates the primary/swirler and dilution/cross flow ratios as in the combusting experiment of Bicen et al. (1990). Previous work by Bicen et al. (1989) has confirmed that case 1 conditions provided a correct simulation of the flow pattern observed in the combusting experiment. Cases 2, 3, and 4 allow the effect of the swirler flow rate to be quantified. These were made with a different swirler, but the work by Palma (1989) shows this to be of insignificant consequence.

According to Bicen and Jones (1986), no significant Reynolds number dependence of the flow is expected at the values of Reynolds number (Table 2) of the present experiment. The reduced importance of the Reynolds number as a flow scaling parameter in model combustors should be born in mind (Beer and Chigier, 1972; Spalding, 1963), since the main parameters on which the flow should be scaled are those related to the relative magnitude of the various streams provided they are turbulent (Bicen et al., 1989).

3 Analysis and Discussion of Results

The velocity results are plotted in non-dimensional form. R_C is the internal radius of the model and U_b is the bulk velocity (0.741 m/s) for case 1. A cylindrical polar system of coordinates (see Fig. 1) was used for representation of the results; however, to facilitate the discussion, different signs are used to identify radial locations in different sides of the centreline. Negative values of radial velocity correspond to flow moving radially towards the centreline. The swirler flow rotates anticlockwise, as viewed in the downstream direction; the swirl velocity is displayed as positive on the right hand side and negative on the left-hand side of the centerline.

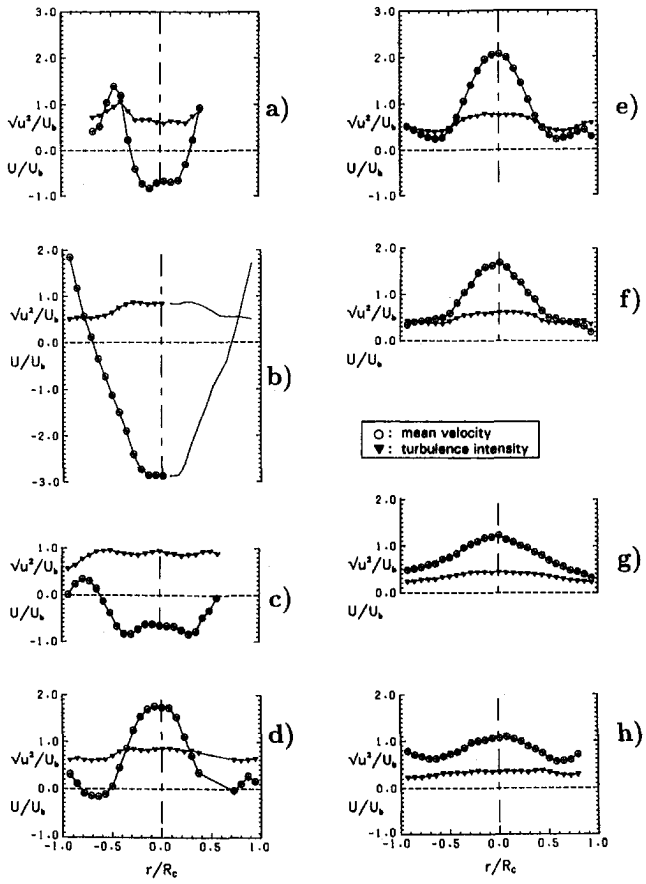

Fig. 4 Measurements of axial velocity in the plane Θ = 0 deg (case 1): (a) z = 8 mm; (b) z = 40 mm; (c) z = 50 mm; (d) z = 60 mm; (e) z = 70 mm; (f) z = 85 mm; (g) z = 110 mm; (h) z = 130 mm

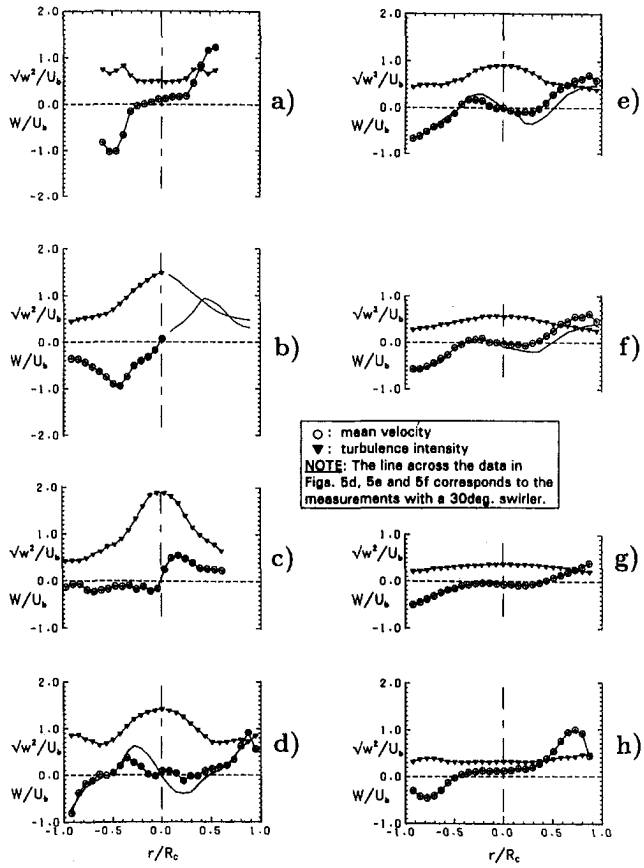

Fig. 5 Measurements of azimuthal velocity in the plane Θ = 0 deg (case 1): (a) z = 8 mm; (b) z = 40 mm; (c) z = 50 mm; (d) z = 60 mm; (e) z = 70 mm; (f) z = 85 mm; (g) z = 110 mm; (h) z = 130 mm

3.1 Standard Case. To facilitate the discussion of the results, schematic views of the mean flow, based in observations and forthcoming velocity measurements, are first described.

Figures 2a and 2b show views in longitudinal planes containing the axes of the first and second row of holes, respectively. The primary jets penetrate almost radially into the combustor and give rise to a toroidal central recirculation zone (zone A) in the head of the combustor. This zone is a prerequisite for stable combustion and, depending on their momentum ratio, the primary region is said to be driven either by the primary jets or by the swirler flow (Lefebvre, 1983). There are gas-turbine combustors without swirlers; however, all seem to have jets discharging through the combustor walls, probably because of the critical stability characteristics of swirling flows, either under isothermal (e.g., Escudier and Zehnder, 1982) or combusting conditions (e.g., Syred and Beer, 1974). In the case of gas-turbine combustors, a so-called precessing vortex core can give rise to an undesirable central core of unmixed fluid throughout the combustor (Koutmos and McGuirk, 1989). Other regions with negative axial velocity are: zone B, near the walls of the combustor head, and zone C, in the wake of the primary jets. Zone B is a consequence of the sudden expansion of the flow leaving the swirler. Its size depends not only on the precise head geometry, but also on the characteristics of both the swirler (higher swirl number may reduce it, e.g., So and Ahmed, 1986) and the primary jet flow (in the limit of no swirler flow this region does not exist and the central toroidal recirculation zone completely fills the combustor head). Region C is typical of jets in crossflow (e.g., Andreopoulos and Rodi,

1984). Neither region B nor region C are requirements of design, and region C is usually referred to as undesirable, since it may provide an extra region for flame anchorage, with damaging consequences to the combustor wall (Bhangu et al., 1983).

The cross-sectional view in Fig. 2(*c*), shows the flow in the primary jet plane for a situation of low swirl momentum. There are two counter-rotating vortices between each pair of jets which, on increasing the strength of the swirling flow, are shifted circumferentially and may even disappear. Provided the momentum fluxes of the jets are all of similar magnitude there is a cyclic repeatability of the mean flow structure and six similar sectors of 60 degree each can be identified. The conditions under which this repeatability can prevail have been addressed by Bicen et al. (1989). The dilution jets, Fig. 2(*d*), are expected to penetrate less compared to the primary jets because of their lower momentum flux ratio relative to the crossflow. The main role of the dilution jets is to decrease the bulk temperature and to ensure an appropriate shape for the temperature profile at the inlet of the turbine. Consequently there is no need for such strong impingement as in the case of the primary jets. Cyclical repeatability may not be observed at the plane of the dilution jets, due to the proximity of the nozzle.

From the description above the individual flow components of the combustor flow may be easily identified. The reason for the extreme complexity of the present flow is the variety of flow patterns that may be set up as the relative "strengths" of these components change. The picture above, though brief, is thought to be sufficient as a visual aid for understanding the following velocity measurements.

The different mass flow ratios of the primary and dilution jets compared with their respective cross flows (1.9 and 1, respectively) show clearly in the centreline axial velocity profile (Fig. 3). Negative values of the axial velocity persist up to the impingement point of the primary jets, with a maximum of three times the bulk velocity at about one combustor radius downstream. The main characteristics of the impingement region around $z = 52$ mm are a strong axial gradient and a peak value of turbulence kinetic energy. At $z = 130$ mm the flow accelerates due to the partial blockage caused by the dilution jets; no jet-on-jet impingement occurs and there is no negative axial velocity, as would be expected in a well-behaved dilution jet system.

Figures 4, 5, and 6 show the radial profiles of the three velocity components in a longitudinal plane containing the axes of two opposed primary holes, centre longitudinal plane. These figures are the quantitative counterpart to the schematic view in Fig. 2(*a*). At $z = 8$ mm the influence of the swirler flow is evident from the positive values of the axial component of velocity for $r/R_C > 0.3$ (Fig. 4(*a*)) and the two maxima in the swirl component with values of 1.1 (Fig. 5(*a*)). Both axial and swirl turbulence intensity are fairly constant over the radius only evidencing small peaks associated with high shear regions. This was the closest location to the swirler that could be measured; the curvature of the head distorted the laser beams and precluded measurements at axial coordinates less than 8 mm. Only measurements with a refractive index-matching technique (Edwards and Dybbs, 1984) would circumvent this problem.

Further downstream, at $z = 40$ mm (Fig. 4(*b*)), the region of backflow extends up to $r/R_C = 0.7$. The inner core of the flow is moving towards the swirler rotating in a solid body fashion up to mid radius (Fig. 5(*b*)). The normal stresses show the high anisotropy, typical of the region surrounding the primary jet impingement; the centreline values of the azimuthal and radial components (Figs. 5(*b*) and 6(*a*)) are twice those of the axial component (Fig. 4(*b*)). In the mean radial component (Fig. 6(*a*)) a nonsymmetrical shape is observed, for which no explanation can be found; the negative radial velocity (flow moving toward the centerline) is due to the clockwise rotation of the central toroidal vortex (region A in Fig. 2(*a*)).

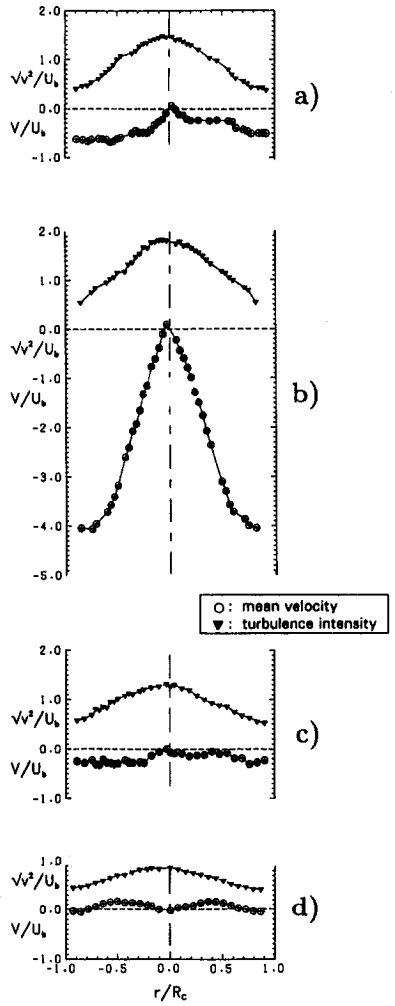

Fig. 6 Measurements of radial velocity in the plane Θ = 0 deg (case 1): (a) *z* = 40 mm; (b) *z* = 50 mm; (c) *z* = 60 mm; (d) *z* = 70 mm

The high anisotropy of the flow is most evident along the axes of the primary holes, at $z = 50$ mm (Figs. 4(*c*), 5(*c*), and 6(*b*)), where the centerline values of the azimuthal and radial turbulence intensities (Figs. 5(*c*) and 6(*b*)) are still higher. The primary jets emerge with a radial velocity of four times the combustor bulk velocity and decelerate linearly between $r/R_C = 0.5$ and the centerline (Fig. 6(*b*)). This linear deceleration was also found along the axial direction (Fig. 3), suggesting an inviscid behaviour close to the impingement point of the six radially impinging jets (Batchelor, 1967), and explaining the sensitivity of calculations of this flow to grid refinement in this zone (McGuirk and Palma, 1993). Little swirl motion has been imparted to the jets (Fig. 5(*c*)) due to their large radial momentum compared to the crossflow momentum. By comparing the profiles of axial velocity at three angular locations, Θ = 0, 15, and 30 deg (Fig. 7), one can see that large positive axial velocity is observed only in planes between the jets (Figs. 7(*b*) and 7(*c*)) and for $r/R_C > 0.7$; furthermore, this is the only region where for any value of Θ the rotation of the flow agrees with the rotation imparted by the swirler (see Fig. 7(*c*)), showing that the swirler flow is mainly transported near the walls, due to the blockage caused by the primary jets. The negative axial velocity of the inner core (Fig. 7), in this region so close to the stagnation point, shows that part of the jet flow after impingement is deflected upstream toward the swirler, giving rise to the toroidal recirculation zone designated above as region A. The swirl component in the inner region, $-0.7 < r/R_C < 0.7$, is dominated by the flow resulting from

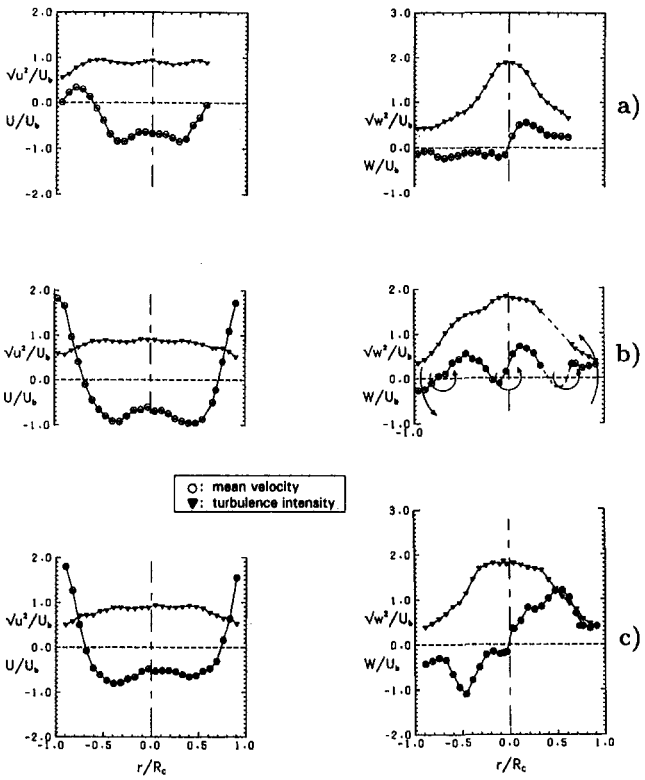

Fig. 7 Measurements of axial and azimuthal velocity in the plane z = 50 mm (case 1): (a) Θ = 0 deg; (b) Θ = 15 deg; (c) Θ = 30 deg

impingement and is strongly dependent on the angular location. To indicate the complex vortex system set up by the primary jet impingement, arrows have been drawn on top of the profile (Fig. 7(b)). Due to interference of the laser beams with the edges of the holes, measurements of the swirl component were not possible around r/R_C = 0.5 (Fig. 7(b)). The points in this region are joined by a dotted line, consistent with our interpretation of the flow pattern.

Bimodal probability density function (PDF) distributions of the swirl velocity, first suggested by the large amplitude variations of the oscilloscope traces, were found in some radial locations at z = 50 mm. The exact location and discussion of the conditions leading to their formation are the subject of Part 2.

Compared to the measurements along the axes of the primary holes (Fig. 6(b)), there is a dramatic decrease of the radial component at z = 60 mm (Fig. 6(c)) just one hole diameter further downstream; a maximum negative value of −0.3 was measured. Also, the turbulence levels of the azimuthal and radial components (Figs. 5(d) and 6(c)) and the angular variations of the azimuthal component (Figs. 8) are much reduced. The axial component reaches its maximum positive value on the centerline in this axial location (see also Fig. 3) and becomes negative in the wake of the jets (Figs. 4(d) and 8(a)), although not in the immediate vicinity of the wall; this is the region mentioned above as zone C.

At z = 70 mm, as the flow readjusts from the centerline towards the low pressure region behind the jets, the radial velocity becomes positive (Fig. 6(d)) and the axial velocity increases near the wall (Fig. 4(e)) compared to the previous axial location. The counter-rotating vortices resulting from jet impingement, rotate via the effect of the enveloping swirler flow and downstream of the primary jets can be observed at Θ = 0 deg (Fig. 5(d)). Note in Figs. 5(d) and 5(e) (at z = 60 and z = 70 mm) the two peaks in the azimuthal velocity on each side of the centerline with a rotation opposite to the rotation of the swirling flow. To illustrate in more detail the flow structure in this region we may refer to Fig. 8, with profiles of azimuthal velocity for three angular locations, at z = 60 mm. The transport of the swirler flow near to the wall can now be observed at all angular locations. The two counter-rotating vortices are centered at a radial location r/R_C = 0.55 and are split by a small region at the combustor centerline where a weak effect of the swirler flow can be noticed. This is much evident at angular locations not aligned with the primary jet axes (Θ = 15 deg and Θ = 30 deg, Figs. 8(b) and 8(c)). The experimental data obtained with the 30 deg swirler is also included (see Figs. 5(d), 5(e), 5(f), and 8(a)). In this case, because of the reduced angular momentum imparted to the jets for a swirler with a lower Swirl number, there is no apparent influence of the swirler around the combustor centerline and the structure of the inner core generated solely by the primary jets flow becomes clearer.

The measurements at z = 70, 85 and 110 mm (Figs. 4, 5, and 6) all show an identical general trend. As the distance from the primary jets increases and the identity of each jet is lost, the swirl component is reduced around the centerline and the turbulence approaches isotropy.

Note that the dilution holes are not aligned with the primary holes and that the location Θ = 30 deg corresponds to the axis of the dilution holes. The comparison between the mid and the central longitudinal plane, Θ = 30 deg and Θ = 0 deg, in Fig. 9, shows that the cross flow accelerates near the wall as it goes between the jets Θ = 0 deg, Fig. 9(a) and that the swirl component is similar in both planes. In contrast to primary jet behaviour, the dilution jets are rotated by the effect of the swirling crossflow (Fig. 9(b)). Virtually zero radial velocities were measured over the entire combustor diameter in the plane between the dilution jets.

Previous work in gas-turbine combustor geometries (e.g., Clarke et al., 1963, Lefebvre, 1983, or the studies related to the current work of Heitor and Whitelaw, 1986 and Koutmos and McGuirk, 1989) showed the combustor flow more like a mass of fluid rotating in a vortex fashion upon which radial opposing jets penetrate and are compelled to follow a helical path. However, the velocity measurements above show that this is not the case under the present conditions. The present flow should rather be viewed as a set of 6 similar 60 degree sectors generated by the impingement of the six radial opposing jets; the cross flow, although rotating, is unable to impart much rotation to the jets and escapes in the gaps between the jets.

3.2 Parametric Study. In the previous section, the results of the standard case were presented and the main features of the combustor flow illustrated. Here, the effect of the swirler flow is studied by: (i) increasing the swirler flow to the maximum possible in the present rig ($\dot{m}_{pr}/\dot{m}_{sw}$ = 1.31, case 2), corresponding to a 30 percent decrease in primary to swirler flow ratio compared to case 1; (ii) reducing the swirler flow to zero ($\dot{m}_{pr}/\dot{m}_{sw} = \infty$, case 3), i.e., the flow inside the combustor is set up only by the primary and the dilution jets; (iii) blocking both the primary and dilution holes ($\dot{m}_{pr}/\dot{m}_{sw}$ = 0 and $\dot{m}_{pr}/\dot{m}_{cross}$ = 0, case 4), i.e., the flow inside the combustor is set up by the swirler flow only. None of these cases will be covered as extensively as the standard case; the measurements were such as to allow the influence of the primary to swirler flow ratio to be assessed.

Comparing Figs. 4(b) and 10(a), we can see that the swirler has contributed to the widening of the region of negative axial velocity and to an increase of the backward flow rate; this is one of the advantages of the swirler flow. The general shape of the velocity profile is similar either with (case 1, Fig. 4(b)) or without swirler flow (case 3, Fig. 10(a)) and this is proof that under case 1 experimental conditions the primary region is dominated by the primary jet flow.

If there is no swirler flow, for symmetry reasons the mean azimuthal component should be zero in longitudinal planes con-

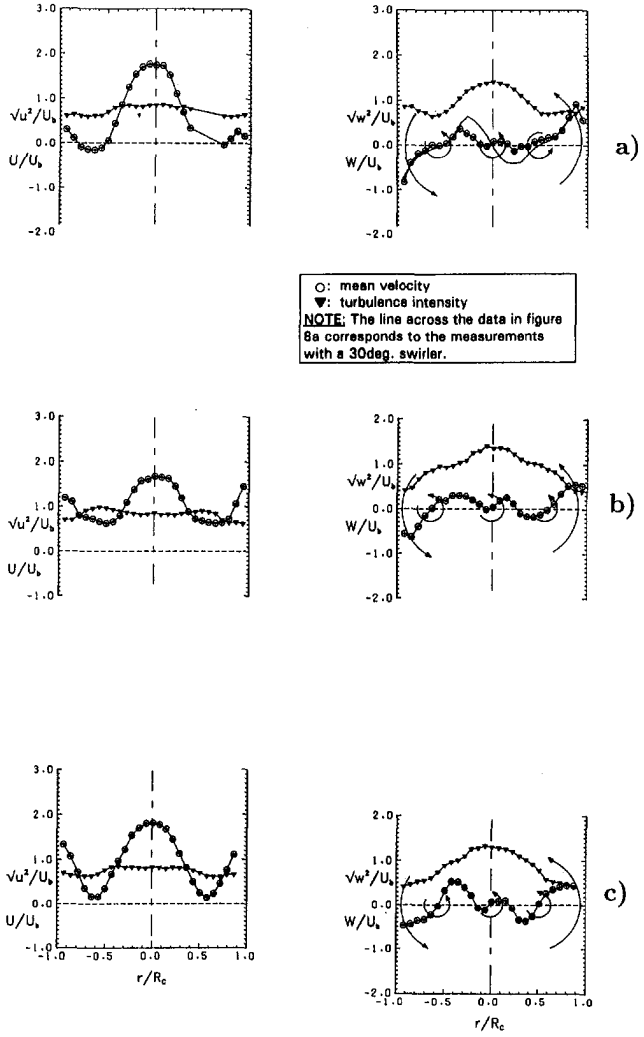

Fig. 8 Measurements of axial and azimuthal velocity in the plane z = 60 mm (case 1): (a) Θ = 0 deg; (b) Θ = 15 deg; (c) Θ = 30 deg

taining the axes of two opposed holes (Θ = 0 deg) or midway between the two holes (Θ = 30 deg). Figure 10(b) violates this condition in a region close to the centerline, which is believed to be related to a small misalignment of the jet impingement, as also suggested in Fig. 11(b). This misalignment was certainly not obvious in case 1 (Fig. 7(c)). The sketches in Fig. 2(c) of the cross-sectional views of the mean flow pattern, with six

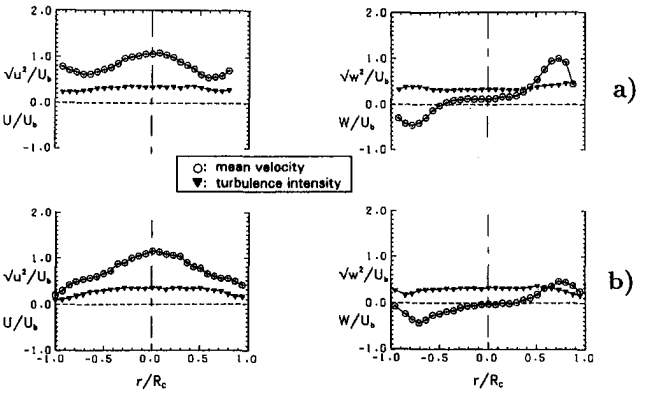

Fig. 9 Measurements of axial and azimuthal velocity in the plane z = 130 mm (case 1): (a) Θ = 0 deg; (b) Θ = 30 deg

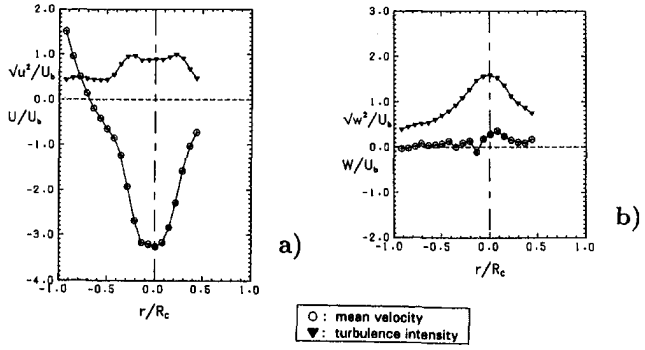

Fig. 10 Measurements at z = 40 mm, Θ = 0 deg (case 3, without swirler flow): (a) axial component; (b) azimuthal component

jets impinging on the centerline, and two equal sized vortices between jets, were idealized sketches. The location of the jet impingement point exactly on the centerline is difficult to achieve experimentally. Work carried out in the context of so-called side-dump ramjet combustors (e.g., Edelman and Harsha, 1978; Nosseir and Behar, 1986; Nosseir et al., 1987) has shown that the jets tend to oscillate due to jet-on-jet impingement and this can give rise to an asymmetric mean flow pattern. Sivasegaram and Whitelaw (1986) also concluded that opposed jets in geometries without cross flow become more sensitive to small geometric or flow asymmetries. The above measurements indicate therefore another important role of the swirler flow under the present flow conditions, i.e., to help re-establish the symmetry of the mean flow pattern and reduce its sensitivity to small jet misalignment.

If we restrict our attention to the axial location z = 50 mm, Figs. 11, 12, and 13 show the influence of the swirler flow for an angular location midway between the jets, starting from a situation with no swirler flow (case 3, Fig. 11) and moving to swirler flow only (case 3, Fig. 13). It becomes obvious that the magnitude and, in particular the anisotropy of the normal stresses are essentially due to primary jet impingement. Fig. 13 (swirler flow only) shows similar and constant values of axial and azimuthal turbulence intensities across the combustor, whereas in Fig. 11(b) (no swirler flow) the peak centerline azimuthal turbulence intensity is 7 times higher than in the case of swirler flow only and about two times higher than the axial turbulence intensity (Fig. 11(a)). These differences are reduced as the primary to swirler flow ratio decreases. This conclusion is apparent from observation of the following sequence of figures: Fig. 11 (case 3, $\dot{m}_{pr}/\dot{m}_{sw} = \infty$), Fig. 7($c$) (case 1, $\dot{m}_{pr}/\dot{m}_{sw} = 1.92$), Fig. 12 (case 2, $\dot{m}_{pr}/\dot{m}_{sw} = 1.31$) and Fig. 13 (case 4, $\dot{m}_{pr}/\dot{m}_{sw} = 0$), arranged in decreasing order of primary to swirler flow ratio.

The profiles of axial velocity in the figures above all show a positive region for $r/R_C > 0.7$, however the negative centerline

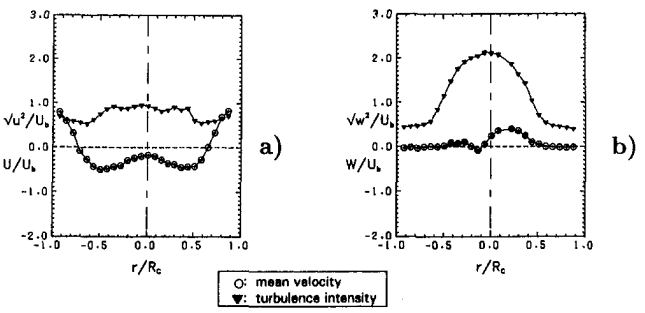

Fig. 11 Measurements at z = 50 mm, Θ = 30 deg (case 3, without swirler flow): (a) axial component; (b) azimuthal component

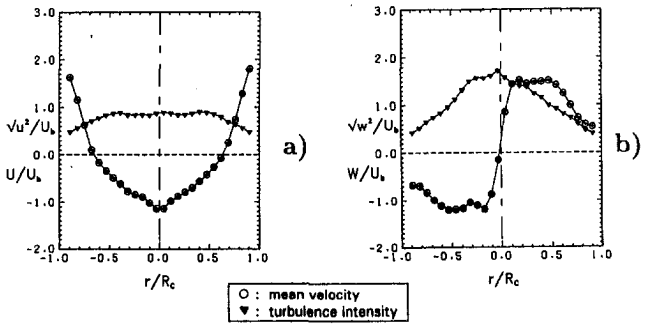

Fig. 12 Measurements at z = 50 mm, Θ = 30 deg (case 2, higher swirler flow rate): (a) axial component; (b) azimuthal component

value throughout the combustor is known, from measurements not included here, to prevail in case 4 only (swirler flow only). In all other cases, the region of negative velocity is terminated by the primary jet impingement. The higher negative axial velocity on the centerline for the case with the highest swirler flow rate (Fig. 12(a)) is due to the increased bending of the jets towards the nozzle rather than any bending of the jets towards the swirler caused by the swirl motion. The measurements of Koutmos and McGuirk (1989) also showed that reducing the primary to swirler flow ratio reduces the primary jet penetration.

Figures 14 and 15 show measurements without swirler flow. Comparing Fig. 14 with Fig. 7(a) one can see the effects of the swirler flow along the axes of the primary holes. A negative axial velocity over the entire combustor diameter and a peak distribution of azimuthal turbulence intensity. Figure 15(b), 10 mm downstream of the primary jets at an angular location rotated by Θ = 15 deg relative to the axis of the primary holes, should confirm the existence of two counter-rotating vortices between the jets, but this was precluded by the low mean azimuthal velocity. The misalignment of the impingement mentioned above may also have changed the relative size of these vortices, in which case the 15 deg plane does not correspond to the center.

4 Conclusions

An experimental study of the flow inside a water model of a gas-turbine combustor was presented. The flow configuration allowed for two rows of radially opposing jets penetrating into a swirling, axially directed stream—a configuration typical of many other fluid devices. The model was a geometrical replica of a combusting model intended to simulate a modern can-type combustor. The main conclusions of the present work were:

1. The flow in the primary region was dominated by the primary jet impingement. The six primary opposed jets penetrate almost radially into the combustor, impinge on each other at the centerline and split giving rise to a toroidal recirculation zone in the head of the combustor. For high primary to swirler flow ratios ($\dot{m}_{pr}/\dot{m}_{sw}$ = 1.92), two counter-rotating vortices are set up in between the jets, a motion that is not as evident for lower primary to swirler flow ratios ($\dot{m}_{pr}/\dot{m}_{sw}$ = 1.31) and gradually disappears with distance from primary jet impingement. For purely swirling flows with no jets a backward axial flow was set up throughout the combustor centerline.
2. The main characteristic of the primary jet impingement was a strong anisotropy of turbulence with the azimuthal normal stress twice as large as the axial normal stress. Both the magnitude of the turbulence intensity and the level of anisotropy are reduced with the primary to swirler flow ratio.
3. Because of the strong backflow created by the primary jet impingement, the swirler flow was transported near to the combustor walls and between the primary jets until it reached the plane of the dilution jets. The swirler flow creates a small recirculation region near the combustor head.
4. Because they are staggered relative to the primary jets, the dilution jets blocked the upstream (swirler fluid) flow near the wall and forced this to mix with the central core, mainly formed by the downstream flow resulting from primary jet impingement.

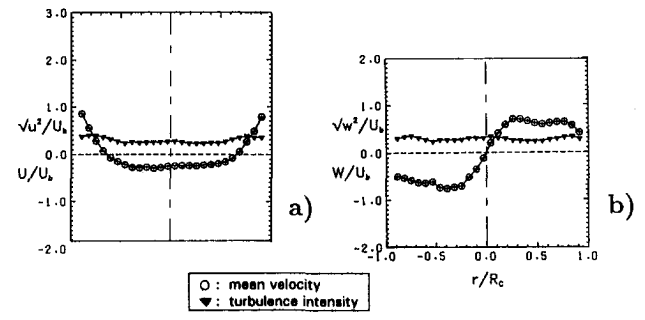

Fig. 13 Measurements at z = 50 mm, Θ = 30 deg (case 4, swirler flow only): (a) axial component; (b) azimuthal component

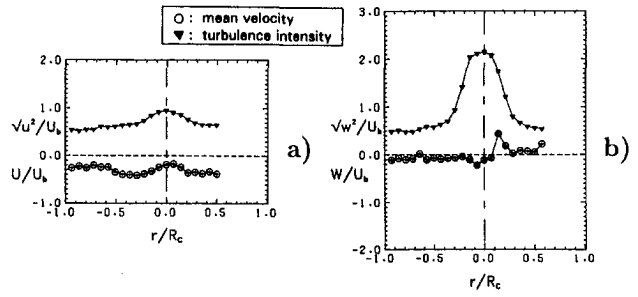

Fig. 14 Measurements at z = 50 mm, Θ = 0 deg (case 3, without swirler flow): (a) axial component; (b) azimuthal component

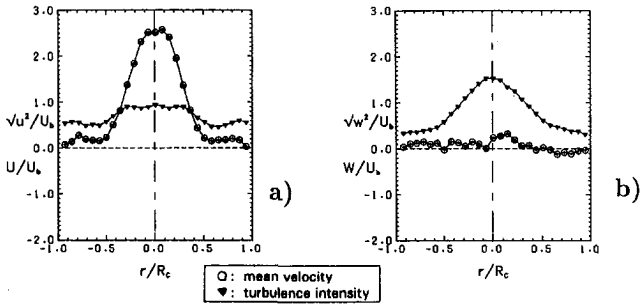

Fig. 15 Measurements at z = 60 mm, Θ = 15 deg (case 3, without swirler flow): (a) axial component; (b) azimuthal component

Acknowledgments

This work was carried out with the support of Rolls-Royce PLC and the Ministry of Defence (UK). The authors would like to thank them for their support and also the technical assistance of Mr. H. Avis and Mr. W. Crew, and the help and useful discussions with Dr. A. Bicen and colleagues at Imperial College, Rolls-Royce PLC and RAE (Pyestock).

References

Andreopoulos, J., and Rodi, W., 1984, "Experimental Investigation of Jets in Crossflow," *Journal of Fluid Mechanics*, Vol. 138, pp. 93–127.

Atkinson, K. N., Khan, Z. A., and Whitelaw, J. H., 1982, "Experimental Investigation of Opposed Jets Discharging Normally into a Cross-Stream," *Journal of Fluid Mechanics,* Vol. 115, pp. 493–504.

Bahr, D. W., 1987, "Technology for the Design of High Temperature Rise Combustors," *Journal of Propulsion,* Vol. 3, No. 2, pp. 179–186.

Batchelor, G. K., 1967, *An Introduction to Fluid Mechanics,* Cambridge University Press, Cambridge.

Beer, J. M., and Chigier, N. A., 1972, *Combustion Aerodynamics,* Applied Science Publishers, London.

Bhangu, J. K., Snape, D. M., and Eardley, B. R., 1983, "The Design and Development of a Low Emissions Transply Combustor for the Civil SPEY Engine," AGARD-CP353, Paper No. 23.

Bicen, A. F., 1982, "Refraction Correction for LDA Measurements in Flows With Curved Optical Boundaries," *TSI Quarterly,* Vol. 8, pp. 10–12.

Bicen, A. F., and Jones, W. P., 1986, "Velocity Characteristics of Isothermal and Combusting Flows," *Combustion Science and Technology,* Vol. 49, pp. 1–15.

Bicen, A. F., McGuirk, J. J., and Palma, J. M. L. M., 1989, "Modelling gas-turbine combustor flow fields in isothermal flow experiments," *Proceedings of the Institution of Mechanical Engineers, Part A: Journal of Power Engineering,* Vol. 203, pp. 113–122.

Bicen, A. F., Tse, D. G. N., and Whitelaw, J. H., 1990, "Combustion Characteristics of a Model Can-Type Combustor," *Combustion and Flame,* Vol. 80, pp. 111–126.

Cameron, C. D., Brouwer, J., and Samuelsen, G. S., 1988, "A Model Gas Turbine Combustor with Wall Jets and Optical Access for Turbulent Mixing, Fuel Effects and Spray Studies," *Proceedings of the 22nd International Symposium on Combustion,* pp. 465–474.

Chleboun, P. V., Craig, P. J., Sebbowa, F. B., and Sheppard, C. G. W., 1982, "A Study of Transverse Turbulent Jets in a Crossflow—Short Communication," *Combustion Science and Technology,* Vol. 29, pp. 107–111.

Clarke, A. E., Gerrard, A. J., and Holliday, L. A., 1963, "Some Experiments in Gas Turbine Combustion Chamber Practice Using Water Flow Visualization Techniques," *Proceedings of the 9th International Symposium on Combustion,* pp. 878–891.

Durst, F., Melling, A., and Whitelaw, J. H., 1981, *"Principles and Practice of Laser-Doppler Anemometry,* 2nd edition, Academic Press, London.

Edelman, R. B., and Harsha, P. T., 1978, "Laminar and Turbulent Gas Dynamics in Combustors—Current Status," *Progress in Energy and Combustion Science,* Vol. 4, pp. 1–62.

Edwards, R. V., 1987, "Report of the Special Panel on Statistical Particle Bias Problems in Laser Anemometry," ASME JOURNAL OF FLUIDS ENGINEERING, Vol. 109, pp. 89–93.

Edwards, R. V., and Dybbs, A., 1984, "Refractive Index Matching for Velocity Measurements in Complex Geometries," *TSI Quarterly,* Vol. 10, pp. 3–11.

Escudier, M. P., and Zehnder, N., 1982, "Vortex-Flow Regimes," *Journal of Fluid Mechanics,* Vol. 115, pp. 105–121.

Founti, M., Vafidis, C., and Whitelaw, J. H., 1985, "Shell-Side Distributions and the Influence of Inlet Conditions in a Model of a Disc and Doughnut Heat Exchanger," *Experiments in Fluids,* Vol. 3, pp. 293–300.

George, W. K., and Lumley, J. L., 1973, "The Laser-Doppler Velocimeter and Its Application to the Measurement of Turbulence," *Journal of Fluid Mechanics,* Vol. 60, pp. 321–362.

Green, A. S., and Whitelaw, J. H., 1983, "Isothermal Models of Gas-Turbine Combustors," *Journal of Fluid Mechanics,* Vol. 126, pp. 399–412.

Heitor, M. V., and Whitelaw, J. H., 1986, "Velocity, Temperature, and Species Characteristics of the Flow in a Gas-Turbine Combustor," *Combustion and Flame,* Vol. 64, pp. 1–32.

Heitor, M. V., Laker, J. R., Taylor, A. M. K. P., and Vafidis, C., 1984, "Instruction Manual for the FS "Model 2" Doppler-Frequency Counter," Imperial College, Fluids Section Report FS/84/10.

Holdeman, J. D., Srinivasan, R., and Berenfeld, A., 1984, "Experiments in Dilution Jet Mixing," *AIAA Journal,* Vol. 22, pp. 1436–1443.

Koutmos, P., and McGuirk, J. J., 1989, "Investigation of Swirler/Dilution Jet Flow Split on Primary Zone Flow Patterns in a Water Model Can-Type Combustor," ASME JOURNAL OF ENGINEERING FOR GAS TURBINES AND POWER, Vol. 111, pp. 310–317.

La Rue, J. C., Samuelsen, G. S., and Seiler, E. T., 1984, "Momentum and Heat Flux in a Swirl Stabilized Combustor," *Proceedings of the 20th International Symposium on Combustion,* pp. 277–285.

Lefebvre, A. H., 1983, *Gas Turbine Combustion,* McGraw-Hill, New York.

McGuirk, J. J., and Palma, J. M. L. M., 1992, "The Influence of Numerical Parameters in the Calculation of Gas Turbine Combustor Flows," *Computer Methods in Applied Mechanics and Engineering,* Vol. 96, pp. 65–92.

McGuirk, J. J., and Palma, J. M. L. M., 1993, "The Flow Inside a Model Gas Turbine Combustor: Calculations," *Transactions of the* ASME JOURNAL OF ENGINEERING FOR GAS TURBINES AND POWER, Vol. 115, pp. 594–602.

McGuirk, J. J., and Palma, J. M. L. M., 1995, "Experimental Investigation of the Flow Inside a Water Model of a Gas Turbine Combustor. Part 2: Higher Order Moments and Flow Visualization," ASME JOURNAL OF FLUIDS ENGINEERING, published in this issue.

McLaughlin, D. K., and Tiedermann, W. G., 1973, "Biasing Correction for Individual Realizations of Laser Anemometer Measurements in Turbulent Flow," *The Physics of Fluids,* Vol. 16, pp. 2082–2088.

Nosseir, N. S., and Behar, S., 1986, "Characteristics of Jet Impingement in a Side-Dump Combustor," *AIAA Journal,* Vol. 24, pp. 1753–1757.

Nosseir, N. S., Peled, U., and Hildebrand, G., 1987, "Pressure Field Generated by Jet-on-Jet Impingement," *AIAA Journal,* Vol. 25, pp. 1312–1317.

Noyce, J. R., Sheppard, C. G. W., and Yamba, F. D., 1981, "Measurements of Mixing and Species Concentrations Within a Gas Turbine Type Combustor," *Combustion Science and Technology,* Vol. 25, pp. 209–217.

Palma, J. M. L. M., 1989, "Mixing in Non-Reacting Gas Turbine Combustor Flows," PhD thesis, University of London.

Rhode, D. L., Lilley, D. G., and McLaughlin, D. K., 1983, "Mean Flow Fields in Axisymmetric Combustor Geometries with Swirl," *AIAA Journal,* Vol. 21, pp. 593–600.

Sivasegaram, S., and Whitelaw, J. H., 1986, "Flow Characteristics of Opposing Rows of Jets in a Confined Space," *Proceedings of the Institution of Mechanical Engineers, Part A: Journal of Power Engineering,* Vol. 200, pp. 71–75.

So, R. M. C., and Ahmed, S. A., 1986, "Effects of Rotation on the Flow Through an Axisymmetric Dump Combustor," *Proceedings of the 3rd International Symposium on Applications of Laser Anemometry to Fluid Mechanics,* Lisbon, Paper N. 1.1.

Spalding, D. B., 1963, "The Art of Partial Modelling," *Proceedings of the 9th International Symposium on Combustion,* pp. 833–843.

Syred, N., and Beer, J. H., 1974, "Combustion in Swirling Flows: A Review," *Combustion and Flame,* Vol. 23, pp. 143–201.

Tennekes, H., and Lumley, J. L., 1972, *A First Course in Turbulence,* MIT Press, Cambridge, MA.

Tse, D. G. N., 1988, "Flow and Combustion Characteristics of Model Annular and Can-Type Combustors," PhD thesis, University of London.

Vu, B. T., and Gouldin, F. C., 1982, "Flow Measurements in a Model Swirl Combustor," *AIAA Journal,* Vol. 20, pp. 642–651.

Yanta, W. J., and Smith, R. A., 1973, "Measurements of Turbulence Transport Properties with a Laser-Doppler Velocimeter," AIAA Paper No. 73-169.

Experimental Investigation of the Flow Inside a Water Model of a Gas Turbine Combustor: Part 2—Higher Order Moments and Flow Visualization

J. J. McGuirk[1]
Professor of Aerodynamics.

J. M. L. M. Palma[2]
Assistant Professor.

Imperial College of Science, Technology and Medicine,
Mechanical Engineering Department,
Exhibition Road,
London SW7 2BX,
England

The measurements of mean and turbulent quantities presented in Part 1 showed a strong influence of the primary jet system and evidence of the existence of bimodal distributions of the azimuthal velocity was also noted. Due to the importance of this phenomenon for combustor operation, a further study was carried out and measurements of higher order moments (skewness and flatness) were taken, followed by spectral analysis and high-speed flow visualization. These showed that, under the present flow conditions, the time behavior of the six radially impinging primary jets is similar to that encountered in single jet instability studies, with a dominant frequency corresponding to a Strouhal number of 0.27, when correlated with the primary jet characteristics. The unsteady nature of the flow around the primary jets and the high turbulence anisotropies observed suggest that accurate calculations of gas turbine combustor flows are likely to be impossible with models based on time-averaged version of the governing equations, even with closure at the second moment level.

1 Introduction

The measurements of mean and instantaneous velocities presented in Part 1 (McGuirk and Palma, 1995), mentioned the presence of bimodal probability distribution functions (PDFs) of the mean azimuthal component around the impingement region of the primary jets. Such bimodal PDFs of the velocity are probably an indication of the presence of large turbulent structures. Distributions of probability with bimodal shape are often associated with the coexistence of two phenomena of distinct frequencies, e.g., a low frequency phenomenon with superimposed high frequency turbulence. If this occurs inside combustors, there is cause for concern as to the origin of the low frequency, intermittent, component since it may affect the performance of the combustor, being a source of noise, flame extinction, combustion instability and probably also structural vibration. Other implications of such phenomena include, for instance the possible abandonment of numerical approaches based on a steady-state formulation of the equations.

There is a wide body of published literature where flow instability is reported, either related to a single jet flow configuration (e.g., Crow and Champagne, 1971; Hussain, 1986), swirling flows (e.g., Cassidy and Falvey, 1970; Syred and Beer, 1974; Escudier and Zehnder, 1982), jets in crossflow (e.g., McMahon et al., 1971), jet-on-jet impingement (Nosseir et al., 1987), impinging wall jets (Ho and Nosseir, 1981), radially discharging jets (Liou et al., 1990; Nosseir and Behar, 1986) or mixing layers (Koochesfahani and Dimotakis, 1986). To a certain extent all of these flows coexist in the present geometry, and the objective of the current study is to identify the location and the reasons for the formation of the azimuthal instability observed in the primary jet plane. Depending on both geometry and experimental conditions, various reasons have been put forward to explain unstable flow behaviour. For instance, in the study of the flow in a side-inlet rectangular combustor, Liou et al. (1990) attributed the phenomenon to the bidirectional characteristic of the flow in this region, whereas Nosseir and Behar (1986) attributed it to the single jet flow instability. Neither of these works encompass the presence of swirl in the crossflow, which by itself can lead to the appearance of low frequency phenomena, this time not related to jets.

Measurements of higher order moments of the three velocity components, velocity spectra measurements and flow visualization by both still and high-speed photography were made, and are discussed in the forthcoming sections. The paper is made up of two main sections: Section 2 describes the experimental techniques being used, and Section 3 includes the discussion of the results. The main conclusions are summarized in Section 4.

2 Experimental Procedures

The combustor model and the main characteristics of the LDV system have all been described in Part 1. In addition, the various flow parameter characteristics (swirler, primary flow rates, etc.) are contained in Table 2 of Part 1 and the same notation is used here for the various experimental conditions (Case 1, 2, 3, etc.).

Spectral measurements were made with a Solartron/Schlumberger 1200. Most of the signal occurred within a range of 4 Hz up to 1 kHz, as was found from a previous sweep over the full range of the instrument (0 up to 30 kHz). The inherent high frequency limitations of the LDV technique, affecting the measurement of the full turbulence spectra (e.g., George and Lumley, 1973; Buchave et al., 1979), were irrelevant for the present study. Uncertainties arising due to spectral measurements originating from an unequal time interval (e.g., Adrian and Yao, 1987) are present but were reduced by increasing

[1] Present address: Loughborough University of Technology, Department of Aeronautical and Automotive Engineering and Transport Studies, Loughborough, Leicestershire LE11 3TU, England.

[2] To whom all correspondence should be addressed. Present address: Faculdade de Engenharia da Universidade do Porto, Departamento de Engenharia Mecânica e Gestão Industrial, Rua dos Bragas, 4099 Porto Codex, Portugal.

Contributed by the Fluids Engineering Division for publication in the JOURNAL OF FLUIDS ENGINEERING. Manuscript received by the Fluids Engineering Division February 15, 1993; revised manuscript received February 23, 1995. Associate Technical Editor: Wing-Fai Ng.

the data rate. This was achieved by decreasing the acceptance threshold level of a valid Doppler burst and increasing seeds by adding a small amount of milk to the water.

For visualization of the mixing process, a solution of rhodamine B diluted in water to a concentration of 1.3 mg/l was injected through the fuel injector. The illumination of the test section was provided by a sheet of light created by a cylindrical lens. 1.2 W argon-ion laser (Spectra-Physics, model 164), tuned at 514.5 nm, was used as the light source. For still photography, a 35 mm standard photographic reflex camera was used with a Kodak TMY black and white negative film. The cine camera was a Photec IV, 16 mm high-speed motion camera. The film was 7250 Eastman Ektachrome Video news high-speed film (tungsten). Without forced processing, 400 ASA, a maximum speed of 400 fps was possible, and according to the Nyquist criterion (Bendat and Piersol, 1986), no phenomenon with a frequency higher than half the frequency of the film (200 Hz) was properly resolved. It is worth noting that the ability to obtain results as good as those shown in the present work at such relatively low frame rate is a consequence of both low molecular diffusivity[3] of rhodamine B (about 2×10^{-5} cm^2/s, i.e., a Schmidt number of 500) and the low velocities typical of water flows.

Given the difficulties of convergence of the higher order statistical moments (Tennekes and Lumley, 1972), special care was taken in the measurements, and also the evaluation of the experimental error of skewness and flatness. For instance, measurements were obtained from up to 32256 samples, by merging the statistics of blocks of 8064 individual samples. To aid graphical presentation, whereas the data points for mean and rms values (in Part 1) were joined by straight lines, in the case of the higher order statistical moments polynomial (Chebyshev series) least-squares fitting was carried out before plotting. To increase the resolution of the fit, and because of the symmetry properties of the flow, data from the two halves of the combustor were first converted into a single half. In addition, within the same profile a weighting factor was attributed to each point, depending on the size of the sample from which it was derived. Once the coefficients of the polynomium were found, the converted half could easily be recovered and the symmetry (or anti-symmetry) of the line plotted through the experimental data points guaranteed. The values on the walls (boundary conditions) were not enforced and the polynomial fitting was terminated at the nearest measured point to the wall. This procedure has proven to be an efficient way to present the data, overcoming the scatter of the results and enabling the identification of trends. Further details are given in Palma (1989).

The average rms distance between the fitted profiles and the raw experimental values was used as a means of estimating the experimental uncertainty of the higher order moments. Moffat (1988) has mentioned this approach as a very simple technique which can provide only an indication of the scatter of the results; the use of Moffat's alternative methodology has not been considered, since it was uncovered only after completion of the present work. Using all points in the profile, a relative error of about 20 and 10 percent, and a mean absolute error around 0.1 and 0.2 were found for the skewness and flatness, respectively.

[3] Taken from Reid et al. (1987), assuming infinite dilution.

3 Analysis and Discussion of Results

Figure 1 shows the skewness (S) and flatness (F) of both axial and azimuthal velocities for case 1 at $z = 50$ mm, the axial location of the primary jets axes, for three different azimuthal planes ($\Theta = 0$ deg, 15 deg, and 30 deg). The values associated with the axial velocity, despite the proximity of the primary jet impingement, 2 mm downstream, show that even at this location the probability density function is, in general, above the gaussian value of 3, with no evidence of axial intermittency. At $\Theta = 15$ deg and 30 deg the flatness increases to a value of 4 towards the wall, due to acceleration of the flow in this region, acquiring features typical of turbulent wall boundary layer flows (Durst et al., 1987). The azimuthal component has different characteristics; the flatness values are relatively low around the centerline with a bimodal shape of the PDF between the primary jets ($\Theta = 30$ deg). The maximum block size of 8064 samples was used in all these probability distributions, and the vertical line in each figure corresponds to zero mean velocity. The PDF furthest away from the centerline ($r/R_C = 0.3$), although also with a low flatness (about 2.5), does not show the double peak structure so clearly; it seems that the bimodal shape is associated with wide regions of flatness below 2.5.

The higher order moments of the radial velocity are included in Fig. 2 for locations around the primary jets. The profile along the jet axes provides the most interesting features of all (Fig. 2(b)). Trends in both skewness and flatness enable a clear identification of the region, at mid radius, where the jets start interacting with the crossflow; there is an inflexion in the flatness and the skewness reaches its highest measured value (1) in this flow, indicating a strongly skewed PDF with a long positive tail, i.e., the presence of turbulent eddies with relatively high positive radial velocity. The behavior around the centerline is similar to that observed previously for the azimuthal component, as it should on simple geometrical grounds.

Measurements of skewness and flatness further downstream at $z = 60$ mm (Fig. 3) and at other locations inside the combustor (Palma, 1989) did not suggest the presence of this bimodal structure, showing that the bimodal behavior was restricted to the area near the primary jets. The higher order moments show values very different from those expected from gaussian PDFs, reinforcing the points made in Part 1 about the nonhomogeneity of turbulence in this type of flow. The maxima of both skewness and flatness for all velocity components are located near the primary jet impingement and both the absolute magnitude and gradients in any direction decrease as the flow evolves downstream, indicating an increased level of mixing.

The conditions favorable to the formation of the bimodal PDF can be made clear by examination of data under different experimental conditions. In Fig. 4(b), corresponding to a loca-

Nomenclature

D_{jet} = jet diameter
f = frequency
F_U, F_V, F_W = flatness factor for axial, radial and circumferential velocities
PDF_U, PDF_V, PDF_W = probability density functions for axial, radial, and circumferential velocities
r = radial coordinate
R = ratio between jet and crossflow velocity
R_C = combustor radius
R_{jet} = jet Reynolds number based on velocity and jet diameter
Re_{bulk} = Reynolds number based on bulk velocity and combustor diameter
St = Strouhal number
S_U, S_V, S_W = flatness factor for axial, radial and circumferential velocities
V_{jet} = jet velocity
z = axial coordinate
Θ = azimuthal coordinate
ρ = fluid density
μ = dynamic fluid viscosity

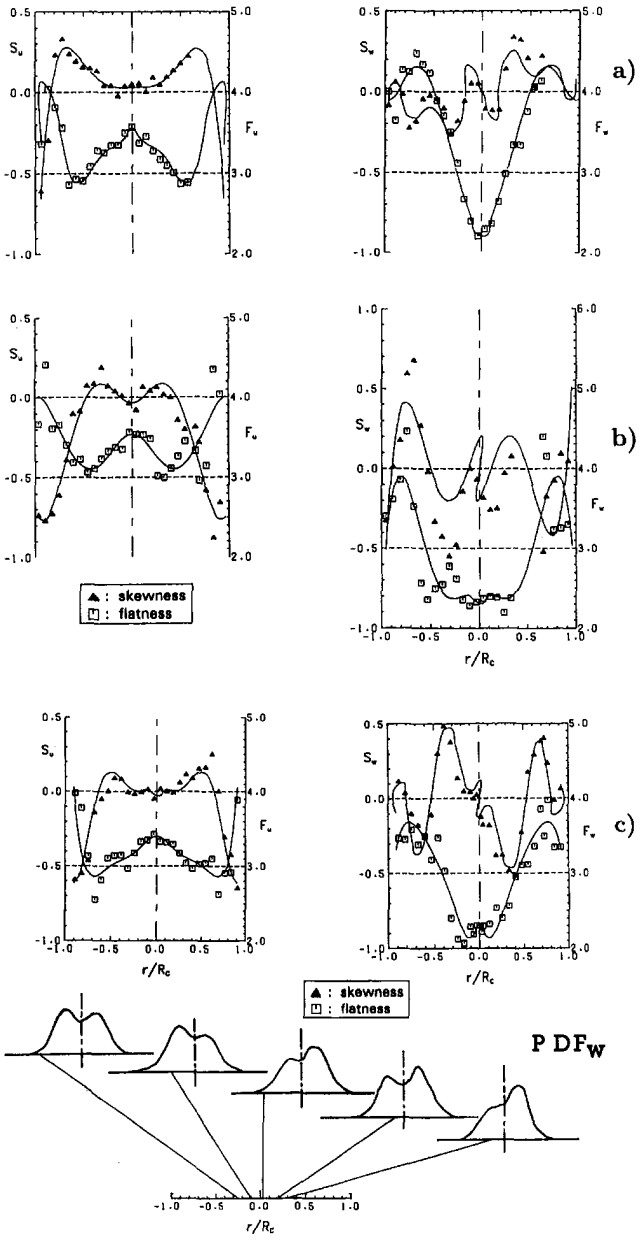

Fig. 1 Higher order moments of axial and azimuthal velocity in the plane z = 50 mm (case 1): (a) Θ = 0 deg; (b) Θ = 15 deg; (c) Θ = 30 deg

tion identical to Fig. 1(c) but without swirler flow, one can see that the discrimination between the two modes of the PDF has been enhanced on removal of the swirler flow; moving from the centreline toward the wall, there is a weakening of one of the peaks, accompanied by a smoothing and "squeezing" of the distribution, leading to flatness values in excess of 3 for $r/R_C > 0.5$. Figure 4(a) shows results along the axes of the primary holes and here there is no evidence of a bimodal PDF, the probability distribution becomes flatter in a much narrower region near the centerline; this can also be seen in the radial profile of F_W.

The flatness shows an abrupt variation (from 2 to 6) at r/R_C = 0.1 and 0.3 (in Figs. 4(a) and 4(b), respectively). Because there is no swirler flow this is a flow with larger azimuthal gradients; note, for instance the different width of the low flatness region at Θ = 0 deg (Fig. 4(a), when aligned with the jets axes) and Θ = 30 deg (Fig. 4(b)). This sudden variation of flatness can also be observed, although not so clearly, under experimental conditions with swirling crossflow (e.g., Fig. 1) and is an indication of a mixing process between shear layers with different scales dominated by mutual penetration rather than by diffusion (Verravalli and Warhaft, 1987).

Results for the azimuthal component in Fig. 4 show the least successful application of the plotting procedure described in Section 2. The skewness profile is assumed to be antisymmetric, an assumption that is not valid in the absence of swirler flow and this partly explains the failure to capture the data trend. We know that these longitudinal planes (Θ = 0 and 30 deg) are planes of azimuthal symmetry, the non-existence of swirler flow ($W \approx 0$) suppresses the azimuthal transport of turbulent stresses and therefore despite the high values of azimuthal turbulence intensity, the skewness is virtually zero.

Other locations, as for instance 10 mm downstream of the jets at an angular location rotated by 15 deg (Fig. 5), show no bimodal distributions. It is now obvious that the bimodal distributions of the azimuthal component of velocity are restricted to the mid longitudinal plane (Θ = 30 deg) at z = 50 mm, although flatness values of 2.2 and high W_{rms} values may persist in a region around the centerline, near the primary jet impingement.

If the removal of the swirler flow enhances the discrimination between the two modes of the PDF, the increase of the swirler flow rate to 0.797 kg/s (the highest in our experiments) removes the bimodal PDF (Fig. 6(b)). The width of the PDFs of the azimuthal component (Fig. 6(b) still increases toward the centerline, but to lower rms and higher flatness levels than in any other case with or without swirler flow. Closer to the centerline, the distribution is symmetrical (Fig. 6(b)), but at r/R_C = 0.25 and −0.25 (locations corresponding to maxima in the radial profile of mean swirl velocity, see Part I) the distributions apart from being strongly skewed are also mirror images of each other, i.e., the skewness has opposite sign; anti-symmetrical images are typical of swirler flows. A flatness value below the gaussian level can still be measured on the centerline but the radial distance over which this low value can spread is much

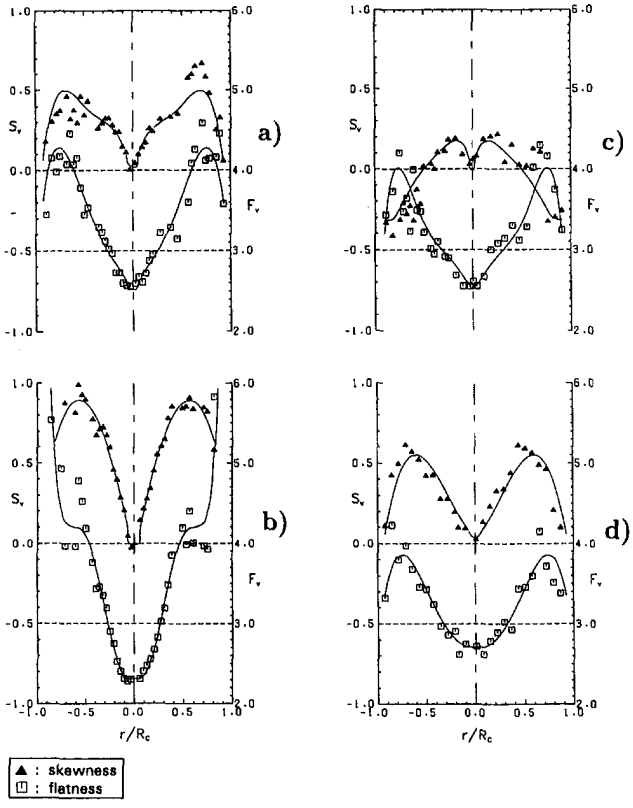

Fig. 2 Higher order moments of radial velocity component at Θ = 0 deg (case 1): (a) z = 40 mm; (b) z = 50 mm; (c) z = 60 mm; (d) z = 70 mm

restricted compared to any of the other experimental conditions. The PDF of the axial component is also shown for this case (Case 2) and here one can see (Fig. 6(a)) a nearly symmetric distribution, becoming progressively more skewed towards the negative side, anticipating the change of sign of the mean velocity which occurs at $r/R_C = 0.65$.

It is likely that the bimodal velocity distributions are related to the two counter-rotating streamwise vortices formed between the jets as described in Part 1. Each mode is associated with a different jet (or vortex) and the reduced discrimination between the modes and their eventual merging as the distance from the jet axes increases is nothing but an indication of the increased mixing between the two jet streams. Increase of either the swirler flow rate or the swirl number will reduce the penetration of the primary jets by simultaneously imparting rotation to the jets and forcing their downstream deflection, therefore reducing the strength of the vortices generated by jet impingement. For low swirler flow rates this will merely rotate the plane of the PDF bimodal shape; whereas for higher levels of swirl it might even give rise to different flow patterns. This evolution of the mean flow pattern is clear from flow visualization based on numerical predictions (McGuirk and Palma, 1992, 1993) of these experiments. The influence of the swirler flow is not surprising since the observed instability is mainly an azimuthal instability removed by the swirler by imparting a preferred rotation to the jets.

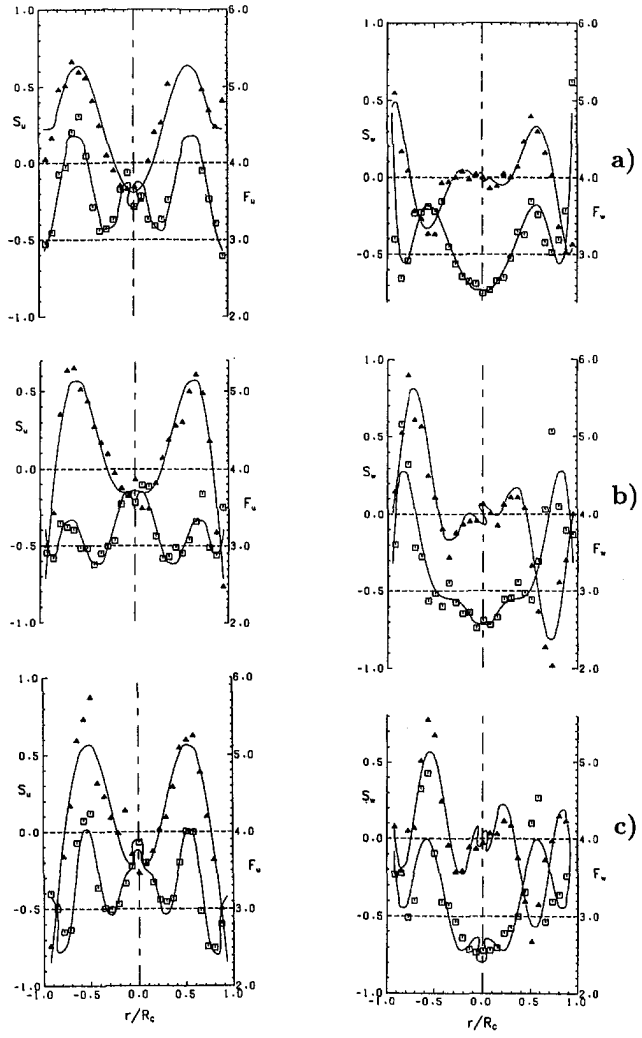

Fig. 3 Higher order moments of axial and azimuthal velocity in the plane z = 60 mm (case 1): (a) Θ = 0 deg; (b) Θ = 15 deg; (c) Θ = 30 deg

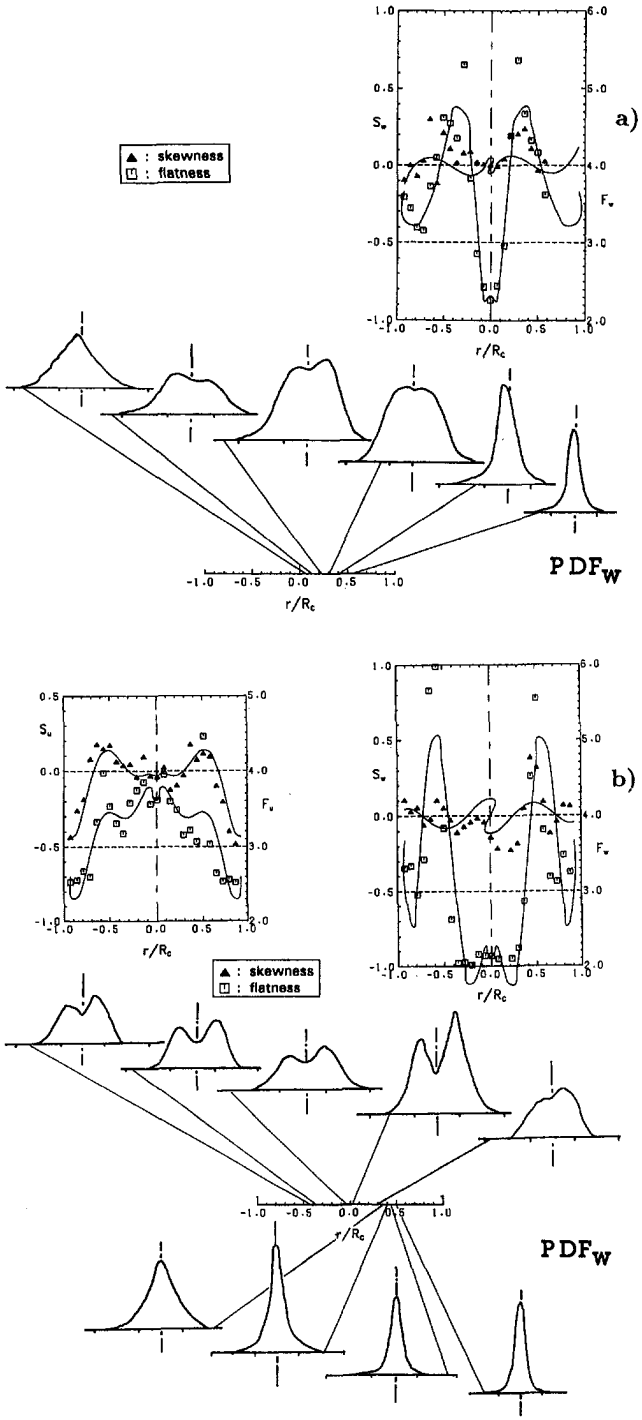

Fig. 4 Higher order moments of axial and azimuthal velocity in the plane z = 50 mm (case 3, without swirler flow): (a) Θ = 0 deg; (b) Θ = 30 deg

The study of the PDF above enabled the identification of both the most probable conditions and the location where the bimodal PDF occurs. The question may be posed as to whether the low frequency contribution arises at a discrete frequency in the spectrum. Spectral measurements on the centerline at the primary jet impingement (z = 50 mm) for the case of no swirler flow did not show any dominant frequency but a broad range of frequencies between 10 and 150 Hz with a maximum at about 60 Hz (Fig. 7). The broad range nature of the spectrum removes any doubts about the turbulent nature of the phenomenon. For a swirler flow of 0.797 kg/s (case 2, $\dot{m}_{pr}/\dot{m}_{sw}$ = 1.31), the energy content of this range of frequencies is reduced (Fig.

8), but a discrete frequency now appears at 10 Hz. This feature is not associated with the counter-rotating vortices as described above, since these weaken as the swirler flow rate increases, it is most likely associated with the precessing vortex core of the swirler flow, as observed in Koutmos and McGuirk (1989). The undesirable consequences of a precessing vortex core inside the combustor (see, for instance, Syred and Beer, 1974) are no less important than the ones associated with the bimodal PDFs of the azimuthal component.

3.1 The Jet Impingement Process. If the bimodal PDF is associated with the interface between the vortices, as suggested above, why does it show up strongly only in the region around the centerline? Assuming that each of the primary jets penetrates into the combustor with negligible expansion, i.e., as a uniform column of fluid, they all meet at 10 mm from the centerline. This cylindrical region, concentric with the combustor centerline, is precisely the region where bimodal distributions were detected and it is thus most likely that the bi-stable behavior is related with the jets themselves.

Because there is no region of constant jet velocity, it is difficult to define a developing region for the present jets. Nevertheless, since the turbulent structure of a free jet shear layer in the developing region is characterized by large turbulent eddies (Townsend, 1976), it is not surprising that, in the present case, the merging of the jet flows is accompanied by very wide distributions of probability. Another conceptual model, equally appealing, is to think of the radially penetrating jet as a cylindrical bar undergoing buckling on impingement. In this case the low frequencies would not only be caused by the merging of the jet shear layers but by collapse of the jet column itself. Both of these aspects, shear layer and jet column instability, have been noted in the literature. Becker and Massaro (1968), for instance, refer to the first reported studies in 1858 by Leconte. The shear layer type of instability shows as ripples on the surface of the jet and scales with the boundary layer thickness at the jet nozzle. The jet column instability is evidenced at low Reynolds number as sinusoidal oscillations of the jet, but for jet Reynolds numbers above 10^4 (as in the range of the present work, Table 1) it assumes the shape of axisymmetric vortex rings. There is some

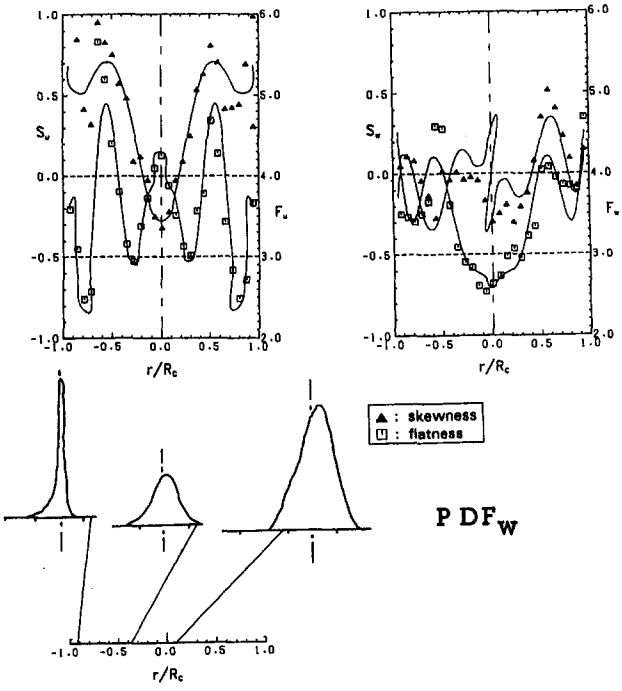

Fig. 5 Higher order moments at z = 60 mm, Θ = 15 deg (case 3, without swirler flow): (a) axial component; (b) azimuthal component

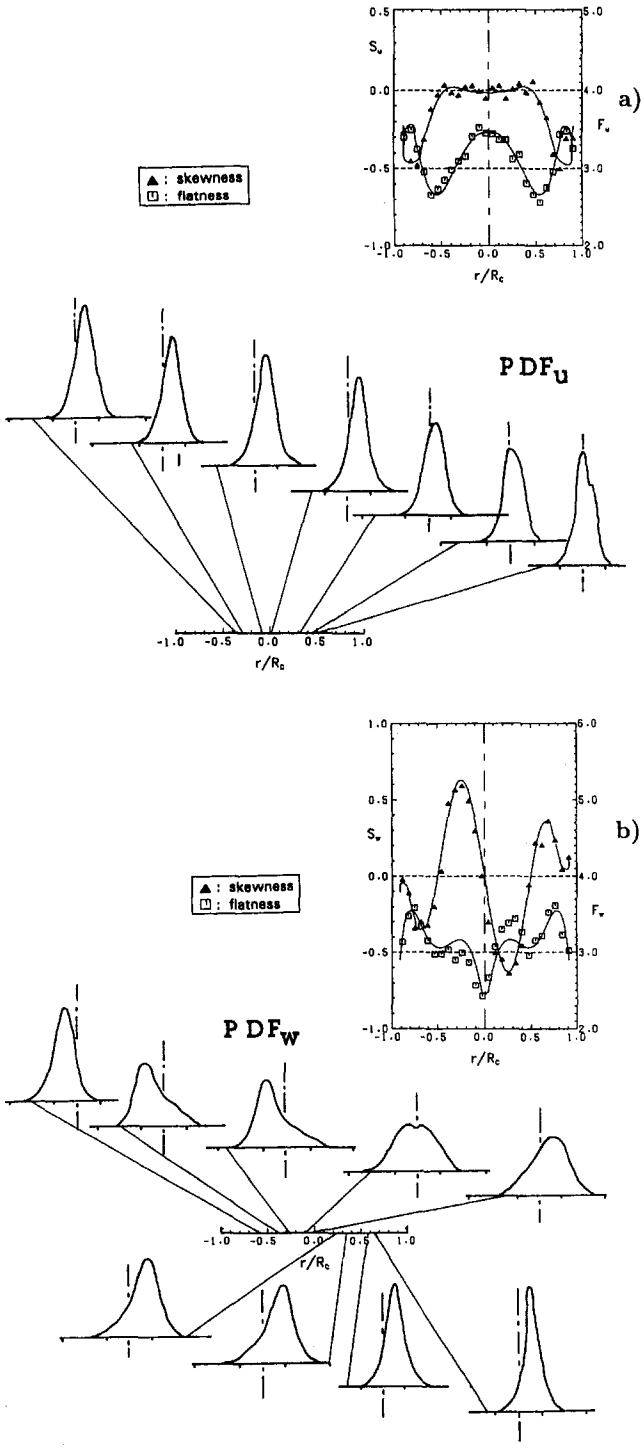

Fig. 6 Higher order moments and PDFs at z = 50 mm, Θ = 30 deg (case 2, higher swirler flow rate): (a) axial component; (b) azimuthal component

controversy about the real origin of these two types of jet instability (c.f., Hussain, 1986 and Petersen and Samet, 1988), and since the present experiment involves rather complex jet structure, here it is not possible, or perhaps necessary, to decide which mode is in operation in our measurements and refer simply to jet instability.

Crow and Champagne (1971), through externally exciting a round free jet, showed that every perturbation is linearly amplified until a saturation level is reached. This saturation reaches its maximum for a jet perturbation with a Strouhal number ($ST = fD_{jet}/U_{jet}$ of 0.30 and occurs 3.7 diameters

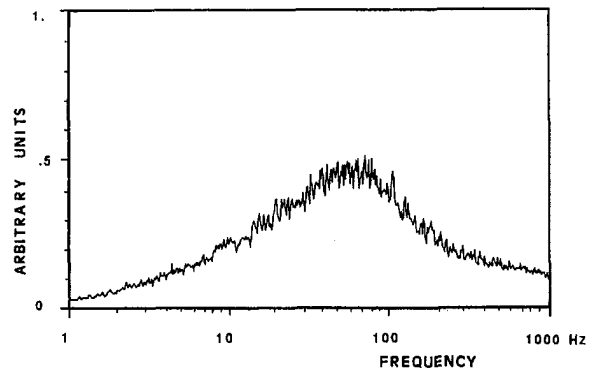

Fig. 7 Spectrum of the W component on the combustor centerline at z = 50 mm (similar to case 1, but with a 30 deg swirler)

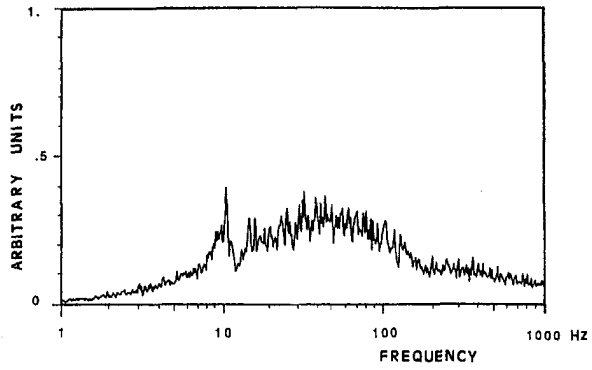

Fig. 8 Spectrum of the W component on the combustor centerline at z = 50 mm (case 2, higher swirler flow rate compared to Fig. 7)

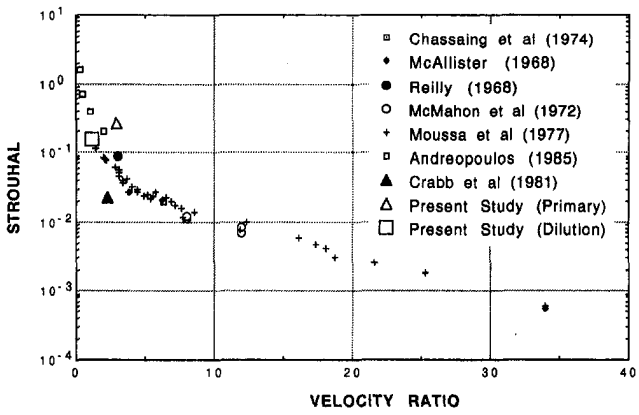

Fig. 9 Strouhal number as a function of the jet to cross-stream velocity ratio

downstream with a wavelength of 2.38 jet diameters. In the present case: (i) the 60 Hz peak in the frequency spectrum (Fig. 7) corresponds to a Strouhal number of 0.27; (ii) the distance between the hole and the centerline is 3.7 jet diameters, as the distance for maximum amplification found by Crow and Champagne, and; (iii) the distance between the jet hole and the point where the bimodal PDFs start is 2.22 jet diameters (r/R_C = 0.4, from Fig. 4(b)), close to the wavelength of the most unstable mode of a free jet. The improved discrimination between the peaks of the bimodal PDF on the jet edges rather than on the jet axes also agrees with free jet observations; since, as Crow and Champagne showed, the energy content of the amplified perturbations is higher in the jet shear layer.

More recent work (Gutmark and Ho, 1983) on jet instability has established a range of Strouhal numbers for jet instability between 0.24 and 0.51. However, despite the differences between the current geometry and the single jet experiment of Crow and Champagne, the agreement between the results is excellent and suggests that the stability characteristics of a free jet are not significantly altered either by jet-on-jet impingement or by interactions between the six jets. There is no destructive interference and the whole system is organized around the most unstable mode of a single free jet. This has already been pointed out by Crow and Champagne to justify the relevance of their experiment to unexcited single jets (". . . *the structure of the big eddies can be expected to pull in around the mode at St = 0.30, which attains the highest possible amplitude under nonlinear saturation.* . . .").

It has been shown that by increasing the swirler flow strength with respect to the primary jet flow ($\dot{m}_{pr}/\dot{m}_{sw}$ = 1.92), the jet impingement is made weaker and the flow acquires a more stable behaviour; however, too high swirler flow rates ($\dot{m}_{pr}/\dot{m}_{sw}$ = 1.31) also give rise to an instability, this time a single frequency attributed to a precessing vortex core. Geometrical alterations available to combustor designers that may also lead to improved stability of the flow (via reduction of the momentum flux of the primary jets) are for instance the increase in the number or size of the primary holes. Any procedure to improve the stability of the flow will lead to a lower level of turbulence intensity, but will improve the mixing process and consequently the combustion characteristics of the combustor. In the present case, the existence of high rms values, especially on the centerline, is due to the convective transport of parcels of fluid (large eddies with a characteristic size of the order of the primary jet diameter, i.e., scales much larger than would be desirable for an intimate mixing of fuel and air) which are not mixed with the crossflow. For improved mixing, the break-up of these large eddies should occur in the shortest time and space

Table 1 Strouhal number as found either in jets in crossflow or jet-on-jet impingement geometries

Authors (Year)	D [mm]	V_{jet} [m/s]	f [z]	R	St	Re_{jet}
McAllister† (1968)	—	—	—	3.83; 34	0.027; 0.0006	7. × 10^3 × 2. × 10^5
Reilly† (1968)	12.7	9.6	65.5	3	0.087	8.1 × 10^3
McMahon et al. (1971)	50.8	183	25	12	0.007	6.1 × 10^5
Chassaing et al. (1974)	40	20.7	11.5	6.35	0.02	5.4 × 10^4
Moussa et al. (1977)	23.6	29.6	$4 < f < 72$	$1.4 < R < 30$	$0.12 > St > 0.001$	4.6 × 10^4
Crabb et al. (1981)	25.4	27.6	25	2.3	0.023	4.6 × 10^4
Andreopoulos (1985)	50	3.48	108	$0.25 < R < 2$	$1.55 > St > 0.194$	1.1 × 10^4
Nosseir and Behar* (1986)	40	0.04	0.3	∞	0.20	3.0 × 10^3
Nosseir et al.* (1987)	97.4	100	$220 < f < 515$	∞	0.21, 0.50	6.4 × 10^5
Present work	10	2.2	60	—	0.27	2.2 × 10^4

* Jet-on-jet impingement with no crossflow.
† Referred by McMahon et al. (1971).

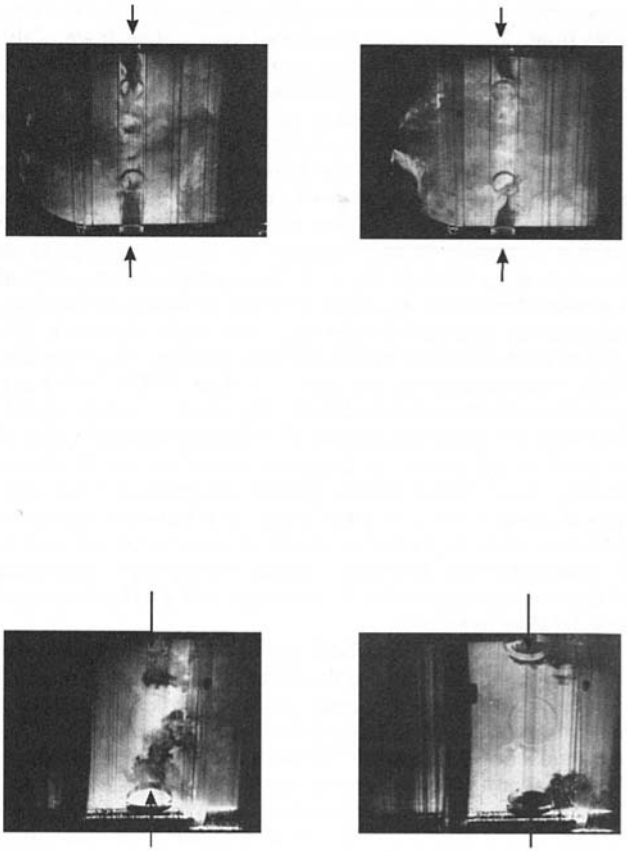

Plate 1 Flow visualization (still photography) by injection of a solution *of rhodamine B diluted in water through the fuel injector–flow conditions* corresponding to cases 2 (left) and 3 (right). Illumination obtained by a vertical laser sheet aligned with the combustor axis, containing the primary holes axes and halfway between the dilution holes axes (centre longitudinal plane). Different flow conditions along lines.

available. These eddies, in the case of increased swirler flow, no longer appear because they have been stretched and broken up due to shear forces caused by the increased angular momentum. The existence of these large structures and their preferential orientation explain the high turbulence anisotropy also measured around the primary jet impingement (in Part 1). The discussion above will be clearer after the visualization study described in Subsection 3.2.

A high turbulence intensity on the axis of the primary jet has already been noticed in previous studies (Green and Whitelaw, 1983; Koutmos 1985; and Heitor and Whitelaw, 1986. Koutmos (1985), for instance, explained this increase on the basis of a sudden deceleration of the jets along their axes, ignoring the strong three dimensional nature of the flow in this region. Heitor and Whitelaw (1986), on the other hand, suggested, by comparing combusting and isothermal flows, that the increased turbulence level was due to the production of turbulence by pressure gradient diffusion. No bimodal PDF structure was found on the primary hole axis and the turbulence kinetic energy was much higher than would be expected from the mean radial gradient. Apart from any doubts introduced by the difficulties of comparing combusting and isothermal situations (the flow pattern is unlikely to be identical in both cases), two reasons may have contributed to the differences between the current data and that of Heitor and Whitelaw: (i) the swirler to primary flow ratio in the Heitor and Whitelaw experiments was much higher, giving rise to a different flow pattern with enhanced flow stability and no bimodal PDF, or (ii) their measurements were restricted to the horizontal plane containing the primary hole axis, a location where even in the current data the bimodal structure is not so evident. Some evidence for the existence of large flow structures may be seen in the temperature measurements of Heitor and Whitelaw (their Fig. 6), where the higher rms of the temperature and flatness values below gaussian are probably associated with intermittency between jet and cross stream flow.

Studies on jets in crossflow have explained the existence of low frequency oscillation on the basis of vortex shedding, by analogy with the flow around a cylinder (e.g., McMahon et al., 1971, Moussa et al., 1977). However, there is evidence that this is not relevant in the present study. First, vortex shedding is strongest in situations with a high jet to cross stream velocity ratio, where there is a greater similarity between the jet and a cylinder in a crossflow; second, vortex shedding occurs only in the wake of the jet and thirdly the relevant Strouhal number, if the jet velocity is used as the reference velocity, is at least twice as low, compared to our measurements. Strouhal numbers from other works (Table 1 and Fig. 9) were evaluated using the jet diameter and velocity as the relevant scales to highlight the different frequencies associated with vortex shedding and jet instability. This supports our point that the phenomenon observed at the impingement is associated with jet instability; a point of view that can also be found in the works of, for instance, Andreopoulos (1985) and, in the context of jet-on-jet impinging flows, either Nosseir and Behar (1986) or Nosseir et al. (1987).

Caution is required in the comparison between our results and those obtained in simpler jet in crossflow geometries. In the present case, there is no obvious cross-stream velocity scale at the plane of the primary jets. Nevertheless, if we use the same bulk combustor velocity (based on the total flow rate) used to non-dimensionalise the velocity measurements, then a velocity ratio of 3 is obtained. Figure 9 shows the Strouhal number from several studies either on jets in crossflow or jet-on-jet impingement. Note that in this figure

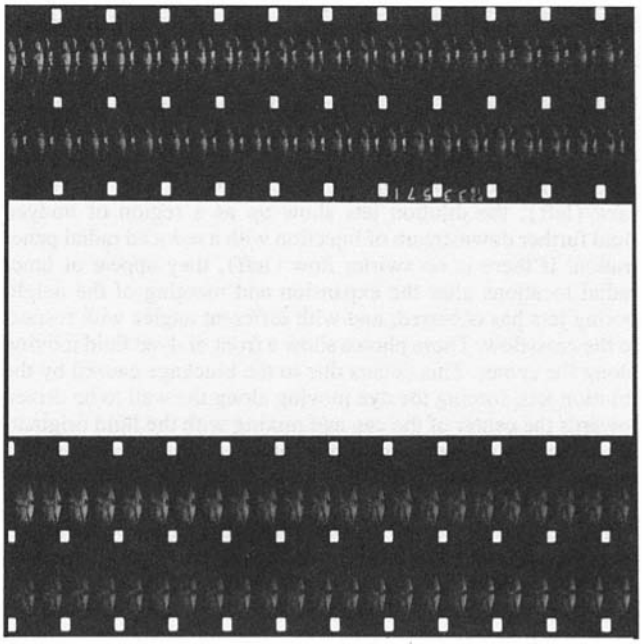

Plate 2 Flow visualization (high-speed photography) by injection of a solution of rhodamine B diluted in water through the fuel injector–flow conditions corresponding to case 3 (combustor flow without swirler flow). Illumination obtained by a vertical laser sheet perpendicular to the combustor axis, containing the primary and dilution holes axes, respectively. Frames should be read from the top to bottom in order to follow the right sequence of events.

the Strouhal number is defined as a function of jet velocity rather than the cross stream velocity as in the majority of the studies available in the literature. These results clearly showed two different trends for velocity ratios lower and higher than 3. This critical value is established mainly by the extensive measurements of Moussa et al. (1977), and this is a feature already pointed out in their study. Andreopoulos (1985) and Krothapalli et al. (1990) also deduce the existence of a critical value which they indicate to be 2 and 5, respectively. Flows with a velocity ratio below the critical value were described as made up of large turbulent structures.

3.2 Flow Visualization and Mixing. Two basic sets of pictures are shown. Plate 1 includes black and white pictures obtained by still photography (1/1000 s), whereas plate 2 includes a sequence of frames taken from the high-speed film.

In the black and white photographs, Plate 1, the white regions correspond to fluorescing dye (orange) and the black regions to pure water (green). These views were illuminated by a vertical laser light sheet originating from below the test section and with the camera orthogonal to the plane of light. Only the visualization of cases 2 and 3 (right and left column, respectively) is shown.

Turning attention to Plate 1 and the two photos of the primary zone (top two pictures), in case 2 (with swirler flow), compared to case 3 (without swirler flow), the penetration of the fuel jets has increased, due to their entrainment by the fluid originating from the swirler. The swirler flow itself is evidenced by the black region near the wall. Other regions of similar low levels of concentration are the wake of the fuel injector and the entry of the primary jets. If the swirler flow is off (column on the left), the preferential transport of "fuel" near the walls and the lower levels of mixing are clearer. Readdressing the coupling between turbulent stresses and mixing, it has been noted above that as the ratio between the primary and the swirler flow rate increases, the overall rate of mixing decreases. This reduced mixing can be seen in the photos on the left through: (i) the central core of the flow, mainly formed by low concentration fluid emerging from the primary holes and (ii) the bigger turbulent structures shown for instance by the impact of the lateral jets on the centre plane as two craters.

The dilution jets are staggered by half a pitch with respect to the primary jets and the vertical plane photographed here (the two photos in the bottom half) is midway between the dilution jets. In case of swirler flow (right) the central core is much more uniform compared to the situation with no swirler flow (left); the dilution jets show up as a region of undyed fluid further downstream of injection with a reduced radial penetration. If there is no swirler flow (left), they appear at inner radial locations after the expansion and merging of the neighboring jets has occurred, and with different angles with respect to the crossflow. These photos show a front of dyed fluid moving along the center. This occurs due to the blockage caused by the dilution jets, forcing the dye moving along the wall to be driven towards the center of the can and mixing with the fluid originating from the primary jets. This pattern is consistent with the temperature measurements performed in a replica of the present model, but under combusting conditions (Bicen et al., 1990).

Plate 2 shows frames obtained from the high-speed film. It is obvious that full advantage cannot be made of the high-speed film here. The model was illuminated by a sheet of laser light perpendicular to its axis and the angle of observation of the camera was at about 30 deg to the combustor axis; this produced an ellipsoid shape with the major axis oriented along the vertical and emphasized the trajectory of the two top and two bottom jets. These frames should be read from left to right in order to follow the sequence of events. Concentrating first on the views of the dilution jets, and in the dilution jet shown on the right of the frames, one can see that the jet progressively increases its penetration into the combustor developing a mushroom shape at its front. This process is terminated by the breakdown of the jet front which develops into an isolated vortex ring and is subsequently distorted and convected by the cross stream fluid. At this stage, the jet is again at its lowest penetration into the combustor and is at the end of a cycle. Most surprisingly, the jet on the left hand side of the frames follows the same cycle but out-of-phase with the jet on the right; this was most evident from the projection of the films and showed that when one of the jets is moving radially inwards the neighbouring jet is on its return stage towards the wall. This cycle seems to occur at a constant frequency, as judged from the projection of the films, although no spectral analysis has been made. However, this pattern went unnoticed when measuring velocity, as no bimodal PDFs were observed in this region (Palma, 1989), which is a probable indication of the relatively low levels of energy associated with this phenomenon and therefore an indication also of its reduced importance. A rough estimate from the 30 frames shot at a frame rate of 200 Hz yields a frequency of the oscillation of about 7 Hz. This corresponds to a Strouhal number of 0.16, i.e., about half of what would be expected in the case of jet flow instability. However, considering the high uncertainty of this evaluation, this flow feature may well also be associated with jet flow instability.

There is nothing new about the structure observed at the front of the dilution jets and the development of the two lateral vortices in the jet shear layer, creating the appearance of a mushroom shape. The dilution jets although possessing a Reynolds number of 1.5×10^4 still show structures typical of laminar flow, similar to those noted in Becker and Massaro (1968). Good pictures of the same phenomenon can be seen for instance in Fig. 1.8 of Hinze (1975) or in Chapter 5 of Van Dyke (1982) for the case of single jets discharging into stagnant surroundings. The novel observation here is the interaction and the apparent out-of-phase relationship between the two neighbouring jets. This is a major observation of the present work and only very recently there was a study by Villermaux and Hopfinger (1994) giving some attention to this aspect. The works on jet flow instability and coherent structures have usually been related to the study of single jet geometries and the interaction between two or more closely spaced jets is certainly an aspect requiring further experimental work. Spectral analysis in the plane of the dilution jets should also be made. The frames corresponding to the primary jets do not suggest the existence of a phenomenon similar to that observed in the dilution hole plane; a random pattern seems to prevail in agreement with the spectral analysis discussed above.

These observations clearly showed the existence of turbulent structures with a scale which invalidates assumptions inherent to gradient transport models (Corrsin, 1974). The works by McGuirk and Palma (1992, 1993) quantify the level of agreement between experimental results and numerical predictions using a gradient transport (k-ϵ) turbulence model. They show the inability of the k-ϵ model to provide accurate prediction of the flow around the primary jets and point towards the need for a time dependent calculation. A recent study by Baker and McGuirk (1991) has also shown the limitations of a steady state calculation based on a Reynolds stress turbulence model for impinging jet flows. The increasing evidence about the unsteady nature of the flow around the primary jets indicates that calculations of gas turbine combustor flows might have to be based on both second moment closure models and time dependent forms of the equations, perhaps even large-eddy simulations.

4 Conclusions

The region around the impingement of six radial jets penetrating into a swirling crossflow was studied.

1. The main characteristics of this region were:

- A strong anisotropy of turbulence characterized by a flatness of around 2.2 and the existence of large scales of turbulence (low frequency eddies) revealed by flow visualization and bimodal PDFs in the plane between the jets.
- Spectral analysis confirmed the turbulent nature of this low frequency which occurred in a broad range between 10 Hz and 150 Hz with a maximum at 60 Hz, corresponding to a Strouhal number of 0.27. The origin of the phenomenon was attributed to jet instability.
- Improved levels of stability and mixing can be achieved if the swirler flow rate is increased but only to a level where it does not give rise to a precessing vortex core along the combustor centerline.

2. The penetration of neighbouring dilution jets occurred alternately and high-speed film suggested a cyclic behavior with a frequency of about 7 Hz, i.e., a Strouhal number of 0.16.
3. The phenomena detailed above are likely to be impossible to compute with models based on time-averaged version of the governing equations, even with closure at the second moment level.

Acknowledgments

This work was carried out with the support of Rolls-Royce PLC and the Ministry of Defence (UK). The authors would like to thank them for their support.

References

Adrian, R. J., and Yao, C. S., 1987, "Power Spectra of Fluid Velocities Measured by Laser Doppler Velocimetry," *Experiments in Fluids,* Vol. 5, pp. 17–28.

Andreopoulos, J., 1985, "On the Structure of Jets in Crossflow," *Journal of Fluid Mechanics,* Vol. 157, pp. 163–197.

Baker, S. J., and McGuirk, J. J., 1991, "Second Moment Closure Predictions on Jet-on-Jet Impingement Flows," *8th Symposium on Turbulent Shear Flows,* Technical University of Munich, September 9-11, paper 13.1.

Becker, H. A., and Massaro, T. A., 1968, "Vortex Evolution in a Round Jet," *Journal of Fluid Mechanics,* Vol. 31, pp. 435–448.

Bendat, J. S., and Piersol, A. G., 1986, *Random Data-Analysis and Measurement Procedures,* 2nd edition (revised and expanded), John Wiley, New York.

Bicen, A. F., Tse, D. G. N., and Whitelaw, J. H., 1990, "Combustion Characteristics of a Model Can-Type Combustor," *Combustion and Flame,* Vol. 80, pp. 111–126.

Buchave, P., George, W. K., and Lumley, J. L., 1979, "The Measurement of Turbulence with the Laser-Doppler Anemometer," *Annual Review of Fluid Mechanics,* Vol. 11, pp. 443–503.

Chassaing, P., George, J., Claria, A., and Sananes, F., 1974, "Physical Characteristics of Subsonic Jets in a Cross-Stream," *Journal of Fluid Mechanics,* Vol. 62, pp. 41–64.

Corrsin, S., 1974, "Limitations of Gradient Transport Models in Random Walks and in Turbulence," *Advances in Geophysics,* Vol. 18A, pp. 25–60.

Crabb, D., Durão, D. F. G., and Whitelaw, J. H., 1987, "A Round Jet Normal to a Crossflow," ASME JOURNAL OF FLUIDS ENGINEERING, Vol. 103, pp. 142–153.

Crow, S. C., and Champagne, F. H., 1971, "Orderly Jet Structure in Jet Turbulence," *Journal of Fluid Mechanics,* Vol. 48, pp. 547–591.

Durst, F., Jovanovic, J., and Kanevce, J., 1987, "Probability Density Distributions in Turbulent Wall Boundary Layer Flows," *Turbulent Shear Flows-5,* Springer-Verlag, Berlin, pp. 197–220.

Escudier, M. P., and Zehnder, N., 1982, "Vortex-Flow Regimes," *Journal of Fluid Mechanics,* Vol. 115, pp. 105–121.

George, W. K., and Lumley, J. L., 1973, "The Laser-Doppler Velocimeter and Its Application to the Measurement of Turbulence," *Journal of Fluid Mechanics,* Vol. 60, pp. 321–362.

Green, A. S., and Whitelaw, J. H., 1983, "Isothermal Models of Gas-Turbine Combustors," *Journal of Fluid Mechanics,* Vol. 126, pp. 399–412.

Gutmark, E., and Ho, C. M., 1983, "On the Preferred Modes and Spreading Rates of Jets," *Physics of Fluids,* Vol. 26, pp. 2932–2938.

Heitor, M. V., and Whitelaw, J. H., 1986, "Velocity, Temperature, and Species Characteristics of the Flow in a Gas-Turbine Combustor," *Combustion and Flame,* Vol. 64, pp. 1–32.

Hinze, J. O., 1975, *Turbulence,* 2nd edition, McGraw-Hill, New York.

Ho, C. M., and Nosseir, N. S., 1981. "Dynamics of an Impinging Jet. Part 1: The Feedback Phenomenon," *Journal of Fluid Mechanics,* Vol. 105, pp. 119–142.

Holdeman, J. D., Srinivasan, R., and Berenfeld, A., 1984, "Experiments in Dilution Jet Mixing," *AIAA Journal,* Vol. 22, pp. 1436–1443.

Hussain, A. K. M. F., 1986, "Coherent Structures and Turbulence," *Journal of Fluid Mechanics,* Vol. 173, pp. 303–356.

Koochesfahani, M. M. and Dimotakis, P. E., 1986. "Mixing and Chemical Reactions in a Turbulent Liquid Mixing Layer," *Journal of Fluid Mechanics,* Vol. 170, 83–112.

Koutmos, P., 1985, "An Isothermal Study of Gas Turbine Combustor Flows," PhD thesis, University of London.

Koutmos, P., and McGuirk, J. J., 1989, "Investigation of Swirler/Dilution Jet Flow Split on Primary Zone Flow Patterns in a Water Model Can-Type Combustor," *ASME Journal of Engineering for Gas Turbines and Power,* Vol. 111, pp. 310–317.

Krothapalli, A., Lourenço, L., and Buchlin, J. M., 1990, "Separated Flow Upstream of a Jet in a Crossflow," *AIAA Journal,* Vol. 28, pp. 414–420.

Liou, T.-M., Wu, S.-M., and Hwang, Y.-H., 1990, "Experimental and Theoretical Investigation of Turbulent Flow in a Side-Inlet Rectangular Combustor," *Journal of Propulsion and Power,* Vol. 6, pp. 131–138.

McGuirk, J. J., and Palma, J. M. L. M., 1992, "The Influence of Numerical Parameters in the Calculation of Gas Turbine Combustor Flows," *Computer Methods in Applied Mechanics and Engineering,* Vol. 96, pp. 65–92.

McGuirk, J. J., and Palma, J. M. L. M., 1993, "The Flow Inside a Model Gas Turbine Combustor: Calculations," ASME *Journal of Engineering for Gas Turbines and Power,* Vol. 115, p. 594–602.

McGuirk, J. J., and Palma, J. M. L. M., 1995, "Experimental Investigation of the Flow Inside a Water Model of a Gas Turbine Combustor. Part 1: Mean and Turbulent Flowfield," ASME JOURNAL OF FLUIDS ENGINEERING, published in this issue, pp. 450.

McMahon, H. M., Hester, D. D., and Palfery, J. G., 1971, "Vortex Shedding from a Turbulent Jet in a Cross-Wind," *Journal of Fluid Mechanics,* Vol. 48, pp. 73–80.

Moffat, R. J., 1988, "Describing the Uncertainties in Experimental Results," *Experimental Thermal and Fluid Science,* Vol. 1, pp. 3–17.

Moussa, Z. M., Trischka, J. W., and Eskinazi, S., 1977, "The Near Field in the Mixing of a Round Jet with a Cross-Stream," *Journal of Fluid Mechanics,* Vol. 80, pp. 49–80.

Nosseir, N. S., and Behar, S., 1986, "Characteristics of Jet Impingement in a Side-Dump Combustor," *AIAA Journal,* Vol. 24, pp. 1753–1757.

Nosseir, N. S., Peled, U., and Hildebrand, G., 1987, "Pressure Field Generated by Jet-on-Jet Impingement," *AIAA Journal,* Vol. 25, pp. 1312–1317.

Palma, J. M. L. M., 1989, "Mixing in Non-Reacting Gas Turbine Combustor Flows," PhD thesis, University of London.

Petersen, R. A., and Samet, M. M., 1988, "On the Preferred Modes of Jet Instability," *Journal of Fluid Mechanics,* Vol. 194, pp. 153–173.

Reid, R. C., Prausnitz, J. M., and Poling, B. E., 1987, *The Properties of Gases and Liquids,* 4th edition, McGraw-Hill, New York.

Syred, N., and Beer, J. H., 1974, "Combustion in Swirling Flows: A Review," *Combustion and Flame,* Vol. 23, pp. 143–201.

Tennekes, H., and Lumley, J. L., 1972, *A First Course in Turbulence,* MIT Press, Cambridge, MA.

Townsend, A. A., 1976, *The Structure of Turbulent Shear Flow,* 2nd edition, Cambridge University, Cambridge, UK.

van Dyke, M., 1982, *An Album of Fluid Motion,* Parabolic Press, Stanford.

Veeravalli, S. and Warhaft, Z., 1987, "The Interaction of Two Distinct Turbulent Velocity Scales in the Absence of Mean Shear," *Turbulent Shear Flows-5,* Springer-Verlag, Berlin, pp. 31–43.

Villermaux, E., and Hopfinger, E. J., 1994, "Periodically Arranged Co-Flowing Jets," *Journal of Fluid Mechanics,* Vol. 263, pp. 63–92.

Unsteady Flowfield and Torque Predictions During the Rotation of the Guidevanes of Hydraulic Turbine

D. E. Papantonis

K. P. Pothou

Department of Mechanical Engineering,
Laboratory of Hydraulic Turbomachines,
National Technical University of Athens,
Athens, Greece 7778367

In the present work, the numerical prediction of the steady as well as of the unsteady flowfield through the cascade of guidevanes of a reaction turbine is examined. The unsteadiness of the flow results from the rotation of the guidevanes around their pivot. The applied numerical procedure is based on the coupling of the boundary element and the vortex particle method and is supplemented by two different procedures for the evaluation of the viscous-inviscid interaction and the boundary layers developed on the vanes. The cinematic conditions at every point of the flowfield are calculated first; however, special attention is paid to the prediction of the torque acting on the cascade and, namely, the variation of the torque during the rotation of the guidevanes, as compared with the torque corresponding to the steady state.

1 Introduction

The cascade of guidevanes of a reaction hydraulic turbine is one of the basic elements of the turbine as it is the main regulating element of the operation point of the turbine. Especially in the case of a Francis turbine, the cascade of guidevanes is the only regulating element of the machine. Apart from the hydraulic criteria that the cascade must satisfy in all the possible inclinations of the vanes, i.e., uniformity of the velocity profile at the exit without recirculation, one of the most important characteristics is the torque acting on the cascade. The calculation of the torque is necessary for the dimensioning of the servomotor controlling the cascade. The servomotor must withstand the torque acting on the cascade when the vanes are motionless and especially the increased torque during an operation corresponding to a rotation of the guidevanes. Due to the lack of a procedure for the calculation of the torque acting on the guidevanes during their rotation, hydraulic turbine designers oversize the servomotor based on unpublished empirical data. The present procedure could be useful for the calculation of the power needed for the servomotor of the guidevane cascade.

A complete description of the problems arising to the designer of the guidevanes of a hydraulic turbine is presented by Moulin et al. (1977). It is clear that the contribution of the developed torque on the design of the cascade is very important. Bovet (1970) gives a complete procedure for the dimensioning of the guidevanes cascade and for the calculation of the main operating characteristics, based mostly on empirical data.

The experimental work of Schweiger and Gregori (1989) and of Korosec and Gregori (1984) shows that the shape of the vanes and the position of the pivot have significant influence on the pressure distribution established around the vanes and consequently on the torque acting on the vanes. Moreover, the magnitude of the torque changes rapidly with the inclination of the vanes, traditionally measured by the corresponding value of the opening A (Fig. 1).

The applied numerical procedure is based on the coupling of the boundary element method with the vortex particle method. The unsteady flow conditions are generated by the rotation of the guidevanes. The examined case corresponds to guidevanes located on the radial plane, normal to the axis of rotation, i.e., to the cascade of the guidevanes of Francis and Kaplan turbines. The pivot of the guidevanes is therefore parallel to the axis of rotation of the runner. Neglecting the boundary layers developed on the two radial disks, the flowfield is considered as two-dimensional located in the radial plane. The boundary layers developed on the vane surfaces are calculated by two different procedures of viscous-inviscid interaction.

The velocity field is represented by means of source and vorticity distributions as well as by point vortices generated from the satisfaction of the unsteady Kutta condition at the trailing edges of the vanes. The source and vorticity distributions are determined by the satisfaction of the physical boundary conditions; on the one hand, the satisfaction of the velocity profile at the inlet perimeter of the considered domain, neglecting disturbances and nonuniformity of the flow due to the cascade of stationary vanes located upstream and on the other, the nonentry condition on the solid surfaces of the vanes. The flow rate i.e., the discharge of the turbine, is represented by a point source located at the axis of the runner. In order to satisfy the mass continuity, the source point is equal to the integral of the radial component of the velocity profile along the inlet perimeter of the considered domain. At the same position a point vortex is also considered corresponding to the circulation of the velocity profile along the inlet perimeter reduced by the initial circulation around the blades.

The main goal of the paper is to present a cost-effective numerical procedure for the estimation of the torque during the rotation of the guidevanes. The grid-free character of the applied method leads to a significant reduction of numerical calculations and computing time. The absence of a grid makes the procedure particularly advantageous for the prediction of the unsteady flowfield during the rotation of the vanes. For this reason all the published works relative to the flowfield prediction through cascades by grid-dependent procedures (by finite differences or finite elements) do not consider the unsteadiness due to the vane rotation.

2 Numerical Procedure

The method is based on the boundary element method and the vortex particle method considering the water as an incompressible inviscid fluid. The numerical procedure applied to the

Contributed by the Fluids Engineering Division for publication in the Journal of Fluids Engineering. Manuscript received by the Fluids Engineering Division February 25, 1994; revised manuscript received August 30, 1994. Associate Technical Editor: L. Nelik.

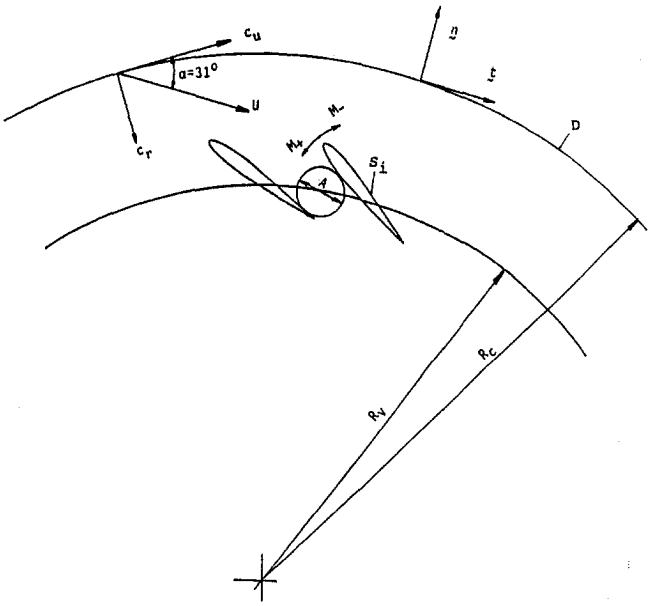

Fig. 1 Definition of the main geometrical characteristics of the guidevane cascade

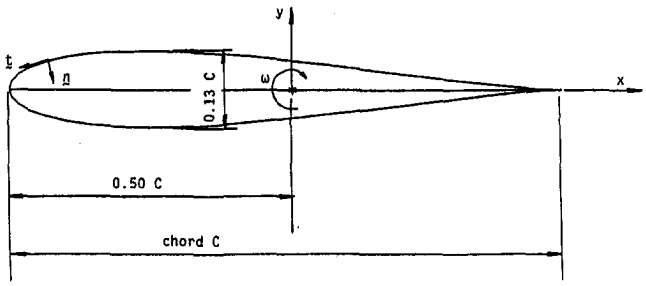

Fig. 2 Shape of the guidevane and definition of the pivot

present work is a modified and adapted version of the procedure developed by Morfiadakis et al. (1991) for the prediction of the unsteady flowfield into a centrifugal pump with spiral casing. In the examined case of the cascade of guidevanes, the spiral casing is replaced by the considered inlet perimeter and all blades are rotating simultaneously around their pivots (Figs. 1 and 2). The unsteadiness of the flow during the rotation of the vanes is taken into account with a time marching procedure.

The boundary of the considered physical domain D (shown in Fig. 1) is composed of the inlet perimeter of radius R_c (external circle) and the perimeters S_i ($i = 1, N_b$) of the N_b vanes. Each vane is motionless or rotating with angular velocity ω (rad/s) around its pivot (Fig. 2).

Let us consider the position (inclination) of the vanes corresponding to the time t. The surface of each vane is divided into N_v flat elements starting from the sharp trailing edge. Their density is increased around the trailing and leading edge in order to define better the expected sharp cinematic gradients. The external circle of radius R_c, on which the inlet conditions are imposed, is also divided into N_c equal flat elements. On each element of the vane surface a uniform source distribution $\sigma_{ik}(t)$ ($i = 1, N_b$ and $k = 1, N_v$) is assumed and along the surface of each blade a uniform vorticity distribution $\gamma_i(t)$ ($i = 1, Nb$) is considered. More clearly, the source intensity varies from element to element while the vorticity $\gamma_i(t)$ is constant for all the flat elements of each vane. Moreover, on each element of the external circle uniform source and vorticity distributions are considered with intensities $\sigma_{ci}(t)$ and $\gamma_{ci}(t)$ ($i = 1, N_c$) varying from element to element. The point source $Q(t)$ and the vortex $\Gamma(t)$ located at the centre are calculated from the conservation of the flow rate and of the circulation at the inlet section respectively (i.e., the imposed inlet boundary conditions).

The circulation $\Gamma_i(t)$ ($i = 1, N_b$) around each blade is equal to:

$$\Gamma_i(t) = \gamma_i(t) L_i \tag{1}$$

where by L_i is denoted the developed length of each vane perimeter and $\gamma_i(t)$ is the uniformly distributed vorticity.

For the calculation of the unknowns of the problem, the source and vorticity distributions, the imposed boundary conditions must be satisfied at the midpoint of each element, i.e., at the inlet section of radius R_c the given radial and tangential components of the velocity and on the vane surface the non-entry condition of the corresponding relative (to the rotating surface) velocity $\mathbf{w}_{ik}$ ($i = 1, N_b$ and $k = 1, N_v$). The relative velocity $\mathbf{w}$ is equal to: $\mathbf{w} = \mathbf{c} - \mathbf{u}$, where $\mathbf{c}$ is the absolute velocity and $\mathbf{u} = \boldsymbol{\omega} \mathbf{x} \mathbf{r}_i$ ($i = 1, N_b$), denoting by $\boldsymbol{\omega}$ the angular speed of rotation of each vane and by r_i the distance of the considered mid-point from the pivot of the vane. Following the non-entry condition the normal to the considered flat element component $(\mathbf{w}_n)_{ik}$ is taken equal to zero: $(\mathbf{w}_n)_{ik} = 0$.

Regarding the unsteady Kutta condition, the procedure proposed by Basu and Hancock (1978) is applied to the modelling

Nomenclature

A = opening between two successive vanes (m)
B = axial length of the vanes (m)
c = absolute velocity (m/s)
C = chord (m)
C_F = friction coefficient
C_M = torque coefficient
C_p = static pressure coefficient
D = physical domain
dl = length of the vortex sheet (m)
dt = time step (ms)
ds = panel length (m)
H = head of turbine (m)
L_i = developed length of the vane perimeter (m)
M = torque (Ntm)
n = speed of rotation (rpm)
$\mathbf{n}$ = unit vector normal on the perimeter
N = number of flat elements and vanes
n_q = specific speed of rotation ($=nQ^{1/2}/H^{3/4}$)
Q = discharge, flow rate (m^3/s)
R, r = radius from the axis of symmetry (m)
S = perimeter (m)
$\mathbf{t}$ = unit vector tangent on the perimeter
t = time (s)
$\mathbf{u}$ = peripheral velocity (m/s)
$\mathbf{U}$ = absolute velocity at the inlet perimeter (m/s)
$\mathbf{w}$ = relative velocity (m/s)
x = length along the chord from the leading edge (m)
α = angle of vanes inclination (deg)
γ = vorticity distribution (m/s)
Γ = circulation (m^2/s)
δ_1 = displacement thickness of the boundary layer (m)
ν = cinematic viscosity (m/s^2)
ρ = fluid density (kg/m^3)
σ = source distribution (m/s)
Φ = potential (m^2/s)
$\boldsymbol{\omega}$ = angular velocity of the vane around its pivot (rad/s)

Subscripts

c = inlet perimeter
b = vanes
n = normal
opt = optimum (or design) point
r = radial

of the vortex shedding from the sharp trailing edge. Following the analysis of Mangler and Smith (1969) and of Mudry (1982) the vorticity at the trailing edge of a blade is shedded tangentially to either one of the two sides of the wedge formed, according to the sign of the circulation around the blade. Let $\mathbf{w}_i^+(t)$ and $\mathbf{w}_i^-(t)$, $i = 1, N_b$, the components of the relative velocity which are tangential to the flat elements surrounding the sharp trailing edge. Then the intensity $\gamma_{wi}(t)$ of the vortex distribution along the straight sheet of length $dl_{wi}(t)$, corresponding to a jump of the tangential velocity, will be equal to:

$$\gamma_{wi}(t) = w_i^+(t) - w_i^-(t) \tag{2}$$

Moreover from Kelvin's theorem we obtain:

$$d\Gamma_i(t) = \Gamma_i(t + dt) - \Gamma_i(t) = \gamma_{wi}(t)dl_{wi}(t) \tag{3}$$

where dt is the time step and:

$$dl_{wi}(t) = 0.50(w_i^+(t) - w_i^-(t))dt \tag{4}$$

Combining Eqs. (2), (3), and (4) the nonlinear equation describing the evolution of $\Gamma_i(t)$ is obtained:

$$\frac{d\Gamma_i(t)}{dt} = \frac{1}{2}(w_i^+(t) + w_i^-(t))(w_i^+(t) - w_i^-(t)) \tag{5}$$

The shed vorticity $d\Gamma_i(t)$ $(i = 1, N_b)$ is convected by the flowfield after its transformation to vortex particles.

The numerical procedure includes two iterative substeps for the orientation of the emitted vortex segments and the calculation of their length $dl_{wi}(t)$. After the solution of the obtained system of linear equations the source and vorticity distributions and the shed vorticity are calculated, permitting the calculation of the cinematic conditions at every point of the flowfield.

The pressure coefficient along the blade's surface is calculated by means of the Bernoulli equation:

$$C_p = 1 - \frac{d\Phi(t)}{dt}\frac{2}{\mathbf{U}^2} + \frac{\mathbf{u}^2}{\mathbf{U}^2} - \frac{\mathbf{w}^2}{\mathbf{U}^2} \tag{6}$$

where $\Phi(t)$ denotes the potential of the velocity on the relative frame, fixed on the blade, $d\Phi/dt$ is a centered in time derivative of the potential Φ and $\mathbf{U}$ denotes the velocity on the inlet perimeter. The velocity field as well as the potential Φ are calculated analytically by means of the source and vorticity distributions obtained at each time step (Coulmy, 1988).

The torque from the axis of rotation developed on one blade is equal to:

$$M = \left(\sum_{j=1}^{N_v} C_{pj}x_j n_j ds_j\right)\frac{\rho}{2}\mathbf{U}^2 B \tag{7}$$

where $\mathbf{x}_j$ $(j = 1, N_v)$ is the control point vector of the jth panel on the relative frame, fixed on the vane (Fig. 2), $\mathbf{n}_j$ is the unit normal vector, $\mathbf{t}_j$ the unit tangential vector of the jth panel, ds_j its length, ρ is the density of the fluid and B the axial length of the vane.

In order to calculate the boundary layer two methods are applied: an integral method and a finite-difference method. The integral method is based on the Pohlhausen solution for the case of the laminar boundary layer, starting from the obtained stagnation point in the vicinity of the leading edge of the blades, and on the Truckenbrodt solution for the turbulent boundary layer (Schlichting, 1968). The finite difference method is the Keller and Cebeci "box" method applied to the Falkner-Skan equation (Cebeci and Bradshaw, 1977).

For the evaluation of viscous-inviscid interaction the nonentry boundary condition on the vane's surface becomes:

$$w_n = \frac{d(w\delta_1)}{dx} \tag{8}$$

where δ_1 is the displacement thickness of the boundary layer and w_n is the normal component of the relative velocity $\mathbf{w}$. Relation (8) results from the application of the continuity equation on the boundary layer region (Moran, 1983).

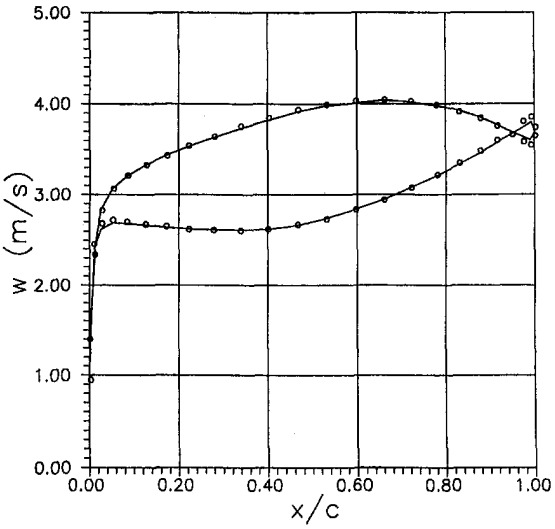

Fig. 3(a) $A/A_{opt} = 1$

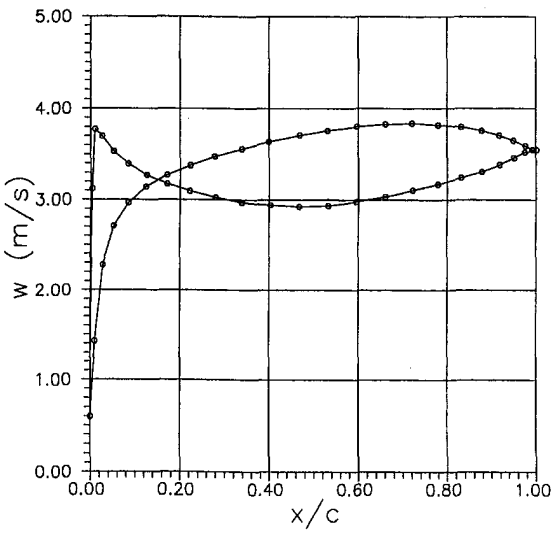

Fig. 3(b) $A/A_{opt} = 0.83$

Fig. 3 Relative velocity distribution w along the vane's surface. —— ω = 0.1 rad/s; ○ ω = 0.7 rad/s

3 Results and Discussion

For the expression of the torque developed on the guidevanes cascade the following dimensionless torque coefficient is introduced:

$$C_M = \frac{MD_v}{\rho Q^2} \tag{9}$$

where M is the torque developed on one guidevane from its axis of rotation (pivot), D_v the diameter of the guidevanes pivot (Fig. 1) and Q the discharge of the turbine (i.e., the flow rate at the inlet perimeter). The sign of the torque M is taken positive if it corresponds to closing (decrease of the opening A, Fig. 1) as negative if it corresponds to opening, increase of the opening A. The coefficient C_M is the same between similar turbines under similar operating conditions.

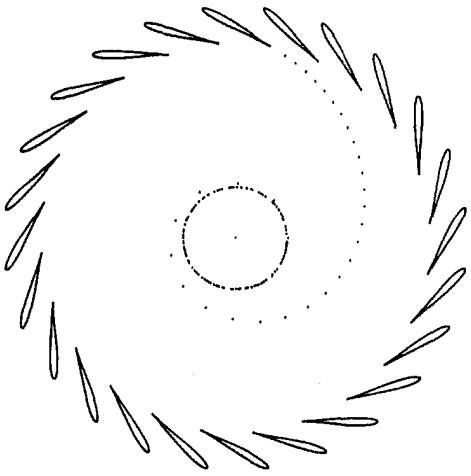

Fig. 4(*a*) ω = 1 rad/s

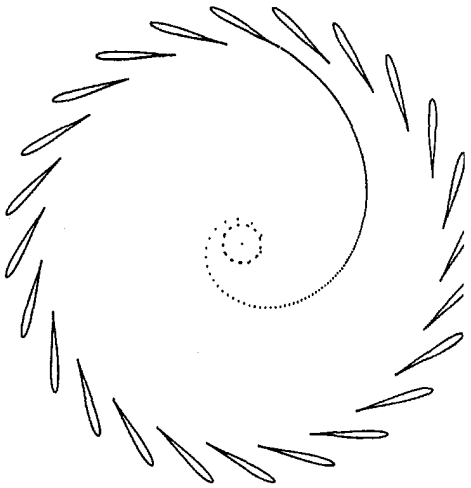

Fig. 4(*b*) ω = 0.7 rad/s

Fig. 4 Position of free vortices for A/A_{opt} = 0.83 (t = 300 dt) starting from A/A_{opt} = 1

The numerical procedure is applied to the guidevanes of a Kaplan model turbine with specific speed of rotation n_q = 110 (metric). The outer runner radius is R_r = 0.2 m, the head of the turbine is H = 8 m and the discharge for the optimum condition is Q = 0.35 m^3/s [3]. The inflow angle α along the inlet boundary is considered as constant, i.e., nondependent on the flow rate or the inclination of the guidevanes as it is imposed by the upstream conditions of the spiral casing and of the stay ring. In the examined case the inflow angle is taken equal to α = 31 deg. It must be noted that the uniformity of the inlet conditions is not a restriction for the procedure nor for the code but it is a reasonable hypothesis which simplifies and accelerates the solution. The number of the guidevanes is taken equal to N_b = 24, with their pivots located at a radius R_v = 0.242 m. The inlet boundary of the domain is defined by the circle of radius R_c = 0.29 m. The dimensioning of the guidevanes cascade as well as the shape of the vane are based on the data given by Bovet (1970). A symmetrical profile is adopted defined by a third order polynomial (Fig. 2) with chord C = 0.0862 m and maximum thickness equal to 0.13C. The axial length B of the vanes is equal to 0.148 m.

The angular velocity of rotation of the guidevanes around their pivot, according to Bovet (1970), is taken equal to ω = 0.1 rad/s, but also an angular velocity of 0.7 rad/s is examined. The discharge of the turbine changes with the inclination of the guidevanes and this change is also taken into account according to the data given by Bovet (1970). The physical properties of the water are taken as follows: density ρ = 1000 kg/m^3 and cinematic viscosity ν = 1.3 10^{-6} m/s^2.

The presented results are obtained with the following discretization:

- number of flat elements on each vane N_v = 48
- number of flat elements defining the inlet boundary N_c = 48.

In Figs. 3(a) and (b) the distribution of the relative velocity along the blade's surface is presented for A/A_{opt} = 1 and A/A_{opt} = 0.83. For each of these openings the relative velocity w is given for the two values of the angular velocity ω = 0.1 rad/s and ω = 0.7 rad/s. Since these are small values, the effect of the angular velocity in the distribution of the relative velocity is almost negligible.

In Figs. 4(a) and (b) the position of the free vortices shedded from one vane is shown at the opening A/A_{opt} = 0.83, starting from the optimum condition (A/A_{opt} = 1) and for ω = 0.1 and 0.7 rad/s. The range from A/A_{opt} = 1 to 0.83 is covered by 300 time steps with time step dt equal to dt = 3.49 ms for ω = 0.1 rad/s and dt = 24.43 ms for ω = 0.7 rad/s.

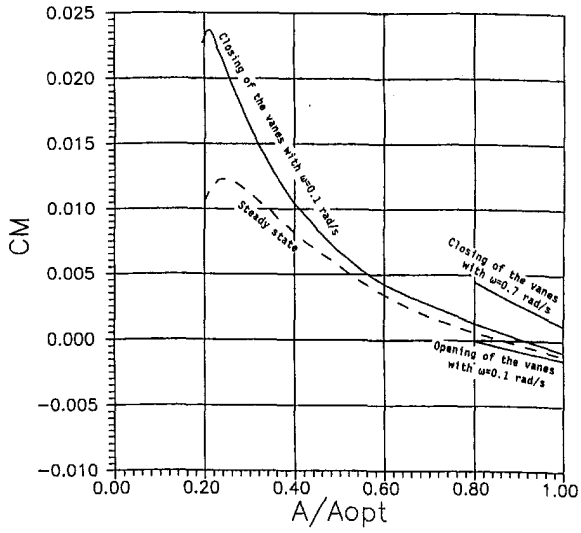

Fig. 5(*a*) Opening and closing with ω = 0.1 rad/s, closing with 0.7 rad/s

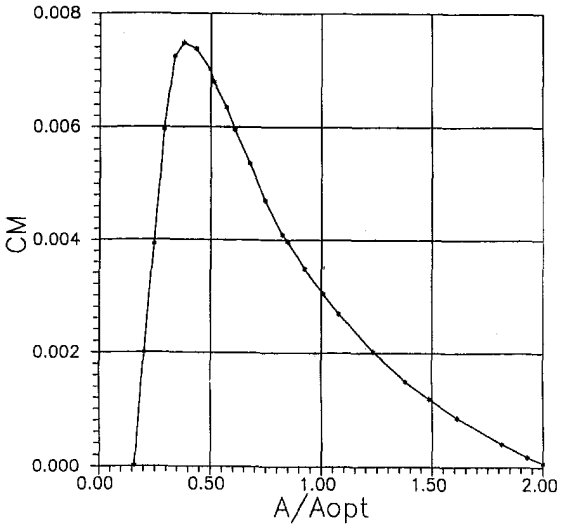

Fig. 5(*b*) Experimental data presented by Schweiger and Gregori [3]

Fig. 5 Torque coefficient C_M versus guidevane opening. – – – steady state; —— unsteady solution (closing or opening)

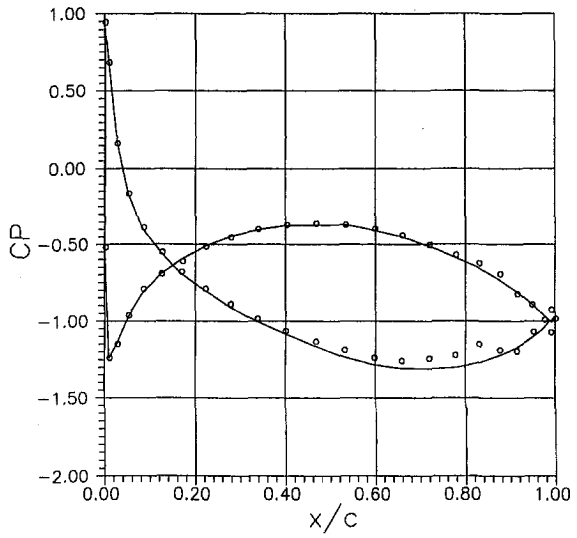

Fig. 6 Pressure coefficient C_p along the vane's surface with and without viscous-inviscid interaction for the optimum condition (A/A_{opt} = 1). —— without viscous-inviscid interaction; ○ with

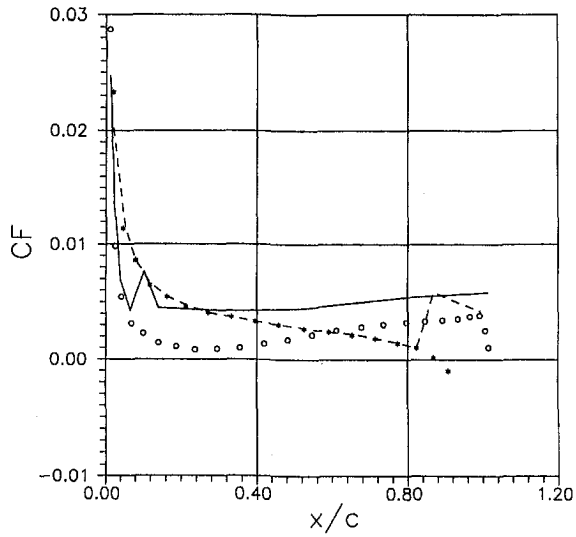

Fig. 7 Friction coefficient C_F along the vane's surface. – – – Pohlhausen-Truckenbrodt, upper side (extrados); —— Pohlhausen-Truckenbrodt, lower side (intrados); * "box" method, upper side, ○ "box" method, lower side

Figure 5(a) gives the torque coefficient C_M versus the guidevane relative opening A/A_{opt} and comparison is made between steady (calculation of C_p from equation (6) with $d\Phi/dt = 0$) and unsteady flow prediction corresponding to opening and closing of the guidevanes with angular velocity $\omega = 0.1$ rad/s. During the closing of the guidevanes the torque is higher than the corresponding value of the steady position while during the opening the torque is smaller than the corresponding value of the steady state. The same Figure gives the torque coefficient C_M versus the relative opening for closing of the guidevanes with angular velocity 0.1 rad/s and 0.7 rad/s. The coefficient C_M increases as the angular velocity ω increases. It is clear that the difference on the C_M between steady state and during the rotation increases as the relative opening A/A_{opt} and the flow rate decreases. This remarkable unsteady effect is due to the acceleration of the fluid in the blade to blade region during the closing of the vanes.

The shape of the obtained curves is similar to the experimental curve presented by Schweiger and Gregori (1989) (Fig. 5(b)). Since this reference does not present the geometry of the profile of the vane it is impossible to proceed in further comparisons of the results.

In Fig. 6 the pressure coefficient distribution is given for A/A_{opt} = 1 with and without the application of the viscous-inviscid interaction procedure. It is concluded that in the examined case the viscous-inviscid interaction modifies slightly the pressure distribution and only around the trailing edge. The resulted modification on the developed torque, as calculated by the viscous-inviscid interaction, is negligible. The friction coefficient C_F, presented in Fig. 7 for the two sides of the guidevane, is obtained by the two viscous-inviscid interaction procedures. The two procedures give similar results while the main difference is the predicted separation of the boundary layer on the lower surface of the vane by the Falkner-Skan equation (box method).

4 Conclusions

The applied method leads to a cost-effective procedure for the prediction of the flow field and the developed torque on a radial cascade of guidevanes in steady state as well as during their rotation. The unsteady effect produced is important. The absolute value of the variation of the torque increases with the angular velocity of rotation while the sign of the variation depends on the operation, opening or closing. The developed torque remains positive over the examined range of inclination of the vanes, corresponding to the closing tendency of the vanes. The viscous-inviscid interaction has no influence on the developed torque since the boundary layer of the vane is not important.

In the cases examined the inlet velocity distributions were uniform but this is not a restriction for the procedure: the influence of the stay ring wake and/or the nonuniformity induced by the spiral casing could also be taken into account.

References

Basu, B., and Hancock, G., 1978, "The Unsteady Motion of a Two-Dimensional Aerofoil in Incompressible Inviscid Flow," *Journal of Fluid Mechanics,* Vol. 87, p. 159.

Bovet, Th., 1970, "Le distributeur de la turbine hydraulique a reaction. Etude de l' aube directrice," Ecole Federale Polytechnique de Lausanne, Publ. No 141.

Cebeci, T., and Bradshaw, P., 1977, *Momentum Transfer in Boundary Layers,* McGraw-Hill, New York, NY.

Coulmy, G., 1988, "Formulation des effets de singularites en domaine bidimensionnel," Notes et Documents LIMSI 85–5, Paris.

Korocec, D., and Gregori, D., 1984, "Torques on Kaplan Guide Vanes," *Proceedings of the Conference on Fluid Flow Machinery,* Lubliana, p. 205.

Mangler, K., and Smith, J., 1969, "Behaviour of the Vortex Sheet at the Trailing Edge," RAE, TR 69049.

Moran, J., 1983, *An Introduction to Theoretical and Computational Aerodynamics,* Wiley, New York.

Morfiadakis, E., Voutsinas, S., and Papantonis, D., 1991, "Unsteady Flow Calculation in a Radial Flow Centrifugal Pump with Spiral Casing," *International Journal for Numerical Methods in Fluids,* Vol. 12, pp. 895–908.

Moulin, C., Wanner, M., Eremeef, R., and Vinh-Phong, 1977, "Methodes de trace des turbomachines hydrauliques," *La Houille Blanche,* No 7/8, p. 617.

Mudry, A., 1982, "La theorie generale des nappes et filaments tourbillonaires et ses applications a l' Aerodynamique instationnaire," D. E. Sc. Physiques, Univ. Pierre et Marie Curie (Paris VI).

Schlichting, H., 1968, *Boundary-Layer Theory,* McGraw-Hill, New York.

Schweiger, F., and Gregori, D., 1989, "Turbine guide vanes torque estimation," S.H.F., XXe *Journees de l' Hydraulique,* Lyon, p. I.7.1.

Measurement and Analysis of Static Pressure Field in a Torque Converter Turbine

R. R. By*
NAO Engineering Center,
General Motors Corporation,
Warren, MI 48090

B. Lakshminarayana
Aerospace Engineering Department,
The Pennsylvania State University,
University Park, PA 16802

In this paper, the static pressure field and performance parameters of a torque converter turbine are measured, analyzed, and interpreted under three speed ratio conditions (0, 0.6, and 0.8). A proven measurement technique was developed for the steady-state measurement of static pressures in the turbine. Results show that: 1) the static pressure field is generally poor at the core section; 2) centrifugal force has the dominant effect on the static pressure drop in the turbine at SR = 0.6 and SR = 0.8; and 3) the static pressure loss due to viscous effects and due to the diffusion of the relative velocity is very pronounced at SR = 0.

Introduction

The automotive torque converter, as shown in Fig. 1, is a complex turbomachine used to transfer power from an engine to a transmission. It consists of a mixed-flow pump connected to the engine crankshaft, a mixed-flow turbine attached directly to the transmission, and either a mixed-flow or an axial-flow stator attached to a stationary housing through a one-directional clutch.

Torque converter flow fields are difficult to measure and to visualize. The geometry of the elements is highly three-dimensional with a high angle of blade turning. Unlike other turbomachines, the torque converter is a closed-loop machine with the same oil circulating through its elements; the flow is highly unsteady as a result of interaction effects between the closely spaced elements. In addition, the torque converter elements operate under an extremely wide range of incidence angle. These physical features give rise to complex three-dimensional flow fields with three-dimensional through-flow distribution, strong secondary-flow phenomena, large flow separation regions, and highly unsteady characteristics that lead to large losses in the performance of the torque converter.

Because of its compact packaging, it is difficult to conduct internal flow measurements in an automotive torque converter. Different packaging arrangements are required for different types of internal flow measurements. To date, there are only a handful of investigators who have studied the flow fields experimentally. Consequently, the amount of published internal flow data is limited and the physics of the flow fields are not well understood.

The objectives of this investigation are: 1) to conduct steady-state static pressure measurement in the turbine of an automotive torque converter under three turbine/pump speed ratio conditions and 2) to understand the measured static pressure field through the use of different analytical methods. The novelty of the present investigation is on the steady-state static measurement of a rotating torque converter turbine. It is hoped that the results will provide important insights into the physics of the turbine flow field. Since this is an experimental investigation, a Navier-Stokes analysis of the flow field is beyond the scope of this paper; additional information may be found in Abe et al. (1991) and By et al. (1993).

Some of the recent experimental investigations are given below. Numazawa et al. (1983) developed a surface flow visualization technique to trace flow patterns on blade and end-wall surfaces of a torque converter. They used this technique to study the effect of axial length on flow fields. Their results, however, were qualitative.

Kubo et al. (1991) used a steady-state five hole probe to measure the three velocity components, static pressure and total pressure in the gap regions of an automotive torque converter under a speed ratio range of 0 to 0.8. The deviation angle was found to be in the range of −5 to 10, 3 to 8, and 10 to 15 degrees at the pump exit, turbine exit, and stator exit, respectively. The measured angles were used to improve the performance prediction of automotive torque converters.

Gruver (1992) used a one component laser velocimeter to measure the three velocity components in the pump of an automotive torque converter under speed ratio conditions of 0.065 and 0.8. Results at both speed ratios show that: 1) about a third of the pump passage (near the core) is not effective; the through-flow velocity is either negative or very small, and 2) a strong secondary flow field was found at the mid-chord and exit planes; the most striking feature is that the secondary flow circulates counterclockwise at the mid-chord plane and switches to clockwise at the exit plane.

By and Lakshminarayana (1991, 1993) measured static pressures in the stator and in the pump of an automotive torque converter. The measurements were taken at the mid-span, core and shell sections under three speed ratio conditions. Results show that: 1) the static pressure distribution is generally poor at the blade core section, 2) centrifugal force has a dominant effect on the static pressure rise in the pump, and 3) the potential flow theory can fairly well predict the static pressure distribution at the blade mid-span, but not at the core and shell sections.

Experimental Facility, Instrumentation, and Measurement Technique

An experimental facility was designed and built to measure static pressures in a torque converter turbine. The experimental facility consists of: 1) an experimental torque converter unit, 2) an input dynamometer to drive the torque converter pump, 3) an eddy-current dynamometer to absorb the output power of the torque converter turbine, 4) a hydraulic system to cool, pressurize and lubricate the torque converter, and 5) a control system to control rotational speeds and torques.

The experimental torque converter has an outer diameter of 230 mm and a peak efficiency of about 82 percent. The pump has 27 blades with 1 mm of constant thickness; an inlet angle

* Presently President, Fluid Machinery Consulting, New Baltimore, MI 48047.

Contributed by the Fluids Engineering Division for publication in the JOURNAL OF FLUIDS ENGINEERING. Manuscript received by the Fluids Engineering Division February 1, 1994; revised manuscript received September 12, 1994. Associate Technical Editor: Wing-Fai Ng.

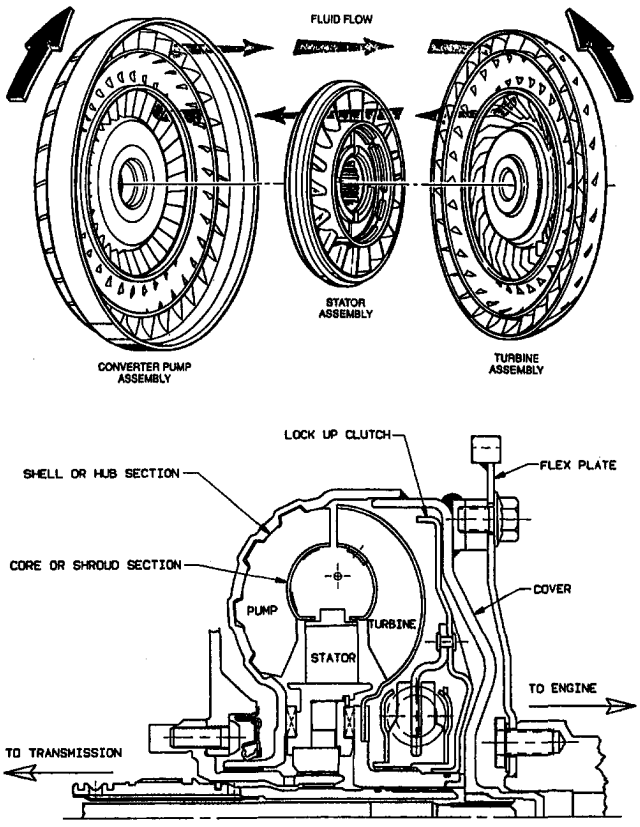

Fig. 1 Components of the automotive torque converter

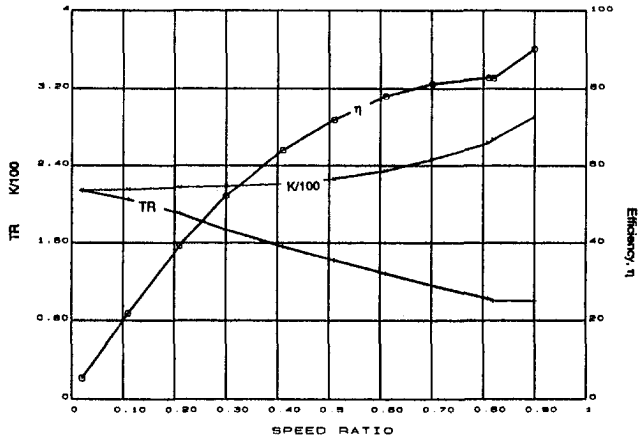

Fig. 2 Steady-state performance characteristics of the experimental torque converter at Tq = 24 Nt-m

of −25 degrees at core and −40 degrees at shell; and, an outlet angle of zero degrees at both blade sections. The meridional blade length of the pump at core is about 3 times shorter than that at shell. The turbine has 29 blades with 1 mm of constant thickness; an inlet angle of 55 degrees at core and 49 degrees at shell; and, an outlet angle of −64 degrees at core and −57 degrees at shell. The meridional blade length of the turbine at core is about 2.5 times shorter than that at shell. The stator has 19 airfoil blades with an inlet angle of about 7 degrees and an outlet angle of 63 degrees at both the core and shell sections.

Steady-state performance characteristics of the experimental torque converter are shown in Fig. 2. It is important to measure static pressures under constant turbine/pump speed ratio conditions, since it is the key independent performance parameter. Static pressure measurement was conducted under three speed ratio conditions: 0, 0.6 and 0.8; 3 speed ratios are enough to cover the range of operation. The three test conditions are shown in Table 1. The incidence angles were obtained from a one-dimensional performance analysis. Fig. 3 shows the range of the inlet flow angle entering the pump, the turbine and the stator. The Reynolds number based on through-flow velocity (W_m) and meridional length at the mid-span (L_{mid}) is 45000, 28000 and 24000 under the speed ratio condition of 0, 0.6 and 0.8, respec-

Table 1 Test conditions for static pressure measurement

	Condition #1	Condition #2	Condition #3
SR	0	0.6	0.8
N_P, rpm	1050	1160	1300
Tq_P, Nt-m	22.8	23.1	23.7
i_P, degrees	−43	+3	+22
N_T, rpm	0	696	1040
Tq_T, Nt-m	51.4	30.6	24.3
i_T, degrees	+18	+11	0
N_S, rpm	0	0	0
Tq_S, Nt-m	28.6	7.4	1.6
i_S, degrees	+67	−2	−47
$U_{\text{tip, }P}$, m/s	12.64	13.97	15.66
$\text{Re}_{L,T}$	45,000	28,000	24,000

Nomenclature

C_p = static pressure coefficient, $C_p = (p - p_{\text{ref}})/(0.5\rho U^2_{\text{tip},P})$
C_T = blade torque coefficient as defined in Eq. (2)
H = blade span or height
i = incidence angle = inlet blade angle − inlet flow angle
K = a pump speed parameter, $K = N/(Tq)^{0.5}$
L = meridional blade length
N = rotational speed in rpm
p = static pressure
P^* = $p + 0.5\rho(W^2 - U^2)$
R = radius from the center of machine axis
Re_L = Reynolds number based on meridional blade length, $\text{Re}_L = W_m L_{\text{mid}}/\nu$
SR = ratio of turbine to pump speed
T = blade torque at a blade section
Tq = torque of all turbine blades or turbine torque
TR = ratio of turbine to pump torque
U = blade speed
V, W = absolute, relative flow velocity
x/L = normalized coordinate in the meridional direction
η = power efficiency, $\eta = SR*TR$
ρ = density in kg/m^3
ν = kinematic viscosity in m^2/s
Ω = angular velocity in rad/s

Subscripts

m = meridional or through-flow component
shell = shell or hub blade section
mid = mid-span blade section
core = core or shroud blade section
p, s = pressure, suction surface
le, te = leading, trailing edge
centr = centrifugal
ref = reference
avg = average or arithmetic mean
tip = tip location of a blade
tap = location of a static pressure tap
1, 2 = inlet, exit of a blade row
P, T = pump, turbine

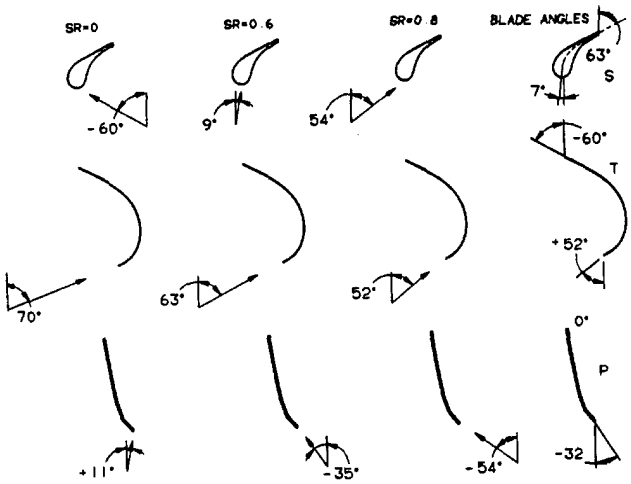

Fig. 3 Range of flow angle entering pump, turbine and stator

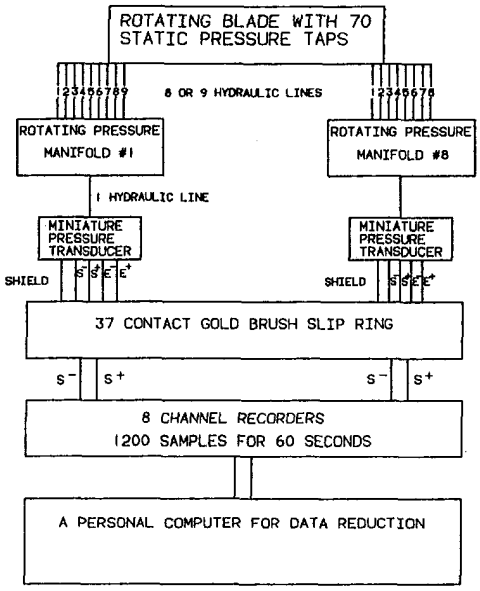

Fig. 5 Schematic diagram of the measurement process

tively. This Reynolds number is well within the range of Reynolds number for passenger car applications.

The measurement of static pressures in a rotating turbine is a challenging and difficult task. For this measurement, innovative design features were devised for the torque converter unit. The torque converter arrangement for the measurement of static pressures is shown in Fig. 4. A multichannel data transmission device is required to transmit pressure signals from the turbine rotating frame to a stationary frame. The data transmission device must be accurate, durable, and able to transmit torque from the turbine to the output dynamometer.

Seventy static pressure taps were drilled along the shell, mid-span and core sections of a blade passage. There were 33, 22, and 15 static pressure taps at the shell, mid-span and core sections, respectively. A soft steel tube, with an inside diameter of about 0.35 mm, was installed in each static pressure tap. One end of each tube was flush with the surface at which static pressure was measured, the another end was connected to a pressure manifold. The fluid flowed past the taps, but remained at rest in the tubes (since their length to diameter ratio was very large).

A schematic diagram of the measurement process is shown in Fig. 5. Tubes were routed from the tap locations to the shell housing where they were connected to eight pressure manifolds. A miniature pressure transducer was mounted to the outlet of each manifold. Eight static pressures were measured simultaneously. Electrical output signals from the eight pressure transducers were connected to an eight-channel slip ring.

A piezoresistive transducer was the only commercial type that satisfied the packaging requirement. Endevco model 8530C-50 was chosen, since it was a high precision type with thermal compensation from −18 to 93 degrees C. The pressure range is from 0 to 345 kPa with a full range output of 0.3 volts at 10 DC volts of excitation. Several transducer units were custom-made and the combined linearity, hysteresis and repeatability was less than ±0.1 percent of full scale outputs.

The slip ring is a brush type with 37 gold alloy rings designed and built by the Quality Aero Technology Corporation. Its outer housing is stationary and carries 3 brushes per ring. The brushes transfer analog pressure signals from rotating rings to terminals on the stationary housing. A separate hydraulic system was built to lubricate and cool the ring/brush assembly. The oil temperature of the slip ring was kept at 60°C (the same as the oil in the torque converter). The noise signature was less than 80 micro volts with a low current source of 20 micro amps (or 0.14 kPa based on the sensitivity of the pressure transducer of about 0.57 mV/kPa at 10 V excitation). The noise to signal ratio was typically less than 0.1 percent.

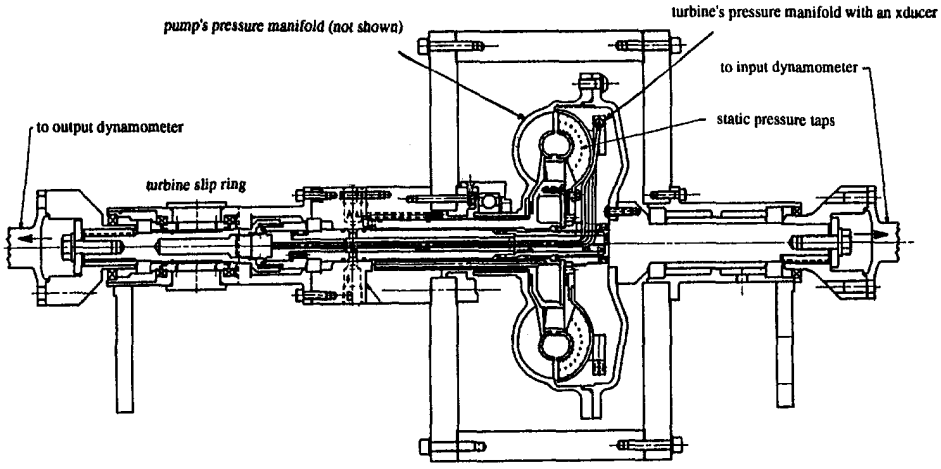

Fig. 4 Torque converter arrangement for the measurement of static pressure in the turbine

Two electronic recorders were used to collect and store output signals from the slip ring. Each recorder is a four-channel strip chart recorder that is capable of storing up to 32K of data per channel and reads data at a frequency range of 20 Hz to 250 kHz. The accuracy is ±0.5 percent of full scale.

Although the transducer units were carefully selected and custom-made, their performance was not reliable enough to give consistent and repeatable results. For this measurement, the transducers had to be mounted to the pressure manifolds and the whole assembly rotated at turbine speed. This design requirement introduced many problems: 1) effects of trapped air in the hydraulic lines on the centrifugal pressure head, 2) effects of rotation on the performance of the transducers, 3) effects of the mounting on the performance of the transducers, 4) effects of the change in oil temperature on the performance of the transducers, and 5) effects of the added mass on the balance of the turbine assembly. Therefore, for this steady-state measurement to be successful, a proven measurement technique had to be carefully developed.

First, an electric heater was added to the oil system to keep a constant oil temperature of 60°C under all operating conditions. The transducers were then operated in an essentially constant temperature environment. Second, air was bled out of the pump's pressure manifolds to minimize the effect of trapped air. Third, an on-line calibration technique was developed to continuously calibrate the Endevco units and to check their accuracy. Fourth, measurements were taken repeatedly and results from the on-line calibration were used to determine the accuracy of all tests. The recorders recorded 1,200 sample outputs during a measurement span of about 60 seconds. Total measurement errors were found to be less than ±1 kPa or ±1 percent of the dynamic pressure based on blade tip speed. The analysis of measurement errors is in the Appendix.

As mentioned previously, small tubes were used to connect the static pressure taps to the pressure manifolds. The pressure transducers were mounted to the manifolds at a radius of 97.76 mm from the machine axis—this was the radius where the centrifugal pressure developed during the measurement process. Therefore, a correction must be used to correct for the difference in centrifugal pressure due to the difference in radius. The correction can be obtained from the radial momentum equation and is of the form

$$\Delta p_{\text{centr}} = \frac{1}{2000}\,\rho\Omega_T^2(R_{\text{tap}}^2 - 0.09776^2) \qquad (1)$$

the correction is 0 kPa at $SR = 0$, −15.21 to 8.30 kPa at $SR = 0.6$, and −33.96 to 18.53 kPa at $SR = 0.8$. This correction is significantly larger than the blade loading.

Results and Discussion

The C_p distributions at the shell, mid-span and core sections are shown in Figs. 6, 7, and 8 for $SR = 0$, $SR = 0.6$, and $SR = 0.8$, respectively. Results are plotted as a function of meridional blade length, so that the area enclosed between the curves can be related directly to the torque exerted by the fluid on the blade. Meridional blade length is normalized by meridional blade length at the shell, since it is the longest length.

Interpretation of the C_p Distribution at $SR = 0$. The blade loading is a maximum at $SR = 0$ for two reasons. First, the through-flow velocity is a maximum; W_m at the turbine inlet is about 33 percent of the pump tip speed. Second, the blade turning is also a maximum. It is seen from Fig. 2 that the blade turning is about 130 degrees.

From a one-dimensional performance analysis, the incidence angle was found to be +18, +21, and +15 at the mid-span, shell and core sections, respectively. The incidence effect is most severe at $SR = 0$ due to the combined effect of the maximum incidence angle and the maximum through-flow velocity. The flow is, therefore, expected to be poorly behaved.

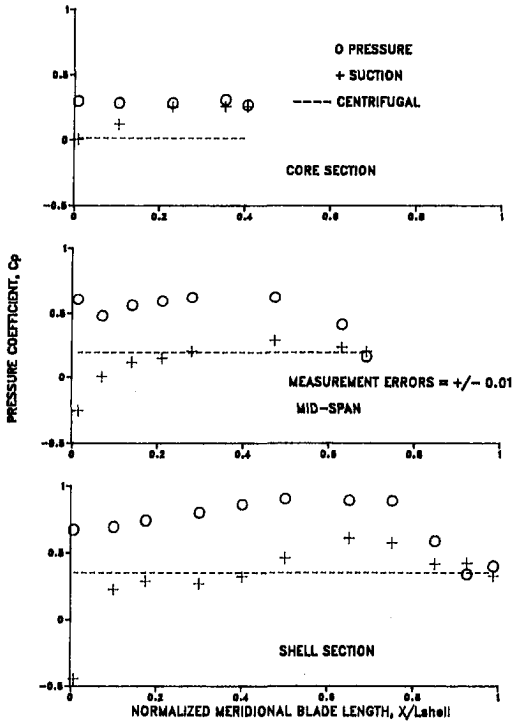

Fig. 6 C_p distribution at $SR = 0$

The static pressure drop from turbine inlet to turbine exit is practically zero at the three blade sections. The effect of the positive incidence angle, as seen in Fig. 6, is indeed very pronounced at the three blade sections near the leading edge. At the mid-span section, the C_p on the pressure surface is significantly higher than that on the suction surface; the difference is about 83 percent of the dynamic pressure based on pump tip speed. At the shell section, the difference is about 112 percent of the dynamic pressure. At the core section, the difference is about 30 percent of the dynamic pressure.

At the core section, the pressure distribution is flat on both pressure and suction surfaces in the last 50 percent of the meridional blade length. That is, the flow is neither accelerated nor decelerated; the through-flow velocity must be very small. As a result, a strong flow separation phenomenon may occur near the core section. This flow separation increases the viscous loss and it reduces the effective through-flow area.

Interpretation of the C_p Distribution at $SR = 0.6$. The blade loading and the incidence effect are expected to be considerably smaller at $SR = 0.6$ than those at $SR = 0$. The through-flow velocity at the turbine inlet is about 19 percent of the pump tip speed. It is seen from Fig. 2 that the blade turning is about 120 degrees. From a one-dimensional performance analysis, the incidence angle was found to be +11, +14 and +8 degrees at the mid-span, shell and core sections, respectively. The flow is, therefore, expected to be better behaved than that at $SR = 0$.

The incidence effect, as seen in Fig. 7, is less severe than that at $SR = 0$. The static pressure drop from turbine inlet to exit is about 24, 24 and 11 percent at the mid-span, shell, and core sections, respectively. There is no noticeable flow separation near the three blade sections.

Interpretation of the C_p Distribution at $SR = 0.8$. The blade loading and the incidence effect are expected to be minimum at $SR = 0.8$. The through-flow velocity is a minimum (W_m is about 14 percent of the pump tip speed). The blade turning is also a minimum of about 110 degrees. The incidence angle

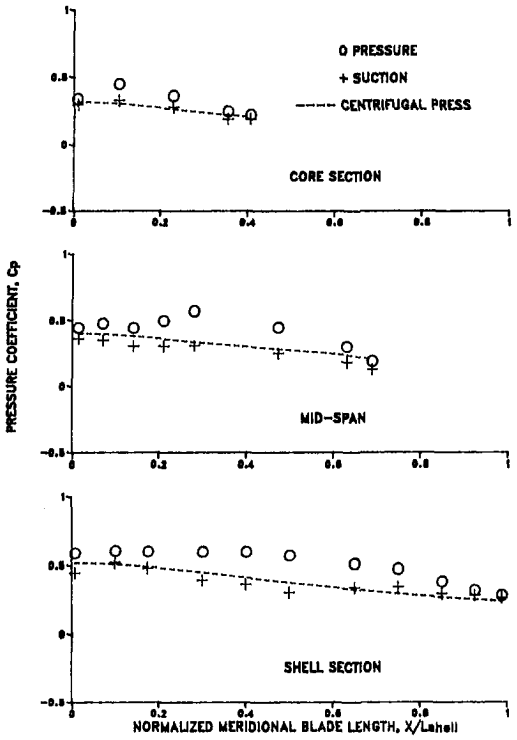

Fig. 7 C_p distribution at $SR = 0.6$

is also a minimum; it was found from a one-dimensional performance analysis to be 0, 3 and −3 degrees at the mid-span, shell and core sections, respectively. The flow is, therefore, expected to be better behaved than that at $SR = 0.6$ and $SR = 0$.

The incidence effect, as seen in Fig. 8, is significantly smaller than that at $SR = 0$, but it is about the same as that at $SR = 0.6$. The turbine static pressure drop, as expected, is significantly higher than that at $SR = 0.6$ (43 versus 24 percent at the mid-span, 45 versus 24 percent at the shell, and 21 versus 11 percent at the core section).

At the mid-section, however, the C_p distribution is poor in the first 30 percent of shell meridional length. This is probably caused by a negative incidence angle. The true incidence angle may be −5 degrees, since the maximum C_p is located on the suction surface (not on the leading edge). A small recirculating region may exist near the pressure surface.

Blade Torque. Blade torque is the torque exerted by the fluid on each turbine blade. Blade torque is an important parameter in the energy transfer between the fluid and blades of the turbine. Since the meridional length of the turbine blade is about 2.5 times longer at the shell than at the core, it is more appropriate to calculate the blade-torque-per-unit meridional length. At any blade section, the blade torque coefficient is

$$C_T = \frac{T}{0.5\rho U_{\text{tip},P}^2 H_1 R_{\text{tip}} L} = \int_{x_{\text{le}}/L}^{x_{\text{te}}/L} \frac{H}{H_1}\frac{R}{R_{\text{tip}}}(C_{p,p} - C_{p,s})\,d\left(\frac{x}{L}\right) \quad (2)$$

In addition to the dynamic pressure based on pump tip speed, two other parameters are used to normalize the blade torque coefficient. The two parameters are blade height or span at the turbine inlet, H_1, and turbine tip radius, R_{tip}. Equation (2) is used to calculate the blade torque coefficient at the shell, mid-span and core sections under the three speed ratio conditions. Results are shown in Fig. 9.

The blade torque coefficient at $SR = 0$ is 0.31, 0.28, and 0.08 at the shell, mid-span and core sections, respectively. The poor result at the core section is evident from the C_p distribution of Fig. 6.

The C_T distribution at $SR = 0.6$ is similar to that at $SR = 0$. It is significantly higher at the shell and mid-span sections than at the core (0.12, 0.13, and 0.06 at the shell, mid-span and core sections, respectively). The poor result at the core section is also evident from the C_p distribution of Fig. 7.

The C_T is almost constant at $SR = 0.8$; it is 0.05, 0.06, and 0.07 at the shell, mid-span and core sections, respectively. This result is different from the trend at $SR = 0$ and $SR = 0.6$. This may be due to the facts that: 1) the blade loading at $SR = 0.8$ is significantly smaller than that at the lower speed ratios and 2) the incidence angle is only a few degrees (at all blade sections).

The Mechanism of Static Pressure Drop. The static pressure drop along a streamline is

$$\frac{p_1 - p}{0.5\rho U_{\text{tip},P}^2} = (C_{p,1} - C_p) = \left(\frac{U_1^2 - U^2}{U_{\text{tip},P}^2}\right) + \left(\frac{W^2 - W_1^2}{U_{\text{tip},P}^2}\right) + \left(\frac{\Delta P^*}{0.5\rho U_{\text{tip},P}^2}\right) \quad (3)$$

The static pressure drop consists of three terms. The first term is the static pressure drop due to centrifugal force. The second term is the static pressure loss due to the diffusion of the relative velocity. The third term is the change of static pressure due to viscous effects.

The static pressure drop due to centrifugal force (the first term in the above equation) is calculated at the shell, mid-span and core sections under the three speed ratio conditions. The calculated pressure drop is compared with the measured static pressure distribution. From the turbine inlet to the turbine exit of any blade section, the difference between the two results

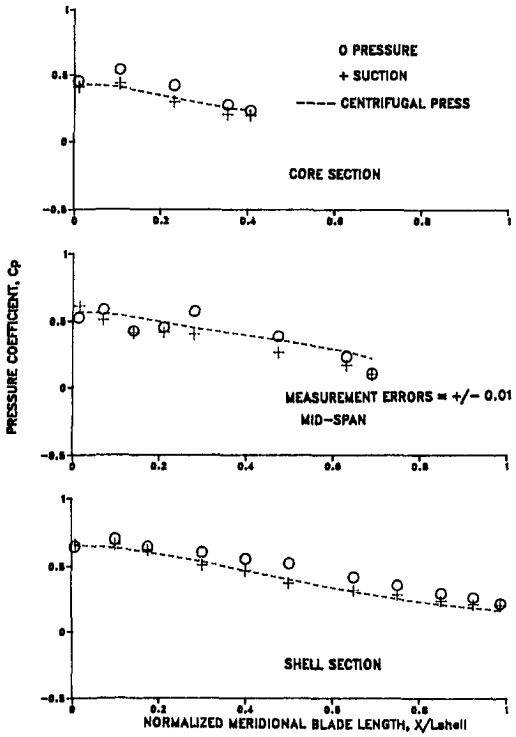

Fig. 8 C_p distribution at $SR = 0.8$

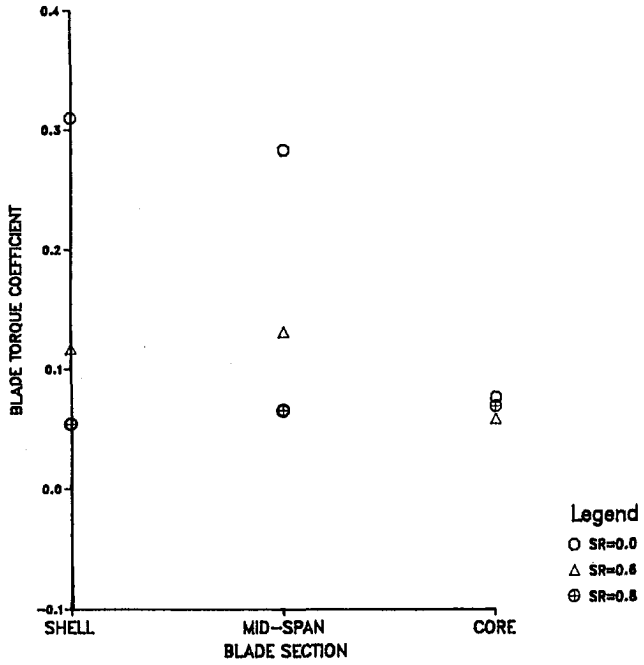

Fig. 9 Distribution of blade torque coefficient (C_T)

represents: 1) the loss of static pressure due to viscous effects and 2) the change of static pressure due to the diffusion of the relative velocity. The comparison is shown in Figs. 6, 7, and 8 for the speed ratios of 0, 0.6 and 0.8, respectively.

The static pressure drop due to centrifugal force is zero at $SR = 0$, since the turbine is stationary. As expected, it is seen from Fig. 6 that the loss of static pressure due to viscous effects and due to the diffusion of the relative velocity is very pronounced.

On the other hand, the static pressure drop due to centrifugal force has the dominant effect at $SR = 0.6$ and $SR = 0.8$. The static pressure loss due to viscous effects and due to the diffusion of the relative velocity is small. The turbine flow field is, therefore, expected to be better behaved at the higher speed ratios. This observation is in agreement with the measured efficiency curve of Fig. 2; the efficiency is 0 at $SR = 0$, 79 percent at $SR = 0.6$ and 82 percent at $SR = 0.8$.

The static pressure drop due to centrifugal force can be accurately predicted from the simple expression given in Eq. (3). However, the static pressure loss due to the diffusion of the relative velocity and due to viscous effects can only be analyzed by a reliable Navier-Stokes code. In addition to the static pressure data, data on the three velocity components is required to calibrate and validate the code. This type of investigation was done for the pump by By et al. (1993) and it should be repeated for the turbine and stator.

Conclusions

The turbine static pressure field changes drastically from the shell to the core section. Hence, the one-dimensional flow theory cannot accurately predict the spanwise distribution of the blade torque coefficient. The static pressure field is generally poor at the core section. Centrifugal force has the dominant effect on the static pressure drop in the turbine at $SR = 0.6$ and $SR = 0.8$. The static pressure loss due to viscous effects and due to the diffusion of the relative velocity is very pronounced at $SR = 0$.

As an extension of this work, a reliable Navier-Stokes code should be used to analyze the static pressure field and the velocity field of a torque converter turbine and a stator. Data on the three velocity components is required to complement the static pressure data. A Navier-Stoke analysis of a pump flow field has already been done.

Acknowledgments

This work was a portion of the first author's dissertation and it was partially supported by the General Motors NAO Engineering Center. The authors would like to express their gratitude to John Cicerone, Ted Hojna, and Roy Harvey for their assistance and contributions in designing, constructing, and testing the experimental facility; and John Mahoney for his continuous support and encouragement.

References

Abe, K., Kondoh, T., Fukumura, and Kojima, M., 1991, "Three-Dimensional Simulation of the Flow in a Torque Converter," SAE Paper #910800.

By, R. R., and Lakshminarayana, B. 1991, "Static Pressure Measurement in a Torque Converter Stator," SAE Paper #911934 and also in the 1992 SAE Journal of Passenger Cars.

By, R. R., and Lakshminarayana, B., 1993, "Measurement and Analysis of Static Pressure Field in a Torque Converter Pump," *The 2nd ASME Pumping Machinery Symposium*, FED-Vol. 154, pp. 253–264 and ASME JOURNAL OF FLUIDS ENGINEERING, Vol. 117, 1995, pp. 109–115.

By, R. R., Kunz, R. F., and Lakshminarayana, B. 1993, "Navier-Stokes Analysis of the Pump Flow Field of an Automotive Torque Converter," *The 2nd ASME Pumping Machinery Symposium*, FED-Vol. 154, pp. 265–274 and ASME JOURNAL OF FLUIDS ENGINEERING, Vol. 117, 1995, pp. 116–122.

Gruver, J. K., 1992, "Laser Velocimetry Measurements in the Pump of an Automotive Torque Converter," Master Thesis, Department of Mechanical & Aerospace Engineering, The University of Virginia.

Kubo, M., Ejiri, E., Okada, K., and Ishii, Y., 1991, "Improvement of Accuracy in Torque Converter Performance Prediction by Internal flow Measurement," JSAE Academic Conference Preprint #912279.

Numazawa, A., Ushijima, F., Fukumura, K., and Ishihara, T. 1983, "An Experimental Analysis of Fluid Flow in a Torque Converter," SAE Paper #830571.

APPENDIX

Analysis of Measurement Errors

The total measurement error (E_T) is the sum of the bias error (E_B) and the precision error (E_P). The bias and precision errors are the fixed and random components of the total error, respectively. If the bias and precision errors are known, the total measurement error can be calculated as follows

$$E_T = \sqrt{(E_B)^2 + (E_P)^2} \tag{4}$$

The bias error consists of errors of the pressure transducers, errors of the slip ring, errors of the data acquisition system, and others. It was the same in every reading and it was reduced to a minimum by calibration. Since 1200 sample outputs were recorded for each reading during a measurement span of 60 seconds, it was possible to place 95 percent confidence limit on the true mean population (p_{avg}). The standard deviation (σ) was less than 2 percent of the mean value. The maximum bias error is about ± 0.04 kPa based on 95 percent confidence level using the t distribution.

The precision error is the error associated with the repeatability of the measurement. It consists of errors associated with the trapped air in the hydraulic pressure lines, errors associated with induced-flow disturbances, and others. The maximum precision error is about ± 0.80 kPa based on 95 percent confidence level using the t distribution. As expected, the precision error is significantly larger than the bias error.

The total measurement error is found from Eq. (4) to be about ± 0.80 kPa or ± 1 percent of the dynamic pressure based on pump blade tip speed.

H. Tsukamoto
Professor,
Faculty of Engineering, Kyushu Institute of Technology,
Tobata, Kitakyushu, 804 Japan

H. Yoneda
Senior Researcher,
Technical Development Bureau, Nippon Steel Corporation,
Futtsu-city, Chiba, 299-12 Japan

K. Sagara
Engineer,
Nagasaki Shipyard & Machinery Works,
Mitsubishi Heavy Industries, Ltd.
Nagasaki, 850-91 Japan

The Response of a Centrifugal Pump to Fluctuating Rotational Speed

A theoretical and experimental study has been made on the dynamic characteristics of a centrifugal pump subject to sinusoidal changes in rotational speed. Time-dependent rotational speed, flow-rate, and total pressure rise are measured for a variety of amplitude and frequency of the fluctuating rotational speed. Measured flow-rate as well as total pressure rise is compared with the quasi-steady ones. Unsteady flow analysis is made for a two-dimensional circular cascade by use of the singularity method. The calculated frequency characteristics are compared with the corresponding experimental ones. The deviation of unsteady characteristics from quasi-steady ones is evident, and the numerical results agree qualitatively with the measured ones. It was found that with the increased frequency of rotational speed fluctuations the dynamic characteristics deviate remarkably from quasi-steady ones. Moreover, a criterion for the assumption of quasi-steady change is presented.

Introduction

The characteristics of a pump under unsteady operational condition have usually been thought to follow along its steady-state characteristic curves (Knapp, 1937). This assumption, called hereafter quasi-steady change, is acceptable in the case of slow change in operational condition. When the rate of change of the operating point exceeds a certain limit, however, the pump cannot respond quickly enough to traverse its steady-state characteristic curves. There has been, therefore, a need for understanding the dynamics of the pump characteristics in unsteady operation.

Dynamic performance of a pump has been investigated intensively for the case in which the flow-rate oscillates periodically about a mean operating point with a small amplitude. In this case, the pump dynamic performance can be described by a transfer matrix representation to relate the quantities at the inlet and exit of the pump (Guarga, 1991). Ohashi (1968), Anderson et al. (1971), Brennen et al. (1976), and Stirnemann et al. (1987) have contributed to such a description. However, most of the works done in the past are limited to the case of constant rotational speed. Therefore we have not known whether such data can be extended to dynamic characteristics in the case of the fluctuating rotational speed or not. The total pressure rise as well as flow rate changes with time when the rotational speed changes periodically around the mean value. This case, therefore, offers far more difficulties than the constant rotational speed case.

The aim of the present study is to make clear the dynamic characteristics when the rotational speed changes periodically with small amplitude around its mean value. And special interest lies on the pumping action during unsteady operation. The present study is, however, done for incompressible and cavitation-free flow so that the knowledge of basic phenomena may be obtained. This paper reports the measured frequency response of total pressure rise as well as flow rate to rotational speed. For the purpose of understanding the basic mechanism of the dynamic characteristics, unsteady flow analysis is made for a two-dimensional circular cascade by use of the singularity method. The calculated frequency characteristics are compared with the corresponding experimental ones.

Experiment

Test Equipment and Method. A single-stage, volute-type centrifugal pump is used for the experiment, and its principal specifications are summarized in Table 1. The arrangement of test setup and instrumentation system is similar to that by Tsukamoto et al. (1986). The test pump is driven by a 2-pole 7.5 kW induction motor. Variable speed operation of the motor is achieved by an inverter. In order to generate sinusoidal perturbations of rotational speed, the inverter is controlled by a microprocessor-based variable frequency device. In the present experiment the pump is excited from 0.57 Hz to 15.3 Hz.

In order to avoid cavitation, water is supplied to the suction port from a large reservoir with a water level of 1 m above the pump center through a short inlet pipe. The discharge line is connected to a large accumulator and thus the fluctuations in flow rate and pressure are limited to the region among the two reservoirs. Before starting each test, the pump and piping loop are completely filled with water. The discharge valve is so adjusted that the mean value coincides with the desired value. The valve setting is not changed during each test. The rotational speed of the pump is detected by the pulse signals (60 pulses a revolution), which are fed to a frequency-analog converter for the recording. The suction and discharge pressure are measured by semi-conductor type pressure transducers, which are installed directly on the pressure taps in order to prevent the decrease of natural frequency in the pressure measurement system.

The flow-rate is measured by an electro-magnetic flowmeter installed in the discharge line. A variable frequency AC excitation of magnet has been adopted to avoid severe drift problems encountered in the DC excited flowmeter and to get better accuracy in instantaneous flow-rate. The instantaneous rotational speed N_i, flow-rate Q_i, suction and discharge pressure, p_s and p_d, are transmitted to an A/D converter, and then recorded on the data file in the computer. From the data on the data file, instantaneous rotational speed $N_i(t)$, flow-rate $Q_i(t)$, total pressure difference between suction and discharge port, $P_i(t)$, are read out as a function of time t. Experimental frequency response data have been obtained over a range of frequencies up to 15 Hz, using frequency control for the inverter controlled motor.

Contributed by the Fluids Engineering Division for publication in the JOURNAL OF FLUIDS ENGINEERING. Manuscript received by the Fluids Engineering Division December 16, 1993; revised manuscript received March 6, 1995. Associate Technical Editor: R. L. Panton.

Table 1 Specifications of test pump

Suction diameter		65 mm
Discharge diameter		50 mm
Impeller:	Outer diameter	137 mm
	Outer passage width	9.3 mm
	Outlet vane angle	20 degs
	Number of vanes	7
Rating:	Rotational speed	3455 rpm
	Flow rate	0.25 m^3/min
	Total head rise	31.5 m

Presentation of Data. In the case of unsteady operation special attention must be paid to the meaning of total pressure rise P of the pump, which is defined usually as the increase of the total pressure from suction to delivery generated by the pumping action. In the case of unsteady flow rate, a part of the total pressure difference is caused by the inertia of water contained in the pump impeller and casing. This part of pressure difference is called the total pressure difference by conduit effect, P_c, (Ohashi, 1968), and is calculated by the equation

$$P_c = -\rho(L_{eq}/A_0)(dQ_i/dt) \tag{1}$$

where the pump is represented by a straight pipe with the reference cross-sectional area A_0, length L_{eq}. The equivalent pipe length L_{eq} of the pump is calculated by the equation

$$L_{eq} = \int_{s=0}^{L} \{A_0/A(s)\}\, ds \tag{2}$$

where s is the distance measured from the suction port, and L is the total path length.

In the present study where we are interested only in the dynamic behavior of the pumping action, therefore, the true total pressure rise containing no inertial effect of the water, P, should be compared with a quasi-steady value in order to discuss the deviation of the dynamic performance from a quasi-steady one. The true total pressure rise by pumping action during unsteady operation, P, can be calculated by subtracting the apparent total pressure difference P_c due to the conduit effect from measured total pressure rise, P_i, as the following equation shows:

$$P = P_i - P_c \tag{3}$$

In order to derive the nondimensional parameters which regulate the frequency characteristics, let us compare the frequency phenomena in the pumping system with geometrically similar pump and piping. Once we fix the following eight parameters, i.e., the representative length of the pump, d, total length of the piping, l_{eq}, density and viscosity coefficient ρ and μ, mean rotational speed N_0, amplitude of variable rotational speed ΔN, pipe resistance ζ, perturbation frequency f; a unique experimental condition can be established, under which a specific frequency phenomenon takes place. According to the theory of dimensional analysis, the above eight physical quantities can be reduced to five independent nondimensional parameters, i.e., normalized piping length l_{eq}/d, Reynolds number $N_0 d^2/(\mu/\rho)$, pipe resistance $\zeta \propto \phi_0/\phi_r$, normalized amplitude of rotational speed $\Delta N/N_0$, and newly introduced reduced frequency $f/(\phi_0 N_0)$. Here ϕ_0 and ϕ_r are mean and rated flow coefficient, respectively.

The latter three parameters can be controlled in the experiment by adjusting the opening of the delivery valve, and the perturbed rotational speed and perturbation frequency. The influence of Reynolds number on frequency characteristics is omitted from the present study.

Test Results. Figure 1 presents the time histories of measured rotational speed, N_i, flow rate, Q_i, and total head difference $H_i = P_i/(\rho g)$ in the case of $\phi_0/\phi_r = 1.0$, $\Delta N/N_0 = 0.12$, and $f = 7.63$ Hz. The data are periodic but nonsinusoidal with random noise as can be seen in this figure. Thus the statistical analysis is carried out to get the frequency response of P and Q_i against N_i.

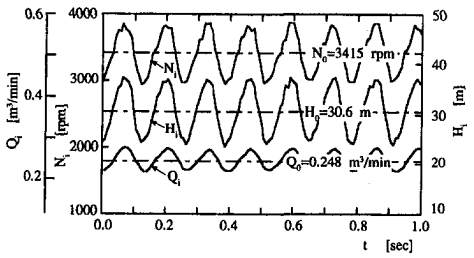

Fig. 1 Time histories of N_i, Q_i, and H_i ($\phi_0/\phi_r = 1.0$, $\Delta N/N_0 = 0.12$, and $f = 7.63$ Hz); experimental uncertainty in $N_i/N_0 = \pm 3.0$ percent, in $H_i/H_0 = \pm 3.5$ percent, and in $Q_i/Q_0 = \pm 5.5$ percent

Before going into the statistical analysis of the measured data, the correlation between input N_i, and output Q_i and P is checked. Figure 2 shows the coherence function between the rotational speed $N_i(t)$ and the other variables $Q_i(t)$, $P_i(t)$ at the forced frequency of the rotational speed. As can be seen in these figures, the measured values of the coherence function are almost unity within the range of the present experiment, and thus the output $Q_i(t)$ and $P_i(t)$ are completely related with the input $N_i(t)$.

Figure 3 shows the plot of the output amplitude, and the phase shift between the output and input $N_i(t)$ as a function of the input amplitude. Figures 3(a) and (b) present the relation of total head rise to the rotational speed and that of flow rate to the rotational speed, respectively. The amplitudes of fluctuations in flow-rate as well as total head rise are proportional to that in rotational speed. On the other hand, the phase lag against the rotational speed is independent of the amplitude of rotational speed and nearly constant under a constant frequency. These results, therefore, demonstrate the linearity of the present experiment.

Figure 4 indicates the measured loci, along which the coordinates of instantaneous flow rate Q_i and total head rise $H = P/(\rho g)$ move during the unsteady operation of the pump. The measured steady-state resistance curves of the piping system are indicated by a dash-line for the three different valve setting of $\phi_0/\phi_r = 0.5$, 1.0, and 1.5. When the fluctuation is sufficiently slow, the instantaneous pressure rise of the pump varies obviously along the steady-state H-Q curve at the instantaneous rotational speed $N_i(t)$. The true quasi-steady pressure rise is that corresponds to the steady-state value for the instantaneous rotational speed and flow rate. In the present case in which the valve setting unchanged during unsteady operation, then, the loci lies on the steady-state resistance curve for low fluctuation frequency. This case may be referred to a quasi-steady change for the convenience sake, although there has been a slight difference between the true quasi-steady change and the present definition.

These loci represent the characteristic curves during the unsteady operation and should be compared with the steady-state

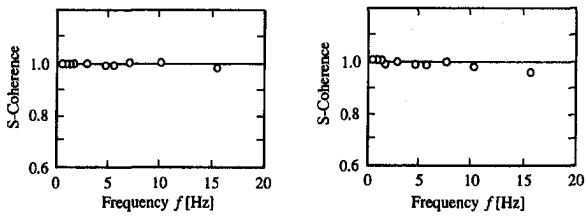

(a) Rotational speed, N_i, vs. total pressure difference, P_i **(b) Rotational speed, N_i, vs. flow rate, Q_i**

Fig. 2 Coherence function between input N_i and output at $\phi_0/\phi_r = 1.0$

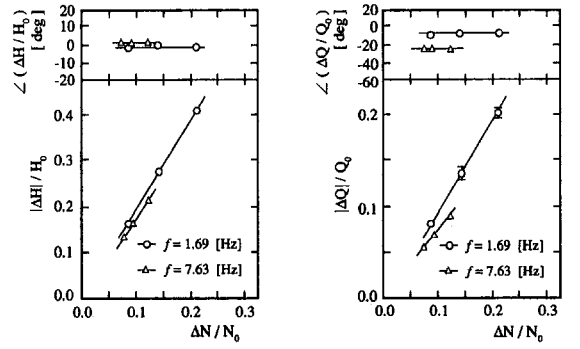

(a) Frequency response of total pressure rise

(b) Frequency response of flow rate

Fig. 3 Dependence of the frequency response on amplitude of fluctuations in rotational speed (ϕ_0/ϕ_r = 1.0); experimental uncertainty in $|\Delta H|/H_0$ = ±3.5 percent, $\angle(\Delta H/H_0)$ = ±3 deg, in $|\Delta Q|/Q_0$ = ±5.5 percent, $\angle(\Delta Q/Q_0)$ = ±3.8 deg, in $|\Delta N|/N_0$ = ±3.0 percent

pipe resistance curve. As can be seen clearly from these figures, the deviation of unsteady characteristics from quasi-steady ones is evident.

Analysis

Flow Model. In a centrifugal impeller, which is our main concern, the impeller blades on the stream surface constitute a rotating circular cascade. Unsteady flow analysis can thus be made for a two-dimensional circular cascade by use of the singularity method similar to that by Tsukamoto et al. (1986).

The configuration of the cascade used in the present analysis is shown in Fig. 5. It is a rotating circular cascade of thin blades with a rotational speed $\Omega(t)$, flow-rate per unit passage width $q(t)$, and number of vanes N. The blade shape chosen herein for analysis is a logarithmic spiral, i.e., a vane of constant angle. Each blade is represented by an identical bound vortex sheet $\gamma(s, t)$ since "in phase" unsteadiness is considered under time-dependent rotational speed and flow rate. According to the change in circulation, each blade sheds vorticity downstream, forming a vortex sheet of strength $\epsilon(s, t)$. Among many existing models of the wake (Mook and Dong, 1994), we use the simple model that this vortex sheet is assumed to be convected along the logarithmic spiral extended from the trailing edge with the mean radial velocity component $q_0/(2\pi r)$. The shed vortex sheet from the first blade extends on the logarithmic spiral from s_2 ($r = r_2$) to ∞. All other vortex sheets have the same extensions.

Vorticity Distribution. The configuration of the singularities mentioned above gives the absolute complex conjugate velocity at the point $z' = R\cdot\exp(i\mathrm{H})$ on the blade as follow:

$$u - i\cdot v = \frac{q(t)}{2\pi z'} + \frac{i}{2\pi}\int_{s_1}^{s_2}\gamma(s, t)G(z, z')ds + \frac{i}{2\pi}\int_{s_2}^{\infty}\epsilon(s, t)G(z, z')ds \quad (4)$$

where, s: coordinate along the logarithmic spiral, u and v: x and y components of the absolute velocity, $z = r\cdot\exp(i\theta)$,

$$G(z, z') = Nz'^{N-1}/\{z'^N - z(s)^N\}.$$

Considering the fact that the strength of free vortices is inversely proportional to the velocity, the distribution of free vortices ϵ can be written as

$$\epsilon(s_2, t_1)w_s(s_2, t_1) = \epsilon(s, t)w_s(s, t) \quad (5)$$

where, w_s: the s-component of the relative velocity,

$$t - t_1 = \int_{s_2}^{s} ds/w_s = (\pi\cos^2\beta/q_0)(s^2 - s_2^2).$$

Further, Kelvin's law for the conservation of vortices leads to the relation that the rate of total circulation change is equal to the total shed vortices from the trailing edge within unit time. This is expressed by

$$\epsilon(s_2, t)w_s(s_2) = -d\Gamma(t)/dt = -d\left\{\int_{s_1}^{s_2}\gamma(s, t)ds\right\}/dt \quad (6)$$

The velocity induced by shed vortices can be rewritten by substituting Eqs. (5) and (6) into Eq. (4).

The boundary condition on the blade requires that there is no flow through the surface in the relative system. This condition is fulfilled for a rotating blade if

$$\mathrm{Im}[\exp(i\alpha)\{u - i\cdot v + i\cdot\Omega(t)\bar{z}'\}] = 0 \quad (7)$$

where, $\alpha = \Theta - \beta$, β: complement of impeller vane angle.

Substitution of Eq. (4), (5), and (6) into Eq. (7) then gives the integral equation for unknown vorticity $\gamma(s, t)$, in which the velocity induced by shed vortices is rewritten in the manner mentioned above.

Now we will consider the case in which the angular velocity of the impeller and the flow rate fluctuate periodically in time around their mean values Ω_0 and q_0, respectively. Using the complex variable notation, the rotational speed and flow rate may be written

$$\Omega(t) = \Omega_0 + \overline{\Delta\Omega}\cdot\exp(j\nu t); \quad (|\overline{\Delta\Omega}| \ll \Omega_0)$$
$$q(t) = q_0 + \overline{\Delta q}\cdot\exp(j\nu t); \quad (|\overline{\Delta q}| \ll q_0) \quad (8)$$

where $\overline{\Delta\Omega}$ and $\overline{\Delta q}$ are constants, and $\nu = 2\pi f$.

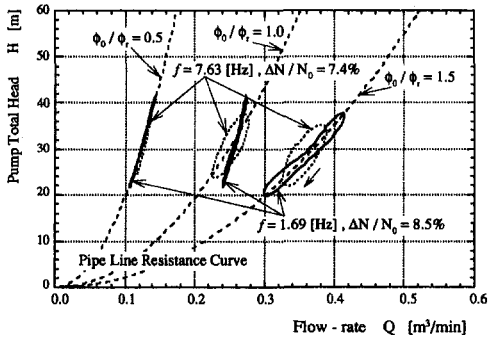

Fig. 4 Dynamic relations of H to Q_l during periodic fluctuations in rotational speed; experimental uncertainty in H/H_0 = ±3.5 percent, and in Q_l/Q_0 = ±5.5 percent

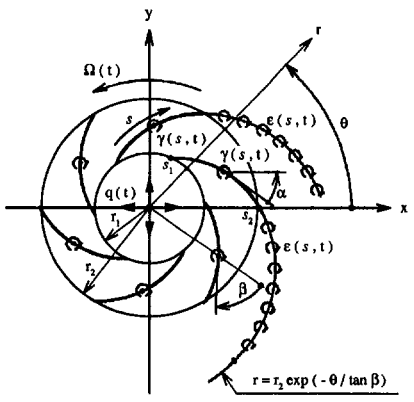

Fig. 5 Model of unsteady two-dimensional rotating circular cascade

The bound vorticity γ consists of mean term γ_0 and unsteady term:

$$\gamma(s, t) = \gamma_0(s) + \bar{\gamma}(s) \exp(j\nu t) \tag{9}$$

The unsteady bound vorticity term is divided to quasi-steady term and wake effect term, and furthermore individual terms consist of terms caused by angular velocity and flow rate changes:

$$\begin{aligned}\bar{\gamma}(s) &= \overline{\gamma_s}(s) + \overline{\gamma_w}(s) \\ &= \{\overline{\gamma_{sN}}(s) + \overline{\gamma_{sQ}}(s)\} + \{\overline{\gamma_{wN}}(s) + \overline{\gamma_{wQ}}(s)\}\end{aligned} \tag{10}$$

where, subscripts s and w express quasi-steady and wake components, and Q and N do the components due to flow rate and rotational speed changes, respectively. Substituting Eq. (8), (9), and (10) to the integral equation for unknown vorticity $\gamma(s, t)$, considering the contribution of each vorticity component to each induced velocity, and introducing the dimensionless quantities, we get the following set of normalized basic integral equations for the unknown vorticity components, γ_0, $\bar{\gamma}_{sQ}$, $\bar{\gamma}_{sN}$, $\bar{\gamma}_{wQ}$, and $\bar{\gamma}_{wN}$:

$$\mathrm{Im}_i\left[e^{i\alpha}\left\{\frac{\phi_0}{z'^*} + \frac{i}{2\pi}\int_{r_1^*}^{1} \gamma_0^*(r^*)G(z^*, z'^*)dr^*/\cos\beta + \overline{iz'^*}\right\}\right] = 0$$

$$\mathrm{Im}_i\left[e^{i\alpha}\left\{\frac{1}{z'^*} + i\int_{r_1^*}^{1} \bar{\gamma}_{sQ}^*(r^*)G(z^*, z'^*)dr^*/\cos\beta\right\}\right] = 0$$

$$\mathrm{Im}_i\left[e^{i\alpha}\left\{\frac{i}{2\pi}\int_{r_1^*}^{1} \bar{\gamma}_{sN}^*(r^*)G(z^*, z'^*)dr^*/\cos\beta + \overline{iz'^*}\right\}\right] = 0$$

$$\mathrm{Im}_i\left[\frac{ie^{i\alpha}}{2\pi}\left\{\int_{r_1^*}^{1} \bar{\gamma}_{wQ}^*(r^*)G(z^*, z'^*)dr^*/\cos\beta - jkF(z'^*)\right\} \times\left\{\Gamma_{sQ}^* + \int_{r_1^*}^{1} \bar{\gamma}_{wQ}^*(r^*)dr^*/\cos\beta\right\}\right] = 0$$

$$\mathrm{Im}_i\left[\frac{ie^{i\alpha}}{2\pi}\left\{\int_{r_1^*}^{1} \bar{\gamma}_{wN}^*(r^*)G(z^*, z'^*)dr^*/\cos\beta - jkF(z'^*)\right\} \times\left\{\Gamma_{sQ}^* + \int_{r_1^*}^{1} \bar{\gamma}_{wN}^*(r^*)dr^*/\cos\beta\right\}\right] = 0 \tag{11}$$

where,

$$r^* = r/r_2, \quad \gamma_0^* = \gamma_0/(r_2\Omega_0)$$

$$\bar{\gamma}_{sQ}^* = \bar{\gamma}_{sQ}/(\overline{\Delta q}/r_2), \quad \bar{\gamma}_{sN}^* = \bar{\gamma}_{sN}/(r_2\overline{\Delta\Omega})$$

$$\bar{\gamma}_{wQ}^* = \bar{\gamma}_{wQ}/(\overline{\Delta q}/r_2), \quad \bar{\gamma}_{wN}^* = \bar{\gamma}_{wN}/(r_2\overline{\Delta\Omega})$$

$$k = \nu r_2/\{q_0/(2\pi r_2)\}, \quad \phi_0 = q_0/(2\pi r_2^2\Omega_0)$$

$$z^* = z/r_2, \quad z'^* = z'/r_2, \quad \bar{\Gamma}^* = \int_{r_1^*}^{1} \bar{\gamma}^*(r^*)dr^*/\cos\beta$$

$$F(z'^*) = \int_{r_1^*}^{1} \exp\{-jk(r^{*2} - 1)/2\} r^* G(z^*, z'^*)dr^*$$

For the numerical calculation, a transformation is made from r and R to new independent variables λ and Λ, via the trapezoidal rule

$$r = r_1 + (r_2 - r_1)(1 - \cos\lambda)/2 \quad (0 \le \lambda \le \pi)$$

$$R = r_1 + (r_2 - r_1)(1 - \cos\Lambda)/2 \quad (0 \le \Lambda \le \pi)$$

The bound vortices can be specified at $(n + 1)$ points

$$\lambda = (k - 1)\pi/n \quad (k = 1, 2, \ldots, n + 1)$$

The values of λ for $k = n + 1$, that is at the trailing edge, is unnecessary since in the integration it is always multiplied by $\sin\lambda = 0$ (Whitehead, 1960). The n values of γ can be determined so as to satisfy equation (11) at n points only, and these points are chosen so as to be allocated midway between the points at which bound vortices are specified.

$$\Lambda = (2k - 1)\pi/(2n) \quad (k = 1, 2, \ldots, n)$$

In this manner, each equation in Eq. (11) yields n simultaneous equations for the n unknowns, $\gamma(s, t)$.

Flow Rate. In the case under consideration the flow-rate changes with time following the rotational speed changes, and therefore an equation is required for determining the instantaneous flowrate in addition to the basic Eq. (11). The instantaneous flowrate was calculated by considering the pressure balance of the piping system:

$$(\rho l_{eq}/A_0)\{dQ_i(t)/dt\} + (\rho\zeta)\{Q_i(t)/A_0\}^2 = P(t) \tag{12}$$

where, l_{eq}: equivalent pipe length of piping system, A_0: nominal flow area, ζ: pressure loss coefficient determined by using Eq. (12) at the steady-state operating condition:

$$\zeta = \psi_0/\phi_0^2 \tag{13}$$

By omitting negligible small terms we can get the following equation for determining the nondimensional oscillatory flow rate $\overline{\Delta q}^*$:

$$(jkl_{eq}^* + \zeta)\phi_0^2\overline{\Delta q}^* = \overline{\Delta P}^*\psi_0 \tag{14}$$

where,

$$\overline{\Delta q}^* = \overline{\Delta q}/(\overline{\Delta q})_s, \quad (\overline{\Delta q})_s = 2\pi r_2^2\phi_0\overline{\Delta\Omega}$$

$$\overline{\Delta P}^* = \overline{\Delta P}/(\overline{\Delta P})_s, \quad (\overline{\Delta P})_s = \rho\phi_0\overline{\Delta\Omega}\Omega_0 r_2^2$$

$$\psi_0 = -N\Gamma_0/(\pi r_2^2\Omega_0), \quad \phi_0 = q_0/(2\pi r_2^2\Omega_0)$$

Pressure Rise. Total pressure rise through cascade, $P(t)$, can be obtained by applying the unsteady Bernoulli's Equation with respect to the moving relative system (Tsukamoto et al., 1986).

$$\begin{aligned}\psi_i(t) &= P(t)/[\rho\{r_2\Omega(t)\}^2/2] \\ &= N\left[\theta_2\{d\Gamma(t)/dt\} - \left\{\int_{s_1}^{s_2} \gamma(s, t)\theta(s)ds\right\}dt\right]\Big/ \\ &\qquad [\pi\{r_2\Omega(t)\}^2] - N\Gamma(t)/\{\pi r_2^2\Omega(t)\}\end{aligned} \tag{15}$$

We will consider the case in which the rotational speed changes sinusoidally with small amplitude around its mean value Ω_0. The oscillatory total pressure rise was calculated by Eq. (15), and higher order small quantities are omitted:

$$\begin{aligned}\overline{\Delta P} = \rho N\left\{j\nu\theta_2\bar{\Gamma} - j\nu\int_{s_1}^{s_2} \bar{\gamma}(s)\theta(s)ds\right\}\Big/(2\pi) \\ - \rho N\{\overline{\Delta\Omega}\Gamma_0 + \Omega_0\bar{\Gamma}\}/(2\pi)\end{aligned} \tag{16}$$

The above equation can be normalized as follow:

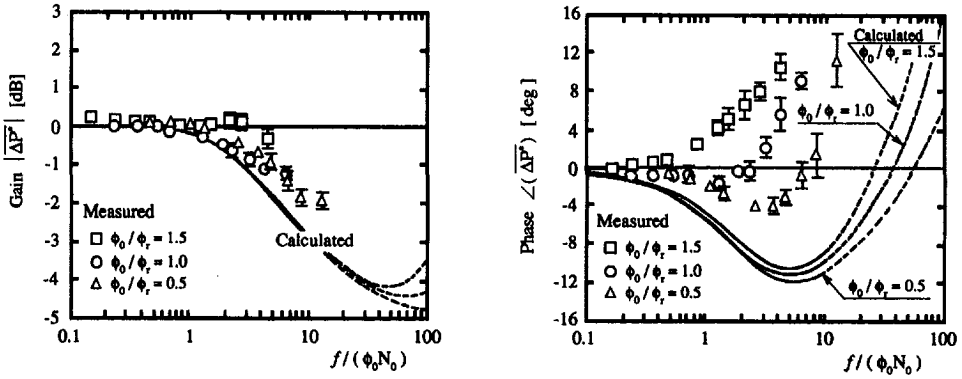

(a) Gain $|\overline{\Delta P^*}|$ vs. frequency

(b) Phase $\angle(\overline{\Delta P^*})$ vs. frequency

Fig. 6 Frequency response of total pressure rise of a centrifugal pump for sinusoidal change in rotational speed; experimental uncertainty in gain = ±0.2 db, in phase ±3 deg; vertical bars show the two sigma error (20 to 1 odds)

$$\overline{\Delta P}^* = -(\pi\phi_0/\Gamma_0^*)\left[jk\phi_0\left\{\theta_2(\bar{\Gamma}_{sQ}^* + \bar{\Gamma}_{wQ}^*) - \int_{r_1^*}^{1}(\bar{\Gamma}_{sQ}^* + \bar{\Gamma}_{wQ}^*)\theta(r^*)dr^*/\cos\beta\right\} - (\bar{\Gamma}_{sQ}^* + \Gamma_{wQ}^*)\right] \times \overline{\Delta q}^* - \left[jk\phi_0\left\{\theta_2(\bar{\Gamma}_{sN}^* + \bar{\Gamma}_{wN}^*) - \int_{r_1^*}^{1}(\bar{\Gamma}_{sN}^* + \bar{\Gamma}_{wN}^*)\theta(r^*)dr^*/\cos\beta\right\} - (\Gamma_0^* + \bar{\Gamma}_{sN}^* + \bar{\Gamma}_{wN}^*)\right]/(2\Gamma_0) \quad (17)$$

After getting the vorticity distributions from Eq. (11), nondimensional oscillatory flow rate and total pressure rise are determined simultaneously by Eqs. (14) and (17).

Discussion

Comparison Between Theory and Experiment. Figures 6 and 7 indicate the frequency characteristics of total pressure rise and flow-rate, respectively. The dynamic results are presented in the conventional manner as the pressure amplitude ratio and the phase shift against a frequency parameter; that is, what is generally termed the "frequency response" or BODE plot. In these figures, the calculated frequency characteristics are compared with the corresponding experimental ones. As the frequency is increased from zero, the amplitude of the pressure rise at first steadily decreases, and the pressure rise lags slightly behind the quasi-steady one. With further increase of the frequency, however, the pressure rise vector leads the quasi-steady one. According to the theoretical calculations by Imaichi et al. (1982), the unsteady torque shows a similar tendency in the case of sinusoidal change in flow rate or rotational speed. The amplitude of flow rate steadily decreases and the phase shows the lag behind the quasi-steady flow rate as the frequency is increased from zero.

Since the analysis was conducted on the basis of inviscid flow, i.e., 100 percent efficiency, the qualitative agreement between theory and experiment is poor. However, the calculated results agree qualitatively with the measured ones and offer a basis of explaining dynamic characteristics during the unsteady operation.

Criterion for Quasi-Steady Change. An increase in the above parameter results in a greater shift from a quasi-steady change. And the assumption of quasi-steady change may be acceptable within the range of $f/(\phi_0 N_0) < 1.0$ as far as the present test pump is concerned. This critical condition has the same order as that by Ohashi (1968) in the fluctuating flow rate case under a constant rotational speed.

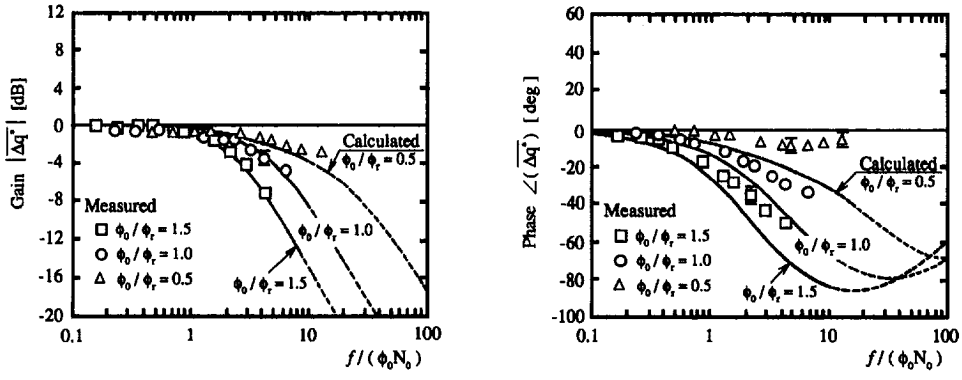

(a) Gain $|\overline{\Delta q^*}|$ vs. frequency

(b) Phase $\angle(\overline{\Delta q^*})$ vs. frequency

Fig. 7 Frequency response of flow rate of a centrifugal pump for sinusoidal change in rotational speed; experimental uncertainty in gain = ±0.2 db, in phase ±3.8 deg; vertical bars show the two sigma error (20 to 1 odds)

Conclusion

The frequency response of a centrifugal pump impeller to the fluctuating rotational speed was studied experimentally and theoretically. When the rotational speed fluctuates quickly, the frequency response of the total pressure rise deviates from the quasi-steady one. The results of the numerical calculations were compared with the experiments, and the following conclusions were drawn:

(1) As the frequency is increased from zero, the amplitude of the pressure rise at first steadily decreases, and the pressure rise lags slightly behind the quasi-steady one.

(2) With further increase of the frequency, however, the pressure rise vector leads the quasi-steady one.

In addition to the above results, nondimensional parameter $f/(\phi_0 N_0)$ was introduced as the parameter which is determinant for the frequency characteristics of a pump at rotational speed fluctuation. An increase in the above parameter results in a greater shift from a quasi-steady change. And the assumption of quasi-steady change may be acceptable within the range of $f/(\phi_0 N_0) < 1.0$.

Acknowledgment

This study was supported by the Harada Memorial Scholarship Foundation. The authors appreciate the dedicated assistance in the experimental work by Messrs. Y. Shimizu and Y. Kaku. The authors' thanks extend also to Mr. T. Ito for his assistance in the preparation of this paper.

References

Anderson, D. A., Blade, R. J., and Stevans, W., 1971, "Response of a Radial-Bladed Centrifugal Pump to Sinusoidal Disturbances for Noncavitating Flow," NASA TN D-6556.

Brennen, C., and Acosta, A. J., 1976, "The Dynamic Transfer Function for a Cavitating Inducer," ASME JOURNAL OF FLUIDS ENGINEERING, Vol. 98, No. 2, pp. 182–191.

Guarga, R., 1991, "Instability due to Performance Characteristics," *Vibration and Oscillation of Hydraulic Machinery,* H. Ohashi, ed., Avebury Technical, Aldershot, pp. 175–196.

Imaichi, K., Tsujimoto, Y., and Yoshida, Y., 1982, "An Analysis of Unsteady Torque on a Two-Dimensional Radial Impeller," ASME JOURNAL OF FLUIDS ENGINEERING, Vol. 104, No. 2, pp. 228–234.

Knapp, R. T., 1937, "Complete Characteristics of Centrifugal Pumps and Their Use in the Prediction of Transient Behavior," *ASME Transactions,* Vol. 59, pp. 683–689.

Mook, D. T., and Dong, B., 1994, "Perspective: Numerical Simulations of Wakes and Blade-Vortex Interaction," ASME JOURNAL OF FLUIDS ENGINEERING, Vol. 116, pp. 5–21.

Ohashi, H., 1968, "Analytical and Experimental Study of Dynamic Characteristics of Turbopumps," NASA TN D-4298.

Stirnemann, A., Eberl, J., Bolleter, U., and Pace, S., 1987, "Experimental Determination of the Dynamic Transfer Matrix for a Pump," ASME JOURNAL OF FLUIDS ENGINEERING, Vol. 109, pp. 218–225.

Tsukamoto, H., Matsunaga, S., Yoneda, H., and Hata, S., 1986, "Transient Characteristics of a Centrifugal Pump During Stopping Period," ASME JOURNAL OF FLUIDS ENGINEERING, Vol. 108, No. 4, pp. 392–399.

Whitehead, D. S., 1960, "Force and Moment Coefficient for Vibration Aerofoils in Cascade," Aeronautical Research Council, Report and Memoranda, No. 3254.

An Experimental Investigation of the Flow Through an Axial-Flow Pump

(Data Bank Contribution*)

W. C. Zierke

W. A. Straka

P. D. Taylor

Applied Research Laboratory,
The Pennsylvania State University,
State College, PA 16804

The high Reynolds number pump (HIREP) facility at ARL Penn State has been used to perform a low-speed, large-scale experiment of the incompressible flow of water through a two-blade-row turbomachine. The objectives of this experiment were to provide a database for comparison with three-dimensional, turbulent flow computations, to evaluate engineering models, and to improve our physical understanding of many of the phenomena involved in this complex flow field. This summary paper briefly describes the experimental facility, as well as the experimental techniques—such as flow visualization, static-pressure measurements, laser Doppler velocimetry, and both slow- and fast-response pressure probes. Then, proceeding from the inlet to the exit of the pump, the paper presents highlights of experimental measurements and data analysis, giving examples of measured physical phenomena such as endwall boundary layers, separation regions, wakes, and secondary vortical structures. In conclusion, this paper provides a synopsis of a well-controlled, larger scope experiment that should prove helpful to those who wish to use the database.

Introduction

Low-speed, large-scale experiments within multiple-blade-row machines have become increasingly important in the field of turbomachinery over the last several years. There are several reasons for this trend. The first is the increasing use of numerical prediction methods in the design and analysis of multiple-blade-row machines. In order to extend the range of confidence that we have in these numerical codes, we must perform some means of validation by comparing the numerical results with data from well-controlled experiments. A second reason for this experimental trend lies in the fact that despite the great advances in numerical prediction codes, many critical calculations required by the designer cannot yet be performed by solving the governing equations from first principles. Engineering models are still required and these models are still empirical in nature and require experimental data for closure. A final reason for the growing number of multiple-blade-row turbomachinery experiments lies in our lack of physical understanding of many of the phenomena involved in this complex flow field. Many of these phenomena are specific to multiple-blade-row turbomachines and have not been addressed with enough detail.

None of the growing number of low-speed, large-scale, multiple-blade-row experiments has dealt with the incompressible flow of water at large blade-chord Reynolds numbers. In order to extend the range of our numerical prediction codes, flow models, and physical understanding to this incompressible flow problem, we need to perform new experiments. ARL Penn State has a high Reynolds number pump (HIREP) facility that can achieve blade chord Reynolds numbers as high as 6,000,000 and can accommodate a variety of instrumentation in both a stationary and a rotating frame of reference. Using HIREP, Zierke et al. (1993) performed an experiment using several types of experimental techniques and their final report gives the details of the experiment, as well as a complete analysis of all the data (including the data uncertainty).

With a complete description of the HIREP geometry, the experimental results provide an excellent test case for comparison with numerical computations. However, considering the large scope of the experiment and subsequent data analysis, we feel that this summary paper would give others a sense of the quantity and quality of the data—allowing them to determine if they would benefit from using these experimental measurements for their code validation. This summary paper briefly describes the experimental facility and, then, describes highlights of the experimental techniques and results as one proceeds from the inlet to the exit of the pump. These experimental results include various types of physical phenomena within this complex flow field.

Experimental Facility

This experiment was performed in the Garfield Thomas Water Tunnel at ARL Penn State. The tunnel has a 1.22-meter diameter, 4.27-meter long test section which supports water velocities up to 18.29 m/s and static pressures ranging from 20 to 414 kPa. Tunnel turbulence is controlled using a honeycomb placed within the plenum, 2.82 meters upstream of the nine-to-one contraction nozzle, giving a measured axial component of the freestream turbulence intensity level to be 0.11 ± 0.01 percent and a longitudinal integral length scale of 13.9 mm ± 1.5 mm with 95 percent confidence. (All subsequent uncertainties within this paper are given to a 95 percent confidence level.) Lauchle et al. (1989) give a detailed description of the tunnel, as well as some of the basic experimental procedures.

HIREP consists of a 1.07-meter diameter pump stage driven by a 1.22-meter diameter downstream turbine—with a constant

* Data have been deposited to the JFE Data Bank. To access the file for this paper, see instructions on p. 544 of this issue.

Contributed by the Fluids Engineering Division for publication in the JOURNAL OF FLUIDS ENGINEERING. Manuscript received by the Fluids Engineering Division November 26, 1994; revised manuscript received April 14, 1995. Associate Technical Editor: L. Nelik.

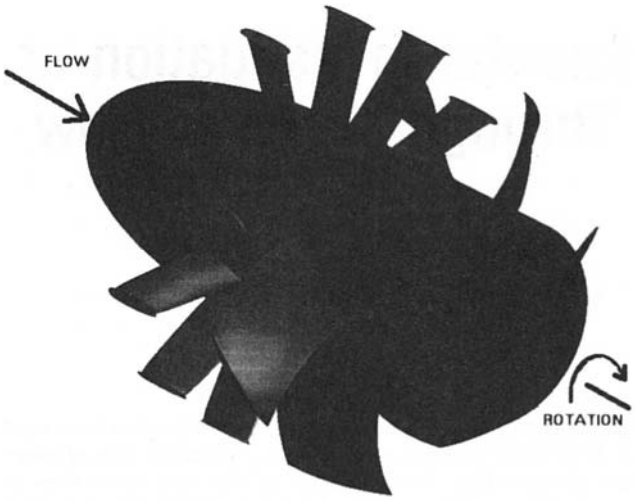

Fig. 1 Computer-generated isometric view of the HIREP blades

hub diameter of 0.53 meters. The two units rotate together on a common shaft in the test section of the water tunnel—such that the main drive impeller of the tunnel overcomes the energy losses within HIREP. The pump includes a row of 13 inlet guide vanes, a row of 7 rotating blades, and three downstream support struts. The turbine includes a row of variable pitch control vanes, a row of rotating blades, and a downstream cruciform support strut.

This HIREP experiment included blade designs as described by Zierke et al. (1993). For the sake of later discussion, some geometric characteristics should be noted here. Each inlet guide vane (IGV) and rotor blade trailing-edge geometry is essentially an asymmetric chisel, with the bevel of the chisel lying on the suction side of the blade and the point of the chisel being somewhat rounded off. All of the inlet guide vanes and rotor blades include fillets where the blades meet the endwalls. The rotor blades are designed with a significant negative blade circumferential lean (such that the suction surface points toward the hub surface), as shown in Fig. 1. Also, a nominal clearance of 3.3 mm exists between the rotor blade tips and the casing. Finally, a ring mechanism allows the inlet guide vanes to be circumferentially indexed in 2 degree increments over 2.5 blade spacings.

At the design point, the rotor blades rotated at 260 rpm which yields a rotor blade tip speed of $U_{tip} = 14.5$ m/s. From similarity considerations, one can derive a volumetric flow coefficient,

$$\phi_{Vol} = \frac{Q}{nD_{tip}^3} \approx \frac{AV_{ref}}{nD_{tip}^3},$$

where Q is the volume flow rate, n is the rotational speed, D_{tip} is the tip diameter, A is the annular area through HIREP, and V_{ref} is the inlet axial velocity. This investigation was completed at the design value of $\phi_{Vol} = 1.36$ with a dimensionless specific speed of $\tilde{n} = 0.89$.

Inlet Conditions

Using a calibrated five-hole pressure probe, we measured the static and stagnation pressures at one circumferential position at the reference plane 37.0 percent IGV chord axially upstream of the inlet guide vanes. Figure 2 shows the location of all pressure probe measurements within HIREP. Both the static and total pressures are provided in the usual coefficient form (C_p). Five-hole probes can also resolve the three components of velocity, as shown for this inlet flow in Fig. 3. The radial and tangential velocities are quite small, as expected, and the measured magnitudes are smaller than the uncertainty of the measurements themselves—except possibly near the tunnel liner. In the past, laser Doppler velocimeter (LDV) measurements have shown that the residual swirl in the bare tunnel is negligible. The axial velocities are nearly uniform—with a slight curvature due to the radial pressure gradient that is visible from streamline curvature calculations. A monitor velocity measurement was acquired with each five-hole probe measurement and Fig. 3 shows these measurements on the tunnel liner which contained the reference static-pressure tap. Using an average static-pressure measurement from this tap of $p_{ref} = 298$ kPa, the monitor velocity gives a nominal reference velocity of $V_{ref} = 10.7$ m/sec. Zierke et al. (1993) performed boundary layer calculations that confirm that a significant turbulent boundary layer exists on the tunnel liner, while a much thinner turbulent boundary layer exists on the hub.

Inlet Guide Vanes

The measured inlet flow establishes a flow through the inlet guide vanes with a chord Reynolds number of 2,300,000. Static-pressure taps allowed us to measure the IGV static-pressure distribution. Zierke et al. (1993) showed that the overall uncertainty in measuring the blade static pressures ranged from 0.4 kPa over regions of minimal streamwise pressure gradients to 0.9 kPa over regions of large streamwise pressure gradients. To be consistent with the analysis further downstream where U_{tip} is the most reliable velocity measurement, we present these data using an alternative definition of the pressure coefficient,

$$K_p = \frac{p - p_{ref}}{\frac{1}{2}\rho U_{tip}^2},$$

using U_{tip} instead of V_{ref}. Figure 4 shows a sample IGV static-pressure distributions at one of the five spanwise measurement locations as well as the design calculations using lifting surface theory.

The spanwise static-pressure distributions show very similar shapes. Boundary layer calculations show that natural transition should begin near 15 percent chord and end near 30 percent chord for both the suction and pressure surfaces. Since no adverse pressure gradient exists in this region, transition simply results from the large Reynolds number. Also, even though the calculations show no separation through the 94.1 percent chord location on the suction surface, calculations in this adverse pressure gradient show signs that separation will occur between 94.1 percent chord and the trailing edge.

We used an oil-paint method to visualize the skin-friction lines in the vicinity of the inlet guide vanes and neighboring endwalls. The skin friction patterns on the hub and casing endwalls show the topology for the formation of a "horseshoe vortex" or "necklace vortex." The pressure side leg of the horseshoe vortex separation line moves downstream into the midpassage region, while the suction side leg of the separation line moves up onto the suction surface. This movement is the result of the flow overturning in the endwall boundary layer region. Near the suction surface trailing edge, this flow overturning causes the skin-friction line patterns near both endwalls to show the presence of three-dimensional corner separation, although the separation region near the hub is larger and more complex than the corresponding region near the casing. Also, a two-dimensional separation occurs over the last 5 percent chord of the suction surface—a separation forced by the chisel trailing edge.

Aside from the small separation regions, the skin-friction line patterns on both the IGV suction and pressure surfaces indicate a rather two-dimensional flow with natural transition ranging from 18 to 40 percent chord on the suction surface and from 15 to 25 percent chord on the pressure surface. However, the oil-paint patterns of transition are difficult to resolve—espe-

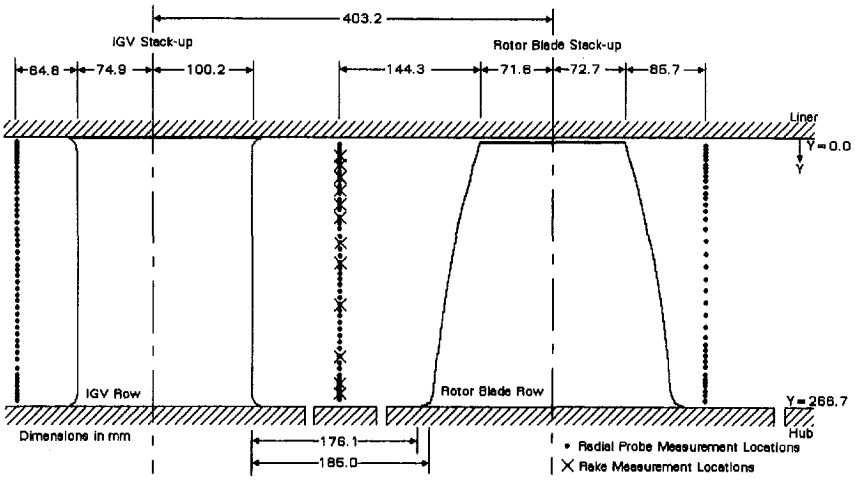

Fig. 2 Pressure probe measurement locations

cially the end of transition. On the pressure surface and near the trailing edge, we found some radial movement of the skin-friction lines away from the design point of maximum lift at 42 percent span. This radial motion of the flow on the pressure surface turns a portion of the spanwise vorticity in the pressure surface boundary layer into the streamwise direction and this streamwise vorticity is shed into the wake as trailing vorticity.

Inlet Guide Vane Exit Flow

At a location 49.7 percent chord downstream of the inlet guide vanes (see Fig. 2), we again used calibrated five-hole pressure probes to measure the flow field. Aside from simple radial surveys, we designed a rake of five-hole probes and installed it into the hub. The five-hole probe rake surveys can measure the total velocity magnitude to within 2.6 percent, while the five-hole probe radial surveys can measure to within 7.7 percent. The rake consisted of a 0.533 m diameter hub that rotated six five-hole probes; each probe attached to a 12.7 mm diameter shaft which fit into a slot in the rake hub. Data from two surveys with the five-hole probe rake were acquired to provide measurements at 11 spanwise locations and at circumferential increments of 0.373 degrees.

Measurements from the five-hole probes show how the axial, radial, and tangential components of velocity vary circumferentially at each spanwise location. Figure 5 shows sample five-hole probe data at 9.5 and 81.0 percent span. The viscous wakes are much deeper near the hub endwall as a result of the small three-dimensional corner separation. Corresponding to the positions of these viscous wakes, the radial velocities vary considerably. Near the hub at the 9.5 percent span location, the radial velocity changes abruptly across the vortex sheet from positive on the suction side to negative on the pressure side. Then, further from the hub (for example, at the 81.0 percent span location), the radial velocity changes abruptly from negative to positive, moving in the same direction. Recall that the location of maximum lift on the inlet guide vanes occurred at 42 percent span and that the streamwise trailing vorticity above and below this location would be of different signs. This is consistent with these radial velocity distributions. Also, the data show excellent agreement with a lifting surface theory calculation. Therefore, the measured variation in radial velocity is an indication of the trailing vortex sheet.

If the trailing vortex sheet was purely radial, only the radial velocities would change across the sheet. However, if the trailing vortex sheet was skewed, the tangential velocity (and to a very small degree, the axial velocity) would also change across the sheet. Since the inlet guide vanes in HIREP turn the flow more near the hub than near the casing, the trailing vortex sheet will become radially skewed as it convects downstream and this skewed sheet leads to a circumferential variation in the tangential velocities. Also, a small portion of the spanwise vorticity in the viscous wakes has been turned into the tangential direction. Away from the endwalls, the data indicate some blade-to-blade differences. For the locations where the data show more overturning than the calculations do, the blade-to-blade differences are probably related to the trailing vortex sheets. In this case, local instabilities of the vortex sheets to small disturbances could deform them and give rise to variations in tangential velocity across the sheets. For the locations where

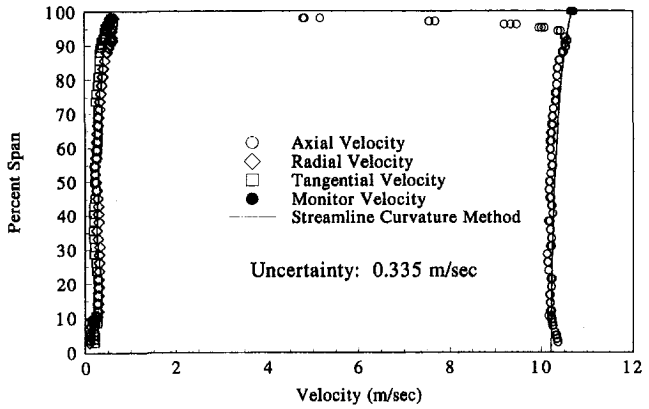

Fig. 3 Inlet velocities from the five-hole probe radial survey 37.0 percent chord upstream of the IGV leading edge

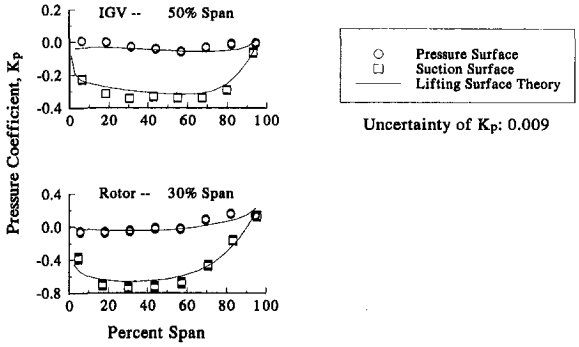

Fig. 4 Sample IGV and rotor blade static-pressure distribution

the data show slightly more underturning than the calculations, the blade-to-blade differences may be related to the separation of the IGV suction surface boundary layers. Local surface irregularities might help explain why the local separation characteristics varied and led to some isolated underturning of the flow. Again, Fig. 5 shows a sample of these tangential velocity variations.

Zierke et al. (1993) also analyzed the five-hole probe data to evaluate harmonic content, average-passage wakes, secondary flow velocity vectors, endwall boundary layers, and circumferentially-averaged velocity components. These local circumferential means involve area averages at each spanwise location over all the IGV passages. The secondary velocity vectors clearly show that the trailing vortex sheet deforms as it convects downstream and rolls-up into two concentrated vortex structures rotating in opposite directions. Passage vortex structures are also evident between vortex sheets from each inlet guide vane. Finally, the five-hole probe data show that the casing endwall boundary layer and the IGV wakes are the primary sources for total-pressure loss.

Moving axially from 49.7 to 88.5 percent chord downstream of the IGV trailing edge, we measured the axial and tangential velocities using a two-component LDV. Figure 6 shows the location of all LDV measurements within HIREP. The precision errors in the mean velocity measurements range from 0.1 to 2.4 percent, with the larger errors corresponding to regions with high turbulence levels. The precision errors in the turbulence intensities range from 6.0 to 8.5 percent. Zierke et al. (1993) discuss possible bias errors. Data were collected using a field point measurement method. In this procedure, the measurement volume remains stationary, and each LDV measurement sample is tagged with the angular position of the rotor—via an optical shaft encoder and a rotating machinery resolver. At this circumferential location, no IGV wakes were present. Upstream of the

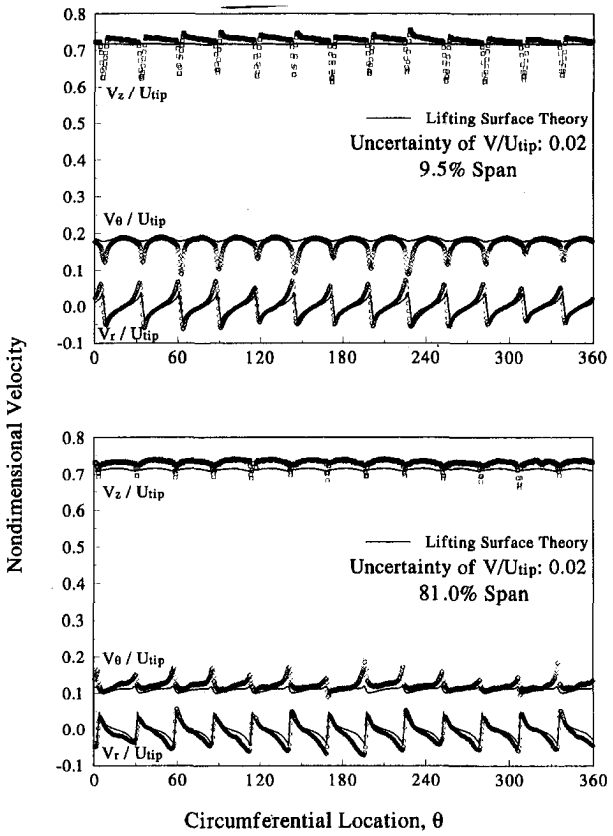

Fig. 5 Circumferential variation of velocity components 49.7 percent chord axially downstream of the IGV trailing edge

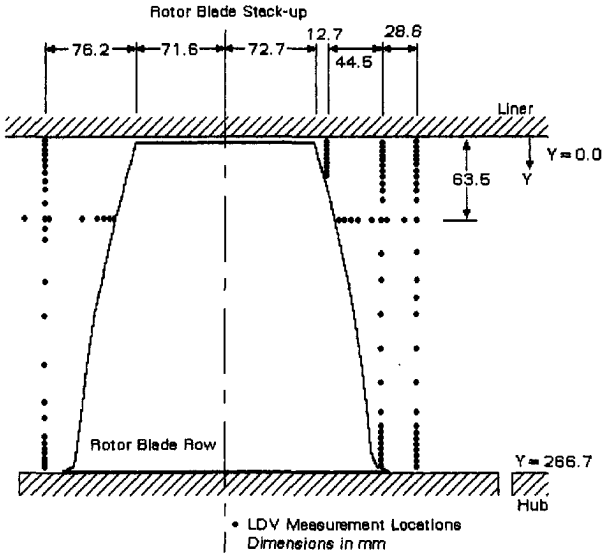

Fig. 6 LDV measurement locations

rotor blades, the LDV data exhibit two interesting phenomena. First, the rotating hub creates a significantly skewed endwall boundary layer; while on the casing endwall, secondary flow leads to a slightly skewed boundary layer. Second, the LDV shows the potential flow effect created by the rotating pressure field from the downstream rotor blades. One axial LDV survey shows how this potential flow effect decays exponentially as one moves upstream from the rotor blade leading edge.

Rotor Blades

The acceleration of the flow through the inlet guide vanes and the larger chord lengths of the rotor blades produce larger chord Reynolds numbers for the rotor blades than for the inlet guide vanes. Using the circumferentially-averaged streamwise (absolute) velocities measured upstream of the rotor blades, we can compute chord Reynolds numbers for the rotor blades ranging from 3,600,000 at 90 percent span up to 3,900,000 at 10 percent span. More appropriately, using relative velocities, the chord Reynolds numbers range from 5,500,000 at 90 percent span down to 4,100,000 at 10 percent span. These chord Reynolds numbers combine with the blade section designs to establish the rotor blade static-pressure distribution shown in Fig. 4 for one of the five spanwise locations of static-pressure taps.

The spanwise static-pressure distributions varied more for the rotor blades than for the inlet guide vanes—especially on the pressure surface. Also, note that integrating the pressure distributions gives values of lift that are about twice as large for the rotor blades than for the inlet guide vanes—with the design value of maximum lift occurring at 22 percent span for the rotor blades. Boundary layer calculations showed that natural transition should take place from 10 percent chord to 20 percent chord on both surfaces. However, the interaction of the rotor blade boundary layers with the periodic passing of the IGV wakes leads to wake-induced transition, which can cause the laminar and transitional boundary layers on the rotor blade to become intermittently turbulent due to the passing of the highly-turbulent IGV wakes.

For time-average measurements of the rotor shaft thrust and torque, we used two pairs of strain gauges. From similarity considerations, one can derive the thrust and torque coefficients,

$$K_T = \frac{F_T}{\rho n^2 D_{\text{tip}}^4} \quad \text{and} \quad K_Q = \frac{M_Q}{\rho n^2 D_{\text{tip}}^5}.$$

Figure 7 shows K_T and K_Q plotted versus ϕ_{Vol}.

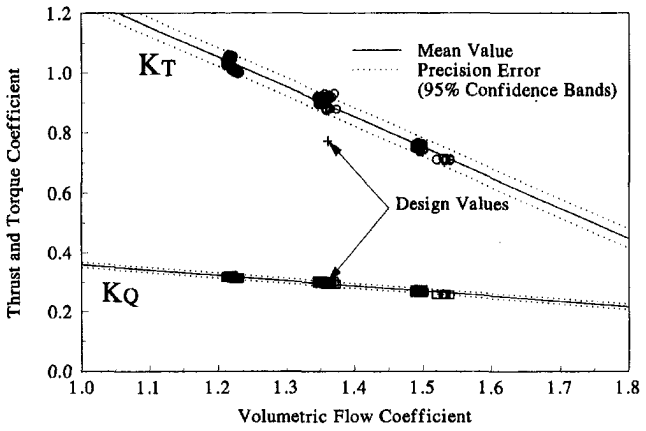

Fig. 7 Variation of rotor shaft thrust and torque with volumetric flow coefficient

The oil-paint surface flow visualization on the rotor blades followed the same procedure as on the inlet guide vanes. Despite the rotation of the blades, the oil-paint patterns are representative of the relative skin-friction lines since the specific gravity of the oil-paint is very close to that of water. As discussed by Zierke et al. (1993), the surface flow visualization shows the topology for the formation of a horseshoe vortex on the rotor hub, a substantial corner separation where the suction surface trailing edge meets the hub, a radial migration of the skin-friction lines along the trailing edge, and a leakage flow across the rotor blade tip. As the leakage flow moves through the clearance—from the pressure surface to the suction surface—it interacts with the throughflow. The interaction of these two flows causes the sheet of vorticity passing through the clearance from the pressure surface boundary layer to roll-up into a tip leakage vortex.

Rotor Blade Exit Flow

Downstream of the rotor blades, we measured the axial and tangential velocities with the LDV in three axial planes as shown in Fig. 6. Before analyzing the LDV data downstream of the rotor blades, we used the upstream five-hole probe data to determine that no IGV wake was present in the vicinity of the LDV measurement volume at any of the three axial measurement planes. With all of the LDV data resolved into one degree storage windows, the axial and tangential velocity measurements clearly show the existence of skewed rotor blade wakes. As an example, Fig. 8 shows a contour plot of the axial velocities at the furthest downstream measurement plane. The rotor blades themselves have 30 degrees of skew and some residual swirl remains in the flow, especially near the hub, creating even more skew within the wakes. Note that the non-uniform nature of the wakes in Fig. 8 arise from computing the contours using data from coarsely-spaced, discrete measurement locations near midspan. An additional LDV survey at 76.2 percent span (see Fig. 6), starting near the rotor blade trailing edge and moving downstream, allowed us to measure the decay of the rotor blade wakes. LDV measurements also show that a flow structure exists near the hub—possibly from the horseshoe vortices. The corner separation has led to much larger wakes in the hub endwall region and, along with the significantly skewed boundary layers and the horseshoe vortices, the hub endwall flow becomes very complex.

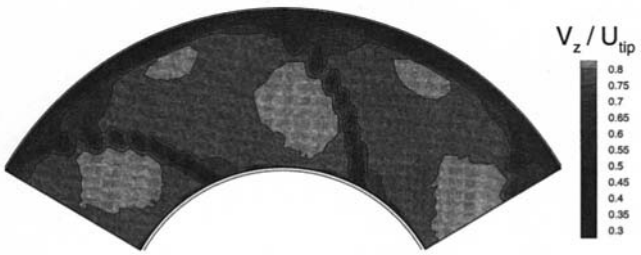

Fig. 8 Axial velocity contours of LDV measurements 32.2 percent chord axially downstream of rotor tip trailing edge

The LDV data also provides details of the dominant flow feature within HIREP: the rotor tip leakage vortex. In order to establish the position of the tip leakage vortex, we used the LDV data along with two types of flow visualization: cavitation visualization and laser light sheet visualization. Aside from giving the location of the tip leakage vortex, both types of flow visualization also showed the unsteadiness of the tip leakage vortex.

The relatively low static pressure within the core of the tip leakage vortex allowed us to visualize cavitation within the core at low tunnel pressures. While some cavitating bubbles originated in the clearance near the rotor blade leading edge, most of the cavitation appears to begin near the suction surface at 15 percent chord—a position very close to the measured minimum pressure point on the suction surface at 90 percent span. At this location, the pressure difference across the clearance reaches a maximum, creating a larger leakage jet. Therefore, the position where the core pressure becomes low enough to establish a cavitating flow marks the origin of the vortex. Downstream of the rotor blades, the LDV data establishes the circumferential position of the tip leakage vortex.

As the tip leakage vortex convects downstream, the position of the vortex core moves radially. Looking through a periscope from a position downstream of the rotor blades, we observed the tip leakage vortex from a video camera during the laser light sheet visualization. Both 10 micron microballoons and cavitation bubbles were illuminated by a laser light sheet in a plane normal to the axial-flow direction. The radial position of the vortex as determined by the laser light sheet visualization and the LDV data compared very well.

The roll-up of the tip leakage vortex produces a swirling flow about the centerline of the vortex. From the LDV data, we determined the tangential or azimuthal velocity about the vortex axis at the three downstream LDV measurement planes. The minimum and maximum values of tangential velocity differ—giving an asymmetric vortex. The presence of the casing endwall seems to interfere with the rolling-up of the tip leakage vortex. Also, a strong coupling exists between the tangential and axial velocities of a vortex. Within HIREP, the LDV measurements showed a wake-like profile in axial velocity for all three axial measurement planes. In the casing endwall region, the axial velocity profiles associated with the tip leakage vortices are much deeper and broader than those associated with the rotor blade wakes. Finally, the presence and proximity of the casing endwall seems to increase the dissipation and unsteadiness of the tip leakage vortex.

Zierke et al. (1993) also analyzed the LDV data to evaluate harmonic content, endwall boundary layers, and circumferentially-averaged velocity components. To complement the circumferentially-averaged velocity profiles at the third LDV measurement plane, we also performed radial surveys with a slow-response Kiel probe, in order to measure the time-average total pressures. Surveys were completed at two different circumferential index positions of the inlet guide vanes. While the laser beams for the LDV measurements entered from the side of the tunnel, the Kiel probe was inserted from the top of the tunnel. Thus, the LDV and Kiel probe measurements were acquired at different circumferential positions and, therefore, at different positions relative to the IGV wakes. Figure 9 shows the results of these total-pressure measurements. For the two circumferential index positions of the inlet guide vanes, the total-pressure

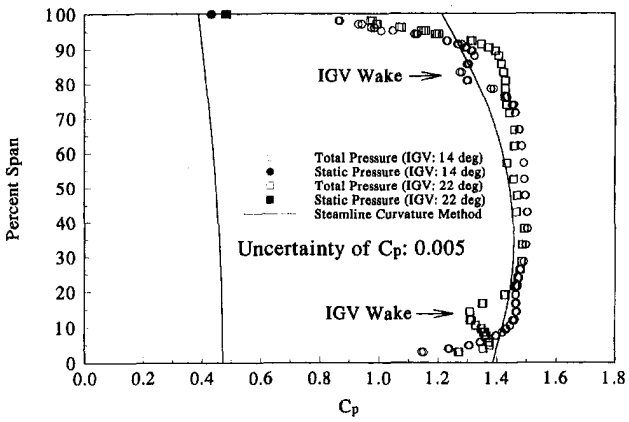

Fig. 9 Spanwise variation of the total pressure coefficient 32.2 percent chord axially downstream of the rotor tip trailing edge for two IGV index locations

deficits shown in Fig. 9 at 11.2 and 83.3 percent span match closely with our analysis of the locations of the IGV wakes.

Again referring to Fig. 9, note that we measured the static pressure on the casing at this axial location. These static-pressure measurements might prove useful in establishing a downstream boundary condition for numerical computations. The static-pressure coefficient did vary slightly with the circumferential position of the inlet guide vanes. The two measured values of $C_p = 0.432$ and $C_p = 0.482$ give an indication of the static-pressure rise through HIREP.

At the same axial measurement plane used to acquire data with the slow-response Kiel probe, we also performed a radial survey using a total-pressure probe with a response time fast enough to resolve the total pressures for instantaneous angular positions of the rotor. In order to achieve this fast response, the probe was equipped with a subminiature piezoelectric pressure transducer, located close to the probe tip. The resulting measurements include the structure of the rotor tip leakage vortices and the skewed rotor blade wakes. The low total pressures in these regions—especially in the tip clearance vortices—indicate that these are regions of large total-pressure losses.

Summary

The high Reynolds number pump (HIREP) facility at ARL Penn State has been used to perform a low-speed, large-scale experiment of the incompressible flow of water through a multiple-blade-row turbomachine. The data shows that three-dimensional effects are significant. Three-dimensional corner separations occur near the blade leading edges and where the suction surfaces meet the endwall in the trailing-edge region. Secondary flows and the relative motion of the stationary and rotating hubs lead to strongly skewed endwall boundary layers, which produce streamwise vorticity. Surface flow visualization shows the topology for the development of horseshoe vortices and vortices emanating from the three-dimensional separation regions on the blades. Flow field measurements show the presence of vortical structures created from the trailing vortex sheet, as well as secondary flows between blade wakes. The dominant secondary flow structure within HIREP is the rotor blade tip leakage vortex. The tip leakage vortex results in large total-pressure losses and vortex cavitation, the limiting form of cavitation within HIREP. A detailed analysis of the tip leakage vortex shows a strong asymmetry. For this small clearance, the presence and proximity of the casing endwall affect the roll-up, shape, dissipation, and unsteadiness of the tip leakage vortex.

In conclusion, the HIREP experimental measurements provide an excellent database for comparisons with three-dimensional, viscous (turbulent) flow computations, as well as other engineering models.

JFE Data Bank Contributions

A number of the results from this axial-flow pump experiment are being added to the *Journal of Fluids Engineering* data bank. The data bank will include the geometry definition, as well as the experimental data summarized in this paper. The data includes time-average static-pressure measurements on both the inlet guide vanes and rotor blades and measurements of rotor shaft thrust and torque. Also, the pressure probe data from the locations in Fig. 2 will be included. The five-hole pressure probe data includes static pressure, total pressure, and all three components of velocity. As located in Fig. 6, the LDV data will include axial and tangential mean velocities, as well as the corresponding variances. All information from flow visualization studies can be obtained from Zierke et al. (1993).

Acknowledgments

This investigation was supported by the Advanced Research Projects Agency.

References

Lauchle, G. C., Billet, M. L., and Deutsch, S., 1989, "High-Reynolds Number Liquid Flow Measurements," *Frontiers in Experimental Fluid Mechanics*, Gad-el-Hak, ed., Springer-Verlag, Berlin, Heidelberg, pp. 95–157.

Zierke, W. C., Straka, W. A., and Taylor, P. D., 1993, "The High Reynolds Number Flow through an Axial-Flow Pump," The Pennsylvania State University, Applied Research Laboratory Technical Report No. TR 93–12.

F. C. Lai
School of Aerospace and Mechanical Engineering, University of Oklahoma, Norman, OK 73019

P. J. McKinney

J. H. Davidson

Particle Technology Laboratory, Department of Mechanical Engineering, University of Minnesota, Minneapolis, MN 55455

Oscillatory Electrohydrodynamic Gas Flows

Prior numerical solutions of electrohydrodynamic flows in a positive-corona, wire-plate electrostatic precipitator are extended to reveal steady-periodic electrohydrodynamic flows. Previously, only steady solutions were reported. The present study includes results for flows with Reynolds numbers from 0 to 4800 and with dimensionless electric number ranging from 0.06 to ∞. Results indicate that two regimes of low frequency oscillatory flow occur. The first regime is characterized by a single recirculating vortex that oscillates in strength between one and five Hertz. The second regime is characterized by two counter-rotating vortices that oscillate in strength at a frequency near one Hertz.

Introduction

It is well known that a corona discharge in air produces a unipolar space charge that, in the presence of a non-uniform electric field, creates a rotational body force acting on the gas. Prior numerical characterizations of the resulting electrohydrodynamic (EHD) flow, known as the ionic or corona wind, have not considered the possibility of electrical generation of an oscillatory flow. Oscillatory flows have been noted in other applications in which the inertial force is the same order of magnitude as, but opposed to or perpendicular to, a buoyancy driven body force (e.g., Nayak and Sandborn, 1977; Lai and Kulacki, 1990a, b).

Most theoretical studies of EHD flows have considered only laminar flow in the wire-plate electrostatic precipitator with a uniform, positive corona discharge along the wire(s). Negative corona is characterized by individual tuft discharges along the wire. Consequently, neither the electrodynamic nor the fluid dynamic process is correctly characterized by a two-dimensional model. All experimental studies have shown negative coronas to create turbulence (e.g., Davidson and Shaughnessy, 1986; Kallio and Stock, 1992). The two-dimensional numerical analysis of positive corona wind by Ramadan and Soo (1969) shows that in the absence of any inlet flow, the electric body force creates a jet originating at the wire and streaming toward the plate. Yabe et al. (1978) predicted similar results. In a more complete study of the interaction of a bulk flow with the corona wind, Yamamoto and Velkoff (1981) solved the two-dimensional, time-dependent, vorticity-stream function form of the Navier-Stokes equations using the finite-difference method. They predicted steady EHD flows in single-wire and double-wire precipitators over a range of inlet velocities and applied voltages. Kallio and Stock (1992) used a finite-difference, κ-ϵ formulation of the steady, incompressible, two-dimensional, time-averaged mass and momentum conservation equations, combined with the turbulence kinetic energy and dissipation transport equations, to predict the turbulent flow field in a wire-plate precipitator with three wires. Their method of solution precludes exposure of an oscillating flow pattern.

In this paper, numerical study of positive corona discharge in a single-wire, wire-plate geometry shows that, in some circumstances, prior predictions of a steady flow are incorrect. The discrepancy in the predictions is attributed to the convergence criteria. Prior solutions (Yamamoto, 1979; Yamamoto and Velkoff, 1981) of the time-dependent equations were assumed to reach steady state when one of the two following criteria was met: (1) the difference in the dimensionless flow variables between two consecutive iterations was less than 2×10^{-4}, or (2) the dimensionless computational time reached 60.0. The second criterion was imposed probably because of a limitation of computational resources. However, it is primarily due to this criterion that the existence of an oscillatory flow was not revealed. In this paper, the work by Yamamoto and Velkoff (1981) is extended by removing the second convergence criterion. Frequencies of the oscillatory flows are presented in terms of the Reynolds number and dimensionless EHD number.

Problem Formulation and Analysis

Assuming a two-dimensional, incompressible, laminar flow in the wire-plate electrostatic precipitator geometry, the governing equations for electric potential (V) and space charge density (ρ_c) are

$$\frac{\partial^2 V}{\partial x^2} + \frac{\partial^2 V}{\partial y^2} = -\frac{\rho_c}{\epsilon_0}, \tag{1}$$

and

$$\rho_c^2 = \epsilon_0 \left(\frac{\partial \rho_c}{\partial x}\frac{\partial V}{\partial x} + \frac{\partial \rho_c}{\partial y}\frac{\partial V}{\partial y} \right), \tag{2}$$

which can be readily derived from the set of reduced Maxwell's equations,

$$\nabla \cdot \mathbf{E} = \frac{\rho_c}{\epsilon_0}, \tag{3}$$

$$\nabla \cdot \mathbf{J} = 0, \tag{4}$$

$$\mathbf{E} = -\nabla V, \tag{5}$$

and the Ohm's law,

$$\mathbf{J} = \rho_c \beta \mathbf{E}. \tag{6}$$

The computational domain, shown in Fig. 1, is one half of the flow channel due to symmetry about the centerline. Boundary conditions on V are:

$$V = V_0, \quad \text{at the wire } (x = 0, y = 0), \tag{7a}$$

$$V = 0, \quad \text{along the plate } (y = d), \tag{7b}$$

$$\frac{\partial V}{\partial x} = 0, \quad \text{along the symmetry line } (x = 0), \tag{7c}$$

Contributed by the Fluids Engineering Division for publication in the JOURNAL OF FLUIDS ENGINEERING. Manuscript received by the Fluids Engineering Division February 5, 1994; revised manuscript received September 7, 1994. Associate Technical Editor: S. P. Vanka.

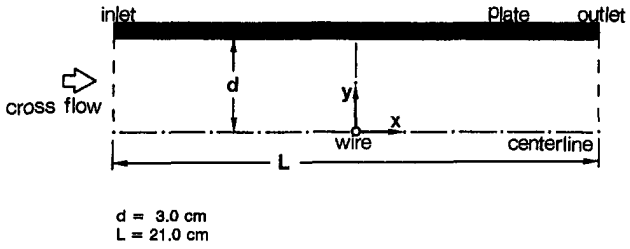

Fig. 1 The two-dimensional computational domain in the wire-plate electrostatic precipitator. The computational domain is one-half of the flow channel.

and

$$\frac{\partial V}{\partial y} = 0, \quad \text{along the centerline } (y = 0). \tag{7d}$$

These simplified forms of the Maxwell's equations and Ohm's law can be solved independently of the flow field equations. This one-way coupling of the electrodynamic and fluid dynamic equations only applies to situations where the ion drift velocity ($\beta \mathbf{E}$) is much greater than the gas velocity.

The numerical scheme employed to solve Eqs. (1) and (2) is identical to the finite difference scheme used by Yamamoto and Velkoff (1981). Electric potential and space charge density are solved for by iterating on Eqs. (1) and (2) with an assumed value of space charge density at the wire (ρ_{c0}). The validity of the solution is checked by comparing total predicted current to measured current at a specific operating voltage. If the currents do not match, a new value of space charge density at the wire is assumed and the calculations are repeated.

The governing equations for the flow field are the two-dimensional, incompressible continuity equation,

$$\frac{\partial u}{\partial x} + \frac{\partial v}{\partial y} = 0, \tag{8}$$

and the momentum equations modified by the addition of a volumetric electric body force, $\rho_c \mathbf{E}$,

$$\frac{\partial u}{\partial t} + u\frac{\partial u}{\partial x} + v\frac{\partial u}{\partial y} = -\frac{1}{\rho}\frac{\partial p}{\partial x} + \nu\left(\frac{\partial^2 u}{\partial x^2} + \frac{\partial^2 u}{\partial y^2}\right) + \frac{\rho_c}{\rho}E_x, \tag{9}$$

and

$$\frac{\partial v}{\partial t} + u\frac{\partial v}{\partial x} + v\frac{\partial v}{\partial y} = -\frac{1}{\rho}\frac{\partial p}{\partial y} + \nu\left(\frac{\partial^2 v}{\partial x^2} + \frac{\partial^2 v}{\partial y^2}\right) + \frac{\rho_c}{\rho}E_y. \tag{10}$$

From the above equations, the vorticity transport equation is expressed as

$$\frac{\partial \omega}{\partial t} = -u\frac{\partial \omega}{\partial x} - v\frac{\partial \omega}{\partial y} + \nu\left(\frac{\partial^2 \omega}{\partial x^2} + \frac{\partial^2 \omega}{\partial y^2}\right) + \frac{1}{\rho}\left[\frac{\partial(\rho_c E_x)}{\partial y} - \frac{\partial(\rho_c E_y)}{\partial x}\right]. \tag{11}$$

In stream function form, the nondimensional vorticity transport equation is

$$\frac{\partial \bar{\omega}}{\partial \tau} = -\frac{\partial \bar{\psi}}{\partial \bar{y}}\frac{\partial \bar{\omega}}{\partial \bar{x}} + \frac{\partial \bar{\psi}}{\partial \bar{x}}\frac{\partial \bar{\omega}}{\partial \bar{y}} + \frac{1}{(\mathrm{Re})_{\mathrm{EHD}}}\left(\frac{\partial^2 \bar{\omega}}{\partial \bar{x}^2} + \frac{\partial^2 \bar{\omega}}{\partial \bar{y}^2}\right) + \left(\frac{\partial \bar{\rho}_c}{\partial \bar{x}}\frac{\partial \bar{V}}{\partial \bar{y}} - \frac{\partial \bar{\rho}_c}{\partial \bar{y}}\frac{\partial \bar{V}}{\partial \bar{x}}\right). \tag{12}$$

Nondimensionalization of this equation is based on scales chosen by Yamamoto and Velkoff (channel half-width d, voltage at the wire V_0, and corona wind velocity u_e). The velocity u_e is defined as

$$u_e = \left(\frac{\rho_{c0} V_0}{\rho}\right)^{1/2}. \tag{13}$$

Note that the electrical vorticity production term in Eq. (12) (the last term on the right-hand side) is determined from the electrodynamic equation alone and thus, is not affected by the

Nomenclature

A = plate area [m^2]
d = distance between wire and plate [m]
$\mathbf{E}$ = electric field [V/m]
E_x = electric field strength in x-direction [V/m]
E_y = electric field strength in y-direction [V/m]
f = flow oscillation frequency [Hz]
$\bar{f}$ = dimensionless flow oscillation frequency, fd/U
I = total electric current [A]
$\mathbf{J}$ = current density [A/m^2]
N_{EHD} = dimensionless electric number, defined in Eq. (12)
p = pressure [Pa]
Re = flow Reynolds number, $u_0(2d)/\nu$
$(\mathrm{Re})_{\mathrm{EHD}}$ = EHD Reynolds number, $u_e d/\nu$
t = time [s]
u = velocity in x-direction [m/s]
$\bar{u}$ = dimensionless velocity in x-direction, u/u_e
u_e = characteristic velocity of ionic wind, defined in Eq. (9) [m/s]
U = uniform gas velocity at the inlet [m/s]
$\bar{U}$ = dimensionless uniform gas velocity at the inlet, U/u_e
v = velocity in y-direction [m/s]
$\bar{v}$ = dimensionless velocity in y-direction, v/u_e
V = electrical potential [V]
$\bar{V}$ = normalized electrical potential V/V_0
V_0 = electrical potential at the wire [V]
x, y = Cartesian coordinates [m]
$\bar{x}, \bar{y}$ = dimensionless Cartesian coordinates, $\bar{x} = x/d$, $\bar{y} = y/d$
β = ion mobility, $\beta = 1.4311 \times 10^{-4}$ $m^2/V \cdot s$ for positive ions in air
ϵ_0 = permittivity of free space, $\epsilon_0 = 8.854 \times 10^{-12}$ F/m
ν = kinematic viscosity of fluid [m^2/s]
ρ = fluid density [kg/m^3]
ρ_c = ionic space charge density [C/m^3]
$\bar{\rho}_c$ = dimensionless space charge density, ρ_c/ρ_{c0}
ρ_{co} = ionic space charge density at the wire [C/m^3]
τ = dimensionless time, $u_e t/d$
ψ = stream function [1/s]
$\bar{\psi}$ = dimensionless stream function, $\psi/u_e d$
ω = vorticity [1/s]
$\bar{\omega}$ = dimensionless vorticity, $\omega d/u_e$

Table 1(*a*) $(Re)_{EHD}$ for all operating conditions

	V_0 (kV)	10.0	12.5	15.0	17.5
	ρ_{c0} (C/m^3)	1.6×10^{-4}	4.4×10^{-4}	8.7×10^{-4}	1.4×10^{-3}
U (m/s)	Re				
0	0	∞	∞	∞	∞
0.02	75	30	57	87	120
0.04	150	15	28	43	60
0.08	300	7	14	22	30
0.15	600	3.7	7.1	11	15
0.23	900	2.5	4.7	7.2	10
0.30	1200	1.9	3.5	5.4	7.5
0.38	1500	1.5	2.8	4.3	6.0
0.46	1800	1.2	2.4	3.6	5.0
0.53	2100	1.1	2.0	3.1	4.3
0.61	2400	0.94	1.8	2.7	3.7
0.91	3600	0.62	1.2	1.8	2.5
1.2	4800	0.47	0.88	1.4	1.9

Table 1(*b*) N_{EHD} for all operating conditions

	V_0 (kV)	10.0	12.5	15.0	17.5
	I (amp)	8.5×10^{-6}	2.2×10^{-5}	4.0×10^{-5}	6.2×10^{-5}
U (m/s)	Re				
0	0	∞	∞	∞	∞
0.02	75	65	169	308	477
0.04	150	16	42	77	119
0.08	300	4.1	11	19	30
0.15	600	1.0	2.6	4.8	7.5
0.23	900	0.45	1.2	2.1	3.3
0.30	1200	0.25	0.66	1.2	1.9
0.38	1500	0.16	0.42	0.77	1.2
0.46	1800	0.11	0.29	0.53	0.83
0.53	2100	0.08	0.22	0.39	0.61
0.61	2400	0.06	0.16	0.30	0.47
0.91	3600	0.03	0.07	0.13	0.21
1.2	4800	0.02	0.04	0.08	0.12

flow field. The EHD Reynolds number, $(Re)_{EHD}$, is equal to $u_e d/\nu$.

Appropriate boundary conditions for the flow field are

$$\frac{\partial \bar{\psi}}{\partial \bar{y}} = \bar{U}, \quad \bar{\omega} = \frac{\partial \bar{u}}{\partial \bar{y}} = \frac{\partial^2 \bar{\psi}}{\partial \bar{y}^2} = 0, \quad \text{at the inlet,} \quad (14a)$$

and

$$\frac{\partial \bar{\psi}}{\partial \bar{x}} = 0, \quad \frac{\partial \bar{\omega}}{\partial \bar{x}} = 0, \quad \text{at the outlet.} \quad (14b)$$

The inlet flow is assumed to be uniform and parallel.

The finite difference scheme employed to solve Eq. (12) is the same as that used by Yamamoto and Velkoff (1981), but with no restriction in computational time. The only other modification is use of a fixed, rather than variable, time-step so that transient and oscillatory flows may be closely monitored. Time is nondimensionalized by the characteristic electric velocity ($\tau = tu_e/d$). The calculation starts with an appropriate initial condition and is advanced in time until a steady state is reached or at least three complete cycles of oscillatory flow patterns are identified. The dimensionless time step is chosen ($\Delta\tau = 5 \times 10^{-4}$) to guarantee numerical stability and accuracy. The stability criterion for the numerical scheme used is given by (Jaluria and Torrance, 1986)

$$\Delta t \leq \frac{1}{2\nu\left[\frac{1}{(\Delta x)^2} + \frac{1}{(\Delta y)^2}\right] + \frac{|u|}{(\Delta x)} + \frac{|v|}{(\Delta y)}}. \quad (15)$$

The test of grid dependence has been performed by the previous authors (Yamamoto and Velkoff, 1981). Therefore, it is not repeated here and the same uniform grids (225×33) are used in the present study for consistency. To verify that flow oscillations are not due to numerical instability, the computations are repeated with reduced time steps ($\Delta\tau = 1 \times 10^{-5}$ and 5×10^{-5}). Identical results are obtained. In some cases, more than 100 hours of CPU time on a HP Apollo 9000/730 workstation are required.

The choice of dimensionless parameters describing the flow phenomenon are flow Reynolds number and an EHD parameter equal to the ratio of electrical body force to fluid inertial force. Yamamoto and Velkoff (1981) chose a dimensionless parameter equal to $(Re)_{EHD}/Re$ or $u_e/2U$. Except in numerical studies, this parameter is very difficult to evaluate since the space charge density ρ_{c0}, needed to define u_e, is not easily measured. An alternate parameter suggested by Davidson and Shaughnessy (1986),

$$N_{EHD} = \frac{Id}{\rho U^2 \beta A}, \quad (16)$$

uses total current rather than space charge density and is based on easily measured quantities.

Table 1(*c*) N_{EHD} for operating conditions of Kallio and Stock (1992)

	V_0 (kV)	32	42
	J (A/m^2)	0.98	2.5
U (m/s)	Re		
0.02	134	11646	29115
0.04	1339	116	291
0.08	2677	29	73
0.15	6693	4.7	11.6
0.23	9370	2.4	5.9
0.30	13386	1.2	2.9
0.38	26227	0.29	0.73

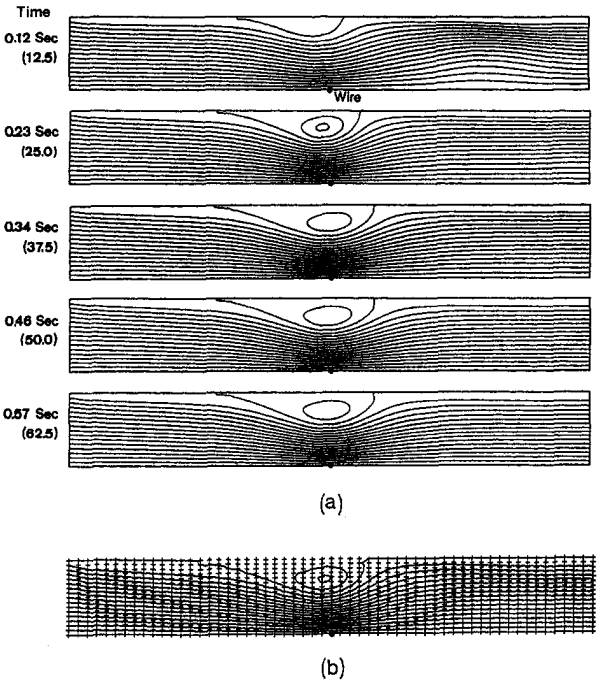

Fig. 2 Variation of flow streamlines with time for V_0 = 15 kV and U = 0.6 m/s (Re = 2400 and N_{EHD} = 0.3), (*a*) present results, (*b*) result of Yamamoto and Velkoff (1981). Dimensionless time is in parenthesis.

In this paper, computations are carried out at applied electric potentials of V_0 = 10, 12.5, 15, and 17.5 kV (the same values used by Yamamoto and Velkoff). For each case, speed of the inlet flow (U) is varied from 0 to 1.22 m/s. Table 1(a) lists electrical and flow conditions and corresponding dimensionless parameters as initially presented by Yamamoto and Velkoff (1981). For the same operating conditions, values of N_{EHD} are listed in Table 1(b). For reference, Table 1(c) contains values of N_{EHD} for the experimental conditions of Kallio and Stock (1992). An infinite value of N_{EHD} occurs when there is no inlet flow.

Results and Discussion

Two possible flow phenomena occur for flows with finite, nonzero N_{EHD} numbers. The solution is initially transient in both cases, and then either reaches steady-state or becomes steady-periodic. As an example of a steady solution, streamlines are plotted at five time steps in Fig. 2(a) for V_0 = 15 kV and U = 0.61 m/s (corresponding to Re = 2400 and N_{EHD} = 0.30). The most prominent feature of the flow is a single counter-clockwise recirculating eddy, or cell, near the wall opposite the wire. A mirror image of the flow field with a second rotating cell would exist in the half of the channel not pictured. For simplicity, the remainder of the discussion considers only the computational domain (shown in Fig. 1) and not the entire flow channel. Streamlines reported by Yamamoto and Velkoff (1981) are included for comparison in Fig. 2(b). Although their solution is successfully reproduced at t = 0.23 seconds (τ = 25.0), the steady-state solution is not actually achieved until t = 0.34 seconds (τ = 37.5).

Streamlines for a steady-periodic solution are shown in Fig. 3 for V_0 = 15 kV and U = 0.15 m/s (Re = 600 and N_{EHD} = 4.8). For this case, N_{EHD} is an order of magnitude greater than in the previous case. Figure 3(a) shows a full period of the established flow pattern, for 4.20 seconds $\leq t \leq$ 4.54 seconds ($460.0 \leq \tau \leq 497.5$). A strong circulatory cell with counter-clockwise rotation is adjacent to the wall and spans almost the entire half-channel. A second, weaker cell with clockwise rotation is downstream of the primary cell, adjacent to the centerline of the channel. At the beginning of the pictured oscillation, t = 4.20 seconds (τ = 460.0) and the dominant cell is fairly symmetric. At t = 4.29 seconds (τ = 470.0), this cell has weakened and is elongated. The primary cell then grows stronger and reaches maximum strength at t = 4.47 seconds (τ = 470.0). From this point until the end of the period at t = 4.54 seconds (τ = 497.5), the cell weakens until it is identical to the condition at the beginning of the period. During the same period, the weaker secondary cell has moved downstream and out of the computational domain and has been replaced by another small cell. Figure 3(b) is a plot of streamlines at t = 0.39 seconds (τ = 42.5), before the steady-periodic solution is revealed. Figure 3(c) is the "steady-state" solution reported by Yamamoto and Velkoff (1981). Comparison of Figs. 3(b) and 3(c) reveals that the prior solution was apparently terminated in the transient phase of the flow and did not capture the true periodic behavior.

An example of a periodic flow in which two nearly equal strength counter-rotating cells coexist is shown in Fig. 4 for V_0 = 15 kV and U = 0.08 m/s (Re = 300 and N_{EHD} = 19.3). The figure shows one complete period of the flow, from t = 3.65 seconds (τ = 400.0) to t = 4.45 seconds (τ = 487.5). Both cells span nearly the channel half-width. The counterclockwise cell is upstream of the wire and the clockwise cell is centered at a point just downstream of the wire. During the period, the clockwise (upstream) cell starts out relatively weak, grows in strength until t = 4.10 (τ = 450.0) and then recedes to its original strength at t = 4.45 (τ = 487.5). The clockwise cell follows exactly the opposite pattern and is strongest at the beginning and end of the period.

To further illustrate the oscillatory nature of the flow, variations in the maximum and minimum values of the stream function are plotted as a function of time in Fig. 5. These solutions

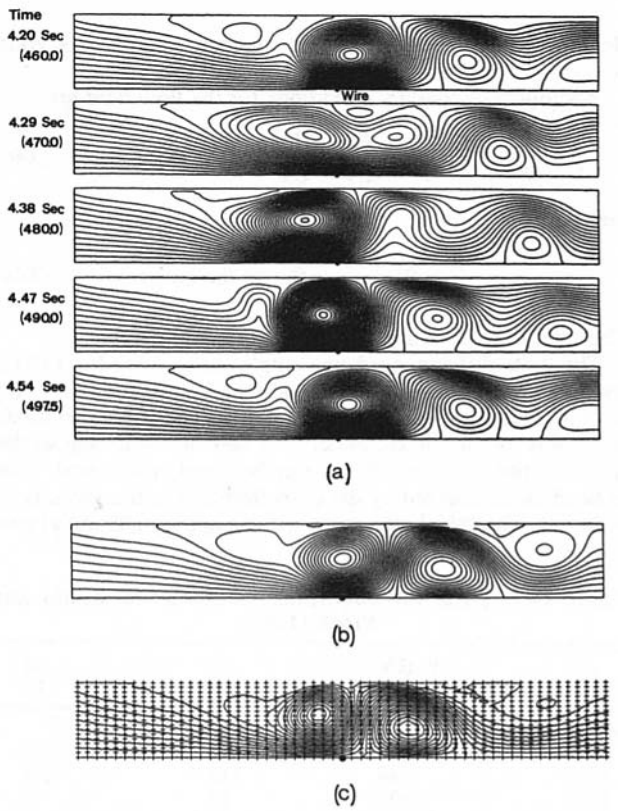

Fig. 3 Variation of flow streamlines with time for V_0 = 15 kV and U = 0.15 m/s (Re = 600 and N_{EHD} = 4.8), (*a*) present results after becoming steady-periodic, (*b*) present results during transient phase, (*c*) result of Yamamoto and Velkoff (1981). Dimensionless time is in parenthesis.

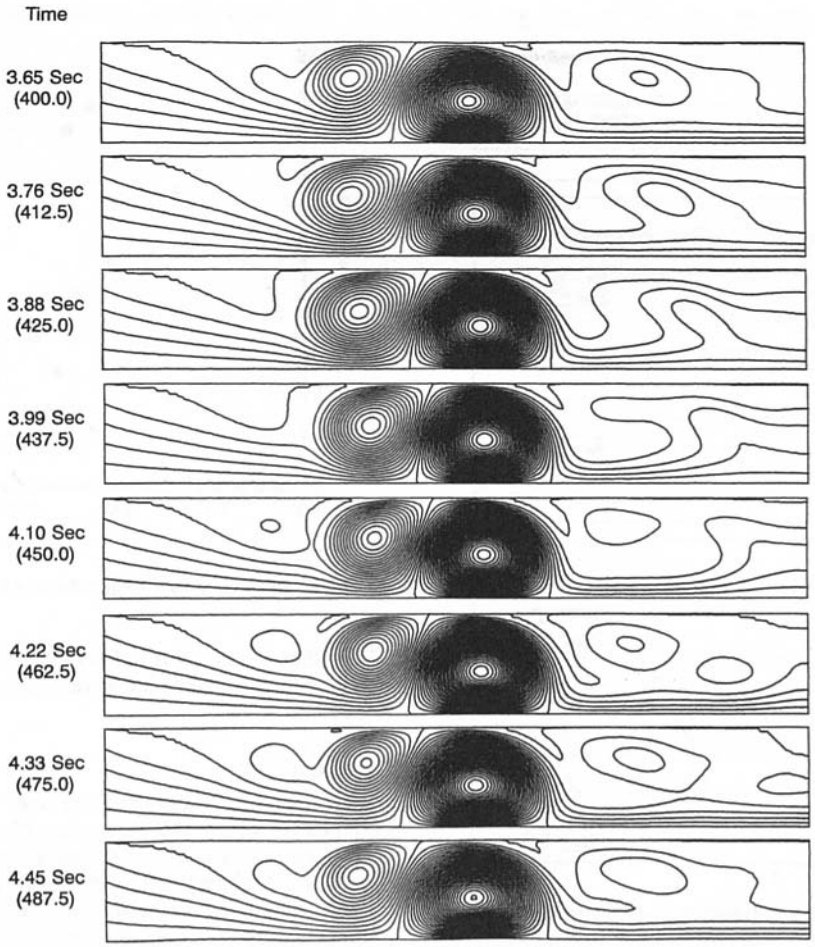

Fig. 4 Variation of flow streamlines with time for V_0 = 15 kV and U = 0.08 m/s (Re = 300 and N_{EHD} = 19.2). Dimensionless time is in parenthesis.

are for V_0 = 15 kV and $0 \leq \text{Re} \leq 2400$ ($\infty \geq N_{EHD} \geq 0.77$). Note that in these plots, changes in flow are due only to changes in inlet flow speed and not electrical conditions. Thus, changes in N_{EHD} are due to changes in U. The maximum value of the stream function represents the strength of the counterclockwise recirculating cell. The minimum stream function corresponds to the clockwise cell. In the absence of a forced flow, a steady-state solution, as shown in Fig. 5(a), is always found. The EHD flow in this case is a pair of symmetrical, counter-rotating vortices, one upstream of the wire and one downstream of the wire. As soon as an inlet flow is introduced, the EHD flow may oscillate. Examples of oscillatory flow are shown in Figs. 5(b) through 5(g). In Figs. 5(b) through 5(d), where $\text{Re} \leq 300$ and the $N_{EHD} \geq 19$, the flow is characterized by two cells oscillating at $f \approx 1$ Hz. At higher Reynolds numbers (and lower values of N_{EHD}), the flow field is characterized by a single counter-clockwise vortex with f = 1.2 to 4.3 Hz, as shown in Figs. 5(e) through 5(g). The absence of the second vortex causes the minimum value of the streamfunction to remain at a steady value in Figs. 5(f) and 5(g). At $\text{Re} \geq 1500$ (Figs. 5(h) and 5(i)), the flow is steady with a single small circulation cell. The flow field at Re = 2400 is also shown in Fig. 2.

Figure 6 shows the oscillatory flow frequency as a function of N_{EHD} for all computed conditions. In this plot, changes in N_{EHD} are due to changes in both inlet gas speed and applied voltage. All EHD flows are steady (f = 0) for $N_{EHD} < 0.8$. At N_{EHD} = 0.8, the inertial and electrical forces are nearly balanced and oscillatory behavior begins with a single circulating cell at f = 4.3 Hz. As N_{EHD} is increased further, the oscillations decrease in frequency. At $N_{EHD} \approx 7.5$, oscillatory flow changes from a single cell to a double cell pattern. Unfortunately, flow oscillations are not completely characterized by N_{EHD}. Four conditions at V = 10 kV and V = 12.5 kV show no oscillatory behavior between N_{EHD} = 5 and N_{EHD} = 90. All four of these flows are characterized by two strong circulatory cells. The double cell structure of the flows is consistent with the oscillatory flows in the same range of N_{EHD}.

The distinction between the one and two cell oscillatory flows is made clear in the plot of dimensionless frequency as a function of N_{EHD} shown in Fig. 7. Dimensionless frequency ($\bar{f}$) equals fd/U. In the single cell oscillatory flows, $\bar{f}$ can be expressed as

$$\bar{f} = 0.60 + 0.70[\log (N_{EHD})], \tag{17}$$

with correlation coefficient 0.933. The two cell flows occur from $N_{EHD} \approx 4$ to $N_{EHD} \approx 300$. In this case, oscillating frequency is given by

$$\bar{f} = -0.49 + 1.15[\log (N_{EHD})], \tag{18}$$

with correlation coefficient 0.991. Obviously, the four steady flows in this regime are not characterized by this expression.

Figure 8 shows the regimes of oscillatory behavior as a function of Re and N_{EHD}. The open symbols denote steady flows. Solid symbols indicate oscillatory flows with two cells. Solid symbols with a center cross represent single cell oscillations. It is evident that the oscillatory behavior is not a simple function of either Re or N_{EHD}. The four cases for which there are steady conditions at relatively high N_{EHD} have the lowest applied voltages. It is not clear why at $N_{EHD} > 1$, some flows oscillate

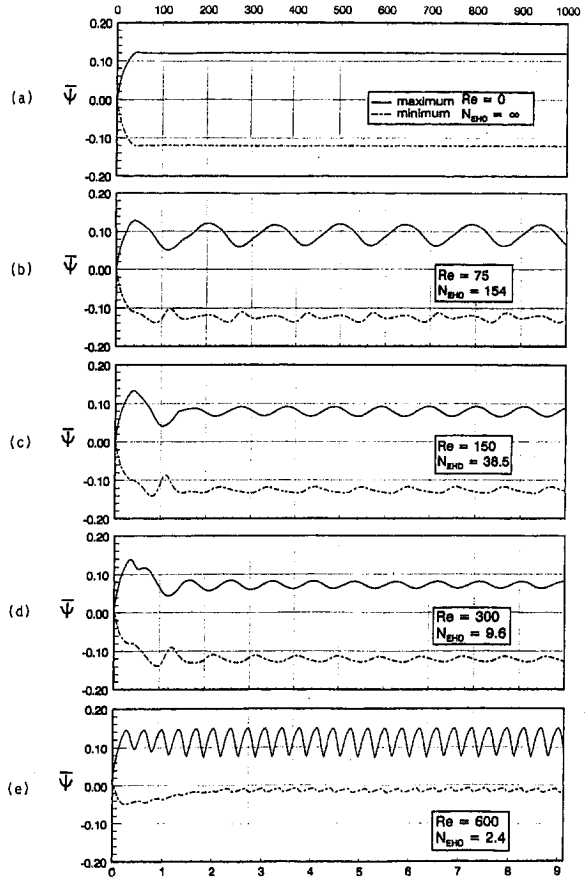

Fig. 5 Variation of minimum and maximum dimensionless stream function values with time for V_0 = 15 kV, (*a*) U = 0 m/s, (*b*) U = 0.02 m/s, (*c*) U = 0.04 m/s, (*d*) U = 0.08 m/s, (*e*) U = 0.15 m/s, (*f*) U = 0.23 m/s, (*g*) U = 0.30 m/s, (*h*) U = 0.38 m/s, (*i*) U = 0.61 m/s

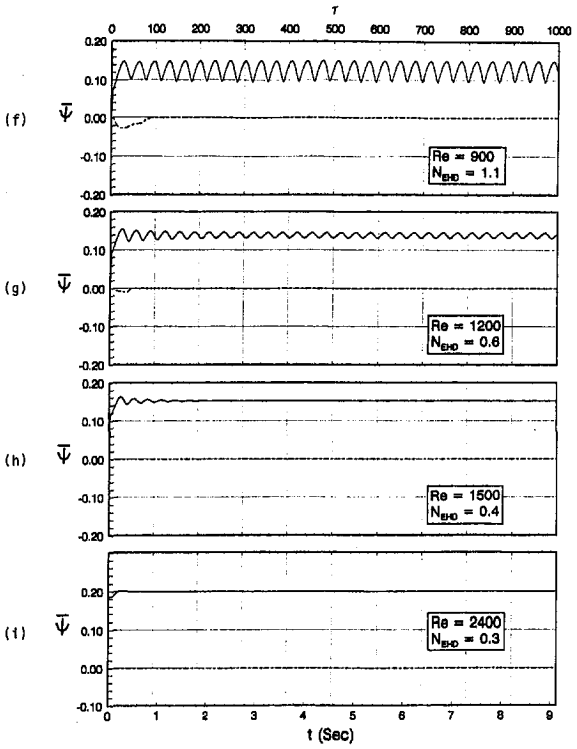

Fig. 5 (cont.)

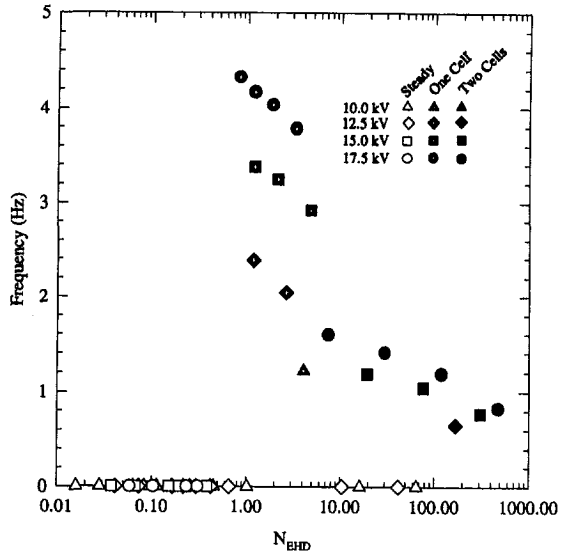

Fig. 6 Oscillatory flow frequency as a function of N_{EHD} number

while others do not. It is unlikely that viscous forces have much effect on the flow since the lowest Reynolds number considered is 75.

Conclusions

Extension of earlier numerical work by Yamamoto and Velkoff (1981) shows that secondary flows in a positive corona, wire-plate precipitator are frequently steady-periodic. Oscillations of 4.3 Hz or less can occur for Reynolds numbers between 75 and 1800 and for electric numbers (N_{EHD}) between 0.8 and 480. Two regimes of oscillation are observed. For $0.8 \leq N_{EHD} < 7.5$, oscillatory flows are characterized by a single eddy that appears opposite the wire and oscillates from 1.2 to 4.3 Hz. The second regime, $7.5 \leq N_{EHD} \leq 480$, is characterized by counter rotating eddies that oscillate at 0.6 to 1.6 Hz. Steady flows also occur in this N_{EHD} range. Steady flows consistently occur for $N_{EHD} < 0.8$ and $N_{EHD} = \infty$ (Re = 0). Work is in progress to extend the range of flow and electrical parameters considered.

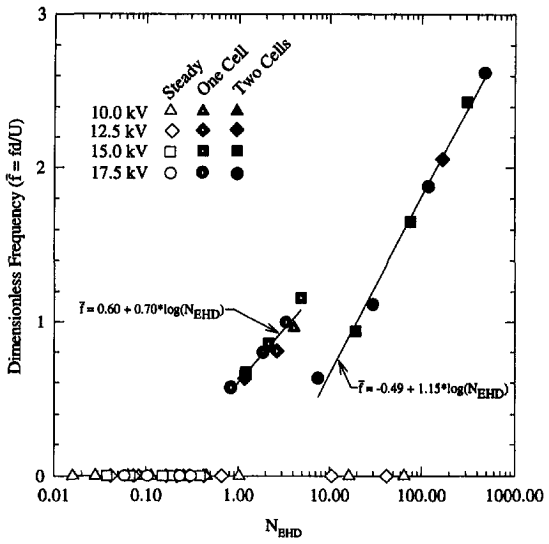

Fig. 7 Dimensionless oscillatory flow frequency as a function of N_{EHD} number

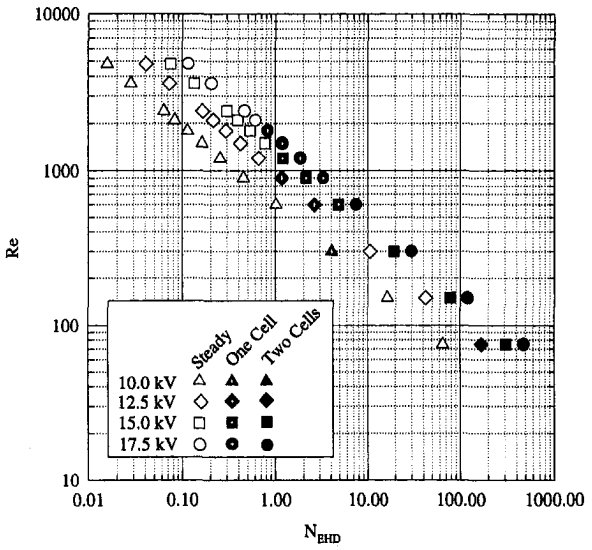

Fig. 8 Regimes of oscillatory flow as a function of N_{EHD} and Reynolds number

References

Davidson, J. H., and Shaughnessy, E. J., 1986, "Turbulence Generation by Electric Body Forces," *Experiments in Fluids,* Vol. 4, pp. 17–26.

Jaluria, Y., and Torrance, K. E., 1986, *Computational Heat Transfer,* Hemisphere, New York.

Kallio, G. A., and Stock, D. E., 1992, "Interaction of Electrostatic and Fluid Dynamic Fields in Wire-Plate Electrostatic Precipitators," *Journal of Fluid Mechanics,* Vol. 240, pp. 133–166.

Lai, F. C., and Kulacki, F. A., 1991a, "Experimental Study of Free and Mixed Convection in Horizontal Porous Layers Locally Heated from Below," *International Journal of Heat and Mass Transfer,* Vol. 34, pp. 525–541.

Lai, F. C., and Kulacki, F. A., 1991b, "Oscillatory Mixed Convection in Horizontal Porous Layers Heated from Below," *International Journal of Heat and Mass Transfer,* Vol. 34, pp. 887–890.

McDonald, J. R., Smith, W. B., Spencer, H. W., and Sparks, L. E., 1977, "A Mathematical Model for Calculating Electrical Conditions in Wire-Duct Electrostatic Precipitation Devices," *Journal of Applied Physics,* Vol. 48, pp. 2231–2243.

Nayak, S. K., and Sandborn, V. A., 1977, "Periodic Heat Transfer in Directly Opposed Free and Forced Convection Flow," *International Journal of Heat and Mass Transfer,* Vol. 20, pp. 189–194.

Ramadan, O. E., and Soo, S. L., 1969, "Electrohydrodynamic Secondary Flow," *Physics of Fluids,* Vol. 12, pp. 1943–1945.

Yabe, A., Mori, Y., and Nijikate, K., 1978, "EHD Study of the Corona Wind Between Wire and Plate Electrodes," *AIAA Journal,* Vol. 16, pp. 340–345.

Yamamoto, T., 1979, "Electrohydrodynamic Secondary Flow Interaction in an Electrostatic Precipitator," Ph.D. dissertation, Ohio State University.

Yamamoto, T., and Velkoff, H. R., 1981, "Electrohydrodynamics in an Electrostatic Precipitator," *Journal of Fluid Mechanics,* Vol. 108, pp. 1–8.

Preliminary Investigation of the Use of Air Injection to Mitigate Cavitation Erosion

R. E. A. Arndt

C. R. Ellis

S. Paul

St. Anthony Falls Hydraulic Laboratory,
University of Minnesota,
Minneapolis, MN 55414-2196

This project was initiated as part of a new research and development focus to improve hydropower generation. One aspect of the problem is severe cavitation erosion which is experienced when hydroturbines are operated at best power or in spinning reserve. Air injection has been used successfully to minimize or eliminate cavitation erosion in other applications. Thus, an investigation was initiated to determine whether or not air injection would be an effective solution for turbine erosion problems. A specially instrumented hydrofoil of elliptic planform and a NACA 0015 cross section was tested at flow velocities up to 20 m s^{-1}, at various values of cavitation index. Although pit sizes were measured on a soft aluminum insert, pitting rate was not measured directly but was inferred from direct measurement of impulsive pressures on the surface of the hydrofoil and by monitoring accelerometers mounted at the base of the hydrofoil. Cavitation noise was also measured by a hydrophone positioned in the water tunnel test section. Air was injected through small holes in the leading edge of the foil. Air injection was found to be very effective in minimizing erosion as inferred from all three cavitation erosion detection techniques.

Introduction

This study is the first phase of a research and development effort to improve hydropower generation within the Pacific Gas and Electric System. Severe erosion has been experienced in the turbine in the Kerckhoff 2 powerhouse. This unit is operated for a considerable amount of time in spinning reserve as well as being operated at power settings above the best efficiency point. Leading edge erosion on the runner as well as erosion at the discharge end of the runner has been experienced. This erosion occurs in spite of the fact that the plant setting is adequate according to US Bureau of Reclamation field experience (c.f. Arndt, 1990). However, this is not unusual for a turbine in this specific speed range. In addition, Arndt et al. (1989) have already found that operating a turbine off peak significantly aggravates the erosion problem.

Two techniques for minimizing cavitation erosion are being studied. Since the unit is operating in spinning reserve as well as best power, a cavitation monitoring system was considered. By using a cavitation monitoring system, operational data necessary for achieving a trade-off between the extra revenue from operation at power settings above the best efficiency point and the extra costs associated with excessive erosion can be obtained.

A cavitation acoustic emission test was performed prior to this study by Shanahan and Abbot (1993) using a cavitation monitoring system developed by Abbot (1989) and Abbot et al. (1991). The results show that operation at maximum power, rather than the best efficiency point, increases erosion rate by a factor of 20 as inferred by acoustic emissions. Severe cavitation is also encountered when operating in spinning reserve. As part of the water tunnel studies reported herein, this system was evaluated under laboratory conditions. Details are presented in Abbot et al. (1993).

In addition to cavitation monitoring, air injection is being considered as a solution to the erosion problem. The efficacy of artificially protecting hydraulic machinery against cavitation damage by injecting small amounts of air into the cavitating region has long been recognized and demonstrated (Huse, 1976). The origin of using this technique for mitigation of cavitation damage in hydrodynamic applications is not known. However, it is not unlikely that the idea followed from observations of reduced cavitation damage in large turbines during seasons when the air content of the reservoir water was high.

The success of this technique in full scale installations is evident from the studies of Okamoto et al. (1975) and Narita et al. (1977). This method of mitigating cavitation erosion has been subsequently applied to conventional (nonducted) propellers. Air injection at high head spillways has become common practice and many older spillways are presently being retrofitted with air injection systems. The exact mechanism for attenuation is not understood. Thus, the efficacy of air injection for eliminating leading edge cavitation erosion in hydraulic turbines is unknown. The present research is directed towards determining whether or not air injection is an appropriate solution for the problem at hand.

Previous Studies

Bubble Dynamics. Arndt (1981a) provides a summary of noise and erosion studies. At the heart of the problem is the impulsive pressures created by collapsing bubbles (Rayleigh, 1917). Recent numerical techniques permit detailed examination of the collapse of individual bubbles (Blake and Gibson, 1987; Zhang et al., 1992). This work is complemented by experimental studies (Tomita and Shima, 1986; Vogel et al., 1989; van der Meulen and van Renesse, 1993). All of these studies indicate that the final stages of collapse of an individual bubble results in the formation of a microjet which can be highly erosive. Estimates of collapse pressures using the water hammer model,

$$p_c = \rho c_o U_j \tag{1}$$

indicate that pressures in excess of 1500 atmospheres are possible. However, Tomita and Shima (1986) suggest that several related mechanisms may be involved. The modes of bubble collapse are dependent on the proximity to a boundary. At the first collapse of a bubble positioned very close to or attached

Contributed by the Fluids Engineering Division for publication in the JOURNAL OF FLUIDS ENGINEERING. Manuscript received by the Fluids Engineering Division April 11, 1994; revised manuscript received April 17, 1995. Associate Technical Editor: O. C. Jones.

to a boundary the following occur: 1) a pressure pulse due to bubble collapse, 2) the impact pressure from a liquid jet formed within the original bubble, 3) impulsive pressures caused by the collapse of many tiny bubbles resulting from the interaction of the outward radial flow following liquid jet impact and the contracting bubble surface and, 4) the impact pressure from a shock wave radiated from the torus like original bubble at its rebound. Very high local pressures may result from the interaction of the micro bubbles in (3) and the shock wave in (4). Vogel et al. (1989) found that the resulting pressure pulses can be of very short duration ranging between 10 and 40 ns. Since these pulse durations are much smaller than the rise time of typical pressure sensing devices, significant measurement errors can occur. They suggest that the peak amplitude of an exponential pulse is too low by a factor of

$$m = \frac{\tau}{\tau_a \ln 2} \tag{2}$$

where τ is the pulse time which is much shorter than the rise time τ_a of the pressure transducer. For typical transducer rise times, this factor can be of the order of 0.01 to 0.05 which explains the unreasonably low values of collapse pressure measured in most experiments. Vogel et al. (1989) measured collapse pressure by measuring the change in refractive index of the liquid using a laser. Their measurements indicate that pressures as high as 60 Kbar can result from spherical collapse of bubbles.

In practical problems, the collective collapse of a cloud of bubbles is an important mechanism. Hansson and Mørch (1980) suggested an energy-transfer model of concerted collapse of clusters of cavities. Because of mathematical difficulties this problem has not been studied in detail until recently (Chahine et al., 1992). Earlier work (van Wijngaarden, 1964) had already indicated the damage potential of a collapsing cloud of bubbles. Recent work supports this contention. Another important feature of cloud physics is that the characteristic oscillation frequencies are in the *tens* of Hertz range. This has important implications for the acoustic monitoring technique used in this study.

This earlier research also provides a clue for understanding the effects of air injection. Presumably additional air bubbles tend to cushion the collapse of vapor filled bubbles. The work of Morch and his co-workers (Morch, 1980 and 1982; Hansson and Morch, 1980; Hansson et al., 1982) suggests that the collapse of a cavitation cloud involves the inward propagation of a shock wave. The geometric focusing of this shock in the center of the cloud enhances the damage potential. This idea has been recently confirmed by Wang and Brennen (1994). The presence of air bubbles will act to significantly reduce the wave propagation speed (van Wijngaarden, 1972) and attenuate this focusing effect.

Cavitation Erosion. Most of the previous research has been directed toward the mechanics of bubble collapse and the associated impulsive pressures as well as a quantification of those material properties that are of importance in resistance to cavitation. Little has been done to correlate cavitation erosion with the properties of a given flow field. However, it is important to have in mind that cavitation erosion will scale with a high power of velocity at a given cavitation number and that cavitation erosion does not necessarily increase with a decrease in the cavitation index. Stinebring et al. (1977) observed that the cavitation pitting rate at constant σ scales with the sixth power of velocity and is measurably reduced with an increased concentration of dissolved gas in the liquid. It is important to note that the pitting rate is not equivalent to the measured weight loss observed in a specially designed erosion test apparatus. In fact, Stinebring et al. have shown that the rate of energy absorbed per unit area is proportional to the *eleventh* power of velocity in the initial stages of pitting. This result has implications for the results in the present study. Since the velocity in a turbine passage is proportional to the square root of head, the magnitude of the erosion problem is expected to be more severe in high-head installations.

In many cases cavitation erosion can be traced to the region at the trailing edge of an attached cavity. The number of bubbles that collapse in this region in a given period of time will be a function of the cavity geometry, which in turn is a function of the cavitation index.

Advanced stages of cavitation erosion can be simulated in the laboratory by a variety of different devices. The most common is the ASTM vibratory apparatus. In order to relate accelerated erosion tests to field applications, Thiruvengadam (1971) suggested that the erosive intensity of a given flow field can be quantified in terms of the product of the depth of penetration per unit time and the strength of the material being eroded. The intensity is a function of a given flow field. The rate of penetration can be calculated from the weight loss per unit time and the surface area of the eroded material. Many different definitions of material strength have been tried. The most used value appears to be ultimate strength, which is basically a weighted value of the area under a stress-strain curve (Arndt, 1990). Thiruvengadam was also able to show that although various materials have different rates of weight loss when subjected to the same cavitating flow and that the rate of weight loss varies with time, a normalized erosion rate versus time characteristic is similar for a wide range of materials. Thus, Thiruvengadam's simplified theory allows for rapid determination of intensity for a given flow by measuring the depth of penetration per unit time for a soft material. The service life for a harder material can then be predicted from the ratio of the strengths of the hard and soft material. A long term objective of the work in progress is to relate pitting rate observed in hydrofoil experiments to pitting rate and subsequent weight loss observed in the ASTM vibratory apparatus.

Water Tunnel Simulations. Recently many researchers have recognized that the basic physics of erosion in a turbine can be simulated by experiments with partially cavitating hydrofoils in a water tunnel (Avellan et al., 1991; Abbot et al., 1993; Le et al., 1993a, 1993b). These studies indicate that maximum erosion occurs in a region of cloud cavitation at the trailing edge of a cavity. The cavitation cloud contains complex vortical

Nomenclature

a = acceleration
c = chord length
c_0 = speed of sound
d_p = pit diameter
f = frequency, Hz
F = force, N
F_0 = impulsive force amplitude, N
L_c = cavity length
m = pressure correction factor
M^2 = transfer function
N = rate of events
p = pressure, Pa
p_o = freestream absolute pressure, Pa
p_c = collapse pressure
p_m = impulsive pressure amplitude
p_v = vapor pressure
q = air injection rate
U_0 = freestream flow velocity, m s^{-1}
U_i = jet velocity, m s^{-1}
V = volts
α = angle of attack
β = void fraction
ρ = fluid density, Kg m^{-3}
σ = cavitation index $\equiv (p_o - p_v)/\frac{1}{2}\rho U^2$
τ = pulse duration, s
τ_a = transducer rise time, s

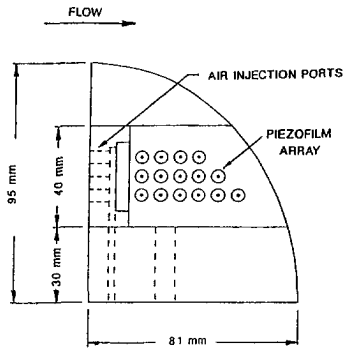

Fig. 1 Details of the hydrofoil with an NACA 0015 cross section

structures which are highly erosive. Several investigators have noted that the erosion process is modulated at a frequency which depends on the cavity length, i.e., $fL_c/U_0 \sim 0.3$. This modulation is easily detected by the methods used in this study.

Kato et al. (1989) performed a series of tests using two different sized foils having a NACA-0015 cross section. Using soft indium inserts mounted on the suction side of the hydrofoil, they were able to quantify the erosion rate using the pit counting technique. They also found that they could simulate either bubble cavitation or sheet cavitation by simply changing the angle of attack. The so-called ductile probe technique was developed by Hackworth and Arndt (1974) for application to measuring cavitation erosion on full scale ship propellers (Hackworth, 1979). A comparison between weight loss and pit counting techniques was studied by Stinebring et al. (1977). Simoneau et al. (1989) have also used hydrofoil tests to develop a unique electrochemical technique for monitoring cavitation erosion. This technique is suitable for monitoring erosion in both turbine models and full scale turbines. This work was extended by Bourdon et al. (1989) who demonstrated through laboratory tests and field experience that hydrofoil cavitation provides a good simulation of hydroturbine cavitation. They used both the electrochemical detection method and the vibratory monitoring technique originally developed by Abbot (1989) and Abbot et al. (1991). Thus, there is ample evidence that cavitation erosion in hydroturbines can be simulated using cavitation hydrofoil tests in a water tunnel.

Experimental Methods

Two experimental facilities were used in this study: the St. Anthony Falls Hydraulic Laboratory (SAFHL) high speed water tunnel and an ASTM vibratory apparatus. Since there is available a great deal of weight loss data obtained using the ASTM vibratory apparatus, it is desirable to relate erosion intensity measured in water tunnel tests to weight loss measured using the vibratory apparatus (described in Paul, 1994). As a first step towards this goal, this apparatus was used for the development of the piezoelectric film transducers, described below. The SAFHL high speed water tunnel (described in Arndt et al., 1991) has several unique features, including the ability to remove as much as 4% by volume of injected air. The test section is separated into two parts by a thin plexiglass sheet. The lower section is 190 mm square and 1250 mm in length and handles flows up to 30 m s^{-1} in velocity. The upper tank contains stagnant water in which an array of hydrophones is mounted. This barrier between the flow and the hydrophones is approximately acoustically transparent.

The hydrofoil designed for this project is similar in overall configuration to hydrofoils being used for other cavitation studies (Maines and Arndt, 1993). It has an elliptic planform with a straight leading edge and a NACA-0015 cross section (Fig. 1). It is mounted in the test section on a circular plug allowing for a setting at any desired angle of attack. The overall dimensions are 95 mm half span and 81 mm chord. This gives an aspect ratio of 3.

The foil is fitted with interchangeable leading edges, one of which has 5 holes at the leading edge of 0.5 mm diameter spaced 5 mm apart. These holes are connected via internal ports to an air supply system. Interchangeable inserts are also provided at mid-span. One type of insert is machined of commercially pure aluminum for pitting studies while another is an instrumented insert machined out of PVC plastic.

The basic instrumentation used in this study consisted of hydrophones, accelerometers, flush mounted piezoelectric transducers, and video recording. Two hydrophones were mounted in the water tank above the test section. The acoustic path between the foil and the hydrophones was one of constant acoustic impedance. Two accelerometers were attached to the outside of the hydrofoil base, one to a bolt threaded into the foil itself, one to a lexan plug on which the foil was mounted. An array of 14 flush-mounted piezoelectric pressure transducers was incorporated into a removable section of the suction side of the foil (Fig. 1).

These custom made transducers, 6.4 mm in diameter and 150 μm thick, were adhered to the surface of the insert. All but the tip and near-base region of the foil was covered with a 150 μm thick adhesive tape which served both to protect and waterproof the transducers and smooth the joints in the surface of the foil. A video camera recorded the tests through a lexan window in the test section.

The transducers were manufactured from piezoelectric film. PVDF film is considered to be specially suitable for recording the impulse pressures due to the cavitation events on the hydrofoil (Paul et al., 1994). However, recent estimates of response time requirements indicate that, in spite of the very favorable response time of the film, obtaining an accurate description of cavitation impulses is a formidable task (Vogel et al., 1989).

Calibration of the piezoelectric transducers was accomplished using a dropping ball technique. Details are given in Paul (1994). Using plastic deformation theory, the sensitivity of the film was calculated to be 2.4×10^5 Pa per Volt. This compares well with the technical specification of the film of 1.05×10^5 Pa per Volt.

The reduction in sensitivity is attributed to the particular method of mounting and coating with protective film. It is important to note that this calibration refers to a uniform pressure over the entire sensitive area. In situations where the excited area is smaller than the active area of the transducer, an important correction is necessary. The correction involves the area ratio. For the 6.4 mm diameter probes used in this study with an excitation area corresponding to a 10 μm pit, this correction is a factor of 4.10×10^5! This may be one of the reasons for the unreasonably low values of impact pressures reported in earlier cavitation studies. Actual values of pressure should be considered to be qualitative at best. The aim of this work is to compare *relative* values of pressure amplitude with and without air injection.

In initial testing of the piezoelectric transducers, the film was mounted on a PVC button which formed the stationary specimen in the ASTM vibratory cavitation setup. At a standoff distance of 1.5 mm from the horn tip vibrating at 20 KHz with a 50 μm peak-to-peak amplitude, an output signal in the range of 3 to 4 Volts could be obtained. The excellent response of the film and the very clean signal made amplification and noise filtering unnecessary.

A Lecroy Model 8210 digital data acquisition system was used for data collection and analysis. The digitized pressure data had a resolution of 9.77 mV which was more than adequate for analysis of the pressure data.

After a preliminary series of tests with the hydrofoil, it was decided to make all comparisons at an angle of attack of 8°. At this incidence, a well developed sheet with cloud cavitation at

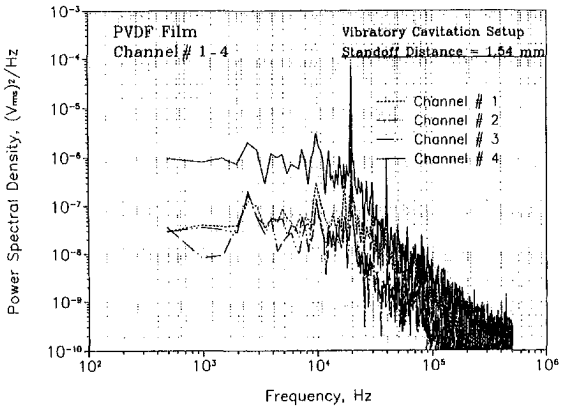

Fig. 2 Measured pressure spectra beneath the horn in the ASTM vibratory apparatus

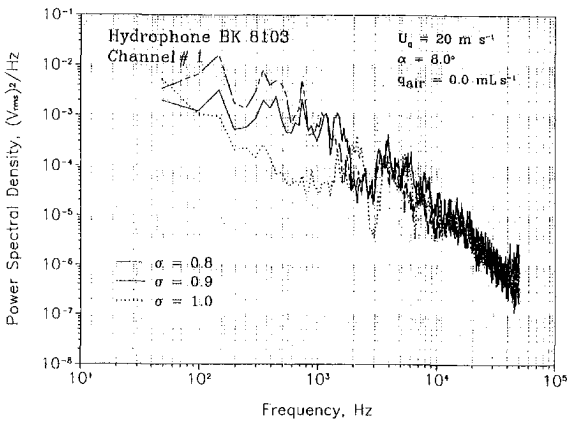

Fig. 3 Cavitation noise spectra measured at U_0 = 20 m s^{-1}

the trailing edge of the sheet occurs over a range of cavitation number, σ. Between σ = 1.0 and 0.6, bubble collapse occurs on the hydrofoil. Below σ = 0.6, the sheet extends beyond the trailing edge of the hydrofoil.

Results and Discussion

Preliminary Tests

Cavitation Inception. Preliminary to selecting the conditions for carrying out a comparative study of cavitation erosion with and without air in the water tunnel, the hydrofoil was tested over a range of velocity and angle of attack. Cavitation data were compared with expected values. The calculations are based on two dimensional flow analysis using classical lifting line theory to compute the lift coefficient. Reasonable agreement between theory and experiment was found. Perfect agreement was not expected because the fit of various components was not perfect.

ASTM Vibratory Apparatus Tests. Several different types of tests were carried out with the vibratory apparatus in the course of developing the PVDF transducers. As previously noted, this apparatus is a convenient test bed for transducer development, but these tests are also the first step towards achieving a comparison between measured weight loss in this apparatus, measured pitting rate and impulsive pressures in hydrofoil tests and vibration and acoustic measurements in full scale hydroturbines.

Figure 2 shows the power spectra measured beneath the vibrating horn with 6.35 mm diameter transducers at a stand-off distance of 1.54 mm. Channel 4 is from a transducer positioned at centerline of the horn. Channels 1, 2, and 3 are from transducers each positioned at a distance of 7.94 mm from the centerline and angles of 0, 90, and 180 deg. A common ground was positioned at 270°. A strong peak is noted at a vibration frequency of 20 KHz with another peak at the first harmonic of 40 KHz. The signal from the centerline transducer is higher, as expected.

A second test was carried out to determine the effect of transducer size. A circular shaped transducer was split into 3 pie shaped pieces having included angles of 60, 120, and 180 deg, respectively. When placed beneath the horn, the signal from each pie shaped transducer was essentially the same, indicating that effect of size was minimal.

Cavitation Noise. Figure 3 contains a comparison of noise spectra collected at σ = 0.8, 0.9, and 1.0 at a velocity of 20 m/s in the water tunnel. The high frequency decay is 6 db/octave which is typical for cavitation noise. The level of low frequency noise increases with decreasing σ, but the high frequency noise appears to be independent of σ. It was also noted that the scaling of cavitation noise with velocity did not agree with the pressure data or the accelerometer data. Presumably the acoustic path between the hydrofoil and the hydrophones was modified by cavitation.

Pressure Pulse Height Spectra. Since it was expected that the pressure signal would be dominated by pressure impulses of high amplitude due to cavitation, pulse height spectra were compared at different velocities. A typical comparison is shown in Fig. 4. The pulse height spectra were computed in terms of the number of pulses per unit time that was recorded within a class interval of 9.77 mV. Only positive voltage pulses were recorded.

Scaling of pressure amplitude with velocity depends on the frequency of occurrence, as expected. Pulses with a high frequency of occurrence correspond to turbulent pressure fluctuations which scale like U_0^2. High amplitude, low frequency of occurrence pulses scale with a much higher power of velocity. Presumably high amplitude pulses are due to cavitation events.

Unfortunately, the measurement technique was not able to accurately resolve the amplitude of cavitation implosions. However, measurements of mean square pressure and pulse height spectra are consistent. The mean square pressure for a series of pulses of amplitude p_m and duration τ is given by

$$\overline{p^2} = Np_m^2\tau \tag{4}$$

Typical values for N and τ at a velocity of 17.5 m s^{-1} are 195 s^{-1} and 5.3 μs, respectively. A measured peak voltage of 0.088 V is in agreement with a measured value of the mean square voltage of 8×10^{-6} V^2 using this equation. This appears

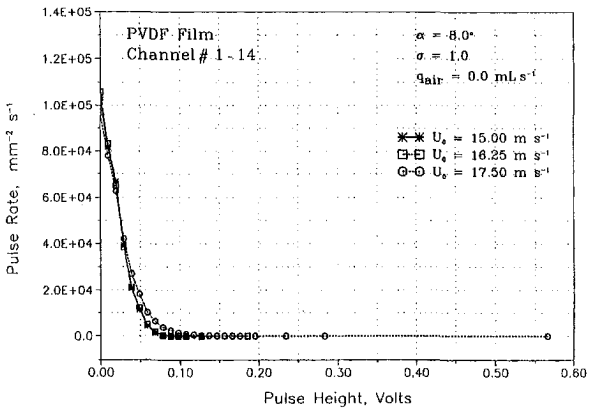

Fig. 4 Comparison of pressure pulse height spectra at different velocities. The measurement error is within 1 percent

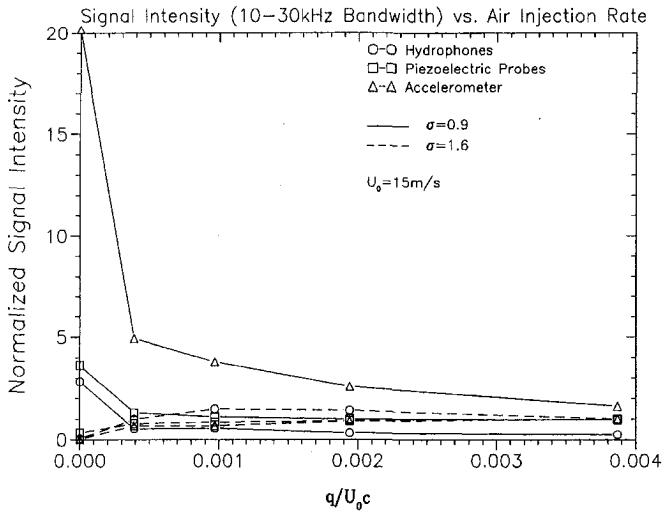

Fig. 5 Comparison of normalized signal intensity versus normalized air flow rate at U_0 = 15 m s^{-1}, σ = 0.9. The amplitude is measured within 1 dB and the normalized rate is within 1.5 percent.

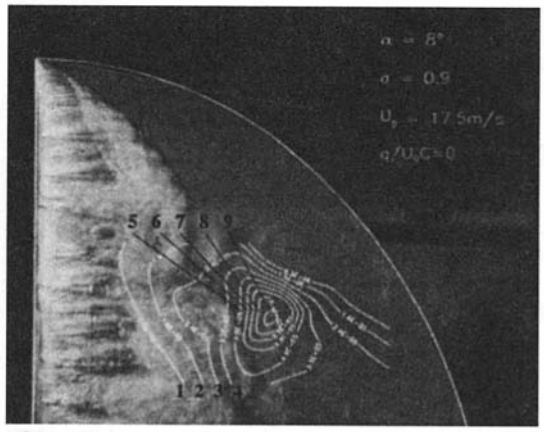

Fig. 6 Photograph of sheet cavitation in the water tunnel (see Fig. 1 for orientation) at σ = 0.9 and U_0 = 17.5 m s^{-1}. Superimposed on the plot are isobars of mean square pressure fluctuations in the 10–30 kHz bandwidth. The numbers represent the amplitude relative to a measured minimum value in the region.

to correspond to very low values of impact pressure. Using the measured rise time of the film, the measured sensitivity and Eq. (2), an estimate of 250 atmospheres was obtained, orders of magnitude below the expected value. However at this flow velocity, the pits formed due to cavitation were measured[1] to be approximately 10 μm. Using the area ratio correction discussed in the experimental methods section, the value of p_m is estimated to be 8,650 MPa for the recorded voltage of 0.088 V. Using these values in Eq. (4), p^2 is calculated to be 7.73×10^{16} Pa^2. This underscores the difficulty in interpreting the transducer output signal as previously discussed. Although pulse height spectra were expected to be a good indicator of cavitation erosion intensity, our initial findings suggest that comparisons of the mean square signal in the frequency band 10 KHz to 30 KHz offer the best indication of erosion rate.

Effects of Air Injection. Since pitting rate with and without air was not measured, the effect of air injection had to be inferred from the change in noise, vibration, and direct measurement of impulse pressure on the surface of the hydrofoil. Several researchers have attempted to achieve a correlation between noise and rate of erosion without success (Kato et al., 1989; Guelich, 1990). A long-range objective of the research in progress is to develop improved diagnostic techniques for determining erosion rates in turbines. Recognizing the difficulties involved in measuring erosion rates in situ, it was decided to compare different measurements known to be *qualitative* indicators of erosion rate. This a comparison is shown in Fig. 5. In this figure erosion rate is considered to be proportional to either: 1) the mean square of the hydrophone signal in the 10 KHz to 30 KHz band, 2) the average of the three most intense mean square surface pressure signals in the 10 KHz to 30 KHz band, or 3) the mean square modulation acceleration (Abbot et al., 1993). The mean square modulation acceleration level is obtained from the spectral density of the full-wave rectified acceleration signal by integrating the spectral energy at an observed modulation frequency. This technique is only valid when shedding of the cavitation cloud occurs at a distinct frequency as discussed subsequently. In each case the signal is normalized to the signal obtained for non-cavitating conditions and maximum flow rate. The air flow rate per unit width, q, in the normalized air flow rate, q/U_0c, is obtained by dividing the total air flow rate supplied by the number of holes (5) and the spacing between holes; c refers to the chord length of 68.87 mm at the position of the center air injection port.

A comparison between normalized flow rate and effective void fraction can only be estimated. This estimate was made assuming that diffusion of all the injected air occurs within the cavitation cloud that is oscillating at the modulation frequency. By equating the flow rate, q, to the product of void fraction, β, the measured modulation frequency, f, and the volume of the cloud per unit span, a relationship between normalized flow rate and β can be obtained if an assumption for the dimensions of the cloud is made. This calculation indicated that the void fraction was approximately 50 q/U_0c, for an assumed cloud volume per unit span of 0.1 c^2.

The favorable influence of air injection is clearly evident. All three indicators of erosion are already markedly reduced at a normalized air injection rate of 0.0004. This corresponds to an equivalent void fraction of about 0.02. The calculations of van Wijngaarden (1972) indicate that the speed of sound in a mixture of air and water can be substantially reduced at this value of void fraction, implying a very favorable cushioning effect. However, the actual mechanism for attenuation of sound, acceleration and surface pressure remains unknown.

It is important to note that the acceleration modulation analysis appears to be much more sensitive to air injection, possibly

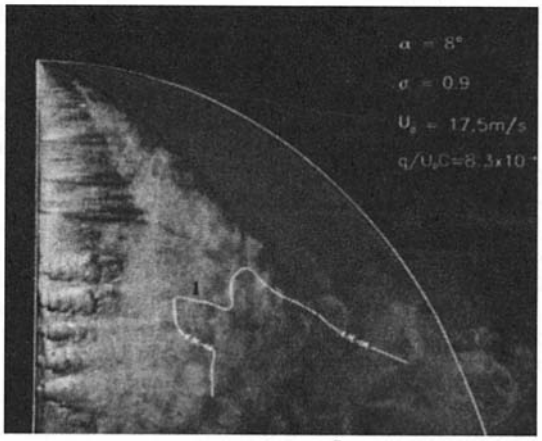

Fig. 7 This is the same situation as in Fig. 6 except for an air injection rate, q/U_0c of 8.3×10^{-4}. Note the dramatic reduction in pressure intensity over the entire surface of the foil (by a factor of 10).

[1] This was done using the aluminum insert in place of the instrumented foil on the hydrofoil. Cavitation number and flow velocity was identical to that when using the instrumented insert.

implying that it is also a better indicator of changes in erosive intensity. However, this conclusion must be made with caution since the air injection could modify the transfer function between the pitting rate and the acceleration. Further discussion of this technique is found in a companion paper (Abbot et al., 1993). Although the modulation method appears to be the most sensitive technique, the effects of air on the pressure pulses are also evident. This is illustrated in Figs. 6 and 7. These are photographs of the sheet cavitation without and with a relative amount air injection of 1.95×10^{-3}. Superimposed on the photographs are contours of the mean square pressure fluctuations in the 10–30 kHz bandwidth relative to a minimum value measured by the piezoelectric transducer array described above. The favorable influence of air injection over the entire surface of the foil is evident.

Modulation Frequency. As discussed in Abbot et al. (1993), there is evidence that erosion intensity is most severe under conditions where a cavitating cloud is modulated. Whether this modulation is a function of the sheet characteristics, the cloud dimensions and void fraction, or a combination of both is not clear at this point.

If one assumes that a sheet has a cyclical life time that scales with the time required for a re-entrant jet travelling forward at a speed of $U_0(1 + \sigma)^{1/2}$ to pinch off the cavity (Stinebring et al., 1980), it follows that

$$\frac{fL_c}{U_0} = C\sqrt{1 + \sigma} \tag{5}$$

where C can be shown to be theoretically equal to 0.25.[2]

Since L_c varies strongly with σ, most of the observed variation in modulation frequency with σ is removed by using L_c as the characteristic length scale. This is shown in Fig. 8 where Eq. (5) is compared with data from this study (labeled NACA 0015) and data obtained with a 2D foil in another water tunnel published by Abbot et al. (1993). The frequency of oscillation is obtained from the modulation analysis and agreed almost perfectly with cavity oscillation frequency data obtained visually using a stroboscope.

Comparison of Modulation Analysis and Measurement of Mean Square Pressure. Abbot et al. (1993) have found very good correlation between hydrofoil erosion rate measurements and the mean square acceleration level. They also found that their mean square acceleration levels had a velocity exponent as high as 11. On the other hand, measured mean square pressure data scaled with velocity to a lower exponent. One possibility for this discrepancy is offered here.

Assuming that each pit formed on the surface of the hydrofoil corresponds to an impulsive force of amplitude F_0 and duration τ, the mean square force $\overline{F^2}$ is then

$$\overline{F^2} = NF_0^2\tau \tag{6}$$

where N is the number of pits per unit time. Mean square acceleration $\overline{a^2}$, and $\overline{F^2}$ are related by a transfer function

$$\overline{F^2} = M^2\overline{a^2} \tag{7}$$

Assuming that F_0 is proportional to peak pressure, p_m, and pit diameter, d_p

$$F_0 \sim p_m d_p^2 \tag{8}$$

then

$$\overline{a^2} \sim \frac{\overline{F^2}}{M^2} = \frac{Np_m^2 d_p^4 \tau}{M^2} \tag{9}$$

Noting that

[2] Unpublished work of the first author.

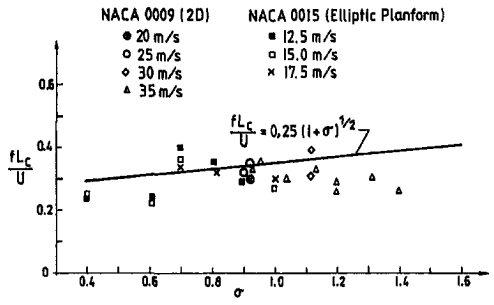

Fig. 8 Cavity oscillation frequency over a range of cavitation number. The NACA 0015 data were measured within 5 percent.

$$Np_m^2\tau = \overline{p^2} \tag{10}$$

we obtain

$$\overline{a^2} \sim \overline{p^2}d_p^4 \tag{11}$$

Using our measured values, $\overline{p^2} \sim U_0^6$, $\overline{a^2} \sim U_0^{11}$, in Equ. 10 it is found that $d_p \sim U_0^{1.25}$ which is fairly consistent with previously reported results for pit volume, $d_p^3 \sim U_0^5$ or $d_p \sim U_0^{1.67}$. These results are very tentative and warrant further study.

Uncertainty Estimates

Measurements of velocity, static pressure, air flow rate and frequency are all within one percent. The measurement of acceleration and acoustic pressure are considered to be within 1 db. During a careful calibration of all the pressure transducers, a confidence interval estimation of 99 percent was measured for the correlation between the peak amplitude of the output signal in volts and the impulse imparted to the film with a dropping ball. However, as discussed in the text, measurements of peak pressure and pulse height spectra are unreliable. Measurements of mean square pressure may be considered reliable within 10 percent.

Conclusions

This study and previous work by others indicate that water tunnel tests are an effective method for isolating the essential flow physics that contribute to cavitation erosion in hydroturbines. The hydrodynamic conditions for the water tunnel

Acknowledgments

The authors gratefully acknowledge the support of the Pacific Gas and Electric Company. Preparation of this paper was supported by the Office of Naval Research under Contract number N/N00014-91-J-1239. Dr. Edwin Rood is the contract monitor. The help of Mr. Brant Maines in the photographic part of this research is also gratefully acknowledged.

References

Abbot, P. A., 1989, "Cavitation Detection Measurements on Francis and Kaplan Hydroturbines," *Proc. ASME Intl. Symp. on Cavitation Noise and Erosion in Fluid Systems,* R. E. A. Arndt, M. L. Billet and W. K. Blake, eds., FED-Vol. 88.

Abbot, P. A., Welsh, J., and Halas, R., 1991, "Cavitation Noise Investigation of a Pump Turbine," *Proceedings International Conference Waterpower,* Denver, CO, July.

Abbot, P. A., Arndt, R. E. A., and Shanahan, T. B., 1993, "Modulation Noise Analysis of Cavitation Hydrofoils," *Proceedings ASME International Symposium on Bubble Noise and Cavitation Erosion in Fluid System,* Winter Annual Meeting, Dec.

Arndt, R. E. A., 1981, "Cavitation in Fluid Machinery and Hydraulic Structures," *Annual Review of Fluid Mechanics,* Vol. 13.

Arndt, R. E. A., et al., 1989, "Cavitation Erosion in Hydroturbines," *Journal of Hydraulic Engineering,* Vol. 115, No. 10, Oct.

Arndt, R. E. A., 1990, "Hydraulic Turbines" Chapter 4 in *Hydropower Engineering Handbook,* J. S. Gulliver and R. E. A. Arndt, eds., McGraw-Hill.

Arndt, R. E. A., Arakeri, V. H., and Higuchi, H., 1991, "Some Observations of Tip-Vortex Cavitation," *Journal of Fluid Mechanics,* Vol. 229.

Avellan, F., Dupont, P., and Farhat, M., 1991, "Cavitation Erosion Power," *Proc. ASME-JSME Cavitation '91 Symp.,* FED-Vol. 116.

Blake, J. R., and Gibson, D. C., 1987, "Cavitation Bubbles Near Boundaries," *Annual Review of Fluid Mech.,* Vol. 19.

Bourdon, P., Simoneau, R., and Lavigne, P., 1989, "A Vibratory Approach to the Detection of Erosive Cavitation," *Proceedings International Symposium on Cavitation Noise and Erosion in Fluid Systems,* R. E. A. Arndt, M. L. Billet, and W. K. Blake, eds., FED-Vol. 88.

Chahine, G. L., Duraiswami, R., and Rebut, M., 1992, "Analytical and Numerical Study of Large Bubble/Bubble and Bubble/Flow Interactions," *Proceedings Symposium,* Seoul, Korea, Aug.

Guelich, J. F., 1990, "Estimation of Erosion Rates and Implosion Pressures in Cavitating Pumps and Cavitation Test Devices," *Vibration and Wear in High Speed Rotating Machinery,* J. M. Montalvao e Silva and F. A. Pina da Silva, eds., Kluwer Academic Publishing.

Hackworth, J. V., and Arndt, R. E. A., 1974, "Preliminary Investigation of the Scale Effects of Cavitation Erosion in a Flowing Media," *Cavitation and Polyphase Flow Forum,* ASME.

Hackworth, J. V., 1979, "Predicting Cavitation Erosion of Ship Propellers from the Results of Model Experiments," *Proceedings International Conference on Erosion by Solid and Liquid Impact,* Cambridge, U.K.

Hansson, I., and Mørch, K. A. 1980, "The Dynamics of Cavity Clusters in Ultrasonic (Vibratory) Cavitation Erosion," *Journal of Applied Physics,* Vol. 51(19), Sept.

Hansson, I., Kredinski, V., and Mørch, K. A., 1982, "On the Dynamics of Cavity Clusters," *Journal of Physics D: Applied Physics,* Vol. 15, pp. 1725–1734.

Huse, E., 1976, "Air Injection to Avoid Cavitation Erosion in Propeller Ducts," *Norwegian Maritime Research,* No. 1.

Kato, H., Ye, Y. P., and Maeda, M., 1989, "Cavitation Erosion and Noise Study on a Foil Section," *Proceedings ASME International Symposium on Cavitation Noise and Erosion in Fluid Systems,* R. E. A. Arndt, M. L. Billet, and W. K. Blake, eds., FED-Vol. 88.

Le, Q., Franc, J. P., and Michel, J. M., 1993a, "Partial Cavities: Global Behavior and Mean Pressure Distribution," ASME JOURNAL OF FLUIDS ENGINEERING, Vol. 115, No. 2, June.

Le, Q., Franc, J. P., and Michel, J. M., 1993b, "Partial Cavities: Pressure Pulse Distribution around Cavity Closure," ASME JOURNAL OF FLUIDS ENGINEERING, Vol. 115, No. 2, June.

Maines, B. H., and Arndt, R. E. A., 1993, "Viscous Effects on Tip Vortex Cavitation," *Proceedings International Symposium on Bubble Noise and Cavitation Erosion in Fluid System,* Winter Annual Meeting, Dec.

van der Meulen, J. H. J., and Nakashima, 1983, "A Study of the Relationship Between Type of Cavitation, Erosion and Luminescence," *Proceedings 2nd International Conference on Cavitation,* Edinburgh, pp. 13–19.

van der Meulen, J. H. J., and van Renesse, R. L., 1993, "The Collapse of Laser Produced Bubbles Near a Solid Boundary and the Generation of Pressure Pulses," *Cavitation and Multiphase Flow Forum,* ASME, FED-Vol. 153.

Mørch, K. A., 1980, "On the Collapse of a Cavity Cluster in Flow Cavitation," *Proc. First Intl. Conf. on Cavitation and Inhomgeneites in Underwater Acoustics,* Vol. 4, Springer Series in Electrophysics, pp. 95–100.

Mørch, K. A., 1982, "Energy Considerations in the Collapse of Cavity Clusters," *Applied Scientific Research,* Vol. 38, pp. 313–321.

Narita et al., 1977, "Investigations of the Ducted Propeller Cavitation and Duct Erosion Prevention by the Air Injection System," *Det Norske Veritas Symp. on Hydrodyn. of Ship and Offshore Propulsion Systems,* Oslo.

Okamoto, H., Okada, K., Saito, Y., and Takahei, T., 1975, "Cavitation Study of Ducted Propellers on Large Ships," *Trans. SNAME,* Vol. 83.

Paul, S., 1994, "Towards Laboratory Prediction of Cavitation Damage Intensities in Prototype Applications," MS Thesis, Univ. of Minnesota.

Paul, S., Ellis, C. R., and Arndt, R. E. A., 1994, "The Use of Piezoelectric Film in Cavitation Research," *Proc. ASCE Symp. on Fundamentals and Advancements in Hydraulic Measurements and Experimentation,* Buffalo, N.Y.

Rayleigh, Lord, 1917, "On the Pressure Developed in a Liquid During the Collapse of a Spherical Cavity," *Phil. Mag.,* Vol. 34, Aug.

Shanahan, T. B., and Abbot, P. A., 1993, "Acoustic Emission Cavitation Test at Kerckoff 2 Powerhouse," ORE Intl., Inc., Falmouth, MA, Accusonic Rep. No. FP22280-1.

Simoneau, R., Avellan, F., and Kuhn de Chizelle, Y., 1989, "On Line Measurement of Cavitation Erosion Rate on a 2-D NACA Profile," *Proc. ASME Intl. Symp. on Cavitation Noise and Erosion in Fluid Systems,* R. E. A. Arndt, M. L. Billet, and W. K. Blake, eds., FED-Vol. 88.

Stinebring, D. R., Arndt, R. E. A., and Holl, J. W., 1977, "Scaling of Cavitation Damage," *Journal of Hydronautics,* Vol. 11, No. 3, July.

Stinebring, D. R., Holl, J. W., and Arndt, R. E. A., 1980, "Two Aspects of Cavitation Damage in the Incubation Zone: Scaling by Energy Considerations and Leading Edge Damage," ASME JOURNAL OF FLUIDS ENGINEERING, Vol. 102, Dec.

Thiruvengadam, A., 1971, Hydronautics, Inc., Laurel, MD, Technical Report 233-15.

Tomita, Y., and Shima, A., 1986, "Mechanisms of Impulsive Pressure Generation and Damage Pit Formation by Bubble Collapse," *Journal of Fluid Mechanics,* Vol., 169.

Wang, Y. C., and Brennen, C. E., 1994, "Shock Development in the Collapse of a Cloud of Bubbles," *ASME Cavitation and Multiphase Flow Forum,* Vol. 153.

van Wijngaarden, L., 1972, *Annual Review of Fluid Mechanics,* Vol. 4, pp. 369–396.

van Wijngaarden, L., 1993, "Bubble Dynamics and the Sound Emitted By Cavitation," *IUTAM Symposium on Bubble Dynamics and Interface Phenomena* Birmingham, United Kingdom, Sept.

Vogel, A., Lauterborn, W., and Timm, R., 1989, "Optical and Acoustic Investigations of the Dynamics of Laser-Produced Cavitation Bubbles Near a Solid Boundary," *Journal of Fluid Mechanics,* Vol. 206.

Zhang, S., Duncan, J. H., and Chahine, G. L., 1992, "Simulation of the Final Stage of Bubble Collapse Near a Rigid Wall," *Cavitation and Multiphase Flow Forum,* ASME, FED-Vol. 135.

Particle Size and Velocity Discrimination in a Sediment-Laden Turbulent Flow Using Phase Doppler Anemometry

S. J. Bennett

J. L. Best

Department of Earth Sciences,
University of Leeds,
Leeds, West Yorkshire LS2 9JT, UK

A series of experiments were performed in a mixing box in order: (1) to investigate the applicability of phase Doppler anemometry (PDA) to discriminate fluid and sediment particle sizes and velocities in sediment-laden turbulent flows; and (2) to relate the size and amount of sediment in suspension to the grid-generated turbulence. Natural impurities within the water provide excellent "seeding" to represent the fluid and can be easily discriminated from spherical glass beads (75–355 μm) used as sediment. Slight asphericity in the glass beads results in larger grain size ranges determined by PDA compared to the nominal sieved sizes. The mean, root-mean-square and skewness of the vertical fluid velocities increase at higher grid oscillation frequencies but decrease with distance from the grid. Similarly, the size and amount of suspended sediment increase with grid oscillation frequency and decrease with distance from the grid. The suspension of sediment is shown to be dependent on the magnitude and anisotropy of the fluctuating vertical component of velocity. Phase Doppler anemometry offers a unique methodology to investigate the complex links between the transport of sediment and the turbulent flow field.

1 Introduction

The interactions between fluid turbulence, sediment transport, and bed configuration in sediment-laden flows are of widespread interest to engineers, sedimentologists, and fluid dynamicists. Such information is a prerequisite to develop and test theories for sediment entrainment and bedload transport, to delineate the mechanisms for the suspension of sediment, and to formulate theories concerning the generation, growth, and stability of bedforms in mobile beds. Simultaneous measurement of turbulent fluid and particle velocities, grain size, and sediment concentration has become possible using phase Doppler anemometry (PDA). PDA, an extension of laser Doppler anemometry (LDA), can determine not only the Doppler shift frequency of light refracted by a particle within the flow (hence its velocity) but also the phase shift as observed at three different receiving locations which can be utilized to derive the diameter of the scattering particle (see Bachalo and Houser, 1984; Saffman et al., 1984; Buchhave, 1987; Bachalo, 1994). While some studies have employed PDA for size determination of fuel droplets in engine injection systems (e.g., Bachalo and Houser, 1984; Saffman et al., 1988), dust in aerodynamic jets (e.g., Hardalupas et al., 1988), cavitation nuclei (e.g., Tanger and Weitendorf, 1992) and the dispersion of fine particles (<50 μm) in jets and wakes of cylinders (see review in Bachalo, 1994), little information has yet been provided on the discrimination of particle size and velocity of the fluid and the sediment in sediment-laden turbulent flows with relatively large sediment particles (>100 μm). Recently, Cioffi and Gallerano (1991) simultaneously measured the size and downstream velocity component of sediment particles (glass beads, 150–250 μm in size) in a laboratory channel using a PDA system, also computing at-a-point suspended sediment concentrations. Their results agree well with theoretical distributions of velocity and sediment concentration in turbulent boundary layers. However, Cioffi and Gallerano did not use the observed size and velocity signals to discriminate "fluid" and "sediment" particles.

The objectives of the present study are: (1) to assess the performance of PDA in discriminating between fluid "seed" particles and sediment grains in a simple experimental configuration; and (2) to relate the size, concentration and dynamics of the suspended sediment to the turbulent flow structure. Here, we use PDA in conjunction with a mixing box, an apparatus which provides an easily controllable source of zero-mean-shear turbulent flow through the oscillation of a grid at the base of the box. Details of the technique, including particle size discrimination and the determination of velocity moments, are presented with a discussion of the implications to sediment-laden geophysical flows.

2 Experimental Equipment and Procedure

2.1 The Mixing Box. The mixing box used in this study (see Fig. 1; the same box as used by Thompson and Turner, 1975, and Huppert et al., 1993) consists of a perspex tank (0.254 × 0.254 × 0.45 m high) with a grid of square bars, 0.01 m wide, 0.22 m long and spaced 0.05 m apart, located near and parallel to the base of the box. This grid is fixed by a central arm to an eccentric drive which provided an oscillation amplitude (perpendicular to the base of the box) of approximately 0.019 m. The center of the grid was maintained at a constant mean height above the base in all experiments (~0.026 m). Grid oscillation frequency, ω, was controlled by a voltage regulator and four frequencies (ω = 1.1, 1.9, 2.7, and 3.4 Hz) were chosen so that each sediment population within a particular experiment remained immobile at the lowest frequency. The zero plane for fluid depth (used here where $Y = 0$) is at the apogee of the grid.

The entire apparatus was mounted to a 1 m^2 baseboard, which had a scissor jack attached at each corner. This configuration allowed the box and its controls to be raised and lowered with an accuracy of ±0.5 mm using millimeter-graduated scales fixed to the sides of the base, thus permitting acquisition of vertical

Contributed by the Fluids Engineering Division for publication in the JOURNAL OF FLUIDS ENGINEERING. Manuscript received by the Fluids Engineering Division May 5, 1994; revised manuscript received October 31, 1994. Associate Technical Editor: M. W. Reeks.

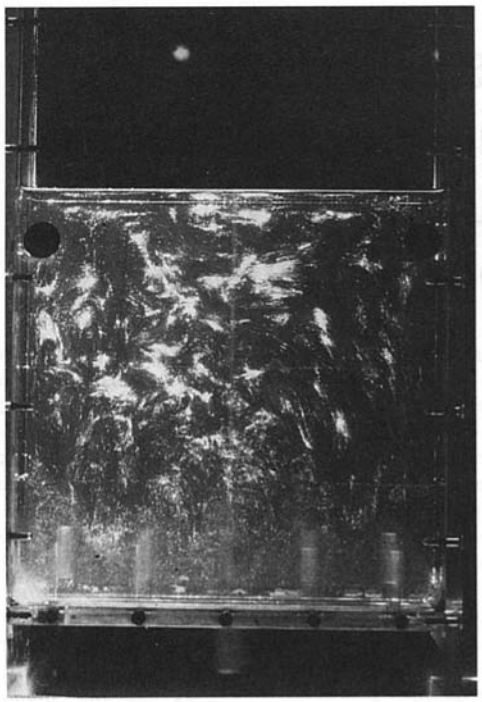

Fig. 1 Photograph of fluid movement within the mixing box as visualized using a vertical laser light sheet. Tracer particles of titanium dioxide-coated mica flakes (5–70 μm diameter) reveal large, energetic vertical jets at the bar intersections and turbulent eddies which extend through the entire flow depth. Oscillation frequency = 3.4 Hz and box width is 0.254 m.

velocity profiles without requiring movement of the laser optics. The mixing box was filled with unfiltered tap water to a depth of 0.25 m (an effective depth, d, of 0.2 m).

2.2 The Discrimination of Fluid and Sediment Particle Sizes and Velocities Using Phase Doppler Anemometry. The simultaneous measurement of particle size and velocity was achieved using phase Doppler anemometry which extends the principles of LDA by detecting the phase difference of a Doppler burst signal as seen at three different locations in the receiving optics (e.g., Saffman et al., 1984; Buchhave, 1987; Bachalo, 1994). As a transparent particle passes through the measurement volume, the interference fringes are refracted by an amount proportional to the diameter of the grain. Three detectors, located at different positions within the receiving optics, will observe the same frequency but with a relative phase shift proportional to the detector spacing divided by the projected fringe spacing. The separation of the projected fringes at a large distance from the measuring volume is proportional to the effective focal length of the particle, which, for a spherical particle, is proportional to the particle diameter. Hence the measured phase shift is proportional to the particle diameter.

Our rationale in these experiments is based on two central points: (1) that spherical glass beads can be used to represent the sediment population whilst natural impurities within the water represent the fluid flow; and (2) the size distributions of the sediment and fluid particles do not overlap, enabling discrimination of the size and velocity of the fluid 'seed' particles and the sediment grains.

The sediment grains used were glass beads (density, σ, of 2600 kg/m^3 with a refractive index of 1.5), chosen because: (1) their shape is close to spherical and they are of quartz density; (2) their transparency allows the PDA to be used in refraction mode; and (3) large quantities sufficient for mobile bed flume experiments can be purchased at moderate cost. Three size distributions of glass beads were used with nominal sieved diameters of 75–95 μm (termed fine), 180–210 μm (medium), and 300–355 μm (coarse). The total dry mass of sediment (concentration) added to the box for the fine, medium, and coarse populations was 5 g (0.31 g/l), 40 g (2.48 g/l) and 100 g (6.20 g/l), respectively. Each sediment population was initially spread evenly across the base of the box. In most experiments, the sediment supply available for suspension was not exhausted and therefore the flow could reach an equilibrium capacity, although no particles remained on the base of the box at the highest oscillation frequencies using the fine sediment.

The PDA used in this study is a two-component DANTEC 100 mW argon-ion, fiber-optic system operated in side-forward scatter mode (at 42 deg outside the tank, 30 deg in the water) with a DANTEC Flow Velocity Analyzer processor (correlation-type), 40 MHz frequency shift, and a 600 mm focal length lens with a beam separation distance of 0.025 m at the lens surface. In the processing software, the maximum phase error was set at 15 deg and the maximum spherical deviation was set at 35 percent. With this configuration, typical uncertainty estimates were 1 percent for the velocity measurements (with a resolution of 0.006 m/s) and 4 percent for the particle size measurements (with a resolution of 2 μm). The laser intersection volume was located within 10–15 mm from a grid bar intersection. At this fixed coordinate, vertical velocity profiles (one component only) were taken through the box to determine the vertical fluid and sediment velocities and suspended sediment fluxes as a function of both height away from the grid and oscillation frequency. A 300 second sample was taken at heights above the grid, Y, of 5, 10, 15, 20, 25, 30, 35, 40, 45, 50, 60, 70, 80, 100, 120, and 150 mm. Typical sampling rates varied from 30–1000 Hz (normally 400 Hz) depending upon the chosen frequency and height above the grid. At each point within a profile, the following moments were determined for both the vertical velocity of the fluid and sediment (see below): arithmetic particle mean velocity ($\bar{V}$; m/s) defined as

$$\bar{V} = \frac{1}{n}\sum_{i=1}^{n} v_i \tag{1}$$

where n is the total number of velocity observations made and v_i is the instantaneous vertical velocity (no attempt was made to correct for velocity bias since this only becomes significant at very large velocities; see Gould and Loseke, 1993); root-mean-square of the velocity (v'; m/s) defined as

$$v' = \sqrt{\frac{1}{n}\sum_{i=1}^{n} (v_i - \bar{V})^2} \tag{2}$$

and skewness of the velocity distribution (κ; dimensionless) defined as

$$\kappa = \frac{1}{n}\sum_{i=1}^{n}\left[\frac{(v_i - \bar{V})}{v'}\right]^3 \tag{3}$$

In addition, the at-a-point volumetric suspended sediment flux (q_S), defined as the time-averaged volume of sediment intersecting the measurement volume per unit cross-sectional area (laser intersection area perpendicular to flow, A, is 1.54 mm^2) per unit time (mm^3/mm^2 s) was determined (assuming spherical grains) using

$$q_s = \frac{1}{At}\sum_{i=1}^{m}\frac{4}{3}\pi\left(\frac{D_i}{2}\right)^3 \tag{4}$$

where m is the total number of sediment grains observed, D_i is the grain diameter, and t is the total sample time length. It should be noted that sediment flux determined by the PDA (using Eq. (4)) is sensitive to signal validation levels and the optical set-up. For example, at very high sediment concentrations the receiving optics may be unable to detect the laser

beam measurement volume due to the flow turbidity, hence the observed concentrations would tend towards zero. As shown below, however, relative sediment fluxes such as those determined in Eq. (4) for dilute flows can be useful for both qualitative and quantitative purposes. A vertical velocity profile was taken for each sediment population used and for each oscillation frequency chosen. In the present study, it is assumed that the turbulent motions within the mixing box quickly attained a steady state since no fluid density contrast was present and the sediment concentrations used in these experiments were relatively small.

3 Results

3.1 Fluid Motion Within the Mixing Box. Visualization of flow within the mixing box using a laser light sheet and highly-reflective titanium dioxide-coated mica flakes (Fig. 1) reveals the gross patterns of flow within the box that have been described in previous studies (Turner, 1968; Thompson and Turner, 1975; McDougall, 1979; Nokes, 1988). Fluid motion comprises a strong oscillatory flow near the grid bars generating energetic vertical jets of fluid whose centerlines pass through the intersection points of the grid (Fig. 1). The PDA measuring volume was positioned close to, but not directly above, one of these intersections in order to measure the turbulent vertical velocities and suspended sediment concentrations related to these upward-directed fluid motions. As these vertical jets rise within the flow, they interact and breakdown, giving rise to turbulence which is advected upwards by the jets (Thompson and Turner, 1975, p. 350). At a height dependent upon the grid oscillation frequency, the vertical jets decay and overturn to produce an area of downward-directed fluid, broadly located above the spaces between the bars. Mixing of the vertical jets above each grid bar intersection also gives rise to a number of strong and visible vortices whose axes are parallel to the grid bars (Fig. 1). These fluid interactions produce zero-mean-shear turbulence beyond a certain distance away from the grid. The decay of this turbulence has been the focus of several fluid dynamic investigations concerning turbulent diffusion and mixing across density interfaces (see reviews in Turner, 1986; Fernando, 1991).

3.2 Size Discrimination Between Fluid and Sediment. In order to evaluate the range of grain sizes detected by the PDA for the fluid and glass beads used, Fig. 2 shows the frequency distributions for all PDA measured grain diameters for each sediment population at two different oscillation frequencies at a fixed height (Y = 5 mm) within the box. The majority of grain sizes observed within the pure fluid experiments (>90 percent) were less than 50 μm, with 85 percent less than 30 μm. These measured grain sizes represent colloidal and natural particulate matter in the water. The frequency distributions for the fine sediment population show peaks at 50–70 μm and 60–90 μm for the low and high oscillation frequencies, respectively. At the lower frequency (1.9 Hz), the signal illustrates the equal detection of fluid particles and sediment grains, while at the higher frequency (3.4 Hz) the signal is completely dominated by the sediment particles in suspension. For the two other sediment populations used, few sediment grain sizes are observed at the lower frequency whereas appropriate peaks are observed at 200–230 μm for the medium sediment and at 310–340 μm for the coarse sediment at the higher frequency. It is apparent that, for a given range of grain sizes introduced into the box, discrimination can easily be made between the particles representing the fluid (<30 μm) and the sediment particles suspended in the flow. However, a larger range of grain sizes is observed by the PDA when compared to the sieved grain size range. The range of grain sizes measured by the PDA varies from about 25–125 μm for the fine sediment, 100–300 μm for the medium sediment, and 200–400 μm for the coarse sediment.

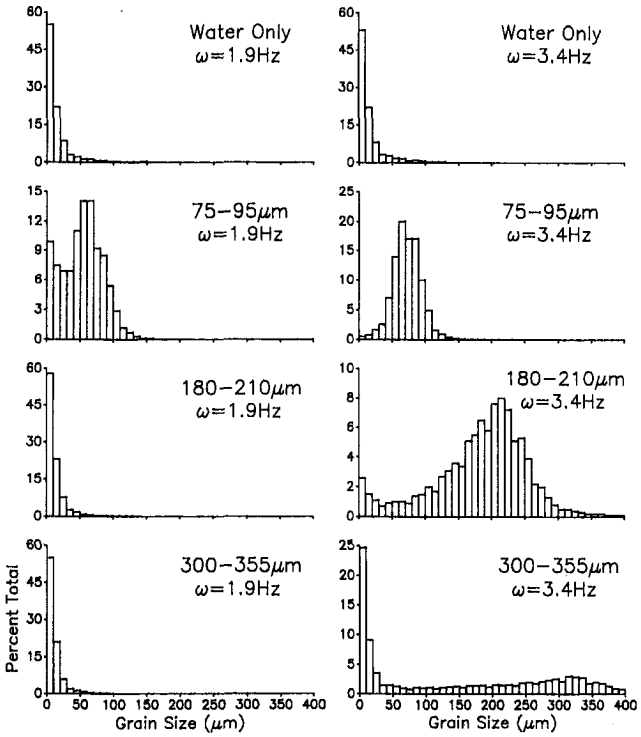

Fig. 2 Grain size frequency distributions for all sediment populations at a height of 5 mm above the grid for oscillation frequencies of 1.9 and 3.4 Hz. Histogram bin size = 10 μm

Independent grain size determination of the fine sediment population using an Elzone electrical resistance particle size analyzer also revealed a range of sizes from 25–115 μm in agreement with the PDA results. Tanger and Weitendorf (1992) also observed a disparity between the sieved size distribution of the sediment and that determined by the PDA. These workers ascribed this disparity to the presence of dirt on the spheres and particle asphericity. Scanning electron microscope photographs have confirmed similar variations in sphericity of the glass beads used herein, and this may also result in aberrant grain size determinations.

Our justification for imposing strict grain size limits upon the PDA-measured experimental distributions is based on the fact that the "fluid" seed distributions do not overlap with the sieved size distributions of the sediment grains: the overlap region measured by the PDA may therefore be filtered from the signal. Proof of the validity of this approach with respect to the velocity statistics of the measured grain size limits is shown in Fig. 3. This plot shows the vertical velocity moments for the medium size particles (180–210 μm) as a function of distance away from the grid at an oscillation frequency of 3.4 Hz but for *differing* imposed grain size limits for this one sediment mixture. It is unmistakable that the moments do not differ significantly with the varying grain size limits imposed. In addition, since data sampling rates were commonly much greater than 400 Hz for a period of 300 seconds, the statistical implications of reducing the sample size by up to 50–75 percent are considered negligible. Thus, in the following sections all of the particles are filtered under the following inclusive constraints: 0–30 μm for the fluid, 75–95 μm for the fine sediment, 180–210 μm for the medium sediment, and 300–355 μm for the coarse sediment.

3.3 Defining the Zero Concentration Limit. As demonstrated above, for a specific sediment population a range of grain sizes are determined by PDA. Since we need to focus on true sediment signals, a measure of zero sediment concentration

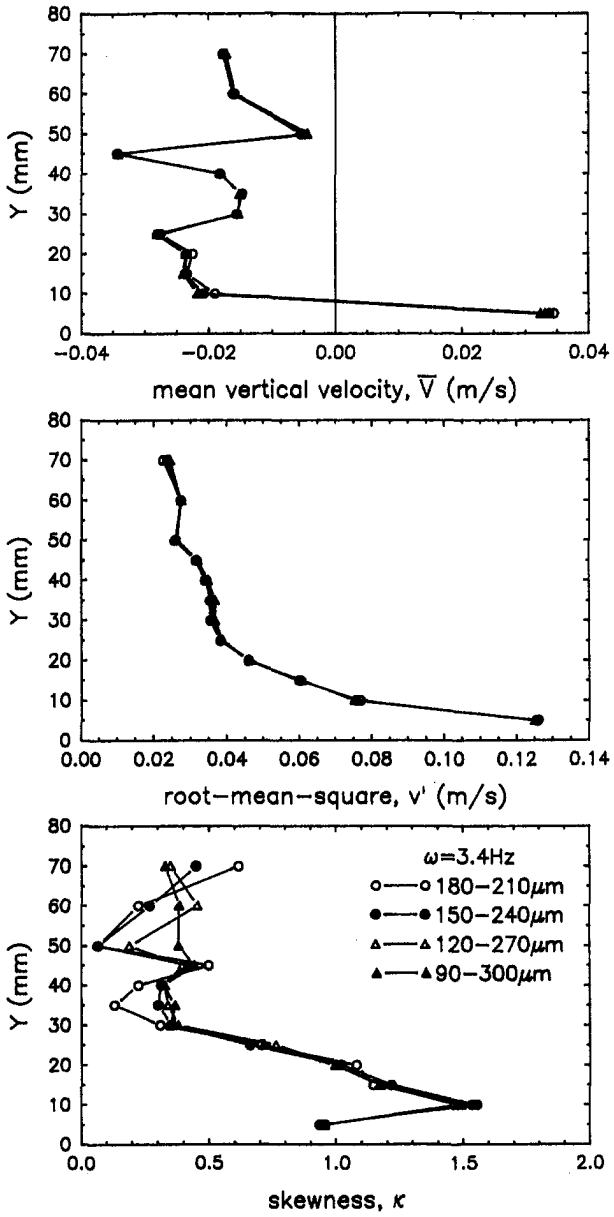

Fig. 3 The variation with height above the grid of the vertical velocity moments determined for the 180–210 μm sediment population as a function of varying grain size range limits. The grid oscillation frequency is 3.4 Hz

must be defined below which it can be assumed no sediment signals were observed. In order to derive this limit, plots of volumetric suspended sediment flux (defined in Eq. (4)) as a function of height away from the grid and oscillation frequency are shown in Fig. 4. In each case, the signature of the sediment flux for the lowest oscillation frequency defines a zero sediment concentration since no sediment was observed in suspension under these conditions. The maximum height (Y_{max}) at which each sediment population is suspended within the flow is also determined from this figure. Therefore, the two limits imposed upon the raw sediment size and velocity data are: (1) the grain size limits of the fluid and the sediment within the box; and (2) the height at which sediment flux goes to zero. In the following sections, these limits are imposed and the vertical velocity moments are calculated and compared accordingly.

3.4 Characteristics of Sediment Concentration as a Function of Oscillation Frequency. Although the sediment mass flux observed by the PDA can depend on the burst validation levels and optical set-up, the sediment flux measured in these low-concentration flows increases at higher oscillation frequencies (Fig. 4). These results agree with visual observations of increased suspended sediment at higher grid oscillations. These data can also be used to determine relative changes in sediment flux as a function of the magnitude of grid-generated turbulence.

The form of the observed suspended sediment flux profiles is the result of both the magnitude of the grid-generated turbulence and the sediment supply. In most geophysical flows, sediment flux decreases exponentially from the base of the flow toward the free-water surface (e.g., Allen, 1985, p. 126). However, it is apparent from the present curves, especially for the fine sediment experiments, that sediment flux can reach a maximum well above the grid, and decrease either asymptotically or log-linearly with increased distance from the grid. As noted earlier, it is the energetic jets located at the bar centers which are responsible for the majority of fluid (hence sediment) transport from the base of the box (e.g., Thompson and Turner, 1975; McDougall, 1979; Nokes, 1988). Because the energy of these jets decreases with increased height above the grid, sediment is transported up into the flow and dissipates sideways, resulting in high sediment fluxes away from the base of the box (Fig. 4). Additionally, the height at which the maximum

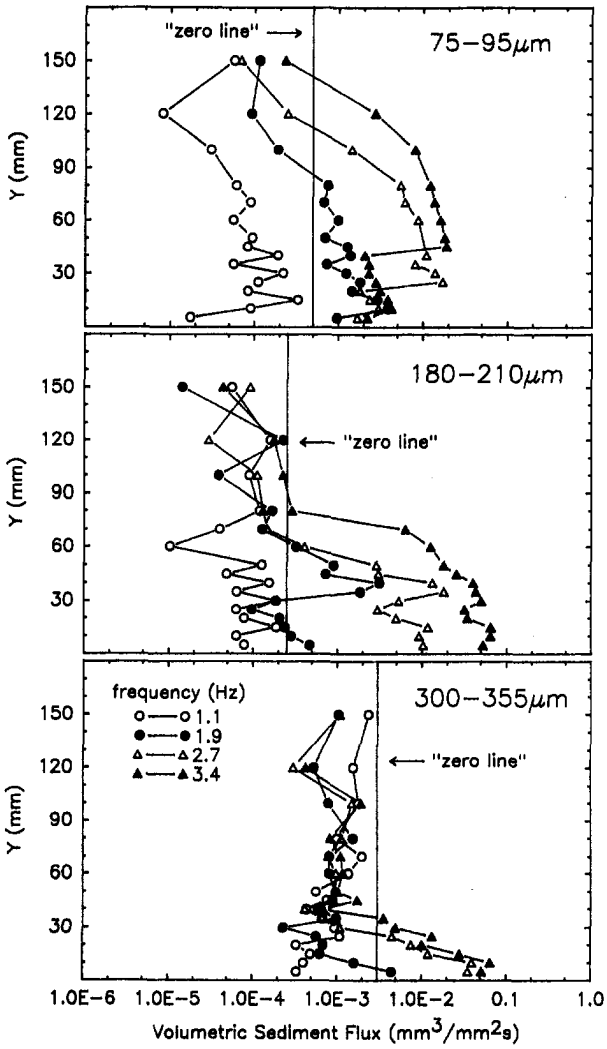

Fig. 4 The variation with height above the grid of the suspended sediment flux (q_s) for the 75–95 μm, 180–210 μm and 300–355 μm sediment populations as a function of oscillation frequency. The "zero line" defines the zero sediment flux criterion

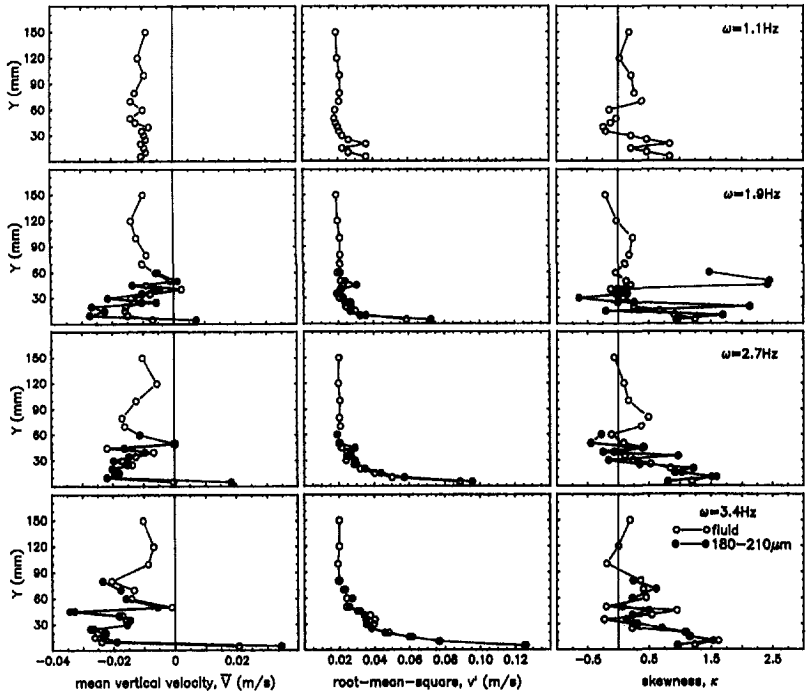

Fig. 5 The variation with height above the grid of the mean ($\bar{V}$; m/s), root-mean-square (v'; m/s) and skewness (κ) of the vertical velocity for both the fluid and 180–210 μm sediment population as a function of oscillation frequency

sediment flux occurs increases at higher oscillation frequencies. As noted by Noh and Fernando (1991), the overall shape of the suspended sediment concentration profile in a mixing box is a function of the propagation of turbulent energy away from the boundary and the upward diffusion of the suspended sediment. The experiments for the fine sediment distribution at the highest frequencies used were supply limited since no sediment was observed on the base of the box and relatively lower sediment fluxes were measured near the base (Fig. 4).

3.5 Variations in Vertical Velocity Moments of the Fluid and the Sediment. The first three moments of the vertical velocity distribution for both the fluid and the 180–210 μm sediment are shown in Fig. 5 for each oscillation frequency. At the lowest oscillation frequency negative mean velocity values, $\bar{V}$ (Fig. 5), illustrate the position of the measurement volume to one side of the weak ascending vertical jets and depict a zone of return flow towards the base of the box. However, increasingly positive vertical velocities near the grid at higher oscillation frequencies reflect the higher magnitude jets which penetrate further laterally and upwards into the flow and suspend sediment to greater heights (Fig. 4). The mean vertical velocity of the sediment differs little from that of the fluid, and the height attained by sediment grains within the box is directly proportional to the oscillation frequency.

Similarly, the root-mean-square of the vertical velocity, v', of both the sediment and fluid increases with grid oscillation frequency (Figs. 5 and 6), with maximum values (~0.12 m/s) occurring closest to the grid and minimum values (~0.02 m/s) occurring well up into the flow. The value of v' decreases exponentially away from the grid, with the fine sediment experiments exhibiting the slowest rate of decay of fluid v' and the coarse sediment experiments exhibiting the fastest rate of decay (Fig. 6). This may reflect the influence of the larger mass and grain size of the 300–355 μm sediment population in reducing the rms values and extracting energy from the fluid, thus acting to suppress the grid-generated turbulence.

The skewness values for vertical fluid and sediment velocities (Fig. 5; also observed using the other sediment populations) become increasingly more positive near the grid as oscillation frequency increases. Skewness values decrease away from the grid at all frequencies, tending towards a non-skewed vertical velocity distribution well into the flow.

The vertical velocity moments of the fluid and sediment particles near the grid show that with increasing grid oscillation frequency, $\bar{V}$ and κ become positive while v' increases substantially. Irrespective of oscillation frequency and grain size, the vertical velocity moments determined for the sediment are very similar to those determined for the fluid. However, the fine sediment population more closely parallels that of the fluid because: (1) the fine sediment has a relatively lower settling velocity, such that its drift velocity is more comparable to that of the fluid (see Noh and Fernando, 1991); and (2) the greater volume and mass of the larger particles extract more energy from the flow (i.e., suppress turbulence).

3.6 Implications for the Suspension of Sediment. The data presented herein have important implications to the study of the physical processes controlling sediment suspension in turbulent flows. These include the dependence of sediment suspension on the magnitude and anisotropy of the turbulent vertical velocity and the suppression of turbulence by the suspension of sediment.

The maximum height attained by suspended sediment within the mixing box for a particular frequency is determined from Fig. 4. This maximum height, Y_{max}, normalised by the effective depth (d) is plotted against the ratio of the maximum root-mean-square vertical velocity (v_b'; at Y = 5 mm) normalised by the grain's settling velocity (V_S; determined using Dietrich's (1982) equation for spheres; Fig. 7). The empirical relation determined for these data has the form:

$$\frac{Y_{max}}{d} = -0.021 + 0.429\left[\log_{10}\frac{v_b'}{V_S}\right] \quad (5)$$

with a correlation coefficient of 0.97. As expected, as more energy is expended upon the sediment grains (in the form of v_b'), the sediment attains greater heights within the box. Simi-

larly, the relative sediment concentration observed by the PDA increases as the local turbulent vertical velocities (v') increase toward the grid (see Figs. 4–6).

The anisotropy of vertical turbulence, whereby a mean upward-directed stress is exerted upon the sediment within the flow, has been suggested as a necessary mechanism for the maintenance of a suspended load (e.g., Bagnold, 1966, 1978; Leeder, 1983; Wei and Willmarth, 1991). This net upward-directed momentum flux may be expressed by the positive skewness of the instantaneous vertical velocity distribution. These vertical velocity distributions (Fig. 5) illustrate a marked positive skewness near the grid and an upwards decline in the flow. Although the location of the measurement volume with respect to the grid determines the exact velocity distribution, these positive skewness values are associated with positive, upward-moving sediment particles very near the grid (see Fig. 6). Similar

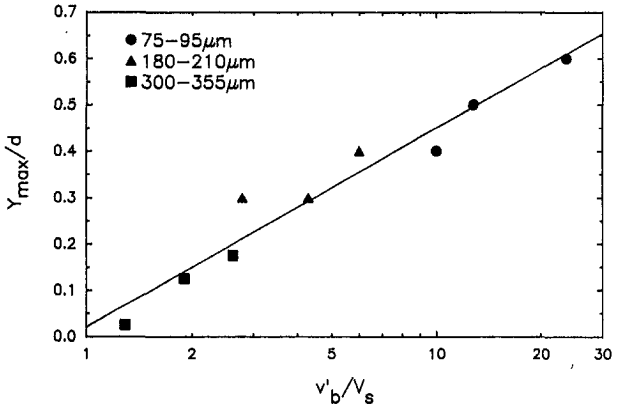

Fig. 7 The variation in the value of Y_{max}/d for all sediment populations as a function of v'_b/V_s. The values of Y_{max} were determined from Fig. 4

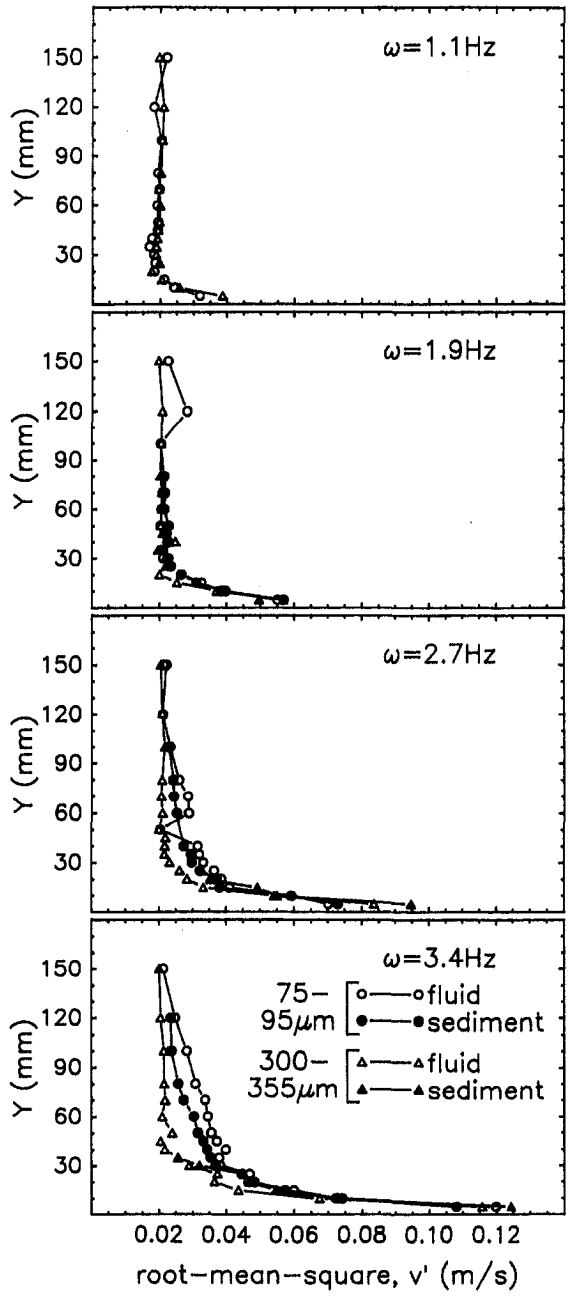

Fig. 6 The variation with height above the grid of the root-mean-square of the vertical velocity (v'; m/s) for both the fluid and 75–95 μm and 300–355 μm sediment populations as a function of oscillation frequency

flow asymmetry was reported by McDougall (1979) who observed that the upward motion of the grid transfers more energy to the flow than does the downward motion of the oscillation cycle. In addition, these increased skewness values are associated with greater sediment concentrations and increased heights attained by the sediment within the box (Fig. 4).

Finally, the greatest rate of decay in the turbulent vertical fluid velocity is shown to occur in the presence of the coarsest sediment population, which also has the greatest total sediment concentration in the box. This suggests that turbulence generated by the grid may be suppressed by the movement and suspension of these larger and more massive grains for the scale of turbulence in relation to particle size present in these experiments. These results are in agreement with several studies documenting turbulence suppression in the presence of appreciable near-bed sediment concentrations (see discussions in Coleman, 1981; Gust, 1984; Parker and Coleman, 1986).

4 Conclusions

Experiments have demonstrated the applicability of phase Doppler anemometry for investigating the dynamic relationships between the suspension of sediment and the characteristics of the turbulence field. Sediment suspension, which requires a net upwards-directed vertical velocity component, has been shown to be associated with high mean vertical velocities, high rms values and a positive skewness in the distribution of vertical fluid velocities near an oscillating grid. For a given grain size, as distance from the grid increases or as grid oscillation frequency decreases, both the fluid vertical turbulence intensity and skewness, together with the size and total sediment maintained in suspension, decrease. These results validate, in a simplified experimental configuration, Bagnold's (1966, 1978) suggestion that turbulence anisotropy is required to maintain a suspended load. Phase Doppler anemometry offers a unique and potentially powerful tool for investigating the complex links between the characteristics of the flow field and the sediment grains in transport.

Acknowledgments

This work has been funded by Natural Environment Research Council grant GR3/8235. JLB gratefully acknowledges award of a Nuffield Foundation Science Fellowship which aided completion of this paper. We wish to thank Phil Fields and Neil Woodhouse for providing technical assistance during these experiments and Graham Hassall and Robert Jaryczewski of DANTEC, Bristol, for providing assistance and advice during the installation of the PDA system. We are grateful to Herbert Huppert and Paul Linden at the University of Cambridge for use of the mixing box and to Charlotte Gladstone, University

of Bristol, for performing the Elzone grain size analysis. Mike Leeder and Henry Pantin are thanked for their constructive comments on an earlier version of the manuscript.

References

Allen, J. R. L., 1985, *Principles of Physical Sedimentology,* Allen and Unwin, London.

Bachalo, W. D., 1994, "Experimental Methods in Multiphase Flows," *International Journal of Multiphase Flow,* Vol. 20, Suppl., pp. 261–295.

Bachalo, W. D., and Houser, M. J., 1984, "Phase/Doppler Spray Analyzer for Simultaneous Measurements of Drop Size and Velocity Distributions," *Optical Engineering,* Vol. 23, pp. 583–590.

Bagnold, R. A., 1966, "An Approach to the Sediment Transport Problem from General Physics," United States Geological Survey Professional Paper 422-I.

Bagnold, R. A., 1978, "Sediment Transport by Wind and Water," *Nordic Hydrology,* Vol. 10, pp. 309–322.

Buchhave, P., 1987, "A New Instrument for the Simultaneous Measurement of Size and Velocity of Spherical Particles Based on the Laser Doppler Method," *Particulate and Multiphase Processes, Vol. 2: Contamination Analysis and Control,* T. Ariman and T. N. Veziroglu, eds., Hemisphere Publ., New York, pp. 55–67.

Cioffi, F., and Gallerano, F., 1991, "Velocity and Concentration Profiles of Solid Particles in a Channel with Movable and Erodible Bed," *Journal of Hydraulic Research,* Vol. 29, pp. 387–401.

Coleman, N. L., 1981, "Velocity Profiles with Suspended Sediment," *Journal of Hydraulic Research,* Vol. 19, pp. 211–229.

Dietrich, W. E., 1982, "Settling Velocities of Natural Particles," *Water Resources Research,* Vol. 18, pp. 1615–1626.

Fernando, H. J. S., 1991, "Turbulent Mixing in Stratified Fluids," *Annual Review of Fluid Mechanics,* Vol. 23, pp. 455–493.

Gould, R. D., and Loseke, K. W., 1993, "A Comparison of Four Velocity Bias Correction Techniques in Laser Doppler Velocimetry," ASME JOURNAL OF FLUIDS ENGINEERING, Vol. 115, pp. 508–514.

Gust, G., 1984, "Velocity Profiles with Suspended Sediment: Discussion," *Journal of Hydraulic Research,* Vol. 22, pp. 263–290.

Hardalupas, Y., Taylor, A. M. K. P., and Whitelaw, J. H., 1988, "Measurements in Heavily-Laden Dusty Jets with Phase-Doppler Anemometry," *Transport Phenomena in Turbulent Flows: Theory, Experiment and Numerical Simulation,* M. Hirata and N. Kasagi, eds., Hemisphere Publ., New York, pp. 821–835.

Huppert, H. E., Turner, J. S., and Hallworth, M. A., 1993, "Sedimentation and Mixing of a Turbulent Fluid Suspension: A Laboratory Study," *Earth and Planetary Science Letters,* Vol. 114, pp. 259–267.

Leeder, M. R., 1983, "On the Dynamics of Sediment Suspension by Residual Reynolds Stresses—Confirmation of Bagnold's Theory," *Sedimentology,* Vol. 30, pp. 485–491.

McDougall, T. J., 1979, "Measurements of Turbulence in a Zero-Mean-Shear Mixed Layer," *Journal of Fluid Mechanics,* Vol. 94, pp. 409–431.

Noh, Y., and Fernando, H. J. S., 1991, "Dispersion of Suspended Particles in Turbulent Flow," *Physics of Fluids A,* Vol. 3, pp. 1730–1740.

Nokes, R. I., 1988, "On the Entrainment Rate Across a Density Interface," *Journal of Fluid Mechanics,* Vol. 188, pp. 185–204.

Parker, G., and Coleman, N. L., 1986, "Simple Model of Sediment-Laden Flows," *Journal of Hydraulic Engineering,* Vol. 112, pp. 356–375.

Saffman, M., Buchhave, P., and Tanger, H., 1984, "Simultaneous Measurement of Size, Concentration and Velocity of Spherical Particles by a Laser Doppler Method," *Proceedings 2nd International Symposium on Applications of Laser Anemometry to Fluid Mechanics,* Lisbon.

Saffman, M., Fraidl, G. K., and Wigley, G., 1988, "Application of Phase and Laser Doppler Anemometry to the Measurement of Droplet Size and Velocity in Gasoline and Diesel Fuel Injection Systems," *Proceedings 4th International Symposium on Applications of Laser Anemometry to Fluid Mechanics,* Lisbon.

Tanger, H., and Weitendorf, E. A., 1992, "Applicability Tests for the Phase Doppler Anemometer for Cavitation Nuclei Measurements," ASME JOURNAL OF FLUIDS ENGINEERING, Vol. 114, pp. 443–449.

Thompson, S. M., and Turner, J. S., 1975, "Mixing Across an Interface due to Turbulence Generated by an Oscillating Grid," *Journal of Fluid Mechanics,* Vol. 67, pp. 349–368.

Turner, J. S., 1968, "The Influence of Molecular Diffusivity on Turbulent Entrainment Across a Density Interface," *Journal of Fluid Mechanics,* Vol. 33, pp. 639–656.

Turner, J. S., 1986, "Turbulent Entrainment: The Development of the Entrainment Assumption, and its Application to Geophysical Flows," *Journal of Fluid Mechanics,* Vol. 173, pp. 431–471.

Wei, T., and Willmarth, W. W., 1991, "Examination of V-Velocity Fluctuations in a Turbulent Channel Flow in the Context of Sediment Transport," *Journal of Fluid Mechanics,* Vol. 223, pp. 241–252.

Developing Lengths in Horizontal Two-Phase Bubbly Flow

B. A. Warren[1]

J. F. Klausner

Department of Mechanical Engineering,
University of Florida,
Gainesville, FL 32611

An air-water two-phase flow facility with a 19.1 mm i.d. test section has been fabricated. Local measurements of pressure drop for two-phase horizontal bubbly flow and single-phase flow downstream of various orifices have been obtained over a range of flow conditions. The wall shear stress developing length is obtained from the pressure drop profile. A developing length correlation is presented in which the relative deviation is 6 percent. The fully developed vapor volume fraction has also been measured up- and downstream of the orifice. A simple correlation for vapor volume fraction is presented in which the relative deviation is 7 percent. Photographs of the two-phase flow pattern in the developing region reveal that the flow structure is extremely complex and continuously evolves until approximately fully developed flow conditions are achieved.

Introduction

Two-phase bubbly flows are utilized in many industrial processes. A number of obstructions to the flow path are common to industrial piping systems, including valves, spacers, pipe fittings, and orifice plates. These peripheral obstructions may have a significant impact on the hydrodynamic structure of the flow. Obstructions typically accelerate the flow, increase pressure losses, enhance heat transfer, and alter the volume fraction. In order to assist in the design of such systems, there exists a need to better understand the hydrodynamic characteristics of a two-phase mixture downstream of a peripheral obstruction. The two-phase pressure drop across a peripheral obstruction has been studied extensively, and many suitable correlations have been developed for its prediction. In contrast, the developing region downstream of an obstruction has received far less attention from investigators. In particular, no correlations are currently available for predicting the two-phase developing length, nor have the important nondimensional parameters which characterize the two-phase developing region been identified. Knowledge of the pressure drop in the developing region and the corresponding developing length are relevant to the accurate prediction of the thermodynamic performance of HVAC equipment utilizing two-phase flow, pressure loss in condensate return lines, pressure drop of petroleum liquids and their vapors in tube stills, among others. In addition, experimentalists measuring pressure drop and vapor volume fraction simultaneously, using the quick closing valve technique (Klausner et al., 1990), need to be concerned with the proximity the valves are placed with respect to the pressure taps in order to avoid bias due to the disturbance created by the valves.

Extensive experimental investigations of two-phase flow through obstructions with air/water mixtures were carried out by Salcudean et al. (1983a, 1983b, 1983c) for horizontal flow and by Salcudean and Leung (1988) for vertical flow. Fully developed regions were observed far up- and downstream of an obstruction. Immediately before an obstruction the flow stagnates, and the pressure levels off. Across an obstruction there is a sudden pressure drop due to the acceleration and increased turbulence. The magnitude of the pressure drop depends on the position of the obstruction within the duct cross section. Downstream of an obstruction there exists a recovery region where the bulk turbulent intensity decays and the two-phase mixture decelerates. Based on visual observations Salcudean et al. (1983b) reported that the length affected by the flow obstruction is about 30 L/D for dispersed flow and 15 L/D for annular flow. The effect of area changes on a two-phase air/water mixture in a square, vertical channel was investigated by Tapucu et al. (1989). A slight decrease in vapor volume fraction was observed just upstream of the blockage, and a larger increase was observed downstream.

When discussing the hydrodynamic developing length in single-phase flow, typically three different developing lengths are referred to: wall shear stress, boundary layer, and velocity profile developing lengths. Because the velocity profile approaches its fully developed value close to the wall sooner than it does near the core, the wall shear stress developing length is always less than that for the boundary layer and velocity profile. Klein (1981) has given an excellent review of the developing region in turbulent pipe flow. Although the influence of inlet conditions are not yet fully understood, the wall shear stress for smooth entrances typically becomes fully developed in 8–15 pipe diameters. For turbulent flow in a 0.305 m i.d. pipe, Wang and Tullis (1974) found the wall shear stress developing length to be 15 pipe diameters. When a peripheral obstruction is placed at the pipe entrance, Sharan (1974) found that the turbulent structure of the single-phase developing region is different than that for smooth entrance flow. He attributed the difference to large eddies which form along the duct wall due to the obstruction. These large intensity eddies significantly influence the shape of the velocity profile but appear to have little effect on the velocity profile and boundary layer developing lengths.

The primary objective of this work is to experimentally investigate the developing region downstream of a symmetrical peripheral obstruction in two-phase bubbly flow. An air/water mixture in conjunction with a closed loop facility is used to carry through the experiments. Measurements of the pressure drop along the length of the 19.1 mm i.d. test section are used to identify the shear stress developing length over a range of flow conditions: mass flux, G = 1277 to 2126 kg/m^2-s; vapor quality, x = 0 to 0.0013; vapor volume fraction, α = 0 to 0.20; absolute static pressure, P = 124 to 222 kN/m^2 and area blockage ratio, A_f/A_c = 0.20 to 0.80, where A_f is the flow area of the orifice and A_c is the cross-sectional area of the test section. The nondimensional parameters which control the flow development are discussed, and a correlation for predicting the wall shear stress developing length is presented.

Experimental Facility

The two-phase air-water experimental facility used to measure the wall shear stress developing length is shown schemati-

[1] Currently at Westinghouse Electric Corp., Orlando, FL.

Contributed by the Fluids Engineering Division for publication in the JOURNAL OF FLUIDS ENGINEERING. Manuscript received by the Fluids Engineering Division December 27, 1993; revised manuscript received January 9, 1995. Associate Technical Editor: O. C. Jones.

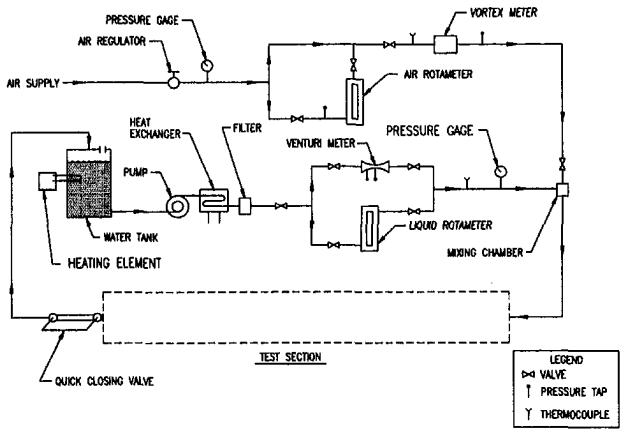

Fig. 1 Schematic diagram of air/water two-phase flow facility

cally in Fig. 1. A $\frac{1}{2}$ kW centrifugal pump provides a maximum liquid flow rate of 0.62 l/s. A resistance heater is used in conjunction with a counterflow heat exchanger to maintain the two-phase mixture at a constant temperature of 30°C. Measurements of the liquid flow rate were made with a venturi in conjunction with a Validyne DP-15 magnetic reluctance pressure transducer. The venturi meter was calibrated using a time-volume method, and based on the standard deviation of the calibration, it has an estimated uncertainty of ±1.6 percent of full scale. Air is supplied to the facility via a 2.1 m^3 compressed air tank. Air flow rates were measured with a rotameter in conjunction with a mercury manometer. The rotameter was calibrated against an Omega electronic mass flowmeter, and based on the standard deviation of the calibration, the rotameter is accurate to within ±1.1 percent of full scale. The air and water streams enter a mixing chamber where a two-phase mixture is produced.

The 19.1 mm i.d. circular test section is preceded by ninety diameters of straight pipe in order to insure fully developed inlet conditions. The test section, which is composed of two pressure tap sections, three capacitance based volume fraction sensors, and an orifice plate section, may be arranged in three different configurations as shown in Fig. 2. Configurations 1–3 are, respectively, used for volume fraction measurements, pressure drop measurements, and flow visualization. In Fig. 2 VFS, PT, and VS, respectively, denote the volume fraction sensors, pressure drop measuring sections, and the visualization sections. The capacitance technique was used to measure the vapor volume fraction. Helical capacitance sensors, which are based on the design of Abouelwafa and Kendall (1979), are located 68 diameters upstream of the orifice and 115 diameters downstream of the orifice. Presumably these sensors are located in the fully developed region. In an attempt to measure the axial variation of volume fraction in the developing region, four ring type capacitance based volume fraction sensors were placed immediately downstream of the orifice, but there remains doubt as to the reliability of their readings, and thus results from these measurements are not reported. The helical capacitance sensors which provided good results were calibrated using the quick closing valve facility. The capacitance across the helical sensors was measured with a Keithley 590 digital CV analyzer. The uncertainty of the volume fraction readings is estimated to be ±1.5 percent. The pressure tap sections were fabricated from 25.4 mm o.d. and a 19.1 mm mean i.d. brass pipe. 43 pressure tap holes, centered along the bottom of the pipe, are spaced at 50.8 mm increments along the length of the test section. The pressure tap diameter to tube diameter ratio is 0.1 and is within the recommendation of Shaw (1960). In order to explore the possibility of the pressure taps distorting the velocity profile, a pitot tube was used to measure the single-phase turbulent velocity profile of air inside the test section. The results were found to agree well with the $\frac{1}{7}$th power law, and it was concluded that the pressure taps do not significantly influence the flow structure. The pressure taps are interfaced with a Validyne DP-15 magnetic reluctance differential pressure transducer via a manifold system, which includes bleed valves for removing air from the pressure lines. Since the pressure taps are centered along the bottom of the test section, and a layer of liquid is maintained over the taps for the entire test duration, gravity prevents air bubbles from entering the pressure lines. The maximum uncertainty associated with the pressure transducer measurement is ±0.25 percent of 665 N/m^2 (±1.3 N/m^2). The visual test section was constructed from 19.0 mm i.d. and 25.4 mm o.d. clear acrylic tube. Six different orifice plates are available to vary the area blockage ratio from 0.20 to 0.80. The analog signals from the capacitance meter and all pressure transducers were recorded with a digital data acquisition facility.

Flow visualization was accomplished with a Videk Megaplus charged coupled device (CCD) camera. The output of the CCD camera is inputted to an Epix 4 megabyte frame grabber. The image may be saved to a computer diskette, displayed on a Sony analog monitor with 1000 lines per inch resolution, or printed out via a laser printer. Since the resolution of the laser printer image is low compared with the monitor, hard-copy images were obtained by photographing the monitor using 35 mm film.

Experimental Procedure

The experimental data were obtained in three stages. The vapor volume fraction measurements were obtained with the test section in configuration 1, and configurations 2, and 3 were used to, respectively, measure the axial variation of the local pressure drop and obtain photographs of the two-phase flow structure. The peripheral obstruction to the flow was created using orifices with area blockage ratios of: 0.20, 0.30, 0.40, 0.50, 0.70, and 0.80. Vapor volume fraction and pressure drop measurements were made for all six orifices using 22 different air-water flow rate combinations. The water flow rate ranged from 0.37 to 0.61 l/s while the air flow rate ranged from 0 to 13.5 l/min. The air-water flow rate combinations were chosen to maintain stable bubbly flow. The maximum vapor volume fraction was 20%.

Nomenclature

A_c = duct cross-sectional area (m^2)
A_b = bubble projected area (m^2)
A_t = orifice cross-sectional area (m^2)
C_d = bubble drag coefficient
D = duct diameter (m)
d_t = orifice diameter (m)
F_d = bubble drag force (N)
f_w = wall friction factor
G = total mass flux (kg/m^2-s)
$\dot{m}$ = mass flow rate (kg/s)
P = pressure (N/m^2)
ΔP = differential pressure (N/m^2)
r_b = bubble equivalent radius (m)
Re = Reynolds number
S = velocity slip
u = mean velocity (m/s)
x = vapor quality
z = axial coordinate (m)
z_{fd} = developing length (m)
α = vapor volume fraction
γ = density ratio, ρ_v/ρ_l
μ = dynamic viscosity (N-S/m^2)
ρ = density kg/m^3
τ_w = wall shear stress (N/m^2)

Subscripts

l = liquid
v = vapor

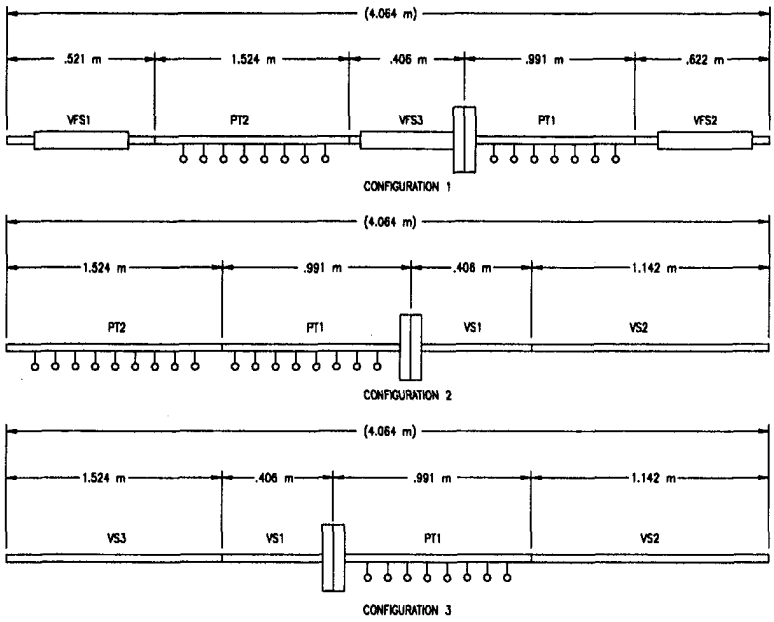

Fig. 2 Different test section configurations

Frictional pressure drop measurements for single phase flow without an orifice were made over an axial distance of 0.45 m for a liquid Reynolds number ranging from 20,000 to 50,000. The maximum error between the measured values and the predicted pressure drops using Blasius' friction factor formula and a mean pipe diameter of 19.1 mm was 4 percent. Thus the pressure drop measurement is believed to be accurate. However, due to manufacturing imperfections, the local pipe diameter along the length of the test section varies from 18.52 to 19.77 mm. Therefore, the measured local pressure drop over a 50.8 mm length can vary by as much as 18 percent over the length of the test section. In order to compare the measured pressure drops based on the same diameter the following procedure is used. According to Blasius' formula $\Delta P \sim D^{-19/4}$, where ΔP is the local pressure drop measured over a length of 50.8 mm and D is the local pipe diameter. The equivalent pressure drop at otherwise identical flow conditions, ΔP_{eq}, based on a mean pipe diameter, $\bar{D} = 19.1$ mm, is calculated from

$$\Delta P_{eq} = \Delta P \left(\frac{D}{\bar{D}}\right)^{19/4}. \quad (1)$$

ΔP_{eq} should be invariant along the length of the test section for single phase flow and when tested over a liquid Reynolds number range of 20,000 to 50,000, ΔP_{eq} was found to have an average variation of 2 percent. The validity of Blasius' friction factor formula for bubbly two-phase flow has yet to be rigorously demonstrated. Nevertheless, measurements for two-phase bubbly flow and no orifice show that ΔP_{eq} is essentially invariant along the test section length. Therefore, when determining the developing length past an orifice based on the axial variation of pressure drop, the comparison is made based on ΔP_{eq}. Extensive efforts were expended validating this procedure and further details are given in Warren (1992).

Experimental Results

Figures 3(*a*)–(*c*) show the two-phase flow structure downstream of an orifice with 50 percent flow blockage. The corresponding liquid Reynolds number, $\mathrm{Re}_l = [G(1-x)D/\mu_l(1-\alpha)]$, is 52,000, and the vapor volume fraction in the fully developed region is 0.09. Figure 3(*a*) corresponds to the region 0.5 to 4.5 pipe diameters downstream of the orifice. The air bubbles appear to be uniformly dispersed across the cross section. The bubbles are approximately spherical, and are small compared to the bubbles in the fully developed region (Fig. 3(*c*). 9 to 14 pipe diameters downstream of the orifice, Fig. 3(*b*) shows that the bubbles are still distributed throughout the test section. The observation that larger bubbles are migrating to the upper half of the test section is evidence of gravitational stratification. Since bubbles are agglomerating, they tend to be larger than those shown in Fig. 3(*a*). Figure 3(*c*) shows the two-phase flow structure in the fully developed region 69 to 72 diameters downstream of the orifice. Due to agglomeration the air bubbles are much larger than those seen in the developing region. Stratification of the two-phase mixture has forced all the bubbles into the upper half of the test section. Clearly, the bubbles are nonspherical and are inclined due to the wall shear. It has also been observed from other photographs that the mean bubble size in the fully developed region decreases with increasing liquid flow rate. The blockage area has virtually no effect on the flow structure in the fully developed region. Increasing the liquid flow rate, vapor volume fraction, or the blockage area enhances the degree of turbulent mixing immediately downstream of the orifice.

Figures 4(*a*)–(*d*) characterize the influence of the area blockage ratio and liquid Reynolds number on the pressure drop, and hence the developing length, downstream of the orifice. In Fig. 4(*a*) it is observed that for $\alpha = 0.09$ and $A_t/A_c = 0.80$, the pressure drop rises rapidly just downstream of the orifice and then gradually approaches a fully developed value. Such behavior is only observed for $A_t/A_c = 0.80$. In Fig. 4(*b*) it is seen that for $\alpha = 0.08$ and $A_t/A_c = 0.70$, the pressure drop downstream of the orifice rises rapidly until it reaches a peak and gradually decreases until the fully developed pressure drop is reached. Thus the pressure drop profile appears to have a "hump." Figures 4(*c*) and 4(*d*), in which the respective area blockage ratio's are 0.50 and 0.30, also display a hump in the pressure drop profile. Similar behavior was observed for all orifices tested in which $A_t/A_c < 0.80$. In Fig. 4(*a*) it is seen that the magnitude of the pressure drop increases with increasing liquid Reynolds number, which is expected. Although, the developing length appears to increase slightly with increasing Re_l, the increase is very marginal. In contrast, Figs. 4(*b*)–(*d*) show that although the developing length increases with increasing liquid Reynolds number, the position of the peak in the pressure drop profile is insensitive to liquid Reynolds

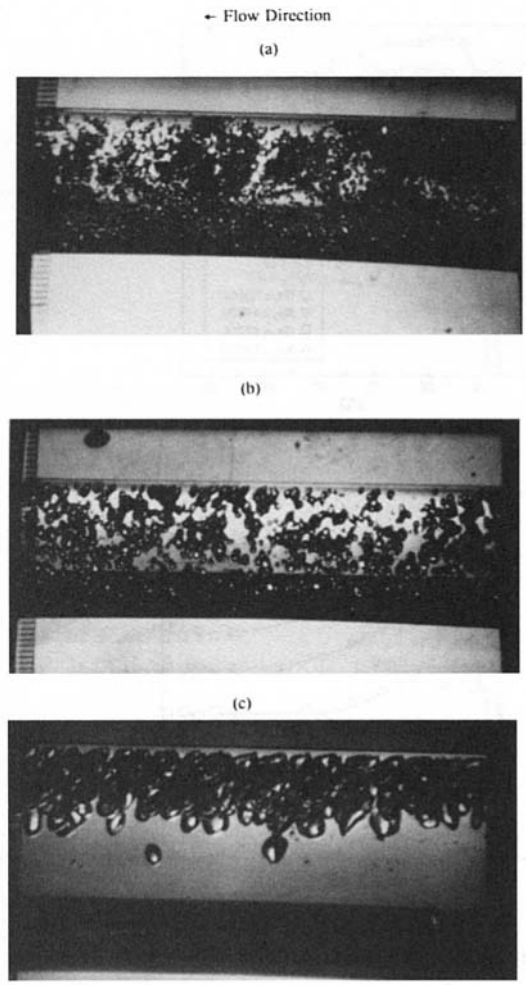

Fig. 3 Vapor bubble distribution downstream of the orifice; (a) 0.5 to 4.5 pipe diameters downstream, (b) 9 to 14 pipe diameters downstream, and (c) 69 to 72 pipe diameters downstream

number and the area blockage ratio. Comparison of Figs. 4(*b*)–(*d*) show a slight increase in developing length with decreasing A_t/A_c.

Figures 5(*a*)–(*d*) characterize the influence of the vapor volume fraction and area blockage ratio on the pressure drop profiles downstream of the orifice. The pressure drop profiles for single-phase liquid flow are also shown in Fig. 5(*a*). These profiles behave in a similar manner as those for two-phase bubbly flow. Thus it reasonable to expect that the mechanisms governing single-phase and two-phase bubbly flow wall shear stress development are the same. The vapor volume fraction does not appear to have a discernable influence on the developing length. However, in Figs. 5(*b*)–(*d*) it is seen that the pressure drop profiles display a hump, and the position of the peak increases with increasing volume fraction. Furthermore, the magnitude of the pressure drop as well as the developing length increases with increasing vapor volume fraction.

The precise determination of the end of the developing region based on visual observations of the above figures is not feasible. Therefore, for correlating purposes, consistent criteria are used for determining the developing length, z_{fd}. For the data in which the pressure drop profiles display a "hump," z_{fd} is taken to be the point past the peak at which $\Delta P_{eq} = 1.05\Delta P_{fd}$. For those data in which no "hump" is observed z_{fd} is taken to be the point at which $\Delta P_{eq} = \Delta P_{fd}$. These criteria allow the developing length to be determined with little ambiguity.

Although, the precise physical mechanism responsible for the hump in the pressure drop profiles is uncertain, the increase in pressure drop is clearly due to enhanced dissipation. For two-phase pipe flow, the location of the hump corresponds to the region where air bubbles are beginning to agglomerate and migrate towards the upper portion of the test section. It is likely that the dissipative processes associated with air agglomeration, the cross trajectory motion of the bubbles, and enhanced turbulence is responsible for the "hump." For single-phase flow, the hump is likely due to enhanced turbulence just downstream of the orifice.

Correlation of the Developing Length

The motion of the two-phase mixture in the developing region is extremely complex and precise analytical modelling of the flow structure does not, at this time, appear to be feasible. However, it is desired to deduce the dimensionless parameters which govern the developing length. Therefore, consideration is given to the control volume (CV) in Fig. 6 which corresponds to horizontal bubbly flow. For bubbly flow with low quality, $x \ll 1$, and low vapor volume fraction, $\alpha < 0.2$, it is expected that the liquid phase should have a dominating influence on momentum exchange in the developing region. A one-dimensional quasi-steady momentum balance on the CV liquid phase results in,

$$[P(z) - P(z + \Delta z)]A_l - \tau_w P_w \Delta z - F_d N = \dot{m}_l(z + \Delta z)u_l(z + \Delta z) - \dot{m}_l(z)u_l(z) \quad (2)$$

where P is pressure, A_l is the cross-sectional area occupied by the liquid, τ_w is the average wall shear stress around the periphery of the duct, P_w is the duct perimeter, F_d is the average drag on a single bubble, N is the number of bubbles in the control volume, $\dot{m}_l$ is the liquid mass flow rate, and u_l is the mean liquid velocity. Introducing the drag coefficient, $C_d = [F_d/\rho_l A_b(u_l - u_v)^2]$, and assuming the gas bubbles are spherical with radius r_b, the bubble drag term may be expressed as,

$$F_d N = \frac{3}{4} C_d \alpha A_c \frac{\Delta z}{r_b} \rho_l (u_l - u_v)^2, \quad (3)$$

where A_b is the projected area of a gas bubble and u_v is the mean velocity of the bubbles. Using Eq. (3) and the fact that $\dot{m}_l(z) = \dot{m}_l(z + \Delta z)$ for quasi-steady flow, Eq. (2) may be divided through by $A_c\Delta z$, and in the limit as $\Delta z \to 0$, (2) becomes

$$-(1 - \alpha)\frac{dP}{dz} = \frac{\tau_w S}{A_c} + \frac{3}{4}\frac{\alpha}{r_b} C_d \rho_l (u_l - u_v)^2 + G(1 - x)\frac{du_l}{dz}. \quad (4)$$

Using the following nondimensional parameters:

$$P^+ = \frac{P}{\rho_l u_{l0}^2} \quad f_w = \frac{\tau_w}{\rho_l u_{l0}^2} \quad z^+ = \frac{z}{D} \quad r_b^+ = \frac{r_b}{D} \quad \text{and} \quad u_l^+ = \frac{u_l}{u_{l0}}$$

Equation (4) may be recast in dimensionless form,

$$-\frac{dP^+}{dz^+} = \frac{4 f_w}{(1 - \alpha)} + \frac{3}{4}\frac{C_d}{r_b^+}\frac{\alpha}{(1 - \alpha)}\left(\frac{u_l}{u_{lf}}\right)^2\left(\frac{d_t}{D}\right)^4 (1 - S)^2 + \left(\frac{d_t}{D}\right)^2\left(\frac{u_l}{u_{lf}}\right)\frac{du_l^+}{dz^+}. \quad (5)$$

Here a circular duct cross-section has been assumed, f_w is the wall friction factor, $S = u_v/u_l$ is the velocity slip, and u_{l0} is a characteristic mean liquid velocity at the throat of the orifice and is defined by $u_{lo} = u_{lf}[(D/d_t)^2]$ where u_{lf} is the fully developed mean liquid velocity, d_t is the orifice diameter, and D is the pipe diameter. The first term on the right-hand side (rhs)

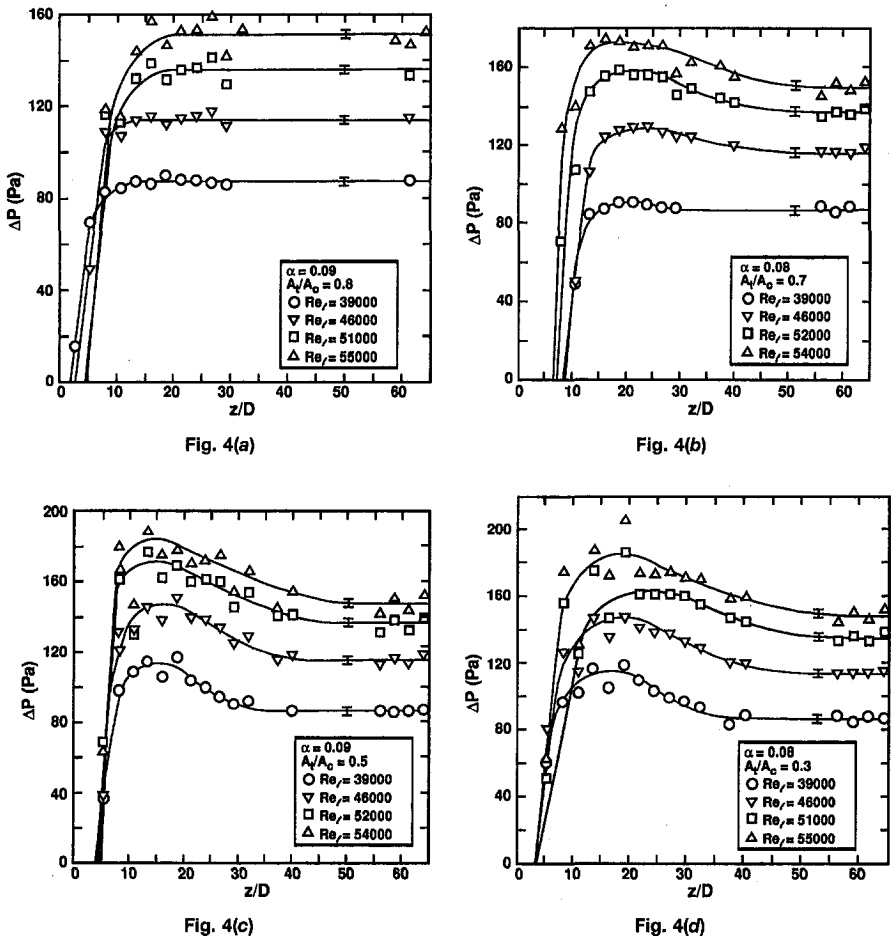

Fig. 4(a) Fig. 4(b) Fig. 4(c) Fig. 4(d)

Fig. 4 Pressure drop profiles for fixed volume fraction and different area blockages and Reynolds numbers

of Eq. (5) is the pressure gradient component due to wall friction; the second term is that due to the relative motion between the liquid and vapor phase; and the third term is the pressure gradient component due to the liquid acceleration. Due to the small inertia of the vapor bubbles compared with the liquid, it is expected that they will closely follow the surrounding liquid. Thus it is not unreasonable to believe that the wall friction and acceleration will control the pressure gradient. Using an analogy with single-phase flow, it is expected that f_w is primarily a function of the liquid Reynolds number, Re_l. Based on these considerations, it is hypothesized that the developing length is a function of Re_l, $(1 - \alpha)$, and (d_t/D).

As was mentioned earlier, the measured developing lengths for the pressure gradient profiles with a hump behaved significantly different than those without a hump. For those data with a hump, it was indeed observed that the ratio, z_{fd}/D, showed a dependence on Re_l, $(1 - \alpha)$, and (d_t/D). Here the vapor volume fraction for fully developed flow is used to evaluate α. Figure 7 shows z_{fd}/D as a function of the grouping $[\mathrm{Re}_l/(1 - \alpha)(d_t/D)^{1/4}]$. As is seen the data are surprisingly well collapsed, and for correlating purposes a linear fit to the data yields,

$$\frac{z_{fd}}{D} = 6.17 \times 10^{-4} \frac{\mathrm{Re}_l}{(1 - \alpha)\left(\frac{d_t}{D}\right)^{1/4}}. \tag{6}$$

The relative deviation of Eq. (6) is 5.6 percent. It is noted that single-phase flow data are also included in Fig. 7 and are simply treated as a special case where the vapor volume fraction is zero.

For those data without a "hump" the ratio, z_{fd}/D, ranged from 8 to 15 and showed a slight dependence on Re_l and virtually no dependence on $(1 - \alpha)$ or (d_t/D).

Vapor Volume Fraction

In order to use Eq. (6) for predicting the developing length, it is necessary to predict the fully developed vapor volume fraction. A number of volume fraction correlations were compared against the present data, but none were successful over the entire range of data considered. Therefore, a simple correlating scheme was attempted. Based on conservation of mass considerations, the local volume fraction may be expressed in terms of the quality, x, velocity slip, S, and the density ratio, $\gamma = \rho_v/\rho_l$ as

$$\alpha = \frac{x}{S\gamma + x(1 - S\gamma)}. \tag{7}$$

For a constant S, which may or may not hold over the range of flow conditions considered, Eq. (7) may be expanded in series form and averaged over the duct cross section,

$$\bar{\alpha} = \frac{1}{S}\overline{\left(\frac{x}{\gamma}\right)} - \frac{(1 - S\gamma)}{S^2}\overline{\left(\frac{x}{\gamma}\right)^2} + \frac{(1 - S\gamma)^2}{S^3}\overline{\left(\frac{x}{\gamma}\right)^3} - \ldots. \tag{8}$$

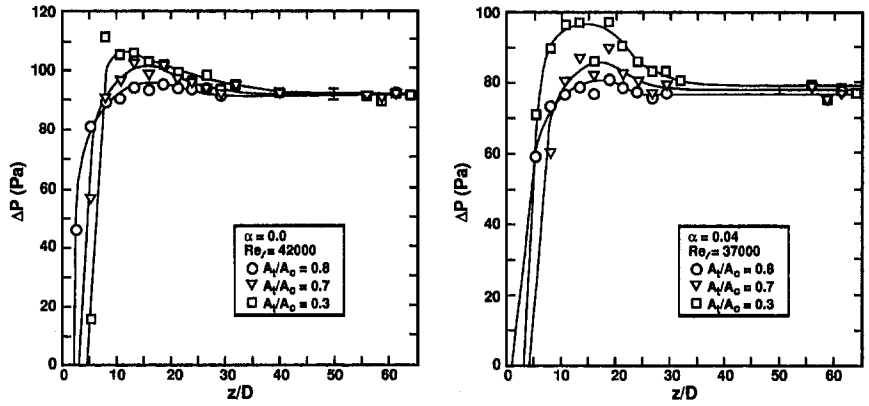

Fig. 5(b)

Fig. 5(c)

Fig. 5(d)

Fig. 5 Pressure drop profiles for different volume fractions and area blockages with Re$_l$ ranging from 37,000 to 58,000

where ($\bar{}$) denotes an area average. One concern with using Eq. (8) is that the area-averaged quality, $\bar{x} = [\dot{m}_v/(\dot{m}_v + \dot{m}_l)]$, is not identical to the measured quality, $x_{\text{meas}} = [\dot{m}_v/(\dot{m}_v + \dot{m}_l)]$. However, at low quality $\bar{x} \sim x_{\text{meas}}$. Since $(1 - S\gamma) \sim 1$, based on Eq. (8), it is expected that $\alpha = \alpha(x_{\text{meas}}/\gamma)$ for constant S. Fig. 8 shows α as a function x_{meas}/γ, and it is seen that to a good approximation, the data are well correlated by,

$$\bar{\alpha} = 0.37 \frac{x_{\text{meas}}}{\gamma}. \tag{9}$$

The relative deviation between the measured and predicted values of vapor volume fraction using Eq. (9) is 6.6 percent. It is not expected that the velocity slip remains constant, but the fact that Eq. (9) correlates the data well provides support that the slip did not vary appreciably over the range of data collected. Numerous studies have shown that a relationship such as Eq. (9) applies only over a limited range of flow conditions with a specific liquid-vapor pair. Therefore, Eq. (9) should not be used outside the range of flow conditions reported herein.

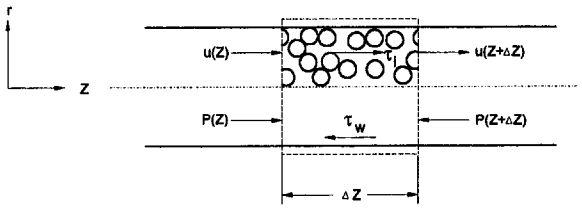

Fig. 6 Control volume for horizontal bubbly two-phase flow

Conclusions

In any two-phase flow encountered, there are a large number of variables which influence the observed hydrodynamics; therefore it is quite difficult to generalize experimental results. Nevertheless, for the flow conditions encountered in this investigation, the following observations have been made:

(i) It has been demonstrated that the wall shear stress developing length for horizontal two-phase bubbly flow and single-

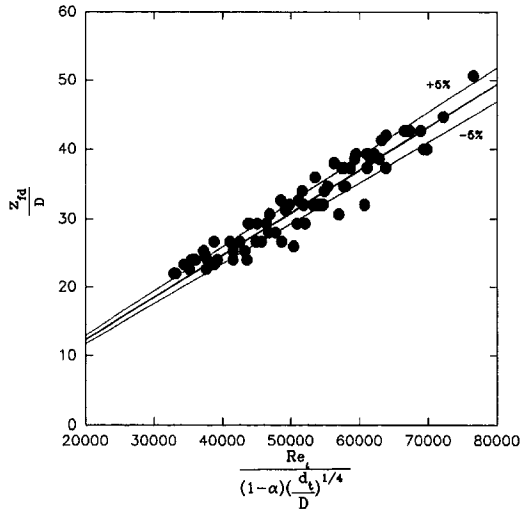

Fig. 7 Correlation for wall shear stress developing length past a peripheral obstruction

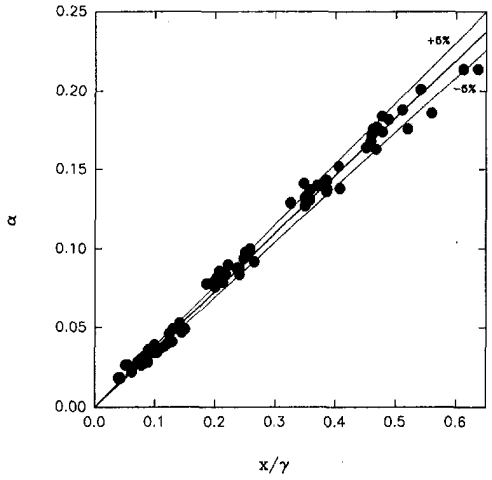

Fig. 8 Correlation of horizontal two-phase bubbly flow vapor volume fraction

phase flow downstream of an orifice is dependent on the area blockage ratio. For $A_t/A_c = 0.80$ it has been found that z_{fd}/D ranges from 8 to 15 and shows only a marginal dependence on α and Re_l. For $A_t/A_c < 0.80$ the developing lengths depends on α, Re_l, and d_t/D, and are well correlated by Eq. (6).

(ii) The pressure drop profiles for $A_t/A_c < 0.80$ display a hump for both single-phase and two-phase bubbly flow. The pressure drop profiles obtained in this study may serve as a benchmark for mechanistic two-phase flow computer codes. For two-phase bubbly flow past an orifice with $A_t/A_c < 0.80$, such codes should be able to capture the hump in the pressure drop profiles shown in Figs. 4 and 5.

(iii) The vapor volume fraction and flow structure in the fully developed region downstream of the orifice is typically not much different than that upstream of the orifice. However, the vapor volume fraction and flow structure changes significantly in the developing region. The fully developed vapor volume fraction is approximately a linear function of the vapor quality for the range of flow conditions considered.

References

Abouelwafa, M. S., and Kendall, E. J., 1979, "Analysis and Design of Helical Capacitance Sensors for Volume Fraction Determination," *Review of Scientific Instruments,* Vol. 50, No. 7, pp. 872–878.

Klausner, J. F., Chao, B. T., and Soo, S. L., 1990, "An Improved Method for Simultaneous Determination of Frictional Pressure Drop and Vapor Volume Fraction in Vertical Flow Boiling," *Experimental Thermal and Fluid Science,* Vol. 3, pp. 404–415.

Klein, A., 1981, "Review: Turbulent Developing Pipe Flow," ASME JOURNAL OF FLUIDS ENGINEERING, Vol. 103, pp. 243–249.

Salcudean, M., Groeneveld, D. C., and Leung, L., 1983a, "Effect of Flow-Obstruction Geometry on Pressure Drops in Horizontal Air-Water Flow," *International Journal of Multiphase Flow,* Vol. 9, No. 1, pp. 73–85.

Salcudean, M., Chun, J. H., and Groeneveld, D. C., 1983b, "Effect of Flow Obstructions on the Flow Pattern Transitions in Horizontal Two-Phase Flow," *International Journal of Multiphase Flow,* Vol. 9, No. 1, pp. 87–90.

Salcudean, M., Chun, J. H., and Groeneveld, D. C., 1983c, "Effect of Flow Obstruction on Void Distribution in Horizontal Air-Water Flow," *International Journal of Multiphase Flow,* Vol. 9, No. 1, pp. 91–96.

Salcudean, M., and Leung, L. K. H., 1988, "Two-Phase Pressure Drop Through Obstructions," *Nuclear Engineering and Design,* Vol. 105, pp. 349–361.

Sharan, V. K., 1974, "The Effect of Inlet Disturbances on Turbulent Boundary Layer Development in a Parallel Pipe," *Journal of Applied Mathematics and Physics,* Vol. 25, pp. 659–666.

Shaw, R., 1960, "The Influence of Hole Dimensions on Static Pressure Measurements," *Journal of Fluid Mechanics,* Vol. 7, pp. 550–564.

Tapucu, A., Teyssedou, A., Troche, N., and Merilo, M., 1989, "Pressure Losses Caused by Area Changes in a Single-Channel Flow Under Two-Phase Flow Conditions," *International Journal of Multiphase Flow,* Vol. 15, No. 1, pp. 51–64.

Wang, J. S., and Tullis, J. P., 1974, "Turbulent Flow in the Entry Region of a Rough Pipe," ASME JOURNAL OF FLUIDS ENGINEERING, Vol. 96, pp. 62–68.

M. Prat

P. Schmitz

Institut de Mecanique des Fluides de Toulouse,
Avenue du Professeur Camille Soula
31400 Toulouse, France

D. Poulikakos

Mechanical Engineering Department,
University of Illinois at Chicago,
842 W. Taylor Street,
Chicago, IL 60607

On the Effect of Surface Roughness on the Vapor Flow Under Leidenfrost-Levitated Droplets

In this paper a theoretical investigation is reported on the effect of surface roughness on the phenomenon of Leidenfrost-levitation of droplets above a hot surface. The problem is solved first approximately using a macroscopic approach in which the roughness is replaced by a semi-empirical slip condition of the Beavers-Joseph type. Next, a microscopic model which determines the vapor flow in the close vicinity of the rough surface is solved numerically. Three basic periodic roughnesses are examined: triangular, rectangular and semi-cylindrical. The effect of the relative size of the droplet and the roughness elements on the vapor flow is investigated in the course of the study.

1 Introduction

The problem of Leidenfrost boiling of liquid droplets on a hot surface has regained interest because of its relevance to several contemporary thermal engineering applications exemplified by spray cooling during the manufacturing of metal sheets and other products, spray cooling of electronic components, and droplet combustion in the vicinity of hot surfaces.

Most of the existing published work on the Leidenfrost boiling problem is focused on flat, smooth, impermeable surfaces or, more recently, permeable ceramic surfaces. To this end, Bell (1967) published a review of the early work on the Leidenfrost problem. Gottfried et al. (1966) studied the film boiling of liquid droplets on a smooth flat plate. Baumeister and Simon (1973) reported results for the Leidenfrost temperature of several types of liquids. More recently, Chandra and Avedisian (1991) reported an interesting study on the thermal interaction between a hot surface and an impinging droplet. Through high-speed photography and temperature measurements they obtained information on the collision dynamics and the bubble formation within the droplet for a wide range of surface temperatures. A companion study to the above for the case of a ceramic surface was also published by Chandra and Avedisian (1992).

The defining feature of the present study is that, unlike the works discussed above, it focuses on the effect of surface roughness on the fluid dynamics of the vapor layer supporting the levitated droplet. The study was inspired by two earlier papers on Leidenfrost boiling on porous (ceramic) surfaces. In the first paper, Avedisian and Koplik (1987) performed an experimental study on levitated boiling of methanol droplets on hot ceramic surfaces. In the context of their work, these authors presented a simple, one-dimensional model of the process, in which the Brinkman extension of the Darcy momentum equation was used. In the second paper, Fatehi and Kaviany (1990) argued that the Darcy flow model, together with the Beavers-Joseph interfacial condition should be used instead of the Brinkman-extended Darcy model to solve the problem. They then proceeded and performed a numerical study of the axisymmetric flow of vapor under a hemi-spherical droplet levitated above a ceramic surface.

Contributed by the Fluids Engineering Division for publication in the JOURNAL OF FLUIDS ENGINEERING. Manuscript received by the Fluids Engineering Division January 7, 1994; revised manuscript received October 31, 1994. Associate Technical Editor: Jong H. Kim.

What is apparent in the last two studies discussed above, is that surface roughness effects, neglected in both studies, may play an important role in the process of Leidenfrost boiling. This is true for both rough impermeable surfaces as well as ceramic surfaces where it is likely that the surface roughness will be of the order of magnitude of the porosity. The present study focuses on the determination of the effect of roughness on the fluid dynamics of Leidenfrost boiling of a droplet over an impermeable surface. Three basic roughnesses are examined utilizing an axisymmetric model: rectangular, triangular and semicylindrical. Two different approaches are adopted in the course of the investigation. The problem is first solved with an approximate macroscopic model. Next, the vapor flow field is determined with a microscopic model which reveals the flow details in the vicinity of the roughness elements. The validity of the macroscopic model is checked against the microscopic model. In the later, the flow field in the vapor region is determined by solving the Navier-Stokes equations around the roughness elements. In the former, the roughness is replaced by a slip condition of the Beavers-Joseph type. It is because of this fact that the microscopic model is expected to be the more accurate (and the more complex) of the two models. The effect of the roughness element size relative to the droplet size is also examined in the course of this study.

2 Mathematical Model

The problem under investigation is shown schematically in Fig. 1(*a*). A droplet is undergoing Leidenfrost boiling over a surface with an axisymmetric roughness. In a realistic application the presence of the roughness introduces three dimensional effects. Since this basic study is a first attempt at investigating the impact of the surface roughness on the already complex fluid dynamics of the vapor layer, three dimensional effects were neglected. In addition, the following assumptions are made following Fatehi and Kaviany (1990) as well as Avedisian and Koplick (1987): The boiling process is quasisteady, the droplet is hemispherical, the droplet is motionless and at saturation conditions, the vapor film is very thin (the heat transfer process within it is conduction-dominated) and, finally, the flow in the vapor film is laminar.

The three roughnesses to be studied (rectangular, triangular and semi-cylindrical) are shown in Fig. 1(*b*). The axisymmetric equations for the conservation of mass and momentum in the

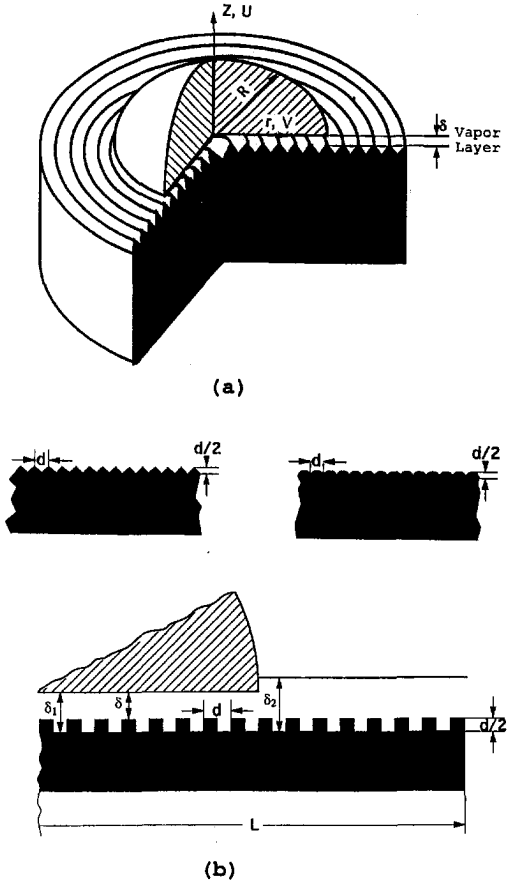

Fig. 1 (*a*) Schematic of the problem of interest, (*b*) definition of the basic roughnesses under investigation. Various symbols are defined in the rectangular roughness schematic.

vapor layer underneath the droplet with respect to the cylindrical coordinate system of Fig. 1 are:

$$\frac{1}{r}\frac{\partial(rv)}{\partial r} + \frac{\partial u}{\partial z} = 0 \tag{1}$$

$$\rho\left(\frac{1}{r}\frac{\partial(rv^2)}{\partial r} + \frac{\partial(uv)}{\partial z}\right) = -\frac{\partial P}{\partial r} + \mu\left(\frac{1}{r}\frac{\partial}{\partial r}\left[r\frac{\partial(v)}{\partial r}\right] - \frac{v}{r^2} + \frac{\partial^2 v}{\partial z^2}\right) \tag{2}$$

$$\rho\left(\frac{1}{r}\frac{\partial(ruv)}{\partial r} + \frac{\partial(u^2)}{\partial z}\right) = -\frac{\partial P}{\partial r} + \mu\left(\frac{1}{r}\frac{\partial}{\partial r}\left[r\frac{\partial(u)}{\partial r}\right] + \frac{\partial^2 u}{\partial z^2}\right) \tag{3}$$

All the symbols in the above equations are defined in the Nomenclature. To complete the model formulation the boundary conditions of the problem need to be stated:

On the rough surface:

$$u = v = 0 \tag{4}$$

At the axis of symmetry,

$$r = 0: \quad v = \frac{\partial u}{\partial r} = 0 \tag{5}$$

At the boiling interface the vapor velocity is assumed to be constant (quasi-steady evaporation) and the no-slip condition is imposed (Fatehi and Kaviany, 1990),

$$z = \delta_1: \quad v = 0, \quad u = -u_0 \tag{6, 7}$$

After flowing past the droplet periphery, the vapor layer experiences an expansion. To account for this expansion, we follow Fatehi and Kaviany (1990) and adopt the computational domain shown in Fig. 1(*b*). To this end, the following additional boundary conditions are required:

$$r = R, \delta < z < \delta_2: \quad u = v = 0$$

$$z = \delta_2, R < r < L: \quad u = \frac{\partial v}{\partial z} = 0$$

$$r = L, 0 < z < \delta_2: \quad u = 0, \quad \frac{\partial v}{\partial r} = 0 \tag{8–10}$$

The lengths L and δ_2 are selected after a trial and error process which insures that increasing these lengths further has no effect on the results. Note that L will take the role of "infinity" in the numerical scheme. In quasi-steady evaporation, the weight of the droplet is balanced by the force caused by the pressure field at the bottom of the droplet:

$$\int_0^R (P - P_0)2\pi r dr = W \tag{11}$$

The weight of the droplet, assuming that the vapor density is much smaller than the density of the liquid constituting the hemispherical droplet, is

$$W = \tfrac{2}{3}\pi\rho_l R^3 \tag{12}$$

Nomenclature

D = characteristic roughness size ($=d/2$)
d = length defining the roughness (Fig. 1)
g = gravitational acceleration
h_{lg} = latent heat of vaporization
k = thermal conductivity
k_l = liquid thermal conductivity
L = length of the computational domain
P = pressure
P_0 = environment pressure
Pe = Peclet number
R = droplet radius
r = radial coordinate
Re = Reynolds number
T = temperature
T_w = wall temperature
T_{sat} = saturation temperature
u = axial velocity
u_0 = axial velocity at the bottom of the droplet
v = radial velocity
W = droplet weight
z = axial coordinate

Greek Symbols

δ = vapor layer thickness, Fig. 1(*b*)
δ_1 = vapor layer thickness, Fig. 1(*b*)
δ_2 = vapor layer thickness, Fig. 1(*b*)
μ = vapor viscosity
ρ = vapor density
ρ_l = liquid density
σ = slip coefficient
τ_e = evaporation time scale
τ_f = flow time scale

Table 1 Values of the dimensionless slip coefficient

Roughness geometry	σ
triangular	6.5
rectangular	28.7
semicylindrical	11.8

The pressure field, needed in Eq. (11) is obtained by integrating Eq. (2) along the vaporization interface

$$P - P_0 = \mu \int_R^r \frac{\partial^2 v}{\partial z^2}\, dr + \rho u_0 \int_R^r \frac{\partial v}{\partial z}\, dr \qquad (13)$$

The vapor velocity at the vaporization interface (u_0) is estimated from:

$$u_0 = \frac{k(T_w - T_{sat})}{\rho h_{lg} \delta} \qquad (14)$$

where δ is the vapor layer thickness between the top of the roughness and the vaporization interface (Fig. 1(b)). Implicit in Eq. (14) is the assumption that the heat transfer in the vapor film is conduction dominated and the temperature distribution is linear. This assumption will be justified a posteriori in Section 5 where the calculated values of the Peclet number will clearly indicate that convection in the vapor film is negligible compared to conduction.

3 A Simple Macroscopic Model

The main premise of the macroscopic model is that the surface roughness is modeled as (and replaced by) a velocity slip condition of the Beavers-Joseph type (Beavers and Joseph, 1967) used commonly at interfaces between fluids and porous materials. In addition, the flow in the vapor layer is assumed to be radial. Based on these assumptions, the macroscopic flow model is:

$$\frac{d^2 v}{dz^2} = \frac{1}{r}\frac{dP}{dr} \qquad (15)$$

at

$$z = 0: \quad v = \frac{D}{\sigma}\frac{dv}{dz}, \quad u = 0$$

at

$$z = \delta: \quad v = 0, \quad u = -u_0 \qquad (16\text{–}19)$$

With reference to the types of roughness considered in the present study, numerical computations showed that the dependence of the slip coefficient, σ, on D/δ can be safely ignored here except for the triangular roughness. For this latter case, the influence of D/δ on σ has been taken into account. In the present macroscopic model, inertia effects are negligible. Hence, the values of the slip coefficient utilized herein are those corresponding to creeping flows. These values are reported in Table 1. The value associated with the triangular roughness is that corresponding to a channel sufficiently wide for σ to be independent of D/δ. The solution of the model is

Table 3 Accuracy test: vapor film thickness for various node arrangements normalized with respect to that for $N_r = N_z = 11$

N_r \ N_z	5	7	9	11
5			0.9913	
7			0.9962	0.9959
9	0.9962	0.9973	0.9981	0.9985
11		0.9989	0.9996	1.0

$$v = \frac{1}{\mu}\frac{dP}{dr}\left[\frac{1}{2}z^2 + Az + B\right] \qquad (20)$$

where

$$A = -\frac{1}{2}\delta^2 \Big/ \left[\delta + \frac{D}{\sigma}\right],$$

$$B = -\frac{D\delta^2}{2\sigma} \Big/ \left[\delta + \frac{D}{\sigma}\right] \qquad (21, 22)$$

In order to obtain the pressure field we express the mass flowrate in the vapor film as follows:

$$2\pi r \rho \frac{1}{\mu}\frac{dP}{dr}\int_0^\delta \left[\frac{1}{2}z^2 + Az + B\right]dz = \pi r^2 \rho u_0 \qquad (23)$$

where u_0 is obtained from Eq. (14). Combining Eqs. (14, 23) and integrating in r over the entire vaporization interface yields

$$P - P_0 = \frac{\mu u_0}{4\left(\frac{\delta^3}{6} + A\frac{\delta^2}{2} + B\delta\right)}(r^2 - R^2) \qquad (24)$$

Combining Eqs. (11), (12), and (24) results in an expression for the vapor layer thickness

$$\sigma\delta^5 + 4D\delta^4 - 12C(T_W - T_S)\sigma R\delta - 12C(T_W - T_S)DR = 0 \qquad (25)$$

where

$$C = \frac{3\mu k}{16 g(\rho_l - \rho)\rho h_{lg}} \qquad (26)$$

The vapor layer thickness results from solving numerically the nonlinear algebraic Eq. (25) for prescribed values of the various parameters and properties.

4 Solution of the Microscopic Model

The governing Eqs. (1)–(3) subject to the boundary conditions (4)–(10) were solved numerically using the finite element method. The discrete computational domain was divided into triangular elements. The velocity functions u and v were chosen to be quadratic in r and z due to the presence of second order partial derivatives in the governing equations. The pressure function P was taken to be linear in r and z. The Galerkin

Table 2 The final grids used in the finite element simulations

Roughness geometry	1 element	2 elements	3 elements	4 elements	5 elements	6 elements	7 elements
rectangular	97 × 81	169 × 71	253 × 71	289 × 61	361 × 61	361 × 51	421 × 51
semicylindrical	65 × 97	113 × 85	169 × 85	193 × 73	241 × 73	241 × 61	281 × 61
triangular	65 × 97	113 × 85	169 × 85	193 × 73	241 × 73	241 × 61	281 × 61

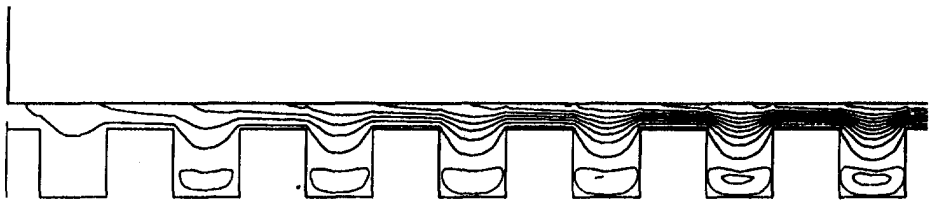

Fig. 2(*a*)

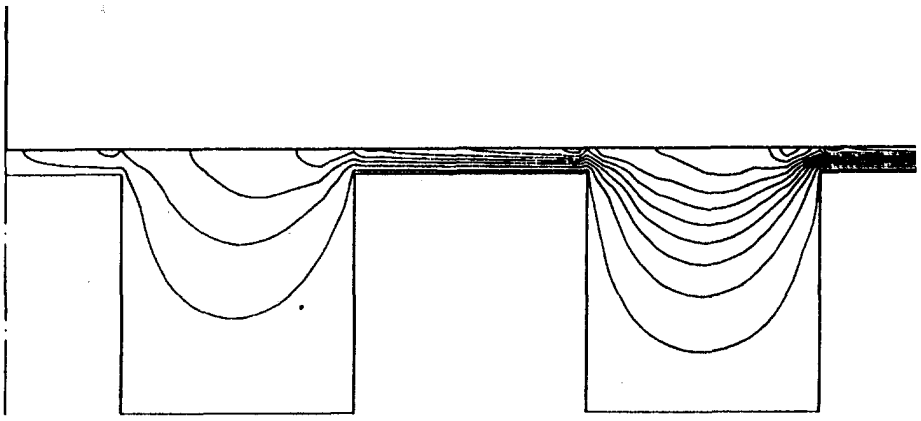

Fig. 2(*b*)

Fig. 2 Dimensionless streamlines illustrating the flow field in the case of the rectangular roughness. The values of the two streamlines in all recirculation regions are: −0.001 and −0.01. The values of the remaining streamlines from left to right starting with the solid wall are: 0.0, 0.01, 0.05, 0.1, 0.15, 0.2, 0.25, 0.3, 0.35, 0.4, 0.45, 0.5. (*a*) Seven roughness elements under the droplet, (*b*) two roughness elements under the droplet.

scheme was applied for the integration of the residue. The integrations on each element were performed using the Hammer direct integration technique on a triangle with 6 points. The final linear system was solved using the classical Gauss direct method.

The final grid fineness for each case considered corresponds to a maximum number of nodes in the r-direction and z-direction reported in Table 2. The standard convergence test, using progressively smaller grid sizes, has been performed. The final choice was a compromise between computational time require-

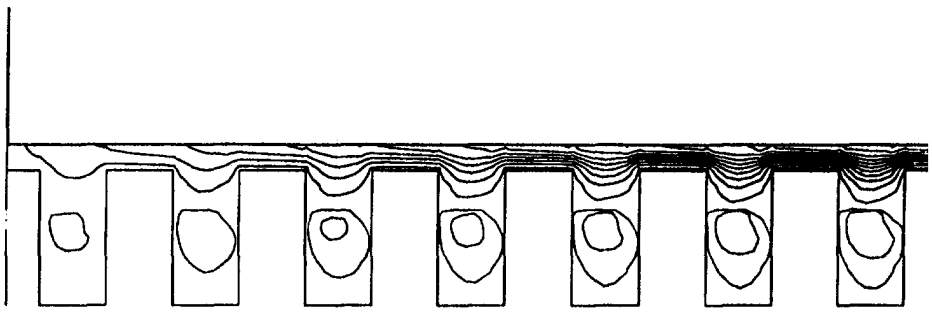

Fig. 3(*a*)

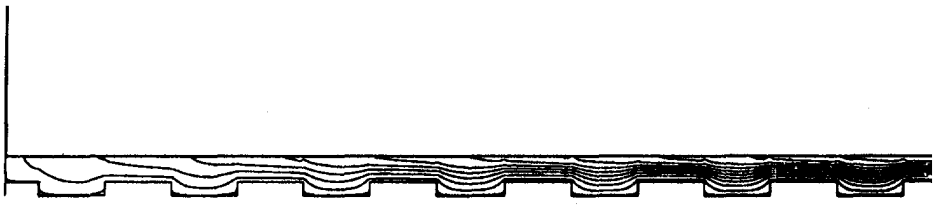

Fig. 3(*b*)

Fig. 3 The effect of the cavity depth on the flow field. (*a*) Cavity depth is twice the cavity length, (*b*) cavity depth is on fifth the cavity length. The values of the streamlines are identical to those in the caption of Fig. 2.

ment and precision. Using finer grids left the results practically unchanged (within one percent). Quantitative evidence of error testing is offered in Table 3 for the case of seven rectangular roughness elements under the droplet. Note that N_r and N_z denote the number of nodes per block in each cell in the radial and axial directions, respectively. Table 3 reports the results on the vapor layer thickness normalized with respect to the thickness corresponding to the finest grid ($N_r = N_z = 11$), which was used throughout this study. The difference in the vapor film thickness obtained between the node fineness used in the computations herein and other coarser arrangements in Table 3 is indeed negligible. For example, going from $N_r = 9$, $N_z = 7$ to $N_r = N_z = 11$ changes the vapor film thickness by less than 0.3 percent. Similar results were found in error tests performed in all the roughness geometries studied in this paper.

An iterative technique was used to obtain the final value of δ using successive corrections of u_0 combined with self-adjustment of the mesh to account for each value of δ corresponding to the corrected value of u_0 according to equation (14). Therefore u, v, and P were calculated at each step throughout the entire computational domain. In these calculations, the vapor film expansion length past the droplet periphery was chosen equal to R ($L = 2R$ in Fig. 1). The thickness of the expansion vapor film above the bottom of the droplet used in the calculations was equal to δ. More specifically, with reference to the rectangular roughness (Fig. 1) $\delta_2 = 2\delta + d/2$. This value of δ_2 was obtained after a trial and error process and it satisfies the criterion that no significant change in the results occurs for larger values of δ_2. In addition, the chosen value of δ_2 agrees with the analogous value of Fatehi and Kaviany (1990) for the case of Leidenfrost boiling over a porous surface. An underrelaxation coefficient equal to 0.5 was implemented to improve the convergence process on u_0. The convergence criterion adopted was 10^{-4} on the normalized value of δ between any two successive computations of the velocity and pressure fields.

5 Discussion of Results

Methanol was chosen as the example fluid for the numerical simulations after Avedisian and Koplik (1987) and Fatehi and Kaviany (1990). The relevant dimensions and thermophysical properties are defined as follows: $\rho = 0.74$ kg m^{-3}, $\rho_l = 773$ kg m^{-3}, $\mu = 204 \times 10^{-7}$ kg m^{-1} s^{-1}, $k = 3.33 \times 10^{-2}$ W m^{-1} K^{-1}, $h_{lg} = 1107.7$ KJ kg^{-1}, $T_{sat} = 337.7$ K, $T_w = 650$ K, $R_0 = 5 \times 10^{-3}$ m. The presentation of the results starts with the flow field over the square roughness shown in Figs. 2(a, b). Clearly, the effect of the roughness on the flow field is significant. Focusing on Fig. 2(a), it is immediately observed that the vapor flow penetrates inside each roughness cavity. A recirculation quickly develops at the bottom of each cavity. This recirculation becomes stronger as the flow moves outward and approaches the droplet periphery.

Upon exiting from underneath the droplet (not shown for brevity), the vapor flow expands. Interestingly, the recirculation pattern outside the area covered by the droplet exhibits little dependence on the radial distance. Also, the penetration of the parallel flow on top of the roughness elements inside the roughness cavities, is significantly less due to the absence of the phase change interface and the vaporization velocity in the axial direction in the region of the flow domain that is not covered by the droplet. Figure 2(b) illustrates the effect of the relative size of the droplet and the square roughness elements. As the droplet size decreases (two roughness elements are present underneath the droplet in Fig. 2(b), compared to seven roughness elements in Fig. 2(a) the recirculation inside the cavities in the region $0 < r < R$ disappears. On the other hand, the flow pattern in the region $R < r < L$ is little affected by the decrease in the droplet diameter relative to the roughness size. The flow penetration inside the cavities under the droplet is enhanced as the droplet diameter decreases (going from Fig. 2(a) to Fig. 2(b).

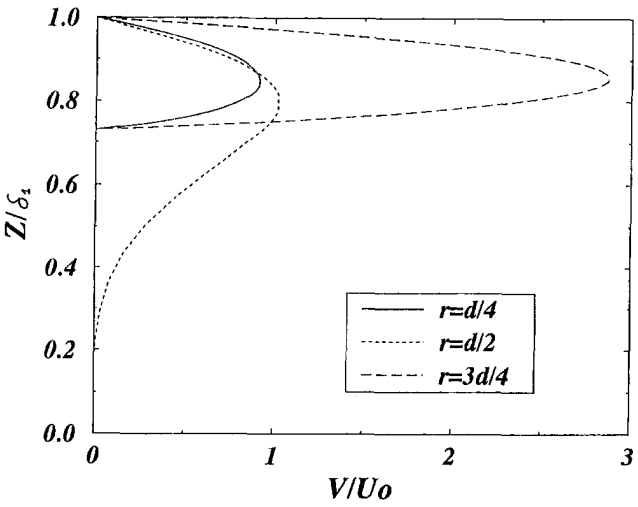

Fig. 4 Velocity profiles for the rectangular roughness case corresponding to Fig. 2(a) right before, at the center and right after the first cavity under the droplet.

As discussed earlier, the droplet was approximated with a hemisphere throughout this study. This approximation leads to the presence of a sharp corner in the location where the lateral surface meets the bottom of the droplet. However, in reality, surface tension rounds off this corner. One may even anticipate that surface tension imposes a related increase in the vapor layer thickness near the outer edge of the bottom region. To assess the importance of these facts additional numerical runs (not shown here due to space limitations) were performed guided by the droplet photographs reported by Avedisian and Koplik (1987). These simulations were performed for a configuration and a set of parameters that are identical to that of Fig. 2 with the exception that the droplet corners were rounded (the rounding was guided by the photographic evidence of Avedisian and Koplik (1987)). The results indicated that the presence of the round corners leaves the flow field practically unchanged. In addition, the calculated thickness of the vapor film δ/R_0 in Fig. 2(a) (sharp corner) was 0.0265 compared to 0.0262 for the identical case but with rounded corners. The above findings clearly indicate that neglecting the roundness of the edge at the bottom of the droplet does not seriously affect the results on the flow field, while it simplifies the modeling process.

The effect of the roughness depth on the flow field is shown in Figs. 3(a, b). Seven roughness elements are present in this case, much like in Fig. 2(a). However, the roughness elements are rectangular to illustrate the change in roughness depth. The depth of each cavity in Fig. 3(a) is twice that of Fig. 2(a). A stronger recirculation develops in the system immediately; it is present in the first cavity away from the centerline unlike in Fig. 2(a). The channel flow on top of the roughness penetrates less inside each cavity. No recirculation regions, for all practical purposes, are observed in the entire flow domain if the roughness size is reduced to one fifth that of Fig. 2(a), as shown in Fig. 3(b). Here, the presence of the roughness simply causes a downward bending of the streamlines over each cavity.

Figure 4 shows radial velocity profiles right before, at the center and right after the first cavity away from the centerline of the geometry in Fig. 2(a). We observe a significant acceleration of the flow as the gas moves downstream. More specifically, the maximum velocity right after the first cavity ($r = 3d/4$) is three times larger than the average velocity right before this cavity ($r = d/4$). The velocity profile at $r = d/2$ reflects the fact that the flow penetrates inside the cavity (a negligibly small recirculation existed in the cavity for $r = d/2$). In the velocity scales of Fig. 4 the negative velocities corresponding to this recirculation region are invisible.

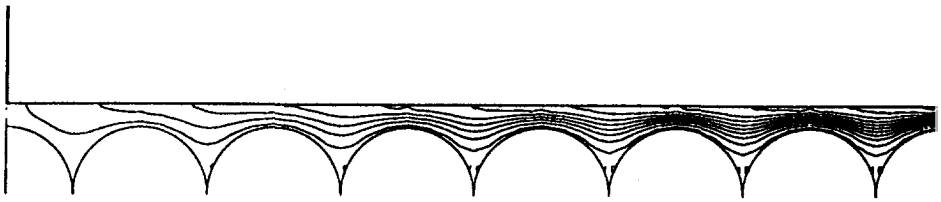

Fig. 5 Dimensionless streamlines illustrating the flow field in the case of the semi-cylindrical roughness. The values of the streamlines are identical to those in the caption of Fig. 2.

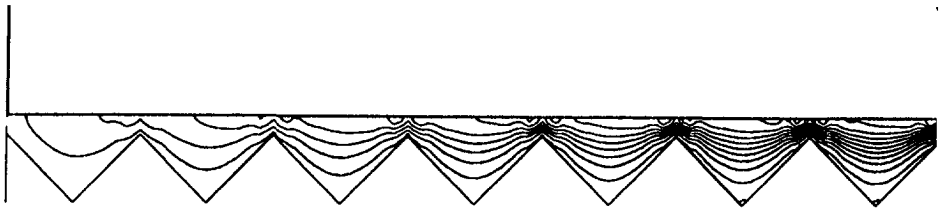

Fig. 6 Dimensionless streamlines illustrating the flow field in the case of the triangular roughness. The values of the streamlines are identical to those in the caption of Fig. 2.

Figures 5 and 6 show the flow field in the vapor region for two other basic roughnesses; a semi-cylindrical and a triangular roughness, respectively. The basic features present in the rectangular roughness flow field exist here as well and will not be repeated, for brevity. It is worth noting, however, that in both cases the recirculation regions are very limited.

In Fig. 7 the predictions of the microscopic and macroscopic models on the vapor layer thickness (δ) are compared and the effect of the relative size of the droplet and the roughness elements on δ is shown. Clearly, increasing the size of the droplet relative to the size of the roughness elements (increasing the number of roughness elements under the droplet) thickens the vapor layer. This effect is weak for the rectangular and semicylindrical roughnesses but it is strong for the triangular roughness. The predictions of the macroscopic model are the best for the rectangular roughness, good for the semicylindrical roughness and not good for the triangular roughness. The two diamond symbols correspond to the case of the rectangular roughness with seven elements under the droplet and they show the effect of roughness depth on δ. Decreasing the cavity depth from $d/2$ to $d/5$ and finally to $d/10$ increases the thickness of the vapor layer. It is obvious from Fig. 7 that the presence of the roughness significantly affects the vapor layer thickness and the flow field and should be accounted for in studies of Leidenfrost vaporization.

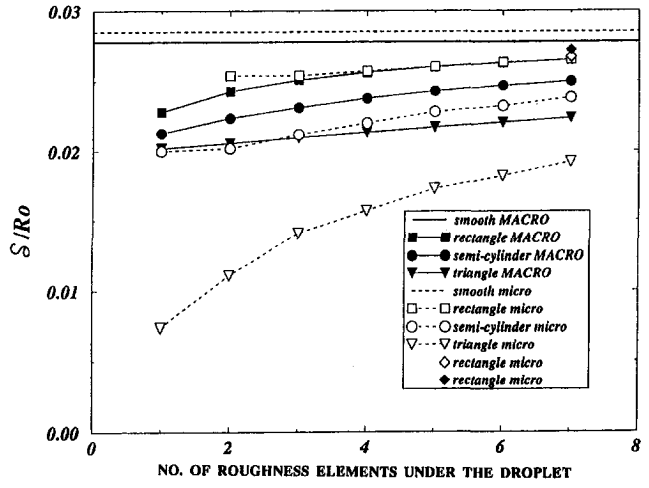

Fig. 7 The dependence of the roughness element size on the vapor layer thickness above the droplet and comparison of the microscopic and macroscopic model results

Before closing this section, it is important to discuss the validity of the assumption following Eq. (14) that the heat transfer in the vapor film is conduction dominated. To this end the value of the Peclet number

$$\mathrm{Pe} = \frac{u_0 \delta \rho c_p}{k} \tag{27}$$

for the flow in the vapor film is estimated. Introducing the Reynolds number based on the vaporization velocity and the droplet radius ($\mathrm{Re} = u_0 R/v$) the above expression becomes

$$\mathrm{Pe} = \frac{\mu \delta c_p \,\mathrm{Re}}{Rk} \tag{28}$$

The simulations showed that $\delta \approx 0.03R$ (or less) and that $\mathrm{Re} \leq 20$. With these values, Eq. (28) results in the estimate that $\mathrm{Pe} \leq 0.8$, which justifies the adopted assumption that conduction is the dominant heat transfer mechanism in the vapor film.

An additional assumption worth checking at this point is that of quasi-steady state conditions (after Avedisian and Koplik, 1987 and Gotfried, 1966) based on which δ was kept constant for each case studied. Utilizing the values of parameters and properties of the present study the evaporation time scale, τ_e = Dropret Mass/$\rho u_0 \pi R_0^2$, was compared to the flow time scale, $\tau_f = R_0/u_0$. It was found that $\tau_e/\tau_f = O(10^3)$. This justifies the quasi steady-state assumption.

Finally, experimental verification of the results in this paper is desirable and it is a recommended topic of future research. Since this study focuses on the fluid dynamics of the phenomenon of interest, relevant experimental results are those on the velocity field and the vapor thickness under the droplet. We were not able to locate such results in the literature, even for a smooth surface (in the absence of the roughness elements). Note, however, that in the limit of a smooth surface the macroscopic model of the present study reduces to an expression identical to that of Avedisian and Koplik (1987) and Gotfried et al. (1966).

6 Conclusions

In this paper a theoretical study is reported on the effect of surface roughness on the vapor flow field underneath a droplet undergoing Leidenfrost vaporization. Three basic axisymmetric roughnesses were examined: rectangular, semicylindrical, and triangular. The problem was solved both by using a macroscopic approach in which the roughness was replaced by a Beavers-Joseph slip condition, as well as by using a microscopic approach in which the flow equations were solved at the roughness level.

It was found that in all cases the presence of the roughness significantly affects the flow field. Flow penetration into the roughness cavities was observed in all cases. In the case of the rectangular roughness sizable recirculation regions were present in these cavities. These regions gradually disappeared as the roughness size decreased. The recirculation regions were less significant in the case of the semi-cylindrical and triangular roughnesses. Axial velocity profiles showed large accelerations near the centerline of the flow field. The thickness of the vapor layer above the roughness increases as the size of the droplet relative to the size of the roughness increases. This effect is more significant for the triangular roughness. Decreasing the height of the roughness elements increases the vapor layer thickness above the roughness.

In short, the presence of the roughness (its size as well as its geometry) severely affects the flow field under the droplet and should be taken into account in studies of Leidenfrost vaporization.

Acknowledgment

Most of the work in this paper was performed when one of the authors (D.P.) was on Sabbatical leave from UIC at IMFT Toulouse. He wishes to acknowledge the warm hospitality of everyone at IMFT and the delightful discussions he had with Dr. Serge Bories (director of research) on science and life in general. We also would like to acknowledge the constructive input of the three anonymous reviewers of the paper.

References

Avedisian, C. T., and Koplik, J., 1987, "Leidenfrost Boiling of Methanol Droplets on Hot Porous/Ceramic Surfaces," *Int. J. Heat and Mass Transfer,* Vol. 30, pp. 379–393.

Baumeister, K. J., and Simon, F. F., 1973, "Leidenfrost Temperature—its Correlation for Liquid Metals, Cryogens, Hydrocarbons and Water," ASME *Journal of Heat Transfer,* Vol. 95, pp. 166–173.

Beavers, G. S., and Joseph, D. D., 1967, "Boundary Conditions at a Naturally Permeable Wall," *Journal of Fluid Mechanics,* Vol. 30, pp. 197–207.

Bell, K. J., 1967, "The Leidenfrost Phenomenon: A Survey," *Chemical Engineering Progress Symposium Series,* Vol. 63, pp. 73–82.

Chandra, S., and Avedisian, C. T., 1991, "On the Collision of a Droplet With a Solid Surface," *Proceedings of the Royal Society of London A,* Vol. 432, pp. 13–41.

Chandra, S., and Avedisian, C. T., 1992, "Observations of Droplet Impingement on a Ceramic Porous Surface," *International Journal of Heat and Mass Transfer,* Vol. 35, pp. 2377–2388.

Fatehi, M., and Kaviany, M., 1990, "Analysis of Levitation of Saturated Liquid Droplets on Permeable Surfaces," *International Journal of Heat and Mass Transfer,* Vol. 33, pp. 983–944.

Gotfried, B. S., Lee, C. J., and Bell, K. J., 1966, The Leidenfrost Phenomenon: Film Boiling of Liquid Droplets on a Flat Plate," *International Journal of Heat and Mass Transfer,* Vol. 9, pp. 1167–1187.

Journal of Fluids Engineering

Technical Briefs

Surface Roughness Effects on Induced Flow and Frictional Resistance of Enclosed Rotating Disks

Andreas Poullikkas[1]

Introduction

Disk friction losses in a pump are caused by the fluid flow in the gap between the impeller and the casing wall as in Fig 1. The classical method of determining these losses is by using a thin plain disk rotating in a close fitting close casing. Rotating disks can be classified in two broad categories:

(i) Free disk, a disk which rotates in a fluid mass of infinite extent and initially at rest. When the disk is rotating fluid is drawn axially toward the disk and is centrifuged off its periphery as a spinning boundary layer. There is no angular momentum in the approach flow so the friction torque is equal to the angular momentum cast off in the boundary layer.

(ii) Enclosed disk, a disk which rotates within a chamber of finite dimensions. When the disk is rotating the whirling flow cast off its periphery eventually returns to the disk retaining some of its angular momentum. For this reason the friction torque on enclosed disks is less than that on free disks.

This investigation concerns the latter case which includes the kinds of conditions encountered in centrifugal machinery where problems of disk friction torque and power loss are related to the circulation and secondary flows induced by the rotating elements. These induced flows are dependent on the geometries of the rotating element and its enclosure and furthermore on the leakage flowrate. The investigation reported here is an attempt to develop a new empirical equation by examining disks with different surface roughnesses within an axially symmetric, right circular cylinder of variable length. There have been several previous studies of this problem, leading to limited correlation between disk friction values and theory.

A new approximate solution was developed using the principles of dimensional analysis and tested against the measured data. Experimental data were obtained for the following variables:

(i) Axial clearances between the disk and the end walls of the casing were varied in a number of finite steps over a range S/R ratios from 0.0333 to 0.1267.

(ii) The tip clearance was constant at t/R ratio of 0.1467 for all runs.

(iii) The disk Reynolds number was constant at Re of 3.83×10^6 for all runs.

(iv) Rotating disk surface roughness were varied at k_a of 0.0261, 0.0163, and 0.0083 mm.

(v) Centerline and peripheral flowrates were constant at Q_L of 1.63×10^{-5} m^3/s.

The flow regimes of an enclosed rotating disk can be classified as follows:

(i) Regime I: Laminar flow, close clearance. Boundary layers on the rotor and stator are merged so that a continuous variation in velocity exists across the axial gap S.

(ii) Regime II: Laminar flow, separate boundary layers. The combined thickness of the boundary layers on the rotor and stator is less than the axial gap S. Between the boundary layers is a core region in which no change in velocity is expected to occur.

(iii) Regime III: Turbulent flow, close clearance. The turbulent counter-part of Regime I, for higher Reynolds numbers and turbulent flow on the circular surfaces.

(iv) Regime IV: Turbulent flow, separate boundary layers. The turbulent counter-part of regime II.

The experiments in the present report are based on Regime IV which is the more likely to occur in centrifugal machinery.

New Empirical Solution

It is generally accepted that there is not an exact mathematical model that can predict the disk friction, therefore a number of empirical equations, depending on experimental results, were suggested by many researchers (Bennet and Worsten, 1960; Daily and Nece, 1960; Watabe, 1965). Figure 2 is the graphical presentation of the experimental results and the results obtained by Daily and Nece (1960a) equation, which is generally accepted as the most accurate:

$$c_m = \frac{0.102(S/R)^{0.1}}{\mathrm{Re}^{0.2}} \qquad (1)$$

The factor of roughness is clearly shown and therefore an expression involving the surface roughness of the disk, k_a, seemed to be attractive.

The following gives a new approximate expression of the disk friction coefficient c_m of an enclosed rotating disk involving

[1] Department of Mechanical Engineering, Frederick Institute of Technology, P.O. Box 4729, Nicosia, Cyprus.

Contributed by the Fluids Engineering Division of THE AMERICAN SOCIETY OF MECHANICAL ENGINEERS. Manuscript received by the Fluids Engineering Division May 28, 1994; revised manuscript received September 6, 1994. Associate Technical Editor: L. Nelik.

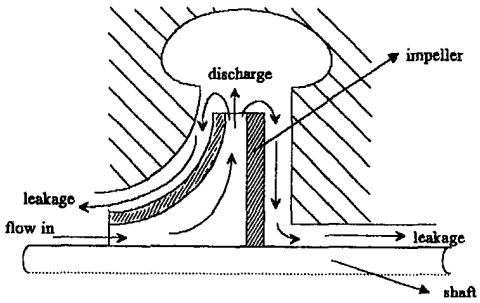

Fig. 1 Disk friction losses in centrifugal pump

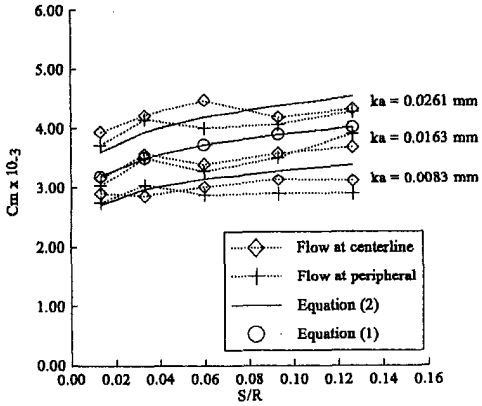

Fig. 2 Comparison of experimental results and approximate theory, c_m versus S/R

the surface roughness parameter k_a. Using the principles of dimensional analysis the following relationship can be written:

$$\frac{M_D}{\rho\omega^2 R^5}(=c_m)=\Phi\left\{\left(\frac{S}{R}\right)^b,\left(\frac{k_a}{R}\right)^c,\left(\frac{1}{\mathrm{Re}}\right)^f\right\}$$

It is generally accepted that for regime IV, the disk friction coefficient c_m is a function of the $\mathrm{Re}^{-0.2}$. Moreover, following Daily and Nece (1960a) approximate analysis, $c_m\mathrm{Re}^{0.2}$ versus $(S/R)^{0.1}$ can be plotted, which appears to be a straight line for all the combinations tested. The mean gradient agreed with the $(k_a/R)^{0.25}$ ratio in all cases between 0.08 to 9.7 percent. Therefore it is possible to write that:

$$c_m=\left(\frac{k_a}{R}\right)^{0.25}\frac{(S/R)^{0.1}}{\mathrm{Re}^{0.2}} \qquad (2)$$

Experimental Work

The general layout of the test stand is indicated in Fig. 3. A 30-hp direct-current motor with a 125–2000 rpm speed range served as the drive unit. Shaft speed was measured by means of a revolution counter and a digital readout. The motor was directly coupled to a 50 mm diameter shaft to which interchangeable disks could be attached. Three different surface roughnesses disks of 150 mm OD and 10 mm thickness were used, as indicated in Table 1.

Table 1 Rotating disks data

Disc No	R (mm)	b (mm)	k_a (mm)
1	150	10	0.0261
2	150	10	0.0163
3	150	10	0.0083

The test fluid was water and a typical leakage flow for a centrifugal pump was allowed during the tests. Although the actual leakage flow is the one indicated in Fig 1, two typical alternatives for a rotating disk were studied, as in Fig 4:

(i) Flow at the centerline
(ii) Flow at the peripheral

The temperature of the water at inlet and outlet was monitored for all test runs by two thermocouples connected to a multichannel digital readout. Torques were measured by means of bonded foil strain gauges. They were positioned on the shaft to give maximum sensitivity to the strains produced by torsion. Four gauges were placed at angles of 45° from the shaft center line, the resulting bridge circuit registering torsional stresses only. Voltage differences from this circuit were taken off through slip rings mounted on the shaft and a dial indicator served as the indicating device. Such arrangement is fully temperature compensated, achieves maximum sensitivity for a given torque, and provides automatic compensation for bending and axial loads.

As suggested by Worster (1957), Bennett and Worster (1960), and Varley (1961) some of the disk friction power eventually returns to the impeller and helps to combat the volume loss. For the purposes of this experimental investigation, the proportion of the disk friction power, which is added to the impeller power, was assumed to be equal with the volume losses. Therefore the loss analysis concentrated only on mechanical loss, disk friction loss, and leakage loss. The mechanical torque losses were determined by running the machine without the disk and with no water in the casing. Since the torque transducer was mounted between the two bearings the only mechanical torque losses measured were due to the bearing before the casing. It was also assumed that the leakage torque losses were in the order of 11.5 percent of the total torque losses. The total torque losses were measured by running the disk in the water under the specified conditions.

The flow rate was measured by means of a variable area flowmeter of an orifice and plug meter type. Water was taken directly from the reservoir. A typical leakage flow for a centrifugal pump of 1.63×10^{-5} m^3/s was applied. This was calculated using I.S.O. data for a 315 mm diameter impeller. The leakage flow rate was kept constant for all runs.

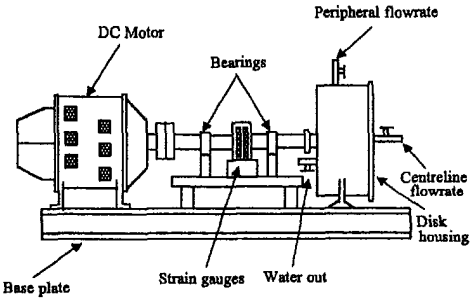

Fig. 3 General layout of the test stand

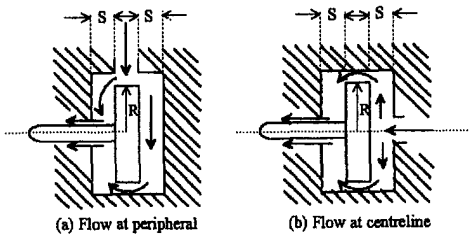

Fig. 4 Alternative flowrates for a rotating disk

Table 2 Precision of test loop instrumentation

Measurement	Range	Accuracy
Speed	0 - 3000 rpm	± 1 rpm
Torque	0 - 20 lb.ft	± 0.01 lb.ft
System temperatures	0 - 150 °C	± 2 °C

Discussion

Figure 2 is the graphical presentation of the results obtained during tests and the results obtained by Eq. (2) for the S/R ratios and disk surface roughnesses tested. In the above equation the effect of surface roughness k_a is introduced. The shape of the curve is exactly the same as Daily and Nece (1960a) Eq. (1), but c_m changes for different disk surface roughnesses from 2.70×10^{-3} to 4.51×10^{-3}. It can be seen that as the S/R ratio increases, c_m increases too and in addition, as the disk surface roughness increases the curve is shifted upwards, giving higher values for c_m. In the case of disk surface roughness k_a of 0.0163 mm, the results obtained are identical to those predicted by Eq. (1). This indicates that the surface roughness of the disk that Daily and Nece (1960a) used for their tests was around 0.0163 mm.

The precision of measurement of parameters recorded for each test condition is described in Table 2. The percentage of the fractional error (Holman, 1994) varied between 1.53 and 1.54 for c_m between 2.5×10^{-3} and 4.5×10^{-3}. The tests were repeated 5 times for each S/R ratio, disk surface roughness, and flow combinations. In both cases—flow at centerline and flow at peripheral—as the disk surface roughness increases the curve is shifted upwards giving higher values for c_m. In addition, the c_m values at the peripheral flowrate were lower than at the centerline flowrate. Experiments from many researchers have indicated that an optimum S/R ratio exist giving a minimum c_m. This optimum ratio appeared to be between 0.010 to 0.015 for a Re of 10^6. Also, it was indicated that a second optimum S/R ratio may occur greater than the above S/R that will give also a second minimum value for c_m. At the centerline flow, the minimum value for the c_m appeared when the S/R ratio was at the minimum of 0.0133 verifying that for smaller S/R ratios an optimum ratio may exists. At the peripheral flow, the minimum value for c_m appeared when the S/R ratio was at the minimum of 0.0133 verifying once again that for smaller S/R ratios an optimum ratio may exist. Moreover a second optimum S/R ratio occurred at 0.0600 giving a second minimum value for c_m.

For the roughest disk with a surface roughness of 0.0261 mm the approximate theory calculation appeared to be between the experimental results with an error of −8.63 to 5.06 percent. Daily and Nece equation (1960) is well below the experimental results. The experimental results for the disk surface roughness of 0.0163 mm appeared to be lower than the approximate theory calculation with an error of 1.27 to 6.01 percent. Daily and Nece (1960) equation coincide with the approximate theory as explained before. For the disk with a surface roughness of 0.0083 mm the approximate theory calculation appeared to be between the experimental results, at the beginning, and then slightly higher with an error of 5.03 percent to −6.57 percent. Daily and Nece equation is well above the experimental results.

Conclusions

The following general conclusions may be drawn from this study, associated with the rotation of different surface roughnesses disks, and, in general, with disk friction losses occurring in centrifugal pumps:

(i) Disk friction coefficient c_m increases with the disk surface roughness k_a.

(ii) Disk friction coefficients c_m at the peripheral flowrate were lower than those on the centerline.

(iii) At the peripheral flow a second optimum S/R ratio of 0.0600 was observed.

(iv) Suggested empirical equations by other researchers agreed with experimental results only in the case of disk surface roughness of 0.0163 mm.

(v) The approximate solution leads to the empirical Eq. (2), which can predict the experimental results with an error of −8.63 to 6.01 percent.

References

Bennet, T. P., and Worster, R. C., 1960, "The Friction on Rotating Discs and the Effect on Next Radial Flow and Externally Applied Whirl," British Hydrodynamic Research Association.

Braske, U. M., 1975, "Investigations on the Pumping Effect of Rotating Discs," *Proceedings of the Institution of Mechanical Engineers,* Vol. 189, pp. 36–75.

Daily, J. W., and Nece, R. E., 1960a, "Roughness Effects on Frictional Resistance of Enclosed Rotating Discs," ASME JOURNAL OF BASIC ENGINEERING, Vol. 82, pp. 553–562.

Daily, J. W., and Nece, R. E., 1960b, "Chamber Dimension Effects on Induced Flow and Frictional Resistance of Enclosed Rotating Discs," ASME JOURNAL OF FLUIDS ENGINEERING, Vol. 82, pp. 217–232.

Goldstein, S., 1935, "On the Resistance to the Rotation of a Disc Immersed in a Fluid," *Proceedings of the Cambridge Philosophical Society,* Vol. 31, pp. 232–241.

Holman, J. P., 1994, Experimental Methods for Engineers, Sixth Edition, McGraw-Hill, New York.

Kurokawa, J., and Toyokura, T., 1976, "Axial Thrust, Disc Friction Torque and Leakage Loss of Radial Flow Turbomachinery," National Engineering Laboratory, International Conference on Pump and Turbine Design and Development, Paper 5-2.

Murata, S., Miyake, Y., and Iemoto, Y., 1976, "A Study on a Disc Friction Pump 1st Report," *Bulletin of the Japanese Society of Mechanical Engineers,* Vol. 19, No. 128, pp. 168–178.

Murata, S., Miyake, Y., and Iemoto, Y., 1976, "A Study on a Disc Friction Pump 2nd Report," *Bulletin of the Japanese Society of Mechanical Engineers,* Vol. 19, No. 236, pp. 160–171.

Osterwalder, J., 1978, "Efficiency Scale-Up for Hydraulic Turbomachines With Due Consideration of Surface Roughness," *Journal of Hydraulic Research,* Vol. 16, No. 1, pp. 55–76.

Poullikkas, A., 1991, "Disc Friction Study," Loughborough University of Technology, Department of Mechanical Engineering (internal report).

Schlichting, H., 1955, *Boundary Layer Theory,* McGraw-Hill, New York.

Stepanoff, J., 1948, *Centrifugal and Axial Flow Pumps,* Wiley, New York.

Varley, F. A., 1961, "Effects of Impeller Design and Surface Roughness on the Performance of Centrifugal Pumps," *Proceedings of the Institution of Mechanical Engineers,* Vol. 184, pp. 955–989.

Watabe, K., 1958, "On Fluid Friction of Rotational Rough Disc in Rough Vessel," *Bulletin of the Japanese Society of Mechanical Engineers,* Vol. 1, No. 1, pp. 68–74.

Watabe, K., 1965, "On Fluid Resistance of Enclosed Rotating Rough Discs," *Bulletin of the Japanese Society of Mechanical Engineers,* Vol. 8, No. 32, pp. 609–619.

Worster, R. C., 1957, "The Effects of Skin Friction and Roughness on the Losses in Centrifugal Pump Volutes," British Hydrodynamic Research Association.

A Note on the Baldwin-Lomax Turbulence Model

J. He[1] and J. D. A. Walker[1]

An analytic expression is obtained for the constant C_{cp} in the Baldwin-Lomax model by comparing self-similar solutions for velocity in a constant pressure incompressible flow that are

[1] Postdoctoral Fellow and Professor, respectively. Department of Mechanical Engineering and Mechanics, Lehigh University, Bethlehem, PA 18015.

Work supported by NASA grant NAE-1-832.

Contributed by the Fluids Engineering Division of THE AMERICAN SOCIETY OF MECHANICAL ENGINEERS. Manuscript received by the Fluids Engineering Division August 23, 1994; revised manuscript received December 16, 1994. Associate Technical Editor: G. Karniadakis.

Table 2 Precision of test loop instrumentation

Measurement	Range	Accuracy
Speed	0 - 3000 rpm	± 1 rpm
Torque	0 - 20 lb.ft	± 0.01 lb.ft
System temperatures	0 - 150 °C	± 2 °C

Discussion

Figure 2 is the graphical presentation of the results obtained during tests and the results obtained by Eq. (2) for the S/R ratios and disk surface roughnesses tested. In the above equation the effect of surface roughness k_a is introduced. The shape of the curve is exactly the same as Daily and Nece (1960a) Eq. (1), but c_m changes for different disk surface roughnesses from 2.70×10^{-3} to 4.51×10^{-3}. It can be seen that as the S/R ratio increases, c_m increases too and in addition, as the disk surface roughness increases the curve is shifted upwards, giving higher values for c_m. In the case of disk surface roughness k_a of 0.0163 mm, the results obtained are identical to those predicted by Eq. (1). This indicates that the surface roughness of the disk that Daily and Nece (1960a) used for their tests was around 0.0163 mm.

The precision of measurement of parameters recorded for each test condition is described in Table 2. The percentage of the fractional error (Holman, 1994) varied between 1.53 and 1.54 for c_m between 2.5×10^{-3} and 4.5×10^{-3}. The tests were repeated 5 times for each S/R ratio, disk surface roughness, and flow combinations. In both cases—flow at centerline and flow at peripheral—as the disk surface roughness increases the curve is shifted upwards giving higher values for c_m. In addition, the c_m values at the peripheral flowrate were lower than at the centerline flowrate. Experiments from many researchers have indicated that an optimum S/R ratio exist giving a minimum c_m. This optimum ratio appeared to be between 0.010 to 0.015 for a Re of 10^6. Also, it was indicated that a second optimum S/R ratio may occur greater than the above S/R that will give also a second minimum value for c_m. At the centerline flow, the minimum value for the c_m appeared when the S/R ratio was at the minimum of 0.0133 verifying that for smaller S/R ratios an optimum ratio may exists. At the peripheral flow, the minimum value for c_m appeared when the S/R ratio was at the minimum of 0.0133 verifying once again that for smaller S/R ratios an optimum ratio may exist. Moreover a second optimum S/R ratio occurred at 0.0600 giving a second minimum value for c_m.

For the roughest disk with a surface roughness of 0.0261 mm the approximate theory calculation appeared to be between the experimental results with an error of −8.63 to 5.06 percent. Daily and Nece equation (1960) is well below the experimental results. The experimental results for the disk surface roughness of 0.0163 mm appeared to be lower than the approximate theory calculation with an error of 1.27 to 6.01 percent. Daily and Nece (1960) equation coincide with the approximate theory as explained before. For the disk with a surface roughness of 0.0083 mm the approximate theory calculation appeared to be between the experimental results, at the beginning, and then slightly higher with an error of 5.03 percent to −6.57 percent. Daily and Nece equation is well above the experimental results.

Conclusions

The following general conclusions may be drawn from this study, associated with the rotation of different surface roughnesses disks, and, in general, with disk friction losses occurring in centrifugal pumps:

(i) Disk friction coefficient c_m increases with the disk surface roughness k_a.

(ii) Disk friction coefficients c_m at the peripheral flowrate were lower than those on the centerline.

(iii) At the peripheral flow a second optimum S/R ratio of 0.0600 was observed.

(iv) Suggested empirical equations by other researchers agreed with experimental results only in the case of disk surface roughness of 0.0163 mm.

(v) The approximate solution leads to the empirical Eq. (2), which can predict the experimental results with an error of −8.63 to 6.01 percent.

References

Bennet, T. P., and Worster, R. C., 1960, "The Friction on Rotating Discs and the Effect on Next Radial Flow and Externally Applied Whirl," British Hydrodynamic Research Association.

Braske, U. M., 1975, "Investigations on the Pumping Effect of Rotating Discs," *Proceedings of the Institution of Mechanical Engineers,* Vol. 189, pp. 36–75.

Daily, J. W., and Nece, R. E., 1960a, "Roughness Effects on Frictional Resistance of Enclosed Rotating Discs," ASME JOURNAL OF BASIC ENGINEERING, Vol. 82, pp. 553–562.

Daily, J. W., and Nece, R. E., 1960b, "Chamber Dimension Effects on Induced Flow and Frictional Resistance of Enclosed Rotating Discs," ASME JOURNAL OF FLUIDS ENGINEERING, Vol. 82, pp. 217–232.

Goldstein, S., 1935, "On the Resistance to the Rotation of a Disc Immersed in a Fluid," *Proceedings of the Cambridge Philosophical Society,* Vol. 31, pp. 232–241.

Holman, J. P., 1994, Experimental Methods for Engineers, Sixth Edition, McGraw-Hill, New York.

Kurokawa, J., and Toyokura, T., 1976, "Axial Thrust, Disc Friction Torque and Leakage Loss of Radial Flow Turbomachinery," National Engineering Laboratory, International Conference on Pump and Turbine Design and Development, Paper 5-2.

Murata, S., Miyake, Y., and Iemoto, Y., 1976, "A Study on a Disc Friction Pump 1st Report," *Bulletin of the Japanese Society of Mechanical Engineers,* Vol. 19, No. 128, pp. 168–178.

Murata, S., Miyake, Y., and Iemoto, Y., 1976, "A Study on a Disc Friction Pump 2nd Report," *Bulletin of the Japanese Society of Mechanical Engineers,* Vol. 19, No. 236, pp. 160–171.

Osterwalder, J., 1978, "Efficiency Scale-Up for Hydraulic Turbomachines With Due Consideration of Surface Roughness," *Journal of Hydraulic Research,* Vol. 16, No. 1, pp. 55–76.

Poullikkas, A., 1991, "Disc Friction Study," Loughborough University of Technology, Department of Mechanical Engineering (internal report).

Schlichting, H., 1955, *Boundary Layer Theory,* McGraw-Hill, New York.

Stepanoff, J., 1948, *Centrifugal and Axial Flow Pumps,* Wiley, New York.

Varley, F. A., 1961, "Effects of Impeller Design and Surface Roughness on the Performance of Centrifugal Pumps," *Proceedings of the Institution of Mechanical Engineers,* Vol. 184, pp. 955–989.

Watabe, K., 1958, "On Fluid Friction of Rotational Rough Disc in Rough Vessel," *Bulletin of the Japanese Society of Mechanical Engineers,* Vol. 1, No. 1, pp. 68–74.

Watabe, K., 1965, "On Fluid Resistance of Enclosed Rotating Rough Discs," *Bulletin of the Japanese Society of Mechanical Engineers,* Vol. 8, No. 32, pp. 609–619.

Worster, R. C., 1957, "The Effects of Skin Friction and Roughness on the Losses in Centrifugal Pump Volutes," British Hydrodynamic Research Association.

A Note on the Baldwin-Lomax Turbulence Model

J. He[1] and J. D. A. Walker[1]

An analytic expression is obtained for the constant C_{cp} in the Baldwin-Lomax model by comparing self-similar solutions for velocity in a constant pressure incompressible flow that are

[1] Postdoctoral Fellow and Professor, respectively. Department of Mechanical Engineering and Mechanics, Lehigh University, Bethlehem, PA 18015.

Work supported by NASA grant NAE-1-832.

Contributed by the Fluids Engineering Division of THE AMERICAN SOCIETY OF MECHANICAL ENGINEERS. Manuscript received by the Fluids Engineering Division August 23, 1994; revised manuscript received December 16, 1994. Associate Technical Editor: G. Karniadakis.

based on the Cebeci-Smith and Baldwin-Lomax models; both models are shown to give identical results when the model C_{cp} has a specific analytical form.

I Introduction

In the numerical computation of turbulent boundary-layer flows, algebraic eddy viscosity models are often the most common choice in Navier-Stokes computer codes. Although such models are known to have certain deficiencies, their relative simplicity leads to minimum requirements in computer time and storage. In addition, the predicted results are often quite credible, at least for attached turbulent boundary layers on a smooth surface. Two formulations in extensive use are the Cebeci-Smith (1974) and Baldwin-Lomax (1978) models, which utilize the same mixing length model for the inner part of the boundary layer but a different eddy viscosity model in the outer part. The outer portion of the Cebeci-Smith model contains the displacement thickness δ^* as what is, in effect, a local representative length scale for the boundary layer. However, for a number of configurations, such as various internal flows or a boundary layer encountering a streamwise feature like a backward-facing step, the determination of δ^* can be problematic. For this reason, Baldwin and Lomax (1978) introduced another outer length scale and determined constants in the new model by comparison with numerical solutions for constant pressure boundary layers at transonic speeds produced using the Cebeci-Smith (1974) model. The model has been applied to a wide variety of two- and three-dimensional flows, with and without boundary layer separation (see, for example, Baldwin and Lomax, 1974; Visbal and Knight, 1984; King, 1987) with varying, but in many cases acceptable, levels of success.

Over the years, other suggestions have been put forward for the modeling constants in the Baldwin-Lomax model (see, for example, Visbal and Knight, 1984) and it has been hypothesized that a variation in the constants is necessary to account for compressibility with increasing mainstream Mach number M_∞. The question of compressibility will be addressed here subsequently. At transonic speeds, compressibility effects in a constant pressure boundary layer are relatively small when compared to a purely incompressible flow ($M_\infty \to 0$). In this note, a systematic way of determining the model constants in the Baldwin-Lomax (1978) model is described. It is shown that analytical solutions can be obtained for constant pressure turbulent boundary layers and with the appropriate choice of the model constants, both models give the identical solution. The resulting analytical formula give results that are close to those originally estimated by Baldwin and Lomax (1978). The present results may be of some utility in parametric studies, particularly in three-dimensional flows, where model constants are sometimes varied.

II Formulation

The equations governing a two-dimensional incompressible boundary layer at constant pressure may be written

$$u\frac{\partial u}{\partial x} + v\frac{\partial u}{\partial y} = \frac{\partial \tau}{\partial y}, \quad \frac{\partial u}{\partial x} + \frac{\partial v}{\partial y} = 0, \tag{1}$$

where τ is a total stress defined by

$$\tau = \sigma + \frac{1}{\mathrm{Re}}\frac{\partial u}{\partial y}, \quad \sigma = -\overline{u'v'}. \tag{2}$$

In these equations, all lengths and velocities are dimensionless with respect to a characteristic length L^*_{ref} and a speed U^*_{ref} and the Reynolds number is defined by $\mathrm{Re} = U^*_{\mathrm{ref}} L^*_{\mathrm{ref}}/\nu$, where ν is the kinematic viscosity. In an eddy viscosity model, the Reynolds stress is expressed in the form

$$-\rho\overline{u'v'} = \epsilon\frac{\partial u}{\partial y}, \tag{3}$$

where ϵ is the eddy viscosity function. In both the Cebeci-Smith and Baldwin-Lomax models, an inner eddy viscosity defined by

$$\epsilon_i = \rho(\kappa y \mathcal{D})^2|\omega|, \quad \mathcal{D} = 1 - \exp(-y^+/A^+), \tag{4}$$

is used, where ρ is the density, κ is the von Karman constant, and $\omega = -\partial u/\partial y$ is the vorticity; thus the inner model is a mixing length model. In addition, $\mathcal{D}$ is the van Driest damping factor, where $A^+ = 26$ and y^+ is the scaled inner coordinate defined by

$$y^+ = \mathrm{Re}\, u_* y, \quad u_*^2 = \frac{1}{\mathrm{Re}}\frac{\partial u}{\partial y}\bigg|_{y=0}, \tag{5}$$

with u_* being the dimensionless friction velocity. In the outer region, an eddy viscosity formula is employed with

$$\epsilon_o = \rho K U_e \delta^* F_{kleb}, \quad F_{kleb} = \left\{1 + 5.5\left(\frac{y}{\delta}\right)^6\right\}^{-1}, \tag{6}$$

for the Cebeci-Smith model, where K is the Clauser constant having a value of 0.0168; U_e is the velocity at the boundary-layer edge, F_{kleb} is an intermittency correction, and δ is the boundary-layer thickness. The intermittency correction represents a curve fit which Klebanoff (1954) originally represented in terms of an error function. In the Baldwin-Lomax model, the outer eddy viscosity formula is

$$\epsilon_o = \rho K C_{cp} F_{\mathrm{wake}} F_{kleb}, \tag{7}$$

where again $K = 0.0168$, C_{cp} is a constant, and $F_{\mathrm{wake}} = y_{\max} F(y_{\max})$; here $y_{\max}$ denotes the location where the function

$$F = y|\partial u/\partial y|\mathcal{D}, \tag{8}$$

reaches an absolute maximum. In addition, the intermittency factor is modified to the form

$$F_{kleb} = \left\{1 + 5.5\left(\frac{C_{kleb} y}{y_{\max}}\right)^6\right\}^{-1}, \tag{9}$$

where C_{kleb} is a constant. In both models the inner formula (4) is joined to either of the outer formula (6) or (7) at the location where both are equal. Baldwin and Lomax (1978) originally suggested values of $C_{cp} = 1.6$ and $C_{kleb} = 0.3$ and in subsequent work, other authors have used different values of the constants; for example, Visbal and Knight (1984) suggest $C_{cp} = 1.2$ and $C_{kleb} = 0.65$ for incompressible flow ($M_\infty \to 0$) and $C_{cp} = 2.08$ for an adiabatic supersonic flow at $M_\infty = 3$. A recent study by He et al. (1995) shows how the Baldwin-Lomax model can be extended to variable density flows with and without heat transfer well up into the low hypersonic range ($M_\infty \sim 10$) using universal values of the constants. Here the objective is to establish the base values of the modeling constants, and this is accomplished by a comparison of equilibrium velocity profiles in a constant pressure flow.

To start with, the intermittency portion of the model, F_{kleb}, will be taken equal to unity; this term is known to have very little effect on the shape of the velocity profile, or the critical features of the turbulence models. In the limit $\mathrm{Re} \to \infty$, it is well known that the turbulent boundary layer is a composite double layer consisting of an outer defect layer and an inner wall layer. In the outer layer, the velocity is of the form

$$u = U_e + u_* \frac{\partial F_1}{\partial \eta} + \ldots, \tag{10}$$

where the defect function $\partial F_1/\partial\eta$ is a function of the scaled

variable $\eta = y/\Delta_o$ for a self-similar flow, with $\Delta_o = \Delta_o(x, \mathrm{Re})$ proportional to the local boundary-layer thickness; for a constant pressure flow Δ_o can be defined by $\Delta_o = U_e\delta^*/u_*$ (Fendell, 1972). The defect function must satisfy the boundary conditions

$$\frac{dF_1}{d\eta} \sim \frac{1}{\kappa}\log\eta + C_o \quad \text{as} \quad \eta \to 0;$$

$$\frac{dF_1}{d\eta} \to 0 \quad \text{as} \quad \eta \to \infty, \tag{11}$$

where C_o is a constant. The first of these conditions is required to match the "law of the wall" in the wall-layer solution, while the second is the statement of matching to the external mainstream. In the wall layer, the velocity is a function of the scaled variable y^+ defined in Eq. (5), and the velocity profile is such that $u = u_*U^+(y^+) + \ldots$, with

$$U^+ = 0 \quad \text{at} \quad y^+ = 0,$$

$$U^+ \sim \frac{1}{\kappa}\log y^+ + C_i \quad \text{as} \quad y^+ \to \infty. \tag{12}$$

Here C_i is a constant generally supposed to have a universal value of $C_i = 5.0$. It is easily shown that the convective terms in Eq. (1) are negligible in the thin wall layer, which is therefore a constant stress layer with $\tau = \tau_w = u_*^2$. This serves to determine the equation for the velocity profile in the inner region, and with the model (4) it is easily verified that

$$\frac{dU^+}{dy^+} + \kappa^2 y^{+2}\mathcal{D}\left(\frac{dU^+}{dy^+}\right)^2 = 1, \tag{13}$$

which can be integrated using conditions (12) to find $U^+(y^+)$.

For large y^+, the damping factor $\mathcal{D}$ approaches unity and from Eq. (4), the inner eddy viscosity becomes linear in y^+. Thus the eddy viscosity for the outer part of the boundary layer may be written as $\epsilon = U_e\delta^*\hat{\epsilon}$ where $\hat{\epsilon}$ is the simple ramp function

$$\epsilon = \begin{cases} \chi, & \eta > \eta_m \\ \kappa\eta, & \eta \le \eta_m \end{cases}, \tag{14}$$

where $\eta_m = \chi/\kappa$, $\chi = K = 0.0168$ for the Cebeci-Smith model and $\chi = KC_{cp}y_{\max}F_{\max}/U_e\delta^*$ for the Baldwin-Lomax model. In the outer layer, the viscous stress in Eq. (2) is negligible, and it is easily shown that the defect function satisfies

$$\frac{d}{d\eta}\left\{\hat{\epsilon}\frac{d^2F_1}{d\eta^2}\right\} + \eta\frac{d^2F_1}{d\eta^2} = 0. \tag{15}$$

The solution satisfying conditions (11) is

$$\frac{dF_1}{d\eta} = \begin{cases} -\sqrt{\dfrac{\pi}{2\chi}}\, e^{-\chi/2\kappa^2}\,\mathrm{erfc}\left\{\sqrt{\dfrac{1}{2\chi}}\,\eta\right\}, & \eta > \eta_m, \\ -\dfrac{1}{\kappa}E_1\left(\dfrac{\eta}{\kappa}\right) + C_o - \dfrac{1}{\kappa}\{\gamma_o - \log\kappa\}, & \eta \le \eta_m, \end{cases} \tag{16}$$

where C_o is the outer region log-law constant given by

$$C_o = \frac{1}{\kappa}\left\{\gamma_o - \log\kappa + E_1(\chi/\kappa^2) - \sqrt{\frac{\pi}{2\chi}}\, e^{-K/2\kappa^2}\,\mathrm{erfc}\left\{\sqrt{\frac{\chi}{2\kappa^2}}\right\}\right\}. \tag{17}$$

In Eqs. (16) and (17) erfc and E_1 denote the complementary error function and exponential integral, respectively, and $\gamma_o = 0.577215\ldots$ is Euler's constant.

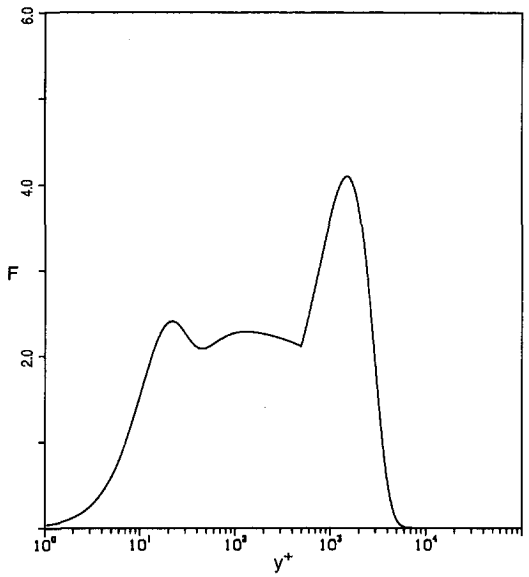

Fig. 1 Variation of F for a constant pressure boundary layer for $\mathrm{Re}_{\delta^*} = 10{,}000$

To determine the value of χ in Baldwin-Lomax model required to reproduce the Cebeci-Smith model, it is necessary to calculate the function F in Eq. (8). A composite profile for the entire boundary layer is formed as follows:

$$u = U_e + u_*\frac{dF_1}{d\eta} + u_*\left\{U^+ - \frac{1}{\kappa}\log y^+ - C_i\right\}, \tag{18}$$

and the function F is plotted in Fig. 1 for $\mathrm{Re}_{\delta^*} = 10{,}000$; here u_* is evaluated from the relation

$$\frac{U_e}{u_*} = \frac{1}{\kappa}\log\{\mathrm{Re}_{\delta^*}\} + C_i - C_o, \tag{19}$$

which must be satisfied so that the inner and outer profiles in Eqs. (10) and (12) match (Fendell, 1972); in addition, $\mathrm{Re}_{\delta^*} = \mathrm{Re}U_e\delta^*$. The corner in F shown in Fig. 1 near $y^+ \simeq 1000$ occurs at the point $\eta_m = \chi/\kappa$. It may be noted that an absolute maximum occurs in F in the outer part of the boundary layer, although local minima occur in the wall layer. For example, an extremum must occur in the overlap zone (for large y^+) in view of the last of conditions (12). However, if the absolute maximum is always selected, $y_{\max}$ occurs in the outer layer and can be chosen uniquely here and in flows with pressure gradient, except in some flows that involve separation (Visbal and Knight, 1984). Since the absolute maximum occurs in the outer layer, it suffices to examine the extrema of $F = \eta\partial u/\partial\eta$, and using Eq. (15), it is easily shown that

$$\eta\frac{d^2F_1}{d\eta^2} = \begin{cases} \dfrac{1}{\chi}\, e^{-\chi/2\kappa^2}\eta\,\exp\left(-\eta^2/2\chi\right), & \eta > \eta_m, \\ \dfrac{1}{\kappa}\exp\left(-\eta/\kappa\right), & \eta \le \eta_m. \end{cases} \tag{20}$$

Therefore the maximum occurs well into the outer part of the boundary layer, and it is easily shown that this occurs at $\eta_{\max} = \sqrt{\chi}$. The corresponding values of $F_{\max}$ and $y_{\max}$ are

$$F_{\max} = u_*\frac{1}{\sqrt{\chi}}\exp\left\{-\frac{1}{2}\left(1 + \frac{\chi}{\kappa^2}\right)\right\}, \; y_{\max} = \frac{\sqrt{\chi}U_e\delta^*}{u_*}. \tag{21}$$

With χ defined for both models following Eq. (14), it may easily be verified that both models are equivalent if

$$C_{cp} = \exp\left\{\frac{1}{2}\left(1 + \frac{K}{\kappa^2}\right)\right\}. \quad (22)$$

Upon substituting $\kappa = 0.40$ and $K = 0.0168$, it follows that $C_{cp} = 1.738$, as compared to the original estimate $C_{cp} = 1.6$ (Baldwin and Lomax, 1978).

In obtaining the result (22), it has been assumed that the intermittency factor (9) is unity and it is of interest to determine if this factor has any significant influence on the location of η_{max}. Consider the equivalent of (15) in the outer region $\eta > \eta_m$ with the factor (9) included; this yields

$$\frac{d}{d\eta}\left\{\frac{\chi}{(1 + 5.5C_{kleb}^6\eta^6/\eta_{max}^6)}\frac{d^2F_1}{d\eta^2}\right\} + \eta\frac{d^2F_1}{d\eta^2} = 0, \quad (23)$$

which is considerably more difficult to integrate analytically. However, the value of η_{max} occurs where $\eta F_1''' + F_1'' = 0$, and using this and Eq. (23), it can be shown that the maximum is located at

$$\eta_{max} = \sqrt{\chi} + 16.5C_{kleb}^6\chi^{7/2}/\eta_{max}^6 + \ldots \quad (24)$$

Thus the maximum is shifted only a minuscule amount from the value $\eta_{max} = \sqrt{\chi}$ calculated when the intermittency correction is not used. Numerical solutions obtained with the intermittency correction show virtually no difference from the analytical solution (16). Thus there does not appear to be a basis for fixing C_{kleb} at a value different from that indicated by Baldwin and Lomax (1978).

III Conclusions

In the present note, an expression for the constant C_{cp} in the Baldwin-Lomax turbulence model has been determined analytically. With a base value of the constant established, the recent study by He et al. (1995) shows how this model (as well as the Cebeci-Smith model) can be extended to account for the effects of variable density in supersonic flow without any changes in the modeling constants.

References

Baldwin, B. L. and Lomax, H., 1978, "Thin-Layer Approximation and Algebraic Model for Turbulent Separated Flows" AIAA Paper 78-257, January.

Cebeci, T., and Smith, A. M. O., 1974, *Analysis of Turbulent Boundary Layers,* Academic Press, New York.

Fendell, F. E., 1972, "Singular Perturbation and Turbulent Shear Flow Near Walls," *Journal of the Astronautical Sciences,* Vol. 20, pp. 129–165.

He, J., Kazakia, J. Y., and Walker, J. D. A., 1994, "An Asymptotic Two-Layer Model for Supersonic Boundary Layers", *1995 Journal of Fluid Mechanics,* Vol. 25, pp. 159–198.

King, L. S., 1987, "A Comparison of Turbulence Closure Models for Transonic Flows About Airfoils," AIAA Paper 87-0418, Jan.

Klebanoff, P. S., 1954, "Characteristics of Turbulence in a Boundary Layer with Zero Pressure Gradient," NACA Tech. Note 3178.

Visbal, M. and Knight, D., 1984, "The Baldwin-Lomax Turbulence Model for Two-Dimensional Shock-Wave/Boundary-Layer Interactions" *AIAA Journal,* Vol. 22, pp. 921–928.

Stability of Computational Algorithms Used in Molecular Dynamics Simulations

Akira Satoh [1]

The present study focuses on a three-dimensional Lennard-Jones system in a thermodynamic equilibrium in order to discuss divergence processes, the relationship between time intervals and divergence times, and the influence of time intervals on thermodynamic quantities and transport coefficients under various number density and temperature. It is found that the velocities of molecules in a system gradually increase with time until the system suddenly diverges exponentially. The time interval-divergence time relationship can be expressed in approximate terms as linear functions if the data are plotted on logarithmic scales, and the system diverges more easily as temperature or number density increases. Thermodynamic quantities show the influence of large time intervals more clearly than do transport coefficients.

1 Introduction

Molecular dynamics (MD) is a molecular simulation method, and is a powerful tool for investigating physical phenomena at the microscopic level (Heermann, 1990). The appearance of supercomputers stimulates the application of MD methods to fluids engineering fields, such as to internal structures of shock waves in liquids (Holian et al., 1980; Holian, 1988; Tsai and Trevino, 1981; Satoh, 1993a), flow around a sphere (Satoh, 1993b), flow around a cylinder (Rapaport, 1987; Satoh, 1993c), Bénard cell problems (Mareschal et al., 1988), and flow in a two-dimensional duct (Mo and Rosenberger, 1991).

Computation time governs the successful application of MD methods to flow problems. These applications need to be extended to larger molecular systems. A reduction in computation time may be attained by adopting an algorithm which can use large time intervals, and by using more efficient techniques for calculating intermolecular forces. Although many computational algorithms have been presented, few studies have attempted to clarify the divergence properties of MD algorithms. Some studies discussed the relationship between energy fluctuations in systems and time intervals for various MD algorithms, while few studies discussed the relationship between divergence times and time intervals. Since divergence properties are not clearly understood in MD algorithms, the values for time intervals which have been empirically used for equilibrium simulations may also be adopted to simulate flow problems. If we simulate normal shock waves with such empirical time intervals, the results of number density profiles will seem reasonable, while pressure may be larger by some orders of magnitude. This is obviously due to too large time intervals, so that we cannot use the empirical time intervals used for thermodynamic equilibrium without sufficient reflection for flow problems.

The purpose of this study is to clarify the relationship between divergence processes and time intervals, and the dependencies of divergence times on time intervals. These results are expected to provide guidance in determining values of time intervals in actual simulations, and also in developing a new algorithm that will not diverge easily.

2 Microcanonical Ensemble Molecular Dynamics

2.1 Lennard-Jones System and Velocity Verlet Algorithm. We assume a model system with number density N and

[1] Department of Mechanical Engineering, Faculty of Engineering, Chiba University, 1-33, Yayoi-cho, Inage-ku, Chiba 263, Japan.

Contributed by the Fluids Engineering Division of THE AMERICAN SOCIETY OF MECHANICAL ENGINEERS. Manuscript received by the Fluids Engineering Division July 11, 1994; revised manuscript received January 20, 1995. Associate Technical Editor: J. A. C. Humphrey.

With χ defined for both models following Eq. (14), it may easily be verified that both models are equivalent if

$$C_{cp} = \exp\left\{\frac{1}{2}\left(1 + \frac{K}{\kappa^2}\right)\right\}. \quad (22)$$

Upon substituting $\kappa = 0.40$ and $K = 0.0168$, it follows that $C_{cp} = 1.738$, as compared to the original estimate $C_{cp} = 1.6$ (Baldwin and Lomax, 1978).

In obtaining the result (22), it has been assumed that the intermittency factor (9) is unity and it is of interest to determine if this factor has any significant influence on the location of η_{max}. Consider the equivalent of (15) in the outer region $\eta > \eta_m$ with the factor (9) included; this yields

$$\frac{d}{d\eta}\left\{\frac{\chi}{(1 + 5.5C_{kleb}^6\eta^6/\eta_{max}^6)}\frac{d^2F_1}{d\eta^2}\right\} + \eta\frac{d^2F_1}{d\eta^2} = 0, \quad (23)$$

which is considerably more difficult to integrate analytically. However, the value of η_{max} occurs where $\eta F_1''' + F_1'' = 0$, and using this and Eq. (23), it can be shown that the maximum is located at

$$\eta_{max} = \sqrt{\chi} + 16.5C_{kleb}^6\chi^{7/2}/\eta_{max}^6 + \ldots \quad (24)$$

Thus the maximum is shifted only a minuscule amount from the value $\eta_{max} = \sqrt{\chi}$ calculated when the intermittency correction is not used. Numerical solutions obtained with the intermittency correction show virtually no difference from the analytical solution (16). Thus there does not appear to be a basis for fixing C_{kleb} at a value different from that indicated by Baldwin and Lomax (1978).

III Conclusions

In the present note, an expression for the constant C_{cp} in the Baldwin-Lomax turbulence model has been determined analytically. With a base value of the constant established, the recent study by He et al. (1995) shows how this model (as well as the Cebeci-Smith model) can be extended to account for the effects of variable density in supersonic flow without any changes in the modeling constants.

References

Baldwin, B. L. and Lomax, H., 1978, "Thin-Layer Approximation and Algebraic Model for Turbulent Separated Flows" AIAA Paper 78-257, January.

Cebeci, T., and Smith, A. M. O., 1974, *Analysis of Turbulent Boundary Layers,* Academic Press, New York.

Fendell, F. E., 1972, "Singular Perturbation and Turbulent Shear Flow Near Walls," *Journal of the Astronautical Sciences,* Vol. 20, pp. 129–165.

He, J., Kazakia, J. Y., and Walker, J. D. A., 1994, "An Asymptotic Two-Layer Model for Supersonic Boundary Layers", *1995 Journal of Fluid Mechanics,* Vol. 25, pp. 159–198.

King, L. S., 1987, "A Comparison of Turbulence Closure Models for Transonic Flows About Airfoils," AIAA Paper 87-0418, Jan.

Klebanoff, P. S., 1954, "Characteristics of Turbulence in a Boundary Layer with Zero Pressure Gradient," NACA Tech. Note 3178.

Visbal, M. and Knight, D., 1984, "The Baldwin-Lomax Turbulence Model for Two-Dimensional Shock-Wave/Boundary-Layer Interactions" *AIAA Journal,* Vol. 22, pp. 921–928.

Stability of Computational Algorithms Used in Molecular Dynamics Simulations

Akira Satoh [1]

The present study focuses on a three-dimensional Lennard-Jones system in a thermodynamic equilibrium in order to discuss divergence processes, the relationship between time intervals and divergence times, and the influence of time intervals on thermodynamic quantities and transport coefficients under various number density and temperature. It is found that the velocities of molecules in a system gradually increase with time until the system suddenly diverges exponentially. The time interval-divergence time relationship can be expressed in approximate terms as linear functions if the data are plotted on logarithmic scales, and the system diverges more easily as temperature or number density increases. Thermodynamic quantities show the influence of large time intervals more clearly than do transport coefficients.

1 Introduction

Molecular dynamics (MD) is a molecular simulation method, and is a powerful tool for investigating physical phenomena at the microscopic level (Heermann, 1990). The appearance of supercomputers stimulates the application of MD methods to fluids engineering fields, such as to internal structures of shock waves in liquids (Holian et al., 1980; Holian, 1988; Tsai and Trevino, 1981; Satoh, 1993a), flow around a sphere (Satoh, 1993b), flow around a cylinder (Rapaport, 1987; Satoh, 1993c), Bénard cell problems (Mareschal et al., 1988), and flow in a two-dimensional duct (Mo and Rosenberger, 1991).

Computation time governs the successful application of MD methods to flow problems. These applications need to be extended to larger molecular systems. A reduction in computation time may be attained by adopting an algorithm which can use large time intervals, and by using more efficient techniques for calculating intermolecular forces. Although many computational algorithms have been presented, few studies have attempted to clarify the divergence properties of MD algorithms. Some studies discussed the relationship between energy fluctuations in systems and time intervals for various MD algorithms, while few studies discussed the relationship between divergence times and time intervals. Since divergence properties are not clearly understood in MD algorithms, the values for time intervals which have been empirically used for equilibrium simulations may also be adopted to simulate flow problems. If we simulate normal shock waves with such empirical time intervals, the results of number density profiles will seem reasonable, while pressure may be larger by some orders of magnitude. This is obviously due to too large time intervals, so that we cannot use the empirical time intervals used for thermodynamic equilibrium without sufficient reflection for flow problems.

The purpose of this study is to clarify the relationship between divergence processes and time intervals, and the dependencies of divergence times on time intervals. These results are expected to provide guidance in determining values of time intervals in actual simulations, and also in developing a new algorithm that will not diverge easily.

2 Microcanonical Ensemble Molecular Dynamics

2.1 Lennard-Jones System and Velocity Verlet Algorithm. We assume a model system with number density N and

[1] Department of Mechanical Engineering, Faculty of Engineering, Chiba University, 1-33, Yayoi-cho, Inage-ku, Chiba 263, Japan.

Contributed by the Fluids Engineering Division of THE AMERICAN SOCIETY OF MECHANICAL ENGINEERS. Manuscript received by the Fluids Engineering Division July 11, 1994; revised manuscript received January 20, 1995. Associate Technical Editor: J. A. C. Humphrey.

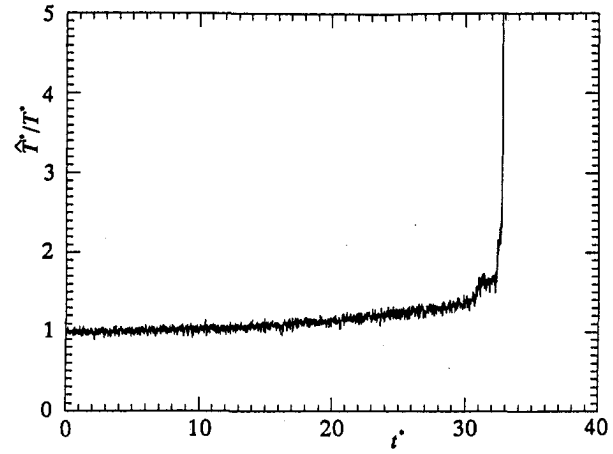

Fig. 1(*a*) Instant temperature

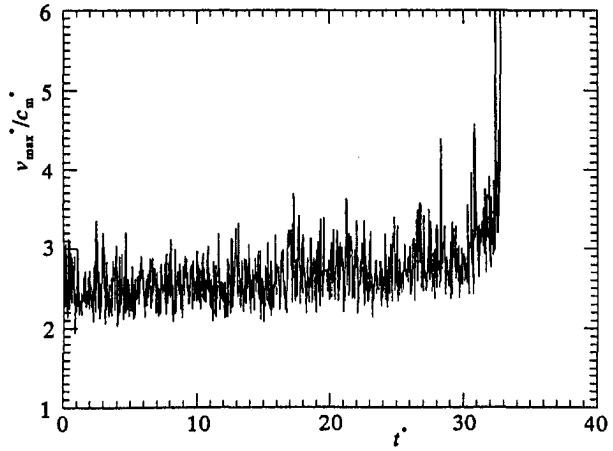

Fig. 1(*b*) Maximum thermal velocity

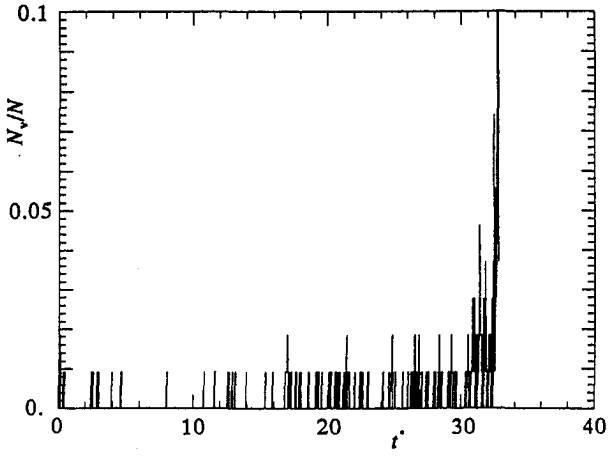

Fig. 1(*c*) Percentage of high speed molecules

Fig. 1 Divergence processes for $n^* = 0.6$, $T^* = 15$, and $h^* = 0.006$

volume V, and take the Lennard-Jones molecule as a molecular model. The potential of this molecule, $u(r)$, is expressed as $u(r) = 4\epsilon\{(\sigma/r)^{12} - (\sigma/r)^6\}$, in which r is the distance between molecules. For Lennard-Jones systems, it is convenient to normalize each quantity by usual representative values (Allen and Tildesley, 1987). For example, lengths are normalized by σ, and energies are normalized by ϵ. From this point on, nondimensional quantities are denoted by the superscript *.

Let us concentrate our attention on the velocity Verlet algorithm (Allen and Tildesley, 1987) which is easy to handle and is relatively accurate. This algorithm advances molecular positions and velocities according to the following equations:

$$\mathbf{r}_i^{*n+1} = \mathbf{r}_i^{*n} + h^* v_i^{*n} + h^{*2} \mathbf{f}_i^{*n}/2, \tag{1}$$

$$v_i^{*n+1} = v_i^{*n} + (\mathbf{f}_i^{*n+1} + \mathbf{f}_i^{*n}) h^*/2, \tag{2}$$

in which $\mathbf{r}_i^*$ is the molecular position vector expressed as (x_i^*, y_i^*, z_i^*), v_i^* is the molecular velocity vector expressed as $(v_{xi}^*, v_{yi}^*, v_{zi}^*)$, $\mathbf{f}_i^*$ is the force acting on the molecule i from the ambient molecules expressed as $(f_{xi}^*, f_{yi}^*, f_{zi}^*)$, and h^* is the time interval. The time step is denoted by the superscript n for simplicity.

2.2 Transport Coefficients and Thermodynamic Quantities. We also discuss the stability of MD algorithms in terms of the influence of time intervals on transport coefficients and thermodynamic quantities. The following summarizes transport coefficient expressions for evaluation by molecular simulations, the derivations of which are referred to in McQuarrie's textbook (1976).

Viscosity:

$$\eta^* = C_\eta \times \int_0^\infty \frac{\langle J_{xy}^*(t^*) J_{xy}^*(0) + J_{xz}^*(t^*) J_{xz}^*(0) + J_{yz}^*(t^*) J_{yz}^*(0) \rangle}{\langle J_{xy}^*(0) J_{xy}^*(0) + J_{xz}^*(0) J_{xz}^*(0) + J_{yz}^*(0) J_{yz}^*(0) \rangle} dt^*, \tag{3}$$

in which

$$C_\eta = \frac{\langle J_{xy}^*(0) J_{xy}^*(0) + J_{xz}^*(0) J_{xz}^*(0) + J_{yz}^*(0) J_{yz}^*(0) \rangle}{3V^*T^*}, \tag{4}$$

$$J_{xy}^*(t^*) = \sum_{j=1}^{N} v_{xj}^* v_{yj}^* + \sum_{j}^{N} \sum_{k>j}^{N} y_{jk}^* f_{xjk}^*. \tag{5}$$

Diffusion coefficient:

$$D^* = C_D \int_0^\infty \frac{\langle v_i^*(t^*) \cdot v_i^*(0) \rangle}{\langle v_i^*(0) \cdot v_i^*(0) \rangle} dt^*, \tag{6}$$

in which

$$C_D = \frac{\langle v_i^*(0) \cdot v_i^*(0) \rangle}{3}. \tag{7}$$

The other notations are as follows: $\mathbf{r}_{jk}^* = (x_{jk}^*, y_{jk}^*, z_{jk}^*) = \mathbf{r}_j^* - \mathbf{r}_k^* = (x_j^* - x_k^*, y_j^* - y_k^*, z_j^* - z_k^*)$, $\mathbf{f}_{jk}^*$ is the force of molecule k acting on molecule j, described as $\mathbf{f}_{jk}^* = (f_{xjk}^*, f_{yjk}^*, f_{zjk}^*)$. t^* is the time and $\langle * \rangle$ represents the ensemble average. Note that the temperature T^* is the time average of instant temperature.

Besides, pressure, internal energy per unit mass, and constant-volume specific heat are written as

$$p^* = n^*T^* + \frac{n^*}{N} \langle W^* \rangle, \tag{8}$$

$$e^* = \frac{3}{2} T^* + \frac{1}{N} \langle \Phi^* \rangle, \tag{9}$$

$$c_v^* = \frac{3}{2} + \frac{1}{T^{*2}N} \langle (\delta\Phi^*)^2 \rangle, \tag{10}$$

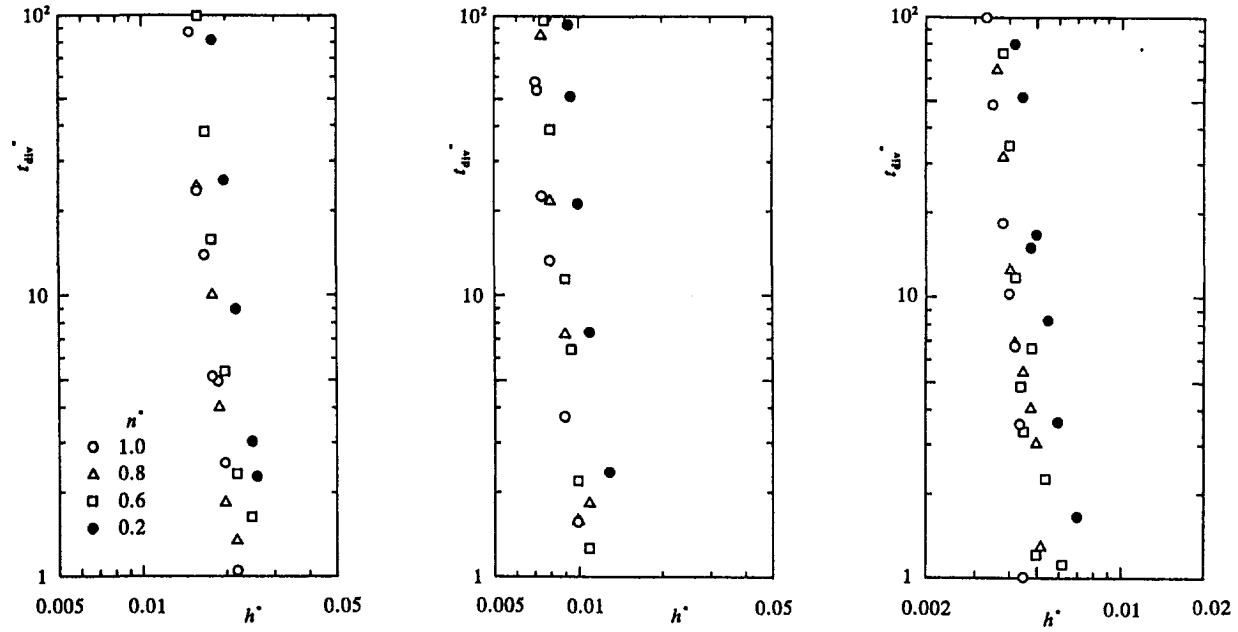

Fig. 2(a) $T^* = 2$ Fig. 2(b) $T^* = 8$ Fig. 2(c) $T^* = 30$

Fig. 2 Relations between divergence times and time intervals

in which

$$\left.\begin{aligned} u^*(r^*) &= 4(1/r^{*12} - 1/r^{*6}), \\ w^*(r^*) &= 24(-2/r^{*12} + 1/r^{*6}), \\ W^* &= -\frac{1}{3}\sum_i^N \sum_{j>i}^N w^*(r_{ij}^*), \\ \Phi^* &= \sum_i^N \sum_{j>i}^N u^*(r_{ij}^*), \\ \langle(\delta\Phi^*)^2\rangle &= \langle\Phi^{*2}\rangle - \langle\Phi^*\rangle^2. \end{aligned}\right\} \quad (11)$$

n^* is the molecular number density and ρ^* is the density. The derivations for these expressions are referred to in Allen and Tildesley's textbook (1987).

3 Parameters for Simulations

The simulation region is assumed to be a cube, and equilibration procedures are carried out at up to 5,000 time steps using a sufficiently small time interval of $h^* = 0.0001$. Desired temperatures can be obtained by scaling the molecular velocities every 500 time steps. Note that the temperature T^* appearing in the following represents the prescribed temperatures, not the average temperatures obtained using the data after the equilibration procedures are completed. The number of molecules, N, is 108, unless otherwise specified, and the cutoff radius r_c^* is 2.5.

4 Results and Discussion

4.1 Divergence Processes and Divergence Times. Figure 1 shows a representative case where the system diverges. The results are obtained for $n^* = 0.6$, $T^* = 15$, and $h^* = 0.006$. Figure 1(a), (b), and (c) indicate the time changes for the instant temperature $\hat{T}^*$, the maximum molecular velocity v_{max}^*, and the number of molecules N_v with a larger velocity than $3c_m^*$, in which c_m^* is the most probable thermal molecular velocity described as $c_m^* = (2T^*)^{1/2}$. Figure 1(a) shows that the instant temperature gradually increases with time from the prescribed temperature at $t^* = 0$ and then diverges exponentially at a certain time. We can see similar properties of divergent processes in Fig. 1(b) and (c), and can derive the following divergent image of the system from these results. The velocities of molecules in the system gradually increase with time as a whole, which leads to an increase in the percentage of molecules with large velocities. This increase causes the velocities of entire molecule groups to become larger, which leads to a further increase in the percentage of molecules with larger velocities. From these additive effects, the system becomes unstable and finally diverges exponentially at a certain time. This

Table 1 Influences of time intervals on thermodynamic quantities and transport coefficients for $n^* = 0.6$ and $T^* = 4$

	h^*	p^*	e^*	c_v^*	C_η	η^*	C_D	D^*
$T^* = 4$	0.004	$5.452^{-0.004}_{+0.005}$	$3.119^{-0.001}_{+0.002}$	$1.782^{-0.001}_{+0.001}$				
	0.005	$5.453^{-0.01}_{+0.001}$	$3.121^{-0.002}_{+0.001}$	$1.775^{-0.004}_{+0.001}$	20.34	$0.996^{-0.03}_{+0.003}$	4.12	$0.523^{-0.012}_{+0.004}$
	0.006	$5.460^{-0.001}_{+0.004}$	$3.125^{-0.001}_{+0.001}$	$1.780^{-0.001}_{+0.002}$	20.33	$0.988^{-0.003}_{+0.049}$	4.17	$0.512^{-0.008}_{+0.002}$
	0.007	$5.469^{-0.001}_{+0.008}$	$3.130^{-0.001}_{+0.004}$	$1.780^{-0.001}_{+0.002}$	20.44	$0.986^{-0.009}_{+0.007}$	4.03	$0.477^{-0.011}_{+0.01}$
	0.008	$5.517^{-0.001}_{+0.009}$	$3.171^{-0.001}_{+0.003}$	$1.786^{-0.001}_{+0.004}$	20.86	$1.019^{-0.003}_{+0.019}$	4.06	$0.529^{-0.022}_{+0.02}$
	0.0087	$5.511^{-0.001}_{+0.003}$	$3.173^{-0.001}_{+0.001}$	$1.780^{-0.001}_{+0.002}$	20.32	$0.969^{-0.012}_{+0.001}$	3.98	$0.467^{-0.007}_{+0.001}$
	0.009	$5.79^{-0.01}_{+0.12}$	$3.47^{-0.01}_{+0.04}$	$1.801^{-0.001}_{+0.004}$	21.13	$1.047^{-0.001}_{+0.028}$	4.25	$0.514^{-0.018}_{+0.008}$
	0.0092	div.						

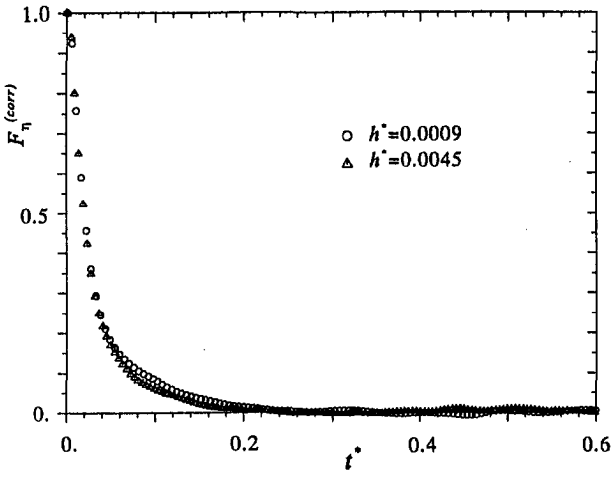

Fig. 3(*a*) Viscosity

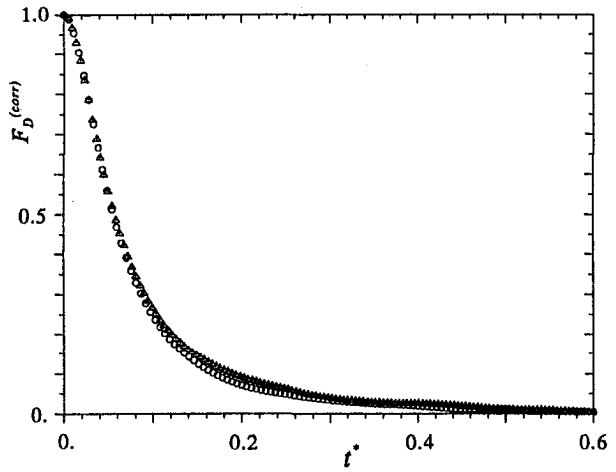

Fig. 3(*b*) Diffusion coefficient

Fig. 3 Correlation functions for $n^* = 0.6$ and $T^* = 15$

divergence is also valid for other number densities, temperatures, and time intervals.

Figure 2 shows the relationship between divergence times t^*_{div} and time intervals h^* for $T^* = 2$, 8, and 30. Each figure shows the results for $n^* = 0.2$, 0.6, 0.8, and 1.0. The relationship between the divergence times and the time intervals can be expressed as linear functions if the results are plotted on logarithmic scales. We see from these relationships that the larger the time interval is, the shorter the divergence time is, so that significantly small time intervals have to be used when the phenomena of interest requires long simulation times. When we simulate a flow which is expected to have high temperature regions (for example, shock waves), we have to use time intervals small enough for a system not to diverge at an expected maximum temperature. Divergence times at first observation are not strongly dependent on the number density. The system diverges more easily, however, as the number density increases.

4.2 Transport Coefficients and Thermodynamic Quantities. Table 1 shows the dependency of time intervals on thermodynamic quantities and transport coefficients for $n^* = 0.6$ and $T^* = 4$. The accuracy of the data is also indicated in the table. Errors in thermodynamic quantities arise from differences in sampling numbers. Accuracy is evaluated from the discrepancy of the mean values obtained by using the data from $t^* =$ 300 to 500 time steps. Uncertainty in transport coefficients occurs from using actual maximum values instead of infinity in integrating each correlation function. The pressure and internal energy values show the influence of time intervals that are too large and not specific heat. Concretely, the pressure and internal energy values agree well at time intervals below $h^* = 0.007$, almost within statistical errors, while the data for these values at time intervals above $h^* = 0.008$ show considerable discrepancy. This shows that the time intervals over 0.008 are too large. Similar observations can be made for other temperature values, although this is not shown in the figures provided. It is not surprising that the critical values for time intervals do not differ much from the maximum values, since divergences in the system arise suddenly, as shown in Fig. 1. The transport coefficients themselves do not show clearly the influences of time intervals that are too large. This is because transport coefficients cannot be used to obtain higher accuracy levels than thermodynamic quantities, which is made clear by comparing the expressions of these quantities, such as Eqs. (3) and (8).

Finally, the correlation functions are shown in Fig. 3 for reference. A comparison of the data for $h^* = 0.0009$ and 0.0045 is made for $n^* = 0.6$ and $T^* = 15$. $F_\eta^{(\text{corr})}$ and $F_D^{(\text{corr})}$ are the correlation functions and the integrants in Eqs. (3) and (6), respectively. The differences in the correlation functions are not so significant, in spite of the fact that the value of $h^* = 0.0009$ is sufficiently small and the value of $h^* = 0.0045$ is high enough to be near the critical value. The differences do not significantly influence the values for the transport coefficients.

5 Conclusions

This study discussed divergence processes, the relationship between time intervals and divergence times, and the influence of time intervals on thermodynamic quantities and transport coefficients. It was found that divergence in a system is not caused by a particular molecule which has suddenly gained an extremely large velocity, but rather by whole groups of molecules which gradually gain greater velocity, causing a system to diverge suddenly. The time interval-divergence time relationship can be expressed in approximate terms as linear functions if the data are plotted on logarithmic scales, and the system diverges more easily as temperature or number density increases.

References

Allen, M. P., and Tildesley, D. J., 1987, *Computer Simulation of Liquids,* Clarendon Press, Oxford.

Ciccotti, G., and Hoover, W. G. (eds.), 1986, *Molecular-Dynamics Simulation of Statistical-Mechanical Systems,* North-Holland Physics Publishing, Amsterdam.

Heermann, D. W., 1990, *Computer Simulation Methods in Theoretical Physics,* 2nd Ed., Springer-Verlag, Berlin.

Holian, B. L., Hoover, W. G., Moran, B., and Straub, G. K., 1980, "Shock-Wave Structure via Nonequilibrium Molecular Dynamics and Navier-Stokes Continuum Mechanics," *Physical Review A,* Vol. 22, pp. 2798–2808.

Holian, B. L., 1988, "Modeling Shock-Wave Deformation via Molecular Dynamics," *Physical Review A,* Vol. 37, pp. 2562–2568.

Mareschal, M., Mansour, M. M., Puhl, A., and Kestemont, E., 1988, "Molecular Dynamics versus Hydrodynamics in a Two-Dimensional Rayleigh-Bénard System," *Physical Review Letters,* Vol. 61, pp. 2550–2553.

McQuarrie, D. A., 1976, *Statistical Mechanics,* Harper & Row, New York.

Mo, G., and Rosenberger, F., 1991, "Molecular-Dynamics Simulations of Flow with Binary Diffusion in a Two-Dimensional Channel with atomically Rough Walls," *Physical Review A,* Vol. 44, pp. 4978–4985.

Rapaport, D. C., 1987, "Microscale Hydrodynamics: Discrete-Particle Simulation of Evolving Flow Patterns," *Physical Review A,* Vol. 36, pp. 3288–3299.

Satoh, A., 1993a, "Molecular Dynamics Simulations on Internal Structures of Normal Shock Waves in Lennard-Jones Liquids," ASME JOURNAL OF FLUIDS ENGINEERING Vol. 117, pp. 97–103.

Satoh, A., 1993b, "Molecular Dynamics Simulation of a Subsonic Flow of a Rarefied Gas past a Sphere," *Advanced Powder Technology,* Vol. 4, pp. 59–70.

Satoh, A., 1993c, "A New Outer Boundary Condition for Molecular Dynamics Simulations and Its Application to a Rarefied Gas Flow past a Cylinder (Periodic-Shell Boundary Condition)," *Advanced Powder Technology,* Vol. 5, pp. 105–117.

Tsai, D. H., and Trevino, S. F., 1981, "Thermal Relaxation in a Dense Liquid under Shock Compression," *Physical Review A,* Vol. 24, pp. 2743–2757.

A Simple, Accurate Integral Solution for Accelerating Turbulent Boundary Layers With Transpiration

James Sucec[1]

The inner law for transpired turbulent boundary layers is used as the velocity profile in the integral form of the x momentum equation. The resulting ordinary differential equation is solved numerically for the skin friction coefficient, as well as boundary layer thicknesses, as a function of position along the surface. Predicted skin friction coefficients are compared to experimental data and exhibit reasonably good agreement with the data for a variety of different cases. These include blowing and suction, with constant blowing fractions F for both mild and severe acceleration. Results are also presented for more complicated cases where F varies with x along the surface.

Introduction

At the second Stanford Conference, Kline et al. (1981) provided a reaffirmation of the value of integral methods in predicting the distribution of the parameters of interest, in turbulent boundary layer flow along a surface, such as skin friction. In an article in Vol. II of the conference proceedings, simplicity, speed, and accuracy are the reasons advanced by Cousteix for integral methods being a viable predictive tool along side of finite difference solutions to the conservation equations.

Some of the more recent articles using integral methods on turbulent flow problems are those of Das and White (1986) and Das (1988) for skin friction, Sucec and Lu (1990) for heat transfer, all with no transpiration, while the contribution of Thomas and Kadry (1990) includes the effect of transpiration. These last two papers contain some favorable comparisons of integral methods with both data and finite difference method results.

Torii et al. (1966) postulate a model for the shear stress distribution across the boundary layer in terms of the distribution for the case of zero transpiration and zero pressure gradient. This is used in an integral x momentum equation to solve by successive approximations for a velocity profile. Then with the aid of an approximation relating the length Reynolds number to the momentum thickness Reynolds number, the x momentum equation for the boundary layer is solved for skin friction. Thomas and Kadry (1990) also began with a shear stress distribution. Use of mixing length expressions relate this shear stress profile to the velocity gradient. Numerical integration of the result yields the velocity distribution. This numerical velocity information is used to numerically integrate two integrals. Finally, finite difference methods are used to solve the x momentum equation for the functions that lead to the skin friction coefficient. Results are compared to experimental data for zero pressure gradient and for an adverse pressure gradient. There is some rather involved numerical work in the method.

In the present work, use will be made of the inner law velocity distribution for transpired flows. The analytical nature of the inner law allows all needed integrals in the x momentum equation to be performed in an exact analytic fashion. The ordinary differential equation, which is left, is easily solved by a Runge-Kutta numerical method to obtain the skin friction coefficient distribution.

Analysis

We consider steady, constant property, turbulent, two-dimensional boundary layer flow over a porous plane surface. Let x and y be coordinates along and normal to the surface, u and u_s be the x component and free-stream velocity, the density is ρ, wall shear stress is τ_w, kinematic viscosity is ν and the boundary-layer thickness is δ. After changing to inner variables, $u^+ = u/u^*$, $y^+ = u^*y/\nu$ and $\delta^+ = u^*\delta/\nu$, with $u^* = \sqrt{\tau_w/\rho}$, the integral form of the x momentum equation can be written as follows:

$$u_s \frac{d}{dx}\int_0^{\delta^+} u^+ dy^+ - \frac{d}{dx}\int_0^{\delta^+} u^* u^{+2} dy^+ + \frac{u_s}{u^*}\frac{du_s}{dx}\delta^+ = \frac{u^{*2} + u_s^2 F}{\nu} \quad (1)$$

The blowing fraction F, in Eq. (1), is defined by $F = v_w/u_s$ where v_w is the surface velocity. Next the needed velocity profile $u^+(x, y^+)$ is taken to be the inner law, or law of the wall, for a transpired flow as given both by experiment and by derivation in Stevenson (1963).

$$u^+ = \frac{v_w^+}{4K^2}\ln^2 y^+ + \frac{1}{K}\left[1 + C\frac{v_w^+}{2}\right]\ln y^+ + C\left[1 + C\frac{v_w^+}{4}\right] \quad (2)$$

K is the von Karman constant and C can, in general, depend upon F or $v_w^+ = v_w/u^*$ and therefore on x.

In general, there is also a wake contribution added to the right-hand side of the velocity profile in Eq. (2), (Coles 1971). However, in the present work, we consider flows with small or negligible wake contributions such as accelerated flows where, if the acceleration parameter $\bar{K}_a = (\nu/u_s^2)du_s/dx$ is large enough, the wake is weak and may even vanish (Mellor and Gibson, 1966; White, 1991). Also, since suction and deceleration push the wake in opposite directions relative to the logarithmic inner region (Julien et al., 1971), there are possibilities for an accurate analysis here using the inner law alone. In other situations where there may be an appreciable wake component, the use of Eq. (2) represents an additional approximation.

Inserting the velocity profile expression, Eq. (2), into the integrals that appear in Eq. (1) and performing the integration gives the following expressions.

$$\int_0^{\delta^+} u^+ dy^+ = \delta^+\left[\Delta - \frac{1}{K} + v_w^+ B_0\right] \quad (3)$$

$$\int_0^{\delta^+} u^{+2} dy^+ = \delta^+[B_0 + B_1 v_w^+ + B_2 v_w^{+2}] \quad (4)$$

The following definitions were used in the equations above.

$$\Delta = \frac{1}{K}\ln\delta^+ + C, \quad B_0 = \Delta^2 - \frac{2\Delta}{K} + \frac{2}{K^2},$$

$$B_1 = \frac{1}{2}\left[\Delta^3 - \frac{3B_o}{K}\right], \quad B_2 = \frac{1}{16}\left[\Delta^4 - \frac{8B_1}{K}\right] \quad (5)$$

[1] Mechanical Engineering Department, University of Maine, Orono, ME 04469-5711.

Contributed by the Fluids Engineering Division of THE AMERICAN SOCIETY OF MECHANICAL ENGINEERS. Manuscript received by the Fluids Engineering Division September 16, 1994; revised manuscript received January 20, 1995. Associate Technical Editor: D. P. Telionis.

Next, v_w^+ is expressed in terms of the blowing fraction F and the skin friction coefficient $C_f = 2\tau_w/\rho u_s^2$.

$$v_w^+ = \frac{F}{\sqrt{C_f/2}} \tag{6}$$

This skin friction is related to the other variables of the problem by evaluating the velocity profile, Eq. (2), at the value of $y^+ = \delta^+$. Using Eq. (6), C_f is given as follows, from Eq. (2), with Δ from Eq. (5).

$$\frac{1}{\sqrt{C_f/2}} = \frac{\Delta}{1 - \dfrac{F\Delta^2}{4}} \tag{7}$$

Inserting the integrals, Eqs. (3) and (4), into Eq. (1), making use of the expressions for v_w^+ and C_f given by Eqs. (6) and (7), and performing the indicated differentiation, Eq. (1) takes the form after defining $P = \sqrt{2/C_f}$.

$$A_1 \frac{d\delta^+}{dx} + A_2\delta^+ \frac{dC}{dx} + A_3\delta^+ \frac{dF}{dx} = \frac{u_s}{\nu}[1 + FP^2 + \bar{K}_a P\delta^+(B - P^2)] \tag{8}$$

The coefficients A_1, A_2, A_3, and the quantity B are given in the Appendix as functions of δ^+ and other variables. u_s and F, the freestream velocity variation and the blowing fraction are given as functions of x in a particular problem. The only remaining question is the possible dependence of C on F or v_w^+.

Specification of the Factor C. For $F < 0$, suction, Bradshaw (1967) recommends a relation that can be written as follows.

$$C = 5 + 1375\, v_w^{+2} \tag{9}$$

More recently, Silva-Freire (1988) determined C by analysis of blowing data endorsed by the second Stanford Conference (Kline et al., 1981), and developed the following relation for $F > 0$.

$$C = 5 - 512F \tag{10}$$

Since the bulk of the data used to determine equation (10) was deemed the most reliable by the evaluation in Kline et al. (1981), it was decided to use Eq. (10) as part of the velocity profile model given by Eq. (2).

With C now specified, Eq. (8) is a nonlinear ordinary differential equation which was solved for $\delta^+(x)$ using a standard fourth order Runge-Kutta method (Ralston and Rabinowitz, 1978). Successively smaller values of lattice spacing $\Delta x/L$ were used until the solution was effectively independent of this spacing. A representative example was the case of $F = -0.00116$ of Simpson et al. (1969) where the lattice spacing was halved until the difference in $C_f/2$ in two successive spacings was less than 0.01 percent, leading to the use of $\Delta x/L = 0.025$. It was preferred to start the calculations using the measured $C_f/2$ at the first data point. However, sometimes the first measured $C_f/2$ seemed clearly out of line with the remaining data points. In these cases, the calculation was started using the first measured value of R_θ. This can be justified because, in the references used, R_θ can be measured with less uncertainty than the quantity $C_f/2$, typically $\pm 1 \rightarrow 3$ percent for R_θ and $\pm 4 \rightarrow 10$ percent for $C_f/2$.

To solve Eq. (8), the initial value of δ^+ at the first calculation point is needed. If, as in most cases, the value of $C_f/2$ is known there, one can use this in Eq. (7) to solve the quadratic equation for the positive root, Δ, and use this to solve for the initial δ^+ from Eq. (5). If, however, the experimental value of R_θ is to be matched at the initial x location, the equations to be solved are implicit in δ^+. So a low value of δ^+, say 50, is used as a trial value. The first of Eqs. (5) gives Δ and Eq. (7) gives C_f. With these, Re_θ is evaluated using Eqs. (3) and (4). This procedure is continued with successively higher values of δ^+ until a δ^+ is reached which gives the calculated Re_θ equal to the measured value.

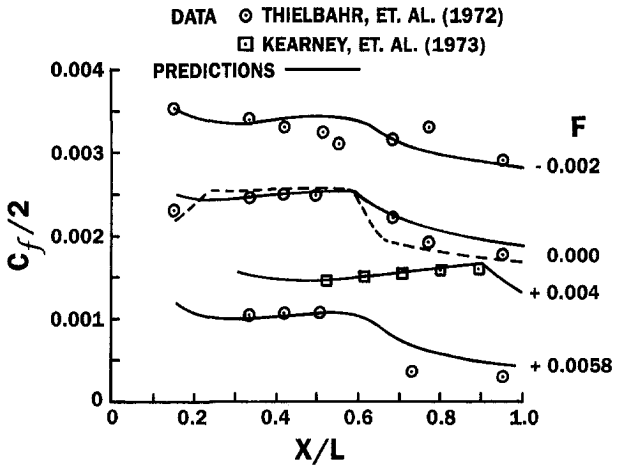

Fig. 1 Predicted skin friction coefficients compared to data of Kearney et al. (1973), L = 1.067 m (3.5 ft), and data of Thielbahr et al., 1972, L = 2.286 m (7.5 ft). Dashed line includes the wake.

Results and Discussion

Consider the case, in Fig. 1, of $F = +0.004$ with data from Kearney et al. (1973). This is a case of strong acceleration, $\bar{K}_a$ nominally about 2.5×10^{-6}, where $u_s(x)$ continually increases until the last data point when it is held constant and causes $\bar{K}_a$ to drop to zero. This condition should lead to very small wake strength values and, therefore, to a velocity profile consisting mainly of the inner law alone. As can be seen, the comparison of predictions with data is very good for this case. Data for the other cases in Fig. 1 are from Thielbahr et al. (1972) where $u_s(x)$ results in a moderately strong acceleration over the first two thirds of the surface. For $F = +0.0058$ the predictions are close to the first three data points, but farther away from the last two points. This is due to the change from a large acceleration factor $\bar{K}_a = 1.45 \times 10^{-6}$ to $\bar{K}_a = 0$ for $x/L > 0.66$. Thus beyond this point, a significant wake component is expected in the actual velocity profile and the predictions are high as would be expected since the calculation procedure does not employ a wake.

The $F = 0.00$ results in Fig. 1 show the predictions using the inner law alone as the solid curve which predicts the experimental data very well in the region, $x/L < 0.59$, where $\bar{K}_a$ is large, 1.47×10^{-6}, where only a very weak wake portion of the velocity profile is expected. Beyond this value of x/L, $\bar{K}_a = 0$, and hence a wake is present as indicated by the overprediction of the last two data points. However, it is seen that the third to last data point is predicted reasonably well in spite of the fact that $\bar{K}_a = 0$ there. The explanation for this lies in the "lag" of the actual relaxing boundary layer, the fact that the full effect of the sudden change in $\bar{K}_a$ at $x/L = 0.59$ does not take place in zero distance, but requires some finite length for the actual velocity profile to make the change from practically an equilibrium profile appropriate to $\bar{K}_a = 1.47 \times 10^{-6}$ to an equilibrium profile characteristic to $\bar{K}_a = 0$. So that third to last data point is still in a region of adjustment and the velocity profile there still contains a lot of past history at $\bar{K}_a = 1.47 \times 10^{-6}$ and hence is still essentially a pure inner law profile. For this case, $F = 0.00$, we also show a solution, with a dashed line, when the combined law of the wall and wake is used to

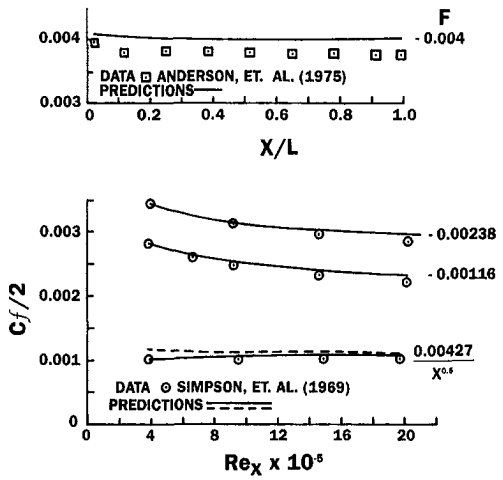

Fig. 2 Predicted skin friction coefficients versus $Re_x = u_s x/\nu$ compared to data of Simpson et al. (1969) and data of Andersen et al. (1975), L = 2.286 m (7.5 ft). Dashed line starts at the initial value of R_θ

solve for $C_f/2$. It is seen that in the region $x/L < 0.59$, the dashed curve and solid curves agree well indicating the relative lack of a wake there and also the existence of a wake component beyond $x/L = 0.59$ as witnessed by the good agreement with data at the last two points for the dashed result which employs the wake. The final curve in Fig. 1 is a case of suction, $F = -0.002$. The agreement seems reasonable, except for the two extreme data points where the error is about 10 percent.

The lower half of Fig. 2 contains cases for which the data are from Simpson et al. (1969). These are cases with zero pressure gradient, $\bar{K}_a = 0$ and include a case, the lowest curve, where the blowing fraction, F, varies inversely as the square root of x. The agreement is surprisingly good when one considers that these flows have a wake. The predictions are higher than the data and this presumably is due to the lack of a wake in the predictive procedure. To illustrate the effect of different starting conditions, the case where $F \sim x^{-0.5}$ shows predictions which start with the measured $C_f/2$, the solid curve, and ones that start with the measured R_θ, the dashed curve. It is seen that there is not too much difference in the predictions with the different starting conditions. The top half of Fig. 2 contains data by Andersen et al. (1975) for $F = -0.004$ and a deceleration, $\bar{K}_a < 0$, with $u_s(x) \sim (ax + b)^{-0.15}$. This deceleration, in the absence of suction could give rise to an appreciable wake component of the velocity profile, thus raising the u^+ versus y^+

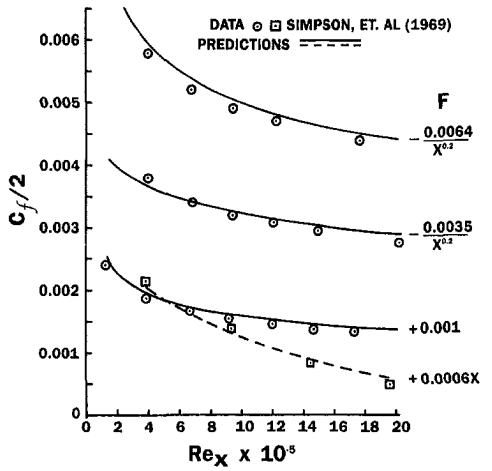

Fig. 3 Predicted skin friction coefficients versus $Re_x = u_s x/\nu$ compared to data of Simpson et al. (1969)

Table 1 Comparison of predicted and experimental R_θ values. Data from Simpson et al. (1969).

$F = 0.0006X$			$F = -0.00116$			$F = -0.00335/X^{0.2}$		
10^{-5} Re_x	Pred. R_θ	Data	10^{-5} Re_x	Pred. R_θ	Data	10^{-5} Re_x	Pred. R_θ	Data
3.9	1235	1235	4.0	952	895	1.4	307	307
9.4	2988	2947	6.7	1371	1238	4.1	444	389
14.5	4969	4840	9.3	1745	1595	6.8	623	530
19.6	7368	7172	14.7	2432	2325	9.5	806	655
			20.3	3093	2940	12.2	991	841
						15.0	1184	1001
						20.3	1552	1438

curve above the logarithmic right side of Eq. (2). However, the effect of suction alone is to depress the velocity profile in the opposite direction, the downward direction (Julien et al., 1971). Looking at the predictions, it is found that they are about 3.5 percent higher at small x/L and 7 percent higher at the last data point. A number of the finite difference methods used at the second Stanford Conference (Kline et al., 1981), for this case, did no better with their predictions than the solid curve of the present integral approach.

In Fig. 3, where all the experimental data comes from Simpson et al. (1969), and is for $\bar{K}_a = 0.0$, the two lowest curves are the predictions for a small, constant blowing fraction and for a blowing fraction which increases linearly with x. For the case of moderately strong, variable suction, $F = -0.0035/x^{0.2}$, the predictions seem reasonable as is also true for the last case shown in Fig. 3, $F = -0.0064/x^{0.2}$.

Some representative results of the predictions of momentum thickness, θ, in the Reynolds number $R_\theta = u_s\theta/\nu$ are given in Table 1. It is seen that agreement is good for the first two cases and perhaps acceptable for the last case where the predicted R_θ average about 14 percent higher than the data.

Concluding Remarks

The inner law, or law of the wall, for a turbulent transpired boundary layer is used as the velocity profile in the integral x momentum equation. The fact that the velocity profile, in inner coordinates, y^+, u^+, is also a law for the wall shear stress, when evaluated at the edge of the boundary layer, provides closure and gives a single nonlinear ordinary differential equation to be solved. Comparison to experimental data in accelerated boundary layers, and in other circumstances where a small wake component of velocity is expected, yields good agreement for a range of positive and negative blowing fractions F including some cases where F varies with x. With the information provided in the work, one can easily write a simple computer program to make the calculations.

References

Andersen, P. S., Kays, W. M., and Moffat, R. J., 1975, "Experimental Results for the Transpired Turbulent Boundary Layer in an Adverse Pressure Gradient," *Journal of Fluid Mechanics,* Vol. 69, pp. 353–375.

Bradshaw, P., 1967, "Mixing Length Velocity Profile in Boundary Layers with Transpiration," *AIAA Journal,* Vol. 5, No. 9, pp. 1674–75.

Coles, D., 1971, "A Survey of Data for Turbulent Boundary Layers with Mass Transfer," *Rand Corporation Report,* No. P-4697, pp. 25-1 to 25-15.

Das, D. K., and White, F. M., 1986, "Integral Skin Friction Prediction for Turbulent Separated Flows," ASME JOURNAL OF FLUIDS ENGINEERING, Vol. 108, pp. 476–482.

Das, D. K., 1988, "A Simple Theory for Calculating Turbulent Boundary Layers Under Arbitrary Pressure Gradients," *International Journal of Engineering Fluid Mechanics,* Vol. 1, pp. 83–99.

Julien, H. L., Kays, W. M., and Moffat, R. J., 1971, "Experimental Hydrodynamics of the Accelerated Turbulent Boundary Layer With and Without Mass Injection," ASME JOURNAL OF HEAT TRANSFER, Vol. 93, pp. 373–379.

Kearney, D. W., Kays, W. M., and Moffat, R. J., 1973, "Heat Transfer to a Strongly Accelerated Turbulent Boundary Layer: Some Experimental Results,

Including Transpiration," *International Journal of Heat Mass Transfer,* Vol. 16, pp. 1289–1305.

Kline, S. J., Cantwell, B. J., and Lilley, G. M., eds., 1981, "*The 1980–81 AFOSR-HTMM Stanford Conference on Complex Turbulent Flows,*" Stanford University, Stanford, CA, Vol. II, pp. 650–67; Vol. I, pp. 112–116; Vol. III, p. 1158.

Mellor, G. L., and Gibson, D. M., 1966, "Equilibrium Turbulent Boundary Layers," *Journal of Fluid Mechanics,* Vol. 24, Part 2, pp. 225–253.

Ralston, A., and Rabinowitz, P., 1978, *A First Course in Numerical Analysis,* Second Edition, McGraw-Hill, New York, pp. 217–222.

Silva-Freire, A. P., 1988, "An Asymptotic Solution for Transpired Incompressible Turbulent Boundary Layers," *International Journal of Heat Mass Transfer,* Vol. 31, pp. 1011–1021.

Simpson, R. L., Moffat, R. J., and Kays, W. M., 1969, "The Turbulent Boundary Layer on a Porous Plate: Experimental Skin Friction with Variable Injection and Suction," *International Journal of Heat Mass Transfer,* Vol. 12, pp. 771–89.

Stevenson, T. N., 1963, "A Law of the Wall for Turbulent Boundary Layers with Suction or Injection," Report Aero No. 166, College of Aeronautics, Cranfield, 18 pages, also available from NTIS as N64-19323.

Sucec, J., and Lu, Y., 1990, "Heat Transfer Across Turbulent Boundary Layers with Pressure Gradient," ASME JOURNAL OF HEAT TRANSFER, Vol. 112, pp. 906–912.

Thielbahr, W. H., Kays, W. M., and Moffat, R. J., 1972, "The Turbulent Boundary Layer on a Porous Plate: Experimental Heat Transfer with Uniform Blowing and Suction, with Moderately Strong Acceleration," ASME JOURNAL OF HEAT TRANSFER, Vol. 94, pp. 111–118.

Thomas, L. C., and Kadry, H. M., 1990, "A One Parameter Integral Method for Turbulent Transpired Boundary Layer Flow," ASME JOURNAL OF FLUIDS ENGINEERING, Vol. 112, pp. 423–436.

Torii, K., Nishiwaki, N., and Hirata, M., 1966, "Heat Transfer and Skin Friction in Turbulent Boundary Layer with Mass Injection," *Proceedings of the Third International Heat Transfer Conference,* Chicago, Vol. 3, pp. 34–48.

White, F. M., 1991, *Viscous Fluid Flow,* Second Edition, McGraw-Hill, New York, pp. 451–452, 459–464.

APPENDIX

Coefficient Expressions for Eq. (8)

$$A_1 = \frac{1}{K}\left[E_0 + \frac{E_1 F}{D_s}\left(1 + \frac{F\Delta P}{2}\right)\right] \tag{A1}$$

$$A_2 = KA_1 + KPB - B_4P^2 \tag{A2}$$

$$A_3 = E_1P/D_s \tag{A3}$$

$$B = B_0 + v_w^+B_1 + v_w^{+2}B_2 \tag{A4}$$

$$B_4 = K\Delta - 1 + \frac{v_w^+KB_0}{4} \tag{A5}$$

$$D_s = 1 - \frac{\Delta^2 F}{4} \tag{A6}$$

$$E_1 = \frac{B_0P^2}{4} + \frac{B\Delta^2}{4} - P(B_1 + 2B_2v_w^+) \tag{A7}$$

$$E_0 = G + H \tag{A8}$$

$$G = K(P^3 - BP) + B\left(1 + \frac{v_w^+\Delta}{2}\right) \tag{A9}$$

$$H = -P\left[\frac{dB_0}{d\Delta} + v_w^+\frac{dB_1}{d\Delta} + v_w^{+2}\frac{dB_2}{d\Delta}\right] \tag{A10}$$